HANDBOOK OF Reflector Antennas and Feed Systems

VOLUME III

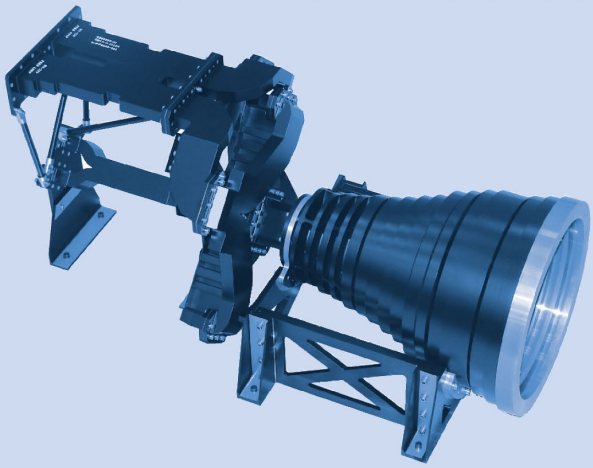

Applications of Reflectors

Sudhakar Rao
Lotfollah Shafai
Satish K. Sharma
editors

Handbook of Reflector Antennas and Feed Systems

Volume III

Applications of Reflectors

For a listing of recent titles in the
Artech House Antennas and Propagation Series,
turn to the back of this book.

Handbook of Reflector Antennas and Feed Systems

Volume III

Applications of Reflectors

Sudhakar Rao
Lotfollah Shafai
Satish Sharma

Editors

ARTECH
HOUSE
BOSTON | LONDON
artechhouse.com

-Library of Congress Cataloging-in-Publication Data
A catalog record for this book is available from the U.S. Library of Congress.

British Library Cataloguing in Publication Data
A catalog record for this book is available from the British Library.

ISBN-13: 978-1-60807-519-5

Cover design by Vicki Kane

Cover photos:
Top picture: An Intelsat satellite that employs multiple reflector antennas to provide shaped beams over a wide area of landmass (courtesy of Intelsat Corporation).

Middle picture: C-band integrated compact feed assembly with dual-polarization, high-power, and low-PIM capability used for uplink and downlink communications links for fixed satellite services (courtesy of Custom Microwave, Inc.).

Bottom picture: Ibaraki No. 3 Earth Station Antenna (29.6m) (courtesy of MELCO, Japan).

10 9 8 7 6 5 4 3 2 1

Contents

CHAPTER 8

CHAPTER 9

Preface

Several books on reflector antennas have been written and the majority of them have given excellent treatment to the theory and analysis of reflector antennas. The intent of this book is to provide practical applications and design information of reflector antennas used for several communications systems. I have been encouraged by my industry colleagues to write such a book documenting the application aspects of reflector antennas for spacecraft and terrestrial communications. With this in mind, I have invited mostly practicing engineers from the antenna industry to write these book chapters. Experts from Northrop Grumman, MELCO, NASA/JPL, Intelsat, Boeing, CMI, AASC, and DUT have largely contributed to this book. Reflector antenna technology has been evolving continuously over the last two decades to cater to new applications. These include large deployable reflectors for mobile satellites, multiple beam reflector antennas for high-capacity satellites, multiband reflector antennas covering multiple frequency bands, terahertz reflectors for radar applications, high-power antenna payloads with low passive intermodulation products, low loss reflector antennas for wide scan applications, reflector antennas for new terrestrial applications, and reflector antennas for remote sensing. This book covers recent developments of reflector antennas used for satellite communications, terrestrial communications, and remote sensing applications. New subjects are introduced for the first time here in a book format dealing with satellite antennas, terahertz antennas, PIM, multipaction, corona, deployable mesh reflector antennas, and mechanical aspects of reflector antennas. A separate topic on integrated feed assembly for reflector antennas covering analysis, design, fabrication, and test has been included in this book.

The organization of this book is as follows. A brief introduction beginning with the history of reflector antennas and its basics is given in Chapter 1. Different types of reflector antennas used for satellite communications, including introduction to payload systems and antenna farm, are addressed in Chapter 2. Contoured beam or shaped beam antennas are described along with analysis results for C-band and Ku-band antennas for fixed satellite services. Gain performance as a function of reflector size is discussed. Dual-reflector Gregorian antenna configuration for shaped beam applications is described. Gridded-reflector antennas with overlapping apertures providing polarization reuse for linear polarization applications are discussed along with design formulae for the grid geometry. The subject of multiple beam antennas is relatively new and is covered in detail in Chapter 2. Design of MBAs, analysis of MBA performance, and several applications of MBAs are discussed.

Advanced feed technologies as well as reflector technologies that improve MBA performance are given with examples. Multiple beam antennas for direct-to-home local channel broadcast and personal communications satellites are addressed.

Chapter 3 provides past and recent developments on reflector antennas for terrestrial communications applications. There are seven sections that cover reflector antennas for different applications. Beam-waveguide fed reflector systems for large earth-station reflector antennas are presented. The shaped Cassegrain antenna fed by a four-reflector beam waveguide feed is described and is a standard for large earth stations all over the world. A trireflector offset antenna for terrestrial microwave relay link systems with very low cross-polar levels is addressed. Reflector antennas used for Japanese communication satellite 2 (CS-2) and an elliptical aperture reflector for satellite news-gathering applications with reduced interference to adjacent satellites are discussed. This latter antenna is an offset Gregorian antenna with elliptical main reflector. Compact dual-reflector elliptical aperture antennas for aeronautical satellite communication systems are presented, including shaping methods. The dual-shaped reflector antenna is realized by using a physical optics shaping technique and achieves excellent electric performance. Reflector antennas used as vessels for mobile communications and terminals for simultaneous communication with broadcast and communication satellites are also discussed.

Use of focusing and nonfocusing reflector systems for terahertz imaging applications is described in Chapter 4. These systems need to steer the beam over the intended field of view with specific spatial resolution. Focal plane arrays that would acquire information from several image pixels simultaneously and reflector antenna systems integrated with mechanical scanners in order to generate the image at terahertz frequencies are addressed here. Relevant analyses for focal-plane and image plane designs are given. Recent developments in the area of multiband reflector antennas and associated feed horns are described in Chapter 5. These antennas are capable of supporting multiple frequency bands that are separated in frequency and covering several octave bandwidths. They have the advantage of using a single antenna instead of several antennas with reduced cost and reduced mass. Advanced reflector technologies—such as stepped-reflector, reflectors with partially reflective surfaces, and shaped reflectors—are presented. Feed advancements in terms of multimode horns with several "slope-discontinuities" and feed assembly developments to isolate the frequency bands are discussed.

Chapter 6 presents reflector antennas used for remote sensing of the Earth and other bodies in the solar system, and relevant sensor technologies to detect and classify objects by means of propagated electromagnetic radiation. Sensors deployed on aircraft or satellites make it possible to collect data on a global scale that would not otherwise be practical to obtain. Remote sensing is used for a wide range of science applications, ranging from global measurement of ocean topography and deforestation to the study of Jupiter's atmosphere. The military employs remote sensing techniques to collect data about opposing forces, weather conditions, and other information relevant to their mission. Chapter 6 also presents technologies related to active and passive remote sensing. For spaceborne remote sensing applications, reflector antennas have historically been the most widely used antenna design. This chapter presents an overview of the various types of reflector antenna designs used for remote sensing applications. Antennas flown on historically significant missions are used to illustrate the practical implementation of each antenna

type. In addition, the chapter presents notable antenna research developments that are regarded as enabling technologies for new types of sensors.

Chapter 7 presents two key sections related to the feed assemblies used for reflector antennas in space and, to a certain extent, in ground applications. It provides the component designs, manufacture, and test results of various types of feed assemblies employed at C-band, Ku-band, and Ka-band. The feed components include horns, orthomode transducers (OMTs), polarizers, filters, diplexers, combiners/dividers, and transitions. Manufacturing approaches that yield precise tolerances required for high-performance feeds are discussed. Advantages of advanced design, analyses, manufacture, and test of integrated feed assembly instead of conventional piece-part design are discussed. The second part of this chapter deals with three important aspects of spacecraft antennas and feeds; namely, passive intermodulation (PIM), multipaction, and corona. These aspects are critical in high-power payloads and multichannel repeaters and significantly impact the feed and reflector design.

Space reflectors having sizes larger than the fairing of the booster need to be "folded up" in some manner for launch, and then "unfurled" on orbit to their full size. These are typically referred to as deployable reflectors, and are the subject of Chapter 8. This chapter is organized into three main sections. The first section deals with reflector classifications either according to the surface geometry or according to the surface type (such as rigid/segmented, semirigid, inflatable/rigidizable, woven-mesh, and knitted-mesh surfaces). The second section deals in more detail with the major constituents/components of the knitted-mesh type reflector, which of all deployable reflectors, is most commonly flown in space. The last section addresses the major design requirements/considerations for a typical deployable reflector subsystem, including electrical, mechanical, thermal, and environmental drivers.

Chapter 9 is intended to provide the reader with a framework and top-level understanding of the elements and requirements that must be considered in the successful design, fabrication, and test of a spaceflight antenna reflector. It is a guide based on over 30 years of professional experience of the authors in engineering, fabricating, and testing spaceflight antenna reflectors and systems. As the state-of-the-art in antenna reflector design continually advances, this chapter is purposely written to provide general recommendations for configuration, design approach materials, and testing. There is a wealth of information available from composite materials suppliers, technical papers, and organizations, such as SAMPE, so it is left to the reader to perform the detailed analyses, engineering, and materials research to establish the best possible specific choices relative to the set of requirements for the particular reflector being considered. A successful antenna reflector design is always a carefully balanced combination of many specific and interdependent choices that must all work together to achieve the best possible results. The mechanical design of the reflector antennas have to satisfy electrical, spacecraft, launch load, vibration, extreme thermal, deployment in space, stowage, low mass, pointing, and structural requirements simultaneously. These are all discussed in Chapter 9.

A professional antenna engineer in the current industrial environment must be skillful in several areas, including theory, analysis methods, design, mechanical consideration, manufacture, test methods, antenna ranges, error analysis, and

related system aspects. More important, he or she should know what types of antennas need to be used for a given application. I have been fortunate to work with excellent mentors Chuck Mok and James Huang at Spar Aerospace Limited, Montreal, Canada (now called MDA). During the 14 years of my early career, I had the opportunity to acquire knowledge about antenna components, reflector antennas for space and ground applications, test range developments, and spacecraft antenna testing. I also had the benefit of leading a group of excellent engineers on IRAD, new business proposals, and space programs. My best learning experience was at Spar and I thank the management for encouraging me with progressively more responsible and challenging jobs during the period 1983–1996. The knowledge and experience I gained at Spar was useful later during my professional career with Hughes/Boeing, Lockheed Martin, and now with Northrop Grumman. I must thank my colleagues Dr. Chih-Chien Hsu, Jim Wang, Minh Tang, Duy Nguyen, Sylvain Richard, Raj Sudarsanam, Joseph Kopal, Dr. Philip Law, Dr. Sebong Chun, Dr. Jon Gulick, and several others with whom I have worked closely and learned much during my association with them. My special thanks to Dr. Kwok-Kee Chan, whom I consider the best antenna consultant in the industry; I had the opportunity to work with him on several difficult antenna projects over the past 30 years. Thanks also are due to Dr. Clency Lee-Yow, President of Custom Microwave Inc., with whom I had worked on advanced feed systems for several flight programs and jointly developed a novel high-power spacecraft thermal vacuum test method using pick-up horns.

I am thankful to my coeditors Prof. Lot Shafai and Prof. Satish Sharma for all the planning, coordination, and motivation during the long and stressful two-year period when the book contents were being finalized. My personal thanks to all the chapter authors who took time in spite of their demanding schedules at work and spending numerous weekends shaping the technical contents of this book. All the authors have shown extreme dedication, professionalism, and cooperation during this project and I am grateful to them for their contributions. I thank Northrop Grumman management of Jon Gulick, Michelle Bailey, and Verne Nagayama for granting me permission to write this book. Special thanks to my best friend Dr. C. S. Rao and his wife Mrs. Chandra for their encouragement. I also want to thank my family friends in Los Angeles for their interest in my work and keeping me relaxed during weekends. Thanks are due to Artech House for guiding me throughout the book development process and special thanks to Samantha Ronan, Lindsay Moore, Jack Stone, Alexis Merry, and Mark Walsh.

Most important, I am grateful to my family for their love and support during this endeavor. Without the help and encouragement of my wife Rajani and daughter Neha, it would not have been possible for me to complete this work.

This book is dedicated to my parents, my wife, and my daughter.

Sudhakar Rao
May 2013

CHAPTER 1

Introduction

Sudhakar Rao, Northrop Grumman Aerospace Systems
Lot Shafai, University of Manitoba

1.1 Introduction

Reflector antennas are widely used for Earth station, satellite, radar, radio astronomy, and deep space communications. The main advantage of reflector antennas is that they provide high gain values using a large passive aperture that reflects the RF signal from the feed without the need for active amplification. It also has the advantages of lower cost, lower mass, lower power, and grating-lobe free radiation when compared to array antennas and lens antennas.

Isaac Newton is the father of modern reflector antennas, having invented the optical reflective telescope in 1672. This type of telescope comprises a concave mirror that reflects light rays to a smaller plane mirror, which in turn focuses into an eyepiece, as illustrated in Figure 1.1. Later developments in reflector antennas occurred during the 17th century through the efforts of Cassegrain and Gregory. Their work resulted in the dual-reflector Cassegrainian and Gregorian reflector configurations that are widely used even today. These two classic reflector configurations are illustrated in Figure 1.2.

During the 1950s and 1960s, reflector antennas found new applications in terrestrial communication systems, radio telescopes, Earth stations, radar antennas, and satellite communications. The use of reflector antennas for satellite communications started in 1960 with the launch of Echo 1, which employed a 30m reflector to test its propagation and transmission techniques. The launch of the Telstar satellite at the C-band (6-GHz uplink and 4-GHz downlink) paved the way to bent-pipe satellites for communication applications. Syncom III, launched in 1964, was a true geostationary satellite. "Early Bird," launched in 1965 by Intelsat, was the first commercial trans-Atlantic satellite with 240 telephone circuits and live TV transmission. In 1965, Russia also launched its first communication satellite in the Molniya orbit.

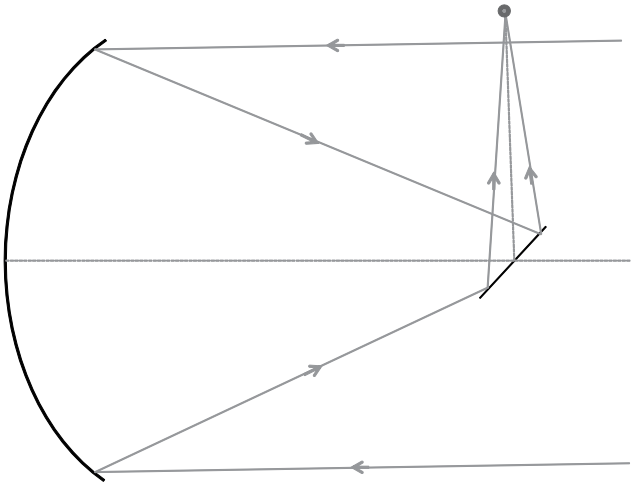

Figure 1.1 Newtonian reflector telescope with planar subreflector.

In the 1970s and 1980s, significant developments occurred in both satellite communication antennas and Earth station antennas. Large Earth stations have been constructed in the United States, Japan, and Europe that employ shaped dual-reflector antennas and fixed-feed beam-waveguide technology with a focus on improving the efficiency of antennas. Gridded reflector technology was developed in Canada and the United States for spacecraft reflector antennas. This technology allowed for reuse of the aperture space for two orthogonally polarized antenna surfaces that are placed one behind the other and fed with two separate feed arrays. This in turn allowed for polarization reuse, which enabled the bandwidth to be increased twofold.

Large-mesh reflector technology was developed in late 1980s and early 1990s by Harris and Astro-Mesh (now Northrop Grumman) for mobile applications. This technology allowed for the use of large reflectors (5 to 12m) that could be folded in a small volume for stowage and deployed in space. More recently, large reflectors of 22m and more have been built and flown by the space industry for both commercial and military applications.

During the late 1980s, another important development occurred in the form of shaped reflector technology [1]. Shaped reflector technology allowed contoured beam shapes to be created by changing the reflector surface shape and using a single-feed instead of large-feed array with a beam-forming network feeding the array. This technology has significant benefits in terms of reducing the overall mass and cost of the payloads. Shaped dual-reflector Gregorian systems have been developed for both linear and circular polarization applications.

Multiple-beam antennas have been developed for mobile and personal communication applications starting in the 1990s. Several satellite systems, such as M-Sat, Anik-E, Globalstar, Inmarsat, ACeS, and Thuraya, have employed multiple beams with frequency reuse schemes to increase the effective bandwidths by factors of 4 to 30. Direct broadcast satellites were developed during the 1990s that resulted in high-power downlink beams providing regional coverage that allowed users to receive signals directly from a satellite using pizza-sized dishes at their homes. Local-

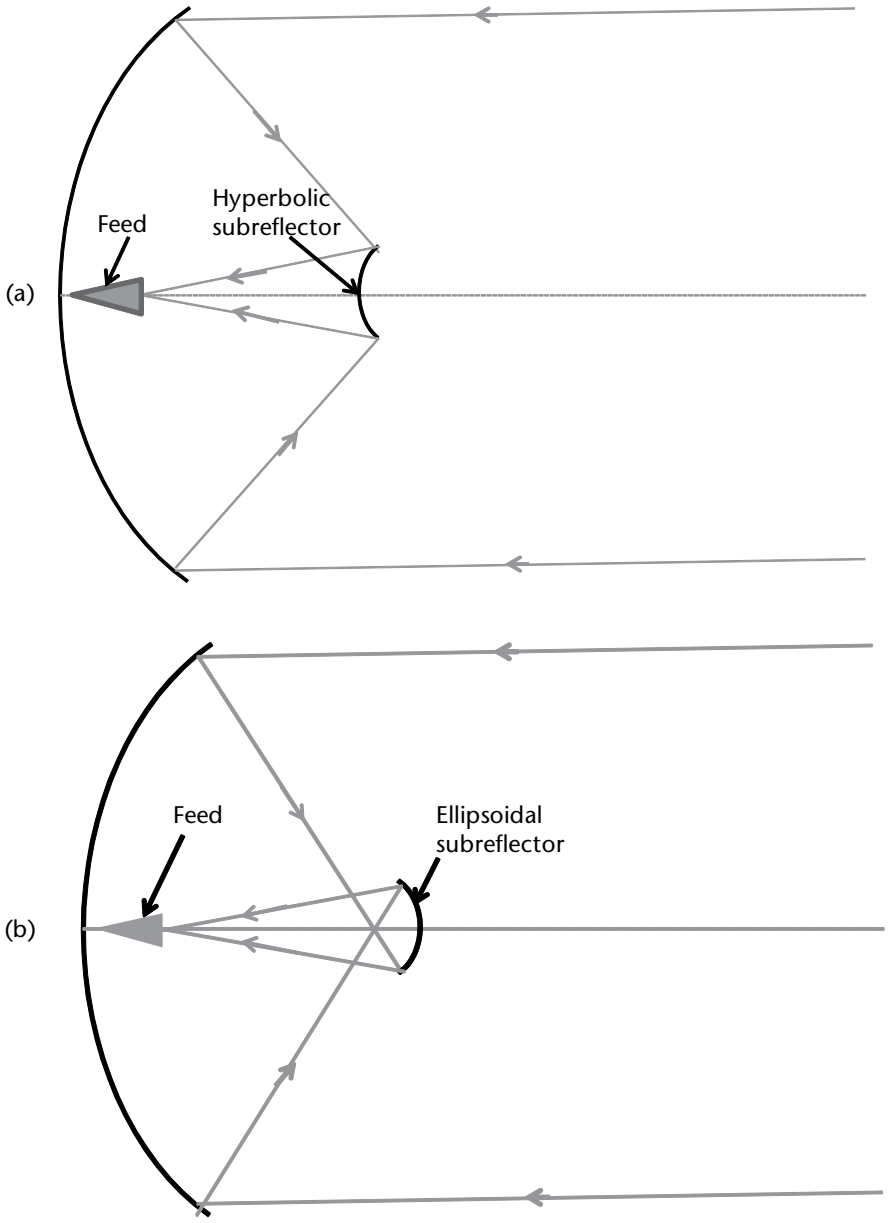

Figure 1.2 Dual-reflector antenna configurations using curved subreflectors: (a) Cassegrain and (b) Gregorian.

channel broadcasts through the use of multiple spot beams augmented DBS service to designated market areas.

With the development of high-power spacecraft buses with 10 to 20 kW of DC power, each satellite was able to carry hybrid payloads offering multiple services. Reflector and feed technologies have been developed in the recent past that allow multiple frequency bands through a single reflector antenna. In addition, compact and low-loss feed assemblies and feed networks have been developed by several manufacturers throughout the world. Advanced designs with low passive

intermodulation (PIM) products and high-power handling technologies have been developed during the past 30 years, thus improving the reliability and extending the capability of the high-power payloads. Reconfigurable reflector antenna technology has been developed for DABS (digital audio broadcast satellites) and has been successfully flown on Sirius-1 and Sirius-2 satellites that operate in highly inclined elliptical orbits. Flat reflector technologies have been developed for radar and remote sensing technologies.

Several excellent books have covered conventional reflector antennas in the past [2–6]. However, developments during the past two decades have not been documented properly. The intent of this volume of the handbook is to address the latest developments in reflector antennas for space, ground, remote sensing, and terahertz applications. This volume will be useful for practicing engineers as well as academic researchers. All of the chapters have been written by experts in the industry and in academia who bring their valuable experience in dealing with practical antennas, hardware design, and related issues. Some of the topics addressed are new and documented here for the first time in textbook form.

The key developments in reflector antennas that have occurred during the past few decades are addressed in this book and include the following topics:

- Contoured or shaped beam antennas;
- Multiple beam antennas;
- Multiband antennas;
- Feed assemblies for reflector antennas: design, fabrication, and test;
- Passive intermodulation products;
- Multipaction and corona;
- Reconfigurable antennas;
- Reflector antennas for terahertz applications;
- Large deployable mesh reflector antennas;
- Remote sensing antennas;
- Large reflector antennas for Earth stations and gateway applications on the ground;
- Beam-waveguide dual-reflector antennas.

1.2 Reflector Antenna Basics

Reflector antennas are used for transmission and reception of RF signals providing high gain. They are preferred over other directive antenna types such as array antennas and lens antennas due to their low cost and low mass and because they do not require active components, they avoid the use of complex beam-forming networks, and they provide large bandwidths. Gain and directivity definitions of reflector antennas are sometimes not correctly used. The directivity of the reflector antenna is defined as:

$$D(\theta_0,\phi_0)=\frac{4\pi\left|E(\theta_0,\phi_0)\right|^2}{\int_0^{2\pi}\int_0^{\pi}\left|E(\theta,\phi_0)\right|^2 \sin\theta\, d\theta\, d\phi} \tag{1.1}$$

The denominator in (1.1) is the total radiated power and $\left|E(\theta_0,\phi_0)\right|^2$ is the power radiated per unit solid angle in the angular direction (θ_0, ϕ_0). Directivity can be obtained by integrating the ideal computed copolar and cross-polar patterns of the reflector antennas. However, gain of the reflector antenna, $G(\theta_0, \phi_0)$, is lower than the directivity and includes feed system and reflector losses. It is given as:

$$G(\theta_0,\phi_0)=\mathrm{D}(\theta_0,\phi_0)-F_L-R_L \tag{1.2}$$

The feed loss F_L includes insertion loss due to all components of the feed assembly (horn, polarizer, orthomode transducers, filters/diplexers, waveguide bends), mismatch losses, and thermal losses as applicable. The reflector loss includes conductive loss, loss due to surface errors, and thermal loss (if applicable) and is given by:

$$R_L = R_C + R_S + R_T \tag{1.3}$$

Conductive loss depends on the material properties of the reflector (graphite, aluminum, etc.) and the surface loss in decibels can be calculated using Ruze's formulation [7] as:

$$R_S = 10\log_{10}\left[e^{-(4\pi\delta/\lambda)^2}\right] \tag{1.4}$$

The thermal loss is accounted for by computing the directivity with reflector surfaces at various temperatures and subtracting the directivity value with ambient surface. This is typically computed since gain measurements with thermal loss are not feasible in practice. Thermal losses include mispointing losses and surface distortion losses.

It is important to optimize the directivity of the reflector antenna by design and minimize the feed and reflector losses through hardware design, manufacture, and implementation. The key system parameters impacted by the reflector antenna design are the effective isotropic radiated power (EIRP) and the gain-to-noise temperature ratio (G/T) and are given as:

$$EIRP(dBW)=10\log_{10}(P_i)+G-L_r \tag{1.5}$$

where P_i is the input power in watts, G is the antenna gain including losses, and L_r is the losses between the amplifier and the antenna interface point.

$$G/T=\frac{Receive\ antenna\ gain}{System\ noise\ temperature} \tag{1.6}$$

The G/T impacts the signal-to-noise ratio (SNR) through

$$SNR = \frac{E_b}{N_0} = \left\{\frac{F_D \cdot \frac{\lambda^2}{4\pi}}{k.R_b}\right\} \cdot \left\{\frac{G}{T_{sys}}\right\} \tag{1.7}$$

In the above equation, F_D is the flux density, k is Boltzmann's constant, R_b is the bit rate, and T_{sys} is the system noise temperature.

The system noise temperature depends on the antenna temperature and the repeater noise figure and is given as:

$$T_{sys} = T_{ant} + 290(F_{RPTR} - 1) \tag{1.8}$$

The antenna temperature depends on the noise environment that the antenna pattern is illuminating and the radiation pattern as:

$$T_{ant} = \frac{1}{4\pi}\int_0^{2\pi}\int_0^{\pi} G(\theta,\phi)T(\theta,\phi)\sin(\theta)\,\mathrm{d}\theta\,\mathrm{d}\phi \tag{1.9}$$

The system link performance of the satellite, depends highly on the transmitting antenna gain and the receiving antenna gain and the link SNR is given as:

$$SNR(Link) = EIRP + \left(\frac{G}{T}\right) - L_s + 228.6 - 10\log(BW) \tag{1.10}$$

where L_s is a large positive number that accounts for all losses in the system, including path loss. The pass loss depends on the path length R from the satellite to ground and can be calculated as $20\log_{10}\left(\frac{4\pi R}{\lambda}\right)$ with R as the path length from the satellite to ground and BW as the bandwidth in hertz. The reflector antenna gains can be improved by designing the feed system to provide optimal illumination taper (typically 12 to 15 dB of taper), minimizing the feed assembly losses, minimizing the surface errors on the reflector system, and minimizing cross-polar levels.

Advanced reflector systems and advanced feed systems have been developed to support multiple frequency bands. An example of an advanced feed assembly supporting C-band transmitting and receiving bands is shown in Figure 1.3. This system isolates the two bands with filters and a symmetric junction and has polarizers at both bands with LHCP and RHCP ports at each band. Losses are kept to a minimum by making the system very compact using advanced manufacturing techniques such as electroforming and minimizing the waveguide flange interfaces.

The directivity of conventional pencil beam antennas can be calculated based on the antenna aperture area and is given as:

$$D = 10\log_{10}\left[\frac{4\pi A}{\lambda^2}\eta_f\right] \tag{1.11}$$

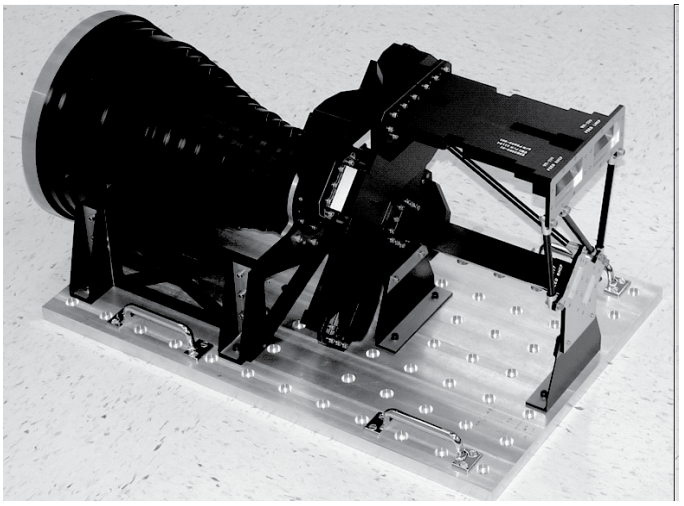

Figure 1.3 A C-band feed assembly with corrugated horn providing dual circular polarization at both the 4- and 6-GHz bands for fixed satellite services. (Courtesy of Custom Microwave Inc.)

where A is the aperture area, λ is the wavelength, and η_f is the overall antenna efficiency and is given by [8, 9]

$$\eta_f = 4\cot^2\left(\frac{\theta_1}{2}\right)\left[1-\cos^n\left(\frac{\theta_1}{2}\right)\right]^2\frac{(n+1)}{n^2} \tag{1.12}$$

Equation (1.12) includes spillover efficiency, aperture efficiency, phase efficiency, and polarization efficiency, and can easily be factored into these four subefficiencies. The feed pattern is assumed to be of the form $\cos^n\left(\frac{\theta}{2}\right)$ in (1.12). The variable n is related to the feed illumination taper T and is given by

$$n = \frac{-0.05T}{\log_{10}\left[\cos\left(\frac{\theta_1}{2}\right)\right]} \tag{1.13}$$

The maximum value of feed efficiency η_f is about 0.81 and occurs when the feed illumination taper T is about 10 to 12 dB. In (1.13), θ_1 is the half-subtended angle from the focus to the reflector edges.

1.3 Organization of Book Chapters

This volume has been organized into the following nine individual chapters:

Chapter 1: Introduction
Chapter 2: Reflector Antennas for Space Communications
Chapter 3: Reflector Antennas for Terrestrial Communications

Chapter 4: Reflector Antennas for Terahertz Imaging Applications

Chapter 5: Multiband Reflector Antennas

Chapter 6: Reflector Antennas for Remote Sensing Applications

Chapter 7: Feed Assemblies, Passive Intermodulation, Multipaction, and Corona Considerations

Chapter 8: Deployable Reflectors

Chapter 9: Mechanical Aspects of Reflector Antennas for Space Applications

Chapter 2 describes the various types of reflector antennas used for satellite communications. An introduction to payload systems and the antenna farms typically used for satellites is given. Different types of reflector antennas used for space are described briefly. Contoured beam or shaped beam antennas are described later along with analysis results for C-band and Ku-band antennas for fixed satellite services. The gain performance as function of reflector size is discussed along with the gain area product, which is sometimes used as the figure of merit of shaped beam antennas. A dual-reflector Gregorian antenna configuration for shaped beam applications is described. Gridded-reflector antennas with overlapping apertures providing polarization reuse for linear polarization applications are discussed along with design formulas for the grid geometry.

The subject of multiple-beam antennas (MBAs) is relatively new and is covered in detail in Chapter 2. Design of MBAs, analysis of MBA performance, and several applications of MBAs are discussed. Advanced feed technologies as well as reflector technologies that improve MBA performance are given with examples. MBAs for direct-to-home local-channel broadcast and personal communications satellites are also discussed.

Chapter 3 provides past and recent developments on reflector antennas for terrestrial communications applications. This chapter describes reflector antennas in practical use, mainly focusing on terrestrial communications. Each of its sections describes reflector antennas for a specific application. Section 3.1 presents design technologies for beam-waveguide feed systems and practical examples in conjunction with large Earth station reflector antennas. The shaped Cassegrain antenna fed by a four-reflector beam-waveguide feed is described. This type of antenna is a standard for large Earth stations all over the world. Section 3.2 introduces a tri-reflector offset antenna for terrestrial microwave relay link systems. The reflector antenna is shown to achieve very low cross-polar levels. Reflector antennas used for Japanese communication satellite 2 (CS-2) are described in Section 3.3. The shape of the wavefront, which corresponds to the desired beam cross section in the sense of geometrical optics, is analyzed, and the method used to synthesize the wavefront is discussed. The reflector shape is determined from the shape of the wavefront by the geometrical optics approach, which is adequate for this application.

Section 3.4 presents the elliptical aperture antenna for satellite news gathering. The antenna is an offset Gregorian antenna with an elliptical main reflector. The elliptical aperture is used to reduce the interference from or to adjacent satellites. Section 3.5 also describes a reflector antenna with an elliptical aperture for aeronautical satellite communication systems. The elliptical aperture allows for the realization of a very low profile antenna under severe envelope constraints

on the airplane. The dual-shaped reflector antenna is realized by using a physical optics shaping technique and achieves excellent electric performance. Section 3.6 introduces the compact reflector antenna for use on vessels for mobile satellite communications. For such a system, the antenna needs to be designed to achieve low sidelobe and low cross-polar characteristics while keeping the antennas efficiency high. Section 3.7 presents a reflector antenna that is used for simultaneous reception from broadcast satellites (BS) and communication satellites (CS). The optimum reflector for a single-reflector wide beam-spacing multibeam antenna is presented on the basis of wave aberration analysis of defocus-fed reflectors.

Terahertz imaging applications rely on the use of focusing and nonfocusing reflector systems. Chapter 4 describes the recent developments in the area of terahertz reflector antennas. These systems need to steer the beam over the intended field of view with specific spatial resolution. One possible solution is to use focal plane arrays (i.e., a camera-like staring imager) that would acquire information from several image pixels simultaneously. In the terahertz regime, this is a feasible solution for passive detectors, such as bolometers or superconducting detectors, commonly used for space applications. However, terahertz heterodyne detector array technology is still under development. In such cases most of the current state-of-the-art imaging systems, especially for terrestrial applications, make use of antenna reflector systems integrated with mechanical scanners in order to generate the image. The properties and typical configurations of focusing reflector systems for both types of image acquisition are addressed in Chapter 4. An analytical expression of the vectorial field in the focal plane of a general focusing system is derived. This derivation is very useful to study the properties of this field and establish equivalence between reflector systems focusing in the near and far regions. Moreover, once this focal plane field is known, it is shown that the power received by an array of antennas in the focal plane can be calculated by using its effective length. With this calculation of the received power, the trade-offs between focal plane sampling and image acquisition velocity for passive detectors and different types of sources (i.e., isolated sources and distributed incoherent sources) can be established.

Recent developments in the area of multiband reflector antennas and associated feed horns are described in Chapter 5. These antennas are capable of supporting multiple frequency bands that are separated in frequency and covering several octave bandwidths. They have the advantage of using a single antenna instead of several antennas, resulting in reduced costs and reduced mass. Advanced reflector technologies such as stepped-reflectors, reflectors with partially reflective surfaces, and shaped reflectors are presented. Feed advancements in terms of multimode horns with several "slope discontinuities" and feed assembly developments to isolate the frequency bands are discussed in Chapter 5.

Chapter 6 presents reflector antennas used for remote sensing of the Earth and other bodies in the solar system and relevant sensor technologies to detect and classify objects by means of propagated electromagnetic radiation. Sensors deployed on aircraft or satellites make it possible to collect data on a global scale that would not otherwise be practical to obtain. Remote sensing is used for a wide variety of science applications ranging from global measurement of ocean topography and deforestation to the study of Jupiter's atmosphere. The military employs remote sensing techniques to collect data about opposing forces, weather conditions and other information relevant to its mission. The chapter presents technologies related

to active and passive remote sensing. Remote sensing system design is driven by the science requirements that define the mission. Consequently, both the system and antenna designs need to be tailored to meet the unique mission science requirements. For spaceborne remote sensing applications, reflector antennas have historically been the most widely used antennas. Characteristics of the antenna such as beam shape, sidelobe levels, cross-polar isolation, efficiency, and scanning capability are driven by specific system design requirements. Chapter 6 also presents an overview of the various types of reflector antenna designs used for remote sensing applications. Antennas flown on historically significant missions are used to illustrate the practical implementation of each antenna type. In addition, the chapter presents notable antenna research developments that are regarded as enabling technologies for new types of sensors.

Chapter 7 presents two key sections related to the feed assemblies used for reflector antennas in space and to a certain extent in ground applications. It provides the component designs, manufacture, and test results for various types of feed assemblies employed in the C-band, Ku-band, and Ka-band. The feed components include horns, orthomode transducers (OMTs), polarizers, filters, diplexers, combiners/dividers, and transitions. Manufacturing approaches that yield precise tolerances required for high-performance feeds are discussed. The advantages of advanced design, analyses, manufacture, and test of integrated feed assembly instead of conventional piece-part design are discussed. The satellite industry has recently recognized the benefits of integrated feed assembly design relative to the conventional discrete component approach and started using this approach for the feed designs. The second part of Chapter 7 deals with three important aspects of spacecraft antennas and feeds: passive intermodulation (PIM), multipaction, and corona. These aspects are critical in high-power payloads and multichannel repeaters and significantly impact the feed and reflector design. Design guidelines and methods to mitigate potential risks due to PIM and multiplication to satellites are discussed.

Space reflectors, whose size is larger than the fairing of the booster that carries them, need to be "folded up" in some manner for launch, and then "unfurled" on orbit to their full size. These are typically referred to as "deployable" reflectors, and are the subject of Chapter 8. This chapter is organized into three main sections. The first section deals with reflector classifications either according to the surface geometry (such as parabolic vs. shaped, circular vs. elliptical, and center-fed vs. offset-fed reflectors) or according to the surface type (such as rigid/segmented, semi-rigid, inflatable/rigidizable, woven-mesh and knitted-mesh surfaces). The second section deals in more detail with the major constituents/components of the knitted-mesh type reflector, which is the most commonly flown reflector in space of all of the various types of deployable reflectors. The third and final section addresses the major design requirements/considerations for a typical deployable reflector subsystem including electrical, mechanical, thermal, and environmental drivers.

Finally, Chapter 9 is intended to provide the reader with a framework and top-level understanding of the elements and requirements that must be considered in the successful design, fabrication, and testing of a spaceflight antenna reflector. It is a guide based on the more than 30 years of professional experience of the authors in engineering, fabricating, and testing spaceflight antenna reflectors and systems. Because the state of the art in antenna reflector design continually advances, this

chapter is purposely written to provide general recommendations for configuration, design approach, materials, and testing. A wealth of information is available from composite materials suppliers, technical papers, and organizations, so it is left to the reader to perform the detailed analyses, engineering, and materials research to establish the best possible specific choices relative to the set of requirements for the particular reflector being considered.

A successful antenna reflector design is always a carefully balanced combination of many specific and interdependent choices that must all work together to achieve the best possible results. The mechanical design of reflector antennas has to satisfy electrical, spacecraft, launch load, vibration, extreme thermal, deployment in space, stowage, low mass, pointing, and structural requirements simultaneously.

This volume provides all aspects of reflector antennas for space and ground applications. As the antenna technology moves towards the terahertz regime, new types of reflector antenna designs and novel manufacturing methods will evolve in the future.

References

[1] B. S. Westcott, *Shaped Reflector Antenna Design*, Research Studies Press, UK, 1983.

[2] R. C. Johnson and H. Jasik, *Antenna Engineering Handbook*, McGraw-Hill, New York, 1984.

[3] W. V. T. Rusch and P. D. Potter, *Analysis of Reflector Antennas*, Academic Press, San Diego, 1970.

[4] A. W. Rudge et al., *The Handbook of Antenna Design*, Peter Peregrinus, London, 1982.

[5] P. J. Wood, *Reflector Antenna Analysis and Design*, Peter Peregrinus, London, 1980.

[6] A. W. Love, "Some highlights in reflector antenna development," *Radio Science*, Vol. 11, pp. 671–684, 1976.

[7] J. Ruze, "Antenna tolerance theory—a review," *Proc. IEEE*, Vol. 54, pp. 633–640, 1966.

[8] P. S. Kildal, "Factorization of the feed efficiency of paraboloids and Cassegrain antennas," *IEEE Trans. Antennas & Propagation*, Vol. 33, pp. 903–908, August 1995.

[9] S. Rao and P. S. Kildal, "A study of the diffraction and blockage effects on the efficiency of the Cassegrain antenna," *Canadian Elec. Eng. Journal*, Vol. 9, pp. 10–15, January 1984.

CHAPTER 2

Reflector Antennas for Space Communications

Sudhakar Rao, Northrop Grumman Aerospace Systems
C. Babu Ravipati, Intelsat Corporation[1]

2.1 Introduction

Reflector antennas are widely used in space applications for communication satellites, military satellites, deep space exploration missions, cross-link communication among satellites, space stations, and remote sensing satellites [1, 2]. The main reasons for the use of reflector antennas as opposed to other types, such as array antennas and lens antennas, are mature technology, low cost, high performance, low losses, low cross-polar levels, light weight, thermal stability, simpler feeds, and wide bandwidths. A good review of conventional reflector antennas has been provided by Rudge [3] and Johnson and Jasik [4]. Although parabolic reflectors were widely used in earlier applications, the design and implementation of advanced reflector antennas has evolved mostly due to the stringent performance requirements and additional capabilities dictated by the space industry operators. Communication satellites have multiple reflector antennas on each spacecraft that cater to various services. Typical satellite services that employ reflector antennas include the following:

- Fixed satellite services (FSS) that provide shaped or contoured beams for domestic or regional satellite services. These antennas operate in the C-band, Ku-band, or Ka-band providing both uplink (satellite receives from ground) and downlink (satellite transmits to ground) beams from the same antenna or using two antennas.
- Broadcast satellite services (BSS) that provide mostly downlink beams over a coverage region such as the continental United States. This type of antenna

1. This work does not reflect the views of the authors' companies (i.e., Northrop Grumman and Intelsat), which assume no responsibility for the material presented.

operates over a narrow transmit (Tx) band (typically the Ku-band or K-band) and provides a highly contoured beam to compensate for the rain attenuation. With the recent approval of local-channel broadcast through satellites, multiple reflector antennas are typically used for providing several spot beams on the ground. Both DirecTV and EchoStar operators have successfully used local-channel broadcast satellites for continental U.S. (CONUS) services and extended CONUS services.

- Personal communication services (PCS) at the K/Ka-band. These systems employ multiple reflector antennas where each reflector uses a large number of feeds for personal communication and data transfer from user-to-user via satellite. Such a system typically employs a forward link from ground-to-satellite-to-user and a return link from user-to-satellite-to-ground. These systems employ a number of overlapping spot beams for both forward and return links. The capacity of the satellite depends on number of factors such as number of beams, frequency reuse scheme, gain of the spot beams, EIRP, G/T, copolar isolation among reuse beams, cross-polar isolation, pointing error of the satellite, and the DC power capability of the satellite.
- Mobile satellite services (MSS) that provide communication to mobile users via satellite. These mobile satellites operate at lower frequencies (the UHF, L-band, or S-band) and, therefore, need to use large deployable reflectors in the range of 5 to 22m that take advantage of mesh reflector technology. The feed array employs a large number of feeds to generate a large number of overlapping beams on the ground. Low-level beam-forming networks combined with matrix power amplifiers (MPAs) for distributed power amplification on the Tx link and low noise amplifiers (LNA) redundancy on the receiving (Rx) end are typically used.
- Intersatellite services (ISS) that provide communication links and data transfers from satellite-to-satellite. This includes, for example, a satellite constellation used for global communications. Such systems typically employ large gimbaled reflectors with autotrack capability. Center-fed dual-reflector systems with tracking feeds are employed while the antenna is mounted on a gimbal mechanism to scan the beam. These are also called cross-link communications antennas.

Communications links are established between satellite and ground, satellite to aircraft, satellite to user, or satellite to satellite. The satellite links for FSS and DBS satellites are illustrated in Figure 2.1. The FSS has both an uplink and a downlink covering the domestic region with contoured beams, whereas the BSS has mainly a downlink contoured beam covering the domestic region; its uplink is provided through spot beams from ground sites.

Typical satellites have a number of reflector antennas and associated repeaters to support hybrid payloads serving, for example, FSS, PCS, and MSS services. The spacecraft bus needs to accommodate several large reflectors stowed in a small volume so that they can fit in the launch fairing envelope, which is about 4 to 5m in diameter. This critical requirement demands that several reflectors be deployed in space from the stowed launch configuration of the spacecraft. The deployed reflectors are mostly accommodated on the east and west sides of the spacecraft and in

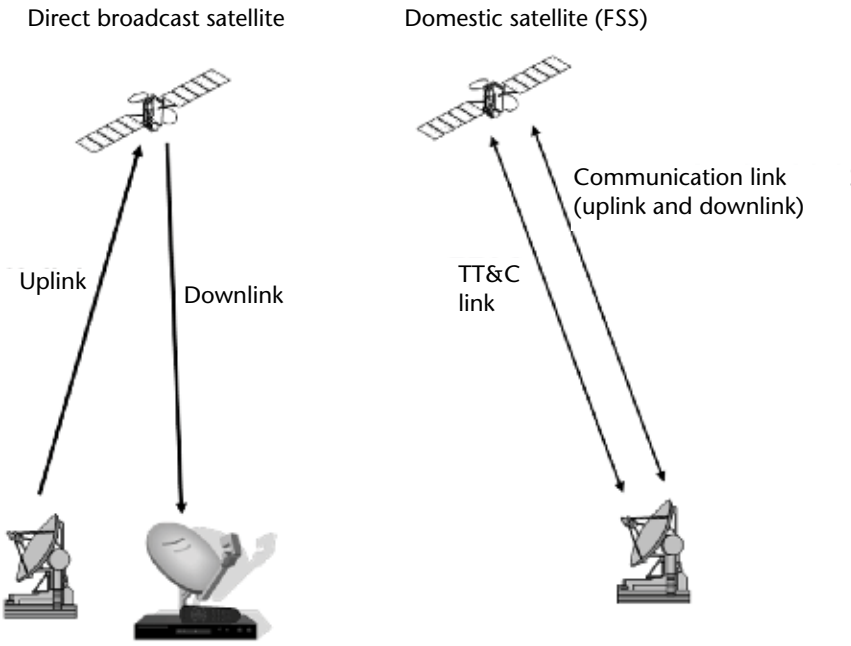

Figure 2.1 Illustration of the various communication links for satellite communications. (© 1985 IEEE. From [13].)

some cases on the nadir deck as well. Fixed smaller reflectors without deployment are placed on the nadir deck of the spacecraft along with tracking, telemetry, and command antennas and global horns. The majority of the reflectors employ an offset configuration to avoid blockage by the feed(s) and/or subreflectors. The feeds for all of the reflectors are fixed on the east-west corners of the spacecraft and on the nadir deck. This is due to the fact that the feed assemblies carry high power and are sensitive to passive intermodulation (PIM). Figure 2.2 shows a typical satellite in the deployed configuration. Solar panels are deployed along the north-south directions to track the sun.

The payload for any satellite service includes the antenna subsystem and the repeater subsystem. The antenna provides the desired radiation characteristics in terms of beam shape tailored to the coverage region, required gain to close the communication links, desired polarization (either single or dual), diplexing function between the Tx and Rx bands, high cross-polar isolation for polarization reuse systems, copolar isolation outside the coverage, and sidelobe shaping as desired by the customer needs.

Figure 2.3 shows the block diagram for a bent-pipe satellite payload providing FSS service. The reflector antenna in this example employs a gridded reflector with two overlapping surfaces where the front reflector provides vertical polarization and the back surface provides horizontal polarization. Each reflector is shaped to provide a contoured beam over the coverage region and is fed with its own horn with either vertical or horizontal polarization. Each feed is diplexed to isolate the Tx and the Rx frequency bands. On the receiving side, the antenna receives the RF signals from ground. The uplink signals go through the input filter assembly (IFA), receivers that downconvert the 6-GHz signals to 4-GHz signals, and then through input multiplexers (IMUX) that separate the wideband signal into various

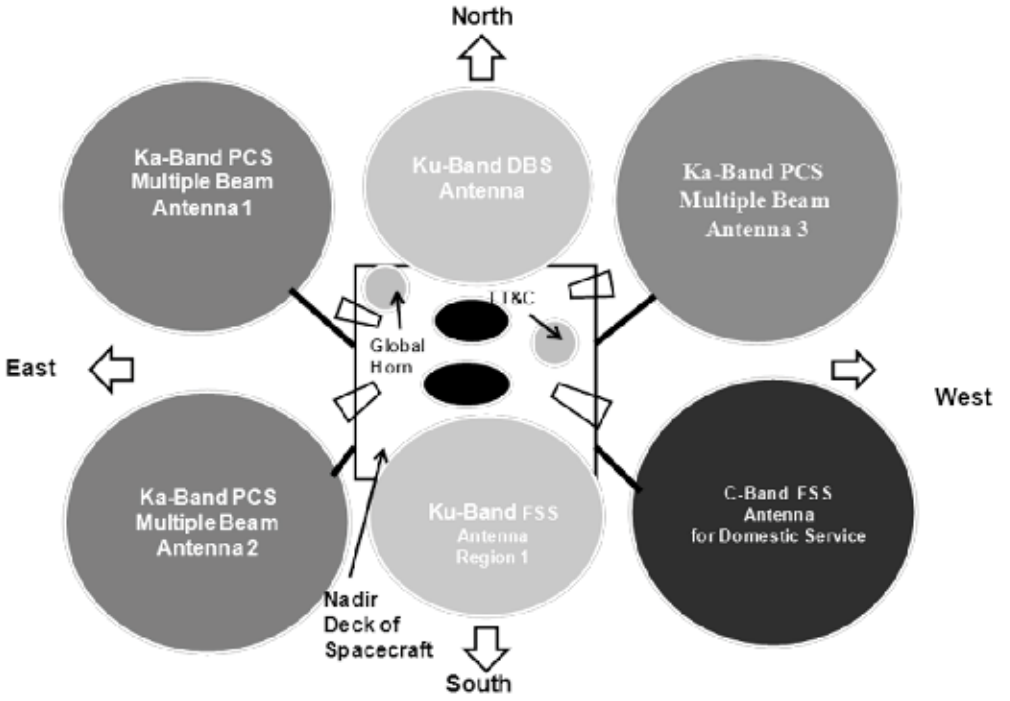

Figure 2.2 Spacecraft layout showing various antennas supporting multiple satellite services.

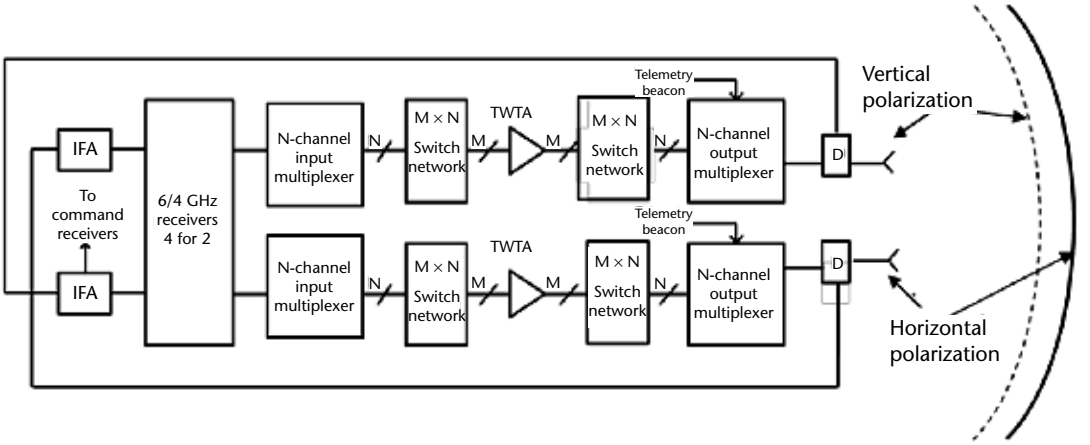

Figure 2.3 Block diagram of typical C-band FSS bent-pipe payload showing dual-gridded reflector for polarization use and repeater block diagrams.

narrowband frequency channels. These narrowband channels are amplified through traveling-wave tube amplifiers (TWTAs) that are designed to provide the required RF power, and combined again through an output multiplexer (OMUX), and then transmitted to ground through the Tx antenna. There are redundant networks for the receivers and TWTAs in case of primary unit failures. These satellites do not have a processor on board and, therefore, they are called *bent-pipe* transponders or receivers.

Key system parameters for the satellites are G/T (gain-to-noise temperature ratio) and EIRP (effective isotropic radiated power). Both of these parameters are the figures of merit for the satellite design and depend on the antenna gain at both the Tx and Rx bands. The communication link quality is determined by the signal-to-noise power ratio, which is defined in decibels as:

$$\begin{aligned} SNR &= 10\log_{10}\left[\frac{Signal\,Power}{Noise\,Power}\right] \\ &= EIRP + G/T + 228.6 + S_L - 10\log_{10}\left(B_w\right) \end{aligned} \tag{2.1}$$

where S_L is the system loss in decibels and B_w is the signal bandwidth in hertz. The EIRP depends on the transmit power, losses from the amplifier output to the antenna, and the antenna gain. The G/T depends on the Rx antenna gain, antenna noise temperature, front-end losses, and noise figure of the LNA. The system losses include free-space path loss from satellite to ground, atmospheric losses, polarization losses, and loss due to satellite pointing errors. The free-space path loss depends on the distance R between the satellite and ground terminal and the wavelength. It is given in decibels as:

$$P_L = 20\log_{10}\left[\frac{4\pi R}{\lambda}\right] \tag{2.2}$$

The loss due to pointing error is generally taken care of in the design by expanding the coverage region with the radial pointing error and synthesizing the shaped beam with the expanded coverage region and computing the minimum coverage area gain. For a spot beam payload, the gain loss (in decibels) due to pointing error is given as:

$$L_{P.E} = -3\left[\frac{P.E}{\theta_{3b}}\right]^2 \tag{2.3}$$

where P.E is the satellite worst-case pointing error, and θ_{3b} is the half beamwidth at the –3 dB level of the spot beam. For shaped beams the loss is smaller due to beam spreading. Antenna gain is very important for satellite designers because it has a significant impact on both the uplink G/T and downlink EIRP. Many designers spend a lot of time optimizing the antenna gain values to the last fraction of a decibel. Other challenges include minimizing the front-end antenna losses, designing the feed components to meet the high-power handling requirements, meeting the low PIM requirements, and improving the copolar and cross-polar isolations of the antenna.

Many types of reflector antennas are used for satellite communications. The type of reflector antenna depends on the satellite payload requirements and the accommodation on the spacecraft. Commonly used reflector antennas for communication satellites are:

- Single-offset reflector (shaped or unshaped).
- Dual-reflector Gregorian in both offset and symmetric configurations (shaped or unshaped).
- Gridded reflector for linear polarization reuse (typically shaped surfaces).
- Center-fed Cassegrain reflector for intersatellite links and offset-fed Cassegrain reflector.
- Large deployable mesh reflectors for mobile services.
- Single reflector imaging antennas.
- Dual-reflector antennas for large scan applications [side-fed offset Cassegrain (SFOC) and front-fed offset cassegrain (FFOC) antennas].
- Confocal reflector antenna.

Some of these reflector antennas are discussed in this chapter; others are presented in other chapters of this three-volume handbook.

2.2 Contoured Beam Antennas

The contoured beam antennas are the most widely used type in satellite communications. They are also called shaped beam antennas. These antennas provide downlink and/or uplink beams that are tailored to fit the geographic coverage region as seen from a geostationary satellite from a given orbital slot. Contoured beams can be generated using phased arrays or reflectors. Phased arrays have these limitations: narrow bandwidth, lower efficiency of SSPAs, higher DC power dissipation, increased delivery schedule, and increased cost and mass. Reflector antennas are most commonly used for contoured beam applications and other satellite applications. Offset-fed reflector configurations (single or dual) are suitable for eliminating the geometrical blockage caused by feeds/subreflectors and are simpler to accommodate on spacecraft. Two methods are used to generate a contoured beam on the ground from a satellite using reflector antennas: (1) a parabolic reflector that is fed with a feed array and (2) a shaped reflector with a single feed.

Satellite payloads prior to 1990 employed parabolic reflectors with a large number of feed horns [5, 6]. The RF signals to the feed array are combined through a beam-forming network (BFN) with appropriate amplitude and phase weightings that are designed to shape the beam. The BFN is realized using a waveguide medium at the Ku-band and higher bands and using a TEM-line medium (also referred as square-ax medium) at the C-band and lower bands to reduce mass. It is designed using a number of couplers with different coupling values, line lengths for phase optimization, phase-slope equalizers for maintaining the phase distribution over the frequency band, and filters to reject frequencies outside the band. Because of the bandwidth limitation of the BFN, the parabolic reflector with feed array requires two such antennas: one for transmitting and another for receiving, which makes it expensive and heavy. The shaped reflector with a single feed avoids the need for a BFN and typically requires a single wideband antenna supporting both Tx and Rx beams. The Tx and the Rx frequency bands are separated through

a diplexer. The two methods of generating the contoured beams are illustrated in Figure 2.4.

2.2.1 Single-Offset Shaped Reflector Antenna for Contoured Beams

This section describes the single-offset solid reflector used for contoured beam applications. The reflectors are typically made of graphite material for thermal stability and lower mass. The primary objective of the design is to maximize the

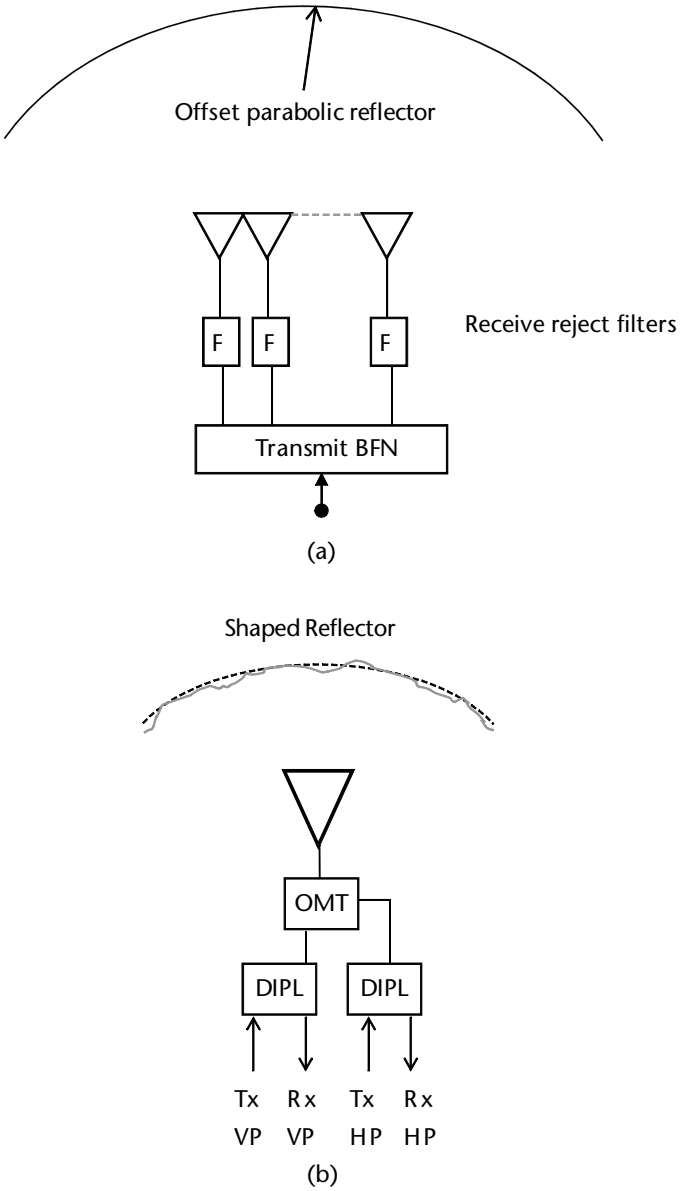

Figure 2.4 (a) Schematic of parabolic reflector with multiple feeds and BFN for contoured beam applications. The Rx antenna is similar to the Tx antenna except for the frequency difference. (b) Schematic of shaped reflector antenna with single feed for contoured beam applications. OMT = ortho-mode transducer, DIPL = diplexer, Tx = transmitting function, Rx = receiving function, VP = vertical polarization, HP = horizontal polarization. (© 1999 IEEE. From [18].)

minimum gain over the coverage region. The coverage region is irregularly shaped to fit a domestic country as seen by the satellite or a region comprising several countries. Other secondary objectives include:

- Maximize the cross-polar isolation over the coverage.
- Maximize the copolar isolation among countries/regions that could potentially use the same frequencies.
- Minimize the antenna losses, including those from the feed assembly, reflector manufacture (surface errors), and thermal distortion.
- Maximize the power handling capability of the feed components.
- Minimize the interference due to PIM products.

The advantages of a shaped reflector relative to a conventional parabolic reflector with a feed array are better antenna directivity due to lower spillover losses, lower insertion loss due to elimination of the BFN, better gain and cross-polar performance due to avoidance of mutual coupling effects among the feed elements, and amplitude and phase variations of the BFN over the frequency and thermal ranges.

The reflector geometry needs to be selected first based on the overall satellite system requirements and the spacecraft constraints. Typical satellites carry hybrid payloads on the spacecraft that cater to multiple services from a single satellite. Several reflector antennas may need to be accommodated on the spacecraft that must fit the limited launch fairing of mostly 4m (in some cases 5m) in the stowed configuration. The reflectors are generally deployed with the feed assembly fixed-mounted on the spacecraft.

The key design parameters for the shaped reflector are reflector diameter (D), focal length (F), offset clearance (h), feed illumination taper or size, and the frequency bandwidth covering both the Tx and Rx bands. The reflector size is dictated by the system and spacecraft requirements. The focal length is dictated by the cross-polar requirements and the beam squint for circular polarizations. The F/D ratio needs to be in the range of 0.8 to 1.4, which is a compromise in terms of achieving good cross-polar isolation and minimizing the beam squint for CP versus mechanical constraints to minimize the deployment boom and mass. The offset clearance h is selected such that there is no blockage from the feed assembly over the coverage region. Good design practices impose a blockage-free condition where the coverage region is expanded by about 3 deg. Figure 2.5 illustrates the geometrical parameters of the reflector antenna. The angular parameters of the starting offset parabolic reflector prior to shaping are given as:

$$\theta_{2,1} = \frac{1}{2}\left(\tan^{-1}\left[\frac{D+h}{F - \dfrac{(D+h)^2}{4F}} \right] \pm \tan^{-1}\left[\frac{h}{F - \dfrac{h^2}{4F}} \right] \right) \tag{2.4}$$

$$\theta_0 = (\theta_2 - \theta_1)/2 \tag{2.5}$$

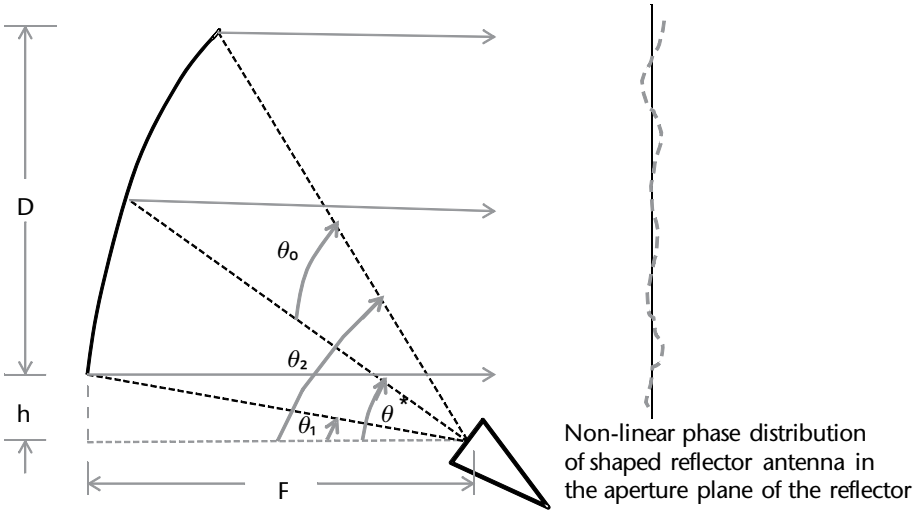

Figure 2.5 Geometrical parameters of the shaped reflector antenna. (© 2003 IEEE. From [19].)

$$\theta^* = \theta_1 + \theta_0 \tag{2.6}$$

The angle θ_0 determines the feed illumination taper on the reflector and is designed with a minimum taper of 15 dB at the lowest frequency of the band(s). It is important when selecting the offset clearance h that consideration be given to maintaining a blockage-free condition for all coverage angles of the contoured beam from the antenna boresight. The maximum angle for blockage-free condition θ_{sm} depends on the offset clearance, focal length, and the diameter d of the feed and is given as:

$$\theta_{sm} = \tan^{-1}\left[\frac{h}{F - \dfrac{h^2}{4F}}\right] - \tan^{-1}\left[\frac{h - 0.5d\cos\theta^*}{F - \dfrac{\left(0.5d\ \cos\theta^*\right)^2}{4F}}\right] \tag{2.7}$$

For linear polarization applications, the cross-polar isolation is intrinsically poor because of the offset configuration of the reflector. Cross-polar suppression in addition to the copolar gain contours needs to be incorporated as part of the synthesis for reflector shaping. However, for circular polarization applications, the reflector does not induce any cross-polar components and the feed assembly cross-polar levels due to the feed horn and polarizer dominate the antenna level cross-polar isolation. The offset geometry causes beam squint in the offset plane and is given approximately as [7, 8]:

$$\theta_{BS} = \sin^{-1}\left[\frac{\lambda_L\ \sin\theta^*}{4\pi F}\right] \tag{2.8}$$

The beam squint occurs in the plane of symmetry and the direction depends on the sense of polarization (LHCP or RHCP). The feed location needs to be displaced

slightly from the reflector focus in order to compensate for the beam squint for single sense of circular polarization application or can be accounted for in the shaping process.

Reflector synthesis can be carried out by two methods. An indirect method involves designing the surface of the reflector such that it produces a given aperture field, which is known to generate a desired far field. The synthesis of the desired aperture field most often involves the iterative solution of partial differential equations that describe the relationship between feed and aperture power distributions, and is based on geometrical optics (GO).

The second method is a direct method and is the method most oftenly used. In this method, the reflector system is designed such that it produces a prescribed far field. The reflector is initially defined in terms of a base surface, for example, a paraboloid, and a perturbed surface is then superimposed on the base surface [9]. The perturbed surface is defined in terms of a series expansion function such as Zernike polynomials or cubic spline functions. At each iterative stage the far field is calculated at a number of sample points and compared to the objective function. This is used to change the coefficients of the expansion until a better match is achieved. Physical optics is used to obtain the far field in each calculation. Typically the expansion functions used are cubic splines because they provide the best fit for rapidly varying surfaces due to their local nature. Zernike polynomials are also used to define the surface. TICRA's POS and GRASP commercial software programs [10] are used as industry standards for synthesis and analysis of shaped reflector contoured beam antennas. A flowchart for the contoured beam design is illustrated in Figure 2.6.

The performance of the contoured beam is sometimes defined in terms of gain area product (GAP). An ideal GAP for a uniformly illuminated coverage area with no radiation outside the coverage is 41,253 [4π steradians = $4*\pi*(180/\pi)*(180/\pi)$]. This is not practical because it requires an infinite size reflector with no spillover and other losses. The GAP for contour beams is generally in the range of 6,000 to 25,000 and is highly dependent on the reflector size relative to wavelength (D/λ), bandwidth of operation, the coverage shape, cross-polar isolation, and sidelobe isolation outside the coverage region. The gain in GAP is the minimum gain over the coverage region, which usually occurs near the edge of the coverage. The gain variation over the coverage region designed with uniform weighting depends on the reflector size and the coverage area and varies in the range of 1.0 to 4.0 dB. A larger reflector tends to have more uniformly shaped contoured beams with less gain variation over the coverage region and hence provides better edge-of-coverage gain.

Ku-Band Contoured Beam Design

Examples of the contoured beam design for Ku-band FSS and BSS payloads are discussed in this section. Two coverage regions, the continental United States (CONUS) and South America (SA), are considered from a geostationary satellite at a 101° W orbital slot. The coverage areas on ground as seen from a geostationary satellite are 13 square degrees for CONUS and 26.45 square degrees for SA. The reflector is illuminated with a corrugated feed having a minimum illumination of 14 dB at Tx frequencies and 19 dB at Rx frequencies. Such high illumination tapers

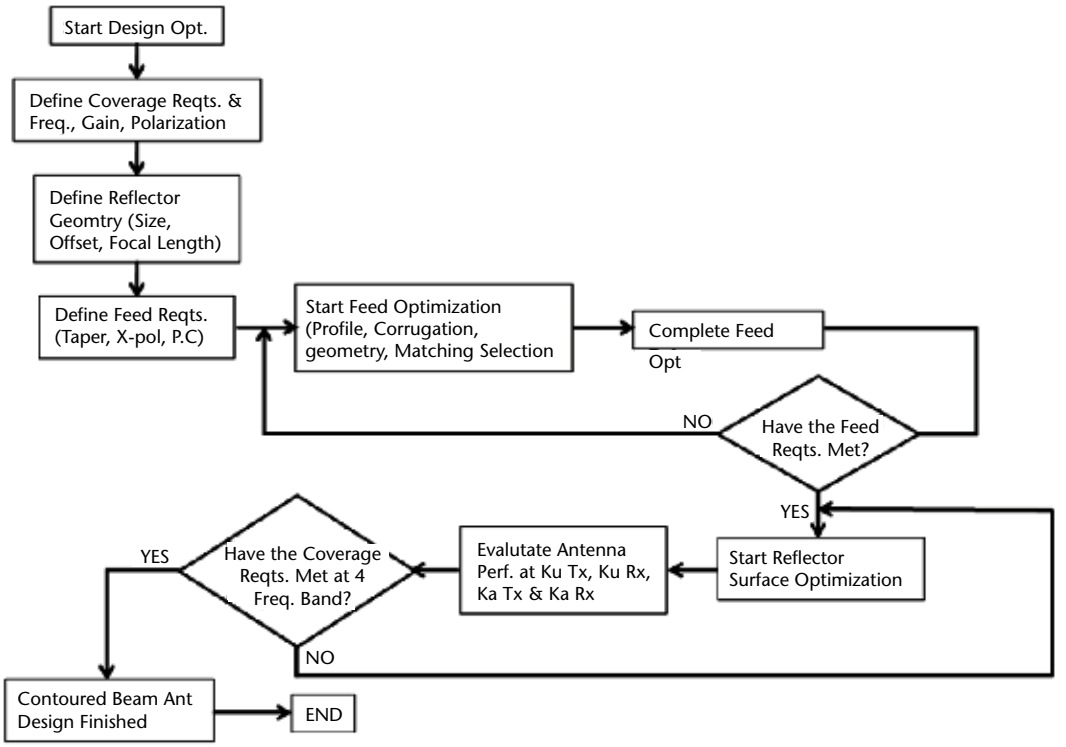

Figure 2.6 Flowchart describing an exemplary iterative procedure for designing multiband contoured beams.

(exceeding 14 dB) are required in order to minimize the spillover losses. Various reflector sizes are considered in this parametric design and results are summarized here for the following FSS and BSS design cases:

Case 1: FSS antenna with Tx band of 10.95 to 12.2 GHz and Rx band of 14.00 to 14.50 GHz.

Case 2: BSS antenna with Tx band of 12.20 to 12.70 GHz.

Synthesized gain contours of Case 1 over CONUS coverage are shown for transmitting and receiving in Figures 2.7 and 2.8, respectively. Minimum coverage gain is 31.7 dBi while the peak gain is 33.1 dBi. There is a 1.4 dB gain variation over the coverage region. Larger variation can be expected if copolar isolation of more than 27 dB needs to be achieved over another spatially isolated region outside CONUS (for example, Brazil). The minimum coverage gain will also be reduced by about 0.5 to 1.0 dB if stringent copolar isolation requirements need to be met. Gain contours over South America for Case 1 are shown in Figures 2.9 and 2.10 for the transmitting and receiving bands, respectively. Minimum gain over the coverage is 29.25 dBi. This gain is 2.45 dB lower than the CONUS gain due to the larger cover region (the SA coverage area is about 2.03 times larger than the CONUS coverage area). Gain variation is about 1.25 dB for this case with no sidelobe constraints.

Case 2 BSS transmit-only design results with weighted coverage gain requirements over the CONUS and SA regions are shown in Figures 2.11 and 2.12, respectively. The weighted coverage requirements are needed to compensate for the larger

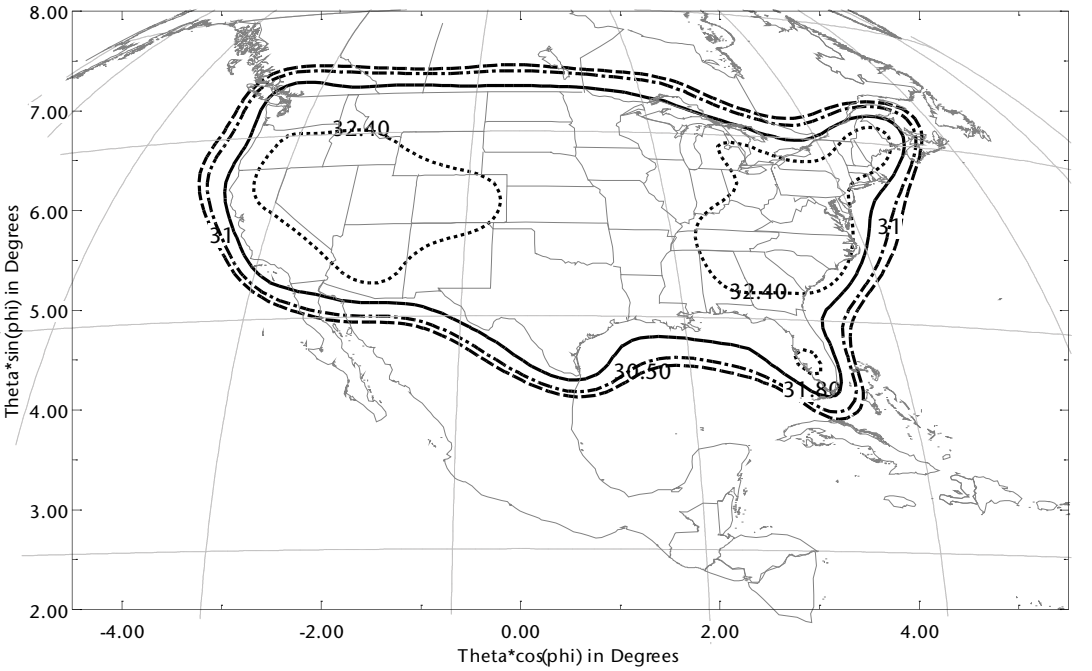

Figure 2.7 Computed gain contours of contoured beam for CONUS coverage at Tx band. (Case 1: 2.3m shaped reflector antenna is designed over FSS Tx and Rx bands.)

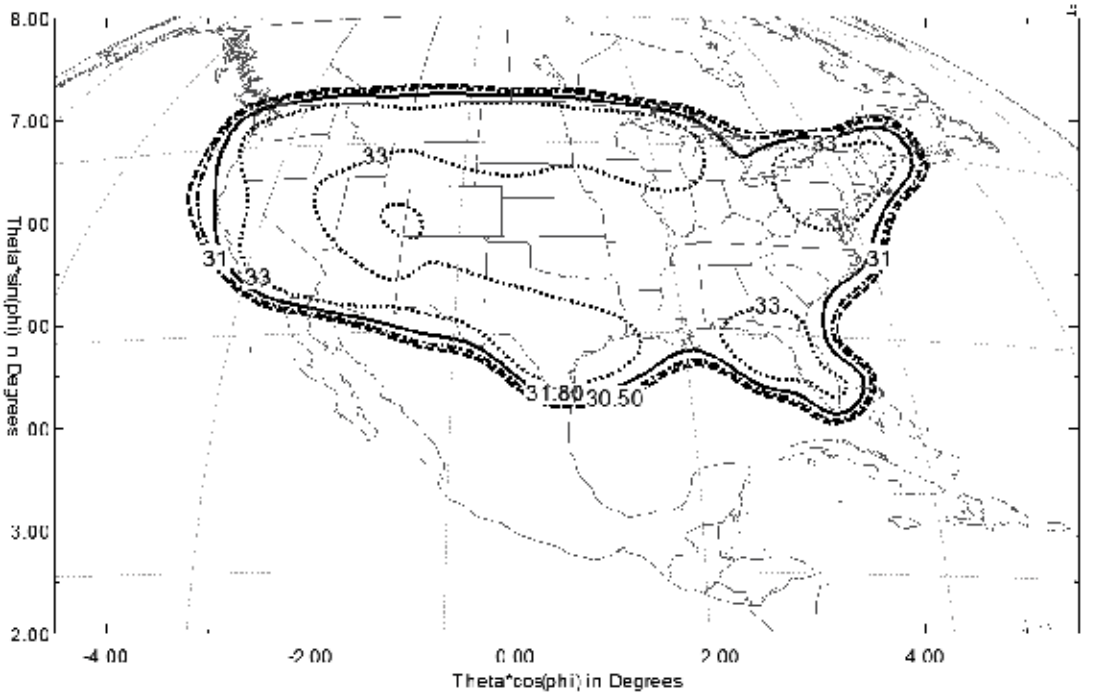

Figure 2.8 Computed gain contours of contoured beam for CONUS coverage at Rx band. (Case 1: 2.3m shaped reflector antenna is designed over FSS Tx and Rx bands.)

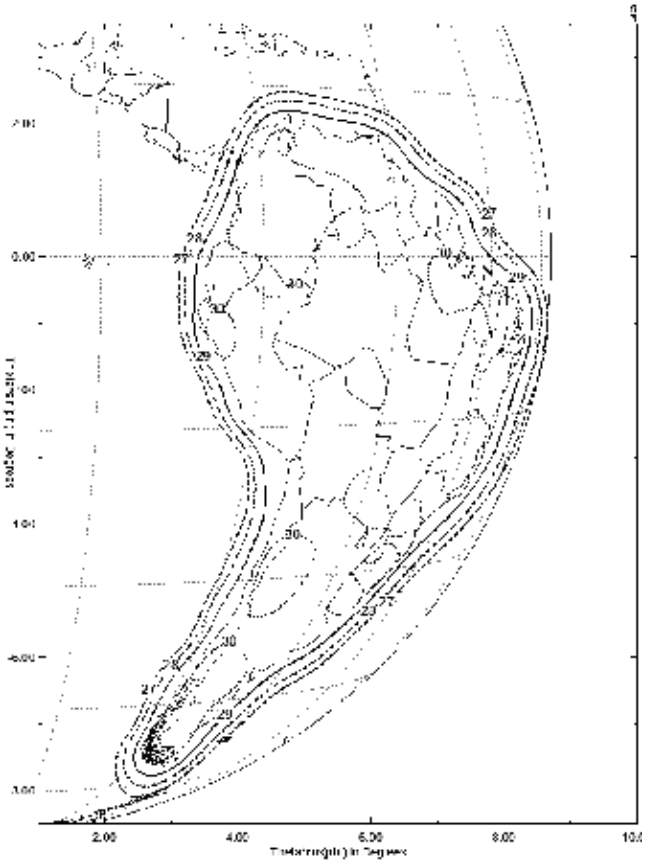

Figure 2.9 Computed gain contours of contoured beam for SA coverage at Tx band. (Case 1: 2.3m shaped reflector antenna is designed over FSS Tx and Rx bands.)

atmospheric attenuation in the rain regions of the coverage with higher antenna gain requirements. Peak to edge variations are larger in the weighted coverage cases (>4 dB) as seen from the plots. Typical cross-polar isolation contours of the FSS antenna with LP are shown in Figure 2.13, which illustrates worst-case cross-polar discrimination (XPD) values of better than 23 dB. The XPD is defined as the worst-case ratio of the copolar signal to the cross-polar signal evaluated at each point within the coverage region. Higher XPD values can be achieved by using longer a *F/D* of the reflector and shaping the surface for XPD suppression.

The GAP depends primarily on the reflector diameter (D/λ) and the coverage area and to a certain extent on the shape of the coverage. Tables 2.1 and 2.2 summarize results for several designs carried out for the CONUS and SA areas at the C-band and Ku-band using the reflector diameter as a variable. The GAP varies from 6,222 to 15,575 for C-band designs and varies from 13,303 to 23,037 for Ku-band designs. The following conclusions are drawn from the results shown in the table and the industry experience:

- The GAP or minimum coverage gain is proportional to the reflector diameter D/λ. Larger reflectors have better shaping capability with lower peak to edge gain variation.

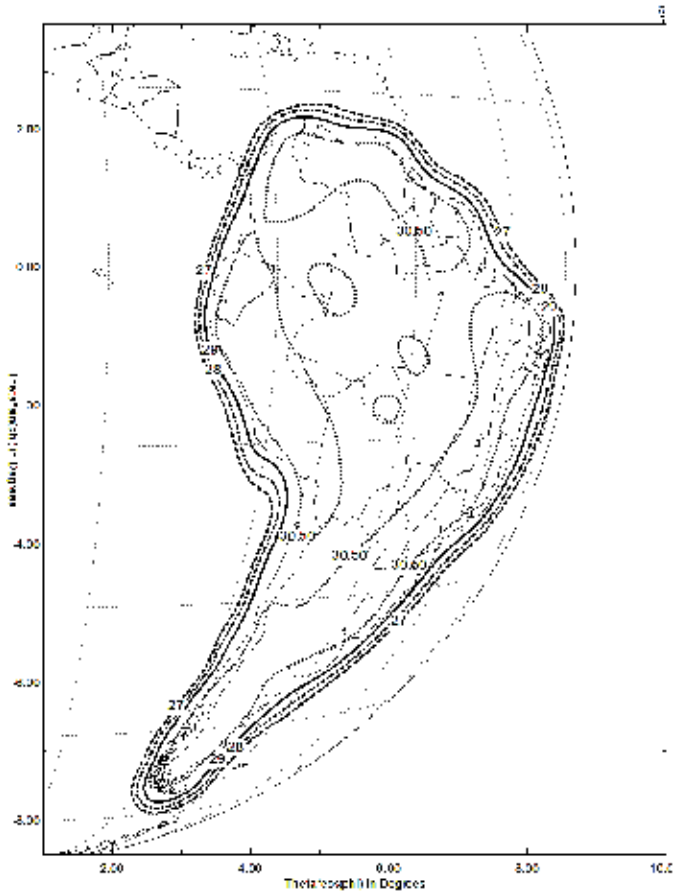

Figure 2.10 Computed gain contours of contoured beam for SA coverage at Rx band. (Case 1: 2.3m shaped reflector antenna is designed over FSS Tx and Rx bands.)

- Larger coverage areas have increased GAP due to better shaping potential with more uniform directivity contours over the coverage and with less peak to edge variation in directivity.
- The GAP also depends on the amount of cross-polar suppression within the coverage region. Note that a single-offset reflector produces significant cross-polar levels for linear polarization (about 20 dB XPD) and needs to be suppressed by about 15 dB in order to meet the cross-polar isolation requirements of better than 30 dB. This suppression can be achieved through shaping of the reflector surface at the expense of lowering the minimum coverage area directivity by about 0.5 dB.
- The GAP also depends on the copolar isolation requirements outside the coverage region. It depends on the spatial distance of other service regions from the designed coverage and the area that needs to be suppressed. The EOC gain impact could be anywhere from 0.0 to 1.0 dB.

Results of the minimum edge of coverage gain as a function of the reflector size are shown in Figure 2.14. Practicing engineers are often interested in how much gain improvement can be made for contoured beam designs if a different reflector

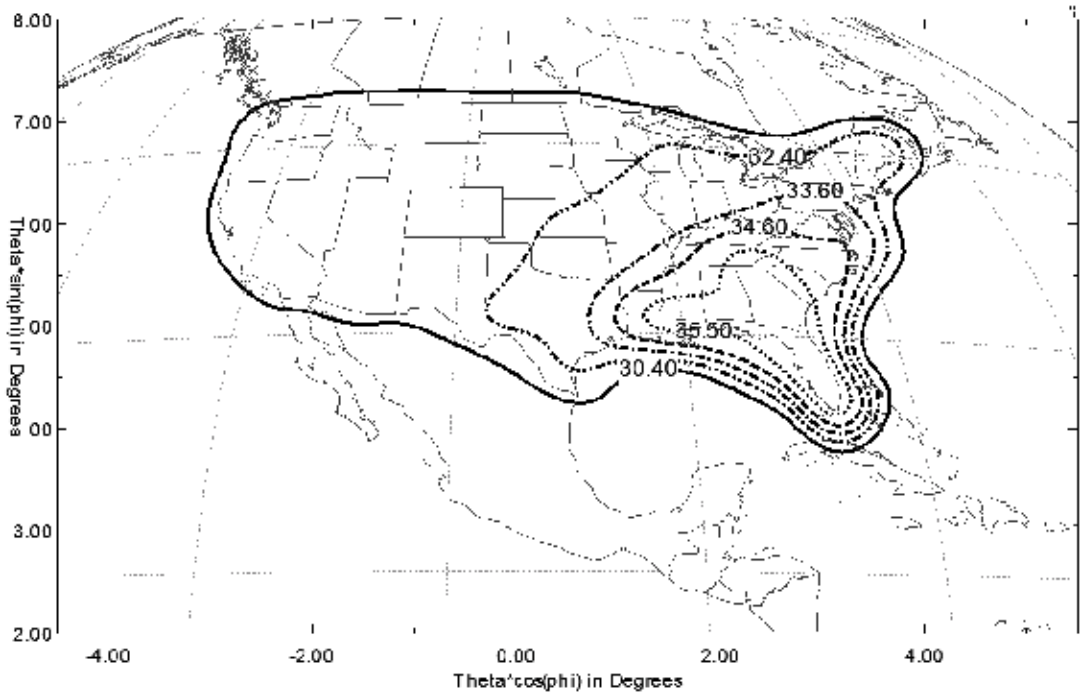

Figure 2.11 Computed gain contours of weighted contoured beam for CONUS coverage at Tx band. (Case 2: 2.3m shaped reflector antenna is designed over BSS Tx bands.)

size is shown. Figure 2.15 shows the EOC gain delta as a function of the reflector size. The gain values with a 1.0m reflector size are used as a reference in the plot shown in Figure 2.15.

2.2.2 Dual-Offset Gregorian Reflectors

The dual-reflector shaped Gregorian is widely used for both FSS and BSS applications. It gives better cross-polar performance relative to a single shaped reflector for linear polarizations. Also, it has two reflector surfaces that provide better shaping potential of the contoured beams. It is well known that an offset dual-reflector antenna can be designed to eliminate geometrical optics cross-polarization in the main reflector aperture [11, 12]. The feed horn is typically larger since it illuminates the smaller subreflector with an illumination taper of better than 15 dB. The subreflector is generally in the near-field region of the feed horn and near-field analysis of the feed horn is required through the use of spherical harmonics. Diffraction effects may increase the cross-polarization in a practical offset dual-reflector system, especially one with small subreflectors. To avoid this, an enlarged subreflector size is often used, particularly at C-band frequencies. Typical sizes of Gregorian reflectors are:

- Deployable reflectors: 2m and higher main and 0.7m sub (at Ku-band).
- Earth deck: 0.8 to 1.5m main and 0.45m sub (Ku-band).
- Steerable beam applications: 0.8 to 1.0m main and 0.4m sub.

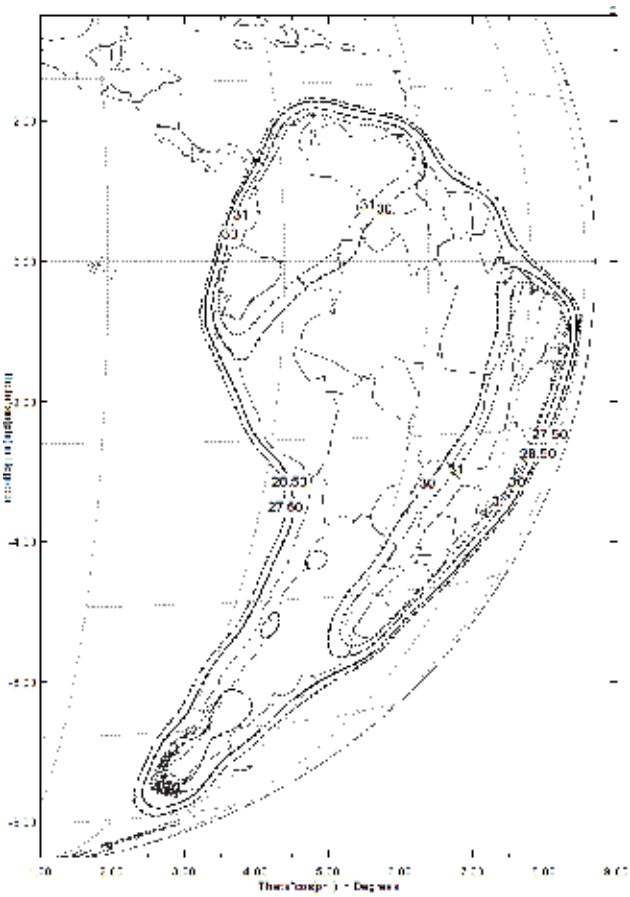

Figure 2.12 Computed gain contours of weighted contoured beam for SA coverage at Tx band. (Case 2: 2.3m shaped reflector antenna is designed over BSS Tx bands.)

The geometry of the dual-offset Gregorian antenna that satisfies the low cross-polar Mizuguchi condition [11] is illustrated in Figure 2.16. The geometry of the system can be specified by the following six parameters:

- Diameter of the main reflector, D.
- Focal length of the main reflector, F.
- Half distance between the focal points of the subreflector, C.
- Eccentricity of the sub reflector, e.
- Angle between the main reflector and subreflector axis, α.
- Angle between the subreflector and feed axis, β.

The Mizuguchi condition, for unshaped reflectors, is given by:

$$M\tan(\alpha/2) = \tan(\beta/2) \tag{2.9}$$

where M is the magnification and is related to the eccentricity as follows:

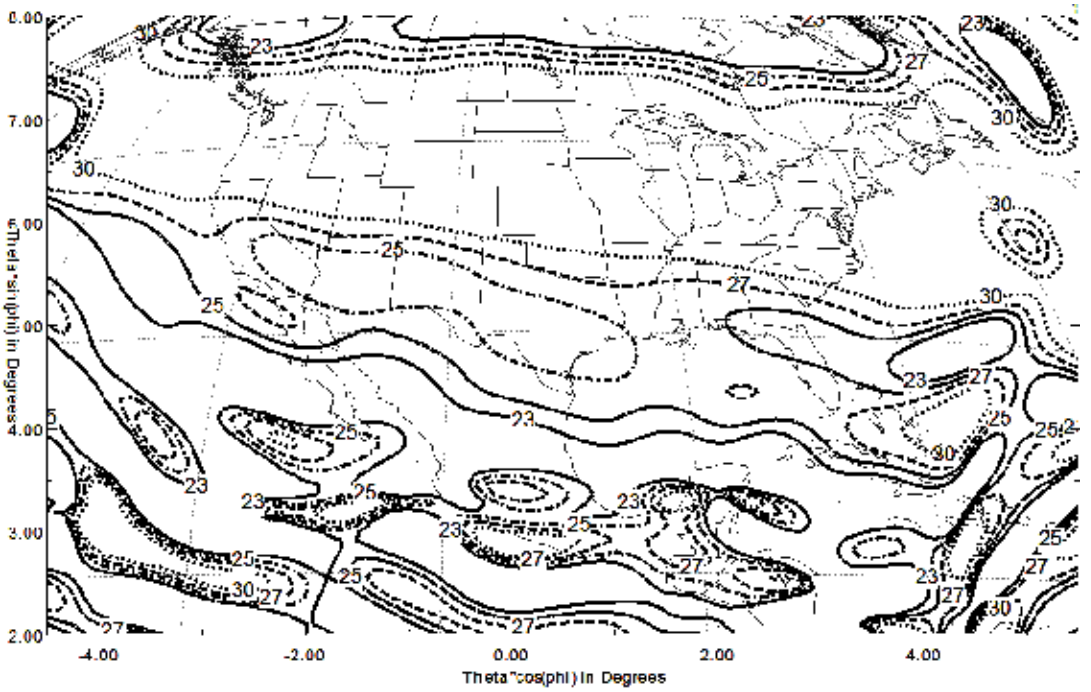

Figure 2.13 Cross-polar isolation contours of FSS Ku-band antenna over the CONUS area. XPD is better than 23 dB and could be improved to 25 dB by shaping the surface with XPD constraints.

Table 2.1 Contoured Beam Design Results at C-Band (EOC Directivity as a Function of Reflector Diameter)

Reflector Diameter (m)	*D/λ*	*CONUS (13 sq. degrees) C-Band*		*South America (26.45 sq. degrees) C-Band*	
		EOC Directivity (dBi)	*GAP*	*EOC Directivity (dBi)*	*GAP*
1.0	12.33	26.8	6,222	25.2	8,758
1.3	16.03	27.8	7,833	26.0	10,530
1.5	18.50	28.4	8,994	26.3	11,283
1.8	22.20	28.8	9,862	26.9	12,955
2.0	24.67	29.0	10,326	27.3	14,205
2.3	28.37	29.4	11,323	27.5	14,874
2.6	32.07	29.6	11,856	27.7	15,575

$$M = (e+1)/(e-1) \tag{2.10}$$

For ellipsoidal subreflectors, e is less than 1.

Any reflector shaping will typically degrade the cross-polar performance, even when the starting geometry satisfies the Mizuguchi condition.

The cross-polar discrimination (XPD) contours computed at the Ku-band with a 2.3m main reflector size over the CONUS and SA are plotted in Figures 2.17 and

Table 2.2 Contoured Beam Design Results at Ku-Band (EOC Directivity as a Function of Reflector Diameter)

Reflector Diameter (m)	*D/λ*	*CONUS (13 sq. degrees) Ku-Band*		*South America (26.45 sq. degrees) Ku-Band*	
		EOC Directivity (dBi)	*GAP*	*EOC Directivity (dBi)*	*GAP*
1.0	36.50	30.1	13,303	27.9	16,309
1.3	47.45	30.7	15,274	28.4	18,299
1.5	54.75	31.0	16,366	28.7	19,608
1.8	65.70	31.2	17,137	28.9	20,532
2.0	73.00	31.4	17,945	29.1	21,499
2.3	83.95	31.7	19,228	29.25	22,255
2.6	94.90	31.9	20,135	29.4	23,037

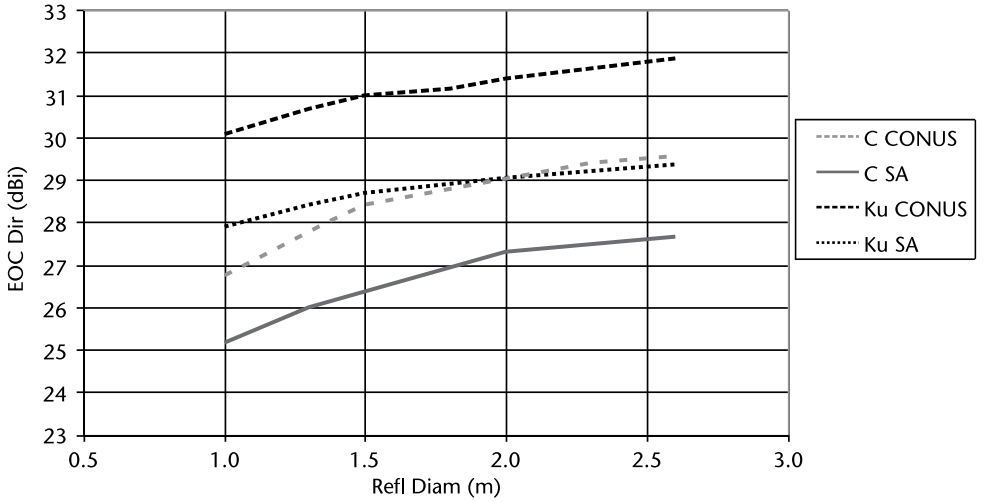

Figure 2.14 EOC directivity variation with the reflector size for different contoured beam designs.

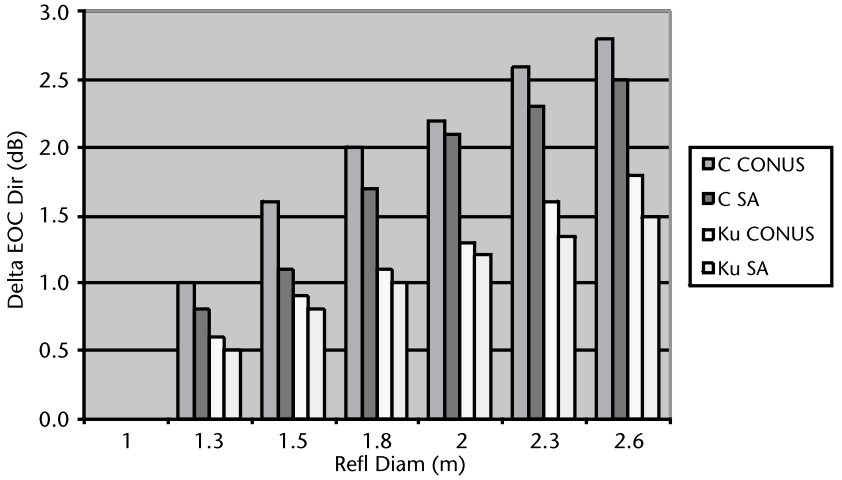

Figure 2.15 EOC directivity improvement with increased reflector size for different contoured beam designs.

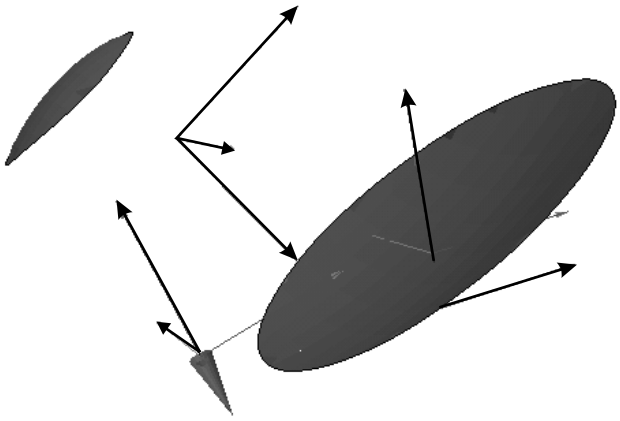

Figure 2.16 Geometry of the dual-offset shaped Gregorian antenna for FSS and BSS applications. The subreflector is typically oversized to minimize diffraction effects.

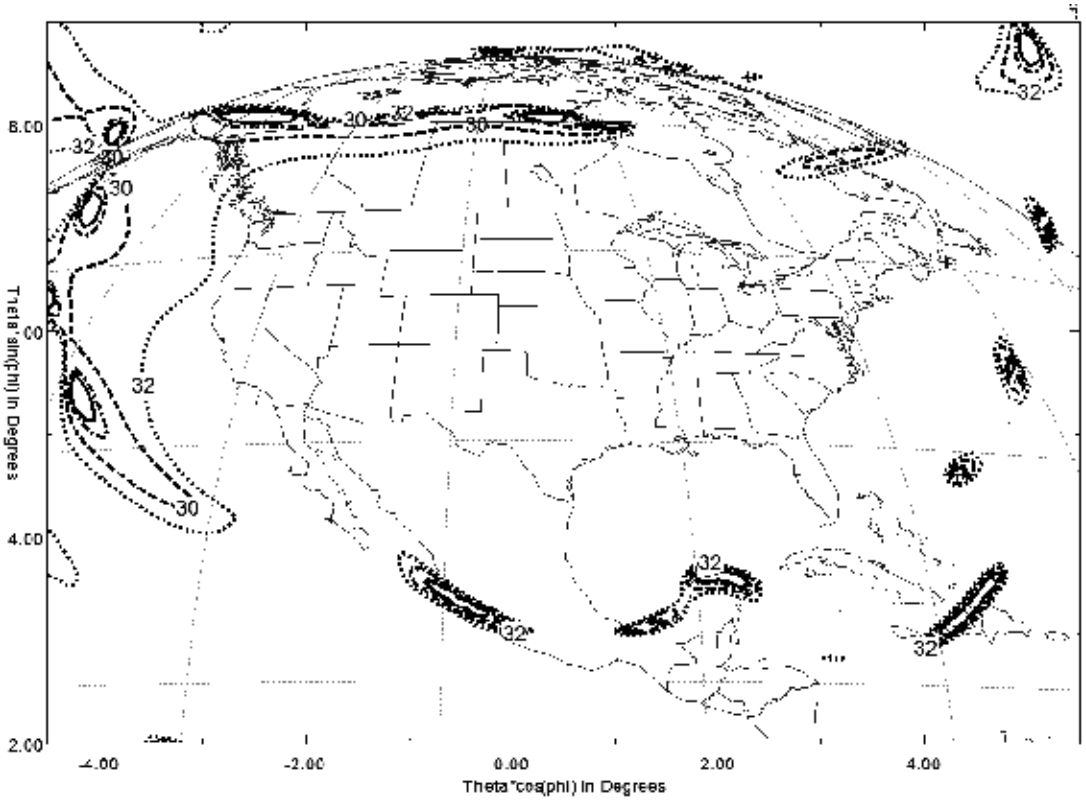

Figure 2.17 Cross-polar discrimination contours of a dual-offset shaped Gregorian antenna over the CONUS area at the Ku-band Tx using a 2.3m main reflector. The XPD is better than 33 dB over the CONUS area.

2.18, respectively. The XPD levels are better than 33 dB for both coverage regions. The copolar patterns are similar to the single shaped reflector patterns shown in Figures 2.7 and 2.9. The XPD with Gregorian is about 10 dB better than the single-offset reflector for linear polarizations.

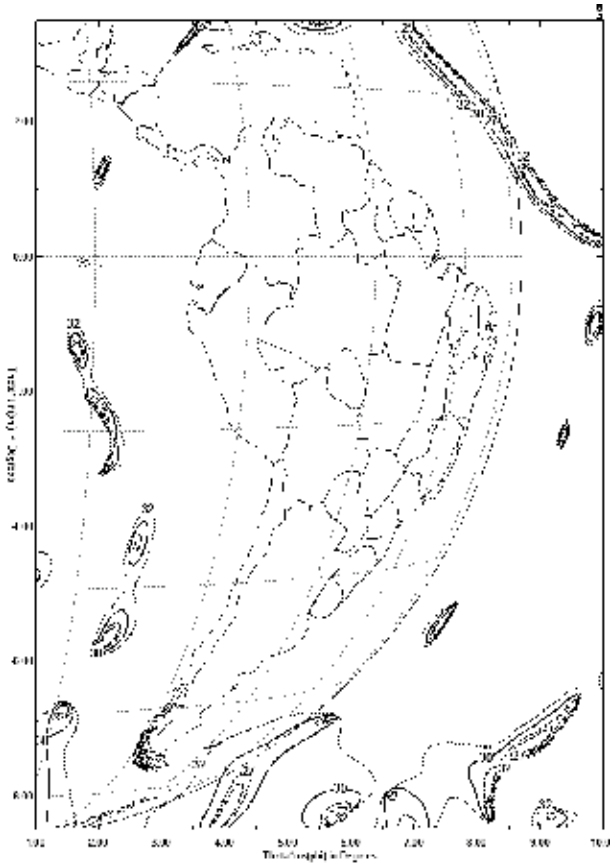

Figure 2.18 Cross-polar discrimination contours of a dual-offset shaped Gregorian antenna over the SA area at the Ku-band Tx using a 2.3m main reflector. The XPD is better than 33 dB over SA.

2.2.3 Gridded-Reflector Antennas

Gridded reflectors are used for dual-linear polarization FSS applications at C-band and Ku-band. The first dual-gridded reflector antenna was developed by SPAR Aerospace Limited and was successfully flown on an RCA Satcom satellite in 1975 and later by Hughes Aircraft Company. It employs two different reflectors with overlapped apertures where the front reflector surface is gridded and the grids are laid in such a fashion that they are parallel to either vertical or horizontal polarizations and the back reflector is either gridded (orthogonal to the front-reflector grids) or solid graphite supporting the opposite sense of linear polarization relative to the front reflector. Each of the two reflectors is illuminated by its own feed horn or horn arrays. The main features and advantages of the gridded reflectors over solid reflectors are as follows:

- Provides twofold frequency reuse through orthogonally polarized (VP and HP) beams.
- The antenna assembly consists of two reflectors with orthogonal grids sharing a common aperture.

- The cross-polar levels of the antenna are lowered by at least 15 dB relative to solid reflectors.
- The reflector assembly comprises two Kevlar honeycomb laminated reflector shells, one in the front and the other in the back, which are connected by an outer ring. Polarization grids are formed by etching copper from the Kapton face sheets.
- VP and HP reflectors employ different focal lengths to spatially separate the two reflector shells and also isolate the two feeds/feed-arrays.

Three types of gridded reflectors are used for satellite communications:

- Dual-gridded parabolic reflectors fed with two feed arrays and corresponding beam-forming networks (DGP).
- Dual-gridded shaped reflectors with two feed horns (DGS).
- Gridded front and solid graphite back shaped reflectors with two feed horns (GS).

The concept of DGP is illustrated in Figure 2.19. Each reflector surface supports one linear polarization (VP or HP) and is illuminated by its own feed array to shape the beam. By optimizing the feed array amplitude and phase excitations, contoured beams are generated. It is common to use rectangular horns for linear polarization applications, since they have excellent cross-polar levels and also allow the number of feeds in the array to be minimized. The horn elements are

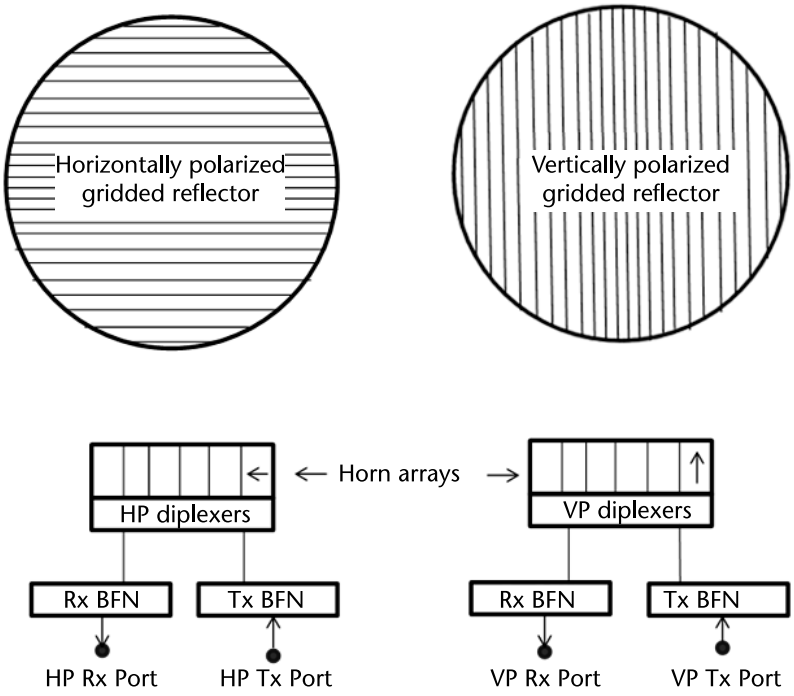

Figure 2.19 Dual-gridded parabolic (DGP) reflector antenna concept.

attached to diplexers in order to separate the Tx and Rx frequency bands. The two outputs of the diplexers for each array element are combined through two separate beam-forming networks, one for transmitting and the other for receiving. The BFNs are implemented in waveguide (Ku-band) or TEM-line media (C-band) using hybrid couplers, loads, and line lengths in order to achieve the desired excitations. Key aspects of the BFN are high power handling, low insertion loss, and minimal variation of excitations over frequency and over temperature range.

The DGS antenna configuration is similar to the one shown in Figure 2.19 with the exception that the reflectors are shaped surfaces instead of parabolic and each feed array is replaced with a feed horn. Advantage of the DGS relative to DGP is that it eliminates the need for BFNs, which results in a significant mass, cost, and schedule savings, lower losses, and better RF performance. The GS configuration is similar to DGS, but the rear surface is solid graphite surface instead of gridded surface. The GS gridded reflectors are most widely used nowadays for fixed satellite services at C-band and Ku-band.

The gridded reflector antennas have two major types: laterally displaced reflectors and a rotated reflector system, as illustrated in Figure 2.20. The laterally displaced system has partially overlapped reflectors and the rotated reflector system has completely overlapped reflectors that are more compact. The feeds of the rotated reflector system are also rotated, providing more spacing between the two horns/horn arrays. The rotated reflector system is most commonly used in spacecrafts due to compact size. The RF analysis of the gridded reflectors needs to take into account the various contributions from the two reflectors, two feeds, and two polarizations for detailed copolar and cross-polar analyses. This is illustrated in Figure 2.21 and the various contributions are explained here:

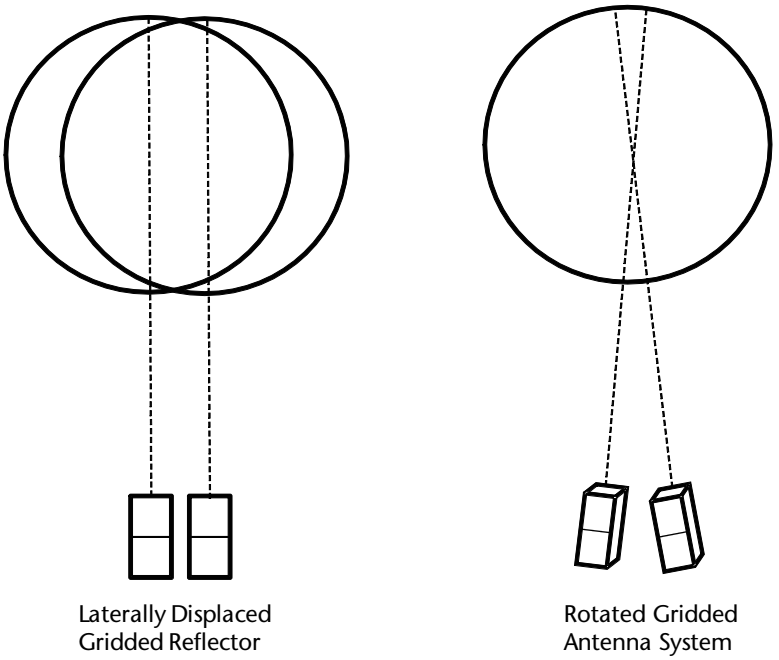

Figure 2.20 Illustration of gridded reflector antenna types. Laterally displaced antenna has partial overlap of the two apertures while the rotated system has complete overlap.

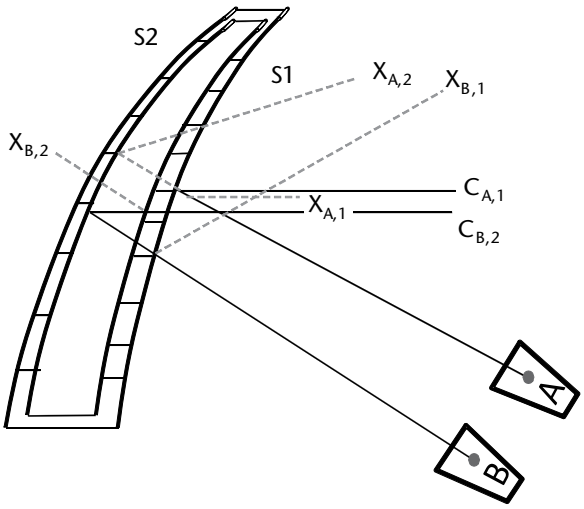

Figure 2.21 Copolar and cross-polar ray mapping of a gridded reflector antenna system.

$C_{A,1}$: copolar signal from feed A reflected from reflector surface S_1.

$X_{A,1}$: cross-polar signal from feed A reflected from surface S_1 with grid suppression of >12 dB.

$C_{B,2}$: copolar signal from feed B reflected from rear reflector surface S_2.

$X_{B,1}$: cross-polar signal from feed B reflected from surface S_1 without any suppression. This signal has the same polarization of $C_{A,1}$ and typically scans outside the coverage due to feed separation. It is important to keep this contribution far outside the coverage so that it does not impact the copolar contours from feed A. Increased feed separation keeps this signal within the coverage region low.

$X_{A,2}$: cross-polar signal from feed A reflected from rear surface S_2 without any suppression. This signal has the same polarization as $C_{B,2}$, but scans outside the coverage region due to spatial separation of the two feeds. It is important to keep this contribution far outside the coverage region with sufficient separation between the two feeds.

$X_{B,2}$: cross-polar signal of feed B leaking through the front shell and reflected back from the front shell out to the rear reflector. This contribution is very low and negligible.

The geometry of the gridded reflector to determine the minimum thickness between the two surfaces is shown in Figure 2.22. The spacing between the shells' "T" is determined based on satisfying the following conditions:

$$(Z_1 - Z_3) - (F_1 - F_2) + T > 0 \tag{2.11}$$

$$(Z_2 - Z_4) - (F_1 - F_2) + T > 0 \tag{2.12}$$

The Z variables in the above equations can be obtained using:

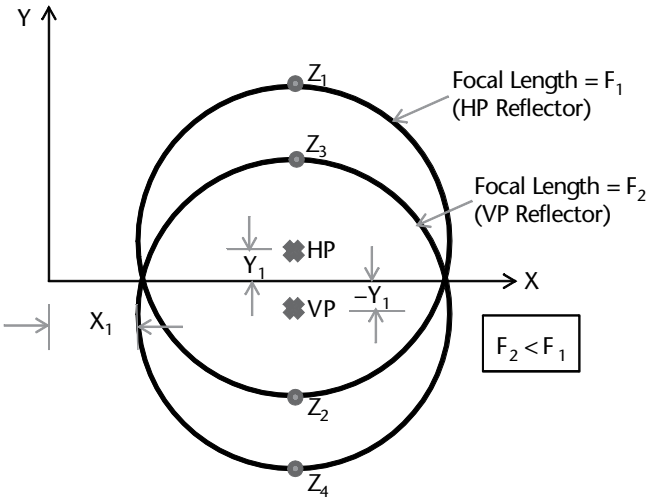

Figure 2.22 Geometry of the gridded reflector antennas to determine spacing between the reflector shells.

$$Z_1 = \frac{(X_1 + 0.5D)^2 + (0.5D + Y_1)^2}{4F_1} \tag{2.13}$$

$$Z_2 = \frac{(X_1 + 0.5D)^2 + (0.5D - Y_1)^2}{4F_1} \tag{2.14}$$

$$Z_3 = \frac{(X_1 + 0.5D)^2 + (0.5D - Y_1)^2}{4F_2} \tag{2.15}$$

$$Z_1 = \frac{(X_1 + 0.5D)^2 + (0.5D + Y_1)^2}{4F_2} \tag{2.16}$$

where D is the projected diameter of the reflector and the variable T also depends on the mechanical design of the dual-shell gridded reflector assembly. The two shells are attached through a ring structure for mechanical design integrity. The choice of the front and rear reflector polarizations depends on where the antenna is placed on the spacecraft. The antenna with worst-case polarization is kept in the back in order to get cross-pol suppression protection from the front shell grids. For an east-west offset when the antenna is deployed in the east or west side of the spacecraft, the cross-pol is the worst for the HP reflector; hence, it is placed on the rear and the VP reflector is placed in the front (closer to the feeds). For antennas placed on the deck of the spacecraft with a north-south offset, the cross-pol is the worst for the VP reflector, so it is placed in the back and HP reflector is in the front shell.

The key design parameters are the grid parameters. These are the width of the strips (W), the center-to-center spacing between adjacent strips (S), and the thickness of the grids (t). The thickness of the grids is a trade-off between minimizing

the thermal distortions and maximizing the conductivity. It is typically selected as follows:

$$T \geq 10S_d \tag{2.17}$$

where S_d is the skin depth of the conducting material. The value of T is about 0.0003 in. for copper grids at Ku-band frequencies. The width of the strips W and the spacing between adjacent strips (S) are selected based on minimizing the insertion loss and maximizing the cross-pol suppression. The spacing S depends on the highest frequency of operation and is determined using 20 strips per wavelength. The spacing and width of girth are given as:

$$\frac{S}{\lambda_b} = 0.05 \text{ and } W/S = 0.30$$

The insertion loss due to the grids is about 0.015 dB and cross-pol suppression is 38 dB. The parametric curves showing the loss versus W/S for various grid spacings are given in Figure 2.23. The cross-polar suppression values as a function of W/S for various S/λ values are plotted in Figure 2.24. These plots are based on an analysis by Chan and Hyjazie [13]. In some cases, the industry uses identical grid configuration for the C- and Ku-bands in order to reduce cost and process-related issues. A compromise design with $W = 0.012$ in., $S = 0.040$ in., and $T = 0.0003$ in. is used for both C-band and Ku-band FSS gridded reflectors. This particular design translates into S/λ values of 0.0125 at C-band and 0.048 at Ku-band. The loss values (signal leakage plus two-way loss) are 0.01 dB at C-band and 0.03 dB at Ku-band. The cross-polar suppression values are 46 dB at C-band and 38 dB at Ku-band.

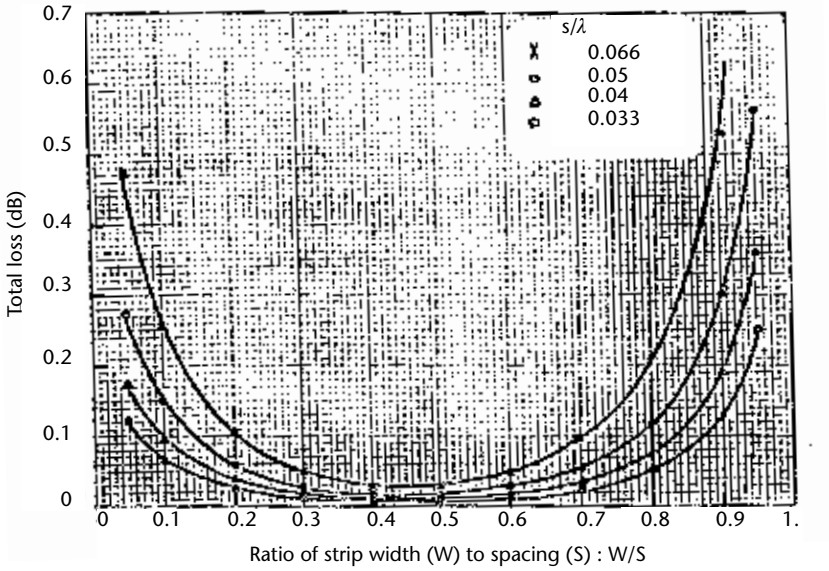

Figure 2.23 Insertion loss of gridded reflector antenna as a function of width to spacing ratio W/S. Parameter of the curves is S/λ.

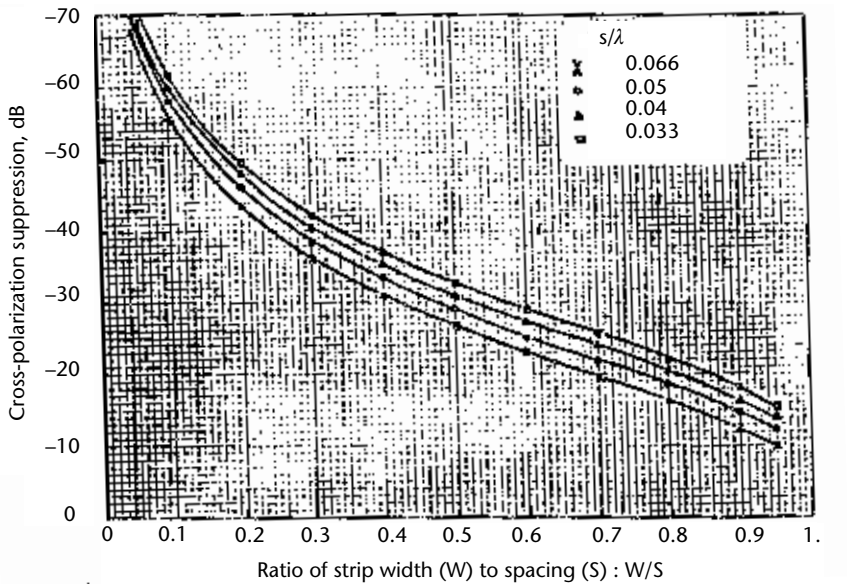

Figure 2.24 Cross-polar suppression (or isolation) of gridded reflector antenna as a function of width to spacing ratio W/S. Parameter of the curves is S/λ.

The cross-polar isolation plots using a gridded reflector antenna (GS) designed for contoured beam application over the CONUS and SA coverage regions, respectively, are shown in Figures 2.25 and 2.26 for Ku-band Tx frequencies. A 2.3m reflector size at Ku-band FSS frequencies is used for this application. The minimum

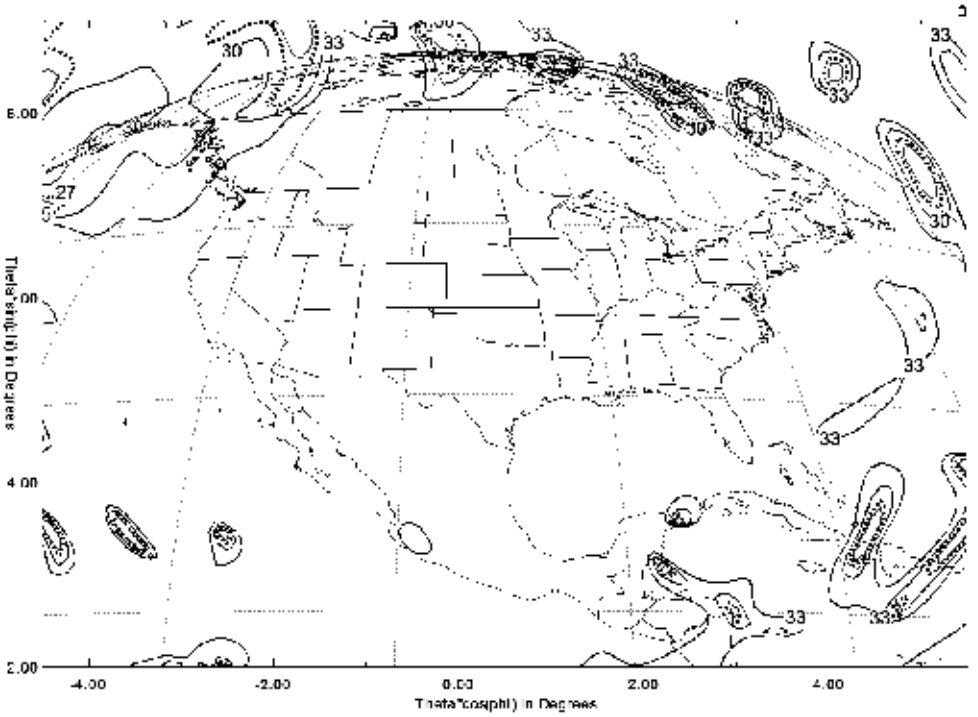

Figure 2.25 Computed cross-polar discrimination (XPD) contours of gridded reflector antenna at Ku-band Tx frequency over CONUS coverage. XPD is better than 34 dB.

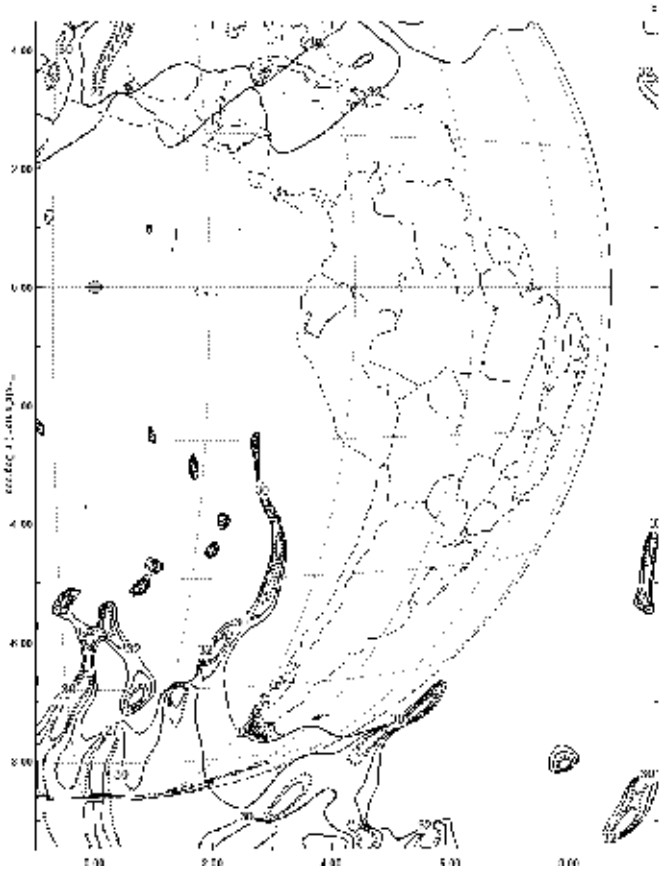

Figure 2.26 Computed cross-polar discrimination (XPD) contours of gridded reflector antenna at Ku-band Tx frequency over SA coverage. XPD is better than 34 dB.

cross-polar isolation over the CONUS region is better than 34 dB. Excellent cross-pol performance is achieved due to the gridded reflector system.

2.3 Multiple-Beam Antennas

2.3.1 Introduction

During the past decade, there has been a tremendous growth in the use of multiple-beam antenna (MBA) technology for satellite payloads for both commercial and military communications. MBAs have been successfully used on several satellite applications, including:

- Mobile satellites (M-Sat, Inmarsat, Thuraya, ACeS, MSV, Iridium, etc.).
- Direct broadcast satellites (DTV-4S, Echostar-10, DTV-7S, Echostar-14, etc.).
- Personal communication satellites (Anik-F, Viasat-1, Jupiter-1, etc.).
- Military communication satellites (WGS, MUOS, DSCS, etc.).

The need for MBA technology arises from the fact that it allows several-fold reuse of the limited frequency spectrum in order to increase the effective bandwidth of the communication payloads and hence the satellite capacity. A large number of overlapping high-gain spot beams are used over the desired coverage region from the satellite orbit instead of a single low-gain coverage beam. The available bandwidth is divided into a number of sub-bands and each of the sub-bands is reused over several spot beams that are spatially isolated within the desired coverage region on the ground as seen by the satellite. As a result, the effective spectrum is much larger than the available spectrum by a factor that is called the *frequency reuse factor* (FRF). The FRF depends on the number of beams and the number of sub-bands. If the sub-bands are all uniform, then the FRF is given simply as the ratio of number of beams used and the number of sub-bands. For nonuniform sub-bands and/or nonuniform layout of beams, the FRF is more precisely given by:

$$FRF = \frac{\sum_{j=1}^{M} \sum_{i=1}^{N} \Delta F_i^j}{\sum_{j=1}^{M} \Delta F^j} \tag{2.18}$$

where i denotes the beam number in each sub-band j, and F_i^j denotes the bandwidth associated with each beam within the sub-band. FRF is a function of the beam size, coverage region, and the number of sub-bands. Although theoretically the FRF could be a very large number, typical values for the FRF are in the range of 4 to 40 for communication satellites. The limiting factors for the FRF are often the spacecraft power limitations and the difficulty associated with accommodating several large reflector antennas on the spacecraft bus within the stowed volume of the launch vehicles

Figure 2.27 illustrates the differences between conventional contoured beam coverage and multiple-beam coverage over the continental United States from a geostationary satellite. The contoured beam coverage shown in Figure 2.27(a) has a typical minimum coverage area directivity (without antenna losses) of about 30 dBi and has no frequency reuse (FRF = 1). The contoured beam coverage is commonly achieved through the use of a single antenna—either a single off-set reflector or a dual-reflector offset antenna where the reflector(s) surface profiles are shaped in order to synthesize a beam whose contour matches with the desired coverage on ground. The multiple-beam coverage shown in Figure 2.27(b) employs 68 overlapping spot beams to contiguously cover the CONUS. The beams are arranged in a hexagonal lattice with adjacent beam spacing of 0.52° and a beam diameter of 0.6° at the triple-beam crossover point, defined as the crossover point of the three adjacent beams forming the equilateral triangle. The minimum coverage area directivity is 45 dBi, which is a 15 dB improvement (31.6 times more power) over the conventional antenna design. In addition, the MBA offers a significant increase in the spectral utilization. FRF values of about 22.67, 17, and 9.71 could be achieved with three-cell, four-cell, and seven-cell reuse schemes, respectively.

The main advantages of using an MBA instead of contoured beam antenna are as follows:

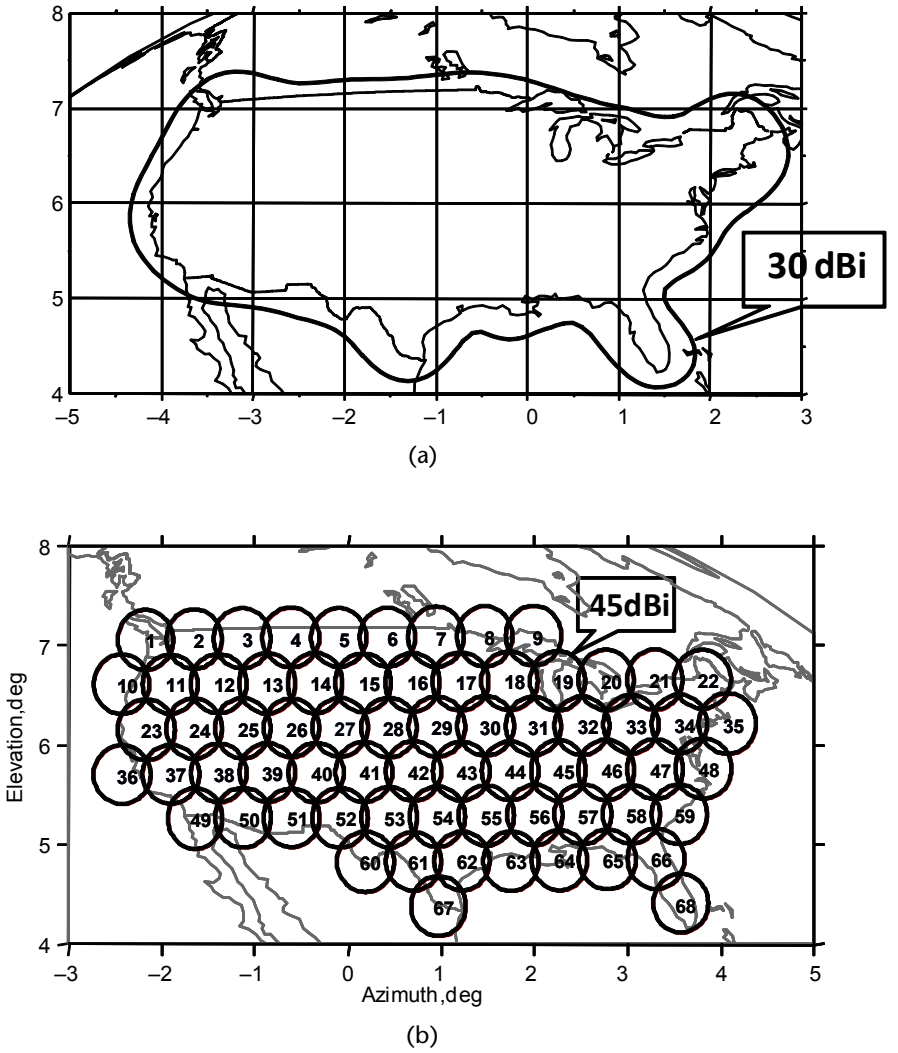

Figure 2.27 Illustration of CONUS coverage (a) with a conventional contour beam antenna design, and (b) with a multiple spot beam antenna design. Coverage shown is from a geostationary satellite.

- A significant increase in antenna gain results from the use of smaller spot beams. This in turn increases EIRP on the downlink and increases G/T on the uplink.
- The effective spectral bandwidth increases by several-fold due to reuse of the frequency channels (sub-bands) over several spot beams.
- Much smaller ground terminals can be used to communicate with the satellite.

Apart from these advantages, it also offers satellite operators the ability to provide a significant capacity increase to their users. This is equivalent to a single satellite launch instead of several satellite launches, which provides significant cost savings.

The coverage region for most applications needs to be contiguously covered by the satellite with multiple spot beams. A hexagonal grid layout is usually preferred due to the need for tight packing of the beams. The optimum beam diameter for a circular coverage region with uniformly sized beams, the total number of beams required for the coverage region, and the adjacent beam spacing are given approximately as:

$$\theta_0 = 0.6155\theta_c / N \tag{2.19}$$

$$N_T = 1 + 3N(N+1) \tag{2.20}$$

$$\theta_s = 0.866\theta_0 \tag{2.21}$$

where θ_0 is the beam diameter at the triple-beam crossover level, N is the number of rings of the hexagonal beam layout excluding the central beam, N_T is the total number of beams, θ_c is the coverage diameter in degrees, and θ_s is the spacing between adjacent beams. A typical beam layout for an MBA providing global coverage from a geostationary satellite is shown in Figure 2.28. The MBA has 91 overlapping spot

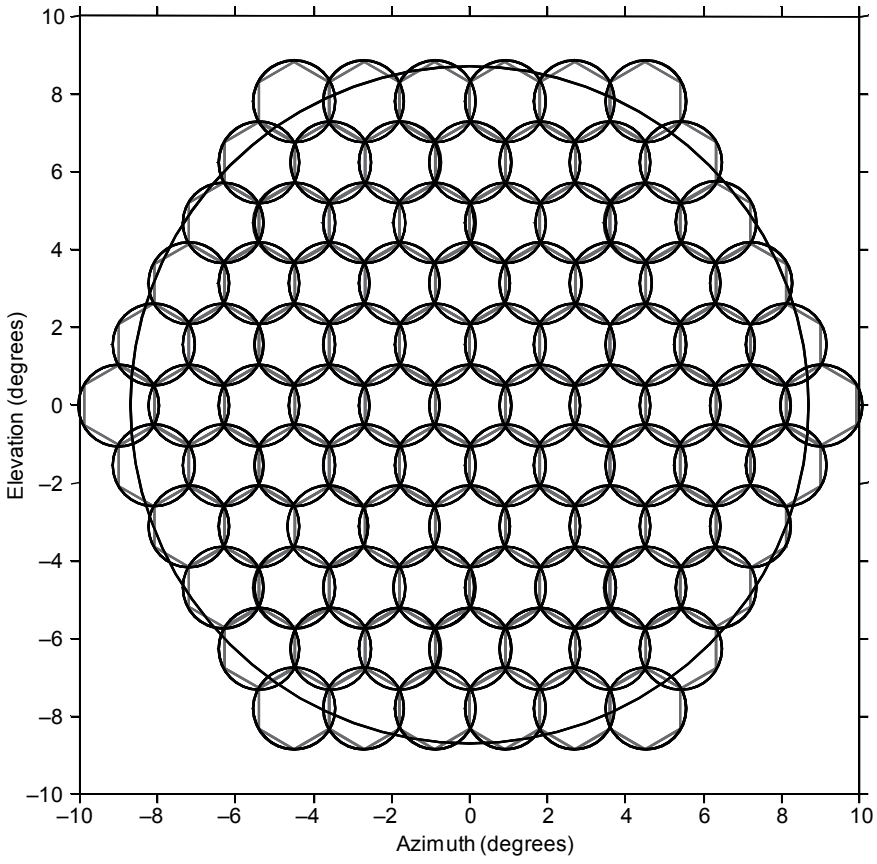

Figure 2.28 Illustration of global coverage of an MBA with 91 overlapping beams.

Table 2.3 Beam Size Versus Number of Beams for a Global Coverage MBA

Beam Diameter (θ_0)	*Beam Spacing* (θ_s)	*Number of Rings* (N)	*Total Number of Beams* (N_T)
0.7	0.606	15	721
0.8	0.693	14	631
0.9	0.779	12	469
1.0	0.866	11	397
1.1	0.953	190	331
1.2	1.039	8	271
1.4	1.212	6	217
1.8	1.559	5	127
2.0	1.732	5	91
2.4	2.078	4	91
2.8	2.425	4	61

beams with a hexagonal beam layout. The spacing between adjacent beams is 1.732 deg and the beam diameter at triple-beam crossover is 2.0 deg. Table 2.3 shows the design variables for a global coverage with a 17.6-deg diameter.

2.3.2 Frequency Reuse Schemes

Various frequency reuse schemes could be used for MBAs. These include regular three-cell, four-cell, seven-cell, or N-cell and also hybrid schemes that employ different schemes over different regions of the coverage region. The generic N-cell frequency reuse scheme involves repeating the frequency cell in a regular pattern such that any particular frequency cell has all of the beams repeated with uniform spacing. There is also a nonuniform cell reuse method that is more appropriate for direct broadcast satellite (DBS) applications, which will be discussed later. Figures 2.29, 2.30, and 2.31 illustrate various reuse schemes and the number of apertures needed. The left side of these figures denotes the beam layout on the ground, the Arabic letters in these beams denote the frequency cell, and the Roman numbers denote the aperture number used for these beams. The apertures are mostly implemented as reflectors, but also as lenses in certain applications. Multiple beams are implemented either using a single aperture or multiple apertures depending on the applications. The number of apertures in a multiaperture design depends on the size and stowage accommodation on the spacecraft bus.

The nonuniform cell reuse and hybrid cell reuse schemes are used primarily for DBS services and in certain cases for personal communication satellite (PCS) services. For DBS satellites, the satellite provides downlink beams for local channel broadcast where the designated market areas (DMAs) are nonuniform in size and spacing. One or more channels serve each beam that covers few DMAs.

Figure 2.32 shows typical coverage of the CONUS using nonuniform beams with nonuniform cell reuse. Smaller beams with higher gain are used in the East Coast beams, whereas large beams are used in the Midwest and in Western beams where the rain rate is low. Thirty-four beams cover the CONUS area with more

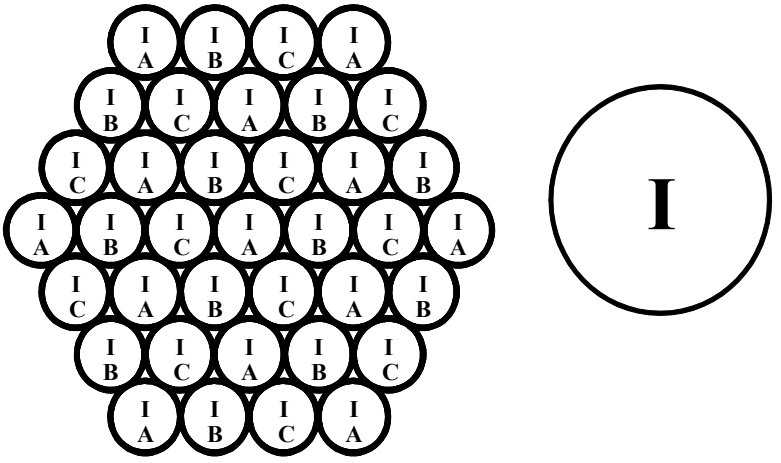

Figure 2.29 Illustration of three-cell frequency reuse scheme using a single aperture. The left side denotes the beam layout on the ground, the Arabic letters in these beams denote the frequency cell, and the Roman numbers denote the aperture number used for these beams. The right side of the figure shows the number of apertures.

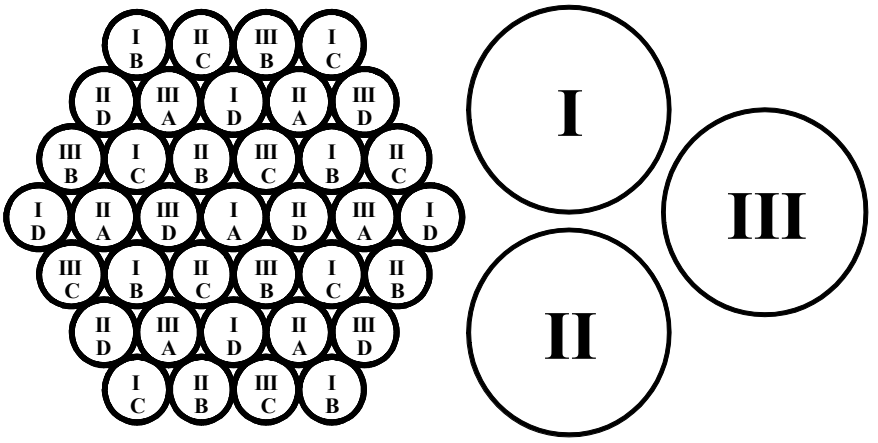

Figure 2.30 Illustration of a four-cell frequency reuse scheme using three apertures. The left side denotes the beam layout on the ground, the Arabic letters in these beams denote the frequency cell, and the Roman numbers denote the aperture number used for these beams. The right side of the figure shows the number of reflector apertures.

than 200 DMAs. The contour levels shown are in EIRP. The beam spacings among the reuse beams are designed to meet the copolar isolation *C/I* of better than 13 dB for most cases. The design employs multiple reflectors in which each reflector is fed with multiple feeds of nonuniform size and with nonuniform spacing in order to achieve various beam sizes.

The design challenge here is to cover the majority of DMAS with fewer beams, allocate DMAs and frequency channels to the individual beams, allocate beams to the reflectors, maximize the copolar isolation among beams re-using the same frequency channels, maximize the cross-polar isolation, allocate beams to the ground hubs, and to maximize the frequency re-use factor. Other challenges invovle selection of beam sizes and spacing among re-use beams for the non-uniform beam layout over the coverage region.

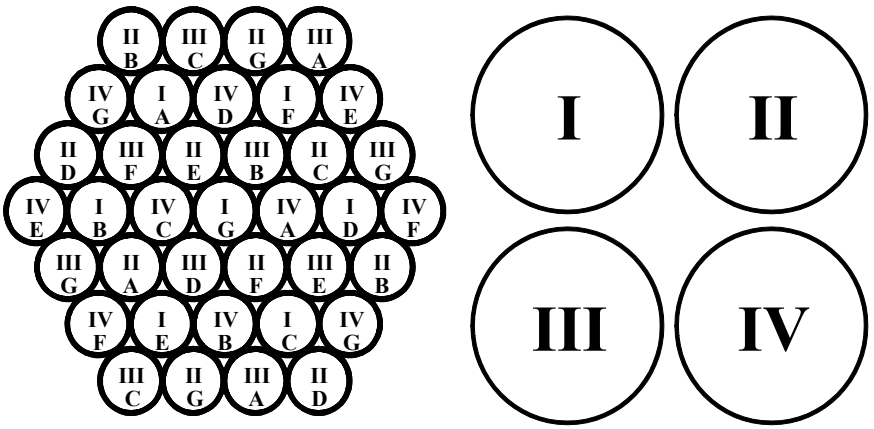

Figure 2.31 Illustration of a 7-cell frequency reuse scheme using four apertures. The left side denotes the beam layout on the ground, the Arabic letters in these beams denote the frequency cell, and the Roman numbers denote the aperture number used for these beams. The right side of the figure shows the number of reflector apertures.

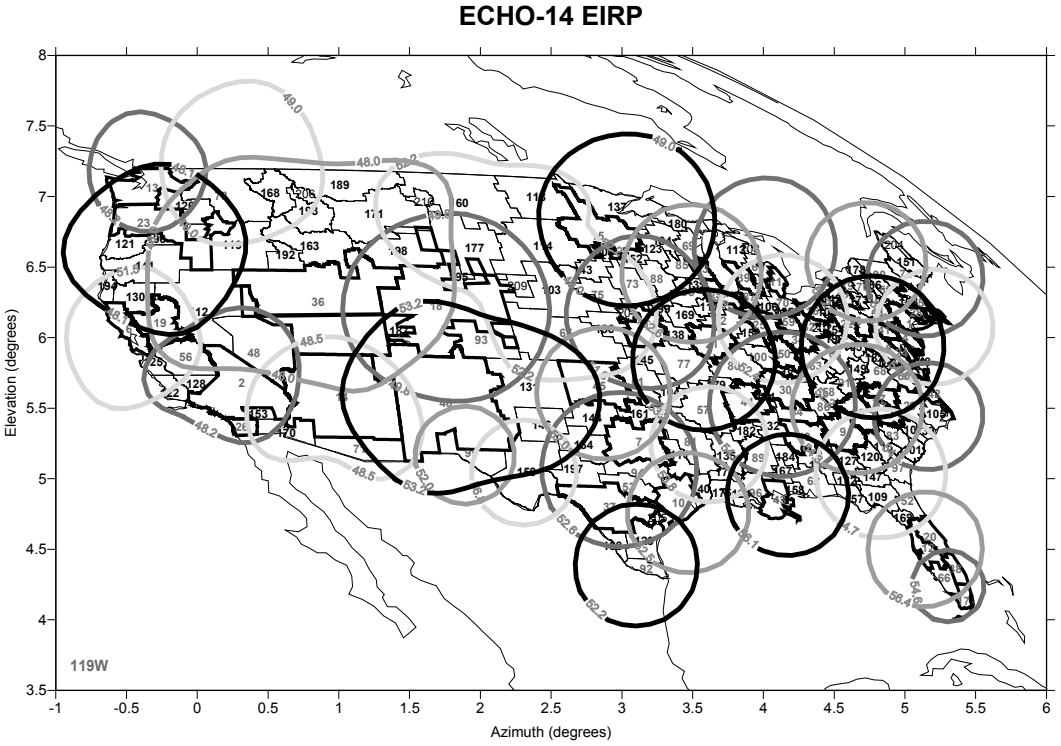

Figure 2.32 Typical coverage of local channel DBS satellite with 34 nonuniform beams covering about 200 DMAs over the CONUS. Each spot beam provides coverage to multiple DMAs.

In contrast, hybrid cell reuse for PCS services employs a uniform beam layout over the coverage region, but uses more channels on the beams requiring higher capacity/bandwidth and fewer channels requiring lower capacity in order to best utilize the available spectrum [14]. This is illustrated in Figure 2.33 where there are 46 beams covering the CONUS from the 105°W orbital slot. The letters within

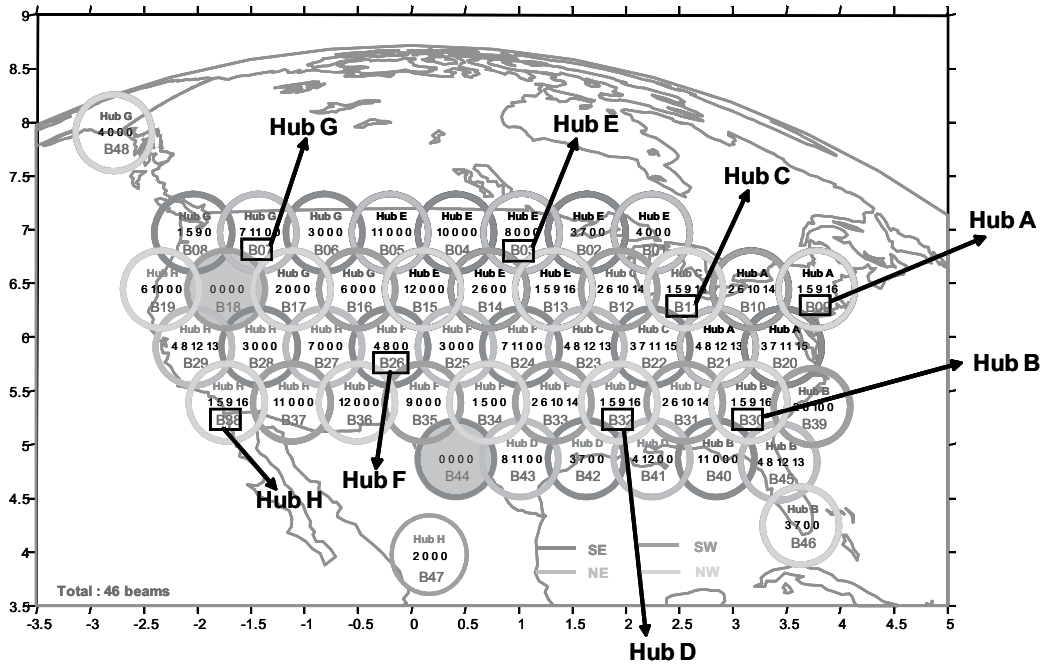

Figure 2.33 CONUS, Hawaii, and Alaska coverage with 46 uniform spot beams using a hybrid cell frequency reuse scheme. The number of channels per beam varies from one to four depending on the population density.

each beam denote the frequency cells. The densely populated East Coast beams of the CONUS are covered with close to three- or four-cell reuse, while the sparsely populated Midwest and Western region beams employ higher cell reuse such as seven or more. It employs eight ground hubs, providing a frequency reuse factor of about 13.

One advantage of this design is that the satellite capacity is weighted based on the population density or operator's requirement and is not wasted in coverage regions with low population density. The East Coast and some of the West Coast beams that cover high population density areas use a large number of cells in each beam and Midwest beams employ one or two cells in each beam.

2.3.3 Multiple-Beam Antenna Types

Practical antenna systems that are suitable and often employed for multiple-beam applications include the following designs:

- Single-reflector antenna with single element per beam;
- Single-reflector design with overlapping feed clusters;
- Multiple-reflector design with single feed per beam;
- Offset hyperbolic reflector with single feed per beam;
- Single-lens antenna;
- Multiple-lens antennas;

- Direct radiating array with passive beam-forming network;
- Phased-array antenna.

The use of a nonfocusing aperture such as a concave hyperboloid with feed located at the imaginary focal point has been explored by Ingerson [15]. Large magnification factor (M) values of greater than 20 are required for practical systems combined with large feed horns. The gain of this imaging system is dictated by M and the feed gain, but is generally independent of the reflector size. Disadvantages of this design are limited scan, higher sidelobe levels with scan, and significantly lower gain than parabolic reflectors. This antenna is not suitable for MBA applications and hence not utilized on practical systems.

The lens antennas have been employed in the past in a DSCS military program employing waveguide lenses. A number of waveguides are densely packed to form the lens and each waveguide length is varied to create a uniform phase front at the radiating side of the lens. Dielectric lenses have also been considered in the past. The main difficulty with these thick lenses is the large mass associated with them. Zoning techniques have been employed to minimize the mass, but the zoning drastically reduces the bandwidth capability of the lens antenna [16]. Dielectric lenses are not considered suitable or space applications because of the electrostatic discharge (ESD) associated with the dielectrics where surface and bulk charges could be developed over the lifetime of the satellite causing multipaction or power breakdown of the payloads. Waveguide and dielectric lenses have fallen out of favor recently due to their increased mass, limited bandwidth, accommodation issues on the spacecraft, poor return loss, and environmental issues such as ESD and power handling.

Direct radiating arrays with passive BFNs are employed when the number of beams is limited and the beams are fixed on ground. On the other hand, phased-array antennas are being employed for space applications requiring agile beams on ground, global coverage, and anti-jamming capability. For commercial satellite applications, reflector MBAs are preferred and most widely used due to their lower mass, lower cost, higher gain, lower losses, mature technology, and simpler accommodation and less power dissipation on the spacecraft.

Single-reflector MBAs are used primarily at low frequencies such as UHF, L-band, and S-band. At these frequency bands, large deployable mesh reflectors ranging from 5 to 22m have been successfully used for mobile satellite communications such as Thuraya, ACeS, Inmarsat, MSV, SkyTerra, and most recently MUOS. Single-reflector MBAs can be implemented using a single feed per beam or multiple feeds per beam (referred to as the *enhanced feed concept*).

A single-feed-per-beam MBA with a single reflector is simpler in terms of hardware since it does not require a beam-forming network. However, the element size required is small and is typically of the order of a wavelength in order to achieve good overlap of about 3 to 4 dB below the beam peak among the adjacent beams. The feed spacing/size depends on the *F/D* ratio of the reflector and is given approximately as:

$$\frac{d}{\lambda} \approx 1.25\left(\frac{F}{D}\right) \tag{2.22}$$

For large deployable reflectors, the F/D ratio is around 0.6 to 0.7 and the feed spacing is around 0.75 to 0.88λ to achieve the desired overlap among adjacent beams. Figure 2.34 shows typical performance of the MBA as a function of feed spacing/size. For a single-reflector MBA with small spacing of about 0.8λ, the beam overlap is very good (less than 3 dB) but the beam efficiency is very low at about 45% and suffers from high sidelobe levels of about 19 dB (below the beam peak). On the other hand, a multiaperture MBA with four reflectors provides alternate beams from the same reflectors, allowing the feed horn spacing/size to increase twice as much compared to a single-aperture MBA. This combined with the large F/D of about 1.0 allows for feed spacings in the range of 2.0 to 3.0λ. For such large horns, each reflector will be illuminated more optimally with a taper of about 10 to 15 dB, increasing the antenna efficiency to about 78% and lowering the sidelobe levels to about 25 dB. Beam overlap is better than 17 dB among the beams generated from the same reflector, allowing reuse of the same frequency for all of the beams.

Because of the low efficiency and high sidelobe levels of a single-feed-per–beam system, single-reflector MBAs employ feed clusters that typically use seven horns per beam. This is called the *enhanced feed concept* [17], in which adjacent beam centers correspond to the feed horn centers, but each beam is broadened and illuminated more efficiently due to the use of the feed cluster. This concept is illustrated in Figure 2.35 where the basic feed concept employs seven horns to illuminate a reflector and produces seven beams in the far field. In the enhanced feed concept, 19 feed horns are used with the reflector to generate seven optimal beams that are larger than the element beams. Each beam is generated using seven horns and produces an optimal illumination on the reflector. Therefore, the composite beams of the MBA are larger than the element beams with higher gain (or efficiency), lower sidelobe levels, and improved overlap among the beams.

The beam layout of the two concepts is illustrated in Figure 2.36. The beams use with the enhanced feed concept are larger than those used with the single-feed concept and there is better overlap among the beams. A single large offset reflector

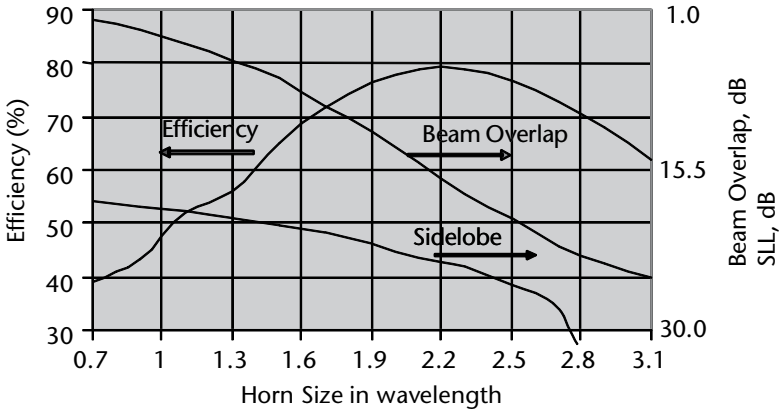

Figure 2.34 Single-reflector MBA RF performance as a function of feed horn size (single horn per beam).

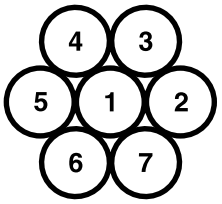

BEAM #	HORN #
1	1
2	2
3	3
4	4
5	5
6	6
7	7

(a)

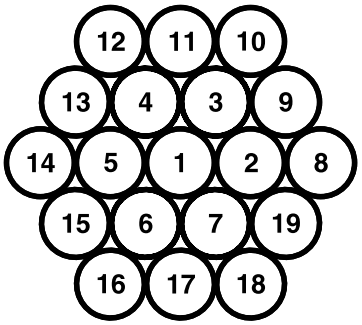

BEAM #	HORN #
1	1, 2, 3, 4, 5, 6, 7
2	1, 2, 3, 7, 8, 9, 19
3	1, 2, 3, 4, 9, 10, 11
4	1, 3, 4, 5, 11, 12, 13
5	1, 4, 5, 6, 13, 14, 15
6	1, 5, 6, 7, 15, 16, 17
7	1, 2, 6, 7. 17, 18, 19

(b)

Figure 2.35 Illustration of feed layout for single-reflector MBA: (a) basic feed concept using single feed per beam, and (b) enhanced feed concept using septet horn array per beam.

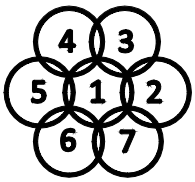

(a)

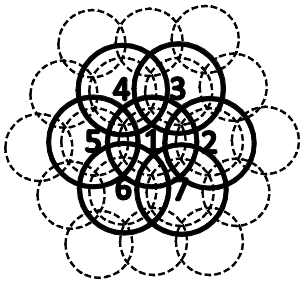

(b)

Figure 2.36 Illustration of beam layout using the two concepts: (a) single element concept and (b) enhanced feed concept. The enhanced feed concept employs seven feeds for each beam while maintaining the adjacent beam spacing identical to the basic feed concept.

being fed with multiple feeds and combined through a matrix power amplifier and low-level beam-forming network is typically used for generating multiple overlapping beams over the desired coverage regions.

Figure 2.37 is a block diagram of the MBA using a single reflector antenna. The Tx MBA shown in Figure 2.37 employs a low-level dividing network that distributes the individual RF signals from each beam to a number of output ports that are eventually connected to a number of feed elements within the large feed array through the matrix power amplifier (MPA) network. The reason for using an MPA is for distributed amplification where each amplifier is shared among multiple beams and for redundancy in case of amplifier failures. The MPA comprises an input hybrid matrix (IHM), power amplifiers, and an output hybrid matrix (OHM), which is connected to bandpass filters and the radiating elements of the feed array. The feed elements illuminate an offset, parabolic mesh reflector providing multiple overlapping beams on the ground, as illustrated earlier in Figure 2.28.

Single-reflector MBAs also employ diplexed antennas serving both Tx and Rx functions as illustrated in Figure 2.38. The antenna is common to both uplink and downlink frequencies. The diplexers behind each element separate the two frequency bands, thus providing the necessary isolation. The Tx path employs the MPA approach as discussed above, and the Rx path employs LNAs behind each diplexer and a low-level BFN for combining a number of closely placed element signals into a number of overlapping beams. The Rx path could also use the MPA approach for LNA redundancy followed by the low-level beam-forming network. The challenge in this approach is to realize the diplexer with large isolation of the Tx frequencies in the Rx path in order to minimize the PIM levels. However, the diplexed design has significant cost and mass advantages compared to the use of separate Tx and Rx antennas.

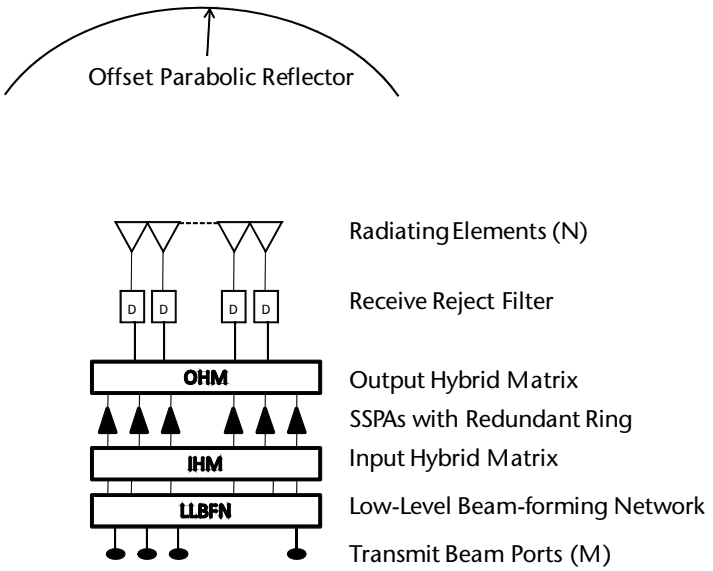

Figure 2.37 Block diagram of typical antenna system for mobile satellite services for the Tx function.

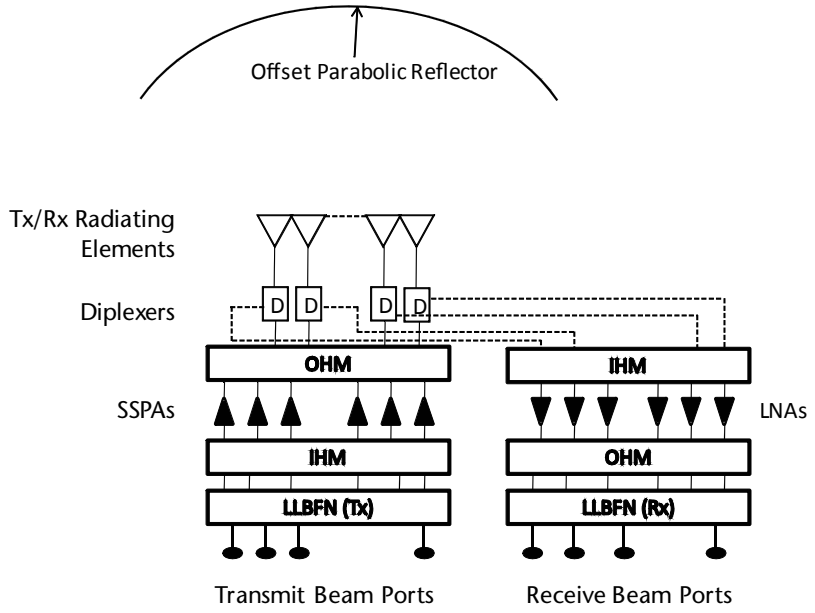

Figure 2.38 Block diagram of a diplexed antenna system for mobile satellite services using a single mesh reflector.

2.3.4 Design and Analysis of Multiple-Beam Reflector Antennas

The design and relevant analysis of reflector antennas for multiple-beam applications are discussed in this section. Key design objectives for the MBAs are:

- Maximize the minimum gain over the spot beam coverage;
- Maximize the copolar isolation (C/I);
- Maximize the cross-polar isolation;
- Minimize the scan loss.

These objectives can be met closely by making the proper design choices for the MBA's reflector and feed systems. A single-reflector antenna with a single feed per beam requires small horns (about 1 wavelength in diameter) in order to achieve high adjacent beam overlap. This results in a low illumination taper on the reflector and increased spillover losses. As a result, the gain values are about 2 to 3 dB lower than what could be achieved with a larger horn with optimal illumination. A single-reflector MBA with overlapping feed clusters improves the gain values, but requires a low-level beam-forming network to provide the element sharing among a number of beams (typically three or seven) and beam-combining functions.

Multiple reflector design with a single feed per beam employs either three or four reflectors on the practical systems used on commercial satellites. These reflectors can easily be deployed to the east and west sides of the spacecraft leaving the nadir deck for other antennas for FSS/BSS and global horns and telemetry, tracking, and control (TT&C) antennas. Adjacent beams are generated from different apertures, as shown earlier in Figures 2.30 and 2.31, forming interleaved but contiguous spot beam coverage on the ground. The closest spacing between adjacent

beams from the same aperture can be increased from θ_s to 1.732 θ_s for a three-reflector MBA, and to 2.0 θ_s for a four-reflector MBA, where θ_s is the center-to-center spacing between adjacent beams of the multiple-beam coverage. The larger beam spacing that accompanies the use of multiple reflectors allows for a proportionate increase in the horn size, which in turn improves the antenna gain through reduced spillover losses and more optimal illumination taper on the reflector.

The following analysis is generic to single- as well as multiple-reflector MBAs. The design of and performance analysis of reflector MBAs is quite tedious. Several iterations are required when designing the feeds, analyzing the primary patterns, and computing the radiation patterns for the reflector antennas for all beams using the physical optics (PO) method of integrating the surface currents on the reflector surface, and then performing the minimum coverage directivity and the *C/I* evaluation for each beam. This process has to be repeated for each iteration and it takes several weeks to arrive at an optimal MBA design. Rao [18, 19] presented a simplified design and analysis method for the multiple-beam reflector antennas that requires only a few minutes to arrive at an optimal design and performance evaluation. The design and analysis are based on approximating the primary and secondary patterns using either Gaussian or non-Gaussian beams and deriving simplified equations for the reflector MBA. This method gives results that are in close agreement with the tedious PO method and provides a good starting solution. The PO method can then be used for the final performance evaluation of the MBA. In addition, this analysis can be applied to the antenna performance analysis of shaped or contoured beams.

MBA design depends on the beam size, which is related to the minimum coverage area directivity requirement. Other key design objectives include minimum scan loss over the coverage, maximum copolar isolation among beams that reuse the same frequency, and maximum cross-polar isolation. For MBAs with uniform size beams arranged in a hexagonal grid, the minimum directivity occurs at the triple beam crossover point of the three adjacent beams as shown in Figure 2.39. Typical beam overlaps used for practical MBAs are 3 dB for two adjacent beams

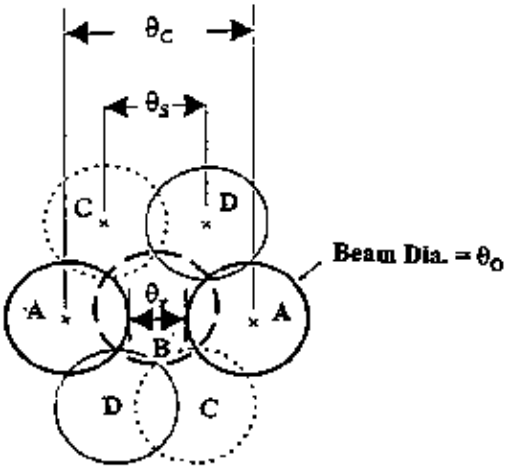

Figure 2.39 Beam parameters of MBA with hexagonal grid layout showing reuse beams and angular parameters for RF analysis

and 4 dB for a three-beam overlap. The optimum overlap depends on the minimum coverage gain, required copolar isolation (*C/I*) among reuse beams, and the frequency reuse scheme (three-cell, four-cell, etc.) of the beam overlap; however, there is a trade-off between achieving the maximum coverage gain and maximizing the *C/I* among the reuse beams. The spacing between adjacent beam centers determines the number of beams for a given coverage and also the maximum feed size that could be used for the reflectors. For the hexagonal grid layout of the beams shown in Figure 2.39, θ_s is given as:

$$\theta_s = 0.866\theta_0 \tag{2.23}$$

where θ_0 is the beam diameter at the triple beam crossover. The minimum number of beams, N_{min}, for a given coverage is given as:

$$N_{min} = C_a \Big/ \left(0.866\theta_s^{\,2}\right) \tag{2.24}$$

where C_a is the coverage area in square degrees and the denominator represents the area of the hexagonal cell associated with each beam. The coverage area includes the expanded coverage with the radial pointing error associated with the station keeping of the satellite. The actual number of beams N_A is typically 15% to 20% larger than N_{min} for an efficient layout of the beams over the coverage such that the triple-beam crossover levels for outer beams occur at the edge of the coverage edge. For a three-reflector (using a three-cell reuse scheme) and a four-reflector (using a four-cell reuse scheme) antenna system, the closest spacing between beam centers reusing the same frequency are given respectively as:

$$\theta_c^3 = 1.732\theta_s \tag{2.25}$$

$$\theta_c^4 = 2.0\theta_s \tag{2.26}$$

The closest spacing between the reuse beam edges, θ_r determines the achievable *C/I*, and is given by $\theta_r = \theta_c - \theta_0$ as shown in Figure 2.39. An important design parameter of the MBA is the feed size and feed design. The optimum adjacent feed spacing (which is close to the maximum feed size) that provides the required beam spacing of θ_s is given by:

$$d_m^{3,4} = \theta_c^{3,4} \big/ S_F \tag{2.27}$$

This equation assumes maximum diameter d_m for the circular horns such that the adjacent feeds from the same reflector are touching each other. The parameter S_F in (2.27) is the scan factor, which is defined as the ratio of the electrical scan angle of the beam to the physical displacement of the feed from the focal point of the reflector. The scan factor is related to the reflector geometry shown in Figure 2.40 and is given by:

$$S_F = \frac{1+x\left(\frac{D}{4F}\right)^2}{1+\left(\frac{D}{4F}\right)^2}\left\{\frac{1+\cos\theta_2}{2F}\right\}\left(\frac{180}{\pi}\right) \tag{2.28}$$

The unit for S_F is degrees per inch and x in (2.28) is related to the feed illumination taper on the reflector and is given as:

$$\begin{aligned} x &= 0.30 \text{ for } T < 6 \\ &= 0.36 \text{ for } T \geq 6 \end{aligned} \tag{2.29}$$

where T is the feed illumination taper (+ve dB) on the reflector edge, D is the projected diameter of the offset reflector, and F is the focal length. The angular parameters of the offset reflector geometry shown in Figure 2.40 are given as:

$$\theta_{2,1} = \frac{1}{2}\left(\tan^{-1}\left[\frac{D+h}{F-\frac{(D+h)^2}{4F}}\right] \pm \tan^{-1}\left[\frac{h}{F-\frac{h^2}{4F}}\right]\right) \tag{2.30}$$

The design variable h is the distance from the vertex to the closest edge of the offset reflector as shown in Figure 2.40. Using the Gaussian model for the main beam of the feed horn, the primary radiation pattern can be expressed as:

$$E(\theta) = e^{-A\left(\frac{\theta}{\theta_b}\right)^2} \tag{2.31}$$

where θ_b is the half 3-dB beamwidth of the horn and is given by:

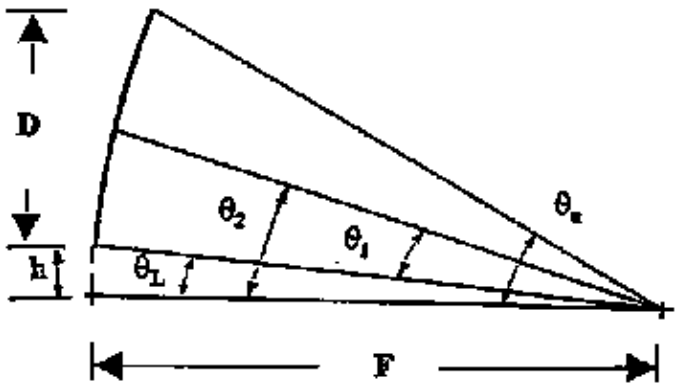

Figure 2.40 Geometry of offset parabolic reflector antenna.

$$\theta_b = C_1 \frac{\lambda}{d_m} \tag{2.32}$$

The constant in this equation depends on the type of horn used and is bounded by 35 for a Potter-type horn and 31 for the dominant TE11 mode circular horn. It varies between the two for high-efficiency horn designs. The constant A in (2.31) is obtained using the following relationship:

$$E(\theta_b) = 0.707 = e^{-A} \tag{2.33}$$

which gives the value of A as 0.3467. The feed illumination taper T at the edge of the reflector can be obtained from

$$T = -20log_{10}[E(\theta_1] = -20log_{10}\left\{e^{-0.3467[\theta_1(d_m/\lambda)/C_1]^2}\right\} \tag{2.34}$$

The secondary pattern half-power full beamwidth for an on-axis beam is given as:

$$\theta_3(\delta = 0) = (0.762T + 58.44)\frac{\lambda}{D} \tag{2.35}$$

where D is the projected diameter of the offset reflector antenna. The above equation is valid for feeds located close to the focal point in the focal plane of the reflector and is modified to include the beam-broadening effect due to scan as [18, 20]:

$$\theta_3(\delta) = \theta_3(0)10^{0.05G_L} \tag{2.36}$$

The gain loss G_L due to beam scan in decibels is given by:

$$G_L = \frac{0.0015\delta^2}{\left[\left(F/D_p\right)^2 + 0.02\right]^2} + \frac{0.011\delta}{\left[\left(F/D_p\right)^2 + 0.02\right]} \tag{2.37}$$

where δ is the number of beamwidths scanned from the antenna boresight [typically it is the ratio of the beam scan from boresight to the 3-dB beamwidth θ_3 (0)], and D_p is the diameter of the parent paraboloid, which is given as $D_p = 2(D + h)$. Equation (2.37) is obtained by interpolating the results published by Ruze [21] in a quadratic form. Note that this analysis can be extended to dielectric or waveguide lenses satisfying the Abbe sine condition (that is, a thin-lens approximation [22]), the gain loss is given as $G_L = 0.07\delta$ instead of (2.37), the feed size can be obtained from $d_m = F\tan\delta_c^{3,4}$ and the illumination angle θ_1 is given by $\theta_1 = \tan^{-1}\left(\frac{D}{2F}\right)$

. The minimum directivity over the spot beam coverage occurs at the triple-beam crossover, and the level at the triple-beam crossover point is given by:

$$B(\delta) = 3\left[\frac{\theta_0}{\theta_3(\delta)}\right]^2 \tag{2.38}$$

where $B(\lambda)$ is the beam overlap in decibels (+ve) below the peak directivity. The above equation for the beam overlap assumes a Gaussian secondary radiation pattern and is a valid assumption over the main beam and over a reasonable scan region of the MBA.

MBA Performance Analysis

This section presents the relevant analysis for evaluating the RF performance of reflector MBAs in terms of minimum coverage area directivity and the copolar isolation (C/I), which are the two critical parameters that define the overall MBA performance. The analysis is generic in nature and can be used for multiaperture or single-aperture MBAs.

Directivity Analysis

The minimum coverage area directivity of the MBA in dBi is given as:

$$D_0 = 10\log_{10}\left[\left(\frac{\pi D}{\lambda}\right)^2 \eta_f\right] - G_L(\delta_m) - B(\delta_m) \tag{2.39}$$

The first term here represents the peak directivity of the boresight beam, and the second term represents the directivity loss due to worst-case beam scan over the coverage region. The third term is the beam overlap at the triple-beam crossover level (+ve dB) below the peak directivity. Equation (2.39) gives a more accurate prediction than the conventional method of using the gain-area product (GAP) that antenna designers employ. The GAP-based method does not take into account several key parameters such as the reflector size and geometry, feed illumination, and the beam scan. The variable η_f in (2.39) is the overall antenna efficiency and is given by [23, 24]

$$\eta_f = 4\cot^2\left(\frac{\theta_1}{2}\right)\left[1-\cos^n\left(\frac{\theta_1}{2}\right)\right]^2 \frac{(n+1)}{n^2} \tag{2.40}$$

Equation (2.40) includes spillover efficiency, aperture efficiency, phase efficiency, and polarization efficiency, and can easily be factored into these four subefficiencies as shown in [23]. The feed pattern is assumed to be of the form $\cos^n\left(\frac{\theta}{2}\right)$ in the above equation. The variable n is related to the feed illumination taper and is given by

$$n = \frac{-0.05T}{\log_{10}\left[\cos\left(\frac{\theta_1}{2}\right)\right]} \tag{2.41}$$

The maximum value of feed efficiency η_f is about 0.81 and occurs when the feed illumination taper T is about 10 dB. Figure 2.41 shows the computed antenna efficiency as a function of illumination taper T. The parameter of the curve is the half-subtended angle of the reflector θ_1.The results show that a smaller θ_1 (in other words, a larger F/D ratio of the reflector) results in better gain performance for the MBA. Typical values of F/D for reflector antennas used for space application range from 0.8 to 1.4 and the choice is often dictated by the reflector size, coverage region, launch fairing envelope, and accommodation on the spacecraft. The reflectors are typically deployed along the east and west sides on the spacecraft body once the satellite is in orbit and are stowed against the spacecraft body during launch. An exemplary sketch of the MBA in the deployed views is illustrated earlier in Figure 2.2.

Copolar Isolation (C/I) Analysis

The copolar isolation of the downlink antenna is defined as the ratio of the copolar directivity of the beam of interest to the combined interference directivity, obtained by adding all of the interferers (using the same frequency as the beam of interest) in

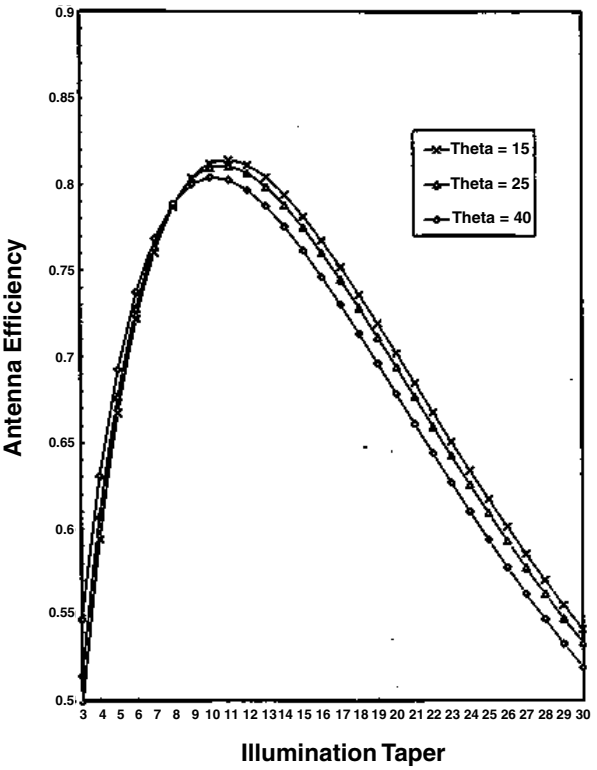

Figure 2.41 Antenna efficiency as a function of feed illumination taper T. The parameter of the curves is θ_1 (half-subtended angle on the reflector edge).

power over each angular location of the beam of interest. Typical beam geometry for *C/I* calculations is shown in Figure 2.42. The worst-case *C/I* occurs at the edge of the beam of interest. The directivity of the beam of interest at the edge is given by:

$$C_0 = 10\log_{10}\left[\left(\frac{\pi D}{\lambda}\right)^2 \eta_f\right] - G_L(\delta_0) - B(\delta_0) \tag{2.42}$$

where δ_0 is the number of beamwidths scanned from the antenna boresight for the beam of interest C_0. The combined interference signal due to N interferers onto the beam of interest at a given angular location within the beam of interest is illustrated in Figure 2.42 and is given as [18]:

$$I_0 = \sum_{n=1}^{N} I_n = 10\log_{10}\left[\left(\frac{\pi D}{\lambda}\right)^2 \eta_f \, 10^{-0.1G_L(\delta_n)} \, 10^{-0.1B_n\left\{\frac{\theta_{ns}+0.5\theta_n}{0.5\theta_n}\right\}^2}\right] \tag{2.43}$$

where θ_n is the diameter of the nth interferer. It is assumed in (2.42) and (2.43) that the antenna efficiency η_f does not change with minor changes in the scan. This is a valid assumption for moderate scans ($\theta_n \leq 7$) and is also valid for wide scans as long as the feeds are located on a spherical cap with a radius R given by $R = F\sec^2\left(\frac{\theta_2}{2}\right)$.

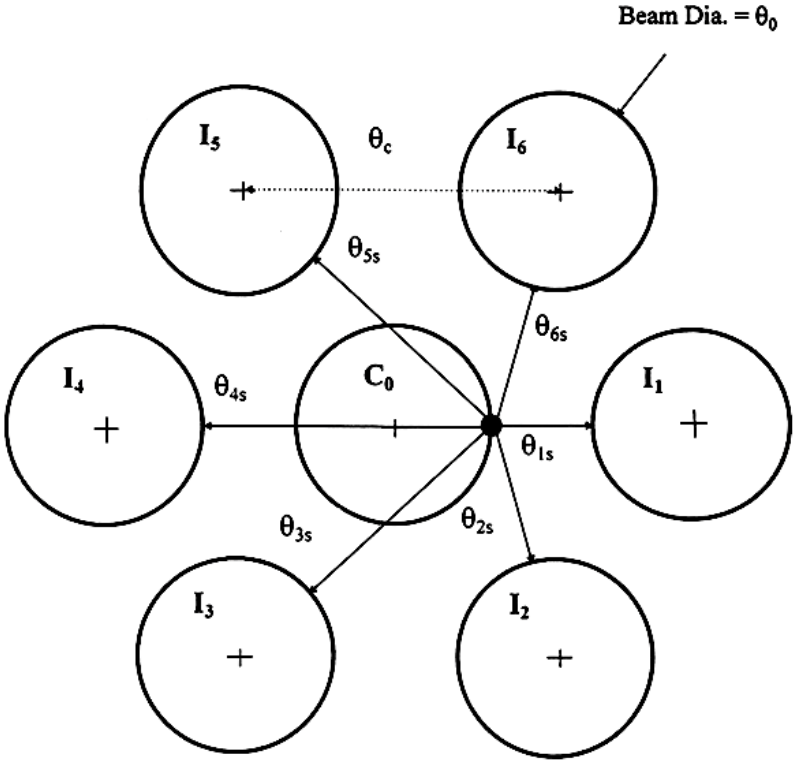

Figure 2.42 The geometry of the reuse beams for C/I calculations.

The dominant interference is from the three closest interferers I1, I2, and I6 (see Figure 2.42) and is assumed to be from the skirt of the main-beam patterns of the interfering beams. This assumption is valid for most of the practical applications with either a three- or four-cell frequency reuse scheme. The impact of sidelobes and coma-lobes due to scan is not considered here, because the levels are very low (of the order of –25 dB relative to peak) and do not significantly impact the copolar isolation values. It is to be noted that (2.43) is valid for most practical F/D values in the range of 0.6 to 2.0.

The cumulative copolar isolation in decibels is given as [18, 19]:

$$C_0 \Big/ \sum_{n=1}^{N} I_n = -G_L(\delta_0) - B(\delta_0) - 10\log_{10} \sum_{n=1}^{N} \left[10^{-0.1G_L(\delta_n)} 10^{-0.1B_n \left\{ \frac{\theta_{ns} + 0.5\theta_n}{0.5\theta_n} \right\}^2} \right] \tag{2.44}$$

The preceding equation is in a generic form and is valid for uniform as well as nonuniform size beams having uniform as well as nonuniform beam spacings. For a regular hexagonal grid arrangement of the beams, as shown in Figure 2.42, the copolar isolation can be simplified by considering the closest six interferers. It is given approximately as:

$$C_0 \Big/ \sum_{n=1}^{N} I_n = -B(\delta_0) - 10\log_{10} \sum_{n=1}^{N} \left[10^{-0.1B_n \left\{ \frac{\theta_{ns} + 0.5\theta_0}{0.5\theta_0} \right\}^2} \right] \tag{2.45}$$

The angular distances in the above equation are given by

$$\theta_{1s} = \theta_c - \theta_0 \tag{2.46}$$

$$\theta_{2s} = \theta_{6s} = \left[\theta_c^2 + 0.25\theta_0^2 - 0.5\theta_c\theta_0 \right]^{0.5} - 0.5\theta_0 \tag{2.47}$$

$$\theta_{3s} = \theta_{5s} = \left[\theta_c^2 + 0.25\theta_0^2 + 0.5\theta_c\theta_0 \right]^{0.5} - 0.5\theta_0 \tag{2.48}$$

$$\theta_{4s} = \theta_c \tag{2.49}$$

The MBA analysis results shown above are compared with the rigorous simulations using PO reflector analysis. Three antenna cases are compared.

Case 1 is a 56-beam MBA with four reflectors that uses a four-cell frequency reuse scheme. The beam is unscanned (δ=0) and the antenna parameters are D/λ = 106.9, F/D = 1.324, h/λ = 50.31, $\theta_0 = 0.545°$, and $\theta_s = 0.472°$. Using the Gaussian beam analysis given in this section, the various design parameters are calculated as $\frac{d_m}{\lambda} = 2.689$, T = 6.4 dB, n = 53.5, $\eta_f = 0.741$, $\theta_3 = 0.592°$, and B = 2.54 dB. The peak and edge of coverage (EOC) directivity values using the Gaussian beam analysis are 49.22 and 46.68 dBi, respectively. The computed directivity values using PO

integration of surface currents on the reflector antenna are 49.11 dBi (peak) and 46.54 dBi (EOC). The *C/I* value using the six closest interferers is calculated as 12.0 dB while the computed value using PO is obtained as 12.5 dB.

Case 2 is the same as Case 1, except that the beam is scanned to 1.666° (δ=2.81) from the antenna boresight direction. The feed design parameters are same as Case 1, and the beam parameters are calculated as $\theta_3(\delta) = 0.619°$ and $B = 2.33$ dB. The improved beam overlap relative to Case 1 is due to a beam-broadening effect with scan. The peak directivity, EOC directivity, and *C/I* (using the three closest interferers) values are 48.84 dBi, 46.51 dBi, and 13.49 dB, respectively, and the computed values are 49.01 dBi, 46.45 dBi, and 13.03 dB, respectively.

Case 3 is a 24-beam MBA with four reflectors and a four-cell reuse scheme. The antenna parameters are $D/\lambda = 79.32$, $F/D = 1.667$, $h/\lambda = 39.66$, $\theta_0 = 1.07°$, and $\theta_s = 0.923°$. Design parameters are calculated as $\frac{d_m}{\lambda}$=4.45, $T = 13.0$ dB, $n = 159$, $\eta_f = 0.802$, $\theta_3 = 0.862°$, and $B = 4.62$ dB. This design example employs a larger beam overlap to improve *C/I*. The calculated values for peak directivity, EOC directivity, and *C/I* (with the six closest interferers) are 46.97 dBi, 42.33 dBi, and 21.2 dB, while the respective values using rigorous PO computations are 46.70 dBi, 41.92 dBi, and 19.8 dB. The calculated values agree well with rigorous computations for all cases and the Gaussian beam analysis could be used for rapid analysis of design trade-offs for practical MBA systems.

Extension to Shaped Beams

The above analysis for MBAs can easily be extended to shaped or contoured beam antennas. This type of analysis is more accurate than using the GAP estimates. The GAP varies for shaped beams in the range of 6,000 to 25,000 depending on the size of the reflector and the extent of shaping. The GAP estimates are very approximate since they do not take into account the reflector size, offset clearance, feed illumination, and so forth. Using the analysis shown in the preceding section, the minimum coverage area directivity, D_{min}, can be estimated as follows:

$$D_{min} = 10\log_{10}\left[\left(\pi D/\lambda\right)^2 \eta_f\right] - M - G_L\left(\delta_m\right) - 10\log_{10}\left[\frac{C_A}{(\pi/4)\theta_M^2}\right] \tag{2.50}$$

where C_A is the coverage area of the shaped beam in square degrees, θ_M is the pencil beam beamwidth at M dB below the beam peak directivity (M is typically 4 for shaped beam designs), and $G_L(\delta_m)$ is the gain loss at a maximum scan angle of δ_m. The maximum scan angle δ_m is given by the coverage requirements and depends on the actual coverage as seen by the satellite and the antenna boresight direction. The variable θ_M is related to the 3-dB full beamwidth θ_3 by

$$\theta_M = \sqrt{\frac{M}{3}}\theta_3 \tag{2.51}$$

The shaped beam example (Case 4) is the contoured beam coverage over South America. Antenna parameters for this design are $D/\lambda = 28.45$, F/D = 0.824, $h/\lambda = 3.18$, $T = 14$ dB, $M = 4$, and $C_A = 23.7$ square degrees. The design parameters are calculated as $\theta_3 = 2.43°$ and $G_L = 0.45$ dB. The calculated minimum coverage area directivity using the analysis shown is 27.66 dBi, while the computed value using the PO method is 27.6 dBi. Another example (Case 5) is a wide area coverage semiglobal beam with antenna parameters as follows: $D/\lambda = 29$, $F/D_p = 0.3125$, $T = 13$ dB, $M = 4$, and $C_A = 79.7$ square degrees. Design parameters are calculated as $\theta_3 = 2.383°$, $G_L = 1.57$ dB, and $\eta_f = 0.79$. The calculated and PO computed minimum directivity values are 21.33 and 21.70 dBi, respectively. The extension of MBA analysis to shaped beams predicts the minimum coverage directivity values within 0.4 dB of the PO computations. The comparison results of the Gaussian-type analysis with PO computations is given in Table 2.4 for MBA and shaped beam antennas.

The analysis method based on the Gaussian beam model is useful for quick analysis and design of MBAs without the need for time-intensive computations and iterations using reflector analysis software. This method gives results close to computations for moderate beam scans and is quite useful for initial design, design trade-offs, and performance evaluation of MBAs. It is widely used in the satellite industry by several companies. Extension of this analysis to shaped beams gives directivity predictions that are close to computed results.

Parametric Analysis of MBAs

The analysis shown in the preceding sections was later generalized [19] using a parametric design that includes feed efficiency and satellite pointing error as variables. For the reflector MBAs, the feed design is most important in dictating the RF performance. Corrugated horns were used in earlier designs, but suffer from low aperture efficiency of about 55% due to the thick walls needed for implementing the corrugations and, as a result, the effective aperture area is much less than the physical area. Potter horns have also been used in multibeam satellites with moderate aperture efficiency of about 74%. High-efficiency horns with aperture efficiencies of about 93% have been realized in the recent past [25–28]. The feed efficiency is a key parameter for optimizing MBA performance parameters. The half-angle of the 3-dB beamwidth of the horn is given by:

$$\theta_b = C_1(\lambda/d_m) \tag{2.52}$$

Table 2.4 Comparison of Analysis Results of MBAs and Shaped Reflectors with Computations Based on TICRA's PO Software

Antenna Case	*Peak Directivity (dBi)*		*EOC Directivity (dBi)*		*C/I (dB)*	
	Analysis	*Computed*	*Analysis*	*Computed*	*Analysis*	*Computed*
Case 1 (MBA)	49.22	49.11	46.68	46.54	12.00	12.50
Case 2 (MBA)	48.84	49.01	46.51	46.45	13.49	13.03
Case 3 (MBA)	46.97	46.70	42.33	41.92	21.20	19.80
Case 4 (shaped beam)	N/A	N/A	27.66	27.60	N/A	N/A
Case 5 (shaped beam)	N/A	N/A	21.33	21.70	N/A	N/A

The constant C_1 in this equation depends on the efficiency of the horn. It is obtained by quadratic interpolation of a few practical designs using low-, medium-, and high-efficiency horns and is given as:

$$C_1 = 31 - 0.0041(93-\eta)^2 + 0.341(93-\eta) \tag{2.53}$$

where η is the efficiency of the feed horn. The above equation works well for efficiency values in the range of 70% to 95%. Computed radiation patterns for three different horn designs with varying efficiency values for a 3.07λ-diameter multimode circular horn are shown in Figure 2.43. The copolar and cross-polar patterns are shown in the 45-deg plane. On-axis directivity values are 18.19, 18.72, and 19.21 dBi for Potter, medium-efficiency, and high-efficiency horns, respectively. The feed illumination taper T values at the reflector edge at 20.95 deg can be calculated using (2.34) and are 9.2, 10.3, and 12.4 dB, respectively, for the Potter, medium-efficiency, and high-efficiency horns. The higher edge illumination taper achieved for the high-efficiency horn designs will illuminate the reflector more optimally and results in higher EOC gain and improved C/I for the MBA.

The secondary patterns of the MBA can be analyzed more accurately using a quasi-Gaussian beam analysis whereby the main beam is represented as a Gaussian beam, the first sidelobe region represented at a constant level, and the sidelobe region beyond the first sidelobe is represented with a slope of –6-dB per octave. The pattern shape is also a function of the horn efficiency value. The secondary pattern in decibels is given by [19]:

$$G(\theta) = 10\log_{10}\left\{A\exp\left[-B\left(0.866\theta/\theta_B\right)^2\right]\right\} \text{ in the region } 1.1547\theta_B \le \theta \le \theta_n \tag{2.54a}$$

$$= -30 \text{ in the region } \theta_n < \theta \le 0.5(\theta_n + \theta_{s1}) \tag{2.54b}$$

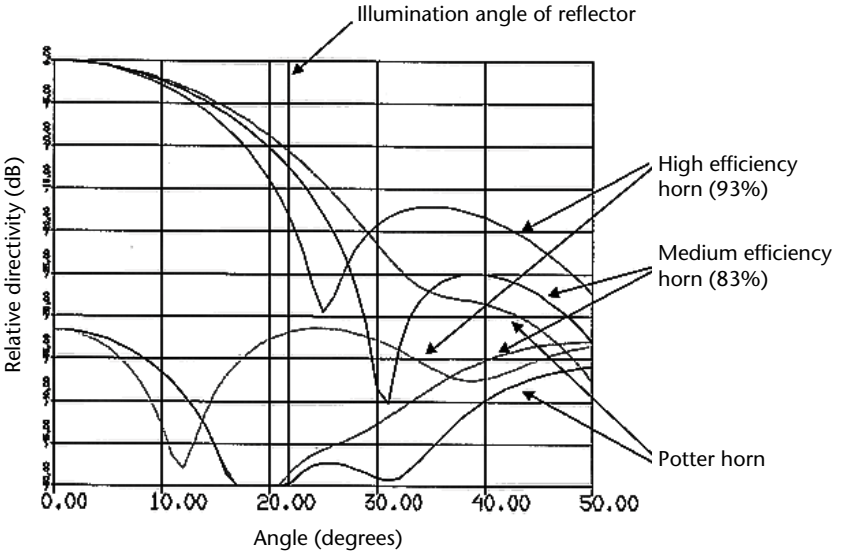

Figure 2.43 Radiation patterns of a 3.07λ-diameter circular horn in the 45° plane. Potter, medium-efficiency, and high-efficiency design cases are shown.

$$= SL \text{ in the region } 0.5(\theta_n + \theta_{s1}) < \theta \le \theta_{s1} \tag{2.54c}$$

$$= SL - 20\log_{10}(\theta/\theta_{s1}) \text{ in the region } \theta > \theta_{s1} \tag{2.54d}$$

where $G(\theta)$ is the gain in dBi, and the constants in the above equation are given by:

$$B = \frac{5.986}{\left(\frac{\theta_n}{1.1547\theta_B}\right)^2 - 1} \tag{2.55}$$

and

$$A = 0.398\exp(B) \tag{2.56}$$

The 3-dB beamwidth of the reflector antenna is interpolated as follows:

$$\theta_3 = 2\theta_B = (0.058T^2 + 0.171T + 58.44)(\lambda/D) \tag{2.57}$$

The other parameters in the above equation are θ_n, the position of first null; θ_{s1}, the angular position of the first sidelobe; and SL, the sidelobe level relative to the beam peak (in decibels). They are given by:

$$\theta_n = (7.8 - 3.16SL)(\lambda/D) \tag{2.58}$$

$$\theta_{s1} = (30.25 - 3.07SL)(\lambda/D) \tag{2.59}$$

$$SL = -0.037T^2 - 0.376T - 17.6 \tag{2.60}$$

where D is the projected aperture of the reflector and T is the illumination taper on the reflector edge. The template model is compared to the computed pattern in Figure 2.44 for $SL = -25$dB. The analytical model agrees closely with the computed patterns in terms of half-power beamwidth and the location of the first null. The above equations are valid for feeds located close to the focal point of the reflector (or for beams close to the antenna's boresight). As the beams are scanned away from the antenna's boresight, the main impacts on antenna radiation are that the main beam broadens, the antenna gain deteriorates due to scanning losses, and the sidelobe levels increase due to coma-lobes. All three effects due to scanning are included in the analysis by modifying the above equations as follows [18, 20]:

$$\theta_3(\delta) = \theta_3 10^{0.05GL(\delta)} \tag{2.61}$$

where $GL(\delta)$ is the gain loss due to scan in decibels, and is given by [16]:

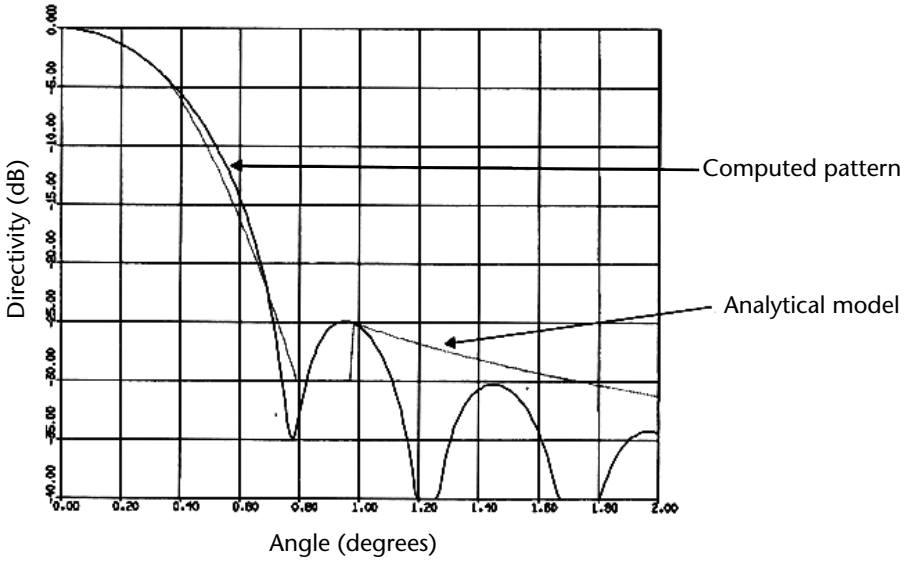

Figure 2.44 Comparison of analytical model with the computed patterns for SL = –25 dB.

$$GL(\delta) = \frac{0.0015\delta^2}{\left[\left(F/D_p\right)^2 + 0.02\right]^2} + \frac{0.011\delta}{\left[\left(F/D_p\right)^2 + 0.02\right]} \tag{2.62}$$

The increase in the sidelobe level due to scanning is obtained by quadratic interpolation:

$$SL(\delta) = SL(\delta = 0) + \frac{0.36\delta}{\left[\left(F/D_p\right)^2 + 0.02\right]} - \frac{0.0026\delta^2}{\left[\left(F/D_p\right)^2 + 0.02\right]^2} \tag{2.63}$$

where δ in the above equations is the number of beamwidths scanned, and D_p is the diameter of the parent paraboloid ($D_p = 2(D + h)$). The angular parameters shown in (2.58) and (2.59) need to be multiplied by the factor $10^{0.5G_L(\delta)}$ in order to account for the beam-broadening effect due to scanning.

Figure 2.45 compares the computed normalized radiation patterns of a 65-in.-diameter parabolic reflector using the three horn designs (Potter, medium-efficiency, and high-efficiency horns) shown in Figure 2.43. It can be seen that the high-efficiency horn gives broader patterns and lower sidelobe levels. This results in improved copolar isolation due to the fact that the interferers are mostly in the sidelobe region.

The electrical performance of the multiple-beam antenna, in terms of the beam directivity and copolar isolation (*C/I*), is analyzed using the following equations developed in this section.

The beam layout including the pointing error is shown in Figure 2.46. The minimum coverage area directivity, taking into account the pointing error ($\Delta\theta^{\mathrm{P}}$), is given by [18]:

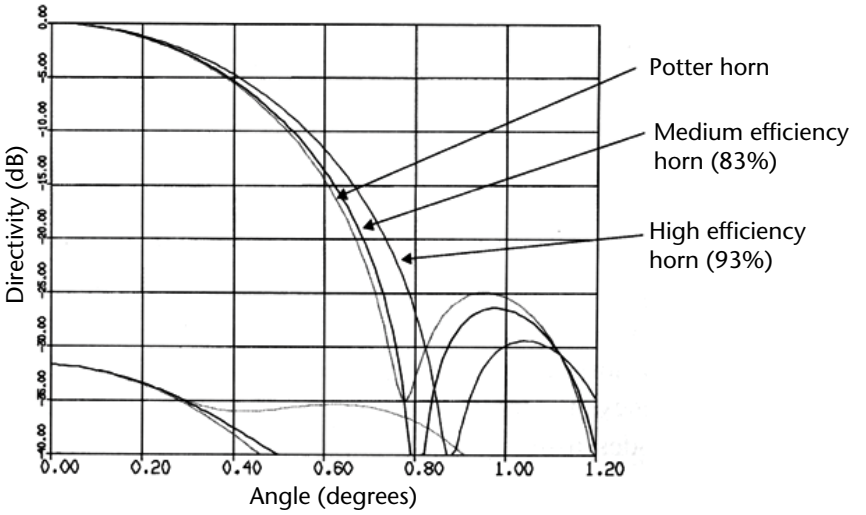

Figure 2.45 Comparison of secondary patterns using Potter, medium-efficiency, and high-efficiency horn designs (shown in Figure 2.43).

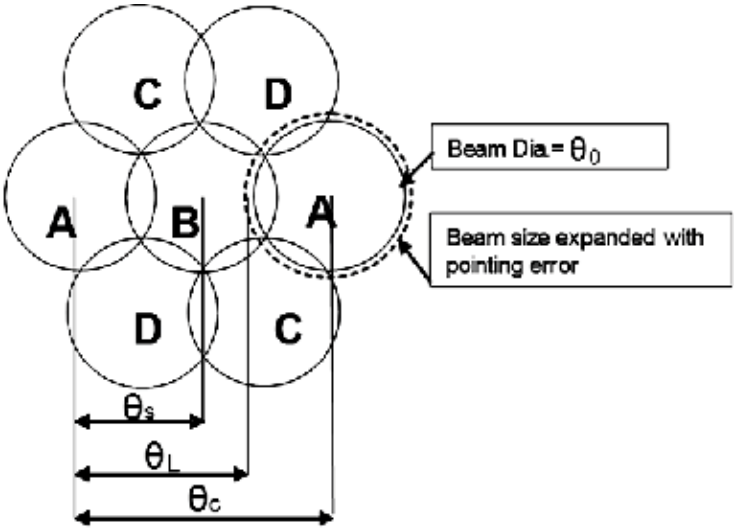

Figure 2.46 Multibeam layout showing the beam expansion with pointing error. Pointing error has impact on the gain as well as C/I.

$$D_C = 10\log_{10}\left[\left(\frac{\pi D}{\lambda}\right)^2 \eta_i\right] - GL(\delta_m) - B(\delta_m) - 10\log_{10}\left(\frac{0.5\theta_0 + \Delta\theta^P}{0.5\theta_0}\right)^2 \tag{2.64}$$

where δ_m is the maximum number of beamwidths the antenna is scanned (defined as the ratio of maximum scan angle to the antenna half-power beamwidth at boresight direction). The first term in the above equation is the peak directivity for the

boresight beam, the second term is the directivity loss due to scan for maximum scan angle, the third term is the peak-to-edge variation for the maximum scanned beam, and the last term is the directivity loss due to the pointing error. The antenna efficiency, η_i, is a function of the feed efficiency, η_f. A Potter horn has a lower taper on the reflector, but has very low spillover loss due to lower sidelobes. The high-efficiency horn, on the other hand, has higher taper on the reflector and high spill-over loss (the sidelobe levels are around 19 dB below peak). The overall antenna efficiency, η_i, is a function of the illumination taper, the reflector geometry, and the feed efficiency, and is given by:

$$\begin{aligned}\eta_i &= 4\cot^2(\theta_1/2)\left[1-\cos^n(\theta_1/2)\right]^2 \\ &\times\frac{n+1}{n^2}\left[1.025+0.5119\left(\eta_f-0.74\right)-7.542\left(\eta_f-0.74\right)^2\right]\end{aligned} \tag{2.65}$$

The above equation includes the aperture efficiency, the spillover efficiency, and the feed horn efficiency. The value of the parameter n in (2.65) is given by

$$n=\frac{-0.05T}{\log_{10}\left[\cos(\theta_1/2)\right]} \tag{2.66}$$

An antenna efficiency value of about 82% is the maximum for a single reflector, and occurs for feed-taper values of about 10 dB. Also, the efficiency value is better for smaller θ_1 values or larger F/D values. The parameter $B(\delta_m)$ in (2.64) is given by:

$$B(\delta_m)=3\left[\frac{\theta_0}{\theta_3(\delta_m)}\right]^2 \tag{2.67}$$

The copolar isolation (C/I) for the downlink antenna is usually more critical than for the uplink antenna, and is defined as the ratio of the copolar directivity of the beam of interest to the combined directivity interference obtained by adding all of the interferers, in power, over the beam of interest. Note that the cross-polar levels are not included in this analysis, due to the fact that the total interference is dominated by the copolar signals from the adjacent beams reusing the same frequency. Self cross-polar interference can be almost neglected in most cases. The cell area of the beam needs to be expanded with the circular pointing error in order to compute the worst-case value. (Also, implementation margins necessary to account for the reflector-surface distortions and range uncertainties need to be added to all interferers to compute the copolar isolation of spacecraft antennas, which are not included here.) The combined interference signal due to J interferers onto the beam of interest is given by [19]:

$$\sum_{j=1}^{J} I_j = 10\log_{10}\left[\sum_{j=1}^{J}\left(\frac{\pi D}{\lambda}\right)^2 \eta_f 10^{-0.1GL(\delta_j)} 10^{-0.1B_n\left(\frac{\theta_{js}+0.5\theta_j-\Delta\theta^P}{0.5\theta_j}\right)^2}\right] \tag{2.68}$$

where θ_j is the diameter of the jth interferer, θ_{js} is the distance from the closest edge of the jth interferer to the beam of interest, and $\Delta\theta^P$ is the maximum pointing error. The copolar directivity, C, is equal to DC, and is given by (2.64). Based on equations (2.64) and (2.68), the copolar isolation, C/I, can be calculated. For example, the angles θ_{js} of the closest six interferers for a four-cell scheme (Figure 2.42) are given by:

$$\theta_{1s} = \theta_{4s} = \theta_C - \theta_0 \tag{2.69}$$

$$\theta_{2s} = \theta_{6s} = \left[\theta_C^2 + 0.25\theta_0^2 - 0.5\theta_C\theta_0\right]^{0.5} - 0.5\theta_0 \tag{2.70}$$

$$\theta_{3s} = \theta_{5s} = \left[\theta_C^2 + 0.25\theta_0^2 + 0.5\theta_C\theta_0\right]^{0.5} - 0.5\theta_0 \tag{2.71}$$

Computed *C/I* results for a four-aperture MBA with $D/\lambda = 100$, $F/D = 1.138$, $h/\lambda = 41.4$, and feed diameter $d/\lambda = 3.01$ using the parametric analysis shown above are given below. Three feed horn designs are used in these calculations: (1) Potter horn with 74% efficiency, (2) medium-efficiency multimode horn with 83% efficiency, and (3) high-efficiency horn with 93% efficiency. Figures 2.47 and 2.48, respectively, show aggregate *C/I* calculated for a four-cell and a seven-cell frequency reuse system. The copolar isolation values shown are the aggregate values where all the copolar interferers are added in power and include a ±0.05° pointing error due to the satellite. The nonmonotonic behavior of the copolar isolation with scan is due to the beam-broadening effect causing the interference signals to shift from the sidelobe region to the main beam roll-off region of the copolar beam and also due to the presence of coma-lobes. For the four-cell and seven-cell reuse schemes, the high-efficiency horn gives about a 1.5 to 2.5 dB improvement relative to the Potter horn, respectively, for moderate scans. For a seven-cell reuse scheme, a high-efficiency horn gives better RF performance, and for a four-cell scheme, either a high- or medium-efficiency horn could be used. For a three-cell reuse scheme, the Potter horn gives better overall performance of the MBA.

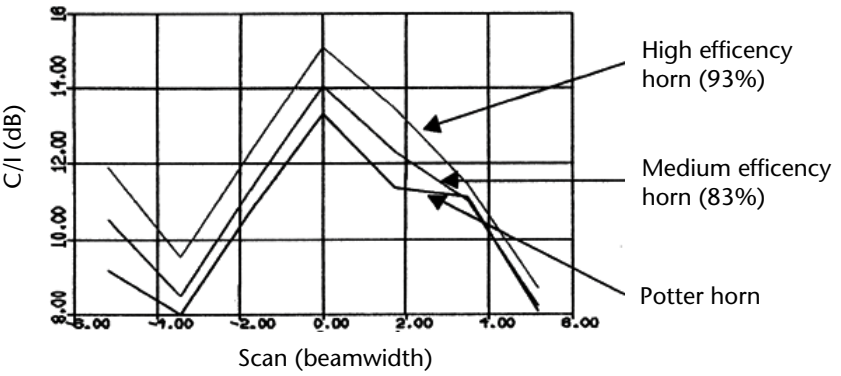

Figure 2.47 Parametric variation of the aggregate copolar isolation (C/I) with scan and horn efficiency for a four-cell reuse scheme and a four-aperture MBA. Results include ±0.05° pointing error.

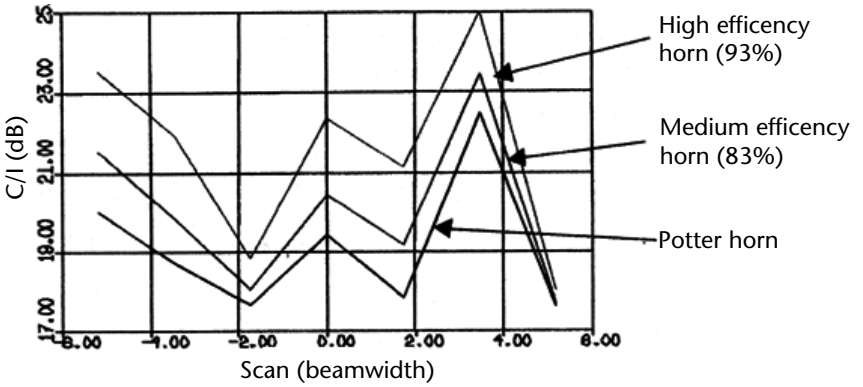

Figure 2.48 Parametric variation of the aggregate copolar isolation (C/I) with scan and horn efficiency for a seven-cell reuse and a four-aperture MBA. Results include ±0.05° pointing error.

2.3.5 Multiple-Beam Antenna Design Examples for Various Satellite Services

This section provides a few design examples of satellite antennas for multiple-beam applications for PCS and DBS services. The evolution of reflector MBA technology is illustrated in Figure 2.49. Configuration A is the conventional reflector MBA for personal communication satellites that employs a separate set of reflectors for uplink and downlink beams. Each set comprises four reflectors where alternate beams are generated using multiple feeds from the same reflector. The uplink reflectors are about 1.5 times smaller than the downlink reflectors. The disadvantage with this configuration is that it requires eight reflectors that need to be accommodated and deployed on the spacecraft bus, which restricts the size of the reflectors and hence the size of the beam.

Configuration B employs dual-band reflector antennas being fed with corrugated horns in order to reduce the number of apertures by half, for example, from 8 to 4. This is a great advantage in accommodating larger reflectors on the spacecraft and, hence, the ability to create smaller beams with higher gain performance. Corrugated horns are used to cover the larger bandwidth of greater than 50% needed to support both uplink and downlink beams. However, this suffers from lower performance due to low efficiency of about 54% for the corrugated horns due to the thick walls needed for corrugations (larger than a quarter wavelength at the lowest frequency of both bands). In addition, it adds mass to the feed assemblies, which is also of prime concern for satellite antennas. The dual-band MBA (DMBA) configuration C overcomes the above limitations by employing smooth-walled high-efficiency horns that support both uplink and downlink frequency bands [25–28].

A novel dual-band MBA using stepped-reflector technology combined with smooth-walled high-efficiency horns has been developed in the recent past [29, 30]. The concept is illustrated in Figure 2.50 and is shown as configuration D in Figure 2.49. It combines the feed horn advancements with stepped-reflector technology in order to achieve significant performance improvements for future MBAs for personal communication satellites. The reflector size is dictated by the downlink frequency band and is typically oversized for the uplink band. The uplink beams using the same reflector as the downlink are about 33% smaller than the downlink beams. The step or steps over optimized annular regions are designed to broaden

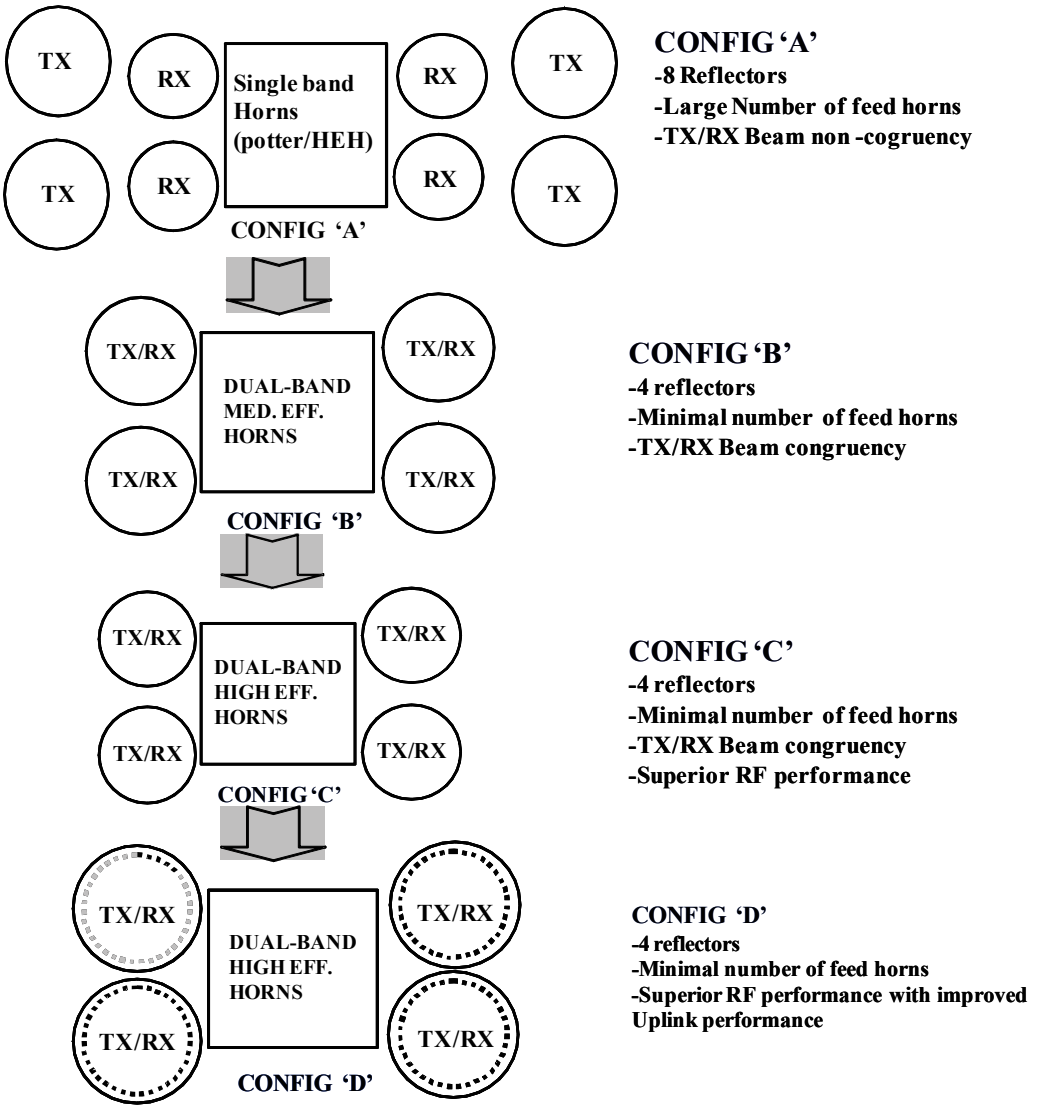

Figure 2.49 Evolution of reflector MBA technology.

the uplink beams by creating a 180-deg phase reversal using steps that gradually blend into the reflector shape avoiding abrupt shape changes. Since the step heights are designed about quarter-wave at the uplink band, the impact on the downlink beam is minimal. The concept and detailed results of stepped-reflector technology have been presented in [29, 30].

The high-efficiency "smooth-walled" horns were initially developed for single narrowband applications where the desired higher order modes are generated by step junctions or discontinuities. To achieve high-efficiency values over both the downlink (transmit) and uplink (receive) frequency bands of the DMBA, a number of slope discontinuities have been used to generate higher order $TE_{1,n}$ modes [27]. Diverging-type slope discontinuities from throat to horn aperture are more suitable

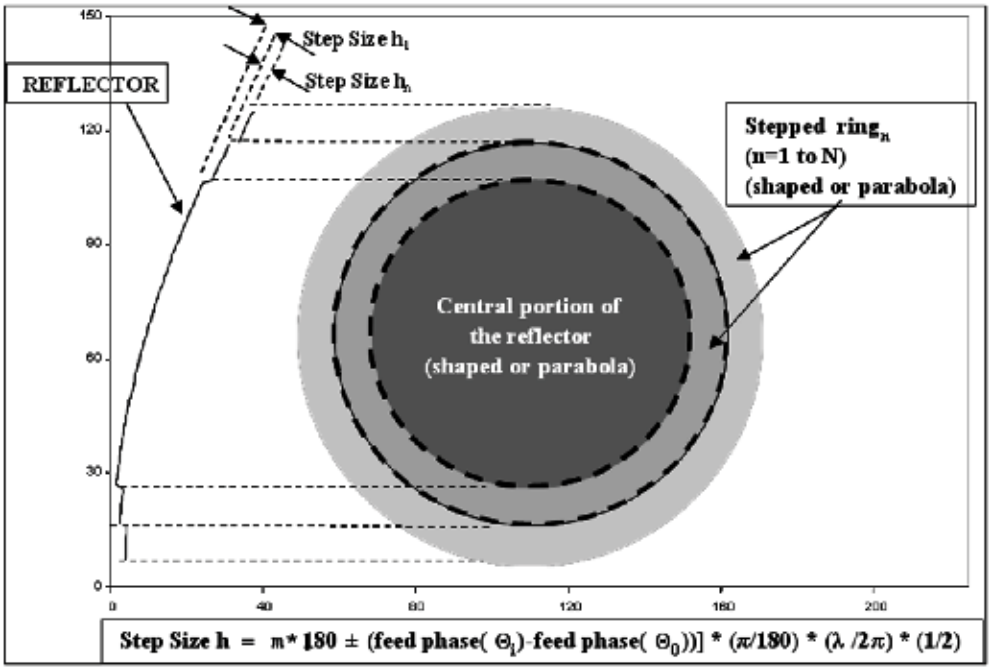

Figure 2.50 The stepped-reflector concept for dual-band and multiband MBAs.

for these applications rather than converging-type slopes because the latter have the disadvantage of trapped modes causing in-band resonances that are undesired for space applications.

The horn geometry is synthesized using iterative analysis that employs a mode-matching technique combined with a generalized scattering matrix (GSM) approach to evaluate the RF performance and optimize the geometry. Desired requirements for the horn efficiency, return loss, and peak cross-polar levels can be specified over discrete frequencies covering both bands and minimizing the cost function using mini-max optimization.

Figure 2.51 graphs the performance of a 2.27 in. diameter, high-efficiency horn compared with a conventional corrugated horn at the K- and Ka-bands. A dual-band reflector performance has been analyzed using both types of horns and an 80 in. reflector diameter with a focal length of 116 in. and an offset clearance of 26 in. The reflector surface is shaped to broaden the Rx beams at the Ka-band for both cases. Table 2.5 summarizes a performance comparison of DMBA with both types of horns. The DBHEH, when compared to a corrugated horn, improves EOC gain by about 0.9 dB at Tx frequencies and by about 2.0 dB at Rx frequencies, and improves *C/I* by about 3.0 dB. DMBA configuration D combines reflector improvements through the use of stepped-reflector antenna (SRA) technology with horn improvements to further improve DMBA performance. A single step is sufficient for most applications, but multiple steps can be employed for tri-band or quad-band applications. Both central and annular stepped regions can be shaped to improve the RF performance, and the transition region can be blended into the reflector to avoid abrupt discontinuities. The height *h* of the step needs to be designed in conjunction with the feed phase characteristics at the Rx frequencies in order to

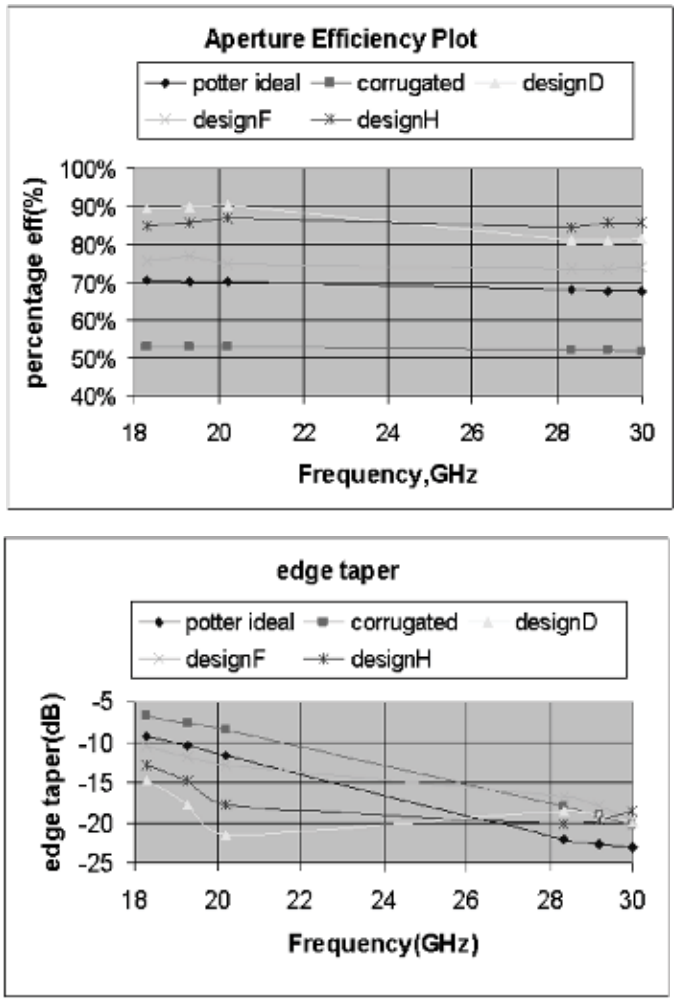

Figure 2.51 Comparison of aperture efficiency and illumination tapers on an MBA reflector for various MBA horn types.

Table 2.5 Performance Comparison of Dual-Band MBA Using Two Types of Horns

Performance Parameter	*Conventional Horn (Corrugated)*	*High Efficiency Horn Design H*
	TX/RX	*TX/RX*
Efficiency %	54/52	85/85
Edge Taper, dB	7/18	13/17
Primary C/X, dB	33/33	20/23
EOC Directivity, dBi	43.8/41.7	44.7/43.7
C/I, 3-cell (dB)	11.1/13.0	14.2/11.6
C/I, 4-cell (dB)	12.0/15.8	15.7/14.5
C/I, 7-cell (dB)	18.2/19.5	22.7/21.9
C/X, dB	30.0/28.0	21./20

provide a 180-deg phase reversal at the step, resulting in a "flat-topped" Rx beam with significantly improved gain and hence *G/T*. The step height is given by:

$$h \leq \lambda_{rm}/4 \tag{2.72}$$

where λ_{rm} is the wavelength at the center frequency of the Rx band. At 30 GHz, the step height h is less than 0.1 in. and can be easily blended with the reflector shape over a small region with gradual shaping. The near-field phase distribution of the SRA at Rx frequency is shown in Figure 2.52, which also shows the desired 180-deg phase reversal near the transition region of the step. As a result, the Rx beam patterns of the SRA shown in Figure 2.53 have flat-topped patterns with increased EOC gain. The Rx beam EOC gain improvement is about 2.0 dB relative to configuration B and about 1.2 dB relative to configuration C. By combining the feed phase quadratic variation with the phase variation due to the step, the step size can be minimized. The SRA for dual-band and multiband applications works well over wide coverage regions with large scan angles. The Tx and the Rx beam patterns of a dual-band MBA are shown in Figures 2.54 and 2.55, respectively. The edge of the beam gains over the scan region are improved at both Tx and Rx bands relative to conventional MBAs.

The BSS satellites for local-channel broadcast over the CONUS area are required to provide coverage to most of the 212 designated market areas (DMAs) throughout the CONUS, Alaska, and Hawaii using a multiple-beam spot beam payload. These payloads typically employ three or four reflectors for spot beam coverage and an additional reflector to provide national broadcasts using a contoured beam. An exemplary MBA using four reflectors (designated as NE, NW, SE, and SW) is used to create 45 spot beams over the CONUS, Alaska, and Hawaii. The beam layout is shown in Figure 2.56. Each reflector has about 10 to 13 feed horns to create the desired spot beams where each beam is designed to

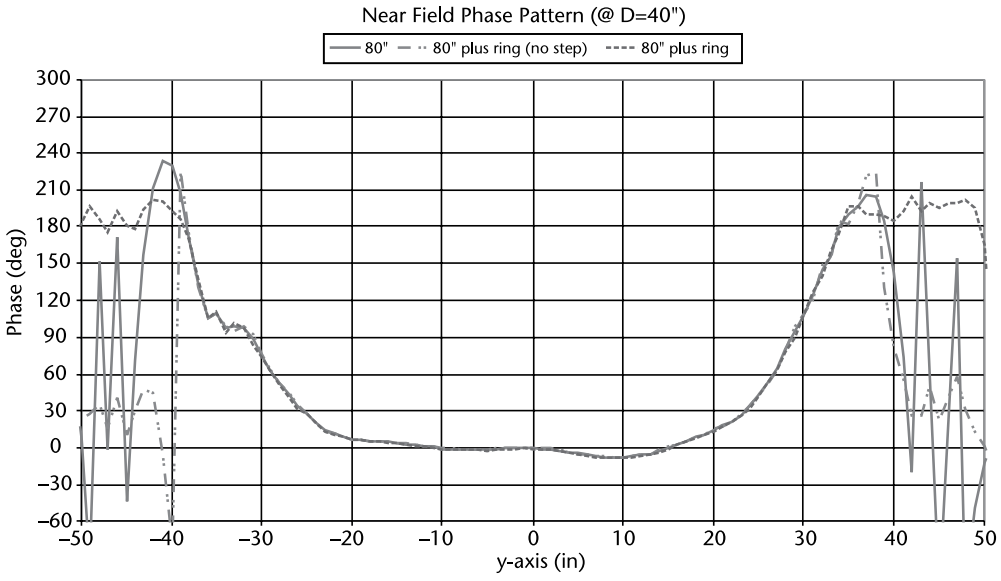

Figure 2.52 Near-field phase distribution creating 180-degree phase reversal due to the step.

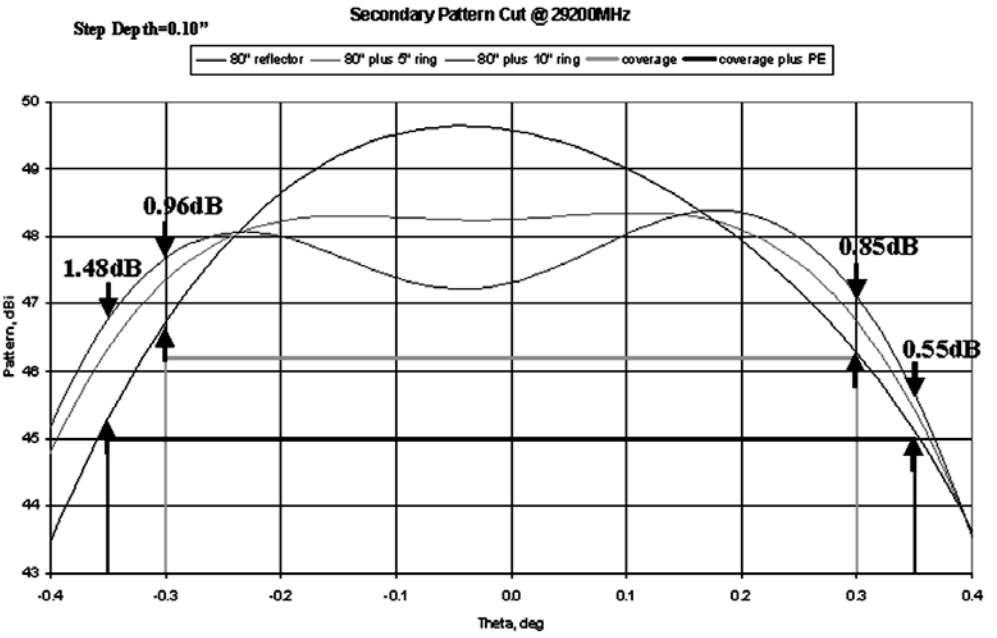

Figure 2.53 Beam shaping of Rx MBA using a stepped reflector.

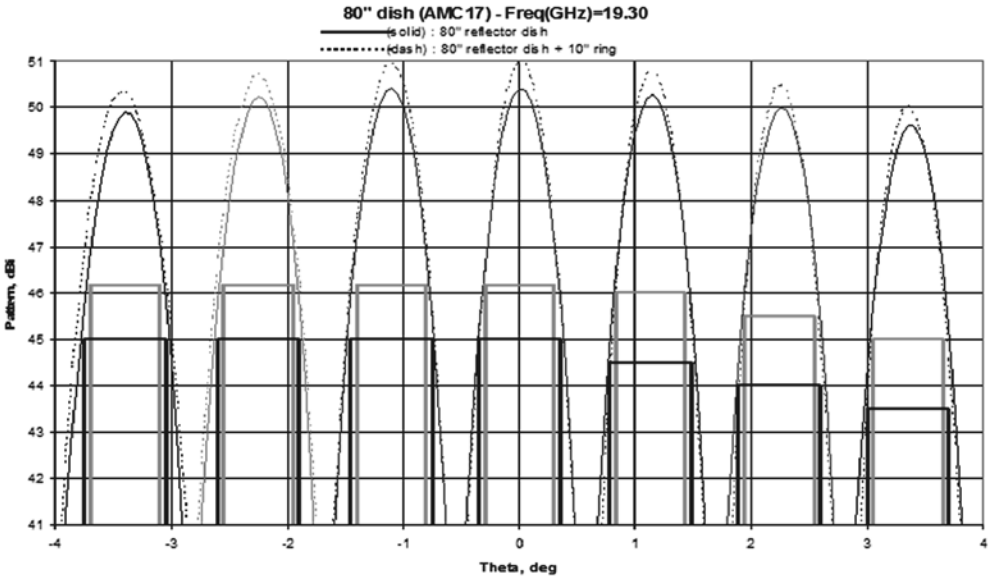

Figure 2.54 Transmit beam patterns of SRA compared to a conventional parabolic reflector MBA over coverage scan.

cover multiple DMAs. The design of these MBAs gets more complicated due to nonuniform beam size, nonuniform spacing among reuse beams, and the need for efficient use of the limited number of frequency channels. Design challenges include combination of DMAs per beam, frequency channels designated to beams, choice of beam diameters/horizons, maximizing the copolar isolation among beams using some frequency channels, and allocation of beams to the hubs on the ground.

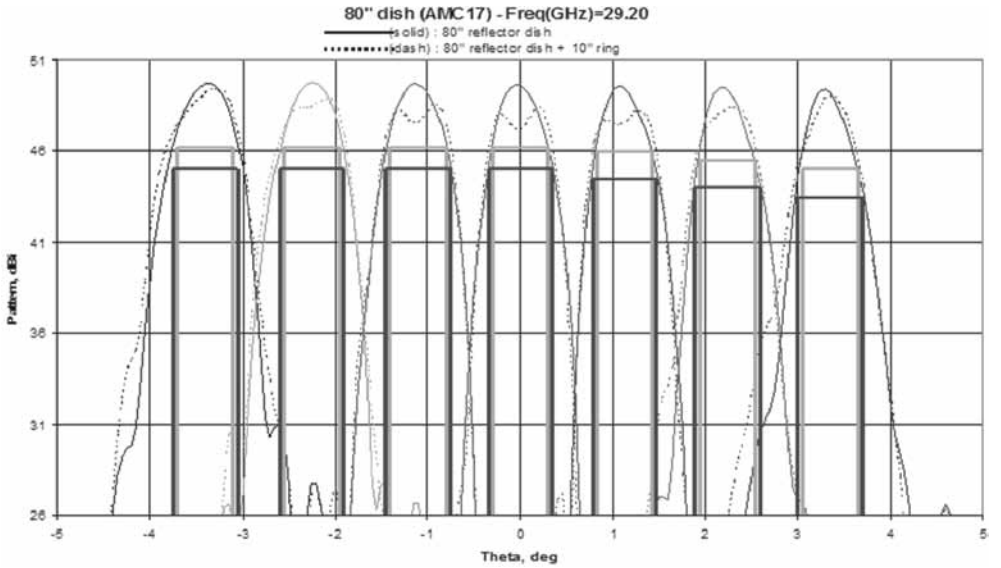

Figure 2.55 Receive beam patterns of SRA compared to a conventional parabolic reflector MBA over coverage scan. Flat-topped beams are achieved with improved edge-of-beam coverage.

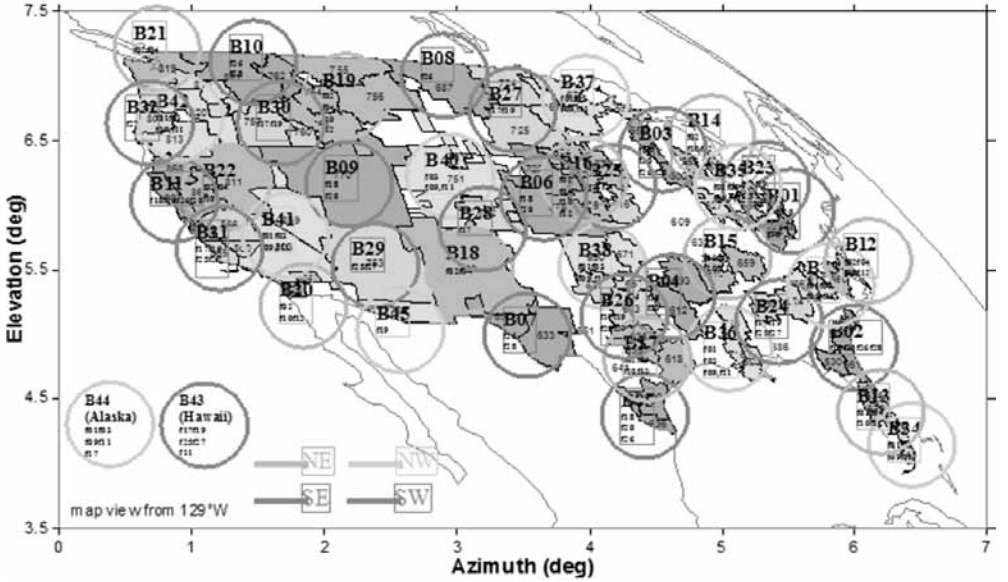

Figure 2.56 Multiple-beam layout for local-channel broadcast satellite covering 205 DMAs with four reflectors and 45 spot beams.

In addition, the power allocated to each DMA varies. Therefore, 0/1 analysis has to be finally carried out and optimized at EIRP level for payload optimization at system level.

References

[1] B. G. Evans, *Satellite Communication Systems*, Peter Peregrinus Ltd., London, 1987.

[2] D. Roddy, *Satellite Communications*, 4th ed., McGraw-Hill, New York, 2006.

[3] A. W. Rudge et al., *The Handbook of Antenna Design*, Peter Peregrinus Ltd., London, pp. 466–505, 1986.

[4] R. C. Jasik, "Satellite Antennas," Chap. 35 in *Antenna Engineering Handbook*, pp. 35-1 to 35-22, McGraw-Hill, New York, 1984.

[5] D. L. Doan, et al., "Design of Anik-D communication antenna," *IEEE APS/URSI Symposium Digest*, pp. 93–96, 1980.

[6] K. K. Chan, et al., "Anik-C antenna system," *IEEE APS/URSI Symposium Digest*, pp. 89–92, 1980.

[7] T. S. Chu and R.H. Turrin, "Depolarization properties of offset reflector antennas," *IEEE Trans. Antennas & Propagation*, Vol. 21, pp. 339–345, May 1973.

[8] N. A. Adatia and A. W. Rudge, "Beam-squint in circularly-polarized offset reflector antennas," *Electronic Letters*, pp. 513–515, October 1975.

[9] B. S. Westcott, *Shaped Reflector Antenna Design*, Research Studies Press Ltd., UK, 1983.

[10] TICRA, "User Manuals for GRASP8, POS, and POD," TICRA Engineering Consultants, Copenhagen, Denmark, 2003.

[11] Y. Mizuguchi, et al., *Elect. & Communications in Japan*, Vol. 61-B, No. 3, p. 58, 1978.

[12] C. Dragone and D. C. Hogg, "The radiation patterns and impedance of offset and symmetric near-field Cassegrain and Gregorian antennas," *IEEE Trans. Antennas & Propagation*, Vol. 12, pp. 472–475, May 1974.

[13] K. K. Chan and F. Hyjazie, "Design of overlapping gridded reflectors for frequency reuse," *IEEE APS/URSI Symposium Digest*, pp. 149–152, 1985.

[14] S. Rao, et al., "Multiple-beam antenna systems using hybrid frequency reuse scheme," U.S. Patent No. 7382743, June 2008.

[15] P. Ingerson and C. A. Chen, "The use of non-focusing aperture for multibeam antenna," *IEEE Antennas & Propagation Symposium Digest*, pp. 330–333, 1983.

[16] K. K. Chan, et al., "Triangular ray-tube analysis of dielectric lens antennas," *IEEE Trans. Antennas & Propagation*, Vol. 45, No. 8, pp. 1277–1285, 1997.

[17] S. Rao, et al., "Development of a 45 GHz multiple-beam antenna for military satellite communications," *IEEE Trans. Antennas & Propagation*, Vol. 43, 1036–1047, October 1995.

[18] S. Rao, "Design and analysis of multiple-beam reflector antennas," *IEEE Antennas & Propagation Magazine*, Vol. 41, pp. 53–59, August 1999.

[19] S. Rao, "Parametric design and analysis of multiple-beam reflector antennas for satellite communications," *IEEE Antennas & Propagation Magazine*, Vol. 45, pp. 26–34, August 2003.

[20] S. Rao, "A template for shaped beam satellite antenna patterns," *IEEE Trans. Antennas & Propagation*, Vol. 36, pp. 1633–1637, November 1988.

[21] J. Ruze, "Lateral-feed displacement in a paraboloid," *IEEE Trans. Antennas & Propagation*, Vol. 13, pp. 660–665, September 1965.

[22] S. Coanbleet, *Microwave Optics,* Academic Press, London, 1976, pp. 374–376.

[23] P. S. Kildal, "Factorization of the feed efficiency of paraboloids and Cassegrain antennas," *IEEE Trans. Antennas & Propagation*, Vol. 33, pp. 903–908, August 1995.

[24] S. Rao and P.S. Kildal, "A study of the diffraction and blockage effects on the efficiency of the Cassegrain antenna," *Canadian Elec. Eng. Journal*, Vol. 9, pp. 10–15, January 1984.

[25] S. Rao and M. Tang, "High-efficiency horns for an antenna system," U.S. Patent No. 7,463,207, December 2008.

[26] C. Hsu and S. Rao, "Horn antenna and system for transmitting and/or receiving radio frequency signals in multiple frequency bands," U.S. Patent No. 8,164,533, April 2012.

[27] K. K. Chan and S. Rao, "Design of high efficiency circular horn feeds for multibeam reflector applications," *IEEE Trans. Antennas & Propagation*, Vol. 56, pp. 253–258, January 2008.

[28] A. K. Bhattacharyya and G. Goyette, "A novel horn radiator with high aperture efficiency and low cross-polarization and applications in arrays and multibeam reflector antennas" Vol. 52, pp. 2850–2859, November 2004.

[29] S. Rao and M. Tang, "Stepped-reflector antenna for satellite communications payloads," U.S. Patent No. 7,737,903, June 2010.

[30] S. Rao and M. Tang, "Stepped-reflector antenna for dual-band multiple beam satellite communications payloads," *IEEE Trans. Antennas & Propagation*, Vol. 54, pp. 801–811, March 2006.

CHAPTER 3

Reflector Antennas for Terrestrial Communications

Yoshio Inasawa, Michio Takikawa, Shin-ichi Yamamoto, and
Yoshihiko Konishi, Mitsubishi Electric Corporation, Information Technology R&D Center, Antennas Technology Department

3.1 Introduction

This chapter discusses past and recent developments on reflector antennas for terrestrial communications applications. Each of the sections describes reflector antennas for a specific application. Section 3.2 presents design technologies for beam-waveguide feed systems and practical examples in conjunction with large Earth station reflector antennas. The shaped Cassegrain antenna fed by a four-reflector beam waveguide feed, which is a standard for large Earth stations all over the world, is described. Section 3.3 introduces a tri-reflector offset antenna for terrestrial microwave relay link systems. The reflector antenna is shown to achieve very low cross-polar levels. Reflector antennas used for Japanese Communication Satellite 2 (CS-2) are described in Section 3.4. The shape of the wavefront that corresponds to the desired beam cross section in the sense of geometrical optics is analyzed using the geometrical optics (GO) approach, and a method for synthesizing the wavefront is also discussed. The reflector shape is determined from the shape of the wavefront by the GO approach, which is adequate for this application.

Section 3.5 presents the elliptical aperture antenna used for satellite news gathering. The antenna is an offset Gregorian antenna with an elliptical main reflector. The elliptical aperture is used to reduce the interference from or to adjacent satellites. Section 3.6 describes a reflector antenna with an elliptical aperture for aeronautical satellite communication systems. The elliptical aperture realizes a very low profile antenna under severe envelope constraints on the airplane. The dual-shaped reflector antenna is realized by using physical optics shaping techniques and achieves excellent electric performance. Section 3.7 introduces a compact reflector antenna for the mobile satellite communications used by vessels. For this type of system, the antenna needs to be designed to achieve low sidelobe and low

cross-polar characteristics while maintaining high antenna efficiency. Section 3.8 discusses the type of reflector antenna used for simultaneous reception from broadcast satellites (BS) and communication satellites (CS). The optimum reflector for a single-reflector type wide beam-spacing multibeam antenna is presented on the basis of wave aberration analysis of a defocus-fed reflector. A novel shaped reflector antenna for base station applications is described in Section 3.9. The antenna radiator vertically shaped six-sector beams simultaneously.

3.2 Large Earth Station Reflector Antenna

Japanese reflector antenna technologies have contributed tremendously to the popularization and advancement of satellite communication systems. In particular, the shaped Cassegrain antenna, fed by a four-reflector beam waveguide feed, is symbolic of the standard reflector antenna for large Earth stations all over the world.

The Cassegrain antenna is a dual-reflector antenna derived from the Cassegrain optical telescope [1]. The fundamental Cassegrain antenna uses a paraboloidal reflector for the main reflector and a small hyperboloidal reflector for the subreflector. This antenna has three advantages when applied as an Earth station antenna:

1. The radiation characteristics of the Cassegrain antenna become equal to those of an equivalent parabolic antenna, the aperture angle of which is the same as the radiating angle of the primary feed horn of the Cassegrain antenna. Accordingly, the Cassegrain antenna has good radiation characteristics because of the equivalently long focal length and small effects of aberrations.
2. The insertion loss between a primary feed horn and a receiver/transmitter is small, because the primary horn can be located at the vertex of the main reflector.
3. The noise temperature becomes smaller than that of the parabolic antenna because the large spillover of the subreflector points toward the cold sky instead of the hot Earth.

The design method and main performance characteristics of large Earth station reflector antennas for satellite communications are described in the following sections.

3.2.1 Design Method

3.2.1.1 Beam-Waveguide Feed Systems

The four-reflector beam waveguide can obtain a symmetrical beam for Cassegrain antennas using an asymmetrically shaped beam-waveguide system [2, 3]. Figure 3.1 shows a model antenna fed by the four-reflector beam waveguide. This beam waveguide consists of two curved reflectors, two plane reflectors, and a horn. The broken lines in Figure 3.1 show image rays due to the plane reflectors. This analysis is only applicable for two curved reflectors. These reflectors are assumed to be quadric surfaces of revolution.

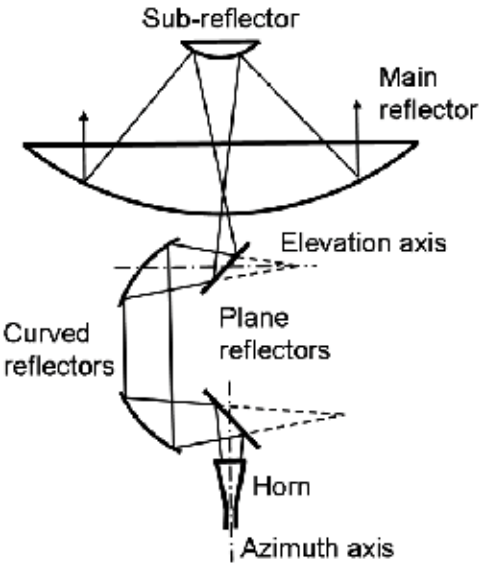

Figure 3.1 A Cassegrain antenna fed by a four-reflector beam waveguide [2, 3].

First, we discuss the relation of rays in one reflector. The incident conical rays from focus F_n, as shown in Figure 3.2, are reflected by the reflector, M_n, and changed into the different conical rays focused on F_{n+1}. The conical rays are expressed by the unit vector of the center axis, $\mathbf{v}_n$, and the cone angle, θ_n. The incident and reflected rays are described by the subscripts n and $n + 1$, respectively. The relationship between the incident and reflected rays can be obtained as follows:

$$\mathbf{v}_{n+1} = \frac{1}{z_n}\left[p_n \left(1 - k_n^2\right)^{\frac{1}{2}} \left\{ \mathbf{v}_n - \left(\mathbf{v}_n \cdot \mathbf{k}_n\right) k_n \right\} + \left\{ K_n \cos\theta_n - \left(\mathbf{v}_n \cdot \mathbf{k}_n\right) \right\} k_n \right] \tag{3.1}$$

$$\cos\theta_{n+1} = \frac{1}{z_n}\left[\cos\theta_n - K_n \left(\mathbf{v}_n \cdot \mathbf{k}_n\right) \right] \tag{3.2}$$

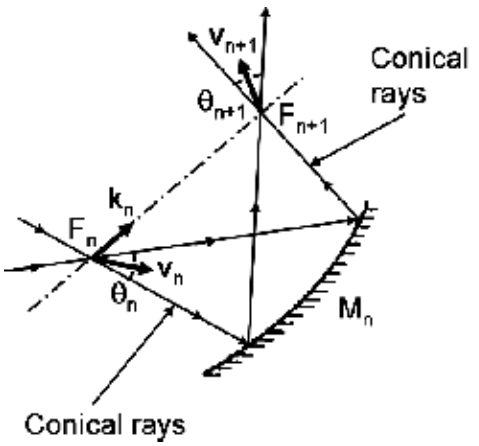

Figure 3.2 The relationship between the incident and reflected conical rays [2, 3].

$$\sin\theta_{n+1} = \frac{1}{z_n}\left(1-k_n^2\right)^{\frac{1}{2}}\sin\theta_n \tag{3.3}$$

where

$$z_n^2 = \left\{\cos\theta_n - K_n\left(\mathbf{v}_n\cdot\mathbf{k}_n\right)\right\}^2 + \left(1-k_n^2\right)\sin^2\theta_n$$

$$K_n = -p_n\delta_n\frac{2e_n}{1+e_n^2}$$

$$p_n = \begin{cases}+1 \text{ hyperboloid}\\ -1 \text{ ellipsoid}\end{cases}$$

$$\delta_n = \begin{cases}+1 \text{ concave reflector}\\ -1 \text{ convex reflector}\end{cases}$$

where e_n is the eccentricity, and $\mathbf{k}_n$ is the unit vector of F_nF_{n+1}, respectively.

In the two-reflector system, as shown in Figure 3.3, all conical rays from F_1 are reflected by the reflectors M_1 and M_2, and changed into the different conical rays from F_3. Here, the unit vector of the center axes, $\mathbf{v}_1$, $\mathbf{v}_2$, and $\mathbf{v}_3$, and the cone angles, θ_1, θ_2, and θ_3, are defined for the reflectors M_1, M_2, and M_3, respectively. The unit vector of the center axis, $\mathbf{v}_3$, associated with the conical rays reflected by M_2, can be obtained from (3.1) to (3.3):

$$\mathbf{v}_3 = \frac{1}{Z_1Z_2}\left[\mathbf{A}+\mathbf{B}\cos\theta_1\right] \tag{3.4}$$

where

$$\begin{aligned}\mathbf{A} = {} & L_1L_2\mathbf{v}_1 - L_2\left(1+L_1\right)\left(\mathbf{v}_1\cdot\mathbf{k}_1\right)\mathbf{k}_1 - L_1\left(1+L_2\right)\left(\mathbf{v}_1\cdot\mathbf{k}_2\right)\mathbf{k}_2\\ & - K_1K_2\left(\mathbf{v}_1\cdot\mathbf{k}_1\right)\mathbf{k}_2 + \left(1+L_1\right)\left(1+L_2\right)\left(\mathbf{v}_1\cdot\mathbf{k}_1\right)\left(\mathbf{k}_1\cdot\mathbf{k}_2\right)\mathbf{k}_2\end{aligned}$$

$$\mathbf{B} = K_1L_2\mathbf{k}_1 + K_2\mathbf{k}_2 - \left(1+L_2\right)K_1\left(\mathbf{k}_1\cdot\mathbf{k}_2\right)\mathbf{k}_2$$

$$L_1 = p_1\left(1-K_1^{\,2}\right)^{1/2}$$

$$L_2 = p_2\left(1-K_2^{\,2}\right)^{1/2}$$

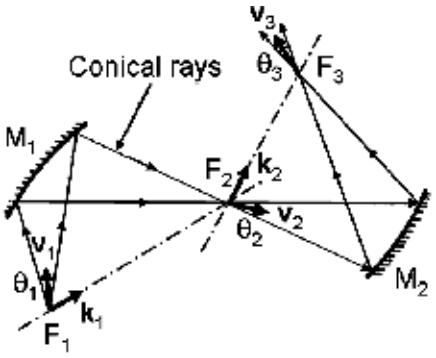

Figure 3.3 Two asymmetric reflectors [2, 3].

The variables **A** and **B** are independent of θ_1. Now, the unit vector $\mathbf{v}_1$ is assumed to be constant, and the beam of the horn is assumed to be symmetric. The unit vector $\mathbf{v}_3$ for the conical rays from the reflector system should be independent of the cone angle θ_1 for the incident conical rays, in order to make the beam from the reflector system symmetric. That is, the vector **B** in (3.4) should be as follows:

$$\mathbf{B} = 0 \tag{3.5}$$

To satisfy (3.5), the parameters of the reflectors should be:

$$\mathbf{k}_2 = \pm\mathbf{k}_1 \tag{3.6}$$

$$K_2 = \pm K_1 \tag{3.7}$$

Finally, from (3.6) and (3.7), the conditions for obtaining a symmetric beam are described as follows:

1. The foci of the two reflectors should be arranged in a straight line.
2. The eccentricities of the two reflectors, e_1 and e_2, should be expressed by $e_2 = e_1$ or $e_2 = 1/e_1$. When these conditions are satisfied, the relationship between the conical rays radiating into and out of the reflector system is as follows:

$$\theta_3 = \theta_1 \tag{3.8}$$

$$\mathbf{v}_3 = \begin{cases} \mathbf{v}_1 & \text{for } p_1 p_2 = +1 \\ -\mathbf{v}_1 + 2(\mathbf{v}_1 \cdot \mathbf{k}_1)\mathbf{k}_1 & \text{for } p_1 p_2 = -1 \end{cases} \tag{3.9}$$

These equations mean that both the beams radiating into and out of the reflector system are identical in shape, and are of the same direction or symmetry with respect to a straight line drawn through the focal points.

Generally, in the primary feeds of Cassegrain antennas, the arrangement of reflectors is restricted. The unit vector $\mathbf{v}_2$ must be arranged on the elevation axis, and the directions of the unit vectors $\mathbf{v}_1$ and $\mathbf{v}_3$ must be nearly 180 deg from each other. That is, from (3.9), the reflector system should consist of hyperboloidal and ellipsoidal reflectors. Only the four types of configurations shown in Figure 3.4 can thus be selected from the many reflector systems satisfying the preceding conditions. Figure 3.4(d) is equivalent to Figure 3.4(a) or 3.4(b) in the case where the focus F_2 is at an infinite distance.

Multiple-reflector systems include beam-waveguide systems, since a series of quadric surfaces of revolution is reported to be equivalent to an offset parabola antenna in terms of geometrical optics [4]. A beam-mode expansion is also appropriate in the analysis and design of beam waveguides [5–7]. The four-reflector waveguide can be designed not only to obtain a symmetric beam, but to also reduce

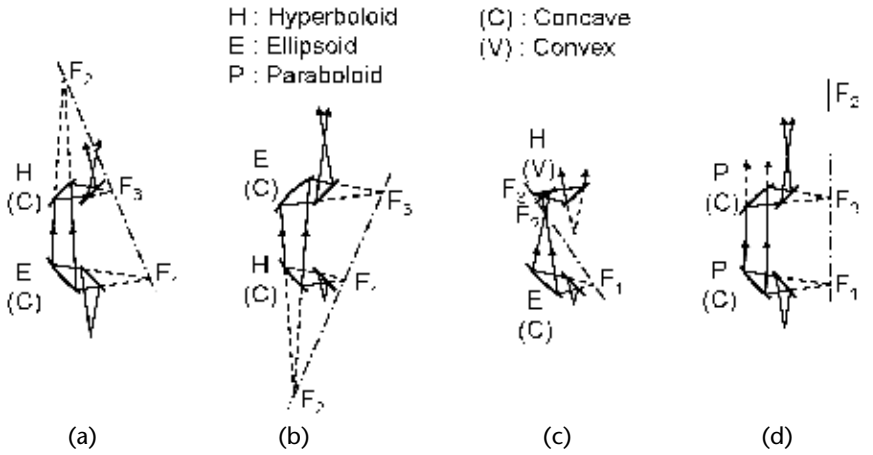

Figure 3.4 Beam-waveguide feeds having rotationally symmetric beams [2, 3].

cross-polarization when the equivalent parabola of the series of quadric surfaces of revolution is chosen to be a symmetrical parabola.

To obtain a symmetrical beam, a corrugated conical-horn antenna is often used as a primary radiator. The corrugated conical-horn antenna consists of a corrugated waveguide instead of a normal waveguide [8–10]. The beam shape of this horn antenna becomes symmetrical due to the symmetrical hybrid EH11-mode aperture distribution. The corrugated horn also has the merit of having broadband frequency characteristics.

3.2.1.2 Reflector Shaping

Another important advantage of Cassegrain antennas over parabolic antennas is the reflector shaping technique, which is a slight modification of the reflector's surface from a quadratic surface of revolution [11, 12]. When reflector shaping is used, the aperture-field distribution can be so tightly controlled that a trade-off becomes possible between the aperture efficiency and the sidelobe characteristics. For an axially symmetric dual-reflector antenna, a shaped-reflector synthesis based on geometrical optics can be carried out by solving a set of ordinary differential equations [13].

Figure 3.5 shows cross sections of a sample shaped Cassegrain antenna having a uniform aperture-amplitude distribution [13]. The nominal Cassegrain antenna has a tapered aperture-amplitude distribution. By applying reflector shaping in order to obtain a uniform amplitude distribution, the thickness of the shaped subreflector becomes large compared with the nominal hyperboloidal subreflector for scattering the electromagnetic wave to the edge area of the main reflector. Also, the shaped main reflector becomes deep (thick) compared with the nominal paraboloidal main reflector, in order to adjust the optical length between the feed horn and the antenna's aperture and in order to obtain a plane aperture-phase distribution.

When the electrical size of the subreflector is small, the scattering pattern of the subreflector needs to be taken into account. Considerations have been made and incorporated for Earth station designs [13, 14]. Figure 3.6 shows an example of subreflector scattering patterns for various subreflector diameter cases, using the

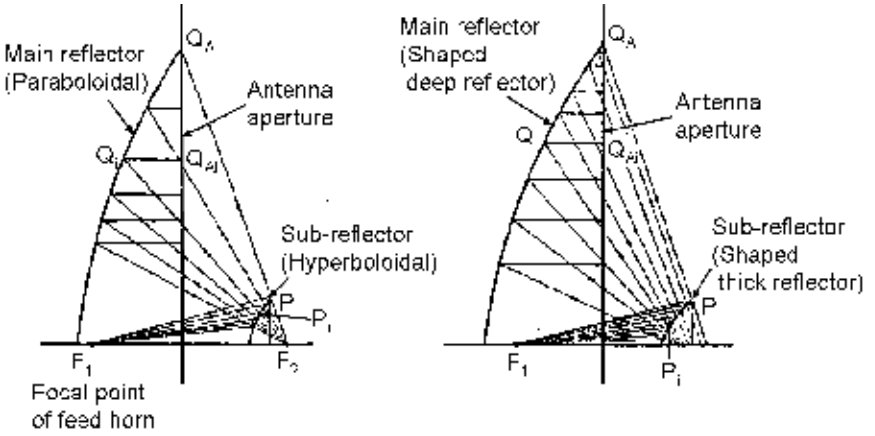

Figure 3.5 Reflector shaping and aperture distribution image.

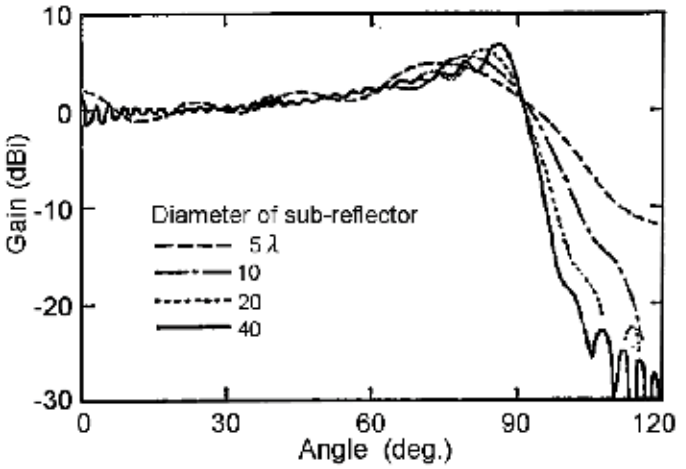

Figure 3.6 Scattering patterns from subreflectors with various diameters [13].

current distribution method when the edge electric-field level of the subreflector is set to be –15 dB and the aperture angle of the main reflector is 90°. From Figure 3.6, the spillover level of the subreflector becomes smaller with increasing subreflector diameter. On the other hand, when the subreflector's diameter becomes large, the blockage area of the subreflector also becomes large, and the aperture efficiency decreases. Accordingly, an optimum subreflector diameter for obtaining maximum aperture efficiency exists based on the main reflector's diameter, as shown in Figure 3.7.

3.2.2 Main Performance

To avoid the offset configuration, a four-reflector beam-waveguide feed system was developed for the Ibaraki No. 3 Earth Station [15, 16]. Figure 3.8 shows the geometry of this Earth station. Tables 3.1 and 3.2 and Figure 3.9 show the electrical performance, a breakdown of the aperture efficiency, and the radiation patterns, respectively.

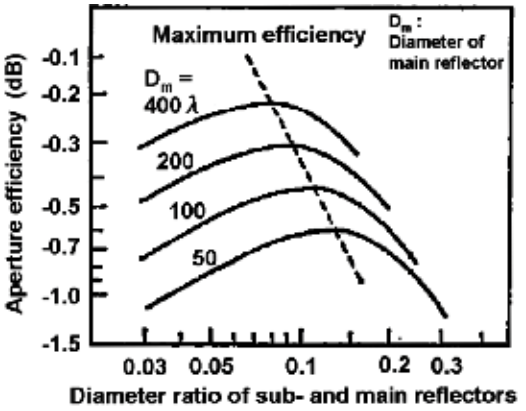

Figure 3.7 Efficiency as a function of the diameter ratio of subreflectors and main reflectors [13].

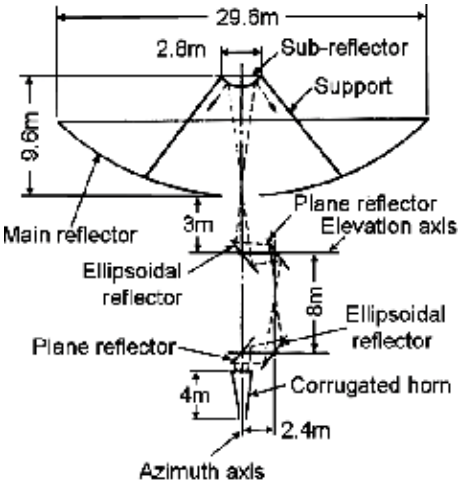

Figure 3.8 Geometry of Ibaraki No. 3 Earth Station [15, 16].

Table 3.3 shows the electrical performances of KDDI Earth stations in Japan. As shown in this table, Yamaguchi No. 2 Earth Station, which is the largest Earth station in Japan, achieved an aperture efficiency of around 80%.

The reflector-shaping technique also results in low sidelobe characteristics, because the edge level of the aperture amplitude distribution can be reduced to a sufficiently low level. The copolarization radiation patterns of Yamaguchi TTC&M/IOT Station, which was constructed in 1980, achieved Recommendation CCIR (now ITU-R) S.465 [17]. Moreover, Yamaguchi No. 2 Earth Station satisfied not only copolarization patterns, but also cross-polarization patterns with this recommendation by using shaped struts for the subreflector [18].

Table 3.1 Electrical Performance of the Ibaraki No. 3 Earth Station [15]

		Receive (Rx)	*Transmit (Tx)*
Frequency (GHz)		4	6
Gain (dBi)		60.6	63.7
Aperture efficiency (%)		75	68
Noise temperature in elevation (K)	5 deg	39	
	30 deg	15	
	90 deg	11	

Table 3.2 Breakdown of Aperture Efficiency for Ibaraki No. 3 Earth Station [15]

	Receive (Rx)	*Transmit (Tx)*
Frequency (GHz)	4.0	6.0
Loss of corrugated horn (dB)	–0.01	–0.01
Loss of horn cover (dB)	–0.01	–0.02
Transmission efficiency of beam waveguide (dB)	–0.13	–0.21
Illumination efficiency (dB)	–0.60	–0.75
Spillover from main reflector (dB)	–0.05	–0.04
Spillover from subreflector (dB)	–0.05	–0.04
Blockage of subreflector and its supports (dB)	–0.22	–0.19
Reduction due to reflector surface tolerance	–0.19	–0.42
Total efficiency	–1.26 dB (75%)	–1.68 dB (68%)

3.3 Tri-Reflector Offset Antenna for Terrestrial Microwave Relay Link Systems

In microwave relay link systems using 4-, 5-, and 6-GHz bands, in order to address congestion and to transition to a digital method from the analog method, it was necessary to develop an antenna that has superior wide-angle radiation properties and cross-polarization properties and that is capable of decreasing interroute interference and differing polarization interference as compared to the conventional horn reflector. To maintain the compatibility of this antenna to the horn reflector [19], the signal must be fed vertically upward. Also, in the digital microwave relay method, in order to apply space diversity to most of the intervals, a new subantenna must be installed at a central height in a preexisting steel tower; therefore, miniaturization and weight reduction are also critical.

To respond to the above-described requirements, an offset antenna comprising a tri-reflector was investigated [20–22]. This tri-reflector composition utilized in the offset antenna allows a degree of freedom in the design. Design parameters can be optimized to decrease the sidelobe and the cross-polarized radiation level, increase efficiency, and perform miniaturization. In this study, there were two types of antennas: (1) an offset antenna with an aperture diameter of 3m comprising a quadratic surface of revolution and (2) an offset antenna with an aperture diameter of 3.6m that corrected the reflector surfaces of a main reflector and subreflectors. Because both of these antennas comprised a geometrical optics reflector surface system, they corrected undulation and achieved good wide-angle radiation properties and cross-polarization properties.

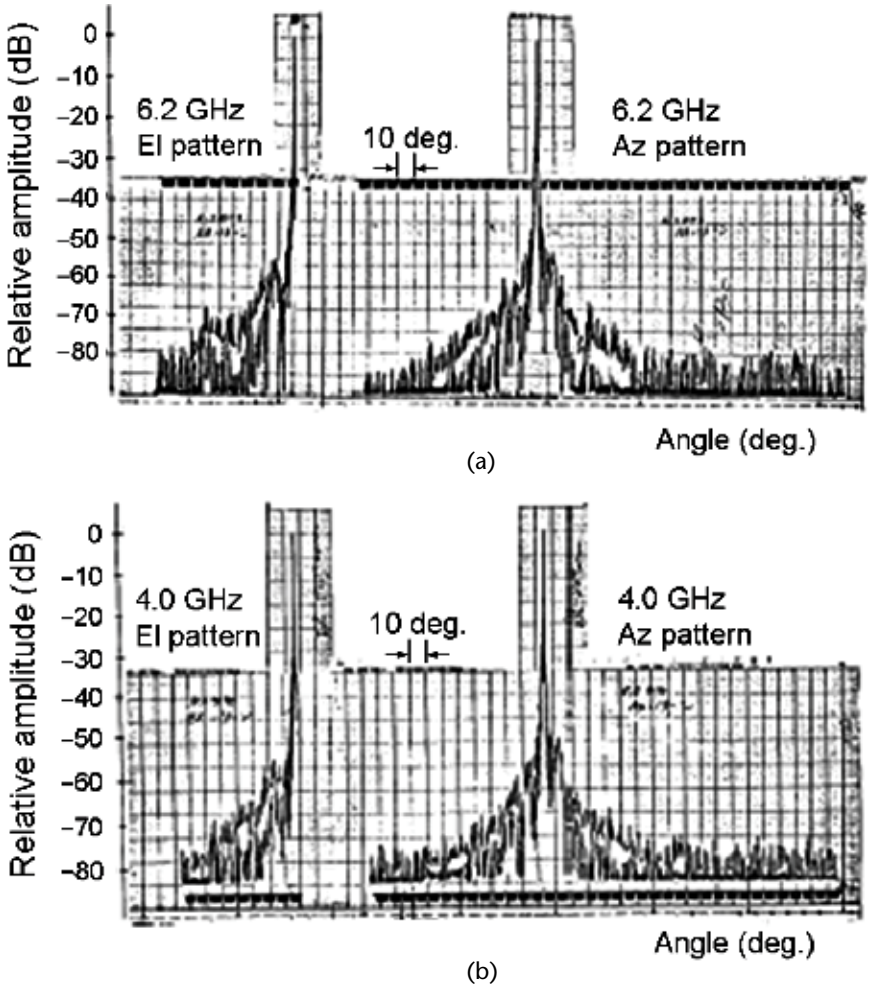

Figure 3.9 The radiation patterns of the Ibaraki No. 3 Earth Station: (a) 6.2 GHz and (b) 4.0 GHz [16].

A general description of how these two antennas are applied to microwave relay link systems is provided here:

1. The high-gain offset antenna with an aperture diameter of 3.6m is used at standard relay distance intervals of 50 km and at the terminal.
2. The offset antenna with an aperture diameter of 3m is used at relay distance intervals shorter than 50 km.

Good wide-angle radiation properties are required even at short distance intervals, due to route congestion. Therefore, wide-angle radiation properties nearly equivalent to that of the offset antenna with a 3.6m aperture diameter were targeted for the offset antenna with a 3m aperture diameter. Because these antennas exhibit excellent electrical and mechanical performance, they are widely used in all microwave relay link systems at 4, 5, and 6 GHz.

The antenna needed to meet the following demands:

Table 3.3 Comparison of the Electrical Performance of KDDI Earth Stations

Earth Station	*Ibaraki No. 1*		*Ibaraki No. 2*		*Yamaguchi No. 1*		*Yamaguchi No. 2*	
Year	1966		1968		1969		1980	
Antenna type	Cassegrain antenna (near-field type)		Horn-reflector fed modified Cassegrain		Horn-reflector fed shaped Cassegrain		Four-reflector beam waveguide-fed shaped Cassegrain	
Mount type	Yoke and tower		Yoke and tower		Yoke and tower		Wheel and track	
Satellite tracking	6m antenna slave tracking		Monopulse tracking		Monopulse tracking		Monopulse tracking	
Aperture diameter (m)	22		27.5		27.5		34	
Performance	*Tx*	*Rx*	*Tx*	*Rx*	*Tx*	*Rx*	*Tx*	*Rx*
Frequency (MHz)	6,337 ±63	4,121 ±63	6,175 ±250	3,950 ±250	6,175 ±250	3,950 ±250	6,175 ±250	3,950 ±250
Gain (dBi) [Frequency (MHz)]	60.0 (6,390)	56.9 (4,170)	62.7 (6,000)	58.9 (4,000)	63.2 (6,000)	59.8 (4,000)	65.6 (6,000)	61.9 (4,000)
Aperture efficiency (%)	46	53	62	58	70	72	79	76
Feed loss (dB)	0.50	0.52	0.11	0.22	0.10	0.21	0.18	0.22
Noise temperature (K) (elevation angle in degrees)		37.4 (30)		42.0 (5)		43.2 (5)		45.1 (5)
Axial ratio (dB)	1.4	0.9	1.0	1.3	1.3	1.5	0.25	0.28
Input VSWR	1.04	1.15	1.10	1.19	1.09	1.18	1.12	1.15

1. Improve the sidelobe and cross-polarization peak level by 10 dB or greater.
2. Miniaturize/reduce weight to be able to install a subantenna at a central height on an existing steel tower, in order to apply space diversity to all intervals.
3. To maintain the high reflector surface precision and assembly precision, after assembly at the factory, the antenna should be transportable without having to disassemble it.

The principal performance of the offset antennas with the 3.6m and 3m aperture diameters that satisfy the above-mentioned requirements are shown in Table 3.4, and the physical appearance of the antennas is shown in Figure 3.10.

3.3.1 Electrical Design

3.3.1.1 Geometrical Optics Cross-Polarization Cancellation [20]

In microwave relay link systems, because two orthogonal polarizations are used to maximize frequency efficiency, cross-polarized components that arise as a result of reflector asymmetry become problematic, as shown in Figure 3.11.

The solution to the problem is mutual cancellation of the cross-polarized components that occur in each reflector of a tri-reflector offset antenna that uses a corrugated conical horn or multimode horn, which generates few cross-polarized components, as the primary radiator. Generally, if there is a desired number of subreflectors existing between a primary radiator and a main reflector that is a rotating quadric surface reflector, it is possible to display an equivalent parabola [23].

Table 3.4 Antenna Primary Performance

	Antenna		*Antenna with Aperture Diameter of 3.6m*	*Antenna with Aperture Diameter of 3m*
Structural Variables	Aperture diameter (m)		3.6	3.0
	Aperture area (m^2)		10.2	7.07
	External dimensions (m)		3.7W × 5.6H × 3.1D	3.2W × 4.9H × 2.6D
	Mass (kg)		1,560	940
Electrical Performance	Frequency band (GHz)		4 (3.6 ~ 4.2), 5 (4.4 ~ 5.0), 6 (5.925 ~ 6.425)	
	Gain	3.9 GHz	40.7	39.0
		6.175 GHz	44.8	43.1
	Input VSWR	4.5 GHz	1.03 or below	
		6	1.025 or below	
	20° directional radiation level (dB)	3.9 GHz	–62	–60
		6.175 GHz	–65	–63
	30° directional radiation level (dB)	3.9 GHz	–68	–65
		6.175 GHz	–75	–72
	XPD (dB)	3.9 GHz	45 or above	43 or above
		6.175 GHz	45 or above	43 or above
Mechanical Performance	Directional adjustment angle (°)		Vertical: ±3, Horizontal: ±45	
	Wind resistance (kPa)		4.7 (equivalent to a wind velocity of 87 m/s)	
	Receiving wind load (at 4.7 kPa) (N)		79, 600	60, 700
	Seismec resistance (m/s^2)		49 (equivalent to 5G)	

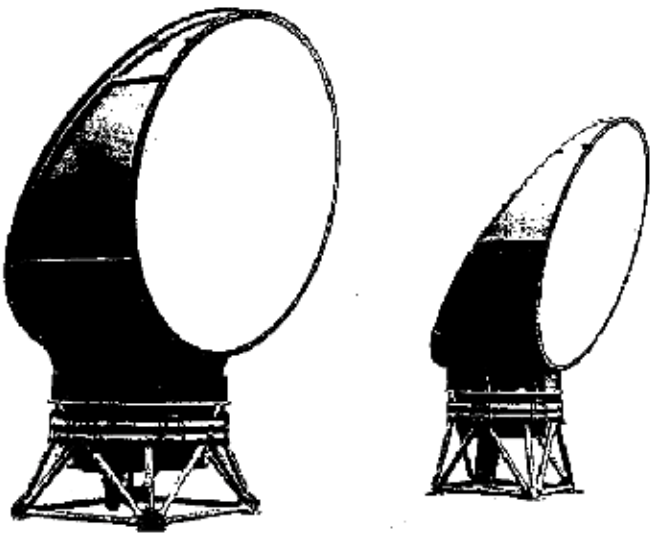

Figure 3.10 Physical appearance of antenna: aperture diameter of (a) 3.6m and (b) 3.0m.

Therefore, the tri-reflector offset antenna shown in Figure 3.12 is displayed as an equivalent parabola in Figure 3.13.

In this equivalent parabola, if the central axis of the primary radiator matches the parabola reflector axis (specifically, if $\varepsilon = 180$ deg), a rotationally symmetric, cross-polarization canceling system arises.

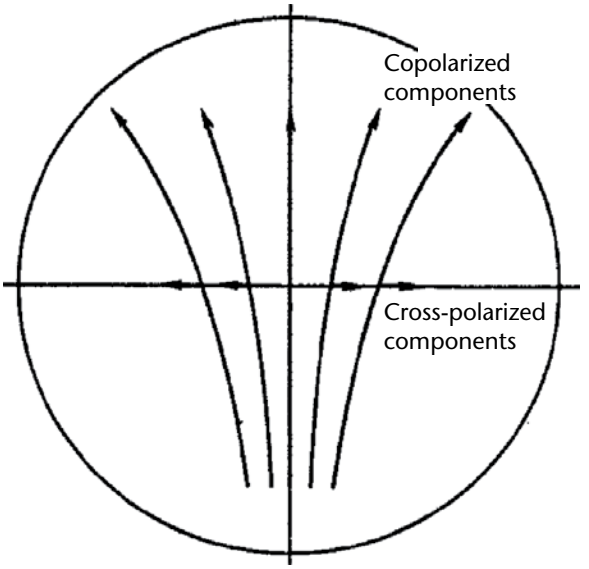

Figure 3.11 Aperture distribution of offset antenna.

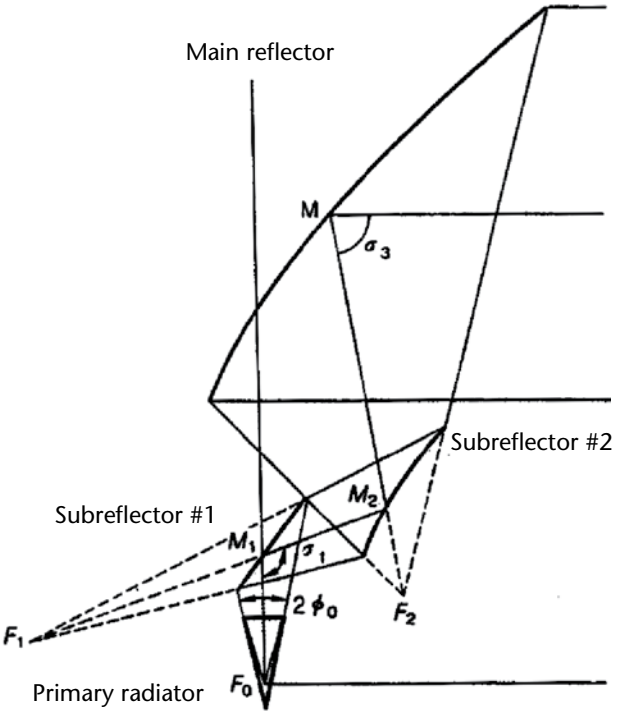

Figure 3.12 Tri-reflector antenna.

A reflector surface system that is capable of geometrical optics cross-polarization cancellation is shown in Figure 3.14, and it can be classified into 18 types according to focal point position differences and so forth.

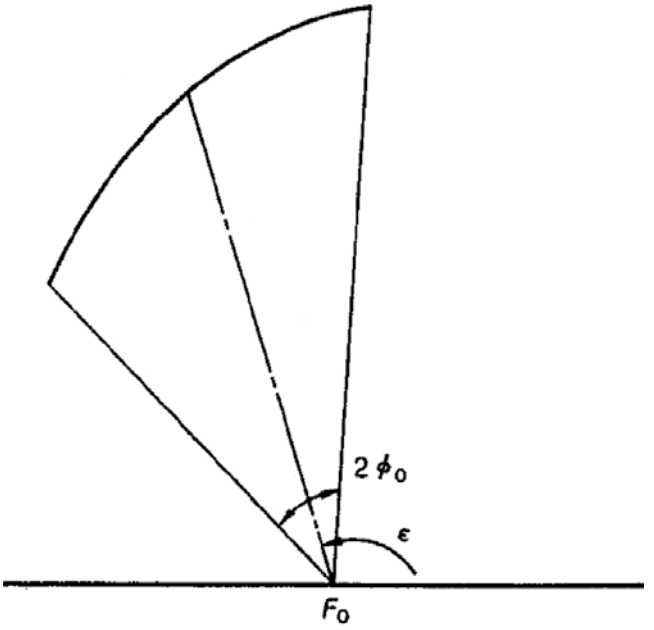

Figure 3.13 Equivalent parabola of tri-reflector antenna.

3.3.1.2 Design of an Antenna That Accounts for Undulation

A tri-reflector offset antenna designed according to the conditions for geometrical optics cross-polarization cancellation will not be a complete cross-polarization cancellation system at 4, 5, and 6 GHz. Therefore, the cross-polarized components at a specified frequency must be evaluated with respect to undulation.

According to the beam-mode expansion method [5], the maximum value C (electrical field) of the cross-polarized components, whose value is based on the maximum value of the copolarized radiation pattern, is provided in the following formula:

$$C = \frac{1}{\sqrt{2e}}\left|\delta_1 e^{j\theta_1}\frac{\omega_1}{f_1}\tan\frac{\sigma_1}{2} + \delta_2\frac{\omega_2}{f_2}\tan\frac{\sigma_2}{2} + \delta_3 e^{j\theta_2}\frac{\omega_3}{f_3}\tan\frac{\sigma_3}{2}\right| \tag{3.10}$$

Here, as shown in Figure 3.12, f_1, f_2, and f_3 are the focal point distances of subreflector #1, subreflector #2, and the main reflector; ω_1, ω_2, and ω_3 represent the beam radius on subreflector #1, subreflector #2, and the main reflector, respectively. Also, σ_i (i = 1, 2, 3) is an angle formed by an incident wave and a reflection wave. As for δ_i, when the main reflector is facing downward, $\delta_1 = \delta_2 = \delta_3 = 1$, and when the main reflector is facing upward, $\delta_1 = 1$ and $\delta_2 = \delta_3 = -1$. Also, the following expressions hold true:

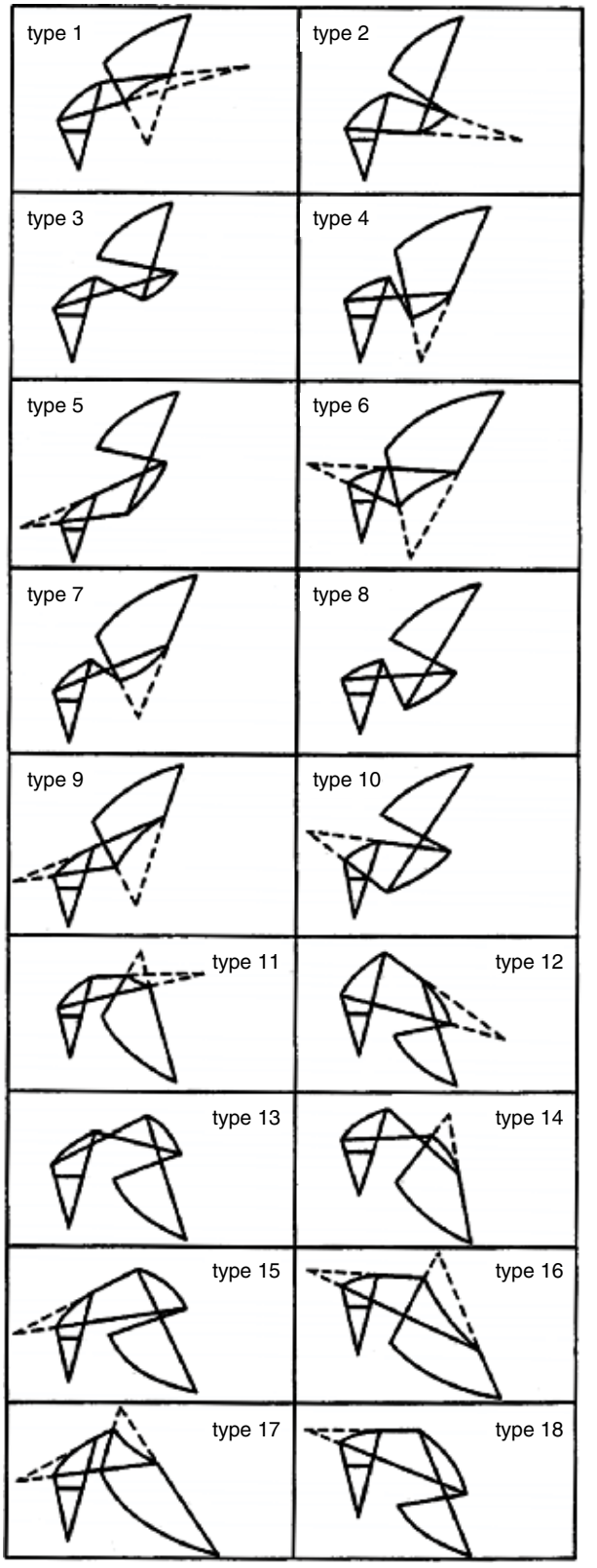

Figure 3.14 Tri-reflector antenna that meets the cross-polarization cancellation condition.

$$\left.\begin{aligned} e^{j\theta_1} &= \frac{1}{u_1}\left(\varepsilon_1\sqrt{u_1^{\,2}-1}+j\right) \\ e^{-j\theta_2} &= \frac{1}{u_2}\left(\varepsilon_2\sqrt{u_2^{\,2}-1}-j\right) \\ u_1 &= \frac{\pi\omega_1\omega_2}{\lambda d_1} \\ u_2 &= \frac{\pi\omega_2\omega_3}{\lambda d_2} \\ \varepsilon_1 &= \sin\left(\frac{1}{R_1'}+\frac{1}{d_1}\right) \\ \varepsilon_2 &= \sin\left(\frac{1}{R_2'}+\frac{1}{d_2}\right) \\ \frac{1}{f_i} &= \frac{1}{R_i}-\frac{1}{R_i'} \end{aligned}\right\} \tag{3.11}$$

where λ is the free-space wavelength. R_i and R_i' are the distance between the intersection point of the central beam on the reflector and the focal point on the incident (reflection) side of the reflector, respectively. They take negative values if there is a focal point at the incident side and reflection side of the reflectors and a focal point in the direction of light beam movement at the distance between the intersection points of the central light beam and the reflectors. Also, d_1 is the distance between the subreflectors measured along the central beam, and d_2 is the distance between subreflector #2 and the main reflector measured along the central beam.

Equations (3.10) and (3.14) are used to evaluate antenna cross-polarization properties. However, if the target value is not met, a correction is made using the abovementioned parameters. Factors other than cross-polarization properties that must be considered are edge level and spillover loss, which can be evaluated according to the results in [6].

3.3.1.3 Selecting Design Targets and a Reflector Surface System

Design targets are shown in Table 3.5. A reflector surface system that meets the target values in Table 3.5 should be selected from among the 18 types of reflector surface systems shown in Figure 3.14. However, the forms in which the main reflector faces upward are excluded, because the adherence of snow could cause properties to degrade. With respect to the remaining 10 types, the required reflector surface system is the geometrical optics cross-polarization cancellation system in which the aperture is 3.6m, and the results of an evaluation using (3.10) are shown in Table 3.6. Considering the results in the Table 3.6, type 10 has the lowest cross-polarization peak level out of the forms that meet the structural requirement of a 6m height or below, and therefore, type 10 is selected as this antenna reflector surface system. An undulation correction is performed for this reflector surface system to optimize wide-angle radiation properties and cross-polarization properties.

Table 3.5 Target Performance

	Antenna		*Antenna with Aperture Diameter of 3.6m*	*Antenna with Aperture Diameter of 3m*
Electrical Performance	Gain (dB)	3.6 ~ 4.2 GHz	39 + 20 log (*f*/3.9) dB or above	40 + 20 log (*f*/3.9) dB or above
		4.4 ~ 5.0 GHz	41 + 20 log (*f*/4.7) dB or above	42 + 20 log (*f*/4.7) dB or above
		5.925 ~ 6.425 GHz	43 + 20 log (*f*/6.175) dB or above	44.3 + 20 log (*f*/6.175) dB or above
	Radiation pattern		$5° \le \theta \le 45.4°$, $20.5 - 33.5 \log \theta$ dBi or below $45.4° \le \theta$, –35 dBi or below	
	Cross-polarization peak level (dB)		–30 or below	–35 or below
	VSWR		1.03 or below	
Structural limitations	Aperture diameter (m)		3	3.6
	Total height (m)		5 or below	6 or below
	Depth (m)		2.2 or below	2.43 or below
	Mass (kg)		1 or below	1.6 or below

Table 3.6 Properties of Each Type

Type	*Height (m)*	*Cross-Polarization Peak Level (dB)*
1	6.1	–25
2	6.0	–31
3	5.6	–20
4	5.4	–26
5	6.0	–25
6	5.7	–23
7	6.0	–23
8	5.5	–19
9	6.1	–25
10	5.8	–32

A reflector surface system with the optimal design is shown in Figure 3.15. Note that the offset antenna with an aperture of 3.6m has the reflector surface system that follows the reflector surface modification described in Section 3.3.1.4.

3.3.1.4 Achieving Asymmetric Aperture Distribution by Modifying the Reflector [22]

Reflector surface modification is not performed in the reflector surface system of the antenna with an aperture diameter of 3m. However, it is performed in the reflector surface system of the antenna with an aperture diameter of 3.6m: The main reflector and subreflector #2 are modified in order to further improve wide-angle radiation properties and cross-polarization properties.

Considering a dual-reflector offset antenna with a hypothetical main radiator whose phase center is at one focal point of subreflector #2, reflector surface modification in the reflector surface system selected in Section 3.3.1.3 is obtained through

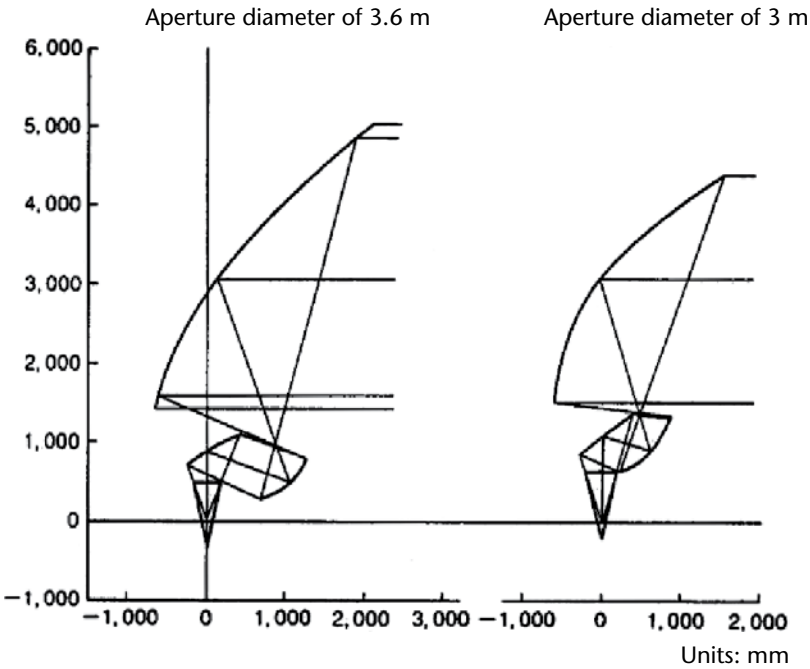

Figure 3.15 Antenna reflector surface shape.

numerical integration of the partial differential equation derived from the rule of reflection at the subreflector under conditions derived from (1) the rule of a fixed optical path length, (2) the axially asymmetric of the aperture distribution, and (3) the energy-saving side.

The result of reflector surface modification is the improvement of radiation properties by combining the aperture surface distribution into a desired distribution shape. For microwave relay antennas in particular, the important countermeasure for interference is to utilize the wide-angle properties of a horizontal surface. Low sidelobe properties that are the same over the entire solid angle are not necessarily required. If aperture distribution is achieved such that only surfaces that absolutely must have low sidelobes are rendered in a low sidelobe shape and all other surfaces are rendered into highly efficient shapes, then it is possible to implement low sidelobes while maintaining aperture efficiency. The target aperture distribution is shown in Figure 3.16.

3.3.1.5 Primary Radiator Selection and Design

If this antenna requires good wide-angle radiation and cross-polarization properties across the 4-, 5-, and 6-GHz bands, then the performance of the primary radiator must be as follows:

1. The main beam is rotationally symmetric.
2. There is little frequency variation of the main beamwidth.
3. Electrical power is high in the main beam.
4. The sidelobes are low and the voltage standing-wave ratio (VSWR) is small.

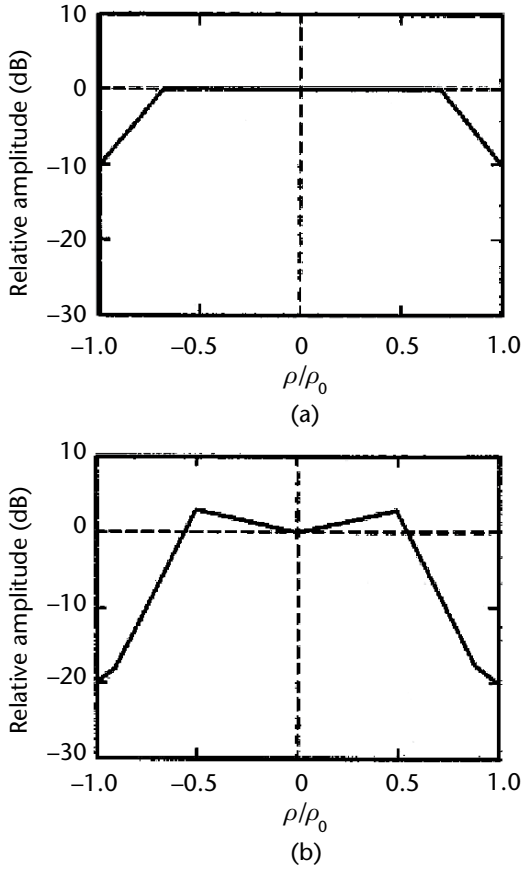

Figure 3.16 Target aperture distribution in a (a) vertical plane and (b) horizontal plane.

5. There is little frequency variation of the phase center.
6. There is a wide frequency range that meets the above-mentioned performance requirements.

A ring-loaded corrugated conical horn was utilized as the primary radiator meeting the above-mentioned performance requirements [24]. There are 35 columns in the corrugated uniform part, and the thickness of the fins is 4 mm. Also, the converter unit comprises a ring-loaded converter with 25 columns, and each dimension is determined such that trap resonance does not occur due to high-order mode waves.

3.3.1.6 Reduction of High-Order Period Components of Reflector Surface Distortion

Degradation of wide-angle radiation properties due to the period components of reflector surface distortion was a problem in the development project for this antenna. Conventional reflectors were made by press-forming. However, because the required reflector surface precision was the highly precise value of 0.3-mm rms, precision was ultimately achieved manually. Therefore, although a reflector surface

precision of 0.3-mm rms was eventually achieved, distortion occurred due to strike-forming at an approximate 300-mm pitch. The fact that distortion due to this high-order period component causes wide-angle radiation properties to degrade was revealed through analytical and experimental results [25].

As described next in Section 3.3.2 on structural design, the countermeasure is to achieve a reflector surface precision of 0.3-mm rms only through press-forming, by producing a highly precise press-forming mold. Figure 3.17 shows the wide-angle radiation properties obtained when using a press-formed reflector and a strike-formed reflector. As is clear from the figure, antennas using press-formed reflectors achieved a maximum improvement of approximately 5 dB from 20 to 30 deg in a horizontal plane, compared to antennas using strike-formed reflectors.

3.3.2 Structural Design

3.3.2.1 Mechanical Performance

After the antenna is lifted to an elevated location, such as a steel tower in a mountainous region or on the roof of a city building, the direction of the antenna is adjusted to match the azimuth and angle of elevation of the opposing antenna to within 1/100th of a degree, and the communication line must be maintained over many years against wind and seismic forces. Various mechanical conditions, such as air-proofing the entire antenna, must be met in order to accurately preserve strength and the relative relationships between the three reflectors and primary radiator, as well as to prevent corrosion of the feed waveguide system. Assembling these antennas under poor conditions, such as in mountainous regions or on the roofs of buildings, creates problems related to both quality and the duration of construction work.

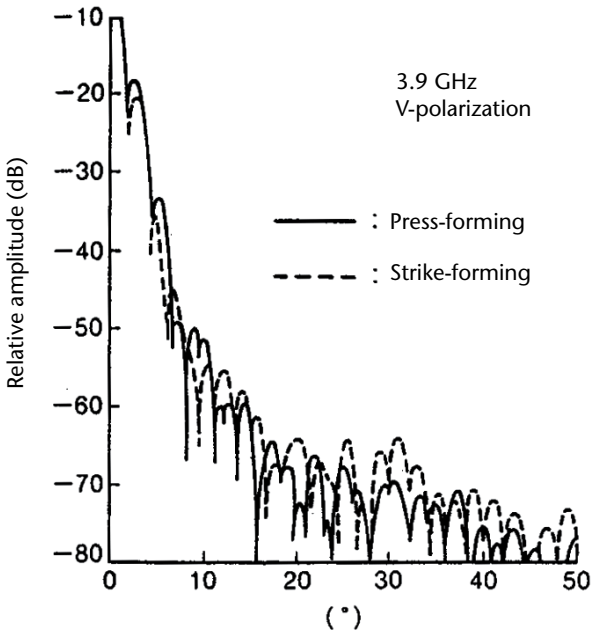

Figure 3.17 Improvement of wide-angle radiation pattern.

Therefore, the offset antenna is completely assembled at the factory, and then transported on a large, specialized vehicle without ever disassembling it. This makes it possible to begin lifting the antenna to the steel tower immediately. The dimensions of the antenna were miniaturized to enable it to be installed at a central height on an existing steel tower. The target mass of the antenna with a 3m aperture diameter was 1,000 kg or less, and the target mass of the antenna with a 3.6m aperture diameter was 1,600 kg or less. Also, the adjustment range of the azimuth angle in the conventional antenna was expanded from ±3 to ±45 deg to increase the location freedom on the steel tower. As for the load the antenna needed to withstand, the goal was to be able to withstand wind forces at a velocity pressure of 4.7 kPa (equivalent to a wind velocity of 87 m/s) and seismic forces at a horizontal acceleration of 49m/s^2 (equivalent to 5G). The physical appearance of the antenna that was designed is shown in Figure 3.18.

3.3.2.2 Shape Design

The shape of the offset antenna should be such that the limits of the inner dimensions are determined by a shape through which radio waves pass that accounts for undulation, and the limits of the outer dimensions are determined by placement/transport restrictions. Because the fundamental shape of the reflector surface system is a quadric surface, the enclosure of the offset antenna must also be a quadric surface, especially one that comprises an assembly of developable surfaces such as cylindrical or conical surfaces suitable for sheet metal processing. Reinforcement materials are almost unnecessary due to the geometrical stiffness of the curved surface, but the design should be such that the curvature and curvature direction do not change suddenly at intersecting parts.

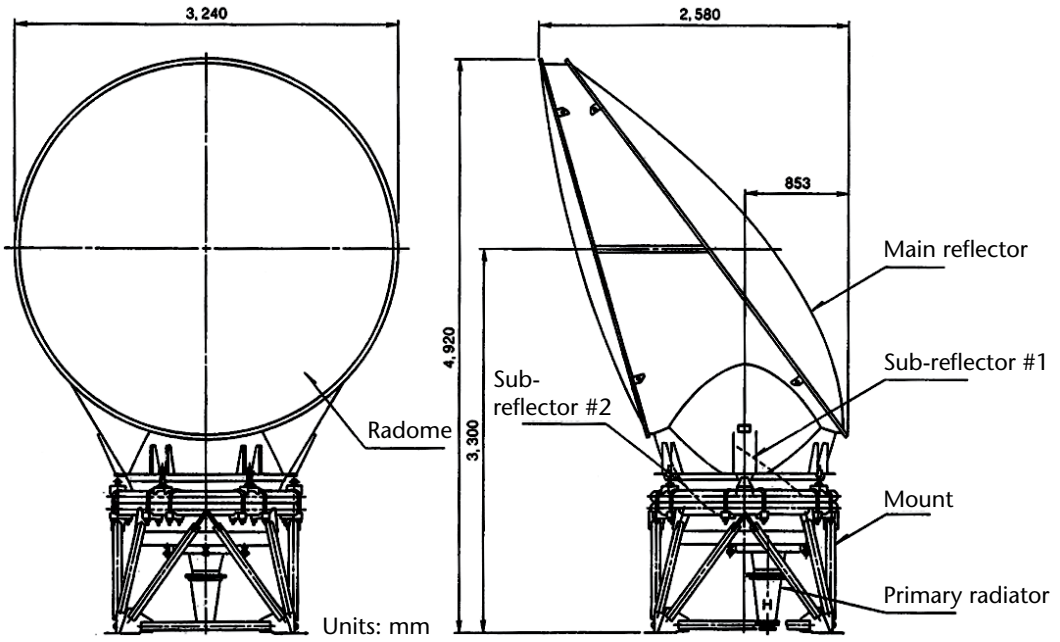

Figure 3.18 Physical appearance of the antenna (aperture diameter of 3m).

The geometrical design of a quadric reflector surface can be represented by a mathematical formula, and therefore is relatively easy to accomplish. However, for modified reflector surfaces expressed by discrete numerical values, a specialized coordinate processing program was developed to enable the coordinates of a desired point to be interpolated at micrometer precision.

3.3.2.3 Strength Design

Wind and seismic forces are representative of loads that act on the offset antenna. By designing an offset antenna with a decreased weight and low center of gravity, the effect of normal seismic forces is decreased compared to that of wind forces. Therefore, wind forces are mainly investigated here.

To prevent the obstruction of radio waves, the enclosure, which is the main structure of the offset antenna, is a thin shell without internal reinforcements and has a streamlined shape. Therefore, it is necessary to consider local negative pressure when investigating wind forces. In creating a strong design, a wind tunnel test is implemented using a reduced model, the pressure distribution of each antenna part is determined for each wind direction, and the strength of each part is confirmed through finite element analysis. In addition, tests are used to check the buckling pressure of the main reflector for which elastic stability (buckling due to wind forces) of the flat shell is problematic. Also, large-deformation analyses and tests are performed to check the strength of the radome, which changes shape several tens of times that of the sheet thickness.

3.3.3 Main Performance of a Prototype Antenna

3.3.3.1 Prototype Antenna Structure

The reflectors of the offset antenna with an aperture diameter of 3m are FRP-formed reflectors, and the reflectors of the offset antenna with an aperture of 3.6m are aluminum alloy press-formed reflectors. Utilizing these forming methods, it is possible to achieve good reflector surface accuracy.

As for other antenna components, the corrugated conical horn and the enclosure are aluminum alloy, and the mount is steel, and they are processed by hot-dip galvanizing. Also, glass fiber-reinforced Teflon is used for the radome, and radio wave absorbers are attached to the inner surface of the enclosure in order to improve wide-angle radiation properties.

3.3.3.2 Gain/VSWR

Table 3.7 shows the gain and VSWR measurement results. VSWR is almost completely determined by the performance of the corrugated conical horn, and a performance of 1.03 or less over the entire bandwidth has been achieved.

3.3.3.3 Near-Axis Radiation Properties

Figure 3.19 shows the measurement results of the paraxial radiation pattern of the offset antenna with an aperture diameter of 3m and the offset antenna with

Table 3.7 Gain/VSWR

		Antenna Aperture Diameter of 3.0 m			*Antenna Aperture Diameter of 3.6 m*		
Gain/VSWR		*V-pol.*	*H-pol.*	*Target value*	*V-pol.*	*H-pol.*	*Target value*
Gain (dB)	3.9 GHz	39.0 (52.8%)	39.1 (54.1%)	39.0 (52.8%)	40.7 (54.4%)	40.7 (54.4%)	40.3 (49.3%)
	4.7 GHz	41.0 (57.7%)	41.0 (57.7%)	41.0 (57.7%)	42.5 (56.6%)	42.7 (59.3%)	42.7 (50.4%)
	6.175 GHz	43.2 (55.4%)	43.1 (54.2%)	43.0 (52.9%)	45.0 (58%)	44.8 (55.7%)	44.3 (49.6%)
VSWR		1.03 or below					

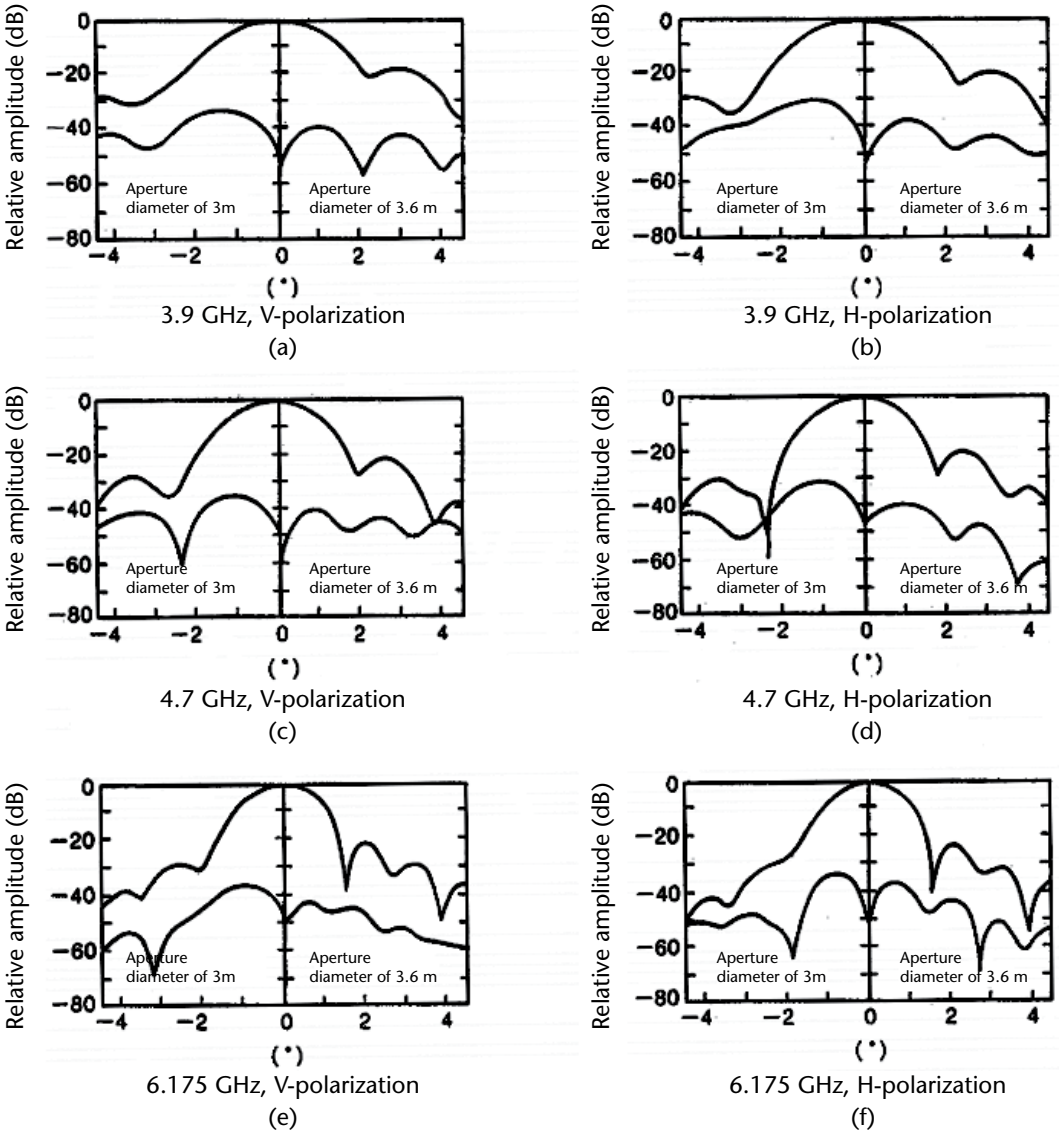

Figure 3.19 Near-axis radiation pattern in a horizontal plane.

an aperture diameter of 3.6m. For the offset antenna with an aperture diameter of 3m, the target value of the peak cross-polarization in a horizontal plane is –30 dB or below. In contrast to this target value, the measured values were approximately –30 dB at 3.9 GHz, approximately –32 dB at 4.7 GHz, and approximately –32 dB at 6.175 GHz. For the offset antenna with an aperture diameter of 3.6m, the target value was –35 dB or below. In contrast to this target value, the measured values were approximately –36 dB at 3.9 GHz, approximately –38 dB at 4.7 GHz, and approximately –38 dB at 6.175 GHz. These values satisfy the target performance.

3.3.3.4 Wide-Angle Radiation Properties

Figure 3.20 shows the wide-angle radiation pattern of the offset antenna with an aperture diameter of 3m and the offset antenna with an aperture diameter of 3.6m. To minimize the degradation of the wide-angle radiation properties that arises from scattered waves inside the antenna, radio wave absorbers are attached to the effective parts of the inner wall of the enclosure. Because FRP-forming and press-forming were utilized to form the reflectors, reflector surface precision is near the limit. Therefore, from the perspective of required gain, considering the fact that the reflector edge level cannot be lowered further, wide-angle properties are almost near the limit.

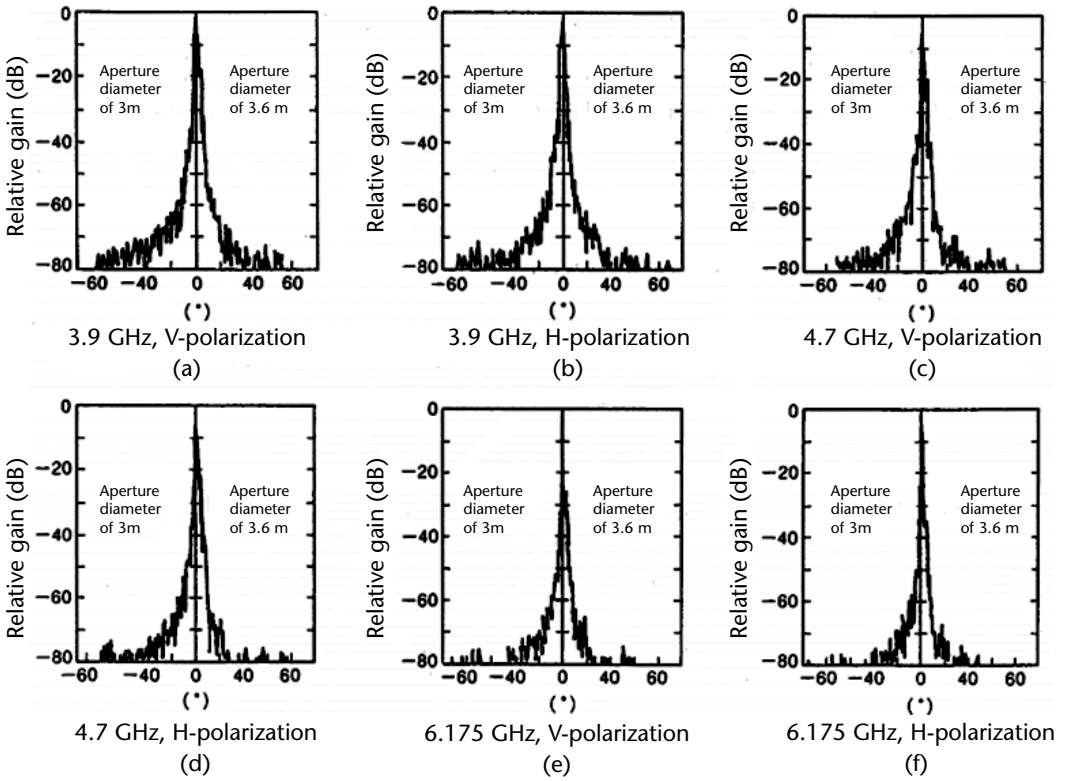

Figure 3.20 Wide-angle radiation patterns in a horizontal plane.

3.3.3.5 Summary

By using an offset antenna form with a tri-reflector, a miniaturized, lighter weight antenna that can be shared on the 4-, 5-, and 6-GHz bands and that has superior wide-angle and cross-polarization properties was achieved. The application of beam-mode expansion allows us to easily obtain properties that require time to calculate, such as aperture distribution variation and cross-polarization peak levels, and facilitates an optimized design for a repetitive multireflector. By achieving axially asymmetric aperture distribution through reflector surface modification, and by achieving highly precise reflectors through the adoption of a ring-loaded corrugated conical horn and press-forming and FRP-forming, wide-angle properties near the limit were achieved. Figure 3.21 shows a photograph of a tri-reflector offset antenna for terrestrial microwave relay link systems.

3.4 Shaped Beam Horn Reflector Antenna for 20/30-GHz-Band Communication Systems

A shaped-reflector antenna consists of a single feed horn and a shaped reflector. Beam shaping can be performed for reflector antennas by controlling one or a combination of the following three parameters: aperture shape, amplitude distribution on aperture, or phase distribution on aperture.

The phase distribution is easily controlled by changing the surface shape. This section presents a reflector design method based on the phase control for a given aperture shape and a primary radiator [26]. The method consists of three steps:

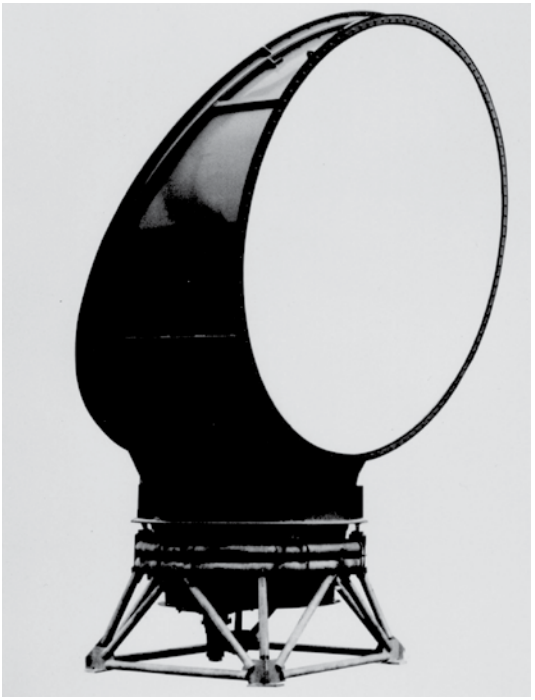

Figure 3.21 Tri-reflector offset antenna for terrestrial microwave relay link systems.

wavefront analysis, wavefront synthesis, and the design of the reflector surface. The design theory is based on geometrical optics.

3.4.1 Design

3.4.1.1 Wavefront Analysis

The inner part of the wavefront is part of a spherical wavefront as described here, and the outer part stays a constant width along the propagation path. In this case the energy in the inner part is spread over the desired service area, and that in the outer part is concentrated on the edge of the desired area in the sense of geometrical optics.

If such a wavefront exists, as shown in Figure 3.22, the normal vector has a constant direction on a curved line that passes the point Q, which lies on the contour of the inner part. Therefore, the curved line must be on a plane that includes Q. The intersection of the plane including the point Q and the plane including the neighboring point on the contour of the inner part of Q is a straight line. Consequently, the curved line mentioned above must be a straight line. In conclusion, the outer part of the wavefront is a ruled surface with the directrix of the contour of the inner part. If the normal vector on the generator passing Q of the ruled surface coincides with the normal vector of the inner part at Q, the ruled surface is the desired shape of the outer part of the wavefront.

To describe the wavefront, a rectangular coordinate system (x, y, z) and a polar coordinate system (r, θ, ϕ) with origin at O are defined as shown in Figure 3.22. The unit vectors tangential to each coordinate curve are designated by $\mathbf{i}$, $\mathbf{j}$, $\mathbf{k}$, and $\mathbf{e}_r$, $\mathbf{e}_\theta$, $\mathbf{e}_\phi$, respectively. The vector $\mathbf{W}$, which goes from O to W, a point on the wavefront, is represented by (3.12) when $\mathbf{W}$ is in the inner part:

$$\begin{aligned} &\mathbf{W} = r_w \mathbf{e}_r \qquad r_w : \text{constant} \\ &\mathbf{e}_r = \sin\theta\cos\phi\,\mathbf{i} + \sin\theta\sin\phi\,\mathbf{j} + \cos\theta\,\mathbf{k} \end{aligned} \tag{3.12}$$

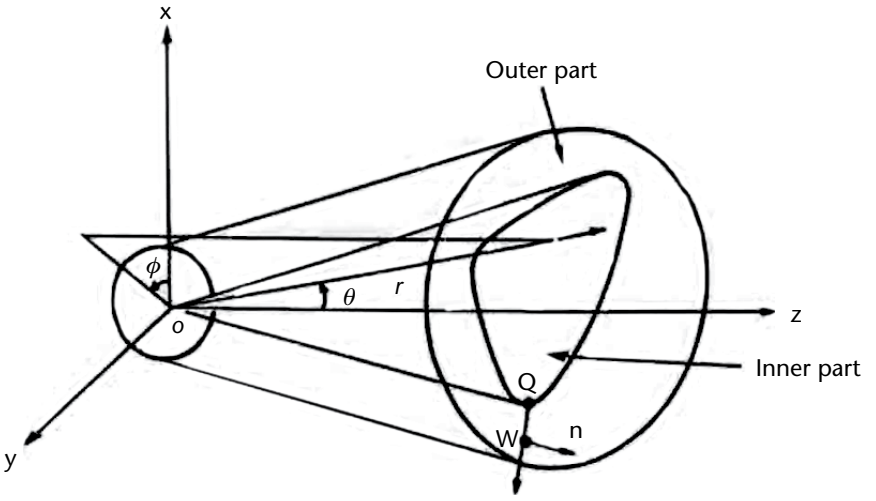

Figure 3.22 Structure of the wavefront.

The unit normal vector of the wavefront is $\mathbf{e}_r$. The contour of the inner part is determined when θ is defined as a function of ϕ.

When W is in the outer part and on the generator passing Q, the vector $\mathbf{W}$ is represented by (3.13), where $\mathbf{e}_s$ designates the unit vector tangent to the generator of the ruled surface, s is the distance between W and Q, and $\mathbf{n}$ is the unit normal vector of the wavefront:

$$\begin{aligned} &\mathbf{W} = r_w\mathbf{n} + s\mathbf{e}_s \qquad r_w : \text{constant} \\ &\mathbf{e}_s = \cos\theta'\cos\phi'\mathbf{i} + \cos\theta'\sin\phi'\mathbf{j} - \sin\theta'\mathbf{k} \end{aligned} \tag{3.13}$$

The unit normal vector $\mathbf{n}$ is constant on the generator passing the point $\mathbf{W}$; accordingly it must coincide with $\mathbf{e}_r$ at Q. From this condition, the parameters θ' and ϕ' in (3.13) are determined as functions of ϕ. In (3.15) θ is a function of ϕ, which defines the contour of the inner part of the wavefront. When χ is defined by

$$\chi = \phi - \phi' \tag{3.14}$$

χ and θ' are represented as

$$\begin{aligned} &\tan\chi = \frac{d}{d\phi}(\log\tan\theta) \\ &\tan\theta' = \tan\theta\cos\chi \end{aligned} \tag{3.15}$$

It is easily seen that the vector $\mathbf{e}_s$ in (3.13) is perpendicular to the normal vector $\mathbf{n}$ of the wavefront. Furthermore it is verified that the vector $\mathbf{e}_s$, is also perpendicular to the tangential vector of the contour of the inner part of the wavefront. Consequently, the outer part of the wavefront may also be defined as a ruled surface whose directrix is the contour of the inner part, and the generator is perpendicular both to the tangent of the contour and to the direction of the propagation of the wavefront at the cross point of the generator and the directrix.

The condition that the outer part of the wavefront can be determined without twist is $(d\chi/d\phi) \leq 1$, and by the relation of (3.15) it is also represented as follows:

$$\frac{d^2}{d\phi^2}(\log\tan\theta) \leq 1 + \left\{\frac{d}{d\phi}(\log\tan\theta)\right\}^2 \tag{3.16}$$

3.4.1.2 Wavefront Synthesis

When the function $\theta(\phi)$ describing the contour of the beam cross section is given and satisfies the condition (3.16), the shape of the wavefront is totally determined by (3.14) and (3.15) as shown previously. From a practical point of view, the desired shape of the beam cross section can be approximated to a polygon and then only the positions of the apices are meaningful. A method to synthesize the wavefront fitting in this case is now discussed.

For an example of the desired beam cross section, a triangle case is shown in Figure 3.23. At the apex A and the point B, whose distance from the beam center C is the local minimum, $\theta(\phi)$ has extremal values. Accordingly at these points $\tan \chi = 0$ is concluded from (3.15), and it means $\phi = \phi'$ by (3.14). From this result the problem is to find the functions θ and ϕ' of ϕ that satisfy the following conditions:

$$\begin{aligned} &\text{at} \quad \phi = \phi_a \quad \phi' = \phi_a \quad \text{and} \quad \theta = \theta_a \\ &\text{at} \quad \phi = \phi_b \quad \phi' = \phi_b \quad \text{and} \quad \theta = \theta_b \end{aligned} \tag{3.17}$$

When χ is supposed to be a linear function of ϕ as shown in Figure 3.24, it is represented by

$$\begin{aligned} \chi &= \frac{\chi_c}{\phi_a - \phi_c}(\phi - \phi_a), \quad \phi_a \le \phi \le \phi_c \\ &= \frac{\chi_c}{\phi_b - \phi_c}(\phi - \phi_b), \quad \phi_c \le \phi \le \phi_b \end{aligned} \tag{3.18}$$

The necessary conditions are :

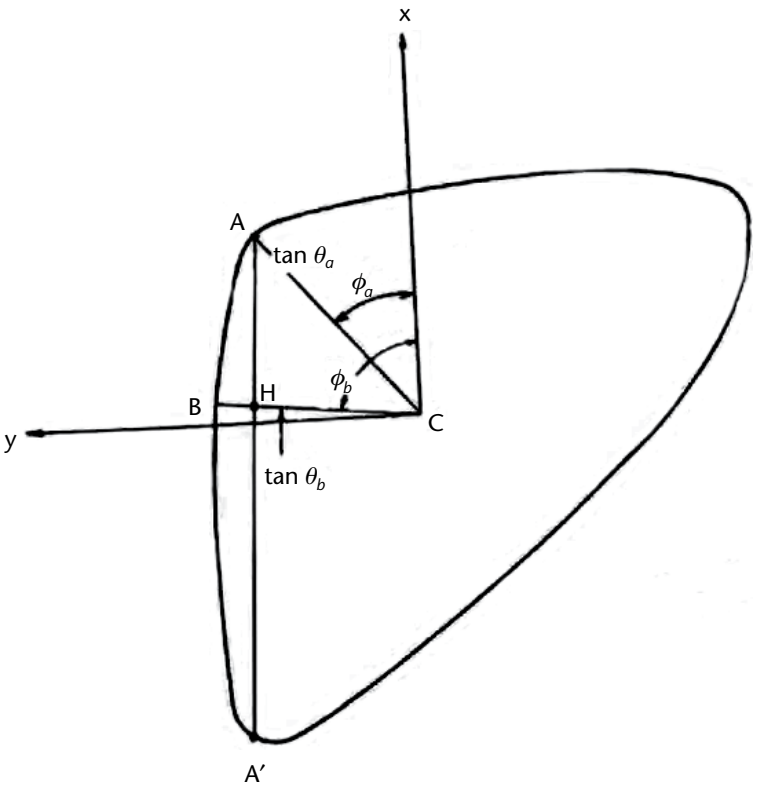

Figure 3.23 Example of a desired beam cross section.

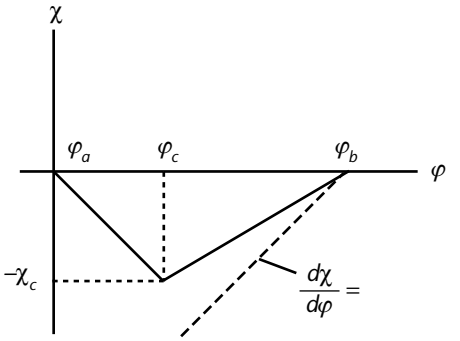

Figure 3.24 Graph of function $\chi = \phi - \phi'$.

$$\begin{aligned} &\phi_a \le \phi_c \le \phi_b \\ &\frac{\chi_c}{\phi_b - \phi_c} \le 1 \end{aligned} \tag{3.19}$$

From (3.15) and (3.17), (3.20) is derived:

$$\int_{\phi_a}^{\phi_b} \tan\chi d\phi = \log\left(\frac{\tan\theta_b}{\tan\theta_a}\right) \tag{3.20}$$

From (3.18), (3.21) is also derived:

$$\int_{\phi_a}^{\phi_b} \tan\chi d\phi = \frac{\phi_b - \phi_a}{\chi_c} \log\cos\chi_c \tag{3.21}$$

These two equations produce a transcendental equation for χ_c:

$$\cos\chi_c = \left(\frac{\tan\theta_b}{\tan\theta_a}\right)^{\chi_c/(\phi_b - \phi_a)} \tag{3.22}$$

The condition that (3.22) has a nontrivial solution is (3.23), which is easily seen from Figure 3.25:

$$\cos(\phi_b - \phi_a) < \left(\frac{\tan\theta_b}{\tan\theta_a}\right) \tag{3.23}$$

Solving (3.22) and choosing ϕ_c to satisfy (3.19), we obtain χ by (3.18). In the following calculation, the value of $\chi_c/(\phi_b - \phi_c)$ is set to 1 for convenience. The case discussed above is for $\phi_b > \phi_a$, but in the case of $\phi_b < \phi_a$ a similar calculation leads to χ with proper consideration of the sign. When $\phi_b - \phi_a = \pi/2$, (3.23) is always satisfied, and consequently χ is determined for arbitrary θ_a and θ_b.

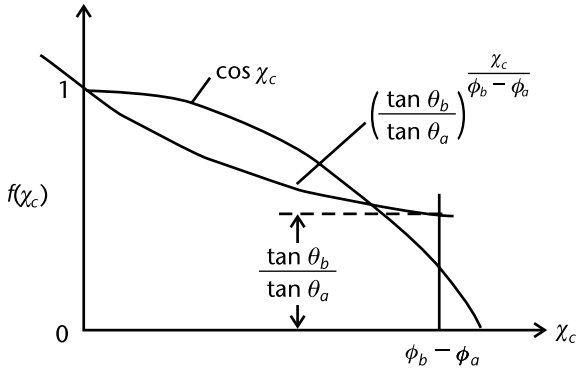

Figure 3.25 Solution of transcendental of (3.22).

Let two apices be designated by A and A' as shown in Figure 3.23. At the point B where the distance from C is the extremal minimum, condition (3.23) must be satisfied, which means that B must be in the exterior of two circles whose diameters are CA and CA'. In the following calculation B is set on the extension of the perpendicular of AA' from C, and the distance CB is given by (3.24), where κ is chosen to be a design parameter and H is the foot of the perpendicular of AA' form C:

$$CB = \kappa CH \tag{3.24}$$

When χ is determined as discussed above, θ is determined as follows:

$$\tan\theta = \tan\theta_a \exp\left(\int_{\varphi_a}^{\varphi} \tan\chi d\phi\right) \tag{3.25}$$

and θ' and ϕ' are determined by (3.14) and (3.15).

In conclusion, the shape of the wavefront is determined by κ and groups of (θ_a, ϕ_a), which represent the apices of the polygon approximated to the desired beam cross section. The resultant shape of the beam cross section is a polygon with rounded corners.

3.4.1.3 Design of the Reflector Surface

The reflector shape that converts a spherical wavefront into a desired wavefront is determined by the law of the optical path. The vector **W** that goes from O to W, a point on the wavefront, is represented by (3.12) and (3.13). The vector **M** that goes from O to M, a point on the reflector as shown in Figure 3.26, is represented by (3.26):

$$\begin{aligned} \mathbf{M} &= r\mathbf{e}_r \quad \text{(inner part)} \\ &= r\mathbf{n} + s\mathbf{e}_s \quad \text{(outer part)} \end{aligned} \tag{3.26}$$

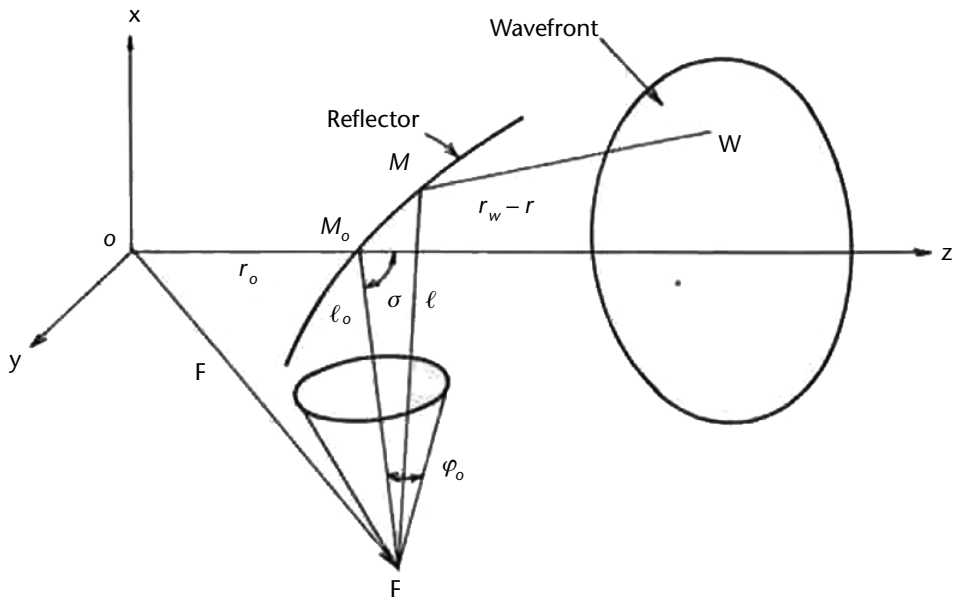

Figure 3.26 Determination of the reflector surface.

When F and $\mathbf{F}$ designate the position of the point source and the vector that goes from O to F, respectively, the condition that M is on the reflector is solved by (3.27), where l designates the distance between F and M:

$$l + r_w - r = c_0 \quad \text{(constant)} \tag{3.27}$$

Because l is equal to $|\mathbf{M} - \mathbf{F}|$, the calculation with the use of (3.26) and (3.27) leads to the following result:

$$\begin{aligned} r &= \frac{|\mathbf{F}|^2 - c_1^{\,2}}{2\{(\mathbf{F}\cdot\mathbf{e}_r) - c_1\}} \quad \text{(inner part)} \\ &= \frac{s^2 - 2s(\mathbf{F}\cdot\mathbf{e}_s) + |\mathbf{F}|^2 - c_1^{\,2}}{2\{(\mathbf{F}\cdot\mathbf{n}) - c_1\}} \quad \text{(outer part)} \\ c_1 &= r_w - c_0 \quad \text{(constant)} \end{aligned} \tag{3.28}$$

The outer contour of the reflector can be determined as the intersection of the extension of the feeding conical horn and the reflector surface. The shape of the aperture of this antenna is not a circle, so the diameter is not defined as one value. For convenience we define the nominal diameter D of the shaped beam horn reflector antenna with a conical horn feed by using (3.29):

$$D = \frac{2l_0 \sin\phi_0 (1 + \cos\sigma)}{\cos\phi_0 + \cos\sigma} \tag{3.29}$$

We presume that the axis of the conical horn passes through F and M_0, the intersection of the z-axis and the reflector. And l_0, ϕ_0, and σ in (3.29) designate the distance between F and M_0, half of the flare angle of the conical horn, and the offset angle as shown in Figure 3.26, respectively. If the given wavefront is a plane, the shape of the aperture is a circle and its diameter is represented exactly by (3.29). When values of design parameters D, ϕ_0, and σ are given, the size of the antenna and the position of F relative to M_0 are determined. One more design parameter is ϕ_1, which is the maximum angle subtended by the inner part of the reflector to F, and this parameter controls the power ratio between the inner part and the outer part. When the value of ϕ_1 is given, the distance between O and M_0, designated by r_0 in Figure 3.26, is determined. Hence, a shaped beam horn reflector antenna with a conical horn feed is designed when values of parameters D, ϕ_0, ϕ_1, σ, κ and (θ_a, ϕ_a) are given.

3.4.2 Performance

A typical antenna of this type is the shaped beam horn reflector antenna used in Japanese Communication Satellite 2 (CS-2) [27]. This antenna was designed by the preceding theory to fit Japanese islands. Figure 3.27 shows the reflector assembly of the antenna. The reflector is made of CFRP skins on an aluminum honeycomb

Figure 3.27 Photograph of the reflector assembly for CS-2 [28].

core. The antenna is used for four frequency bands: 4, 6, 20, and 30 GHz. The reflector shaping works effectively in the 30/20-GHz bands, and it does not affect the desired pencil beam in the 6/4-GHz bands. Figure 3.28 shows measured radiation patterns in each frequency band. The performance of the antenna is summarized in Table 3.8.

3.5 Offset-Shaped Dual-Reflector Antenna with an Elliptical Aperture for Satellite News Gathering

The satellite news gathering (SNG) systems transmit directly from the coverage spots, such as image material transmission and event relay. This section describes the features of and the design method for an in-vehicle station antenna used as a mobile station for an SNG system [28–30].

3.5.1 Reflector Design

This antenna is an offset Gregorian type, with an elliptical-aperture main reflector with an effective aperture of 2m (orbit plane) × 1m (orthogonal plane), and with reflector modification applied on the main and subreflectors. Additionally, the primary horn is a double-flare type, triple-mode horn with a rotationally symmetric beam for both its transmission and reception bands and a low cross-polarization component.

The major advantages of this antenna are that it is very efficient as has an excellent wide-angle radiation pattern and cross-polarization, which are intended to reduce radio wave interference with nearby satellites. (Interference is a particular problem with small-diameter antennas.) On-board vehicle antennas can be set on the roof of a small four-wheel-drive vehicle and electric power can be used to expand and retract them and establish satellite connections. Furthermore, all of the satellite communications equipment, including the main and subreflectors, is built for mounting to and dismounting from a vehicle and can be taken apart (like a portable station) so that in places where a vehicle cannot easily pass, the necessary equipment can be carried in and used as a portable station antenna.

The reflector system of the antenna is the offset Gregorian type and uses a main and subreflector for reflector modification. The reflector modification method used here began with selecting a quadratic reflector, which is the standard form, then gradually changing the form of the subreflector from a quadratic reflector. Then

Table 3.8 Performance of the CS-2 Antenna [28]

	Requirements		*Measured*	
	6/4-GHz band	*30/20-GHz band*	*6/4-GHz band*	*30/20-GHz band*
Frequency (GHz)	Tx: 3.7–4.2 Rx: 5.925–6.425	Tx: 17.7–19.45 Rx: 27.5–29.25	Tx: 3.7–4.2 Rx: 5.925–6.425	Tx: 17.7–19.45 Rx: 27.5–29.25
Polarization	Tx: RHCP, Rx: LHCP			
Gain (dBi)*	Tx: >25 Rx: >25	Tx: >33 Rx: >33	Tx: >26.3 Rx: >27.0	Tx: >34.5 Rx: >33.8

*Coverage area is all Japanese territory for the 6/4-GHz band, and the main Japanese island for the 30/20-GHz band.

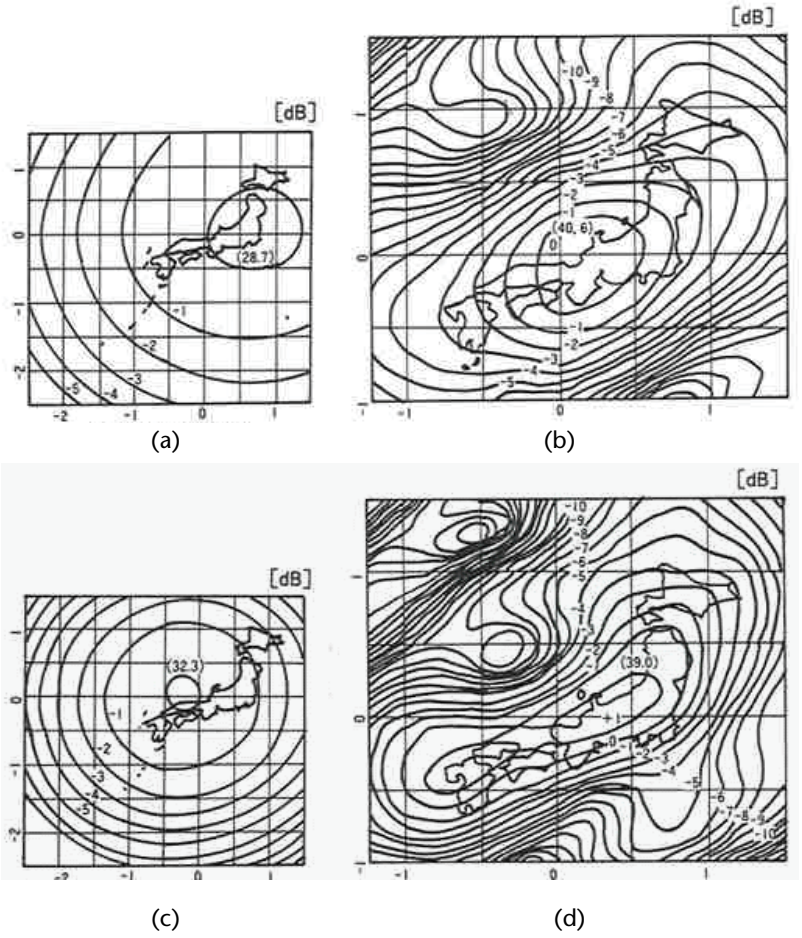

Figure 3.28 Measured radiation patterns of the communications antenna for CS-2: (a) 3.95 GHz, (b) 19.45 GHz, (c) 6.15 GHz, and (d) 29.25GHz [28].

the main reflector corresponding to the subreflector was determined based on the optical path length.

A coordinate system describing the main and subreflectors is shown in Figure 3.29. The rectangular coordinate system XYZ is set such that the Z-axis corresponds to beam direction and the ZX-plane corresponds to the central cross section of the antenna; **i**, **j**, and **k** are unit vectors of each axis. The rectangular coordinate system $X_1Y_1Z_1$ is set such that the direction of the central axis of the cone from origin O to the subreflector is defined as the Z_1-axis, and the Z_1X_1-plane corresponds to the central cross section of the antenna. The unit vectors of each respective axis are $\mathbf{i}_1$, $\mathbf{j}_1$, and $\mathbf{k}_1$, and the polar coordinates θ and ϕ are defined in relation to this coordinate system.

In Figure 3.30, r, the distance from origin O to any point R on the subreflector, is given by a function of θ and ϕ:

$$r = r(\theta, \phi) \tag{3.30}$$

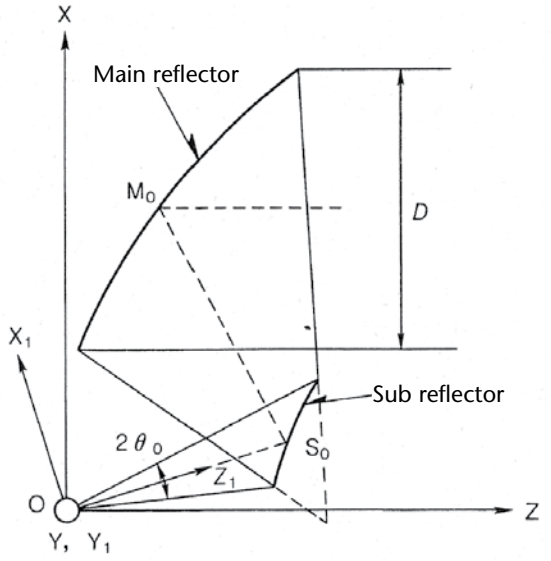

Figure 3.29 Reflector system and coordinate system.

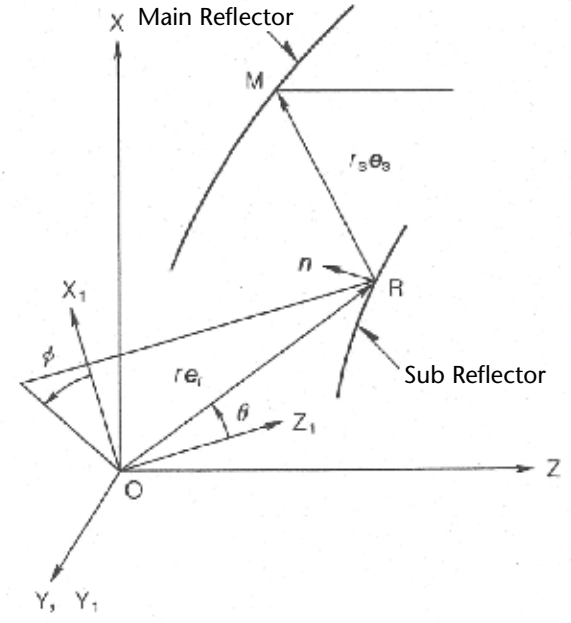

Figure 3.30 Main and subreflectors.

Then, if the vector from origin O to point R is labeled $r\mathbf{e}_r$, the vector from point R to point M on the main reflector is labeled $r_s\mathbf{e}_s$, and the vector from origin O to point M is labeled $\mathbf{r}_m$. These have the following relationship to each other, where $\mathbf{e}_r$ and $\mathbf{e}_s$ are unit vectors:

$$\mathbf{r}_m = r\mathbf{e}_r + r_s\mathbf{e}_s \tag{3.31}$$

$$r + r_s - \mathbf{r}_m \cdot \mathbf{k} = c \quad \text{(const.)} \tag{3.32}$$

$$\mathbf{e}_r = \sin\theta\left(\mathbf{i}_1 \cos\varphi + \mathbf{j}_1 \sin\varphi\right) + \mathbf{k}_1 \cos\theta \tag{3.33}$$

The following can be derived from (3.31) and (3.32):

$$r_s = \frac{c - r\left(1 - \mathbf{e}_r \cdot \mathbf{k}\right)}{1 - \mathbf{e}_s \cdot \mathbf{k}} \tag{3.34}$$

Using unit normal vector $\mathbf{n}$ at point R on the subreflector as $\mathbf{e}_s$ provides the following:

$$\mathbf{e}_s = \mathbf{e}_r - 2\left(\mathbf{e}_r \cdot \mathbf{n}\right)\mathbf{n} \tag{3.35}$$

$$\mathbf{n} = \frac{\dfrac{\partial r\mathbf{e}_r}{\partial\theta} \times \dfrac{\partial r\mathbf{e}_r}{\partial\varphi}}{\left|\dfrac{\partial r\mathbf{e}_r}{\partial\theta} \times \dfrac{\partial r\mathbf{e}_r}{\partial\varphi}\right|} \tag{3.36}$$

Finally, if θ and ϕ are given (which means that $\mathbf{e}_r$ is given), this in turn determines r from (3.30), $\mathbf{e}_s$ from (3.35) and (3.36), and $\mathbf{r}_s$ from (3.34). Then coordinate $\mathbf{r}_m$ of point M on the main reflector is determined from (3.31). Thus, the antenna radiation properties depend on $r(\theta, \phi)$, which determines the form of the subreflector. In this reflector design method, $r(\theta, \phi)$ chooses a quadratic reflector as the basis form, and transforms the shape according to the purpose:

$$r(\theta, \varphi) = r_0(\theta, \varphi) + \sum_i f_i(\theta, \varphi) \tag{3.37}$$

$$r_0 = \frac{\delta p a(\overline{e}^2 - 1)}{1 + \overline{e}(\mathbf{e}_r \cdot \mathbf{l})} \tag{3.38}$$

$$\overline{e} = \delta p e \tag{3.39}$$

Here, $r(\theta, \phi)$ is a nominal quadratic reflector and $f_i(\theta, \phi)$ is a reflector modification function; $\mathbf{l}$ is a unit vector from one focus O of the quadratic surface to another focus F; a is a constant; e is the eccentricity of the quadratic surface; δ is 1 for a concave mirror and –1 for a convex mirror; and p is 1 for a rotational hyperboloid mirror and –1 for a rotational ellipsoid mirror. The reflector modification function $f_i(\theta, \phi)$ is appropriately chosen in the function corresponding to the aperture shape or aperture field distribution.

The following points were taken into consideration in the design:

1. The antenna has a circular aperture equivalent to 1.4m. To avoid the interference in a satellite orbit plane, the real aperture size is set to an ellipse of 2m × 1m.
2. To make the antenna compact, the distance between the main and subreflectors should be as short as possible, and the structure should be designed so the feed does not overflow from the back of the main reflector.
3. After reflector modification, the reflector structure should be such that there is as little cross-polarization as possible.

The outline of the designed antenna is shown in Figure 3.31. The aperture distribution was set to make the edge level as low as possible; about 80% of aperture is uniform. The calculated values for the radiation pattern are shown in Figure 3.32. Calculated gains are 43.5 and 44.4 dB (including 0.2 dB of feed loss), respectively, for 12.25 and 14.5 GHz.

3.5.2 Mechanical Structure

A small on-vehicle station for SNG was put into practical use. The antenna consisted of actuator support parts and a radiation-feed system, which consisted of the main and subreflectors, the primary horn, and the feed system. Because the antenna is designed to be on board a vehicle, the wind load needed to be as small as possible and the antenna light and of a simple structure so that it would be easy to transport, assemble, and set up. The mechanical and electrical performances of this antenna are shown in Tables 3.9 and 3.10, respectively.

The main reflector, built of sheet molding compound (SMC) using aluminum-coated glass fiber as its reflective surface, divides into three reflector parts. The subreflector has a metal reflector made by pressing an aluminum panel, which keeps both the weight and cost low. To realize a weight savings for the feed system, aluminum material was used. The feed system is divided into two pieces in the symmetry plane, but it is a single piece in the axial direction.

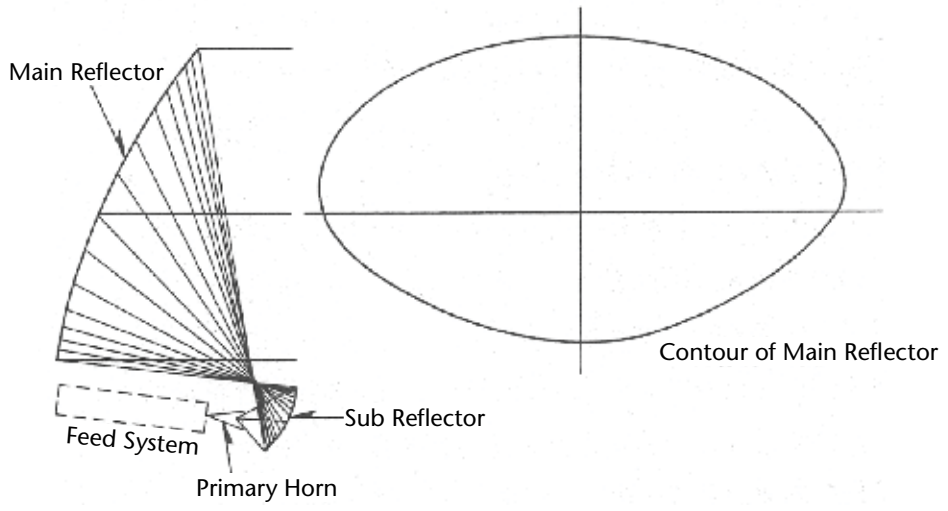

Figure 3.31 Outline of the designed reflector system.

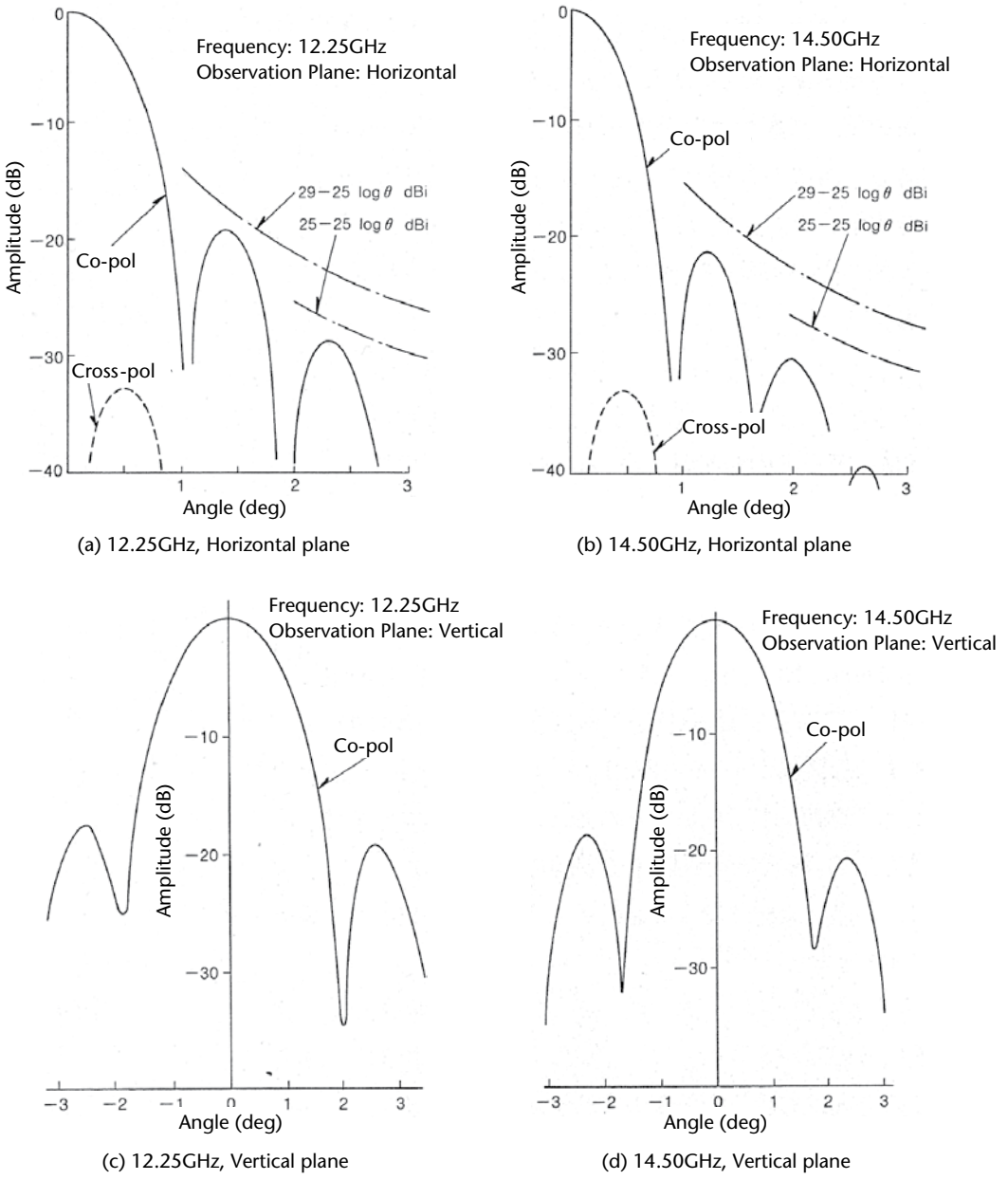

Figure 3.32 Calculated radiation patterns: (a) 12.25 GHz in the horizontal plane, (b) 14.50 GHz in the horizontal plane, (c) 12.25 GHz in the vertical plane, and (d) 14.50 GHz in the vertical plane.

The on-board station antenna is shown in Figure 3.33. This antenna can be set on top of a small four-wheel-drive vehicle and the antenna can be electrically expanded and retracted. It also has a direction sensor and incline sensor. It can automatically point its main beam in the direction of the satellite and also automatically set the polarization plane from the satellite and present position. The drive

Table 3.9 Mechanical Performance of SNG Antenna

Aperture diameter	1.4m equivalent (2m × 1m)
Mount	AZ-EL mount
Drive System	Electrical
Drive Range	AZ: ±180 deg EL: 30–60 deg
Weight	110 kg and below
Wind Velocity proof	During operation: 20 m/s max Deployable: 25 m/s max

Table 3.10 Electrical Performance of SNG Antenna

	Tx	*Rx*
Frequency (GHz)	14.0–14.5	12.25–12.75
Gain (dBi)	44.8	43.6
Aperture efficiency (%)	71	70
[Frequency (GHz)]	[14.25]	[12.5]
Noise temperature (K)	—	32
Sidelobe level (90% peak value)		
Cross polarization discrimination (dB)	35	
Polarization	Tx/Rx orthogonal linear polarization	
VSWR	1.3 and below	
Isolation (dB)	80 and above	
Maximum power	600W (CW) —	

part consists of a worm-drive reducer mechanism and brushless DC motor that can switch between two speeds: fast (5°/s) and slow (1°/s).

3.5.3 Main Performance

The antenna gains at the input port of the feed system are 44.8 dBi at 14.25 GHz and 43.6 dBi at 12.5 GHz. The aperture efficiency except the feed loss is 70% or greater at transmission and reception bands, thus achieving a high level of efficiency. The radiation patterns in the near axis and wide angle are shown in Figures 3.34 and 3.35, respectively. The radiation pattern has a cross-polarization discrimination of greater than 35 dB. The radiation pattern also has a low sidelobe that meets the condition of being $29 - 25 \log \theta$ dBi (1 deg $\leq \theta \leq$ 58 deg) and –15 dBi (58 deg $< \theta$), in spite of the antenna having a small aperture of only about 60 wavelengths. The noise temperature characteristics of the antenna in elevation angle at the output port of the feed system are shown in Figure 3.36. At an angle of elevation of 30 deg, it was under 35K. The measurement results confirm that all properties were achieved as indicated by the design values. The design method for the high-efficiency elliptical beam, the cross-polarization elimination reflector system, and the double-flare type, triple-mode horn are appropriate.

Figure 3.33 On-vehicle antenna mounted on the vehicle.

3.6 Low-Profile Dual-Shaped Reflector Antenna with an Elliptical Aperture for Aeronautical Satellite Communication Systems

Mobile satellite communication systems can provide global services without a terrestrial communications network by using artificial satellites. Several mobile satellite communications systems for engineering tests and commercial services have been reported [31–36]. To provide worldwide services, satellite communications antennas are required to point in almost all directions of an upper hemisphere. In addition, the antennas must have a low profile because of mounting restrictions.

A planar phased-array antenna [31, 32] is an attractive candidate for a low-profile satellite tracking antenna; however, it cannot achieve high antenna performance up to the low angle of elevation due to an effective aperture area reduction. On the other hand, a mechanically scanning antenna maintains high antenna performance up to a low angle of elevation. The aperture shape of a mechanical scanning antenna needs to be elliptical to prevent the increase of antenna height at any elevation beam direction. A dual-shaped reflector antenna with an elliptical aperture is employed for the mechanical scanning antenna that realizes a low-profile and high antenna performance.

The design of a low-profile dual-shaped reflector antenna with high antenna performance follows two procedures. First, the low-profile reflector antenna with an elliptical aperture is designed by using Aoki's geometrical optics (GO) shaping technique. The reflector antenna thus obtained realizes a low-profile antenna at

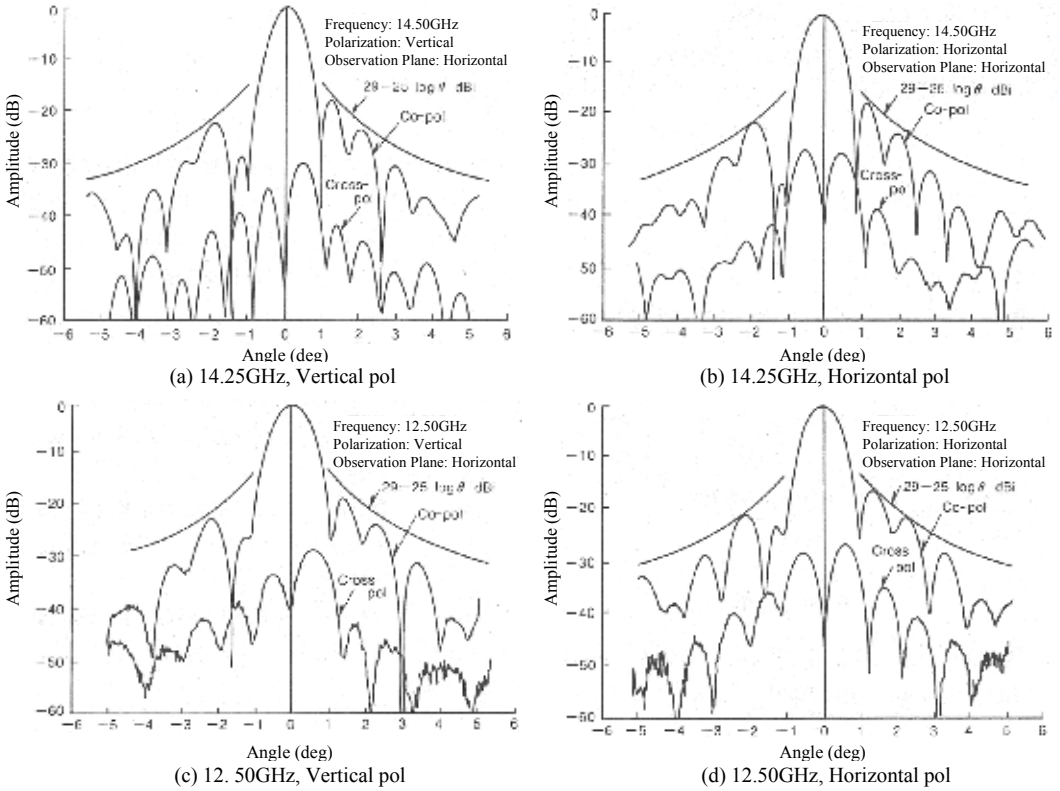

Figure 3.34 Near-axis measured radiation patterns.

any angle of elevation rotation. Next, the initial reflector antenna obtained by using GO shaping is shaped again to achieve the desired antenna performance by the suppression of undesired power. Here the antenna performance and the undesired power are evaluated by means of physical optics (PO). The desired antenna performance is expected to be achieved because the risk of antenna performance degradation is reduced by suppressing the undesired scattering. The resulting antenna is a low-profile reflector antenna that can be enclosed within a fixed circle to achieve the desired performance.

3.6.1 Design Method

3.6.1.1 Dual-Shaped Reflector Antenna with an Elliptical Aperture

The antennas for satellite communications that provide worldwide services must have the ability to cover almost all of the beam directions in the upper hemisphere. Here we present the basic concept for a low-profile dual-shaped reflector antenna that can be mechanically turned in up to the direction of a low elevation angle. The height of the main reflector edge is chosen as the focal length f of the paraboloid for taking the maximum aperture diameter. The main reflector is shaped to be enclosed within the circle viewed from the elevation axis of rotation. The diagrams of the antenna described above are shown in Figures 3.37 and 3.38. The proposed antenna maintains a low profile even in the direction of low elevation angle because all parts

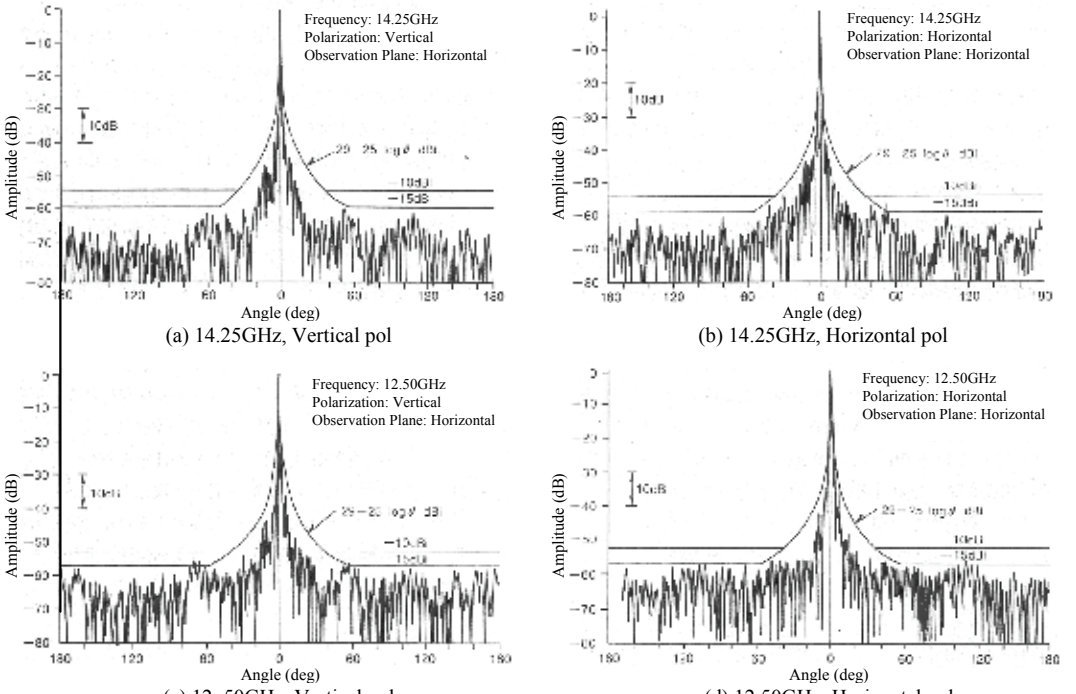

(a) 14.25GHz, Vertical pol (b) 14.25GHz, Horizontal pol

(c) 12. 50GHz, Vertical pol (d) 12.50GHz, Horizontal pol

Figure 3.35 Wide-angle measured radiation patterns.

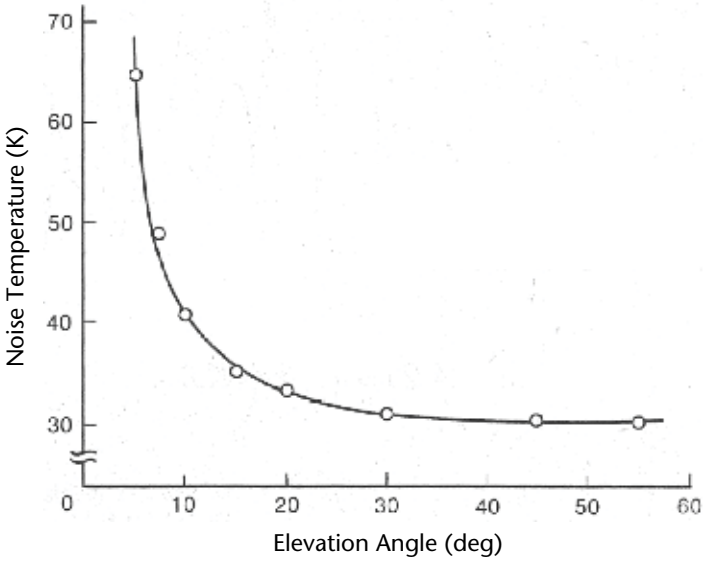

Figure 3.36 Noise temperature.

of the reflector antenna are enclosed within the fixed circle. The major and minor diameter, D_x and D_y, of the elliptical aperture are determined on the condition that the area of the elliptical aperture moves to a maximum.

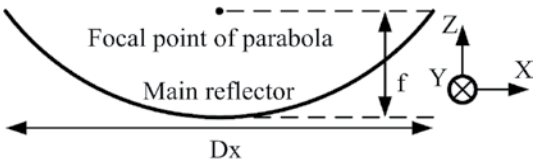

Figure 3.37 Side view of the main reflector.

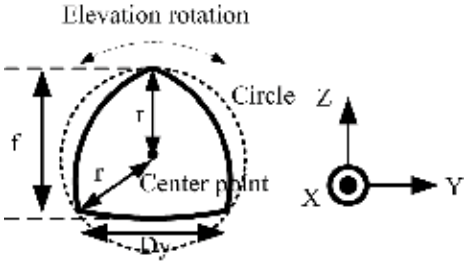

Figure 3.38 Diagram viewed from the elevation axis of rotation.

3.6.1.2 Initial Design

Several design methods for dual-shaped reflector antennas with an elliptical aperture have been proposed [29, 30, 37–39]. Here the reflector shaping technique based on GO proposed by Aoki [29, 30] is employed. Aoki's design method with modified shaping functions is presented in this section.

The coordinate system to define the parameters of a main reflector and a subreflector is shown in Figure 3.39. The rectangular coordinate system (X,Y,Z) is defined so that the aperture plane is parallel to the XY-plane. The phase center of a feed horn is set at the origin O. The unit vectors **i**, **j**, and **k** are the directions of the X, Y, and Z axes, respectively. The coordinates of subreflector and main reflector are defined by the spherical coordinates (r, θ, ϕ). Here r is the distance from O to the point **S** on the subreflector and a function of θ and ϕ.

The point **S** is expressed by using the direction vector $\hat{\boldsymbol{e}}_r$ as follows:

$$\boldsymbol{S}(\theta,\phi) = r(\theta,\phi)\hat{\boldsymbol{e}}_{\mathrm{r}} \tag{3.40}$$

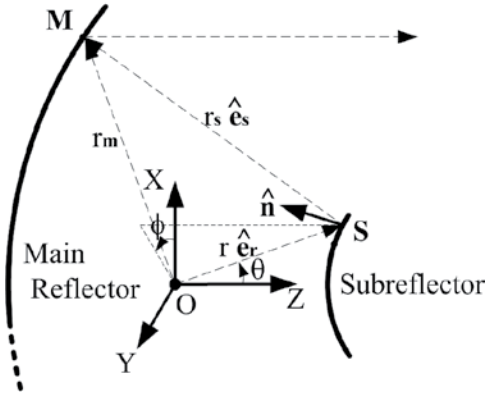

Figure 3.39 Coordinate systems of dual-shaped reflector antenna.

$$\hat{\boldsymbol{e}}_{\mathrm{r}} = \sin\theta\cos\phi\boldsymbol{i} + \sin\theta\sin\phi\boldsymbol{j} + \cos\theta\boldsymbol{k} \tag{3.41}$$

Once the coordinates of the point **S** have been determined, the corresponding point **M** on the main reflector is determined by GO [29, 30]. The vector $\hat{\boldsymbol{e}}_s$ is defined by the law of reflection on the subreflector and r_s is determined by the law of optical paths.

In this design method, r (θ, ϕ) is defined by a linear combination of some shaping functions added to the initial function representing a conventional quadric surface of revolution:

$$r(\theta,\phi) = r_0(\theta,\phi) + \sum_i f_i(\theta,\phi) \tag{3.42}$$

$$r_0(\theta,\phi) = \frac{a\left(1-e^2\right)}{1-e\left(\hat{\boldsymbol{e}}_{\mathrm{r}}\cdot\boldsymbol{k}\right)} \tag{3.43}$$

where $r_0(\theta, \phi)$ represents an initial quadratic surface of revolution, that is, ellipsoid or hyperboloid of revolution; $f_i(\theta, \phi)$ represents the reflector shaping functions; e and a are the eccentricity and constant of the subreflector, respectively. Two kinds of shaping functions are specified, one to modify the aperture shape and the other to modify the aperture field distribution. The functions to modify the aperture shape are:

$$f_1(\theta,\phi) = x_1 t^4\left(1-\cos 2\phi\right) \tag{3.44}$$

$$f_2(\theta,\phi) = x_2 t^4\left(\cos\phi - \cos 3\phi\right) \tag{3.45}$$

where $t = \theta/\theta_0$, and θ_0 is half of the angle subtended by the subreflector to the origin O. The functions f_1 and f_2 include t^4 instead of t^2 or t^3 in the conventional shaping functions [29]. Aoki's method sometimes yields a meaningless reflector with locally reversed surfaces. This problem is resolved by using an appropriate value for the exponent. The power of t is modified to realize a highly distorted reflector (described later). The function f_1 modifies the width of the aperture in the YZ plane while keeping the width of the aperture in the ZX-plane. The function f_2 modifies the asymmetry of the aperture shape with respect to the YZ-plane while keeping the widths in the YZ- and ZX-planes. The coefficients x_1 and x_2 control the magnitude of modifications. The functions f_1 and f_2 are mainly used to modify the aperture shape, but will also modify the aperture field distribution. Therefore, the above shaping functions should be determined before the modification of the aperture field distribution.

The shaping functions to modify the aperture field distribution are:

$$f_3(\theta,\phi) = \sum_{p=1}^{2}\sum_{q=1}^{3} y_{pq}\left\{G_{pq}(\theta)H_q(\phi) - G_{pq}(\theta_0)H_q(0)\right\} \tag{3.46}$$

$$
\begin{aligned}
G_{1q}(\theta) &= \exp\left(-\alpha_{1q}t^2\right) + \alpha_{1q}\exp\left(-\alpha_{1q}\right)t^2 - 1 \\
G_{2q}(\theta) &= -\left\{\exp\left(-\alpha_{2q}\right) - 1 - 2\alpha_{2q}\exp\left(-\alpha_{2q}\right)\right\}t^3/3 \\
&\quad -\left\{1 - \exp\left(-\alpha_{2q}t^2\right)\right\}t
\end{aligned}
\tag{3.47}
$$

$$
\begin{aligned}
H_1(\phi) &= 1 \\
H_2(\phi) &= 1 + \cos 2\phi \\
H_3(\phi) &= 1 - \cos 2\phi
\end{aligned}
\tag{3.48}
$$

Here the appropriate shaping functions are selected and modified from the conventional shaping functions. The function f_3 is modified to satisfy $f_3(\theta_0, 0) = 0$. The target reflector shape can be easily realized because of the fixed shape in the xz-plane. The coefficients α_{1q} and α_{2q} change the curves of $G_{1q}(\theta)$ and $G_{2q}(\theta)$, respectively. The function f_3 controls the aperture field distribution, while keeping the aperture shape approximately. The functions $G_{pq}(\theta)$ and $H_q(\phi)$ control aperture field distributions depending on θ and ϕ, respectively. The coefficient y_{pq} controls the magnitude of the modification. To keep the aperture shape, $G_{1q}(\theta)$ and $G_{2q}(\theta)$ satisfy the following condition:

$$
\left.\frac{dG_{1q}(\theta)}{d\theta}\right|_{\theta=\theta_0} = \left.\frac{dG_{2q}(\theta)}{d\theta}\right|_{\theta=\theta_0} = 0 \tag{3.49}
$$

Under this condition, a ray from the edge of the subreflector will not change the direction, so the aperture shape will be kept approximately, in that it will change slightly according to the change in position of the subreflector edge. The desired aperture field distribution is realized by using shaping function f_3.

3.6.1.3 Final Design

The low-profile dual-shaped reflector antenna enclosed within a fixed circle can be realized by the GO shaping described in the previous section. This method can successfully control the outline of the dual-shaped reflector antenna. However, the desired antenna performance cannot be achieved, especially for the small reflector antenna. The partial power reflected by the subreflector returns to the aperture of the horn antenna and the subreflector blocking region on the main reflector. The former power causes the degradation of the return loss and yields undesired scattering by the horn aperture. The latter power also yields undesired scattering and causes degradation of antenna performance. The undesired power must be suppressed to obtain the desired antenna performance.

Meanwhile a ring-focus type reflector antenna [40] does not yield the above undesired power in the sense of geometrical optics. However a ring-focus type reflector antenna with a highly distorted elliptical aperture cannot be realized by the presented GO shaping technique. The presented GO shaping technique does not

restrict the sign of the differential coefficient of the main reflector $dM(\theta, \phi)/d\theta$ and yields a meaningless reflector surface on the condition that negative differential coefficients occur at the main reflector.

The design conditions for a ring-focus type reflector antenna with a highly distorted elliptical aperture are very severe. It is difficult to keep a positive sign for the differential coefficients on the entire surface. Therefore, a design for a low-profile dual-shaped reflector antenna with high antenna performance is proposed that involves the following two procedures. First, the low-profile reflector antenna with elliptical aperture is designed by using the presented GO shaping technique. The reflector antenna thus obtained maintains a low profile at any angle of elevation rotation. Next, the initial reflector antenna is shaped again to achieve the desired antenna performance by the suppression of undesired scattering.

The undesired power from the subreflector on the aperture of both the horn antenna and the blocking region by the subreflector on the main reflector must be suppressed to reduce undesired scattering. The desired antenna performance is achieved by suppressing the undesired power to reduce the risk of antenna performance degradation. The antenna performance and the undesired power are evaluated by PO because GO does not predict the precise electromagnetic fields of an electrically small reflector. The initial reflector is shaped again by using PO. The reflector shaping based on PO has been reported on in [41]. The proposed method optimizes the suppression of undesired power as well as the antenna performance.

The functions for PO shaping are added in (3.42):

$$f_4(\theta,\phi) = \sum_{n=0}^{2}\sum_{m=1}^{2} z_{nm} J_n\left(\lambda_{nm}\,\theta/\theta_0\right)\cos n\phi \tag{3.50}$$

where λ_{nm} is the mth root of nth Bessel function of the first kind. The edge of the subreflector is fixed because of $f_4(\theta_0, \phi) = 0$. The objective function is defined by suppressing the undesired power as well as achieving desired antenna performance. The objective function is defined as the summation of individual objective functions associated with the antenna gain, the radiation pattern, and the undesired power on both regions.

Analytic optimization methods such as the conjugate gradient method are not suitable for optimizing the objective function G_{total} because the differentiation value of the objective function cannot be determined. We employ the genetic algorithm (GA) [42, 43], which can be easily applicable to various optimization problems. The coefficients z_{nm} of the shaping function $f_4(\theta, \phi)$ are represented as the chromosome, and the value of the objective function is treated as the fitness in the GA optimization procedures. The GA searches the optimization solution by changing the values of the chromosomes, in other words, changing the shape of the reflector surface. The optimum reflector shape is determined after the GA finds the optimum values of the coefficients z_{nm}.

3.6.2 Main Performance

The dual-shaped reflector antenna is designed by using the proposed method and evaluating the validity of the obtained reflector antenna. A Cassegrain antenna is used for the initial dual-reflector antenna before performing reflector shaping. The

target diameter of a circle shown in Figure 3.38 is 221 mm in consideration of the severe mounting restrictions. The parameters of the initial subreflector in (3.43) are $a = 103.157$, $e = 1.738$, and $\theta_0 = 30.184°$. A corrugated horn antenna with an aperture diameter of 64 mm is used as the primary radiator.

The reflector antenna can be shaped to be enclosed within the above circle by using the GO shaping technique described in Section 3.6.1.2. The coefficients of shaping functions defined in (3.44) and (3.45) that are used for changing the aperture's shape are $x_1 = -12.3$ and $x_2 = -21.36$, respectively. The aperture field distribution is also modified by using the shaping function $f_3(\theta, \phi)$ because initial conditions before PO shaping are significant to obtain better antenna performance.

The dual-shaped reflector antenna as thus far described realizes a low profile enclosed within a fixed circle. The initial reflector antenna is obtained by using GO shaping. However, the desired antenna performance cannot be achieved. So the initial reflector antenna is shaped again to achieve the desired antenna performance by using the proposed PO shaping described in Section 3.6.1.3. The parameters of PO shaping are presented. The reflector antenna is optimized at the center frequency of both the receiving band (11.2 to 12.8 GHz) and transmitting band (14.0 to 14.4 GHz). The coefficients of objective functions are determined so that antenna gains at both bands are preferentially optimized. The diagram of the designed dual-reflector antenna is shown in Figure 3.40.

The proposed PO shaping controls the antenna performance as well as the undesired scattering by the undesired power on the horn antenna and blocking region on the main reflector. The calculated electric field distributions at 12 GHz on the horn aperture are shown in Figure 3.41. The undesired power on the horn aperture is successfully reduced up to the design value. Achievement of the desired antenna performance is expected because the risk of antenna performance degradation is reduced by suppressing the undesired scattering.

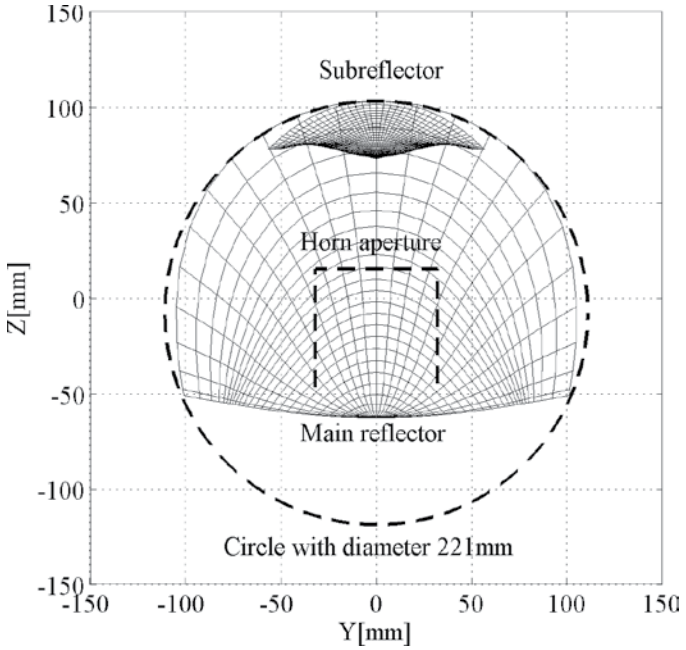

Figure 3.40 Diagram of designed low-profile dual-reflector antenna.

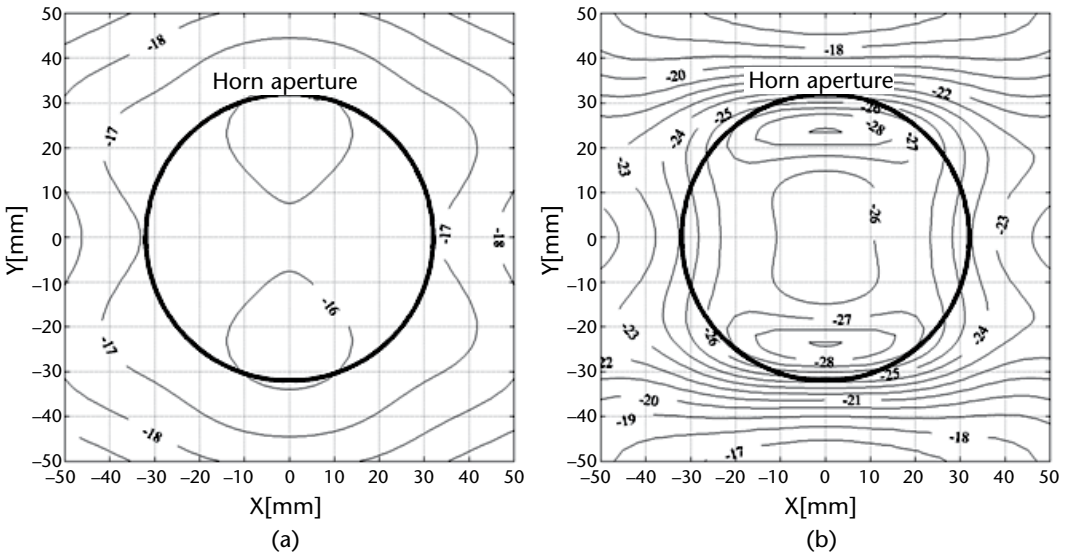

Figure 3.41 Electric field distribution (dBV/m) on the horn aperture at 12 GHz: (a) initial reflector and (b) designed reflector.

The calculated and measured antenna gain and antenna pattern are presented to investigate the proposed method. The measured antenna gain of the prototype antenna is compared with the calculated values, as shown in Figure 3.42. The measured antenna gain of the initial reflector is also presented. The proposed method successfully resolves the degradation of the antenna gain caused by the undesired power. The desired antenna gain is achieved in both the receiving band (11.2 to 12.8 GHz) and transmitting band (14.0 to 14.4 GHz).

The measured antenna patterns of the fabricated prototype antenna at the center frequency of both the Rx and Tx bands are shown in Figure 3.43. The proposed method successfully resolves the degradation of the antenna pattern caused by the

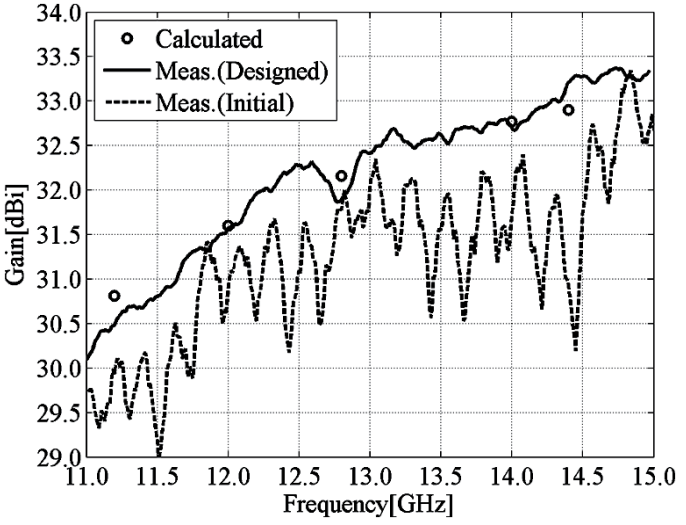

Figure 3.42 Comparison of calculated and measured antenna gain.

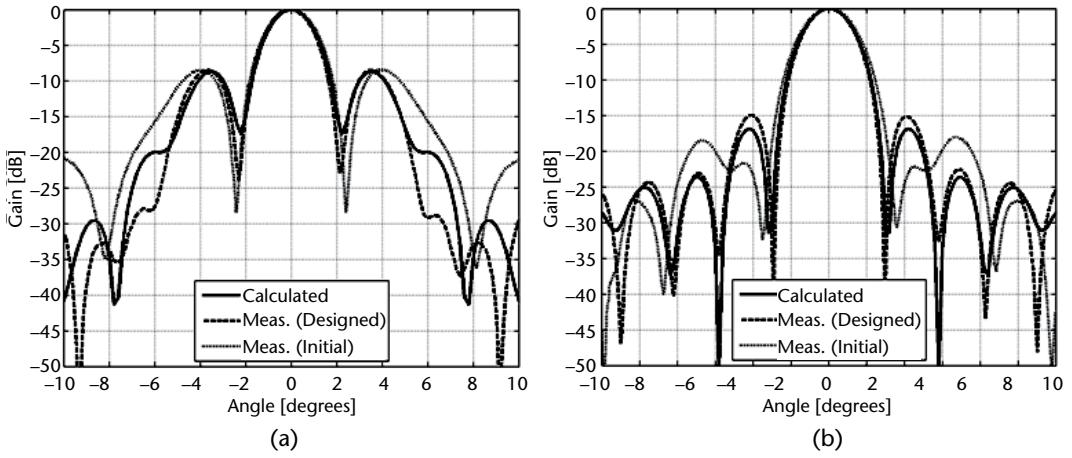

Figure 3.43 Comparison of calculated and measured radiation pattern at 12 GHz: (a) azimuth plane and (b) elevation plane.

scattering of the undesired power. The desired sidelobe level is also achieved in both bands. The calculated antenna patterns almost agree with the measured ones. It is shown that the degradation of antenna performance caused by the undesired scattering is prevented by the suppression of undesired power. The validity of the proposed method is supported by the measurements. Figure 3.44 shows a dual-shaped reflector antenna with an elliptical aperture for aeronautical satellite communication systems [36, 44].

3.7 Compact Reflector Antenna for Ku-Band ESV and VSAT

There is a growing need for broadband moving-vehicle satellite communication services for aircraft, ships, automobiles, and other moving vehicles [36, 44, 45]. Purposes include providing Internet service to passengers, traffic control, and the

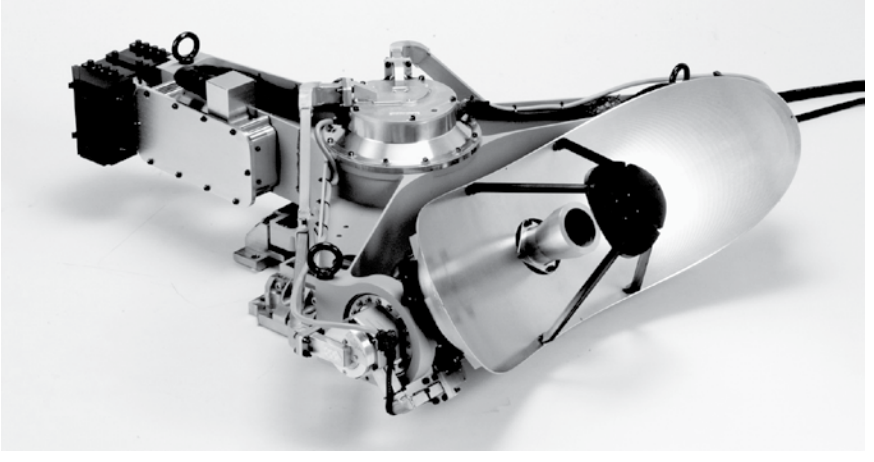

Figure 3.44 Ku-band elliptical aperture dual-reflector antenna for aeronautical satellite communication systems.

transmission of high-definition video from the scenes of disasters and incidents. Such systems require that moving vehicles be equipped with high-gain beam-scanning antennas. A great deal of research and development has already taken place on planar active phased-array antennas (APAAs) because they are easily modified into low-profile antennas and are excellent for installing in moving vehicles [33, 46]. However, APAAs have a complex structure and require numerous modules, so the cost problems are significant. On the other hand, there is a structure that would mechanically drive a compact reflector antenna that could achieve the necessary functioning and performance at a reasonable cost [36, 44, 45].

Generally speaking, if a reflector antenna can use a reflector large enough relative to the wavelength, it can easily realize high performance with just a simple structure. For that reason, such antennas are widely used for fixed satellite communications. However, smaller reflectors do not work well enough as ideal mirrors and thus their properties are degraded. For that reason, it has been a challenge to achieve the required performance given the size limitations of compact reflector antennas.

This section presents the problems with compact reflector antennas and discusses solutions to them. It also describes, as a design example, a compact reflector antenna developed for use as a Ku-band broadband ship satellite communications terminal, or an ESV (Earth station on vessel).

3.7.1 Compact Reflector Antenna Problems

The typical reflector antenna structures are classified into the offset type and center feed type. Figure 3.45 compares the two structures assuming that they have the same aperture size, which is a major parameter determining antenna performance. In the offset type, there is no blockage in the direction of radiating from the main reflector, but the antenna structure is rather large. In the center feed type, the primary radiator or the subreflector, which is located at the front of the main reflector, blocks the radiation from the main reflector, but this arrangement allows for a compact structure. Thus, the center feed type is effective for applying compact reflector antennas.

In terms of antenna radiating properties, blocking makes it difficult to achieve high efficiency and low sidelobes. Generally speaking, the lower the ratio of blocking area diameter to antenna aperture diameter, the better the performance. The aperture efficiency and sidelobe level achievable under blocking conditions and the ideal aperture distribution are known [47]. Thus, the problem in terms of a reflector antenna that needs to achieve both a small size and high performance (high efficiency and low sidelobe) is how to achieve an optimal aperture distribution close to the ideal while minimizing the blocking in a small center feed type.

To reduce blocking, making the primary radiator smaller is important in the case of a single-reflector antenna. For this, a backfire-type primary radiator is effective [48, 49]. A backfire primary radiator is self-supporting, so it has the advantage of avoiding the blocking caused by a support structure. However, primary radiation patterns cannot be finely controlled with backfire primary radiators, so there are limits on how far the aperture distribution can be optimized.

Dual-reflector antennas have the advantage of being able to optimize aperture distribution by using reflector surface modification technology. The diameter of the

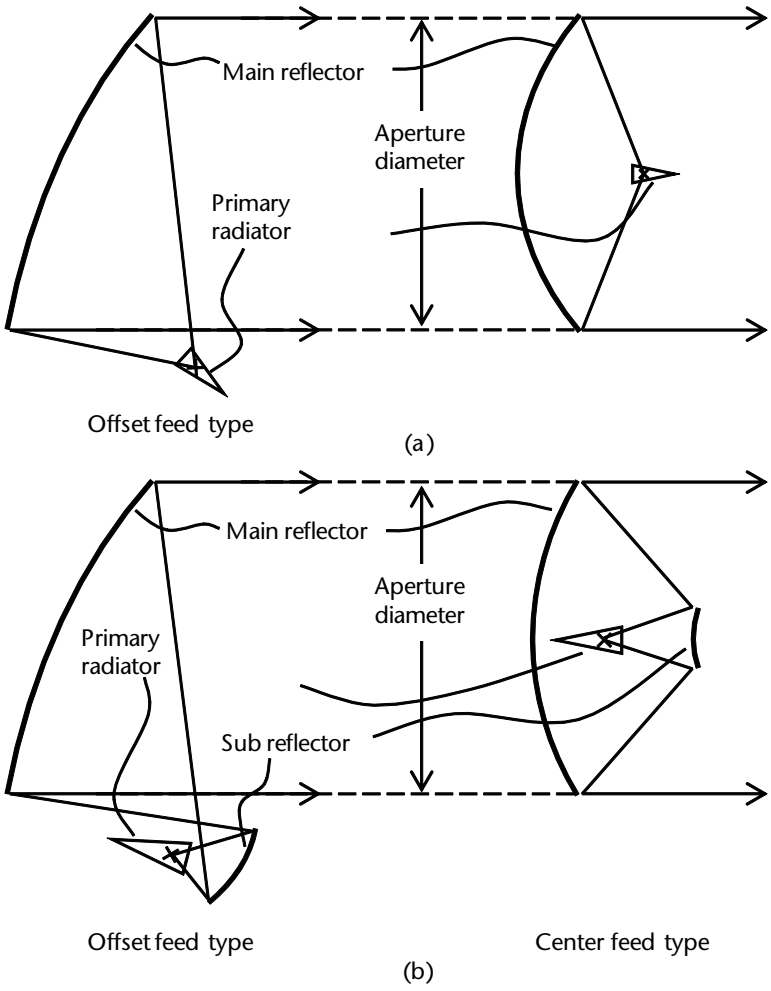

Figure 3.45 Comparison of offset type and center feed type antennas for (a) single reflector and (b) dual reflector.

subreflector must be several wavelengths at least, in order to function as a mirror and to realize optimum aperture distribution.

The results of the above discussion are summarized in Table 3.11. In cases where the antenna aperture is relatively large and the blocking of a subreflector is acceptable, a dual-reflector antenna that has excellent optimization of its aperture distribution is advantageous. Single-reflector antennas are advantageous if the antenna aperture is small and blocking of a subreflector is not acceptable. Thus, it is necessary to select an antenna structure suited for the desired radiating characteristics and size, especially the antenna aperture.

Figure 3.46 shows design examples for a compact reflector antenna for mobile satellite communications Earth stations. Figure 3.46(a) shows a 1m antenna (dual-reflector antenna) for a Ku-band broadband satellite communications terminal on board a vessel (Ku-Mate® SX-5300), which is certified for Eutelsat Standard M type approval. Figure 3.46(b) shows a Ku-band Helisat 40-cm antenna (a single-reflector antenna using a backfire primary radiator), compatible with HD video transmission on board a helicopter.

Table 3.11 Compact Reflector Antenna Problems and Solutions

Problem	*Solutions*
Compact antenna	Use center feed type
High efficiency	Reduce blocking
Low sidelobe	Use backfire-type small primary radiator (single-reflector type)
	Decrease diameter of subreflector (dual-reflector type)
	Optimize aperture distribution
	Optimize primary radiation pattern (single-reflector type)
	Modify reflector surface (dual-reflector type)

(a) (b)

Figure 3.46 Compact reflector antennas for mobile satellite communications Earth station: (a) Ku-band ESV (1m dual-reflector antenna, Ku-Mate® SX-5300) and (b) Ku-band Helisat (40-cm single-reflector antenna).

3.7.2 Design Example

We next discuss a design example for a Ku-band ESV antenna with a 1m aperture.

3.7.2.1 Design Procedures

The design procedures are as follows:

1. Select antenna configuration.
2. Determine antenna structure.
3. Optimize aperture distribution by reflector surface modification.
4. Confirm radiating properties.

The design process was conducted as follows for each step:

1. *Select antenna configuration*. The single-reflector type and double-reflector type were comparatively examined. Based on the results, the double-reflector type was chosen because the antenna aperture was relatively large at 50 wavelengths. A ring-focus Gregorian antenna structure was chosen in order to reduce the effects of subreflector blocking and to ensure freedom of design of the primary radiator. The reflector configuration is shown in Figure 3.47.

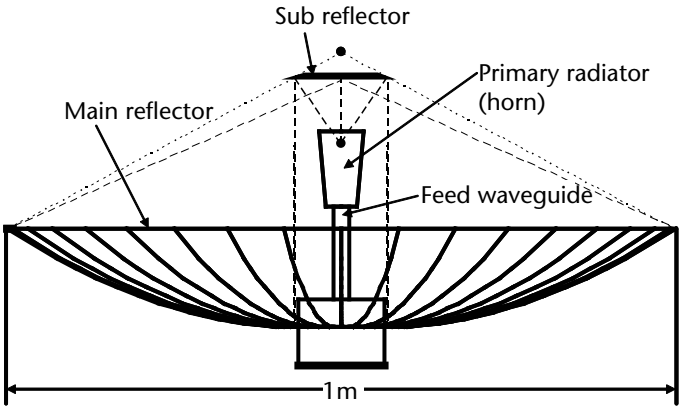

Figure 3.47 Reflector configuration.

2. *Determine antenna structure*. The beam is scanned with a mechanical drive mechanism across the entire antenna, because it tracks a satellite in response to changes in ship position and attitude. Thus, to achieve a compact antenna structure, the focal length of the main reflector was based on a length that would minimize the swept volume of the antenna sweeps across the entire scanned range. The subreflector diameter was set to six wavelengths, the minimum necessary to optimize aperture distribution in the range where blocking is acceptable.
3. *Optimize aperture distribution by reflector surface modification.* The ideal aperture distribution under the condition that there will be blocking is known [47], but is hard to actually achieve with a compact reflector antenna. Therefore, the first step was to modify the reflector surface using geometrical optics. Then the surface was corrected using wave theory analysis to optimize the aperture distribution, getting close to the ideal distribution. Analytical precision is a problem with wave theory analysis since the subreflector diameter is small. Here, analysis precision was enhanced by the finite element method (FEM), wherein analysis was conducted on the feed waveguide, the primary radiator horn, and the subreflector.
4. *Confirm radiating properties.* As in step 3, precision was enhanced by using the results of FEM analysis, taking the main reflector as the radiating wave source. The current induced on the main reflector was calculated by a physical optics (PO) approximation and the antenna radiating properties were analyzed.

3.7.2.2 Reflector Surface Modification Using Wave Analysis

Next we describe a correction of the aperture phase distribution based on wave theory analysis.

The phase distribution in the E- and H-planes at the antenna aperture before correction is shown in Figure 3.48, with radial coordinates on the horizontal axis. The figure shows that there is a gap of up to 60 deg (±30 deg) from the ideal uniform phase distribution.

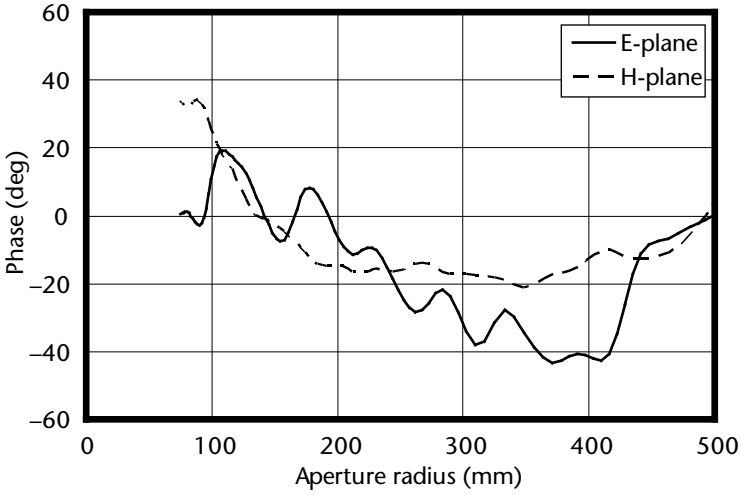

Figure 3.48 Aperture phase distribution before modification.

The aperture phase distribution shown in Figure 3.48 can be made close to the ideal uniform phase distribution by modifying the main reflector's surface . The amount of modification in the main reflector's axial direction is shown in Figure 3.49. Because an axisymmetrical main reflector is easily manufactured, the average of the main reflector across the circumferential direction was used as the amount of modification. Figure 3.50 illustrates the radiation pattern before and after reflector surface modification. It shows that the first and second sidelobes in the E-plane and the first sidelobe in the H-plane were reduced as a result of reflector surface modification.

3.7.3 Main Performance

Measured radiation patterns are shown in Figure 3.51. Also shown in this figure is the off-axis radiation standard for EIRP density as in Eutelsat Standard M. The

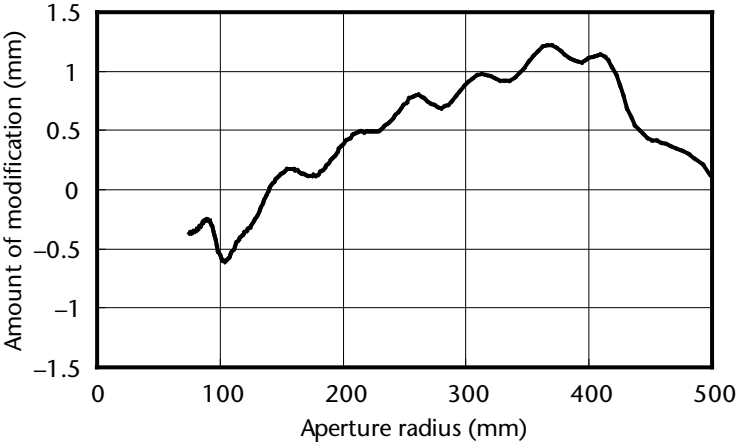

Figure 3.49 Amount of modification in the main reflector's axial direction.

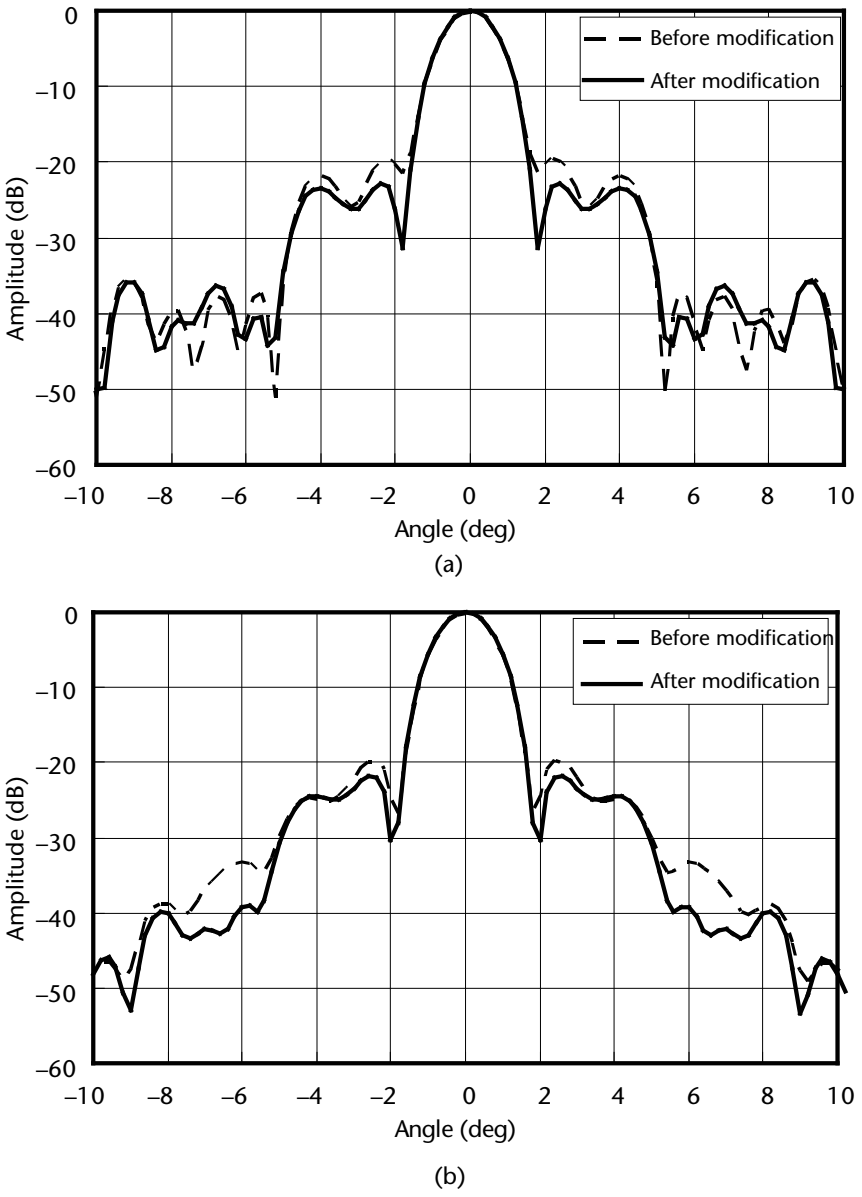

Figure 3.50 Comparison of main reflector's radiation patterns before and after reflector surface modification: (a) E-plane and (b) H-plane.

vertical axis is the EIRP density. The radiation pattern has a peak value of 39.7 dBW/40 kHz, the maximum EIRP density approved under Eutelsat Standard M. This is an extremely high peak electric power density for a certified 1m-class antenna (maximum EIRP density: 39.7 dBW/40 kHz).

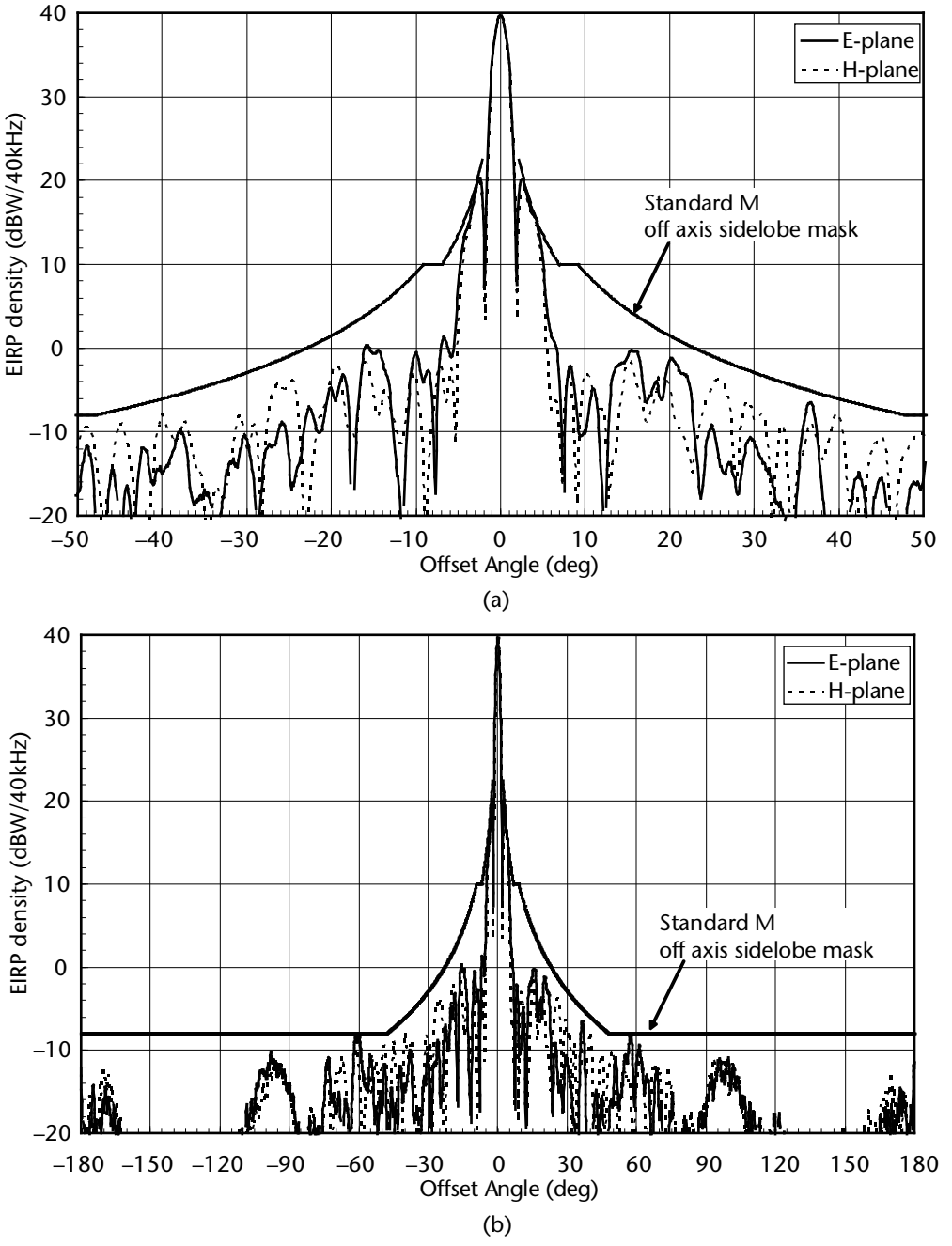

Figure 3.51 Measured radiation patterns (14.25 GHz): (a) near-axis pattern and (b) wide-angle pattern.

3.8 Single-Reflector Wide-Beam-Spacing Multibeam Antennas

Japanese commercial communications satellites (CSs), which are 50 to 60 deg apart from Japanese broadcasting satellites (BSs), are scheduled to start direct broadcasting service. A multibeam antenna with wide beam spacing is desired for simultaneous reception of broadcasting from BSs and CSs. A multibeam antenna for this

purpose, using a merged parabola, has been reported [50]. This section presents an optimum configuration for a multibeam antenna with wide beam spacing.

3.8.1 Design

3.8.1.1 Wave Aberration of a Defocus-Fed Parabolic Reflector

The configuration of a defocus-fed parabolic reflector is shown in Figure 3.52, where F is the focus of the parabolic reflector, M_0 is the center of the parabolic reflector, and $\mathbf{n}$ is the normal vector of the reflector at M_0. Wave aberration δ_p at an aperture of a defocus-fed parabolic reflector is expressed as follows:

$$\delta_p = a_2 r_a^{\,2} + a_3 r_a^{\,3} + a_4 r_a^{\,4} + \cdots \tag{3.51}$$

where r_a is a component of the polar coordinates in the aperture plane.

In this handbook, only the lowest term of the equation, $a_2 r_a^{\,2}$, is considered to simplify the analysis [51]. The term a_2 is expressed as follows:

$$a_2 = U + S\sin 2(\phi_a + \phi) \tag{3.52}$$

$$U = \frac{1}{l} - \frac{1}{l_0}\frac{\left\{1+\cos^2(\theta_0/2)\right\}\left\{1+\cos^2(\theta/2)\right\} - \sin^2(\theta_0/2)\sin^2(\theta_0/2)\cos 2\phi}{\cos(\theta_0/2)\cos(\theta/2)} \tag{3.53}$$

$$\phi = \frac{1}{2}\tan^{-1}\frac{1}{2}\frac{\sin^2(\theta/2)\left\{1+\cos^2(\theta_0/2)\right\} - \sin^2(\theta_0/2)\left\{1+\cos^2(\theta/2)\right\}\cos 2\varphi}{\sin^2(\theta_0/2)\cos(\theta/2)\sin 2\phi} \tag{3.54}$$

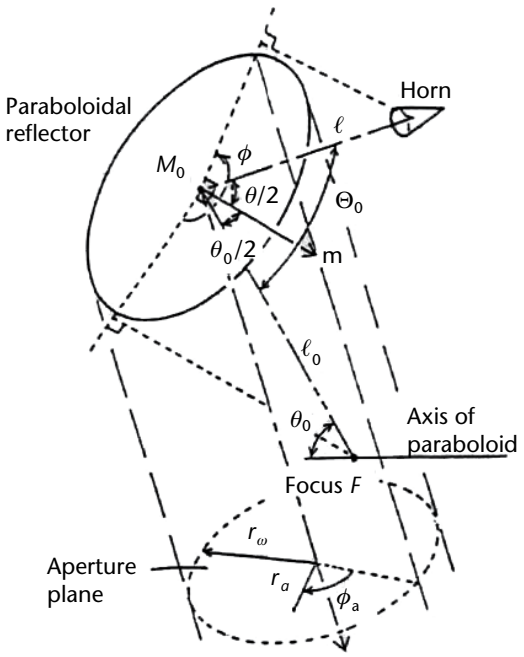

Figure 3.52 Parameters of a defocus-fed parabolic reflector.

$$S^2 = \left(\frac{1}{8l_0}\right)^2 \frac{\left[\begin{matrix}\{1+\cos^2(\theta_0/2)\}\{1+\cos^2(\theta/2)\} \\ -\sin^2(\theta_0/2)\sin^2(\theta/2)\cos 2\phi\end{matrix}\right]^2 - 16\cos^2(\theta_0/2)\cos^2(\theta/2)}{\cos^2(\theta_0/2)\cos^2(\theta/2)} \tag{3.55}$$

where ϕ_a is a component of the polar coordinates in the aperture plane, l_0 is a distance between F and M_0, l is a distance between the horn and M_0, $\theta_0/2$ is an offset angle of F from **n**, $\theta/2$ is an offset angle of the horn from **n**, and ϕ is a rotation angle of the horn from F around **n**. The offset angle Θ_0 of the horn from F is expressed as

$$\cos\Theta_0 = \sin(\theta_0/2)\sin(\theta/2)\cos\varphi + \cos(\theta_0/2)\cos(\theta/2) \tag{3.56}$$

From (3.53) U can be eliminated with appropriate l. From (3.55) and (3.56), the condition for minimum S with constant Θ_0 is given by (3.57), which indicates that the horn is located on the symmetrical plane of the reflector:

$$\theta = |\theta_0 - 2\Theta_0|, \quad \varphi = \begin{cases} 0^\circ & (\theta_0 - 2\Theta_0 \geq 0) \\ 180^\circ & (\theta_0 - 2\Theta_0 < 0) \end{cases} \tag{3.57}$$

From this equation, $\theta = \Theta_0$ and $\phi = 180°$ in the case of $\Theta_0 = \theta_0$. Therefore, from (3.55) S is eliminated. In other words, second-order wave aberration $a_2 r_a^2$ could be eliminated when the horn is located on the ray starting from the focus F and reflected at M_0.

The relationship between θ and the directive gain is shown in Figure 3.53 for the case in which $\theta_0 = 60°$, aperture diameter $2r^\omega = 25\lambda$, and the horn is located on the symmetrical plane of the reflector. Directive gain could be predicted by subtracting gain reductions caused by second-order wave aberration $a_2 r_a^2$, aperture distribution, and spillover from 100% gain. In the case of $r^\omega/l_0 = 0.25$, the predicted directive gain agrees well with the PO result. But in the case of $r^\omega/l_0 = 0.50$, the

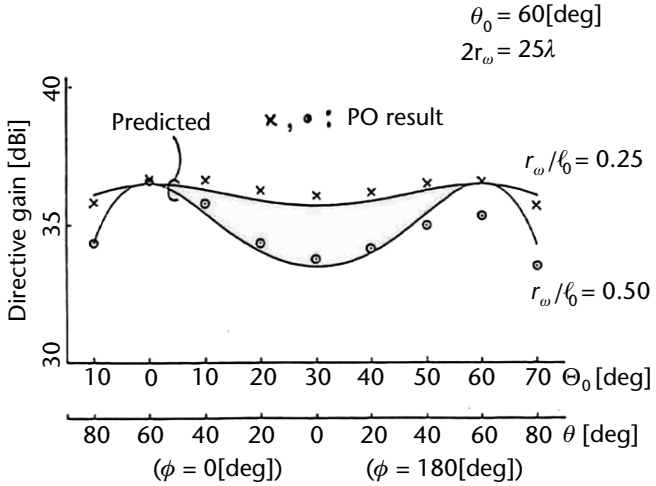

Figure 3.53 The relation between θ, the horn position shown in Figure 3.52, and the directive gain [52].

predicted results disagree with the PO result around $\theta = 60°$ and $\Theta = 60°$. This disagreement results from the aberration of higher-order terms such as $a_3 r_a^3$, $a_4 r_a^4$ ⋯, which are neglected in the above analysis.

3.8.1.2 Design Example

A multibeam antenna with wide beam spacing is designed with a 695-mm-diameter parabolic reflector for simultaneous reception of broadcasting from BSs and CSs. Primary radiators for CSs are located near the focus of the parabolic reflector, and a primary radiator for BSs is located close to the ray, starting from the focus and reflected at the center of the parabolic reflector. Figure 3.54 shows the calculated radiation pattern.

Calculated results agree well with experimental results. The antenna is confirmed to receive broadcasting from BSs and CSs simultaneously.

3.8.2 Performance

The multibeam antenna under discussion is shown in Figure 3.55 and its performance in terms of simultaneous reception of broadcasting from BSs and CSs is summarized in Table 3.12.

3.9 Multisector Omnidirectional Offset-Shaped Reflector Antenna for 26-GHz-Band Fixed Wireless Access Base Station

Point-to-multipoint (P-MP) fixed wireless access (FWA) systems are possible candidates for solving the so-called last-one-mile-problem of "fiber to the home" (FTTH), that is, the problem of cost and time to install the last-one-hop optical fiber cables to subscribers [53, 54]. For base station antennas in such systems, offset single-reflector antennas were developed to radiate a beam with a sector shape in

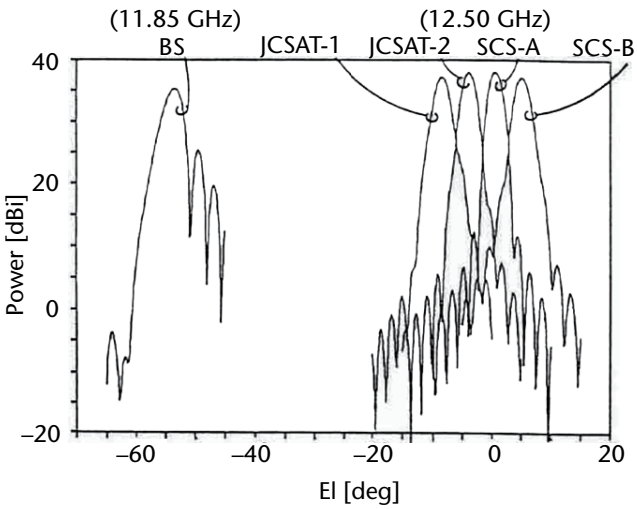

Figure 3.54 Calculated radiation pattern.

Figure 3.55 A multibeam antenna for simultaneous reception of broadcasting from BSs and CSs.

Table 3.12 Performance of Multibeam Antenna for Simultaneous Reception of Broadcasting from BSs and CSs

	CS		
	Superbird-B	*JCSAT-2*	*BS*
Type of antenna	Offset single reflector with three horns		
Frequency (GHz)	12.25–12.75		11.71–12.01
Gain (typical) (dB)	35.5		32.5
Polarization	Vertical	Horizontal	Right-hand circular
Diameter (mm)	ϕ600		

the horizontal plane and a cosecant-square shape in the vertical plane [55, 56]. In these antenna designs, a skilled reflector shaping technique was applied to achieve excellent beam shaping. However, these reflectors were required to be as large as several tens of wavelength in size. Furthermore, since these antennas radiated single beams, multiple antenna reflectors were required in order to cover multiple sector areas.

In this section, a novel shaped reflector, six-sector antenna is proposed for a base station antenna in P-MP FWA systems. The antenna is advantageous for radiating vertically shaped six-sector beams simultaneously with a compact configuration.

3.9.1 Design

3.9.1.1 Antenna Configuration

The antenna configuration is illustrated in Figure 3.56. The antenna is composed of a reflector and six feed horns with an omnidirectional horn reflector [57, 58] type

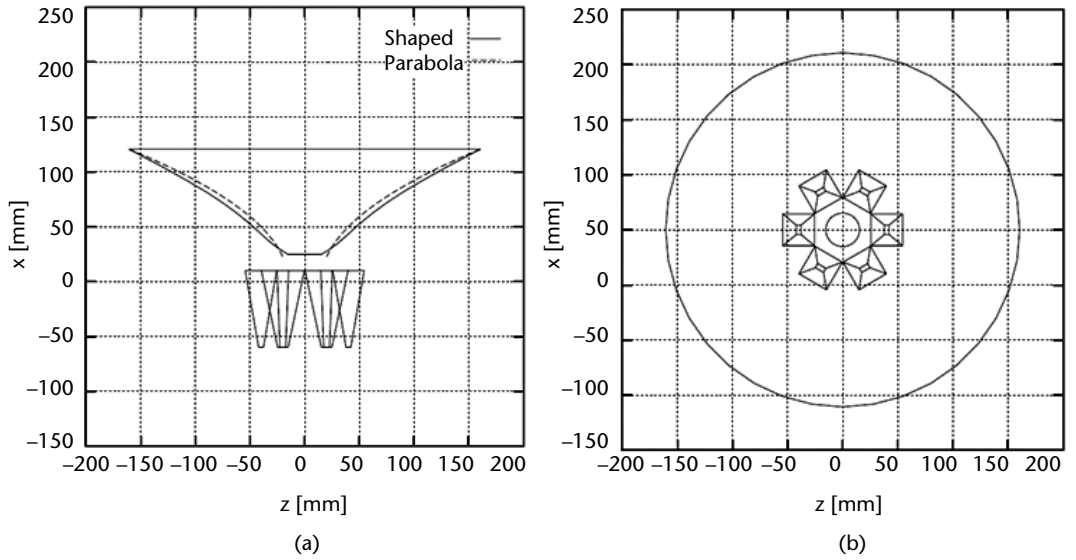

Figure 3.56 Antenna configuration: (a) side view and (b) bottom view.

arrangement. The reflector is a funnel-shaped torus reflector whose axis of rotation is the *x*-axis. The rotation radius is designed to achieve the required beamwidth of 60 deg in a horizontal plane. The generation line of the torus reflector is shaped from a parabola to achieve a cosecant-square-like radiation pattern in a vertical plane, as described in the following section. Being different from an omnidirectional horn reflector antenna, the six feed horns are symmetrically installed on the locus circle of the initial parabola focus. In the current design, the feed horns are conventional square aperture horns excited by the fundamental mode for a simple feed structure.

3.9.1.2 Reflector Shaping

The shaped torus reflector results from the generating line shaped from a parabola. The generating line shaping is based on the path length difference (aberration) in the *xz*-plane including both a feed and the reflector symmetrical axis (*x*-axis). Figure 3.57 shows a schematic cross-sectional illustration of generating line shaping in the *xz*-plane. In this figure, *F* is a feed point, *M* is an arbitrary point on the generating line, and $\mathbf{e}_s$ is a unit vector from *F* to *M*. The generating line is assumed to be shaped along $\mathbf{e}_s$ by amount *s* from an initial parabola. Path length increase *d* due to shaping is given for rays on the *xz*-plane by:

$$\delta = s(1 - \mathbf{e}_s \cdot \mathbf{k}_B) = s(1 - \gamma) \tag{3.58}$$

where $\mathbf{k}_B$ is a unit vector representing the initial parabola axis.

On the other hand, we assume that the desired aberration δ is represented by a power series of an appropriate coordinate *t* of the point on the generating line [59] as:

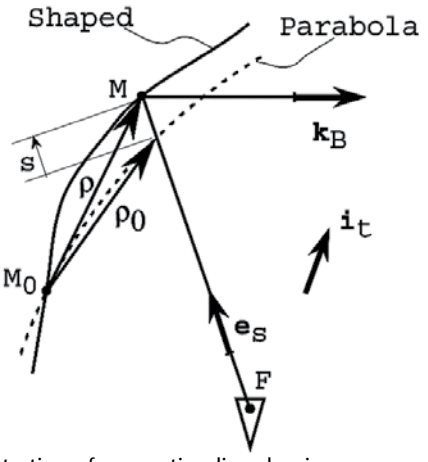

Figure 3.57 Schematic illustration of generating line shaping.

$$\delta = \sum_m a_m t^m \tag{3.59}$$

$$\begin{aligned} t &= \rho \cdot \mathbf{i}_t = (\rho_0 + s\mathbf{e}_s) \cdot \mathbf{i}_t = t_0 + \alpha s \\ t_0 &= \rho_0 \cdot \mathbf{i}_t, \quad \alpha = \mathbf{e}_s \cdot \mathbf{i}_t \end{aligned} \tag{3.60}$$

where ρ_0 and ρ are the position vectors of M on the initial parabola and a shaped generating line from the origin M_0, respectively, and it is the unit vector of the appropriate coordinate frame for t. We can calculate the shaping amount s by substituting (3.60) into (3.59) and equating with (3.58).

Provided that the power series coefficients a_m are determined, we can calculate the radiation pattern from the shaped reflector using the shaping amount s. Therefore, we can design the shaped reflector to achieve a desired radiation pattern shape by minimizing the square sum of the difference between desired and calculated patterns with respect to optimization variables . In the current design, we apply the conjugate gradient method to minimization, and approximate the calculated radiation pattern by a summation of contributions from divided small segments of the reflector for calculation convenience.

3.9.1.3 Design Example

Figure 3.56 shows a designed antenna. For the initial parabola, the focal length is 25 mm, the inclined angle is 90 deg, and the subtended semiangle is 45 deg. The radius of the locus circle of the initial parabola focus is 40 mm. For the reflector shaping, the origin M_0 is at the top of the initial parabola, the coordinate frame for t is the $-x$ direction, and orders of the power series considered in (3.59) are $m = 1$ to 5 [59]. Radiation patterns designed at 26.125 GHz are shown in Figure 3.58. The patterns include only a contribution from current on the reflector, which is

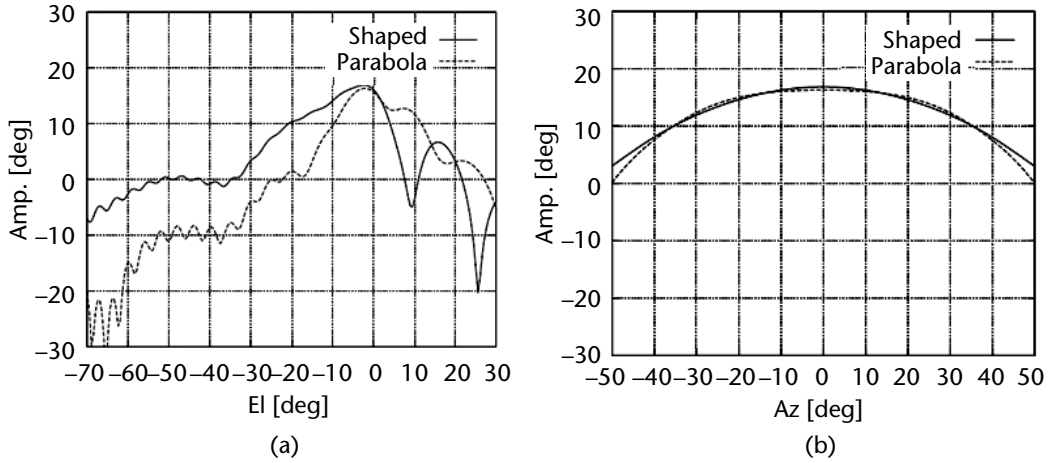

Figure 3.58 Comparison of calculated radiation pattern for shaped and nonshaped reflectors (26.125 GHz): (a) vertical plane (AZ = 0 deg) and (b) horizontal plane (EL = –1.7 deg) [60].

considered in reflector shaping. The radiation pattern in the vertical plane is well shaped to a cosecant-square-like shape, but the pattern in the horizontal plane has about a 60-deg beamwidth regardless of the reflector shaping.

Figure 3.59 shows the measured radiation patterns for the prototype antenna, and Figure 3.60 shows the actual prototype. For comparison, Figure 3.59 includes actual calculated patterns, including contributions from both the reflector current and the feed horn. The patterns also include the 3-dB loss of a switch connected to the feed horn. In the vertical plane, although partial level reduction and some ripples appear in the measured pattern caused by the unexpected blocking and scattering by the structural parts, the measured pattern agrees well with the calculated pattern. In the horizontal plane, the agreement between the measured and calculated values is better. These experimental results validate the antenna design.

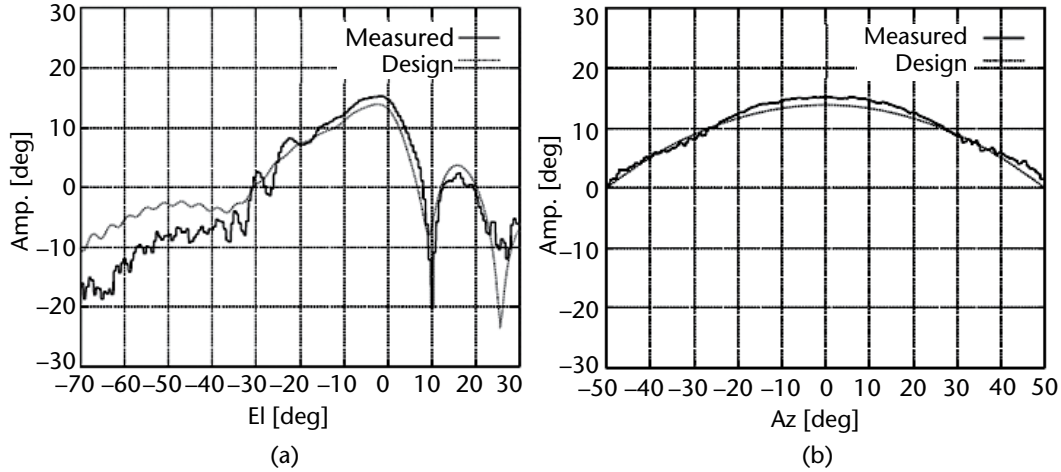

Figure 3.59 Measured radiation pattern (26.125GHz): (a) vertical plane (AZ = 0 deg) and (b) horizontal plane (EL = –1.7 deg) [60].

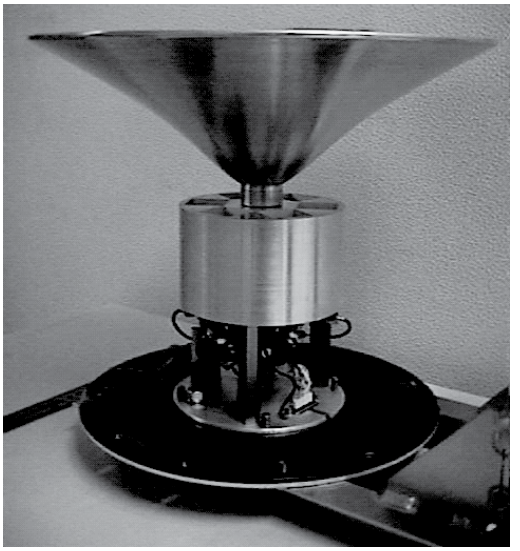

Figure 3.60 The prototype antenna [60].

3.9.2 Performance

The base station antenna for a P-MP FWA system is shown in Figure 3.61 and its performance summarized in Table 3.13.

Figure 3.61 A base station antenna used in P-MP FWA systems [61].

Table 3.13 Performance of the BS Antenna for P-MP FWA Systems [62]

	Principal Characteristics
Type of antenna	Six-sector cylindrical horn reflector antenna with sector changing pin-diode switch
Frequency (GHz)	25.25–27.00
Polarization	Linear (vertical)
Radiation pattern	In horizontal plane:
	>6 dBi for <±30 deg
	<–15 dBi at ±60 deg
	<30 dBi for >±90 deg
	In vertical plane:
	Cosecant-square-like beam shape
Dimension (mm)	Diameter: 400
	Height: 300

References

[1] P. W. Hannan, "Microwave antennas derived from the Cassegrain telescope," *IRE Trans. Antennas and Propagation,* AP-9, No. 2, pp. 140–153, March 1961.

[2] M. Mizusawa and T. Kitsuregawa, "A beam-waveguide feed having a symmetric beam for Cassegrain antennas," *IEEE Trans. Antennas and Propagation,* AP-21, No. 6, pp. 884–886, Nov. 1973.

[3] I. Chiba and Y. Konishi, "Development of large earth-station reflector antennas in Japan," *IEEE Antennas and Propagation Magazine*, Vol. 53, No. 6, pp. 245–257, Dec. 2011.

[4] M. Mizusawa and T. Katagi, "A property of the series of mirrors of quadric surface of revolution," *IECE Trans. Commun.*, 53-B, No. 11, pp. 707–708, Nov. 1970 (in Japanese).

[5] K. Katagi, S. Urasaki, T. Ebisui, and S. Betsudan, "Analysis and design method of beam waveguide feeds by beam mode expansion," *IECE Trans. Commun.*, J66-B, 3, pp. 305–312, March 1983 (in Japanese).

[6] S. Betsudan, T. Katagi, and S. Urasaki, "Design method of four-reflector type beam waveguide feeds," *IECE Trans. Commun.*, Vol. J67-B, No. 6, pp. 622–629, June 1984 (in Japanese).

[7] M. Masuda, S. Betsudan, S. Kobayashi, and S. Tachikawa, "Design and characteristics of a large Ku/C band earth station antenna," *IECE Trans. Commun.*, J68-B, No. 9, pp. 1044–1052, Sep. 1985 (in Japanese).

[8] A. F. Kay, "The scalar feed," TRG Science Report 5, AFCRL Project 4600, Contract No. AF 19(604)-8057, March 1964.

[9] P. J. B. Clarricoats and P. K. Saha, "Propagation and radiation behavior of corrugated feeds, Part 2 corrugated conical horn feed," *Proc. IEE*, 118, No. 9, p. 1177, Sep. 1971.

[10] M. Mizusawa, F. Takeda, and S. Betsudan, "Radiation characteristics of a corrugated conical horn," *IECE Trans. Commun.*, Vol. J56-B, No. 1, pp. 14–19, Jan. 1973 (in Japanese).

[11] K. A. Green, "Modified Cassegrain antenna for arbitrary aperture illumination," *IEEE Trans. Antennas and Propagation,* AP-11, No. 5, pp. 589–590, Sep. 1963.

[12] V. Galindo, "Design of dual-reflector antennas with arbitrary phase and amplitude distributions," *IEEE Trans. Antennas and Propagation,* AP-12, No. 4, pp. 403–408, July 1964.

[13] M. Mizusawa, "Effect of the scattering pattern of the subreflector on the radiation characteristics of shaped-reflector Cassegrain antennas," *IECE Trans. Commun.*, 52-B, No. 2, pp. 78–85, Feb. 1969 (in Japanese).

[14] T. Kitsuregawa and M. Mizusawa, "Design of the shaped-reflector Cassegrain antenna in consideration of the scattering pattern of the subreflector," *IEEE 1968 G-AP International Symposium,* Boston, Sep. 1968.

[15] M. Tomita, S. Itohara, T. Kitsuregawa, and M. Mizusawa, "Cassegrain antenna fed by four-reflector beam-waveguide for satellite communications earth station," *1971 International Symposium on Antennas and Propagation,* 2-11 A3, pp. 101–102, Sep. 1971.

[16] S. Itohara, S. Endo, K. Hatakeyama, M. Mizusawa, and S. Betsudan, "Cassegrain antenna fed by four-reflector beam-waveguide," *IECE Technical Report,* AP71-39, Oct. 1971 (in Japanese).

[17] Recommendation ITU-R S.465-5, "Reference earth-station radiation pattern for use in coordination and interference assessment in the frequency range from 2 to about 30GHz," 1970-1974-1986-1990-1992-1993.

[18] T. Satoh, S. Endo, N. Matsunaka, S. Betsudan, T. Katagi, and T. Ebisui, "Sidelobe level reduction by improvement of strut shape," *IEEE Trans. Antennas and Propagation,* AP-32, 7, pp. 698–705, July 1984.

[19] K. Ohashi, S. Kato, Y. Numano, H. Morikawa, Y. Higashino, and T. Kitsuregawa, "Horn reflector antenna," *Mitsubishi Denki Giho* (Technical Report of Mitsubishi Electric Corp.), 36, No. 5, pp. 601–607, 1962 (in Japanese).

[20] S. Urasaki, S. Makino, and T. Katagi, "Tri-reflector antennas with no cross-polarized component," *IEICE Trans. Commun.*, Vol. J67-B, No. 10, pp. 1119–1125, 1984 (in Japanese).

[21] N. Nakajima, Y. Shimanuki, K. Abe, and T. Furuno, "4,5,6 GHz band offset antenna featuring low sidelobe and high cross polarization discrimination," *IEICE Trans. Commun.*, J67-B, No. 2, pp. 194–201, 1984 (in Japanese).

[22] M. Karikomi and Y. Yamada, "Characteristics improvement by synthesizing non-axisymmetrical aperture distribution," *IEICE Trans. Commun.*, J72-B-2, No. 10, pp. 549–559, 1989 (in Japanese).

[23] M. Mizusawa and T. Katagi, "The equivalent parabola of a multi-reflector antenna and its application," *Mitsubishi Denki Giho* (Technical Report of Mitsubishi Electric Corp.), 49, No. 11, pp. 729–732, 1975 (in Japanese).

[24] F. Takeda and T. Hashimoto, "Broadbanding of corrugated conical horns by means of the ring-loaded corrugated waveguide structure," *IEEE Trans. Antennas and Propagation,* AP-24, No. 6, 1976.

[25] M. Karikomi, Y. Yamada, and K. Kagoshima, "Wide angle radiation pattern improvement of a shaped offset tri-reflector antenna by reducing higher order periodical reflector distortion," *IEICE Trans. Commun.*, Vol. J73-B-2, No. 12, pp. 852–859, 1990 (in Japanese).

[26] T. Katagi and Y. Takeichi, "Shaped-beam horn-reflector antenna," *IEEE Trans. Antennas and Propagation,* Vol. AP-23, No. 6, pp. 757–763, Nov. 1982.

[27] T. Okamoto, C. Hakoishi, Y. Nagai, and T. Kadowaki, "Communications antenna for CS-2," *Proc. 13th Int. Symp. Space Technology Science,* pp. 763–768, 1982.

[28] T. Kitsuregawa, *advanced Technology in Satellite Communication Antennas Electrical & Mechanical Design*," Artech House, Norwood, MA, 1990.

[29] K. Aoki, S. Makino, T. Katagi, and K. Kagoshima, "Design method for an offset dual-shaped reflector antenna with high efficiency and an elliptical beam," *IEE Proc.*, Part H, Vol. 140, No. 2, pp. 121–128, April 1993.

[30] K. Aoki, N. Miyahara, S. Makino, S. Urasaki, and T. Katagi, "Design method for offset shaped dual-reflector antenna with an elliptical aperture of low cross-polarisation characteristics," *IEE Proc.*, Part H, Vol. 146, No. 1, pp. 60–64, Feb. 1999.

[31] S. Ohmori, Y. Hase, H. Wakana, and S. Taira, "Experiments on aeronautical satellite communications using ETS-V satellite," *IEEE Trans. Aerosp. Electron. Syst.*, Vol. 28, No. 3, pp. 788–796, July 1992.

[32] S. Ohmori, "Vehicle antennas for mobile satellite communications," *IEICE Trans.*, Vol. E74, No. 10, pp. 3210–3221, Oct. 1991.

[33] K. Nishikawa, "Land vehicle antennas," *IEICE Trans. Commun.*, Vol. E86-B, No. 3, pp. 993–1004, March 2003.

[34] E. Laase, "Aeronautical internet services via satellite—Present and planned systems," *Proc. 21st AIAA Intl. Commun. Satellite Systems Conf. and Exhibit (ICSSC) Colloquium,* April 2003.

[35] T. Mizuno, "Aeronautical internet services via satellite—Overview of key technologies," *Proc. 21st AIAA Intl. Commun. Satellite Systems Conf. and Exhibit (ICSSC) Colloquium,* April 2003.

[36] Y. Konishi, M. Miyazaki, M. Tsuchiya, and S. Makino, "Airborne antenna for broadband aeronautical satellite communication systems," *IEICE Trans. Commun.* Vol. J88-B, No. 9, pp. 1613–1623, Nov. 1988 (in Japanese).

[37] B. S. Westcott, R.K. Graham, and F. Brickell, "Systematic design of a dual offset reflector antenna with an elliptical aperture," *IEE Proc.*, Part H, Vol. 131, pp. 365–370, 1984.

[38] B. S. Westcott, F.A. Stevens, and F. Brickell, "GO synthesis of offset dual reflector," *IEE Proc.*, Part H, Vol. 128, No. 1, pp. 11–18, Feb. 1981.

[39] H. H. Viskum, H. Wolf, and A. Lindley, "A dual band (11/12/14 GHz) dual polarized shaped dual offset reflector system for high efficiency steerable elliptical beam coverage for the fixed satellite system," *Proc. 14th AIAA Intl. Commun. Satellite Systems Conf. and Exhibit (ICSSC),* pp. 1542–1551, March 1992.

[40] C. Granet, "A simple procedure for the design of classical displaced-axis dual-reflector antennas using a set of geometric parameters," *IEEE Antennas and Propagation Magazine*, Vol. 41, pp. 64–72, Dec. 1999.

[41] S. Nomoto and F. Watanabe, "Shaped reflector design for small-size offset dual reflector antennas," *IEICE Trans. Commun.*, Vol. J71-B, No. 11, pp. 1338–1344, Nov. 1988 (in Japanese).

[42] R. L. Haupt, "Thinned arrays using genetic algorithms," *IEEE Trans. Antennas and Propagation,* Vol. AP-42, No. 7, pp. 993–999, July 1994.

[43] Y. Keen-Keong and L. Yilong, "Sidelobe reduction in array-pattern synthesis using genetic algorithms," *IEEE Trans. Antennas and Propagation,* Vol. AP-45, No. 7, pp. 1117–1122, July 1997.

[44] Y. Inasawa, S. Kuroda, K. Kusakabe, I. Naito, Y. Konishi, S. Makino, and M. Tsuchiya, "Design method for a low-profile dual-shaped reflector antenna with an elliptical aperture by suppression of undesired scattering," *IEICE Trans. Electron.*, Vol. E91-C, No. 4, pp. 615–624, April 2008.

[45] M. Sato, H. -B. Li, Y. Fujino, H. Wakana, A. Miura, Y. Ozaki, H Sato, E. Watanabe, and M. Sawa, "Helicopter-satellite communication system developed for transmission of disaster and emergency information," *21st International Communication Systems Conference and Exhibit,* AIAA 2003–2319, 2003.

[46] Y. Konishi, "Phased Array Antennas," *IEICE Trans. Commun.*, Vol. E86-B, No. 3, pp. 954–967, March 2003.

[47] N. Goto, and F. Watanabe, "Optimum aperture efficiency of Cassegrain antennas with a specific sidelobe level," *IEICE Trans. Commun.*, Vol. J61-B, No. 5, pp. 321–326, May 1978 (in Japanese).

[48] P. S. Kildal, "The Hat Feed: A dual-mode rear-radiating waveguide antenna having low cross polarization," *IEEE Trans. Antennas and Propagation,* Vol. AP-35, No. 9, Sep. 1987.

[49] J. Yang and P. S. Kildal, "Calculation of ring shaped phase centers of feeds for ring-focus paraboloids," *IEEE Trans. Antennas and Propagation,* Vol. 48, No. 4, April 2000.

[50] R. Iwata and S. Tamagawa, "Five beam antenna for simultaneous reception of Japanese broadcasting satellite and communication satellites," *1990 Autumn Nat. Conv. Rec. IEICE, B-116,* Oct. 1990 (in Japanese).

[51] R. E. Collin and F. J Zucker, *Antenna Theory*, Part 2, pp. 60–62, McGraw-Hill, New York, 1969.

[52] I. Naito, M. Yamato, M. Ohno, S. Makino and T. Katagi, "An antenna for simultaneous reception of broadcasting from BS and CS's," *Proc. of ISAP'92,* pp. 325–328, Sep. 1992.

[53] Y. Ito, "Goal of broadband wireless access systems 5: Business opportunities," *IEICE Soc. Conf. 1998,* PB-2-5 (in Japanese).

[54] M. Ito, "Traffic design of point to multipoint broadband wireless access systems," *IEICE Technical Report,* RCS98-140, Oct. 1998 (in Japanese).

[55] T. Yamada, K. Kagoshima, and Y. Itami, "Design and characteristics of sector/cosecant-square shaped beam antenna," *IECE Trans.*, Vol. J67-B, No. 12, pp. 1452–1461, Dec. 1984 (in Japanese).

[56] S. Nomoto and F. Watanabe, "Highly contoured beam antennas for 21GHz-band LDR hub stations," *IEICE Trans.*, Vol. J72-B-II, No. 4, pp. 150–161, April 1989 (in Japanese).

[57] Y. Takeichi and T. Katagi, "Experimental results of the omni-directional horn-reflector antenna," *1969 Joint Convention of IEE,* 1419, 1969 (in Japanese).

[58] Y. Takeichi and T. Katagi, "Omni-directional horn-reflector antenna," *1970 IEEE G-AP International Symposium,* pp. 40–47, Sep. 1970.

[59] I. Naito, K. Kakizaki, N. Miyahara, and T. Haruyama, "Aperture phase distribution for cosecant square beam shaping representing by a power series of a 1-dimensional aperture coordinate," *IEICE Technical Report,* AP98-79, Oct. 1998 (in Japanese).

[60] I. Naitoh, T. Fukui, Y. Inasawa, T. Hamada, S. Makino, and S. Urasaki, "Shaped reflector 6-sector antenna for base station application in fixed wireless access systems," *Proceedings of the 2000 International Symposium on Antennas and Propagation,* ISAP2000, 2A4-6, Vol. 2, pp. 517–520, Aug. 2000.

[61] "FWA base station antenna," 2001 R&D 100 Awards, *R&D Magazine*, 2001.

[62] K. Kishi, T. Hamada, S. Matsubara, and Y. Asano, "Development of P-MP FWA system," *25th Asian Info-communications Council,* Shanghai, China, April 2001.

[63] I. Naitoh, T. Fukui, Y. Inasawa, T. Hamada, S. Makino and S. Urasaki, "An omni-directional horn-reflector type shaped reflector 6-sector antenna for base station application in P-MP fixed wireless access systems," *IEICE AP99-261 Technical Report,* 1999 (in Japanese).

CHAPTER 4

Reflector Antennas for Terahertz Imaging Applications

G. Chattopadhyay, Jet Propulsion Laboratory, California Institute of Technology[1]
A. Freni, University of Florence
N. Llombart and A. Neto, Delft University of Technology

4.1 Introduction

The term *terahertz* has been ubiquitous in the arena of new technological advances during the past couple of years. New applications are emerging every day that are exploiting the promises of terahertz: its small wavelength; its ability to penetrate dust, clouds, and fog; and the possibility of having a large instantaneous bandwidth for high-speed communication channels. Until very recently, space-based instruments for astrophysics, planetary science, and Earth science missions have been the primary motivator for the development of terahertz antennas, sensors, sources, and systems. In recent years, however, emerging areas such as imaging from space platforms, surveillance of person-borne hidden weapons or contraband from a safe stand-off distance and reconnaissance, medical imaging and DNA sequencing, and the world of high-speed communications have been the driving forces for this area of research.

Terahertz science is fascinating. One of the most pivotal quests for humans has been to find the answer to the vital question of "Where did we all come from?" It turns out that the answer to that lies in the cosmic signatures of the terahertz part of the electromagnetic spectrum. It is well known that most of the radiation in the universe is emitted at wavelengths longer than 10 microns (<30 THz), and this peaks at about 100 microns (3 THz), if we exclude contributions from the cosmic microwave background. By studying the minute fluctuations of the electromagnetic waves coming from the distant stars and galaxies at terahertz frequencies, one can study how stars are formed, how galaxies evolve, and how planetary systems come

1. Part of this was carried out at the Jet Propulsion Laboratory, California Institute of Technology, under contract with the National Aeronautics and Space Administration.

about. Even for our own planet Earth, terahertz radiation is an indicator for tracers of global warming and ultimately the health of the planet on which we live. For planetary bodies beyond our own planet, terahertz emission is associated with atmospheric dynamics and trace constituents in planets, moons, and comets. Instruments at the terahertz frequencies have the potential to reveal information about planetary atmospheres, surfaces, and subsurface water and ice contents [1–3].

The study of terahertz frequencies has been very important for astrophysicists for a long time. The studies of the birth of our universe, which started with a big bang almost 15 billion years ago, has been the most fascinating topic for physicists and ordinary people alike to explore. Exploring this extraordinary event in the history and evolution of our universe using electromagnetic waves has been the primary tool of astronomers for a long time. However, when we look back in time by observing distant stars and galaxies through the prism of the electromagnetic spectrum, we can go back only to approximately 400,000 years after the big bang when the first lights emerged from the primordial soup of the nascent universe [4]. The primordial plasma—the hot, dense soup of subatomic particles that filled the early universe—was opaque to electromagnetic radiation; any emitted photons were scattered by the subatomic particles. The first electromagnetic waves—cosmic microwave background (CMB) radiation, the cooled radiation that has permeated the universe for nearly 15 billion years—was emitted approximately 400,000 years after the big bang, when electrons and protons first combined to form hydrogen atoms. CMB was discovered by Penzias and Wilson in 1965, which led to their receiving a Nobel Prize in 1978. The microwave radiation of CMB is confined to 1- to 5-mm wavelengths, peaking at 2-mm wavelengths (150 GHz)—in the territory of the terahertz frequencies.

Another area of astrophysics that plays a key role in understanding the nature and evolution of our universe is the high-resolution spectroscopic observations at terahertz frequencies [5]. The importance of this is emphasized by the key role of heterodyne spectrometers in different space-based and ground-based instruments such as the Herschel Space Observatory, Atacama Large Millimeter Array (ALMA), and the airborne Stratospheric Observatory for Infrared Astronomy (SOFIA). Star formation and key phases of galaxy evolution occur in regions enshrouded by dust, obscuring these processes at infrared and optical wavelengths. Meanwhile, the temperature in these regions of the interstellar medium is in the range of ten to a few thousand kelvin, which excites a wealth of submillimeter-wave spectral information. With high-resolution spectroscopy, resolved line profiles reveal the dynamics of star formation, exposing the details of turbulence, outflows, and core collapse. Observations of emission from ionized species such as the C + fine structure transition at 1900.53690 GHz (158 μm) allows direct measurement of the diffuse components of the interstellar medium as it cools, the amount of "dark gas" in the medium, and analysis of the large-scale motions of this material from which giant molecular clouds form.

Instruments at the terahertz frequencies have the potential to reveal information about planetary atmospheres, surfaces, and subsurface water and ice contents [6]. Recently, through a high-resolution spectrometer at terahertz frequencies operating in space, we learned that the water on planet Earth might have come from comets and that water molecules are formed in stars at an astonishing rate. Moreover, a

recent study with a terahertz spectrometer found that the water in a young Sun-like star shoots out like high-velocity "bullets" moving at more than 200,000 km/h from the star [7]. This can be compared to the velocity of a bullet from an AK47 rifle, which is traveling at 2,500 km/h or 80 times slower. It is a surprise that water molecules are observed at this high velocity—they should have been destroyed in the shock where temperatures exceed 100,000 degrees. Observations reveal that water very likely re-forms rapidly in the hot and dense shocked gas. The conditions are so favorable that approximately 100 million times the amount of water in the Amazon River is formed, every second. Discovery of this fascinating bit of information was possible due to instruments operating at terahertz frequencies.

Heterodyne spectrometers and imagers at terahertz frequencies also provide highly sensitive measurements of our own atmosphere. This is essential for making informed policy decisions affecting ozone chemistry, climate, and air quality. These measurements have been a key component to help answer a fundamental question scientists are grappling with today: "How is the global Earth climatologic system changing and what are the consequences for life on Earth?" They have enabled studies of fast tropospheric processes using the terahertz limb sounding technique, with vertical resolution and cloud and aerosol penetration capability [8, 9].

An emerging area of terahertz applications is security imaging. Demand for new surveillance capabilities for use in airport screenings and battlefield security checkpoints has led to the development of terahertz imagers and sensors. Imaging at terahertz frequencies has several advantages compared to microwave or infrared imaging: The wavelengths in this regime are short enough to provide high resolution with modest apertures, yet long enough to penetrate clothing. Moreover, unlike with infrared, the terahertz frequencies are not affected by dust, fog, and rain [10].

Several groups around the world are working on the development of terahertz imagers for various applications. One option is to use passive imaging techniques, which were very successful at millimeter-wave frequencies, by scaling frequencies to the terahertz range. However, the background sky is much warmer at terahertz frequencies due to high atmospheric absorption. Because passive imagers detect small differences in temperatures from radiating objects against the sky background, at these frequencies passive imagers do not provide enough scene contrast for short integration times. In contrast, in an active imager, the object is illuminated with a terahertz source and the resulting reflected/scattered radiation is detected to make an image. However, the glint from the background clutter in an active terahertz imager makes it hard to provide high-fidelity images without a fortunate alignment between the imaging system and the target. The group at NASA's Jet Propulsion Laboratory (JPL) has developed an ultra-wideband radar-based terahertz imaging system that addresses many of these issues and produces high-resolution through-clothes images at stand-off distances [11]. The system uses a 675- GHz solid-state Tx/Rx system in a frequency-modulated continuous-wave (FMCW) radar mode working at room temperature. The imager has subcentimeter range resolution and comparable cross-range resolution at a 25m stand-off distance with a 1m aperture mirror. Figure 4.1 shows a radar image taken in 1 sec using the 675- GHz FMCW radar at a 25m stand-off distance.

Figure 4.1 Photos showing through-clothes concealed weapon imaging with a 675- GHz FMCW radar at a 25m stand-off distance [11].

Communications at terahertz frequencies have gained attention in recent years. The high fractional bandwidth at these frequencies potentially offers multigigabit per second wireless data links [12]. Although the data rate increases linearly with the carrier frequency for a fixed fractional bandwidth, the free-space path losses increase with the square of frequency, quickly leading to limited transmission ranges unless very high power and phased-array based transmitters are used. However, in specific applications where communication requirements include very high data rates over short distances, terahertz communications are going to play a key role in those areas in the not-so-distant future. Some examples of these applications are high-speed wireless data transfer between handheld devices such as smart phones, home entertainment devices to high-definition television sets, and super-high-speed wireless links between high-volume servers in data centers. It will not be unreasonable to think that we will have 10 Gb/s or higher wireless communication links over short distances pretty soon, even with simple data modulation schemes.

The majority of the terahertz applications mentioned above use instruments with single-pixel detectors with reflector antennas. For imaging applications, the single-pixel receivers are raster scanned to produce the terahertz images. However, there is an increasing need for multipixel arrays of detectors and sensors at terahertz frequencies to produce high-fidelity real-time images, mappings of large areas of the sky, and spectroscopic imaging of a large swath of our atmosphere.

Large focal plane arrays at terahertz frequencies are required for direct detector instruments to measure the polarization of the CMB, for moderate spectral resolution spectrometers, and for heterodyne instruments with very high resolution spectroscopic mapping. Many direct detector instruments are currently being designed

at these frequencies requiring large focal plane arrays backed by reflector antennas [13–15]. However, in the case of heterodyne instruments, the majority of them at these frequencies have been single pixel.

Although the possibility of multipixel array detectors at terahertz frequencies was first suggested way back in 1979 [16], progress was very slow in developing such instruments, although there has been some real progress during the past several years [17–19]. But the cost and complexity of building many parallel terahertz sources and receivers has been a hindrance to rapid progress. The conventional approach of building single-pixel receivers and stacking them to assemble multipixel array receivers is not suited to terahertz frequencies. What one needs are novel ultracompact receiver architectures that are easy to fabricate, preferably by lithographic techniques, to build multipixel heterodyne array receivers where the majority of the front-end components along with the antenna element can be integrated in a small form factor. Antennas play a pivotal role in the successful development of a large focal plane of direct detector arrays as well as multipixel heterodyne array receivers at terahertz frequencies. For fielding these large focal plane instruments for ground-based, airborne, and space-based applications, careful design of the reflector systems is required [20].

In this chapter, the main properties of terahertz reflector systems for imaging applications are addressed in detail. Figure 4.2 shows a conceptual sketch of such an imaging system. The backend electronics, that is, the receiver (in the case of passive systems) or the transceiver (in the case of active systems), are located in the *focal plane* of the reflector system, whereas the reflector system is used to generated an image of the *target plane*. This plane is located at a *target distance* R_f from the reflector system aperture. The different pixels in the image can be measured by creating a multibeam antenna using a *focal plane array* (FPA) with many beams pointing to different *pointing directions* θ, or by *mechanically rotating* the pointing direction of the reflector antenna, or by a combination of both. The image will be generated over a certain *field of view* (FoV) defined by the maximum pointing angle θ of the beam in each plane. The different antenna pointing directions and pattern shapes create a *footprint* at the target plane. This footprint defines the *resolution* of the image and has to be optimized to achieve high image acquisition speeds.

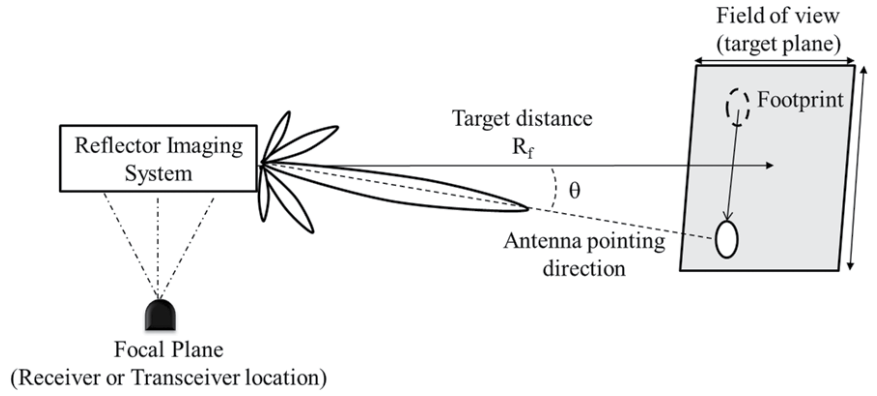

Figure 4.2 Conceptual sketch of an imaging reflector system.

In this chapter, we address the properties and typical configurations of terahertz imaging reflector systems for both FPAs and mechanical scanners. To study the properties of these systems, we derive an analytical expression of the vectorial field in the focal plane of a general focusing system. (Appendix 4A provides the detailed derivation for this field.) This analytical expression helps us to study the properties of the field at both the focal plane and target plane.

By studying the field in the target plane, we can define some important parameters of the reflector imaging systems such as resolution, depth of focus, and FoV. Moreover, it leads us to the derivation of equivalence between reflector systems focusing in the Fraunhofer and Fresnel regions. Several design examples of this equivalence are provided throughout the chapter.

Moreover, starting from the analytical derivation of the field in the focal plane, we introduce a new formulation that allows us to conveniently calculate the power received by each detector that composes the focal plane array. We show how the power received by an array of antennas can be calculated by using its effective length (parameter calculated for the antenna in transmission instead of reception) and the field in the focal plane. This formalism is very useful for optimizing the array element in relation to the imaging acquisition speed. Therefore, by using this new formalism, we can derive some trade-offs on the optimal focal plane sampling for FPAs based on active and passive detectors.

In the last section of this chapter, a detailed description of imaging reflector systems based on mechanical scanners is provided. We summarize the general properties of raster and conical scanners, together with the most common types of mechanically scanned terahertz reflector systems.

4.2 Reflector Systems Focusing in the Fresnel Region

Reflector antennas are very common in microwave telecommunication systems, where in most situations, the object being illuminated is in the far field, that is, in the Fraunhofer region. In this case, the surface of the main reflector is a parabola, which in optical terms means that the field focuses in the infinity [see Figure 4.3(a)]. This is also typical in terahertz imaging reflector systems for space applications, where the targets are at very far distances. However, terahertz imaging reflector systems for terrestrial applications usually have the target in the Fresnel region, the radiative near field, of the focusing main reflector. In this case, to have a well-focused field, the main reflector surface needs to be an ellipsoid with the second foci in the target position [see Figure 4.3(b)].

In this section, we briefly address the properties of the reflectors focusing in the Fresnel region. We will see that the field radiated around the focal point by a focusing aperture such as the one from an ellipsoidal reflector has all the properties of the far field [21, 22]. Moreover the field distribution in the focal region of a focusing device is nearly independent of the location of its focal point, provided it is not too close to the antenna. Thanks to this property, we can establish an equivalence between a reflector focusing in the infinity and in the Fresnel region in order to facilitate the design of advanced near-field focusing multireflector systems (i.e., with reduction of the cross-polarization, improved focal plane performances, lower offset aberrations).

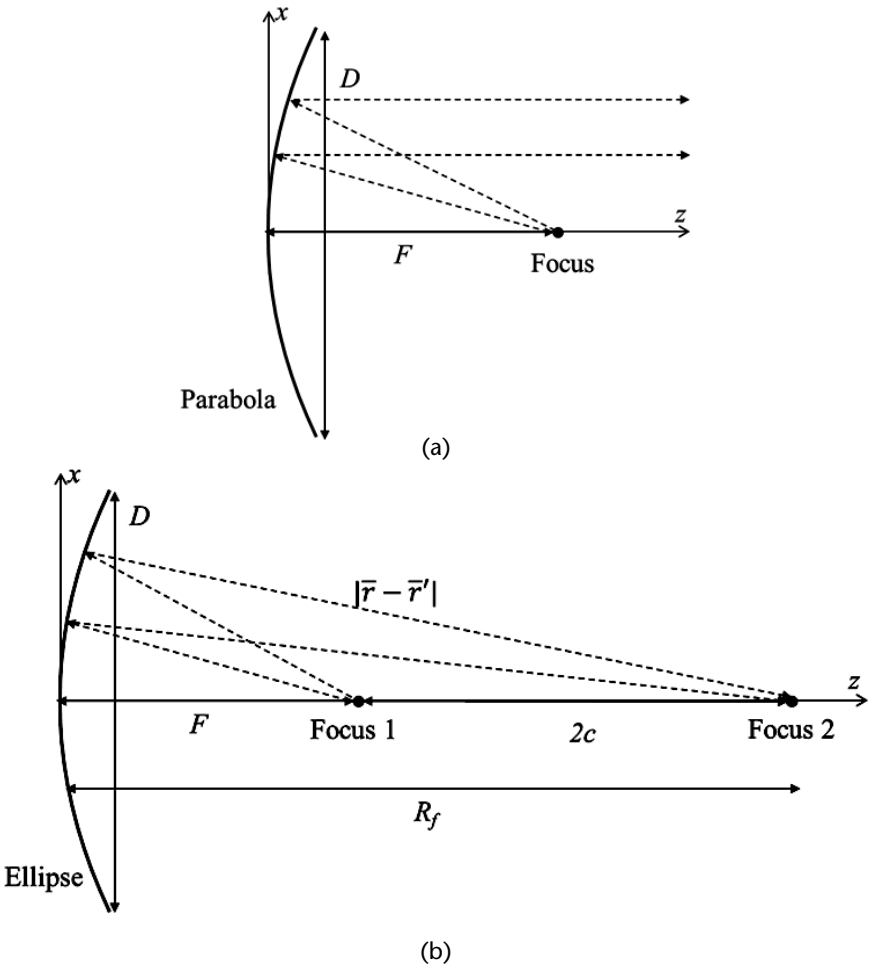

Figure 4.3 Geometry of (a) parabolic and (b) elliptical reflectors with a diameter *D* and focal distance *F*. The secondary focus of the elliptical reflector is at 2*c* from the primary focus, and Rf is the focusing distance from the elliptical reflector aperture to the secondary focus, that is, $R_f = F + 2c$.

4.2.1 Focusing in the Fresnel or Fraunhofer Region

The Fraunhofer region is the region where the antenna radiated field can be computed assuming that the paths associated with each individual contribution from the radiating aperture are parallel. This assumption is only completely true in the infinity; however, one can find a boundary distance where the errors due to the approximation become negligible. The definition of what is negligible is slightly different in the microwave and optical regimes. In the microwave regime, a more conservative definition than in the optical regime is usually taken: Differences in the path length smaller than a sixteenth of the wavelength between the individual contributions and a contribution coming from the origin of the coordinate system are allowed in the microwave far-field region [23]. Instead, path length differences of an octave of the wavelength are allowed in the optical regime [24].

To calculate the value of the boundary between the near- and far-field regions, let us start by specifying the path length $|\bar{r}-\bar{r}'|$ from each of the aperture infinitesimal contributions in the reflector aperture to the observation point

[see Figure 4.3(b)], where we would like to calculate the radiated field (the target plane) as follows:

$$|\bar{r}-\bar{r}'|=\sqrt{(x-x')^2+(y-y')^2+R_f^2} \tag{4.1}$$

In the region where $(x-x')^2+(y-y')^2$ is much smaller than R_f^2, we can apply the Taylor expansion to the path length and retain only the significant terms:

$$|\bar{r}-\bar{r}'| \cong z+\frac{x^2+y^2}{2R_f}-\frac{xx'+yy'}{2R_f}+\frac{x'^2+y'^2}{2R_f}\ldots \tag{4.2}$$

In the analysis of the fields in the Fraunhofer region, only the first three terms of (4.2) are included, whereas we need also the fourth term for calculating the fields in the Fresnel region. Therefore, the impact of this last term determines the boundary between the two regions. In the microwave regime, this term is usually neglected when it is smaller than a sixteenth of the wavelength, leading to a phase error smaller than $\pi/8$. By imposing this phase limit, one arrives at the definition of the boundary distance between the near- and far-field regions: $R \le \frac{2D^2}{\lambda}$. In the optical regime the boundary is usually defined for phase errors smaller than $\pi/4$, leading to a boundary of $R \le \frac{D^2}{\lambda}$.

Figure 4.4 shows the field radiated at 600 GHz by a symmetric parabolic reflector with a diameter of 10 cm and a uniform illumination. It has been simulated by the commercial antenna software package GRASP [25]. This software will be used for all of the simulations shown in this chapter. Figure 4.4(a) shows an *xz*-cut of the radiated field by such a reflector. The white lines represent the spherical cuts where the field is computed as shown in Figure 4.4(b). In that figure, the solid curve represents the far-field distribution, while all the other curves show the field computed in the near region at different spherical cuts defined by different distances *R* from the aperture center. The far-field boundary is located at *R* = 20m or *R* = 40m considering the optical or microwave phase error limit, respectively. From Figure 4.5(b) it is evident that for distances above the optical boundary the differences between the normalized field patterns are very small. Below this boundary, the main beam starts to widen, clearly affecting the quality of the focused pattern.

Considering this same example, if we need to image a target at a distance R_f lower than 20m, we need a better focused field at this distance than the ones shown in Figure 4.4(b). Thus we need to introduce a proper quadratic phase distribution over the reflector aperture. This phase distribution can be achieved either by using a parabolic reflector and defocusing its feed location or by using an elliptical reflector. The defocusing option does not introduce a perfect quadratic phase on the reflector aperture and, therefore, the radiated field can suffer from aberrations.

4.2.2 Field in the Target Plane of a Focusing Reflector

When we are imaging in the Fresnel region, the main reflector should be an elliptical one as described previously. In this case, the target plane will be located at the

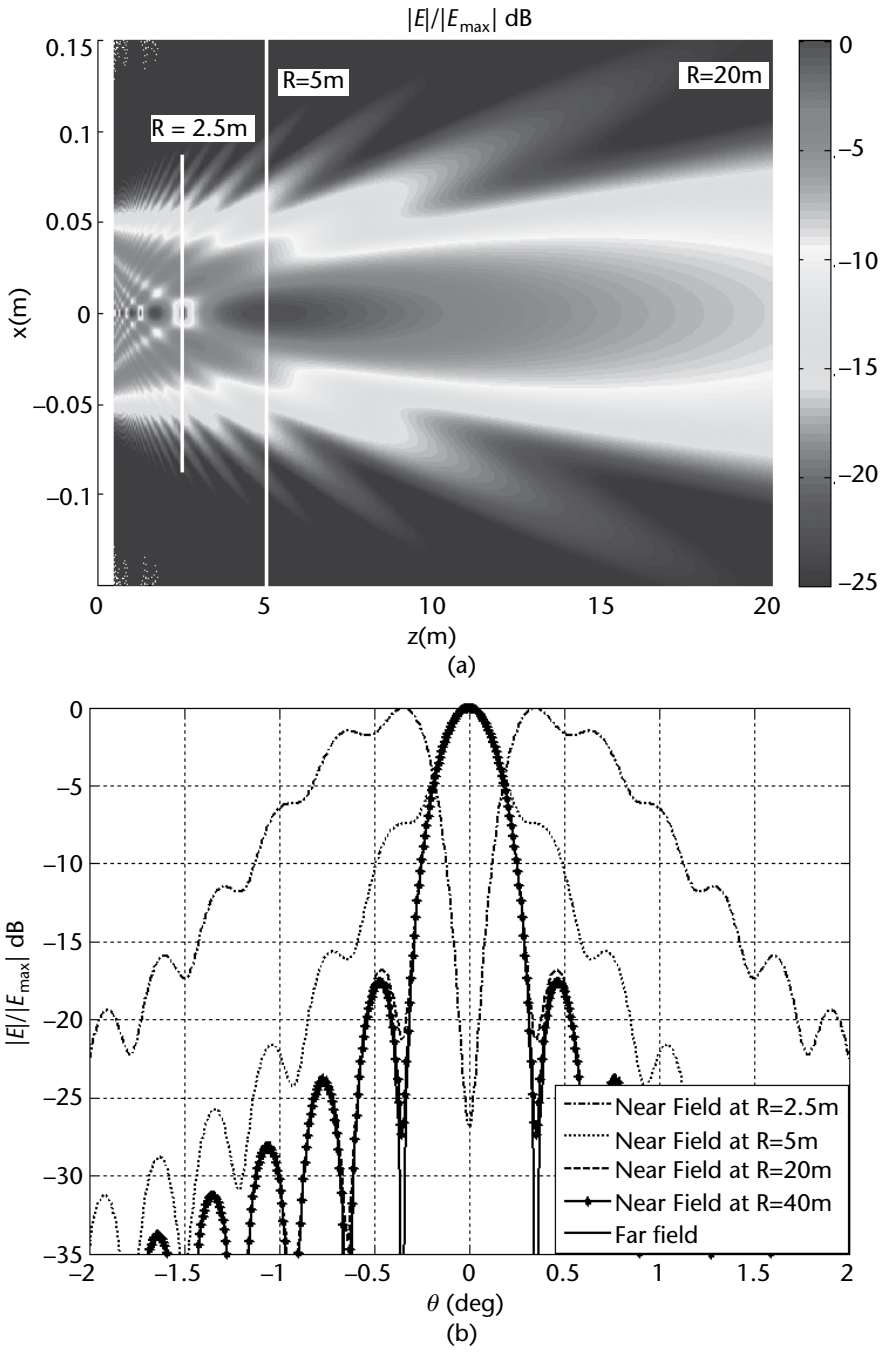

Figure 4.4 Field radiated by a parabolic reflector, with uniform illumination, at 600 GHz with F = 10 cm and D = 10 cm: (a) xz-cut and (b) spherical cuts at several radial distances R from the reflector aperture. These cuts are indicated by white lines in part (a).

secondary focus of the ellipse [see Figure 4.3(b)]. To obtain an expression for the field in this target plane, we can use Appendix 4A, where an analytical expression of the field in the focal plane of a generic focusing reflector is derived assuming a

series of incident plane waves. The expression given in (4A.15) can also be used to describe the y component of the field in the target plane of an elliptical reflector:

$$E_f^y(x,y)=\frac{-je^{-jkR_f}e^{-jk\frac{x^2+y^2}{2F}}}{2\pi R_f}\iint_{S_r} e(x',y')m_x(x',y')k_z e^{jk\frac{x'x}{R_f}}e^{jk\frac{y'y}{R_f}}dx'dy' \tag{4.3}$$

where R_f is the target distance and $e(x', y')$ is the equivalent aperture field generated in the elliptical reflector by a series of plane waves coming from the first focus, excluding the quadratic phase distribution necessary to focus at R_f. In the case of a symmetrical elliptical reflector with large R_f/D, the polarization effect of the reflector on the aperture field can be neglected $m_x(x', y') = 1$ and $k_z \approx k$. Thus, (4.3) can be rewritten as follows:

$$E_f^y(x,y)=\frac{-jke^{-jkR_f}e^{-jk\frac{x^2+y^2}{2R_f}}}{2\pi R_f}\iint_{S_r} e(x',y')\,e^{jk\frac{x'x}{R_f}}e^{jk\frac{y'y}{R_f}}dx'dy' \tag{4.4}$$

It then results that the target field can be expressed directly as the Fourier transform of the reflector equivalent aperture distribution, $e(x', y')$, as:

$$E_f^y(x,y)=\frac{-jke^{-jkR_f}e^{-jk\frac{x^2+y^2}{2R_f}}}{2\pi R_f}E(kx,ky) \tag{4.5}$$

where $E(k_x, k_y)$ is the Fourier transform of $e(x', y')$ evaluated in $k_x=\frac{kx}{R_f}$ and $k_y=\frac{ky}{R_f}$. Therefore, the target field resembles, in first-order approximation, the spectrum of the incident field at the reflector, but spatially compressed by $\frac{kx}{R_f},\frac{ky}{R_f}$ thanks to the focalization effect of the reflector.

Equation (4.5) is the same expression as the one obtained in [21], which was derived starting from the scalar diffraction field. A similar procedure will lead to the derivation of a similar expression for the magnetic field in the target plane of a focusing reflector. Therefore, one can conclude that the target field of a focusing aperture with large R_f/D has all the properties of the far field, that is, the field amplitude is proportional to the Fourier transform of the aperture distribution, and the electric and magnetic field are orthogonal and related by the free-space wave impedance.

Equation (4.5) also implies that the field distribution in the target region is nearly independent of the location of its focal point, provided it is not too close to the antenna. Indeed, the Fraunhofer field of a parabolic reflector and the Fresnel field of an elliptical reflector with large R_f/D number are equivalent. Therefore, also for elliptical reflectors the same techniques of modification of the field aperture used for parabolic reflectors can be exploited to reduce the sidelobes and for beam shaping. Figure 4.5(a) shows a comparison of the near field of an elliptical reflector focusing at $R_f = 2.5$m, with the far field of a parabolic reflector having the same diameter and focal distance F as the elliptical reflector (see Figure 4.3). The field radiated by the elliptic reflector is plotted as a function of θ, which is

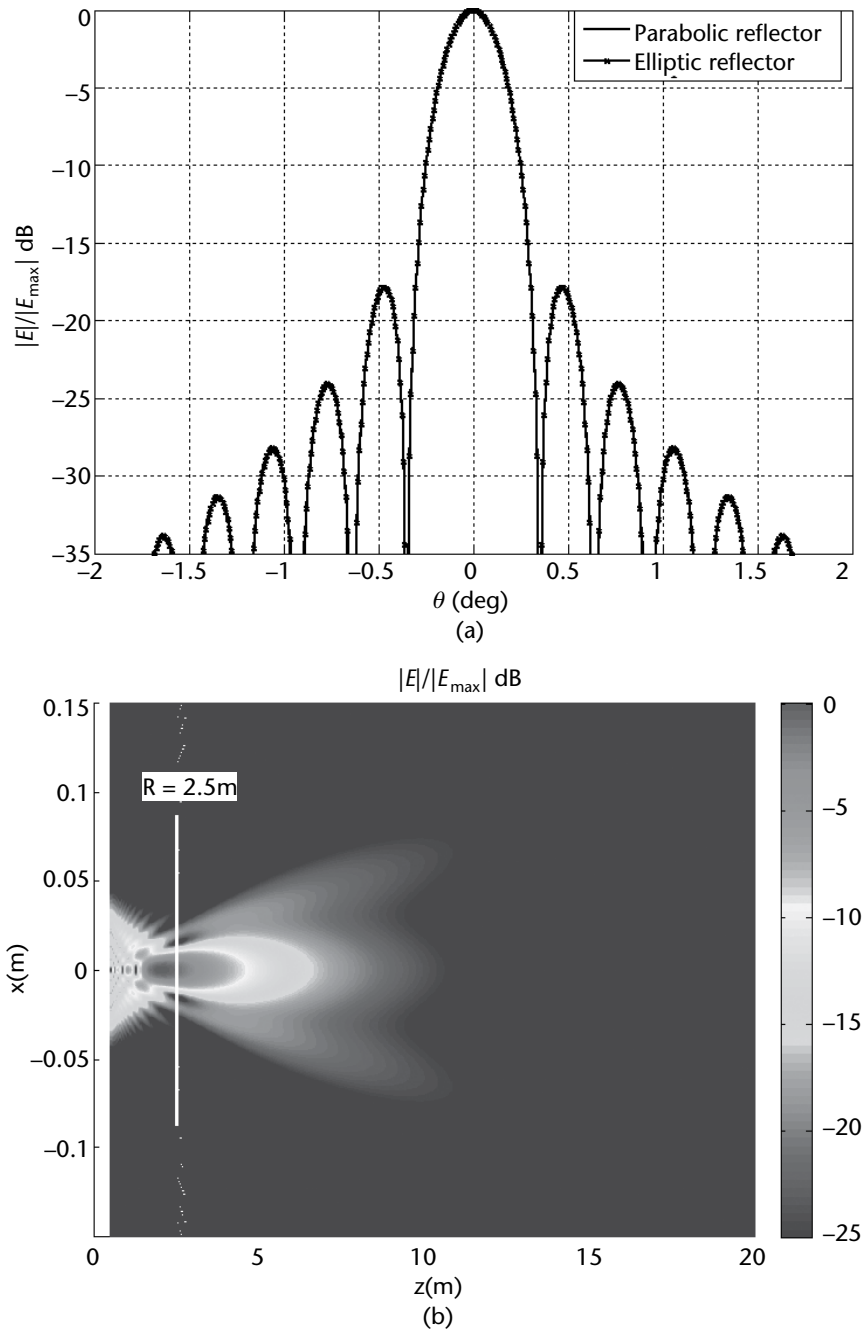

Figure 4.5 Field radiated by an elliptical reflector with uniform illumination at f = 600 GHz (F = 10 cm, D = 10 cm, 2c = 2.4m): (a) spherical cut at R = 2.5m compared to the far-field spherical cut of the parabolic reflector shown in Figure 4.3(a) and (b) an xz-cut where the position of the spherical cut is also indicated.

approximately $\frac{x}{R_f}$ for large R_f/D. Figure 4.5(b) shows an xz-cut of the radiated field by such an elliptical reflector as simulated with GRASP.

4.2.3 General Properties of the Field in the Target Plane

4.2.3.1 Resolution

One of the most important parameters in an imaging system is the resolution because it is directly related to the possibility of distinguishing two objects in an image. There are two main definitions of resolution depending on whether the desired imaging is coherent or incoherent. For coherent imaging, where the receiver couples to the electric field distribution generated by the reflector on the focal plane (e.g., heterodyne receiver), the resolution is usually established to be equal to the antenna half-power beamwidth (HPBW) [26], that is, one-way HPBW. In reality, the imaging resolution of a coherent imager will also depend on the antenna pattern sidelobes and actual directivity achieved. In contrast, for incoherent radiometric imaging, the brightness in the FoV is typically reconstructed by resorting to Fourier transformations (FT) of samples acquired over the entire focal plane. Because these samples are obtained as convolutions of the real brightness and the radiotelescope antenna pattern, as discussed in [26, 27], this procedure limits the resolution to HPBW/2.

If we considered only the HPBW as a measure of the resolution, the best resolution (i.e., the smallest resolution) that can be obtained with a certain reflector diameter is when it is uniformly illuminated. In the optical domain, an imaging system providing the smallest possible resolution is usually referred to as *diffraction limited*.

The field in the target plane of a focusing reflector with a uniform circular aperture can be calculated from (4.5). One only needs to use the Fourier transform of a *circ* function [i.e., a constant function defined on a circular domain with $circ(\rho, D/2)=1$ for $\rho=\sqrt{x^2+y^2} < D/2$, which is commonly known as an *Airy pattern* in the optical domain and has the following expression:

$$E^i\left(\frac{kx}{R_f}, \frac{ky}{R_f}\right) = \pi \frac{D^2}{2} \frac{J_1\left(\frac{k}{R_f}\rho D/2\right)}{\frac{k}{R_f}\rho D/2} \tag{4.6}$$

The HPBW of the field distribution provided in (4.6) can be calculated directly from the –3-dB radial distance, $\rho_{-3\text{dB}}$, which can be calculated using $\frac{\frac{k}{R_f}\rho_{-3\text{dB}} D}{2} = 0.51\pi$. Using $\rho_{-3\text{dB}}$, one can calculate the resolution for coherent imaging to be:

$$\Delta\rho_{\text{HPBW}} = 2\rho_{-3\text{dB}} = 1.02\frac{\lambda}{D}R_f \tag{4.7}$$

A third definition for resolution is for active coherent imaging systems when the transmitter and receiver patterns are the same (e.g., the Tx and Rx antennas are placed at the focal point of the reflector). In such a case, the resolution is defined by taking into consideration the antenna pattern to the second power (i.e., $|E|^2$), that is, the two-way HPBW. By finding the –3-B distance of (4.6) to the second power, the two-way HPBW can be calculated to be:

$$\Delta\rho_{\text{HPBW}}^{\text{two-way}} = 0.74\frac{\lambda}{D}R_f \tag{4.8}$$

4.2.3.2 Depth of Focus

Imaging reflector systems based on ellipsoidal reflectors are designed to have a well-focused beam at a certain distance R_f where the object to be imaged is located. Unlike with parabolic-based systems, where the beam angular profile remains the same from the far-field region boundary to the infinity, the elliptical-based systems are only well focused over a certain region along the axial direction that depends on the Fresnel number $N = \frac{D^2}{4\lambda R_f}$. Figure 4.6 shows the near field, calculated with GRASP, along the axial direction of an elliptical reflector focusing at $R_f = 2.5$m for two different Fresnel numbers. This field is characterized by having a maximum at a z-quote smaller than the target distance R_f. This effect is called *focal shift* and it has been studied by many authors [28]. However, note that even if the maximum peak of the field is at a different location, the field at the target distance R_f is always well focused, as has been shown in earlier examples. Therefore, when designing imaging reflector systems for a specific focusing distance, this shift can, in practice, be ignored. Actually, the near-field distribution due to a parabolic reflector also presents a localized maximum along the axial direction before it is well focused [see Figure 4.4(a)]. In contrast, this shift is relevant when defining the depth of focus of the imaging system, that is, the region where the field remains well focused, as we will see next.

Figure 4.6 also shows, for comparison purposes, the approximated electrical field along the axis calculated with the expression derived in [29] and reported here:

$$\left|E^{axial}\right| \cong \left(1 - \frac{z - R_f}{R_f}\right)\frac{\sin\left(\frac{\pi}{2}N\frac{z - R_f}{R_f}\right)}{\frac{\pi}{2}N\frac{z - R_f}{R_f}} \tag{4.9}$$

Starting from this formula, one can calculate the position of the maximum field, $z_{\max} = R_f + \Delta R_f$, and from this the focal shift, by finding the zero of the following transcendental equation:

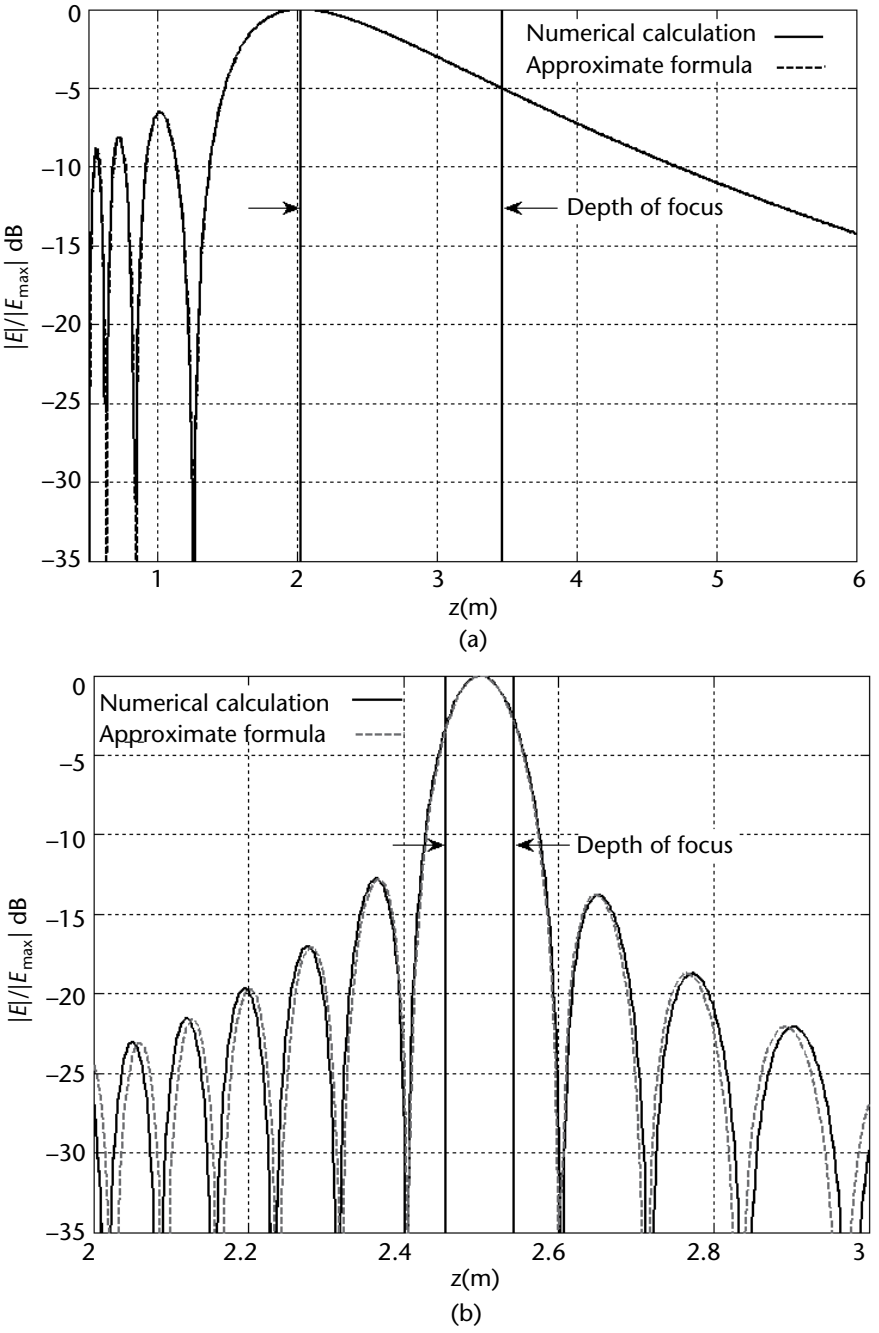

Figure 4.6 Axial field of an elliptical reflector focusing at Rf = 2.5m with (a) $D = 10$ cm and $N = 2$ and (b) $D = 50$ cm and $N = 50$.

$$\frac{\tan\left(\frac{\pi}{2}N\frac{z-R_f}{R_f}\right)}{\frac{\pi}{2}N\frac{z-R_f}{R_f}}=1-\frac{z-R_f}{R_f} \tag{4.10}$$

A useful approximate formula of the focal shift ΔR_f has been provided by [28] as follows:

$$\Delta R_f \cong -\frac{R_f}{1+\frac{\pi^2}{12}N^2} \tag{4.11}$$

Figure 4.7(a) shows such a shift, as a function of the Fresnel number, when the root of (4.10) has been found both numerically or with expression (4.11). It can be seen from the figure that this approximate expression is only valid for $N > 5$.

The most relevant parameter for imaging applications is the axial HPBW, Δz_{HPBW}, which defines the axial region with a field decay of less than 3 dB with respect to its maximum at $R_f + \Delta R_f$. By using this parameter, we can define an axial region where the field is well focused, usually referred as depth of focus in the optical domain. Figure 4.7(b) shows the axial HPBW as a function of the Fresnel number calculated through (4.9). By considering only the first term of the right side of such equation, an approximate expression of such axial width can also be calculated as follows:

$$\Delta z_{\text{HPWB}} \cong 1.77\frac{R_f}{N} \tag{4.12}$$

This expression agrees with the one given in [30], where tapered apertures are also considered. Figure 4.7(b) also shows the approximate expression for the axial HPBW for comparison. Again, the approximate expression is only valid for $N > 5$.

For large Fresnel numbers, the axial field amplitude distribution around the focus is symmetric because the first term on the right side of (4.9) is almost equal to unity. In such a case, the field is symmetric around $z_{max} = R_f + \Delta R_f$, and we can easily define a region where the field remains well focused as $[z_{max} - \Delta z_{HPBW}/2, z_{max} + \Delta z_{HPBW}/2]$. Instead, when there is a significant focal shift, that is, $N < 5$, the radiated field along the axial distance is not symmetric with respect to either the focal distance R_f or with respect to the maximum field at $z_{\max}$. Indeed, the transverse near-field field quality presents a very rapid decay for axial distances smaller than $z_{\max}$ due to diffraction effects. In this situation, it is more difficult to define the depth of focus. In these cases, as a rule of thumb, we can say that the axial region where the field remains well focused is approximately $[z_{max}, z_{max} + \Delta z_{HPBW}]$. Figure 4.8 shows the field at the extremes of the depth-of-focus region, for two different Fresnel numbers, with the field at the target plane.

4.2.3.3 Refocusing

We have just said that a focusing reflector has a limited axial region where the field remains focused. In remote terahertz imaging applications, especially for large distance security applications, the target is not stationary and the system is required to perform images at different distances. Therefore, a way of changing the target distance is needed, that is, a method for refocusing. Here we are going to study a simple symmetrical elliptical reflector. A large amount of literature can be found on complicated zooming systems (see [31] for instance), especially those that use dielectric lenses in the optical domain and all-refractive mirrors in the infrared.

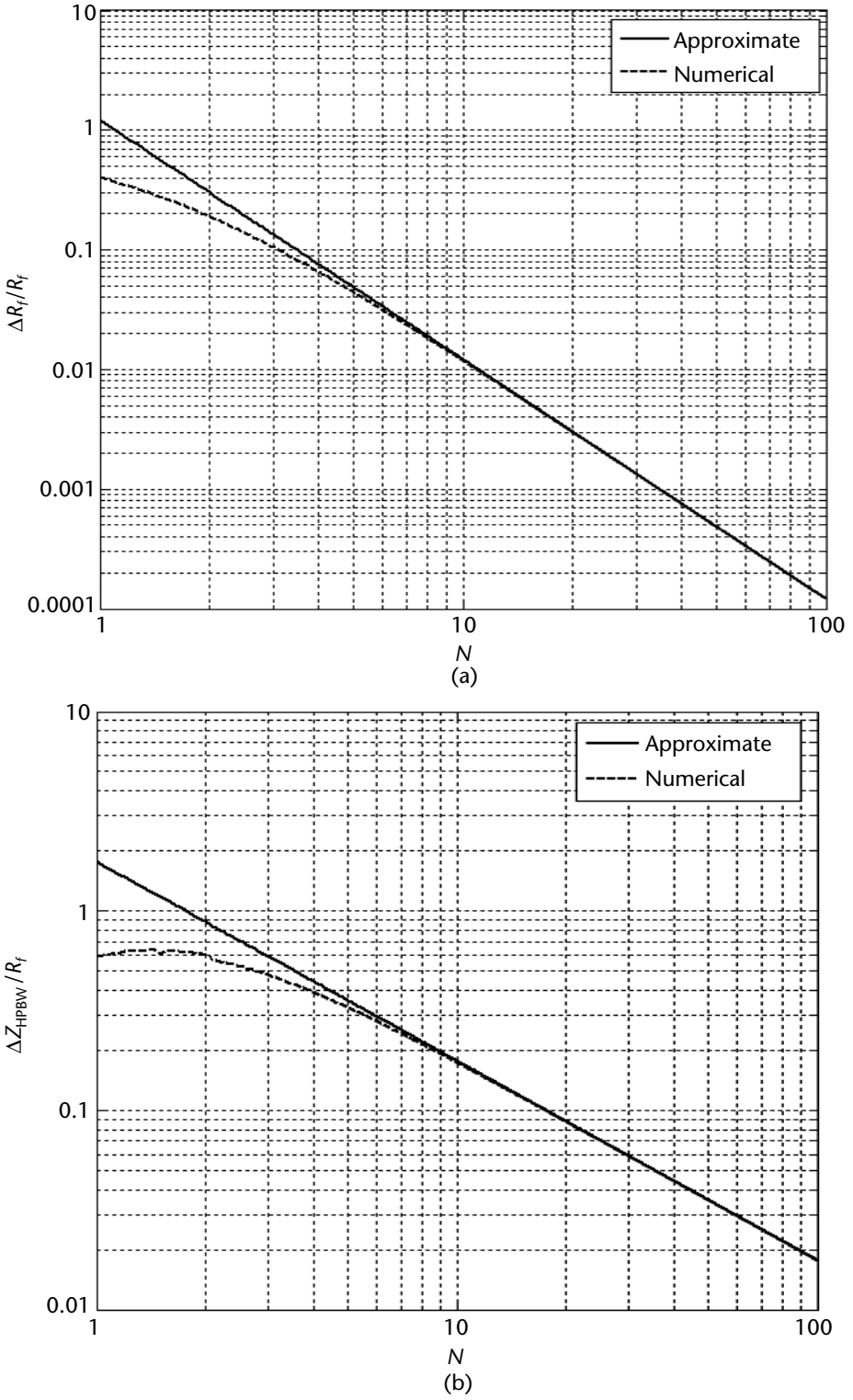

Figure 4.7 (a) Axial shift and (b) axial HPBW as a function of the Fresnel number N.

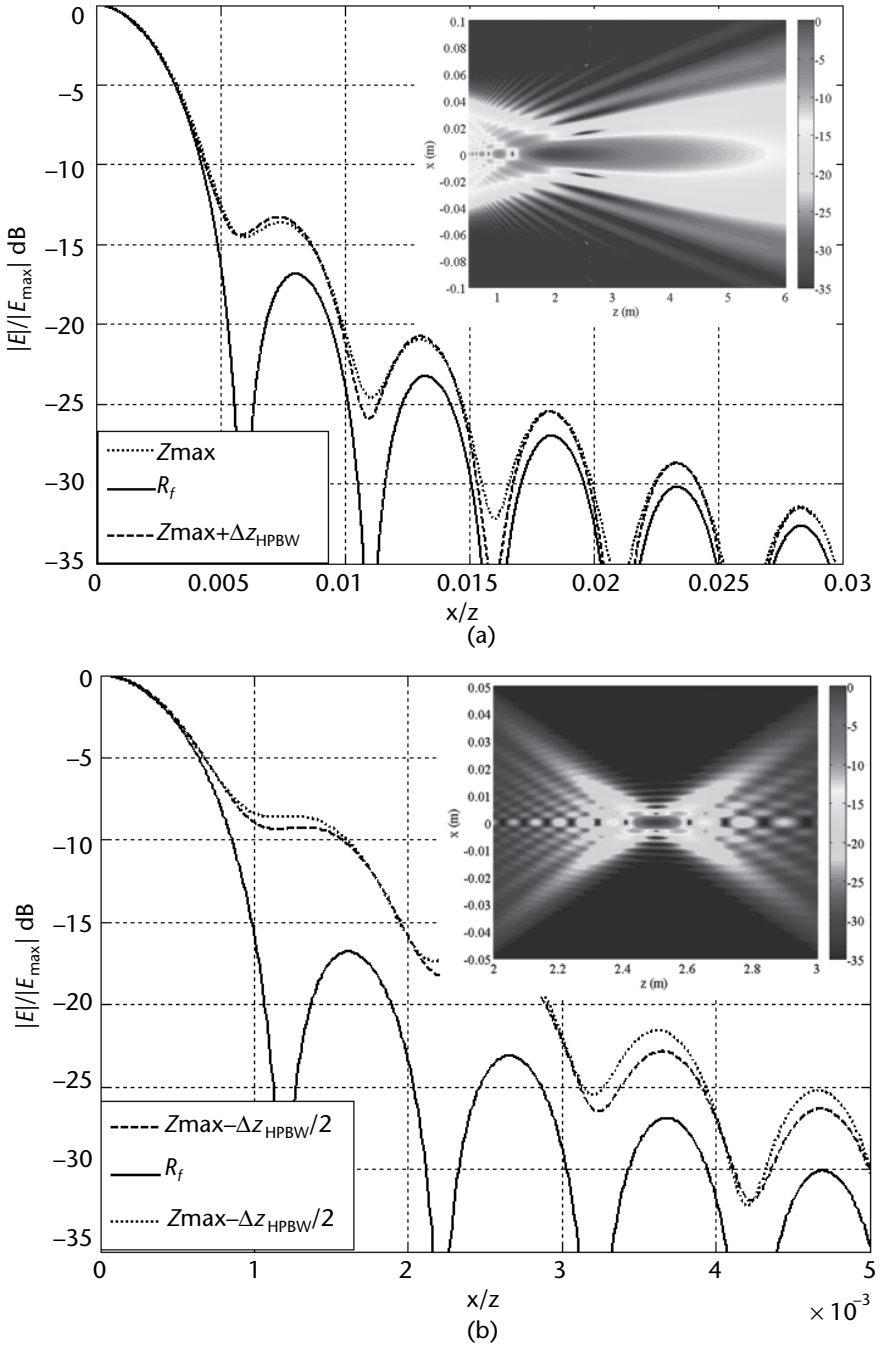

Figure 4.8 Fields radiated at the target plane and extremes of the depth of focus region for the same two cases shown in Figure 4.6: (a) $N = 2$ and (b) $N = 50$. The insets show the radiated field in an xz-cut.

Considering the elliptical reflector shown in Figure 4.9, a displacement Δz_f along the axial direction of the feed will be translated into a shift ΔR_f of the target focusing distance. This is because the defocusing of the feed modifies the quadratic phase distribution over the reflector aperture. Figure 4.10 shows the simulated

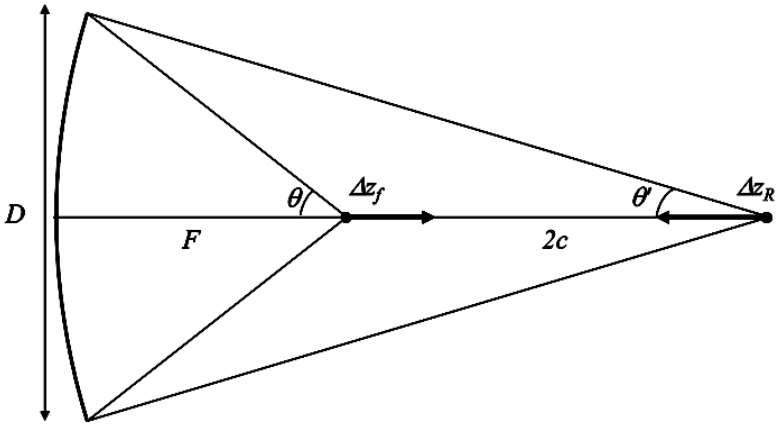

Figure 4.9 Geometry of an elliptical reflector with a defocusing of the feed, Δz_f.

fields for the $N = 2$ case previously studied in Figure 4.8, where a defocusing shift of $\pm\Delta z_f / F = 0.01$ has been considered. Figure 4.10(a) shows the fields radiated along the axial direction. Once again, there is a focal shift with respect to the optimal focus associated with the maximum of the axial field amplitude. Figure 4.10(b) shows the transversal fields at the refocused target plane in each case. It is worth nothing that the curves related to the field of a focused or refocused system, when plotted as a function of x/z, are identical. This is because the target field is proportional to the Fourier transform of the aperture current distribution as indicated in (4.5) and evaluated on x/z and y/z.

One can also change the focusing distance of a parabolic reflector from infinity to a certain close distance R_f by displacing the feed away from the reflector. This solution provides good results as long as the reflector aperture is symmetric or has a small offset displacement from the axis of revolution.

Table 4.1 provides an overview of all the properties of the target field that have been discussed in this section.

4.2.4 Equivalence Between Offset Parabolic and Elliptical Reflectors

All previous examples have been oriented to symmetrical reflectors. In this case, it is straightforward to establish an equivalence between a parabolic and an elliptical reflector—we need merely to assume that both reflectors have the same feed focal distance, F, and that the target distance of the elliptical reflector is equal to $R_f = F + 2c$, where c is the distance between the ellipse foci (see Figure 4.3 for clarification of the geometry).

Let us now consider an offset parabolic reflector, as shown in Figure 4.11(a), with a circular projected aperture, D. A geometrical mapping of the parabolic main reflector to the corresponding elliptical reflector can be done as proposed in [32]. This mapping consists of having the same values of the central ray L and the offset distance X_o for both types of reflectors, as well as having the secondary focus of the elliptical reflector in front of the aperture at the desired focusing distance R_f. In such a case the axis of revolution of the ellipse is tilted with respect to that of the parabolic reflector; therefore, this mapping allows us to maintain the same

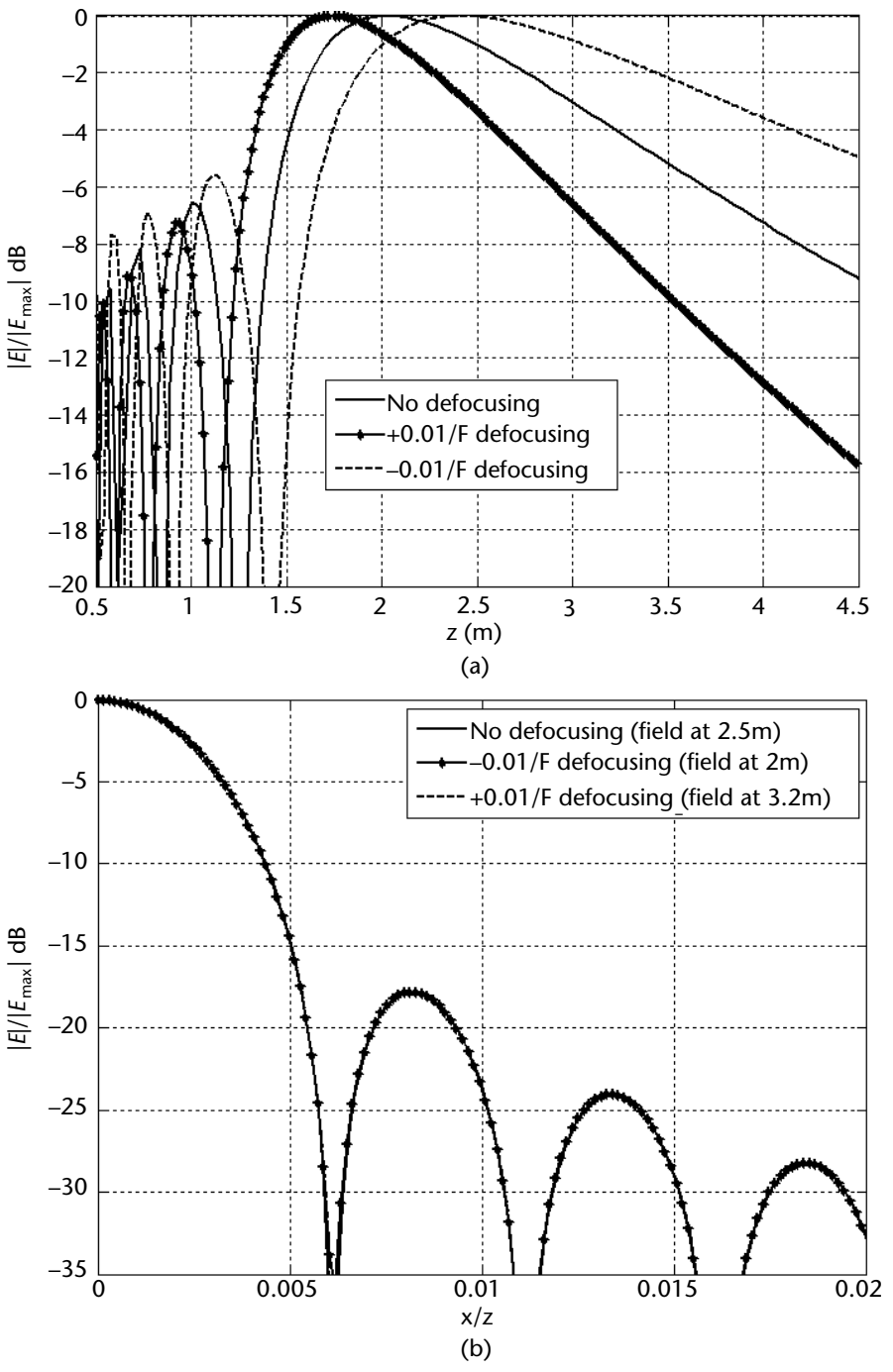

Figure 4.10 Field along the (a) axial direction and (b) at the refocused distance simulated by GRASP for the $N = 2$ case of Figure 4.6 and a defocusing shift of $\pm\Delta z_f/F = 0.01$. The field with no defocusing is also shown for comparison.

definition for the aperture dimensions, D. However, this mapping leads to slightly larger values for the cross-polarized focused field with respect to the far field generated by the equivalent parabolic reflector. This is associated with the fact that the

Table 4.1 Main Properties of the Radiated Field in the Target Plane

Parameter	*Formula*
Field radiated in the target plane by a general aperture distribution	$E_f^y(x,y)=\frac{-jke^{-jkR_f}e^{-jk\frac{x^2+y^2}{2R_f}}}{2\pi R_f}E\left(\frac{kx}{R_f},\frac{ky}{R_f}\right)$
Field radiated in the target plane by uniform aperture distribution	$E_f^y(x,y)=\frac{-jke^{-jkR_f}e^{-jk\frac{x^2+y^2}{2R_f}}}{2\pi R_f}\pi\frac{D^2}{2}\frac{J_1\left(\frac{k}{R_f}\rho D/2\right)}{\frac{k}{R_f}\rho D/2}$
HPBW in the target plane of a uniform aperture distribution	$\Delta\rho_{\text{HPBW}}=1.02\frac{\lambda}{D}R_f$
Two-way HPBW in the target plane of a uniform aperture distribution	$\Delta\rho_{\text{HPBW}}^{\text{two-way}}=0.74\frac{\lambda}{D}R_f$
Field radiated by uniform aperture distribution in the axial direction	$\left\|E^{axial}\right\|\cong\left(1-\frac{z-R_f}{R_f}\right)\frac{\sin\left(\frac{\pi}{2}N\frac{z-R_f}{R_f}\right)}{\frac{\pi}{2}N\frac{z-R_f}{R_f}}$
Axial shift	$\Delta R_f\cong-\frac{R_f}{1+\frac{\pi^2}{12}N^2}$
Maximum axial field distance	$z_{\max}\cong R_f+\Delta R_f$
Axial HPBW	$\Delta z_{\text{HPBW}}\cong 1.77\frac{R_f}{N}$
Depth of focus ($N > 5$)	$[z_{\max}-\frac{\Delta z_{\text{HPBW}}}{2},z_{\max}+\frac{\Delta z_{\text{HPBW}}}{2}]$
Depth of focus ($N < 5$)	$[z_{\max},z_{\max}+\Delta z_{\text{HPBW}}]$

offset portion of the ellipse being used, with respect to the axis of revolution, is larger due to the axis of revolution tilt.

Instead, a different mapping can also be considered when the axis of revolution is not tilted with respect to the parabola axis, as shown in Figure 4.11(b). This mapping leads to similar levels for the cross-polarized field. In this case, the elliptical surface is defined by means of the major axis distance $2a = R_f + L$, and the foci distance $2c$. However, in this case, the reflector aperture is tilted by an angle α. To establish the equivalence, both reflectors need to have the same aperture dimensions, D, as indicated in Figure 4.11. Figure 4.12 shows the field simulated with GRASP for the parabolic and an equivalent elliptical offset reflector that focuses at 2.5m. The geometrical parameters of these two reflectors are provided in Tables

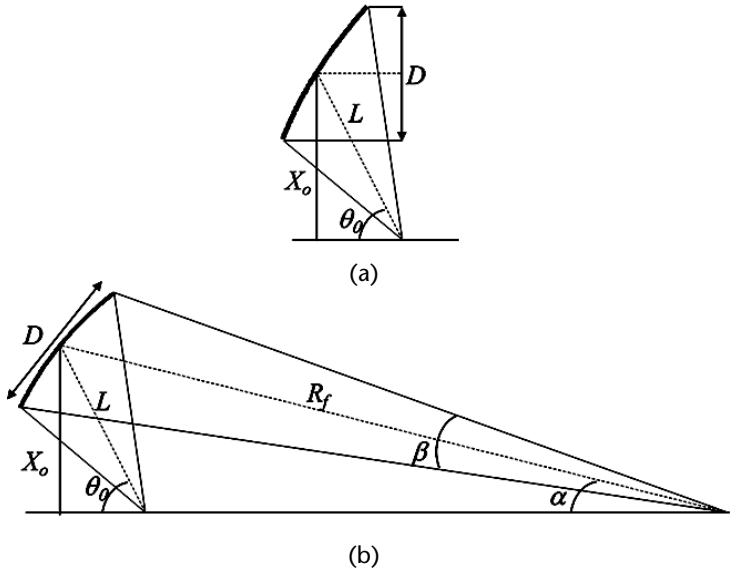

Figure 4.11 Equivalent parabolic and elliptical offset reflectors.

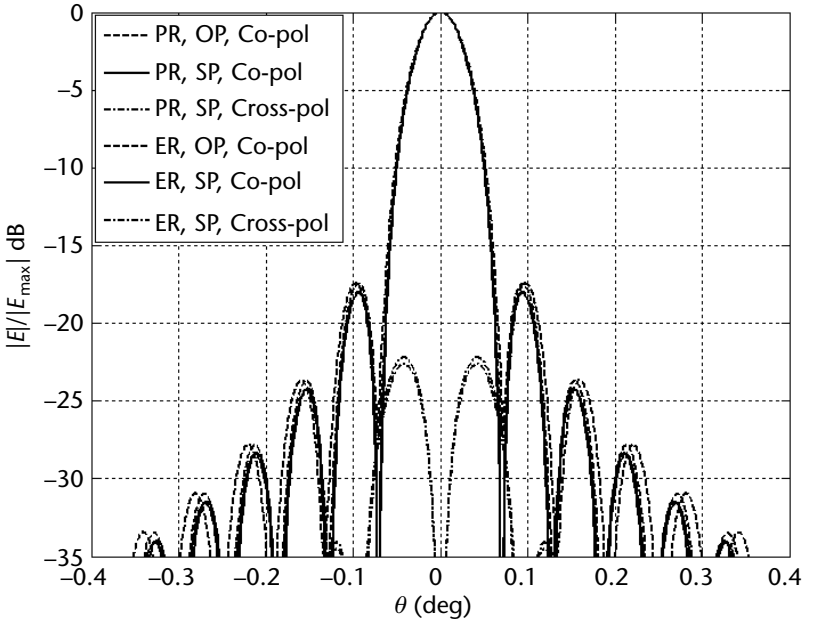

Figure 4.12 Radiated field by an offset parabolic (PR) and elliptical (ER) reflector in the offset (OP) and symmetric (SP) planes. The dimensions of the reflectors are provided in Table 4.2 and 4.3.

4.2 and 4.3. One can appreciate the similarities of all of the radiated field components, even at the level of the cross-polarization ones. Small differences are appreciated in the cross-polarization field because of the relatively close focusing distance.

Thanks to this equivalence, one can use the classical design formulation for multireflector systems based on a parabolic reflector as the main antenna (e.g., compensation of cross-polarization, reduction of off-focus aberrations) with an

Table 4.2 Geometric Parameters of the Offset Parabolic Reflector

Symbol	*Quantity*	*Value*
F	Focal distance	50 cm
D	Aperture diameter	50 cm
X_0	Offset height	62 cm

Table 4.3 Geometric Parameters of the Offset Elliptic Reflector

Symbol	*Quantity*	*Value*
$2c$	Interfocal distance	2.114m
$2a$	Vertex distance	3.192m
X_0	Offset height	62 cm
D	Aperture diameter	50 cm
R_f	Target distance	2.5m
α	Aperture tilt	14.36 deg
β	Output angle	11.42 deg

equivalent main elliptical reflector. Several examples of this equivalence are shown later in this chapter.

4.3 Imaging with Focal Plane Arrays

Figure 4.13 shows a typical configuration representing the key parameters of an imaging system obtained with a FPA. A multibeam antenna is then achieved by placing an array of antennas at the focal plane of a reflector, characterized with diameter D and focal distance F. When an antenna is laterally displaced from the reflector focal point, the field radiated by the reflector is scanned toward a certain angle θ_{out}, as shown in Figure 4.13. This angle can be calculated as $\theta_{out} = BDF\theta_{in}$ [33], where BDF stands for beam deviation factor. Therefore, an array located at the focal plane of a reflector antenna, usually referred as a focal plane array (FPA), generates multiple independent beams pointing to different directions in the FoV, which can image multiple pixels simultaneously (as much as array elements) and, correspondingly, decrease the acquisition time of the image.

When designing a FPA for imaging applications, the most important parameter is the sampling of the focal plane by the array elements, that is, the spacing d of the array. The optimum sampling in terms of antenna efficiency and acquisition time depends on the imaging architecture (active or passive system, coherent or incoherent). The signal-to-noise ratio (S/N) is directly proportional to the reflector illumination efficiency and will play a key role in the FPA optimization.

Terahertz imaging systems can be distinguished between narrowband and broadband systems, depending on the frequency characteristics associated with the detectors considered. Terahertz active imaging systems, in which the S/N can be increased by generating more power if high-power sources and amplifiers are available, are generally narrowband systems. The most common active imaging systems

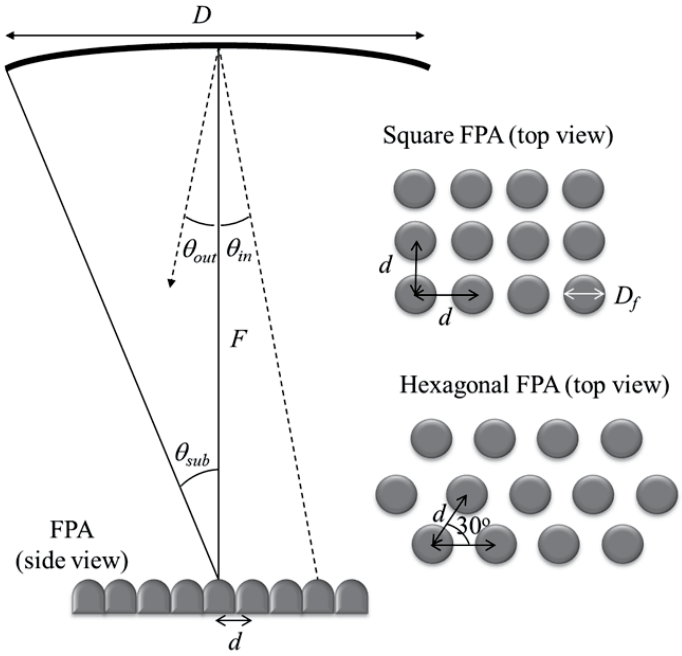

Figure 4.13 Schematic view of the reflector and focal plane array.

are heterodyne systems with microwave types of detectors (i.e., semiconductor diodes). In this case, the sampling of the FPA can be simply optimized at the central frequency of the band as described in Section 4.3.2.

Instead, passive systems are usually designed with broadband detectors to improve the S/N, which makes the selection of the sampling difficult. Moreover, the optimum sampling in this case also depends on the type of source that we are imaging (isolated or continuous), on whether the receiver is background limited or quantum noise limited, and on the noise generated by signals coming from the instrument itself. All these aspects are addressed in Section 4.3.3.

4.3.1 Relationship Between the Reflector Aperture Efficiency and the Power Received by an Antenna in the Focal Plane of the Reflector

The S/N of any imaging system is directly proportional to the actual power received by the antennas in the FPA. Therefore, to optimize the sampling of the focal plane in terms of acquisition speed by keeping a certain level of the S/N, we need to calculate this received power. It is proportional to the actual illumination efficiency of the reflector (i.e., the aperture efficiency) as we will show next.

In (4A.13) of Appendix 4A at the end of this chapter, an analytical expression for this received power is provided for a plane wave impinging on the reflector from (α, β) with an amplitude $E_e(\alpha, \beta)$. This expression can be simplified if we consider the following specific case: The antenna is modeled by a magnetic current distribution along x as described in Appendix 4C, the incident plane wave on the reflector is polarized along y, and the reflector is characterized by large F/D numbers. Under these assumptions $\overline{U}(x',y')\dfrac{\overline{r}'}{r'}\times\overline{\overline{I}}\cdot\dfrac{\overline{m}_a(x,y)}{\zeta I_0}\cong k\dfrac{m_a(x,y)}{\zeta I_0}$, and (4A.13) becomes:

$$P_n^e(\alpha,\beta)=\frac{\left|E_e(\alpha,\beta)\right|^2}{2\zeta}\frac{k^2\eta_{loss}\chi_{match}}{(2\pi F)^2}\frac{\left|\iint_{S_r}\iint_{S_a} f_a(x,y)e^{jk\frac{x'}{F}(x_n+x)}e^{jk\frac{y'}{F}(y_n+y)}e^{-jk_x x'}e^{-jk_y y'}dx'dy'dxdy\right|^2}{\iint_{S_a}\left|f_a(x,y)\right|^2 ds} \tag{4.13}$$

This is a general expression for the voltage induced on the antenna that can be transformed into a double integral either on the reflector aperture S_r by invoking the Fourier transform of the antenna current normalized distribution F_a as

$$P_n^e(\alpha,\beta)=\frac{\left|E_e(\alpha,\beta)\right|^2}{2\zeta}\frac{\eta_{loss}\chi_{match}}{F^2}\frac{\left|\iint_{S_r} F_a\left(k\frac{x'}{F},k\frac{y'}{F}\right)e^{jk\frac{x'}{F}x_n}e^{jk\frac{y'}{F}y_n}e^{-jk_x x'}e^{-jk_y y'}dxdy\right|^2}{\iint_{S_a}\left|F_a(\theta,\phi)\right|^2\sin\theta d\theta\phi} \tag{4.14}$$

or on the antenna aperture S_a by invoking the Fourier transform of the reflector current distribution, which in this case is uniform leading to the well-known Airy pattern distribution, as follows:

$$P_n^e(\alpha,\beta)=\frac{\left|E_e(\alpha,\beta)\right|^2}{2\zeta}\left(\frac{k}{4F}D^2\right)^2\eta_{loss}\chi_{match}\frac{\left|\iint_{S_a} f_a(x,y)\frac{J_1\left(\frac{k}{F}\rho_r D/2\right)}{\frac{k}{F}\rho_r D/2}dxdy\right|^2}{\iint_{S_a}\left|f_a(x,y)\right|^2 ds} \tag{4.15}$$

where $\rho_r=\sqrt{\left(x+x_n-\frac{F}{k}k_x\right)^2+\left(y+y_n-\frac{F}{k}k_y\right)^2}$ represents a translation of the Airy pattern as a function of the antenna location and plane wave incidence.

Equation (4.14) can be expressed as a function of the reflector aperture efficiency, η_{ap}, by multiplying both the numerator and denominator to the reflector area:

$$P_n^e(\alpha,\beta)=\frac{\left|E_e(\alpha,\beta)\right|^2}{2\zeta}A_{ref}\eta_{loss}\chi_{match}\eta_{ap}(\alpha,\beta) \tag{4.16}$$

where

$$\eta_{ap}(\alpha,\beta)=\left(\frac{1}{F}\right)^2\frac{\left|\iint_{S_r}F_a\left(k\frac{x'}{F},k\frac{y'}{F}\right)e^{jx'\left(k\frac{x_n}{F}-k_{xi}\right)}e^{jy'\left(k\frac{y_n}{F}-k_{yi}\right)}dx'dy'\right|^2}{A_{ref}\int_0^{2\pi}\int_0^{\pi}\left|F_a(\theta,\phi)\right|^2\sin\theta d\theta d\phi} \tag{4.17}$$

The exponential terms in (4.17) are related to the antenna location and the direction of the incoming plane wave. The aperture efficiency will be maximized when these phase terms cancel out, which occurs when the antenna is placed at $x_n = F \sin\beta \cos\alpha$ and $y_n = F \sin\beta \sin\alpha$.

Equation (4.17) can be transformed into spherical coordinates by using an angular parameterization of the reflector aperture where $x' = F \tan\theta \cos\phi$ and $y' = F \tan\theta \sin\phi$. In such a case, (4.17) becomes:

$$\eta_{ap}(\alpha,\beta)= \frac{4}{\pi}\frac{F^2}{D^2}\frac{\left|\int_0^{2\pi}\int_0^{\theta_{sub}}F_a\begin{pmatrix}k\ \tan\cos\phi,\\ k\ \tan\sin\phi\end{pmatrix}e^{j\tan\theta\cos\phi\left(k\frac{x_n}{F}-k_{xi}\right)}e^{j\tan\theta\sin\phi\left(k\frac{y_n}{F}-k_{yi}\right)}\frac{\tan\theta}{\cos^2\theta}d\theta d\phi\right|^2}{\int_0^{2\pi}\int_0^{\pi}\left|F_a(\theta,\phi)\right|^2\sin\theta d\theta d\phi} \tag{4.18}$$

where θ_{sub} is the angle subtended by the reflector (see Figure 4.13). Note that for large *F/D* cases $\tan\theta \cong \sin\theta$ and $\cos\theta \cong 1$.

Equation (4.15) can also be expressed as a function of the reflector aperture efficiency by relating the constant at the beginning of the equation to the area of the reflector $A_{ref}=\frac{\pi D^2}{4}$ and to the integration of the square of the Airy pattern function centered at the origin: $\int_0^{2\pi}\int_0^{\infty}\left|\frac{J_1\left(\frac{k\rho}{F}D/2\right)}{\frac{k\rho}{F}D/2}\right|^2\rho d\rho d\phi=4\pi\left(\frac{F}{kD}\right)^2$. Therefore, the received power can be calculated using (4.16), where the reflector aperture efficiency η_{ap} is calculated as the coupling integral between the antenna feed aperture current distribution, $f_a(x, y)$ and the Airy pattern $\frac{J_1\left(\frac{k}{F}\rho_r D/2\right)}{\frac{k}{F}\rho_r D/2}$, translated as a function of the antenna location and plane wave incidence, as follows:

$$\eta_{ap}(\alpha,\beta)=\frac{\left|\iint_{S_a}f_a(x,y)\frac{J_1\left(\frac{k}{F}\rho_r D/2\right)}{\frac{k}{F}\rho_r D/2}dxdy\right|^2}{\iint_{S_a}\left|f_a(x,y)\right|^2 ds\int_0^{2\pi}\int_0^{\infty}\left|\frac{J_1\left(\frac{k\rho}{F}D/2\right)}{\frac{k\rho}{F}D/2}\right|^2\rho d\rho d\phi} \tag{4.19}$$

Both (4.17) and (4.19) lead to the same results, meaning that one can calculate the reflector aperture efficiency either on the reflector aperture, by using the Fourier transform of the antenna current distribution, or in the antenna plane by using the Airy pattern. Moreover, these expressions (valid for $F/D > 1.5$), calculated in reception, lead to the same efficiency values calculated by using the standard definitions of spillover η_{so} and taper efficiencies η_t, as given in [23], which are calculated in transmission. The aperture efficiency in transmission is obtained as the product of the spillover and taper efficiencies (i.e., $\eta_{ap} = \eta_t \eta_{so}$).

As an example we consider a reflector antenna with $F/D = 3$ illuminated by the two different antenna feed aperture distributions described in Appendix 4B: a uniform distribution and a –16-dB taper distribution. The far field patterns for both distributions are shown in Figure 4.14(a). Figure 4.14(b) shows the spillover and taper reflector efficiencies for a fixed $F/D = 3$ as a function of the feed diameter when calculated with the definitions provided in [23]. Figure 4.14(b) also shows the aperture efficiencies calculated with (4.17) and (4.19) or equivalently in transmission by $\eta_{ap} = \eta_t \eta_{so}$.

4.3.2 Focal Plane Sampling in Active Systems

Let us consider an active imaging system realized with a FPA. The source of the active system can be located either outside the reflector imaging system leading to a broad illumination of the target, or inside the reflector imaging system leading to a single pixel illuminated each time. In the first case, the resolution of the system will be the one-way HPBW, and the antennas in the FPA will receive power that comes from directions all over the target (i.e., different plane waves are arriving at the reflector). In such a case, FPA sampling should be optimized by computing the electric field generated by all of these plane waves. However, in most terrestrial applications, the active systems are designed with the transmitter and receiver inside the reflector system to illuminate and measure a single pixel with each antenna pointing direction. Such a configuration leads to significantly larger signal to noise levels and better resolution (i.e., two-way HPBW), but at the cost of higher technological complexity. In this case, the sampling of the FPA can be done by optimizing the received signal from a single plane wave (i.e., by maximizing the reflector aperture efficiency). Actually, the received signal also depends on the reflector illumination of the transmitter, which as demonstrated previously, is the same as the efficiency in reception if the same antennas are used in the transmitter and receiver. In the following, the optimum FPA sampling of this second case is addressed in detail.

Three parameters characterize the performance of a FPA system: the antenna pointing direction separation, $\Delta\theta$; the reflector diameter, D; and the focal distance, F (see Figure 4.13). Let us consider a parabolic reflector focusing at infinity. The beam separation $\Delta\theta$ in the FoV can be approximated for a relatively low number of scanned beams where $BFD \approx 1$ as follows:

$$\Delta\theta \cong \tan(\Delta\theta) = \frac{d}{F} \tag{4.20}$$

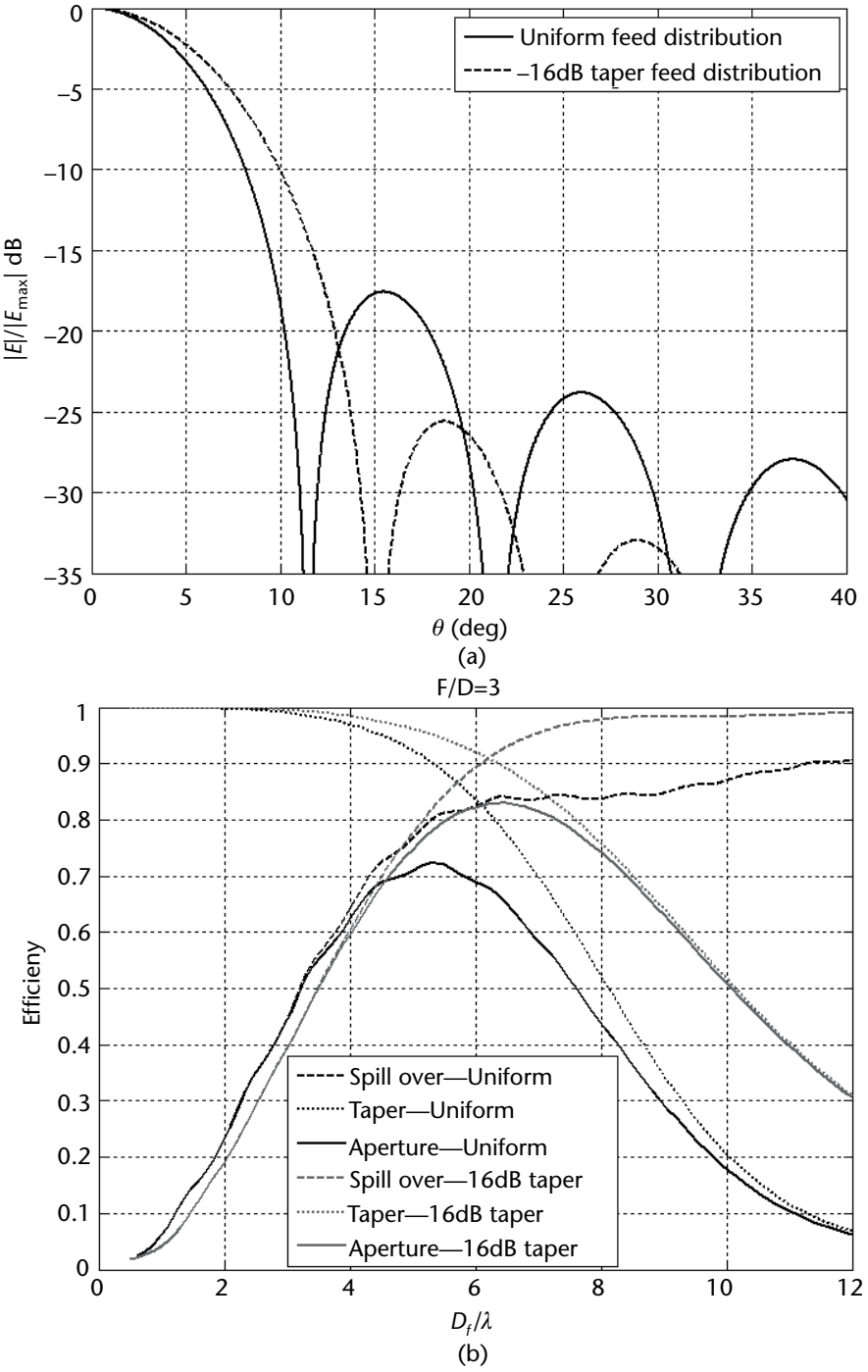

Figure 4.14 (a) Far field of a uniform and tapered feed aperture with $D_f = 6\lambda$ and (b) reflector efficiency versus the feed diameter.

This condition resembles the one derived in the previous section for the antenna position to cancel the phase term in (4.17) and maximize the antenna efficiency.

Note that, if instead of a parabolic reflector, an elliptical reflector focusing at a distance R_f is considered, the beams in the FoV will be separated by a distance $\Delta\rho = \Delta\theta\, R_f$. For the rest of this section, for the sake of simplicity, we will derive the trade-offs for a parabolic reflector, because the same conclusions can be extrapolated to the elliptic reflector case.

In a fully sampled imaging system, the beam separation should be the same as the resolution, which in a two-way active system is associated with the two-way HPBW. From the previous section, we know that for a uniform aperture: $\Delta\theta_{\text{HPBW}}^{\text{two-way}} = 0.74\frac{\lambda}{D}$. Using this definition in (4.20), we can derive a simple condition for the array spacing as follows:

$$\mathrm{d}_{\text{single}}^{\text{two-way}} \cong 0.74\frac{\lambda}{D}F \tag{4.21}$$

which will be referred to from now on as the single sampling case. Figure 4.15 shows the antenna beams generated in the FoV by a FPA sampled following the condition of (4.21).

Let us now consider what (4.21) implies in terms of reflector illumination efficiency. From Figure 4.14(b) it is evident that the spillover efficiency improves as the diameter of the feed increases. However, in a FPA, this diameter is limited by the sampling condition as given in (4.21). Since the feed diameter for a two-way system and $F/D = 3$ is limited to 2.22 wavelengths, the spillover loss for a uniform feed will

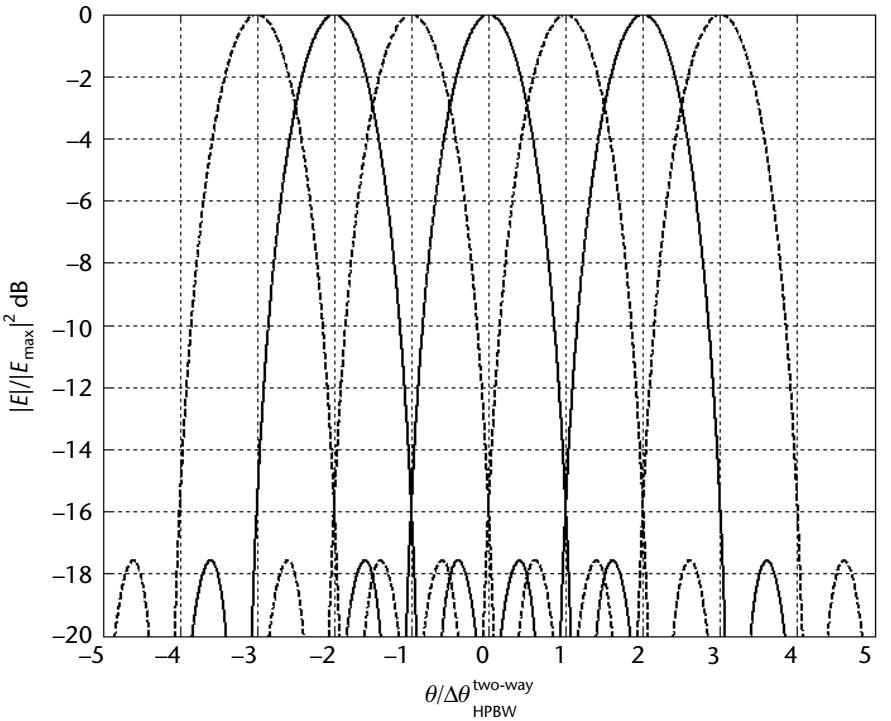

Figure 4.15 Antenna patterns in the field of view for a well-sampled FPA. The dashed lines are the missing beams in the case where the FPA is designed with a double sampling condition.

be –5.5 dB (the received signal in a two-way system will be affected twice by this loss). This efficiency problem in the single sampling condition is independent of the *F/D* ratio because the feed aperture is in any case limited by the sampling condition, which is directly proportional to *F/D*. This means that a very significant part of the power is lost. To avoid such a high loss, it is convenient to design the FPA using a double or third sampling condition:

$$\mathrm{d}^{\text{two-way}} \cong n0.74\frac{\lambda}{D}F \tag{4.22}$$

where n is the sampling order (i.e., n = 1, 2,3, ...). Increasing this sampling order allows us to use larger apertures and improve reflector efficiency. For the double condition, the aperture efficiency loss is reduced to –1.6 dB. Obviously, the focal plane will not be fully sampled, and half of the beams will be missing (see the dashed lines in Figure 4.15). In this case, it is common to use a technique called jiggling [34], which is used, for example, in the Herschel telescope. It consists of rotating a small mirror to cover the missing beams. To optimize the focal plane and the speed, a trade-off between the system S/N and acquisition speed to cover the FoV should be done.

Actually, the optimum aperture efficiency obtained for a uniform feed is achieved at a feed diameter of around 5.3 wavelengths as shown in Figure 4.14(b). This efficiency is limited to about 72%, due to the high sidelobes associated to the distribution given in (4B.6) (see Appendix 4B). To improve this efficiency, one can use a tapered field distribution on the feed aperture. For instance, the –16-dB distribution given in (4B.8) gives an 82% efficiency for a feed diameter of 6.4 wavelengths. To achieve this aperture efficiency in the two-way system, one would need to use the third sampling condition leading to a feed maximum diameter of 6.6 wavelengths.

The reflector taper efficiency is important for imaging applications because it is directly related to the resolution, that is, the HPBW. As a rule of thumb, we can calculate how much the one-way HPBW increases when the reflector is not illuminated uniformly as would be the case for the double or third sampling conditions. For that, we can recall that the taper efficiency relates the achieved directivity *dir* with the maximum directivity $dir_{\max}$ that one could obtain from the reflector aperture, that is, $\eta_t = dir/dir_{\max}$. Then, by considering the Kraus approximation for directive rotationally symmetric patterns [23], that is, $dir \approx 4\pi/\Delta\theta^2_{\text{HPWB}}$, we can compute the increase of the resolution X_{res} as a function of the taper efficiency. Note that this approximation is done for antennas having a single main lobe. For a two-way system, this increase will affect the system twice; therefore:

$$X_{res} = \frac{\Delta\theta^{\text{two-way}}_{\text{HPBW}}}{\left(\Delta\theta^{\text{two-way}}_{\text{HPBW}}\right)_{\min}} \approx \frac{1}{\eta_t} \tag{4.23}$$

This means that the sampling conditions calculated before are affected by this resolution factor, that is, the actual condition will be scaled by X_{res}. For the previous example, we have an increase of X_{res} = 12% for the –16 dB taper feed aperture

at the third sampling condition. This means that the array spacing can actually be increased by approximately 12% [(4.22) is actually $\frac{0.74}{\eta_t}\frac{\lambda}{D}F$] and the antenna diameters can be kept to 6.4 wavelengths, giving some room for the fabrication of the array antennas.

Equation (4.22) is appropriate when we are dealing with a linear FPA (one dimension). However, the sampling of the FoV in a two-dimensional (2D) array has to take into account the lattice of the array itself as well. For example, let us consider a standard 2D FPA (see Figure 4.13) with a square lattice with the element spacing d fixed by the single sampling condition. The black circles in Figure 4.16(a) represent the footprint on the target plane generated by the HPBW of the different antenna patterns created by the different pointing directions associated with each array element position. One can observe that along the vertical and horizontal axes, the beams overlap just at the HPBW level, and these directions are correctly sampled. In contrast, there are unsampled spots along the ϕ = 45-deg direction. To eliminate these spots, and have a fully sampled FoV, the single sampling condition needs to be more restrictive by including a factor associated with the array lattice: $X_{lattice} = \cos\alpha$ with α being the lattice skew angle of periodicity (see Figure 4.13).

In summary, a general expression for the sampling condition including the array lattice and taper factors can be derived as follows:

$$\mathrm{d} \cong n0.74\frac{\lambda}{D}X_{res}X_{lattice} \tag{4.24}$$

The lattice factor reduces further the sampling spacing and therefore the reflector illumination efficiency of the FPA. For the previous example, the array element aperture would be limited to 4.7λ for the third spacing condition leading to a reflector illumination loss of –1.5 dB.

It is well known that better FoV coverage is obtained with a hexagonal lattice where α = 30 deg, as shown in Figures 4.13 and 4.17. If we do not consider, for the moment, the lattice factor on the sampling condition, the illumination efficiency of the reflector is the same as that of the square array of Figure 4.16(a), but with better coverage over the FoV as evident when comparing Figures 4.16(a) and 4.17(a). Nevertheless, there are still some spots missing along the 60-deg direction. To reduce these spots, we need to apply the lattice factor to the sampling condition leading to the footprint of Figure 4.17(b) and obtaining a slightly larger spacing than a square FPA. In the example before, the third sampling condition would be 5.7λ and the spillover loss –0.9dB for a –16-dB taper feed aperture.

Let us now briefly consider the double sampling condition and the jiggling mechanism. The footprint of the FPA in the imaging plane is shown in Figures 4.18(a) and 4.18(b) for the rectangular and hexagonal lattice cases, respectively, when a double sampling condition that includes the lattice factor is applied. The gray circles are the beams directly generated by the FPA. To fully cover the FoV, we need to put into the reflector system a mirror that by wobbling displaces the footprint in different directions (jiggling). For the square lattice, the mirror has to wobble in four directions to virtually displace the FPA and fully cover the FoV, as

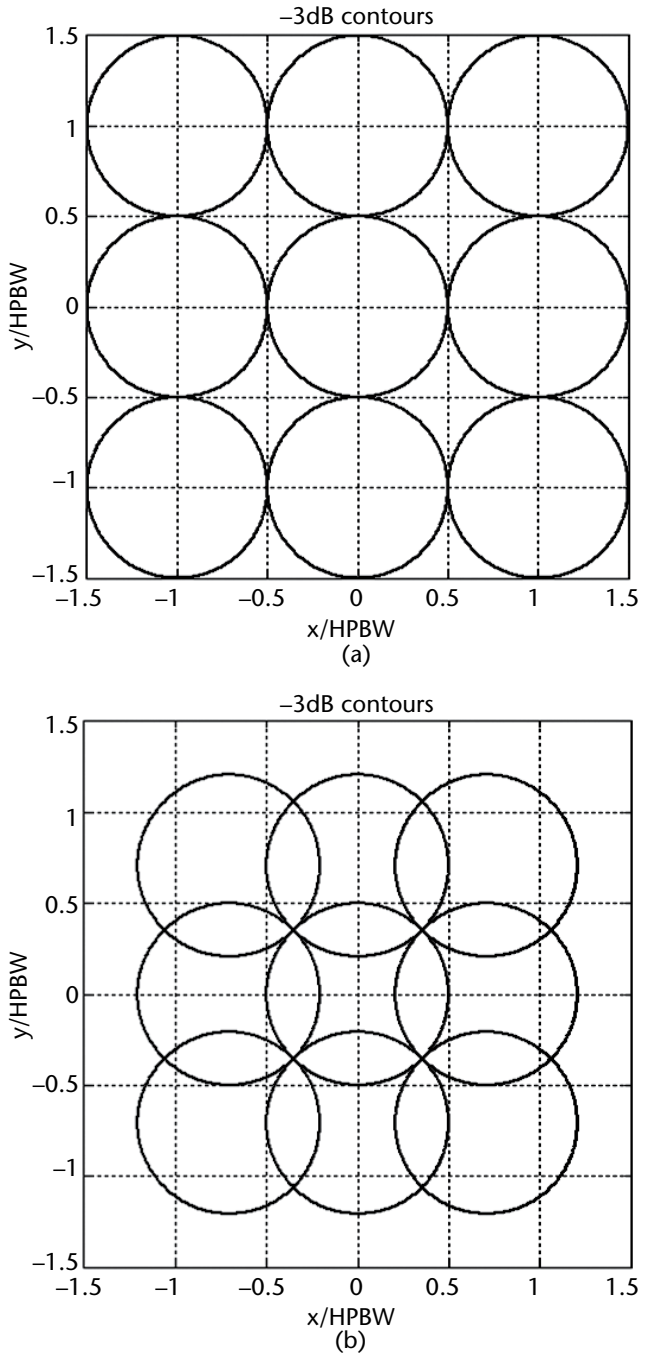

Figure 4.16 HPBW footprint of a square FPA with single sampling condition (a) excluding and (b) including the array lattice factor.

graphically shown in Figure 4.18(a) with different dashed line circles. Similarly, in the case of the hexagonal lattice, the FPA has to be displaced virtually by the four positions shown in Figure 4.18(b). Instead, if we use the double sampling condition without the lattice factor, we would need to displace the footprint in eight different positions, as shown in Figure 4.18(c).

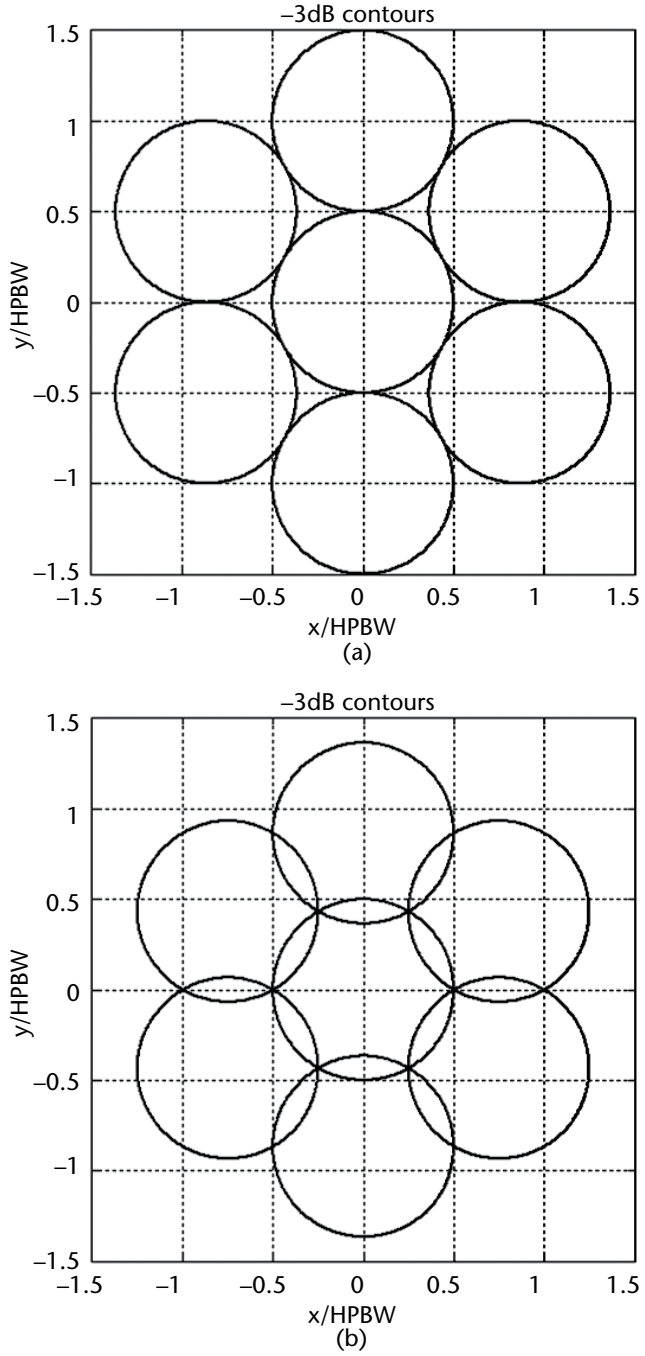

Figure 4.17 HPBW footprint of hexagonal focal plane patterns in the image plane (a) excluding and (b) including the array lattice factor.

Table 4.4 summarizes for different sampling conditions for the two-way loss in the reflector illumination for the case of a –16-dB taper aperture, together with the factor of increase of the image acquisition time. This factor is directly proportional to the number of pointing directions needed by the jiggling mechanism to fully cover the FoV. The final system implementation is a trade-off between the

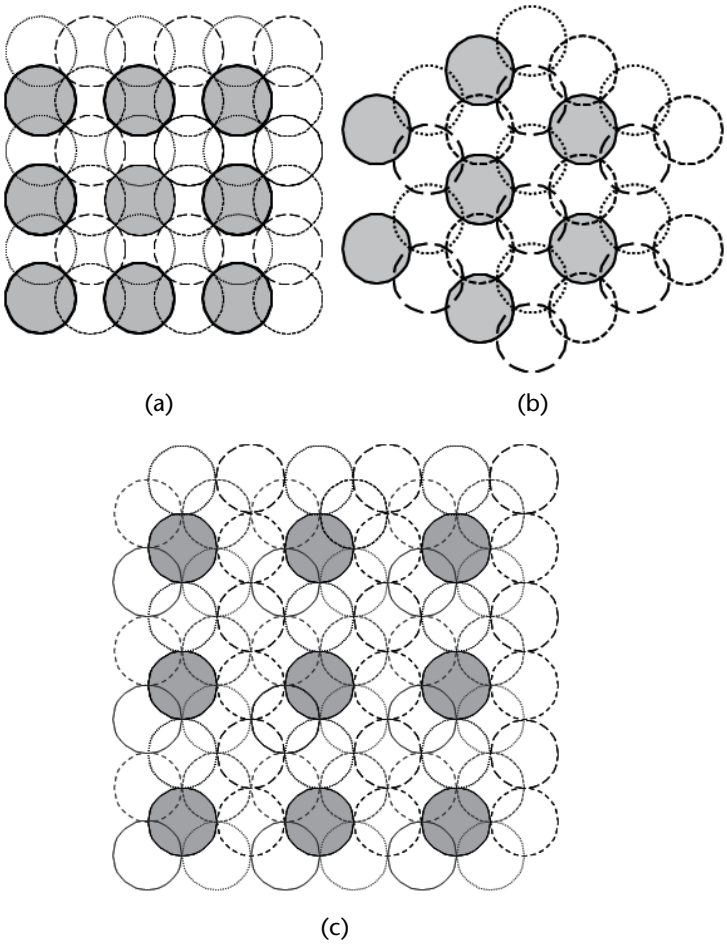

Figure 4.18 A –3-dB footprint in the image plane of (a) a rectangular and (b) hexagonal (b) FPA with compensated double sampling condition, and (c) rectangular FPA with regular sampling condition.

Table 4. 4 Active FPA Sampling

Sampling Condition (d)	*Grid*	*Two-Way Reflector Illumination Loss (dB)*	*Acquisition Time Increase Factor*
$0.74\lambda\frac{F}{D}$	Square	–12.6	2
$1.48\lambda\frac{F}{D}$	Square	–3.4	8
$1.48\lambda\frac{F}{D}\cos(45)$	Square	–7.5	4
$1.48\lambda\frac{F}{D}\cos(30)$	Hexagonal	–4.9	4
$2.22\lambda\frac{F}{D}\cos(30)$	Hexagonal	–1.8	9

maximum loss permitted (i.e., larger FPA spacing), the mutual coupling between the active elements that can affect the performances of an active systems, and the image acquisition speed.

4.3.3 Focal Plane Sampling in Passive Systems

The purpose of radiometric imaging is to obtain the spectral distribution of the incoming radiation for every point in the FoV. This is a typical application for terahertz imaging in astronomy applications, where large FPAs can be fabricated by using superconducting or bolometer-type detectors. In such a case, the speed of the image acquisition is ultimately limited by the S/N at the receivers, which affects the necessary integration time for each pixel to image the FoV with enough sensitivity.

As discussed in a key article [35], different focal plane architectures with advantages and disadvantages in terms of relative observing speed can be calculated on the basis of reasonable assumptions and typical array parameters. A typical configuration representing the key parameters of a radiometric telescope system is shown, in a 2D view, in Figure 4.13. During two-way active imaging, as well as in a typical telecommunication multibeam application, every beam of the FPA looks in a separate direction. For radiometric purposes, the brightness in the sky is reconstructed by resorting to Fourier transformation (FT) of samples acquired over the entire focal plane. As discussed in [26, 27], this process sets a lower limit to the resolution $\Delta\theta = 0.5\lambda/D$ and, correspondingly, to the smallest useful separation between the different focal plane elements ($d = 0.5\ F/D$). Larger samplings d would normally lead to lower resolutions; however, this effect can be compensated for by jiggling the telescope pointing direction, as explained in the previous section. Clearly the observation time with this mode of operation grows proportionally to the number of positions that have to be filled (i.e., to the pixel integration time). In the following we discuss different array sampling configurations and compare them in terms of acquisition speed. To do this, we will focus on a square array configuration and consider three sampling cases: $d_{0.5} = 0.5\ F/D\lambda$, $d_1 = F/D\lambda$, and $d_2 = 2\ F/D\lambda$. These sampling are associated with the standard half, single, and double conditions, without including the lattice and taper factors for the sake of simplicity. The extension to the cases that include those factors will be straightforward by using the formalism introduced here.

The quantity of interest to optimize the acquisition speed is the S/N after the detection. This ratio can be related, as detailed in Appendix 4D, to the integration time, the postdetection bandwidth, and the two major contributions to the noise in passive detectors: the receiver and photon noises. The relative weight of these two noises can be quantified by introducing a constant that is equal to 0 when the photon noise is dominating (background limited detectors) and equal to 1 when the receiver noise is instead dominating. Overall, the required integration time, provided in (4D.4) (see Appendix 4D), depends on the useful (signal) power received $\langle P_n^e \rangle$ as well as the contribution coming from the instrument itself $\langle P_n^i \rangle$, which is typically referred to as the instrument background contribution.

The optimal radiometric mapping of the sub-millimeter-wave spectrum of the sky leads to different antenna designs depending on the distributed or isolated nature of the sources. While the isolated sources case typically leads to the same antenna trade-offs that are also used in telecom and radar designs (see previous

section), where the aperture efficiency is maximized, the distributed sources cases lead to more compact array designs.

As a test case, we will assume that the reflector system is perfectly focalizing; this means that a single point source at infinity, generating a plane wave, and impinging on the main reflector aperture, is mapped in the focal plane as a clean Airy pattern. This hypothesis is verified for large *F/D* ratios. In this section we use the formulation derived in Appendix 4B to optimize the acquisition speed versus the FPA sampling by computing analytically the fraction of power received, $\langle P_n^e \rangle$, by each antenna in a focal plane array for both types of sources, isolated and distributed.

4.3.3.1 Isolated Sources

For the case in which an isolated point source is much stronger than the other contributions, the received power is expressed as a function of the coupling efficiency related to the squared reaction integral between the aperture field distribution and the Airy pattern of the reflector, accounting for the proper phase associated with the alignment of the source, and the feed in the focal plane, as derived in (4.19).

The optimum speed, that is, the shortest integration time expressed in (4D.4), for an isolated source is obtained when maximizing the received signal, which is equivalent to maximizing the coupling efficiency of the aperture distribution to the Airy pattern generated by the point source on the focal plane. Figure 4.19 shows

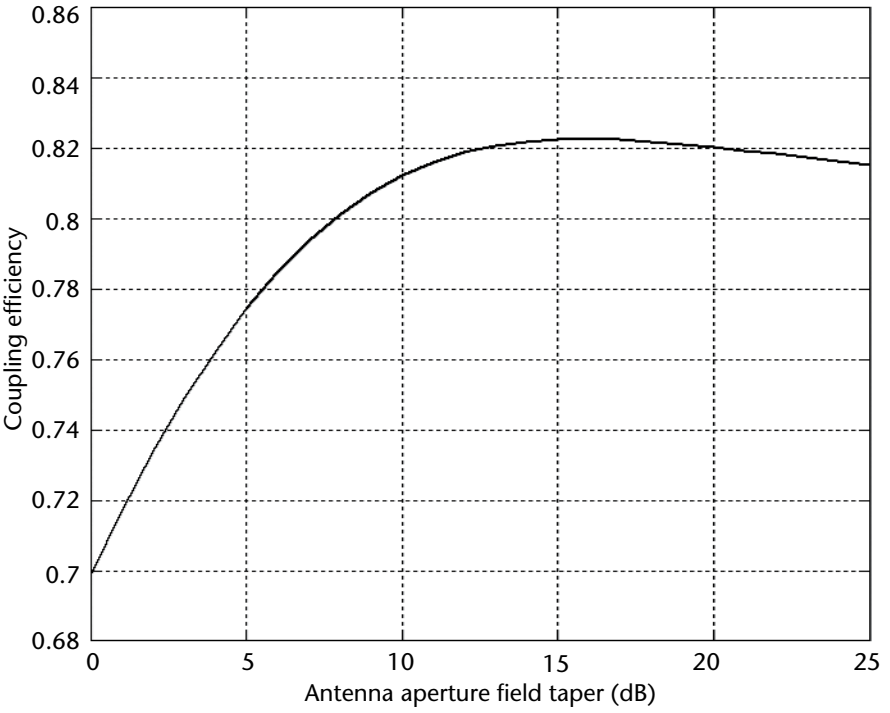

Figure 4.19 Coupling efficiency for a point source on axis incident on a $F/D = 3$ reflector and a receiving antenna aperture of $2F/D\lambda$ versus the field taper in the antenna. The inset shows the Airy pattern generated by the reflector together with an antenna field distribution with a –16 dB field taper.

this coupling efficiency for an antenna aperture limited by the standard double sampling condition (i.e., $2F/D\lambda$) as a function of the field taper at the antenna aperture edge [see (4B.7)]. The coupling efficiency is maximized for a taper of –16 dB. The inset of Figure 4.19 shows the Airy pattern together with the antenna distribution for a $2F/D\lambda$ sampling case.

Now we can take the –16-dB taper antenna and $2F/D\lambda$ sampling FPA as a baseline for comparison with other FPA configurations. To compare the acquisition speed, we can calculate the ratio between the speeds of the different configurations by assuming that the same type of detector is used in all configurations and there is no instrument contribution to the noise. This ratio can then be computed as the summation of the powers received in each element of the arrays, (4.16), as follows:

$$\frac{s_p}{s_q}=\frac{\sum_{p=1}^{n_p}\eta_{loss}^{p}\chi_{match}^{p}\eta_{ap}^{p}}{\sum_{q=1}^{n_q}\eta_{loss}^{q}\chi_{match}^{q}\eta_{ap}^{q}} \tag{4.25}$$

where s_p is the acquisition speed of the generic pth FPA configuration.

Figure 4.20 shows the speed ratios for these FPAs with respect to the baseline as a function of the antenna field taper. If the source is on axis, the –16-dB $2F/D\lambda$ sampling case will always be the optimal one because it maximizes the reflector efficiency. This is because the smaller apertures cannot be as efficient as the perfectly matched distribution when the latter is aligned with the incoming signal. Even so, the smaller cells will still contribute with a portion of the power, and that is why these cases are not too bad in terms of speed.

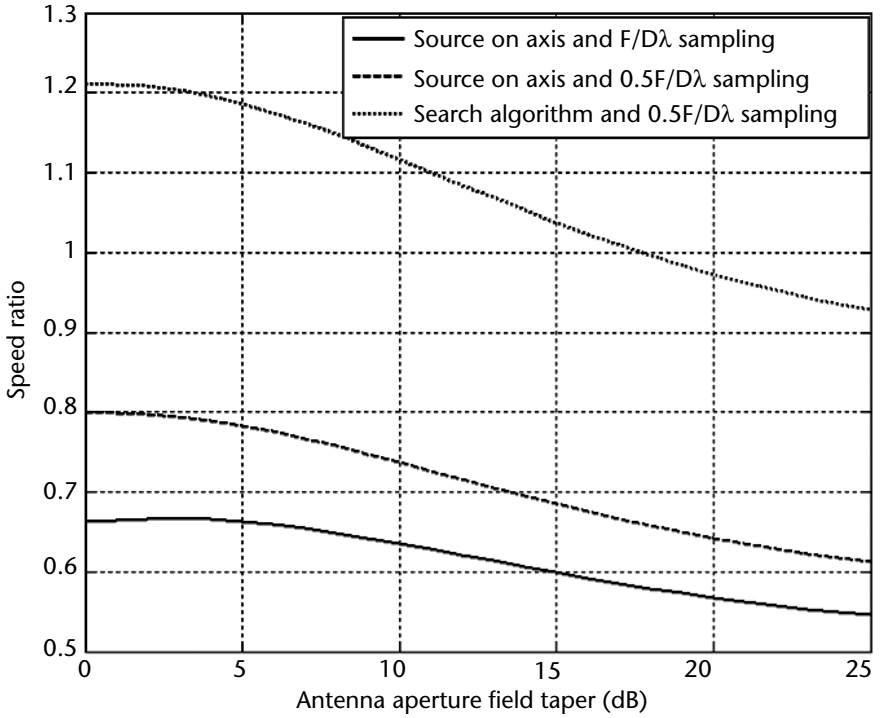

Figure 4.20 Speed ratio with respect to the –16-dB $2F/D\lambda$ sampling case when the source is the on-axis case and when a search algorithm is used.

However, when the point source position is not known, the $2F/D\lambda$ case has a drawback: The system has to be aligned with the actual source position because of the missing beams in the FoV. Therefore, the antenna system needs first to look for the actual position of the source. Known search algorithms typically imply a certain loss of time that can be quantified in about 0.66 of loss of efficiency [35]. Thus, when comparing the optimal case with the multiple subpixel architectures, one should consider this loss of time in the denominator of (4.25). Figure 4.20 also shows the speed ratio for this case, where the $0.5F/D\lambda$ sampling is slightly faster than the $2F/D\lambda$ when uniform apertures are considered.

4.3.3.2 Noncoherent Distributed Sources

Let us now consider the case in which we would like to image noncoherent distributed sources. This case can be modeled as a series of plane waves impinging on the reflector distributed over angles up to $\beta_{\max}$. Because the different plane waves are incoherent, the total power received by the antenna will be directly calculated as the summation of all the powers associated with each of the plane waves (α, β):

$$P_n^e = \int_0^{2\pi} \int_0^{\beta_{\max}} P_n^e(\alpha,\beta) \sin\beta \, d\beta \, d\alpha \tag{4.26}$$

Recalling the expression of the power received by an antenna in the focal plane of a reflector, that is, (4.16), we can express (4.26) as

$$P_n^e = \frac{1}{2\zeta} A_{ref} \eta_{loss} \chi_{match} \int_0^{2\pi} \int_0^{\beta_{\max}} \left|E_e(\alpha,\beta)\right|^2 \eta_{ap}(\alpha,\beta) \sin\beta \, d\beta \, d\alpha \tag{4.27}$$

The actual received power can only be calculated when the radiation distribution, $|E_e|^2$ (α, β) from the distributed sources is known. Instead, one can estimate the average of the received power from a continuous distribution of noncoherent sources and use this information for the optimization of the FPA sampling. The average power received by the antenna can then be calculated as:

$$\left\langle P_n^e \right\rangle = S_{ave}^e A_{ref} \eta_{loss} \chi_{match} \int_0^{2\pi} \int_0^{\beta_{\max}} \eta_{ap}(\alpha,\beta) \sin\beta \, d\beta \, d\alpha \tag{4.28}$$

where $S_{ave}^e = \dfrac{\left\langle \left|E_e(\alpha,\beta)\right|^2 \right\rangle}{2\zeta}$ is the average Poynting vector of the source in the FoV (i.e., the external brightness).

When comparing arrays with half, single, and double sampling conditions, it is apparent that the option $d_{0.5}$ implies a need for 16 times more elements to cover the entire focal plane than the d_2 configuration. This could be prohibitive if the receiver's costs are dominant in the overall architecture; however, this is typically not the case in a space science context with cryogenic detectors. Moreover, different samplings also imply that the beams arising from the d_2 configuration map the field

of view at larger intervals, as explained previously (see Figure 4.18). The voids can be imagined to be filled with successive orientations of the main dish or by jiggling a small mirror to achieve, eventually, the maximum resolution of the $d_{0.5}$ case. In the following we use τ_p to indicate the acquisition time and $n_p = 4/p^2$ (with $p = 0.5$, 1, 2) to indicate the number of receivers in the area defined by the double sampling condition that corresponds to each configurations. The configuration d_p covers a field of view region in $\tau_p 16/n_p$, which accounts for the time of each acquisition multiplied per the number of required movements. As a consequence, the speed of acquisition of configuration p is $s_p = \dfrac{n_p}{\tau_p 16}$. When comparing the relative performances of two different FPA configurations, p and q, the significant parameter is the ratio between the acquisition speeds. Assuming that the same type of detectors is used in all configurations, this ratio can be calculated using (4D.4):

$$\frac{s_p}{s_q} = \frac{n_p}{n_q}\frac{\tau_q}{\tau_p} = \frac{n_p}{n_q}\frac{\left\langle P_p^e \right\rangle}{\left\langle P_q^e \right\rangle}\frac{1+\dfrac{\left\langle P_q^i \right\rangle}{\left\langle P_q^e \right\rangle}}{1+\dfrac{\left\langle P_p^i \right\rangle}{\left\langle P_p^e \right\rangle}} \tag{4.29}$$

First we will assume that the instrument is sufficiently cold so that the internal contribution to the noise is negligible. Then, when the average power received [from (4.28)] is introduced in (4.29), we obtain the following expression for the acquisition time ratio:

$$\frac{s_p}{s_q} = \frac{n_p}{n_q}\frac{\eta_{loss}^p \chi_{match}^p \int_0^{2\pi}\int_0^{\beta_{max}} \eta_{ap}^p(\alpha,\beta)\sin\beta d\beta d\alpha}{\eta_{loss}^q \chi_{match}^q \int_0^{2\tau}\int_0^{\beta_{max}} \eta_{ap}^q(\alpha,\beta)\sin\beta d\beta d\alpha} \tag{4.30}$$

Let us consider two specific cases: an FPA of corrugated horns with a 100% horn aperture efficiency, that is, the field over the horn aperture is uniform in amplitude and phase; and a FPA of lenses with a –16 dB taper aperture (these lenses are fed by an antenna with an appropriate lens edge taper). Figure 4.21 shows the speed ratio between FPAs at $0.5F/D\lambda$ and $F/D\lambda$ samplings with respect to a double sampling FPA having an antenna with a –16-dB taper. Looking at the antenna efficiencies in (4.30), it is apparent that the aperture efficiency is the one that is most drastically affected by the physical dimension of the antennas in the focal plane and, therefore, will drive the trade-off. For these examples, we assume that all the antennas are perfectly matched and have no losses. From Figure 4.21 it is evident that it is more convenient to use a $0.5F/D\lambda$ sampling, even if the spillover loss is larger anyway than in the other sampling cases. This is because we are assuming no noise contribution from the instrument itself; therefore, the spillover does not really contribute to the noise. The use of $0.5F/D\lambda$ sampling for antennas has usually been avoided [26, 35, 36] because it is understood that the antenna performances degrades when the aperture is small. This is indeed true, but only for $F/D < 2$.

Now we can study what happens if there is a contribution to the noise coming from the instrument itself. The average power received by the detector can be computed using the effective height of the antenna as described in Appendix 4E. In

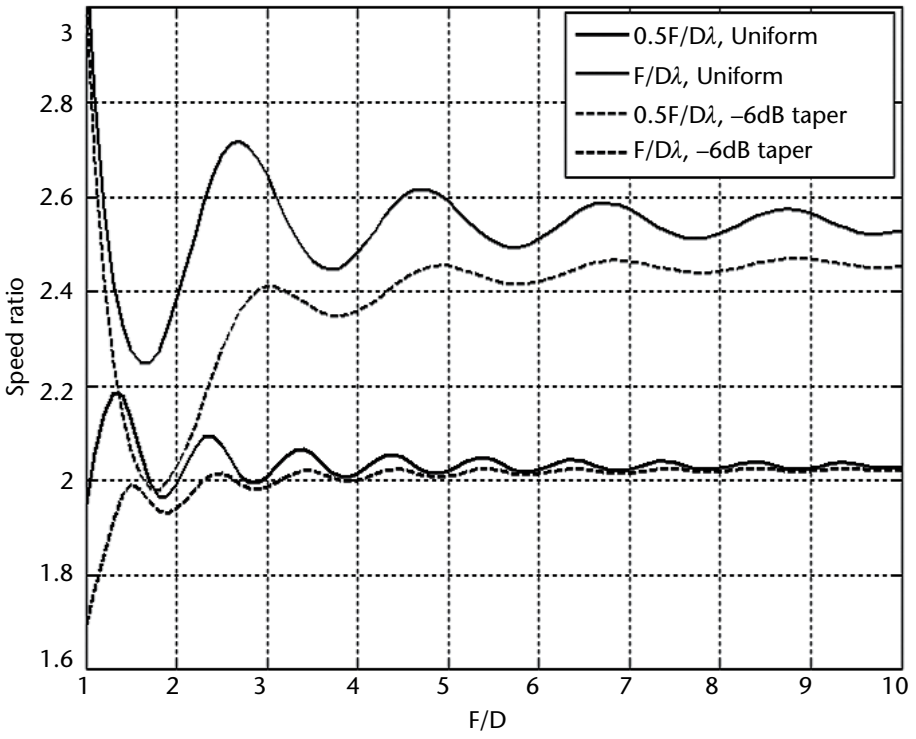

Figure 4.21 Speed ratio with respect to the –16-dB 2F/Dλ sampling case for noncoherent distributed sources and several FPA configurations without any instrument noise contribution

this case the ratio between the received powers from signals coming internally and externally to the reflector system will drive the speed optimization. This ratio can be expressed, by using (4.28) and (4E.3), as follows:

$$\frac{\left\langle P_q^i \right\rangle}{\left\langle P_q^e \right\rangle} = \frac{S_{ave}^i}{S_{ave}^e} \frac{A_a \int_0^{2\pi} \int_{\theta_{sub}}^{\pi} \eta_{ap}^a(\alpha,\beta) \sin\beta \, d\beta \, d\alpha}{A_{ref} \int_0^{2\pi} \int_0^{\beta_{max}} \eta_{ap}(\alpha,\beta) \sin\beta \, d\beta \, d\alpha} \tag{4.31}$$

where S_{ave}^i is the average brightness internal to the instrument, A_a is the area of the feed antenna, $\eta_{ap}^a(\alpha,\beta)$ is the aperture efficiency of the antenna as given in (4E.4), and θ_{sub} is the angle of the reflector rim.

Figure 4.22 shows how the speed ratio of uniform apertures with respect to the –16 dB 2*F/D*λ sampling case changes as a function of the ratio between the internal and external brightness. It is evident that the *F/D*λ sampling case presents very small degradations in the performance provided that the internal brightness is less than 10% of the external one. Instead the 0.5*F/D*λ sampling case starts to worsen already from a 1% of the external brightness.

4.3.4 Typical Reflector Systems

Systems with two reflectors are the preferred solution for designing multibeam imaging arrays because they present low off-axis scan degradations. A review of the design of dual-reflector systems can be found in [33]. Typical symmetrical

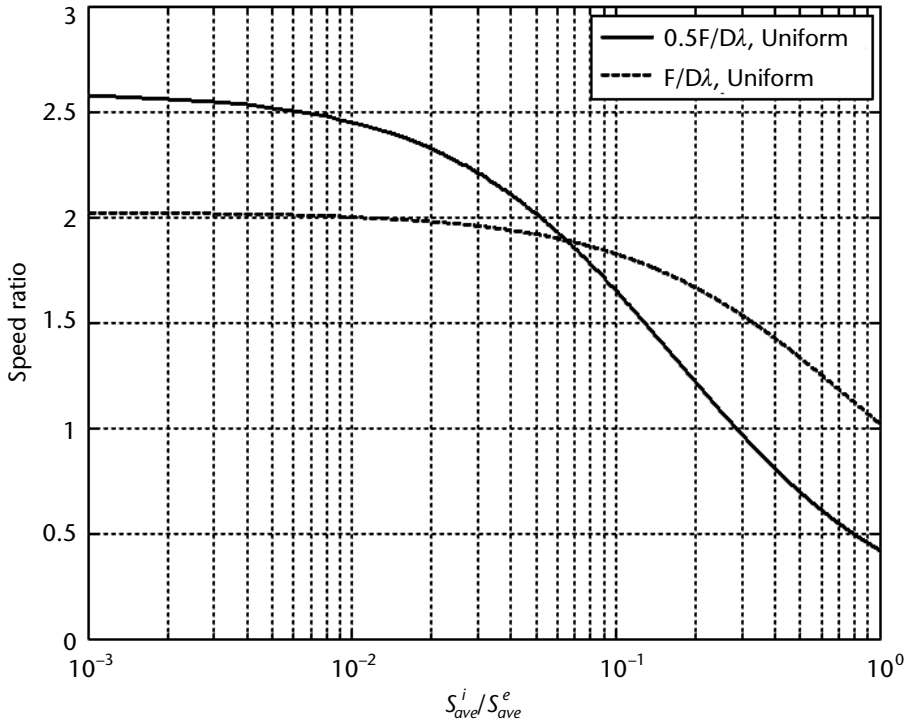

Figure 4.22 Speed ratio with respect to the –16-dB $2F/D\lambda$ sampling case for noncoherent distributed sources as a function of the ratio between the internal and external average brightness

surface-based solutions, such as a Cassegrain or Gregorian system have been used successfully in a large number of terahertz instruments since they present very low degradation because of the surface symmetry.

One eminent example is the Cassegrain system designed for the Herschel telescope [37]. The main drawback of such designs is the blockage of the electromagnetic wave by the secondary reflector, which leads to a reduction of the useful antenna aperture and an increase in the sidelobes. Therefore, frequently, offset surface-based solutions are preferred, such as in the case of the Planck telescope [37]. Offset surface portions introduce a significant amount of cross-polarization (see Figure 4.12) and very poor off-axis scan performances. To reduce these drawbacks, dual-reflector systems, both Cassegrain and Gregorian, with compensated cross-polarization (i.e., to fulfill the Mizuguchi condition) have been designed [38] leading to the possibility of using large FPAs.

A considerable amount of information can be found in the literature on designing cross-polarized compensated dual reflectors. For instance, in [38], some simple design rules are given for a Gregorian system. Taking these rules, the Gregorian system shown in Figure 4.23(a) has been designed with the main paraboloid reflector geometrical parameters being those of Table 4.2. The dimensions of the secondary reflector are given in Table 4.5. Figure 4.23(b) shows the radiated field, which has considerably reduced cross-polarization with respect to that shown in Figure 4.12. Applying the equivalence that we established in Section 4.1.5 between an offset paraboloid and ellipsoid, we can use the same Gregorian system to reduce also the cross-polarized field for a field focused in the Fresnel region. Figure 4.23(b)

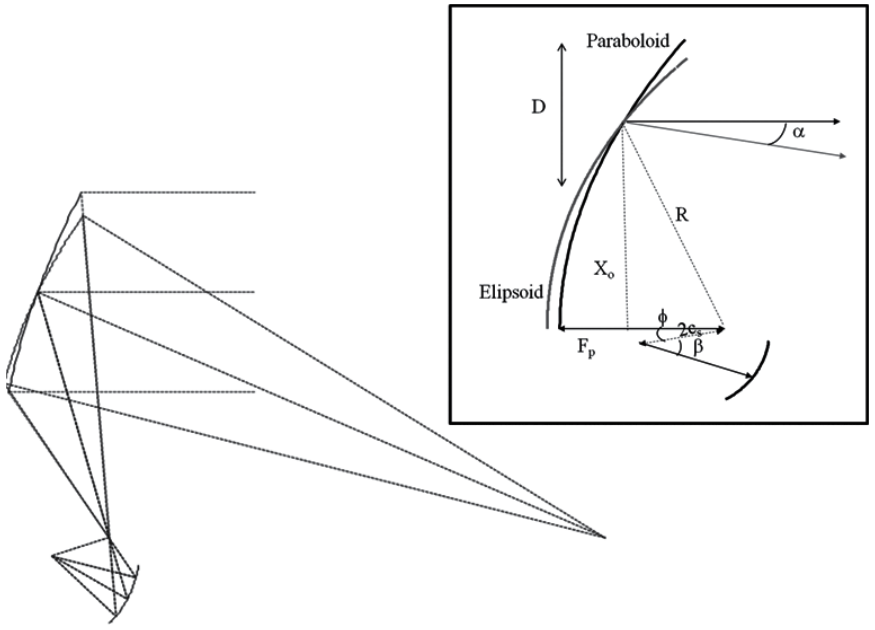

(a)

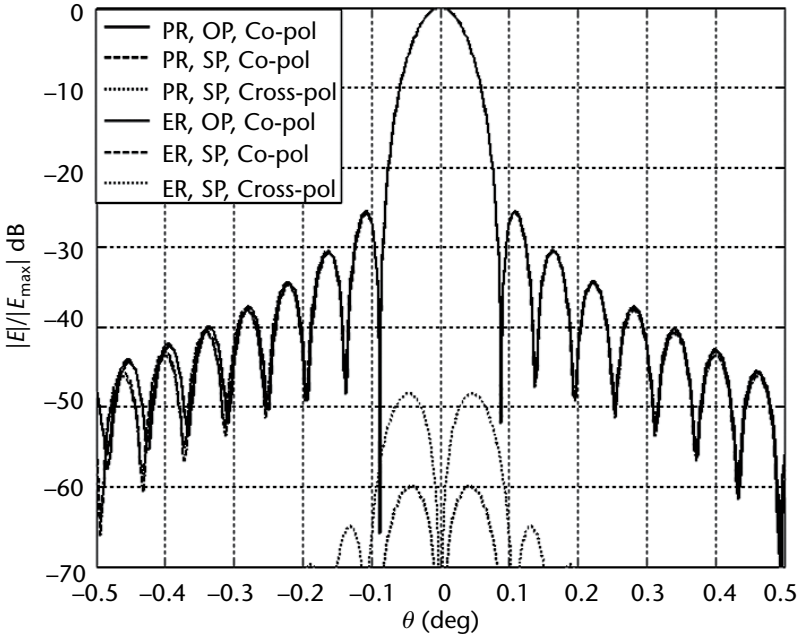

Figure 4.23 Offset Gregorian example of cross-polarization reduction: (a) geometry and (b) simulated fields, where PR and ER stand for parabolic and elliptic reflector, respectively, in the offset (OP) and symmetric (SP) planes.

shows the comparison between the far field and near field of the paraboloid and the equivalent ellipsoid system focusing at 2.5m (the dimensions of the elliptical mirror were given earlier in Table 4.3). The reduction of the cross-polarized field is slightly worse in the elliptical reflector because of the original small differences in the cross-polarized field of the offset reflectors shown in Figure 4.12.

Table 4.5 Geometric Parameters of the Subreflector in the Gregorian System

Symbol	*Quantity*	*Value*
M	Magnification	5
$2Cs$	Interfocal distance	0.2524m
$2As$	Vertex distance	0.515m
ϕ	Subreflector axis tilt	10 deg
β	Feed pointing angle	28.7 deg

The equivalence of the fields generated by the paraboloid and ellipsoidal reflectors is not only valid for the central pattern, but also for the scanned patterns associated with off-focus reflector feeds as long as the feed displacement from the focal point is relatively small. This means that we can also use dual-reflector systems optimized for focal plane arrays to design focusing imaging reflectors. Figure 4.24 shows an example of such a system based on a Dragonian top-fed system designed following the rules provided in [39]. The geometry is shown in Figure 4.24(a) and the geometrical parameters are provided in Tables 4.6, 4.7, and 4.8. The radiated fields in the far and 2.5m near regions for a paraboloid and ellipsoid-based system, respectively, are shown in Figure 4.24(b) for both the center and scanned beam. The fields are indeed very similar up to the level of the sidelobes.

4.4 Imaging with Mechanical Scanners

To generate an image, the antenna reflector system needs to steer the beam along the whole FoV with the proper resolution. One possibility is to use FPAs (camera-like solution), as described in the previous section, which would require information to be acquired from several image pixels simultaneously. This is the most common solution for the passive detectors, such as bolometers or superconducting detectors [40, 41], commonly used for space applications and some terrestrial applications. Nevertheless, terahertz heterodyne detector array technology is still under development [42], and most of the current state-of-the-art imaging systems based on this technology use antenna reflector systems integrated with mechanical scanners to generate the image [32].

4.4.1 Types of Mechanical Scanners

Two different types of motions can be used to realize mechanical scanners: translation and rotation. Rotation motors are usually preferred for designing terahertz antenna systems aiming at long imaging distances and operating at close to real-time speeds. Although the translation of a reflector would perform beam steering, this type of motion is instead limited to small scanning ranges. In fact, the maximum velocity achievable for translation motors is slower than that for rotating motors. Therefore, translation motors are only used in terahertz imaging systems where the sample is displaced to create the image, such as in time domain spectrometers [43]. In such cases, the target is usually very close to the antenna system and the focus of the technology is not on the image acquisition speed but on the S/N.

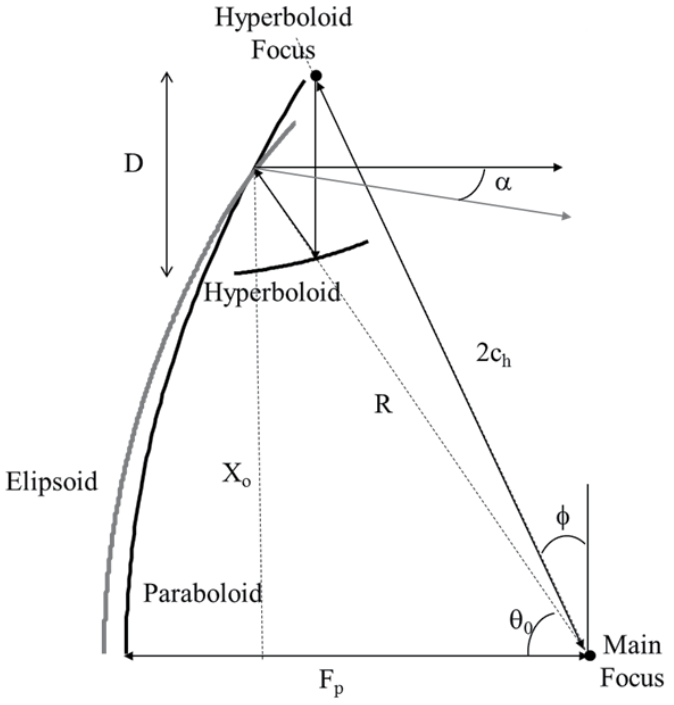

(a)

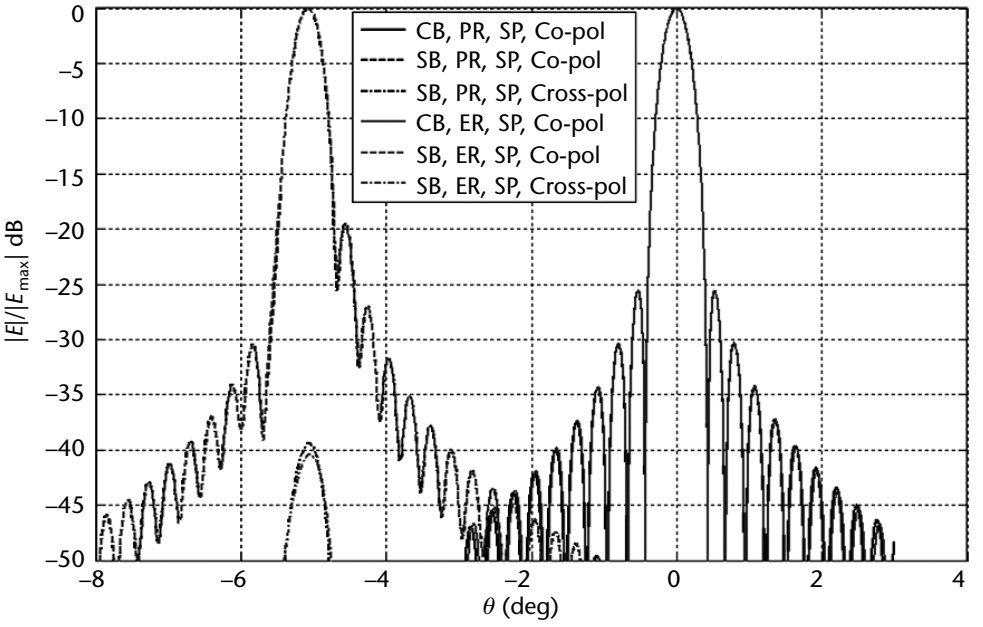

(b)

Figure 4.24 FPA in a Dragonian reflector system with near and far focusing: (a) geometry and (b) simulated fields (CB = center beam, SB = scanned beam, SP = symmetric plane).

By using rotating motors, it is possible to realize raster and conical scans. A raster scan consists of two rotating motors in two orthogonal directions (i.e.,

Table 4.6 Geometric Parameters of the Subreflector in the Dragonian System

Symbol	*Quantity*	*Value*
$2c$	Interfocal distance	55.74 cm
$2a$	Vertex distance	26.96 cm
L_0	Offset height	23.56 cm
ϕ	Axis tilt	25 deg

Table 4.7 Geometric Parameters of the Offset Paraboloid Reflector in the Dagronian System

Symbol	*Quantity*	*Value*
F	Focal distance	40.72 cm
D	Aperture diameter	10 cm
X_0	Offset height	43.47 cm

Table 4.8 Geometric Parameters of the Offset Ellipsoid Reflector in the Dagronian System

Symbol	*Quantity*	*Value*
$2c$	Interfocal distance	2.17m
$2a$	Vertex distance	3.02m
X_0	Offset height	43.47 cm
D	Aperture diameter	10 cm
R_f	Focusing distance	2.5m
α	Aperture tilt	10.01 deg
β	Output angle	2.29 deg

horizontal and vertical) as shown in Figure 4.25(a). The rotation velocity of the two motors will determine the footprint of the reflector scanning system at the target plane. Imagine that we want to create a staircase-type footprint, like that shown in Figure 4.25(b). The vertical motor rotates at a constant velocity to create a vertical line, then stops; and the horizontal one rotates at a constant velocity to displace the pointing direction to the next line. In this case one obtains the same footprint that is obtained using a 2D focal plane array. Therefore, to achieve a full sampling of the FoV, the raster scan rotation step or sampling step in both directions has to be:

$$\Delta\theta_{scan} = \Delta\theta_{resolution} \cos 45 \tag{4.32}$$

where $\Delta\theta_{resolution}$ is the resolution (e.g., $\Delta\theta_{\text{HPBW}}/2$ for radiometric systems, $\Delta\theta_{HPWB}^{two-way}$ for two-way active systems).

Then, the motors have to rotate at a maximum velocity lower than the ratio between the scan rotation step and the integration time, t_p, of the receiver:

$$v \leq \frac{\Delta\theta_{scan}}{t_p} \tag{4.33}$$

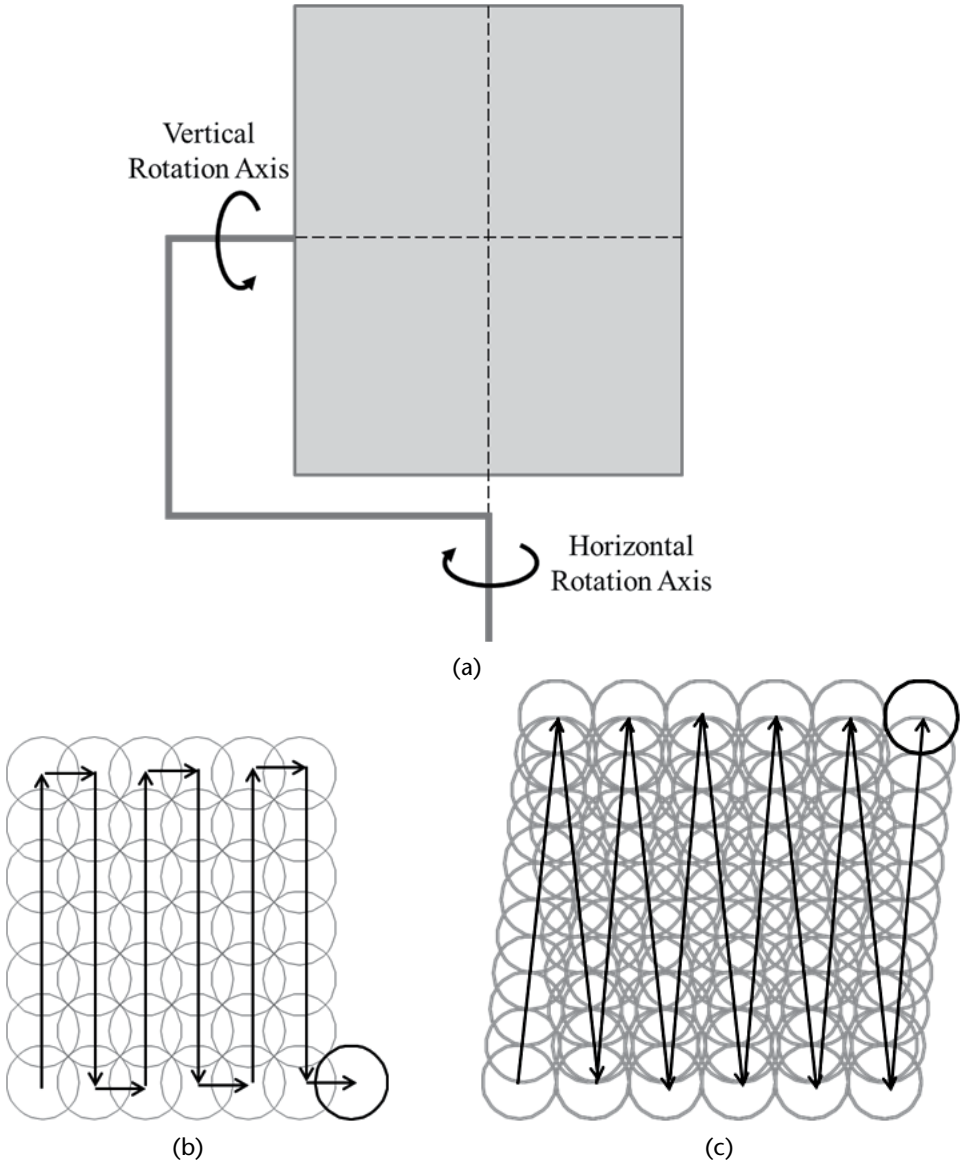

Figure 4.25 Sampling of the FoV with a raster scan: (a) geometry, (b) staircase footprint, and (c) footprint generated by a continuous motion.

The previous staircase movement creates a well-sampled FoV; however, it is very slow because only one motor is working each instant of time. Therefore, for applications requiring high acquisition speeds, one motor is usually rotated at a constant low speed (e.g., the horizontal one), whereas the other motor is accelerated and decelerated at high speed. This solution has successfully been used in [44]. In this case, the footprint created by the raster scan will be like the one shown in Figure 4.25(c). In this case, the sampling has to be done at half the resolution $\Delta\theta_{scan} = \frac{\Delta\theta_{resolution}}{2}$ to have a fully sampled FoV. In such a case, the total number of vertical and horizontal acquired pixels, $N_{v/h}$, will be:

$$N_{v/h} = \frac{FOV_{v/h}}{\Delta\theta_{scan}} \tag{4.34}$$

The vertical scanning can be accomplished with a fast precision rotator that accelerates for the first half of the scan and then decelerates for the second half to achieve a "bang-bang" control approach. The scan time of this configuration will be limited by the maximum motor torque.

A different approach is to use a conical scanner where the mirror spins around a tilted axis of rotation, as shown in Figure 4.26. The rotation axis is tilted with respect to the normal direction of the mirror surface by an angle α. This tilt creates an elliptical footprint in the target plane. To study the rotation properties of the tilted spinning mirror, we need to calculate the dynamic vector normal to the mirror as follows:

$$\hat{n} = \sin(\alpha)\cos(\theta_m)\hat{x} - \sin(\alpha)\sin(\theta_m)\hat{y} + \cos(\alpha)\hat{z} \tag{4.35}$$

where θ_m is the spinning angle. The output ray $\hat{o}$ can then be related to the incident ray $\hat{i}$ by using the following expression:

$$\hat{o} = \hat{i} - 2\hat{n}\left(\hat{n}\cdot\hat{i}\right) \tag{4.36}$$

Let us first consider that the incident ray arrives parallel to the z-axis, that is, $\hat{i} = -\hat{i}_z$. In this case, the output ray angle, θ_o, is equal to two times the tilt angle: $\theta_o = 2\alpha$, whereas the output ray azimuthal angle ϕ_o is equal to the spinning angle . Therefore, the footprint created by this conical scan is a circle. For a generic incidence, we can compute the pointing direction (θ, ϕ) of the output ray by using the previous expressions. Figures 4.27(a) and 4.27(b) show the output angles as a function of the spinning angle, whereas Figure 4.27(c) shows the footprint generated

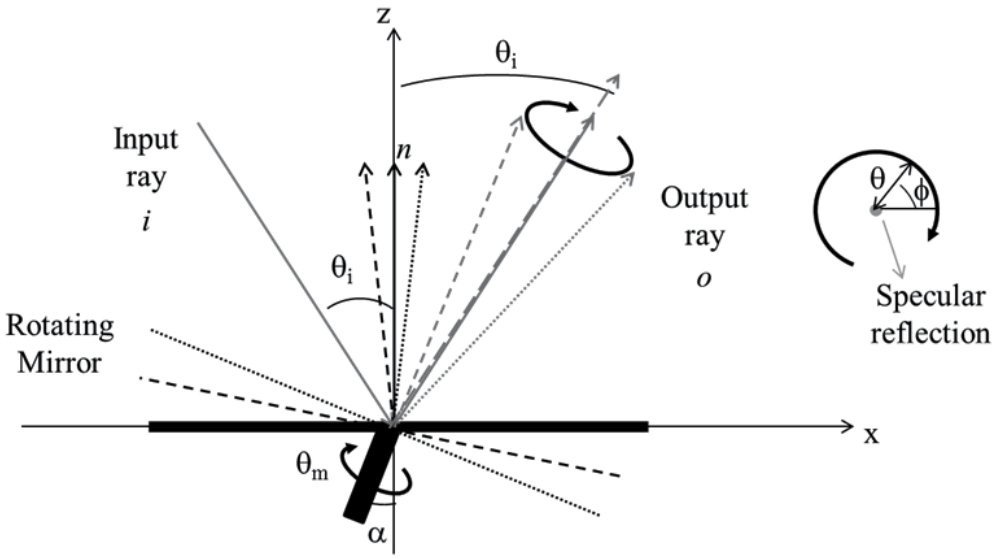

Figure 4.26 Conical mechanical scanner geometry.

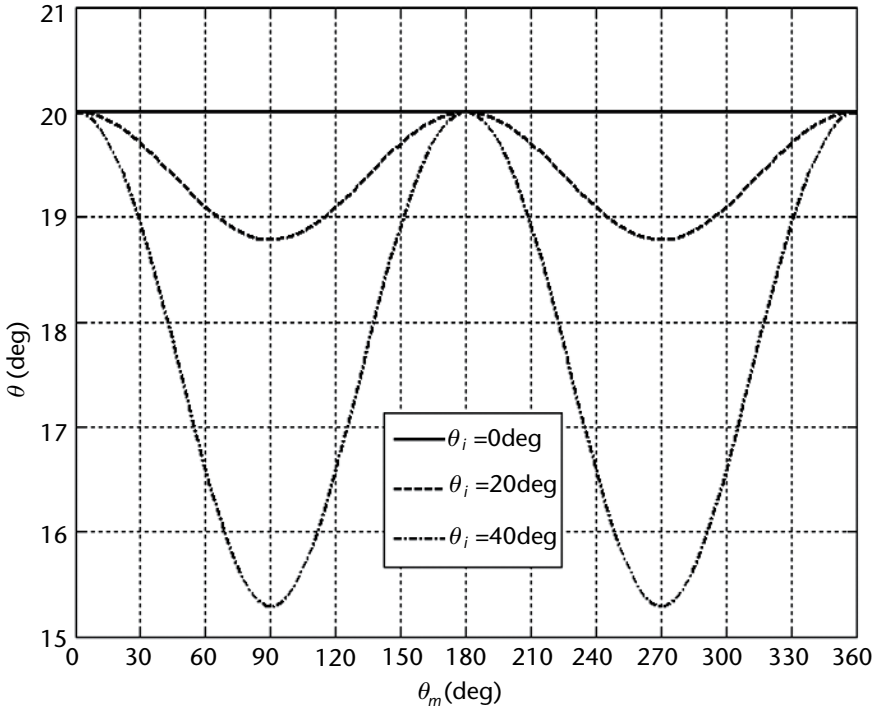

(a)

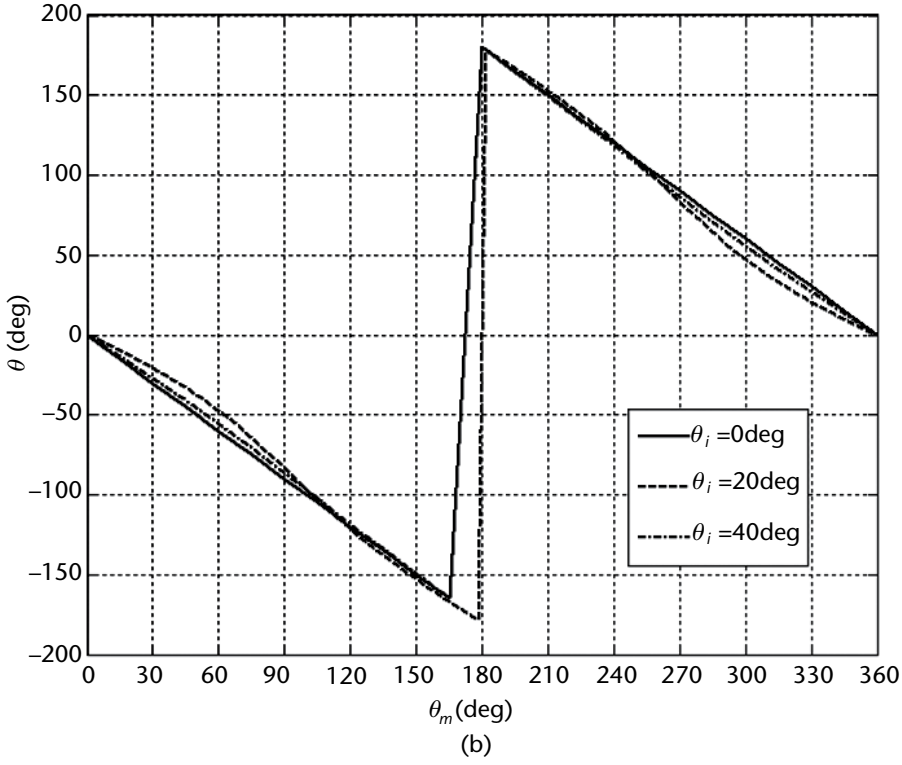

(b)

Figure 4.27 Conical scan with $\alpha = 10$ deg for a few incident angles: (a) θ and (b) ϕ output angles with respect to the specular reflection, and (c) footprint generated by the output ray.

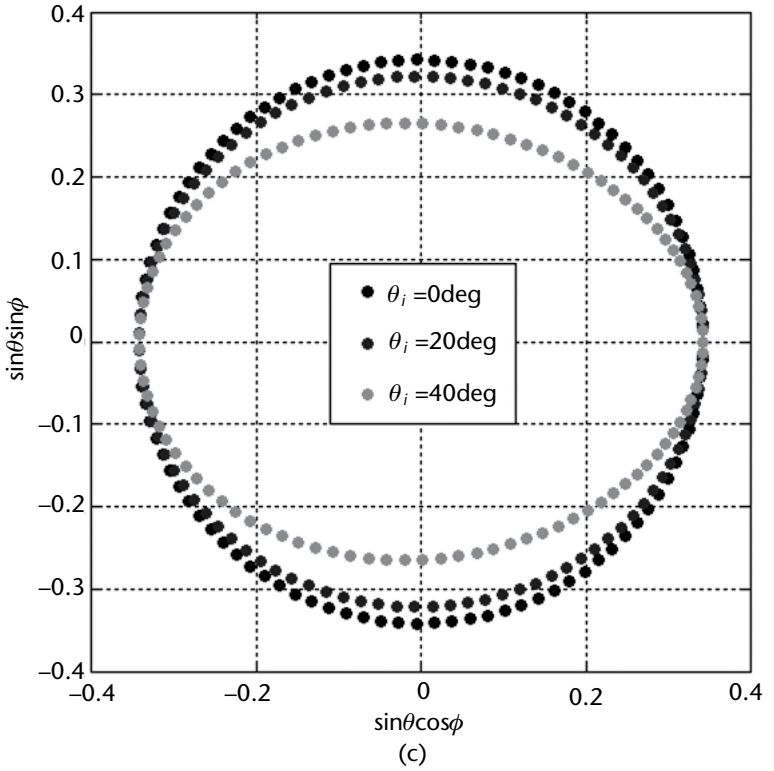

Figure 4.27 (continued)

by the output ray. If the incident ray arrives with an incident angle θ_i, the output ray creates an elliptical footprint around the specular reflection ray (the one that we would obtain without any mirror tilt). The major axis of the generated ellipse is found in the same plane of the incident beam (i.e., ZX or $\phi = 0$ in the example of Figure 4.26), and is equal to θ=2α, whereas there is a reduction of the output angle in the orthogonal plane (i.e., ZY or $\phi = 90$), leading to a minor axis of the ellipse of $\theta = 2\alpha \cos(\theta_i)$. Figure 4.27 shows the output ray angles and footprints for several incident angles.

To achieve a full 2D FoV by using such conical mirror, a second motion is needed. This second motion can be achieved by using a slow rotating motor in the horizontal direction in order to fully sample the FoV by displacing horizontally the elliptical footprint created by the conical mirror. This configuration will generate the footprint show in Figure 4.28(a). This is a common solution in airborne laser scanning systems [45]. The main advantage of this solution is that the fast rotating mirror can be spun at a constant angular velocity without the problem of torque due to the acceleration and deceleration mechanism. However, as can be seen from the footprint of Figure 4.28(a), the sampling of the FoV is not as uniform as it was for the raster scan. Note that some areas are well oversampled. To deal with this FoV oversampling and generate the image, special postprocessing algorithms are needed. This solution has successfully been applied in [46] and in [47, 48] where a linear array of detectors was used instead of the slow horizontal motor creating a similar footprint.

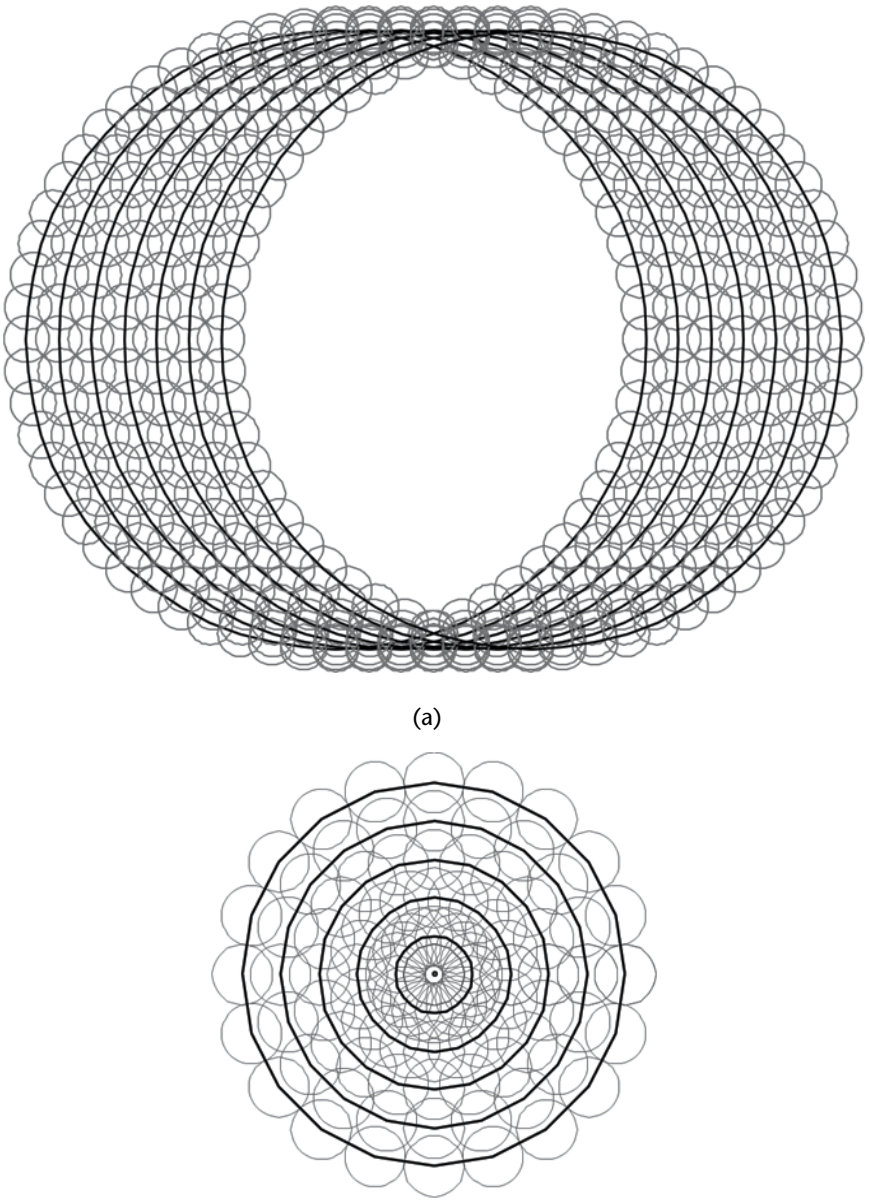

Figure 4.28 Footprints created by conical scanner with (a) a horizontal rotating mirror and (b) a motor changing the conical tilt angle.

Another possibility is to use the second motor to change the tilt angle of the spinning mirror, α. By changing α, the radius of the circle created by the spinning mirror is also modified (i.e., the radius is 2α). Therefore, one can create a spiral footprint like the one shown in Figure 4.28(b). This is the solution that was used in [49]. Once again the image is oversampled; in this case, the oversampling is around the center of the FoV.

More advance scanning systems can be obtained by more than one spinning mirror. Such systems are common in the infrared spectral region [50]. Let us

consider the geometry of Figure 4.29, where we have two rotating mirrors with the rotation axes tilted by α and α', respectively. We can study the footprint generated by such a system by applying a ray-tracing analysis similar to that described in (4.35) and (4.36) for each of the two mirrors. The generated footprints, centered around the specular reflection, depend on the relative phase difference between the two spinning motors:

1. If the spinning motors are rotating in the same direction but out of phase, the generated footprint is an ellipse whose minor and major axis dimensions depend on the phase difference between the motors, ψ. In this case, the spinning rotation angles are related by $\theta'_m = \theta_m + \psi$. Figure 4.30 shows the output angle, with respect to the specular reflection, for different phases. For $\psi = 0$ the output major and minor axes are equal to θ_o=2(α+α') and 2(α+α'), respectively. For larger phases the ellipse axes are reduced until ψ = 180 degrees, where the footprint is basically a point. Using this configuration, one could sample the whole FoV by progressively changing the phase difference between the motors and obtaining a footprint similar to that shown in Figure 4.28(b). The drawback is again that the FoV would not be uniformly sampled.
2. In contrast, if the spinning motors are rotating in opposite directions including a phase difference, that is, $\theta'_m = \theta_m + \psi$, then the footprint is almost a line for which the orientation depends on the phase difference, ψ. The smaller the tilt angle, the more the footprint resembles a line. Figure 4.31 shows the output angles for this configuration and several ψ phases. For ψ = 0 a horizontal line is generated by a maximum side length of θ_o=2(α+α'). Note that for a complete spinning loop (i.e., 0 to 360 deg), the pointing direction goes up and down twice through the line. For larger phases, the

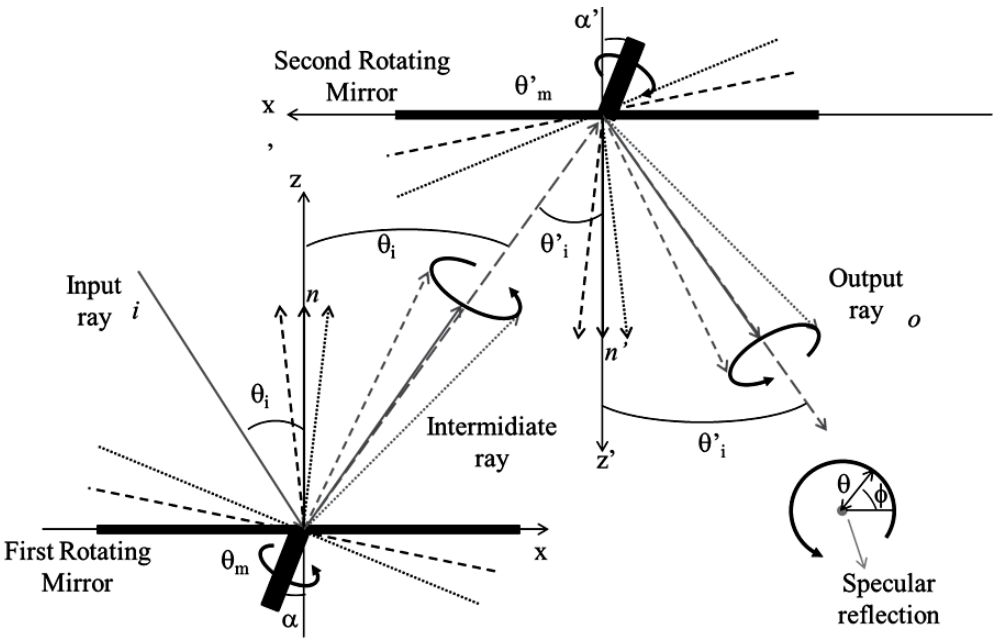

Figure 4.29 Geometry of two conical mirrors.

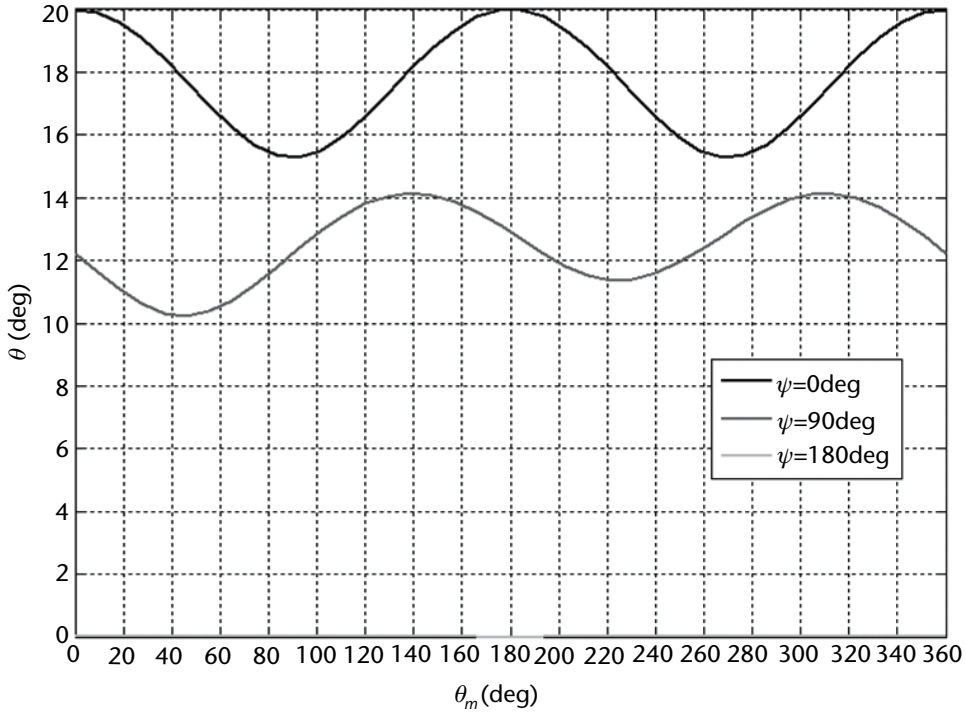

(a)

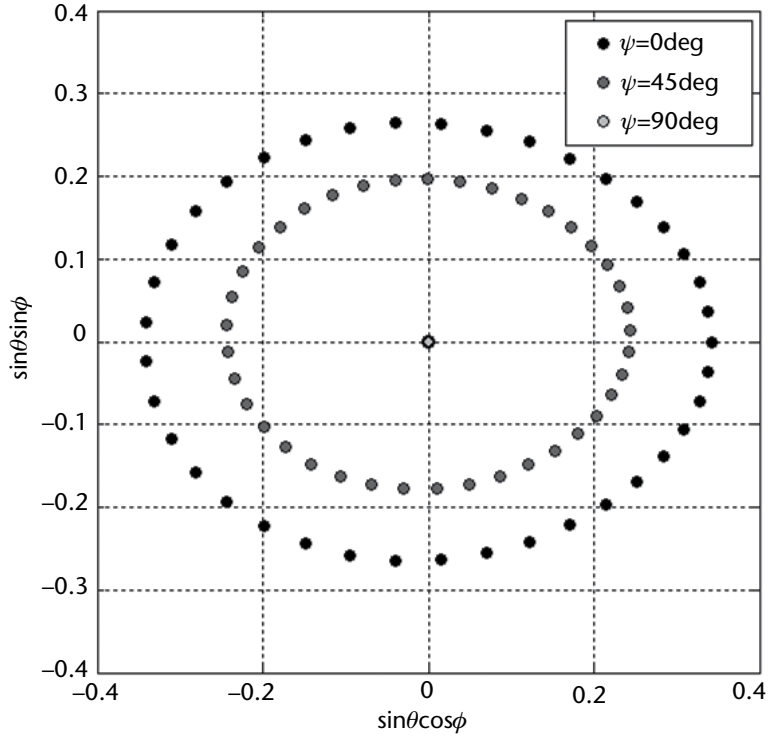

(b)

Figure 4.30 Two-mirror-based conical scan with motors rotating in the same direction and different phases with $\alpha = \alpha' = 5$ deg and $\theta_i = 40$ deg: (a) θ output angle and (b) footprint generated by the output ray.

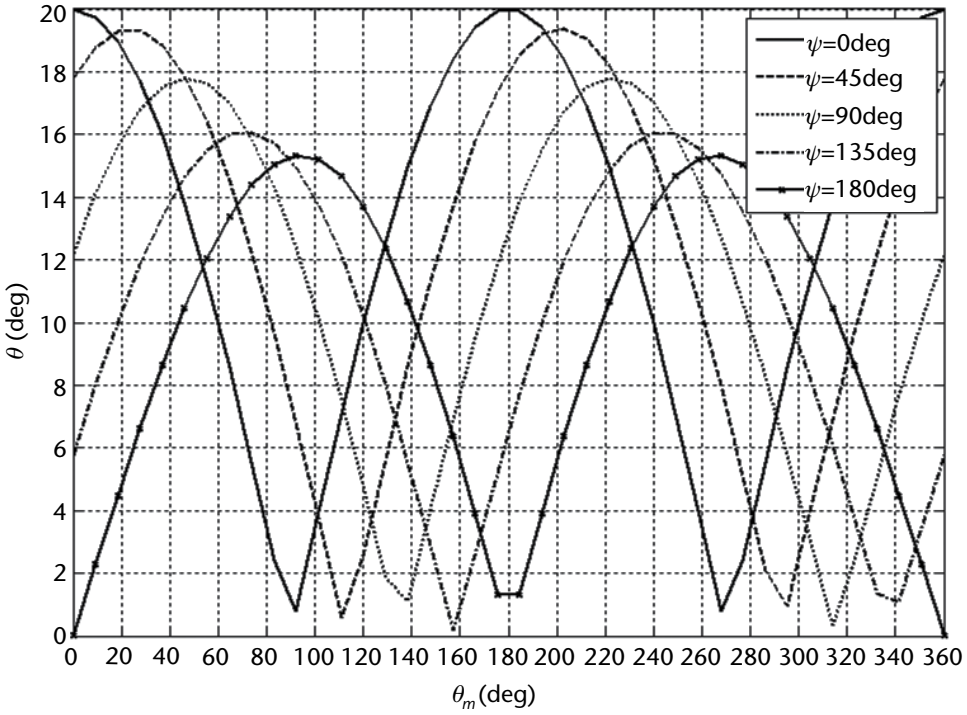

(a)

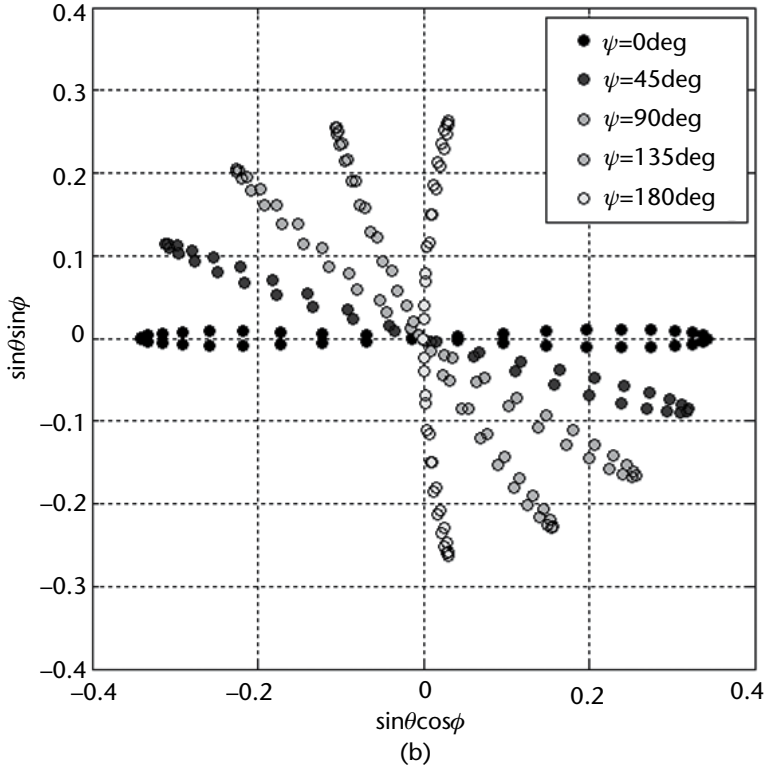

(b)

Figure 4.31 Two-mirror-based conical scan with motors rotating in opposite directions for several phase differences ψ with $\alpha = \alpha' = 5$ deg and $\theta_i = 40$ deg: (a) θ output angles with respect to the specular reflection and (b) footprint generated by the output ray.

line is rotated as shown in the Figure 4.31(b). The length of the line is reduced up to a minimum length of $\theta_o=2(\alpha+\alpha')\cos(\theta_i)$ proportional to the minor elliptical axis of the previous case. Again, using this configuration one could sample the whole FoV by progressively changing the difference in phase between the motors, but with a nonuniform sampling.

A nice scanner has been described in [51], where two spinning mirrors rotating in opposite directions were used to generate a linear footprint. A third slowly rotating motor was then used to fill the FoV by displacing this linear footprint laterally. This solution avoids the problem of motor torque because the fast spinning mirrors are rotating continuously at a constant angular velocity, whereas the footprint in the range plane is practically a raster scan, similar to the one shown in Figure 4.25(c), that prevents the problem of oversampling the FoV.

4.4.2 Typical Reflector Systems

When designing reflector systems that make use of mechanical scanning capabilities to generate the image from a single receiver, one has to take into account a trade-off between the possible aberrations introduced by the scanning antenna system and the acquisition time of the image. If the system has the focus on the beam quality rather than on the speed, it is more convenient to place the scanning system after the main aperture. In such a case, the scanning system should be composed by flat mirrors that do not introduce any phase aberrations. With such a configuration, one could cover large FoVs with high-quality antenna patterns. The only optical aberration present is the Petzval field curvature when working with near-field focusing reflectors. This aberration is associated with the fact that, when scanning, the pattern is well focused along a surface instead of along the target plane.

On the other hand, when the application requires operation at fast imaging speeds, the previous solution is only suited for small FoVs or when the diameter of the primary aperture (and therefore of the scanning system) is relatively small (typically below 30 cm). For larger diameters the weight of the scanning mirrors starts to become prohibitive for high-speed rotation. In such cases, it is more convenient to implement the mechanical scanning system at the level of a secondary reflector where a magnification factor is used to reduce the dimensions of the rotating component. Obviously, in this case, the rotation will introduce aberrations on the antenna pattern, and one should arrive at a compromise between the FoV, beam quality (i.e., resolution), and imaging speed.

When the target plane is at large distance with respect to the main aperture (i.e., R_f/D >10), Cassegrain or confocal systems with an elliptical main reflector are a good solution to obtain a certain magnification. These solutions would reduce the rotating mirror diameter while maintaining a good-quality antenna pattern over the field of view. For instance, a confocal-based reflector system was used in [32, 44] to generate the images shown in Figure 4.1. The images were created at 670 GHz by using an active imager with an elliptical reflector focusing at 25m. The reflector system used is shown in Figure 4.32(a), consisting on a primary aperture of 1m and a magnification of 10, leading to a rotating mirror of approximately 10 cm in diameter. The reflector system is based on a confocal Gregorian system consisting of two paraboloid reflectors sharing a common focus [52] and the equivalence

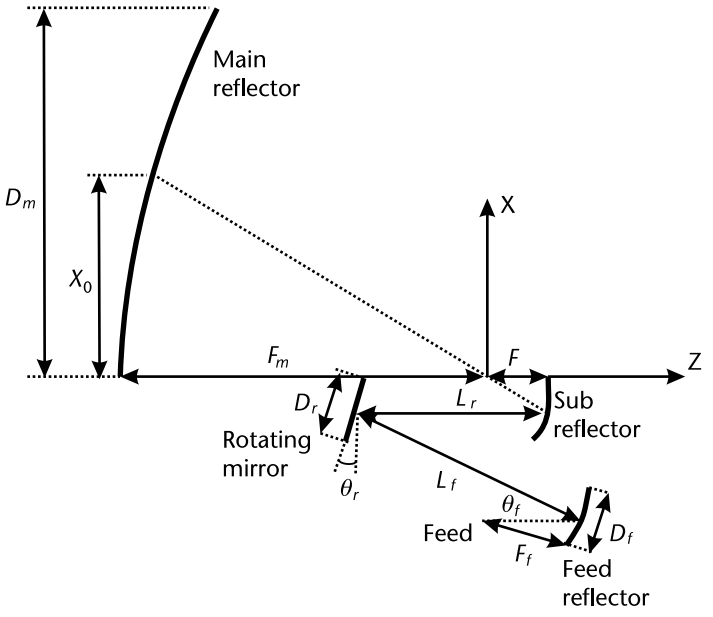

(a)

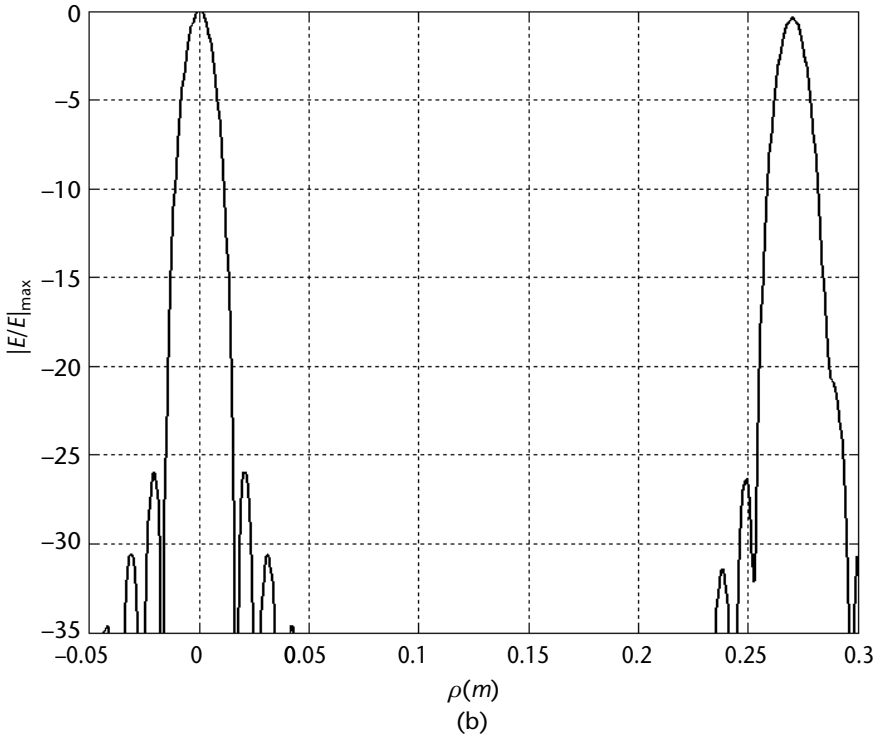

(b)

Figure 4.32 Confocal Gregorian reflector system: (a) geometry and (b) simulated near fields for D = 1m and Rf = 25m.

between the parabolic and elliptical reflector described previously. In the design, the rotating mirror is illuminated by a collimated beam. This is important because

it relaxes the tolerance on the position of the rotating mirror's principal axes, which otherwise would be difficult to align at high frequencies. Such a reflector configuration presents a cancellation of the coma aberrations that are normally present in more conventional reflector configurations, and that is the reason why it presents very good scanning properties. Figure 4.32(b) shows the simulated near fields at the center and at the edge of the FoV.

In [30], some simple design formulas for ellipsoidal confocal reflector systems were provided. The properties of the antenna pattern over the FoV depend on the path length rms, δ, of all the rays, which start at a rotating mirror and end at the target plane, where the bundles of rays are supposed to converge for adequate near-field scanning of the antenna. By doing an intensive parametric study, an empirical formula to calculate this rms path length was derived:

$$\sigma = 0.144M\frac{\rho^3 D}{4c^2 F_m} \tag{4.37}$$

where M is the magnification of the system, D is the primary reflector diameter, F_m is the primary focal distance, c is half the interfoci distance of the elliptical surface of the primary reflector, and ρ is the scanned distance over the FoV. The maximum FoV can be defined directly from the rms path length as described here. Considering a uniform aperture and allowing a maximum decay of the antenna field over the FoV of X_{dB} decibels, the rms path length becomes $\sigma = 0.15\sqrt{X_{dB}}\lambda$, as demonstrated in [30]. Therefore, the field of view of the antenna can determined to be the double of the scanned distance, leading to the following rms path length value:

$$FoV_{\max} = 2\left(0.1667\sqrt{X_{dB}}\frac{c^2 F_m}{MD}\lambda\right)^3 \tag{4.38}$$

When the target plane is relatively close to the main aperture (i.e., $R_f/D < 10$), the design of scanning reflector systems with low aberrations becomes extremely difficult. This type of system resembles the optical reflective systems used for microscopes [53] and spectrometers [54]. A nice system that presents low aberrations is the Offner imaging spectrometer [55]. It consists of three spherical reflectors: two offset ones and a symmetrical one, as shown in Figure 4.33(a). The smaller reflector can be rotated from its center to achieve a mechanical scanned imaging system. The radius of curvature and centers of the three reflectors can be optimized to achieve clean antenna patterns over the whole FoV as in Figure 4.33(b), where the near fields at both the center and the edge of the FoV are shown.

Appendix 4A Derivation of Field in the Focal Plane of a Focusing Reflector

In this appendix, we introduce a simple formulation to compute the field in the focal plane of a general focusing aperture as a superposition of plane waves. This

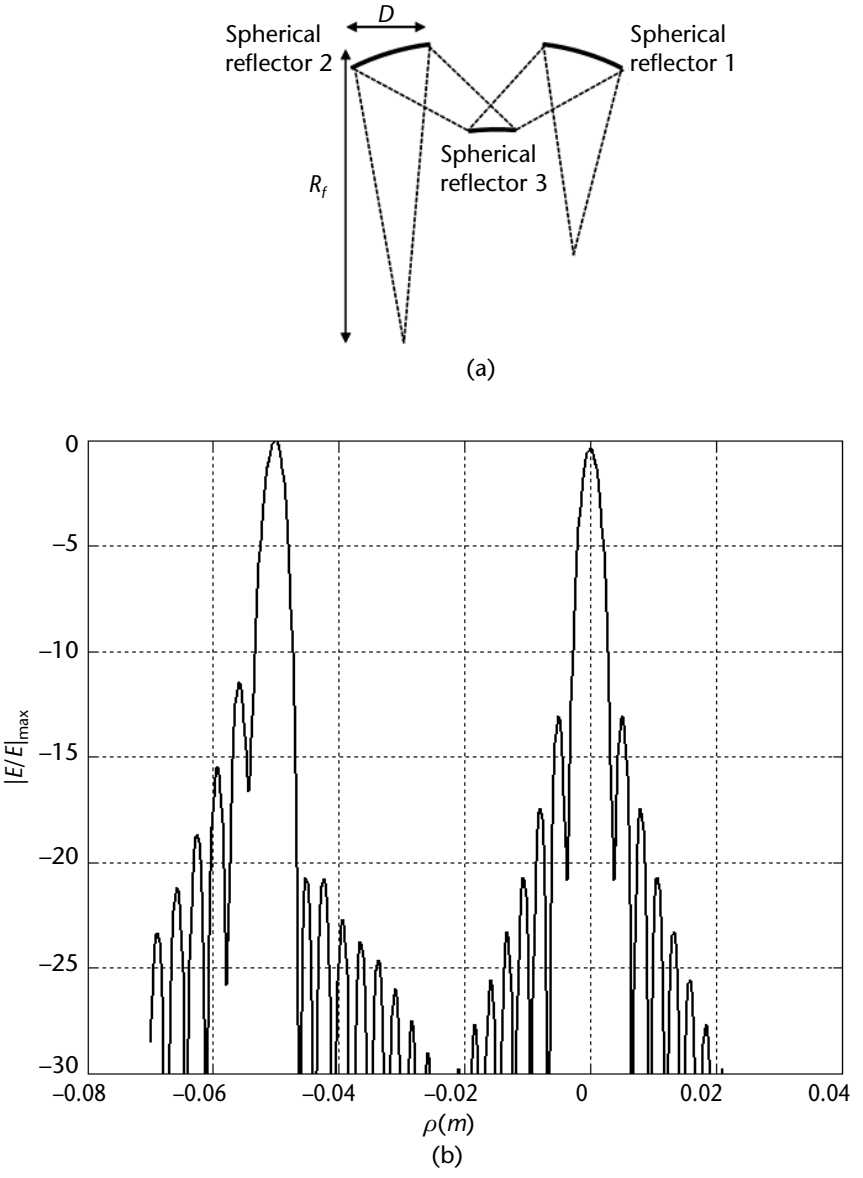

Figure 4.33 Offner reflector system: (a) geometry and (b) simulated near fields for D = 30 cm and Rf = 50 cm.

formulation can then be used to calculate the power received by reflector antenna feeds by using its effective height, as shown in Appendix 4B.

A real reflector system is composed of a cascade of many reflectors, but the basic design trade-offs can be performed considering a single equivalent reflector [33]. Let us define this equivalent reflector with a certain aperture of diameter D and focal distance F, as shown in Figure 4A.1.

For analyzing the radiation characteristics of a reflector antenna, two techniques are commonly used: the equivalent current distribution on the reflector method, and the aperture distribution method [23]. For the current distribution method, a physical optics approximation is assumed to compute the equivalent

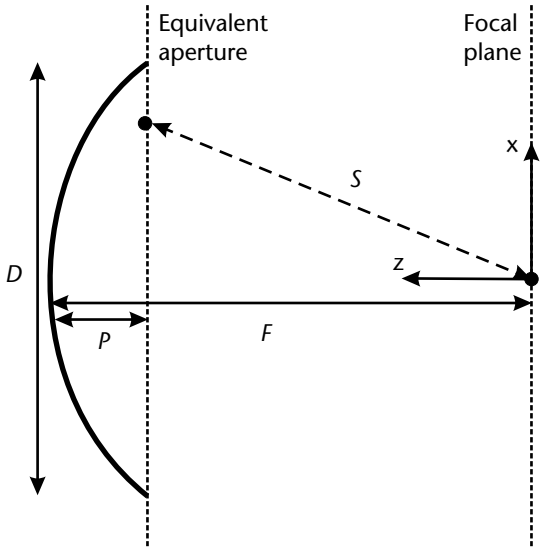

Figure 4A.1 Schematic view of a focusing reflector and its equivalent aperture.

currents along the reflector surface, and the radiated field is then obtained by integrating these currents. In contrast, for the aperture distribution method, the field reflected by the surface is found over a plane normal to the axis of the reflector by using ray-tracing techniques. Then these aperture fields are integrated to obtain the radiation characteristics of the reflector. This method is actually more convenient for analyzing a focusing aperture because it allows for expressing implicitly the quadratic phase distribution of the field aperture. This quadratic phase will be cancelled when calculating the field at the focal plane.

We can define an equivalent aperture in front of the reflector at a distance P from the apex of the reflector. As a starting point we are going to consider the focalization system under the incidence of a plane wave coming from $\hat{k}_i = k_{xi}\hat{x} + k_{yi}\hat{y} + k_{zi}\hat{z}$ with an amplitude $E_i(k_{xi}, k_{yi})$. The field distribution generated by the reflector over such an equivalent aperture can be formulated using the following general expression:

$$\vec{E}^{ap}(x',y') = E_i\left(k_{xi},k_{yi}\right)e^{-jk_{xi}x'}e^{-jk_{yi}y'}\hat{e}_{inc}\cdot\overline{\overline{R}}\left(k_{xi},k_{yi},x',y'\right) \tag{4A.1}$$

where $E_i(k_{xi}, k_{yi})$ is calculated at $z' = 0$, $\hat{e}_{inc}$ is the incident field polarization unit vector, whereas $\overline{\overline{R}}\left(k_{xi},k_{yi},x',y'\right)$ is a dyadic function that represents the effect of the reflector in the aperture field distribution (e.g., the induced cross-polarization). In the case of near-normal incidence, the phase of the field reflected by the reflector at the equivalent aperture, located at $(x', y', z' = F - P)$ results in $e^{-jk(2F-S)}e^{-j\psi}$ with $S=\sqrt{x'^2+y'^2+(F-P)^2}$ as shown in Figure 4A-1. Assuming that the reflector is characterized by large F/D (i.e., $F >> D$) we can approximate the distance S as $S \approx (F-P)+\dfrac{x'^2+y'^2}{2F}$; therefore, the phase can be written as $e^{-jk(F+P)}e^{jk\frac{x'^2+y'^2}{2F}}e^{-j\psi}$. Since the initial phase ψ is arbitrary, we can always express the phase variation of the

reflected field on the equivalent aperture plane directly as $e^{jk\frac{x'^2+y'^2}{2F}}$. Accordingly, for near-normal incidence, we can assume that the effect of the focusing system on the phase and polarization of the incoming plane wave is as follows:

$$\overline{\overline{R}}\left(k_{xi},k_{yi},x',y'\right)=e^{jk\frac{x'^2+y'^2}{2F}}\overline{\overline{S}}\left(k_{xi},k_{yi},x',y'\right) \tag{4A.2}$$

where $\overline{\overline{S}}$ is the dyadic function that characterizes the effect of the reflector.

Invoking the Schelkunoff theorem [56], the field in the focal plane can be expressed in terms of a radiation integral involving only magnetic equivalent currents. Note that this radiation integral is expressed as a function of a reference system center in the focal plane. Accordingly, by considering $F - P >> \lambda$:

$$\overline{E}_f(x,y)=\iint_{S_r}\overline{\overline{G}}(x,y,0,x',y',F-P)\cdot 2\vec{E}^{ap}(x',y')\times\hat{i}_z dx'dy' \tag{4A.3}$$

where $\overline{\overline{G}}$ is the dyadic Green's function in free space and S_r is the integration domain over the reflector aperture.

Denoting with $\overline{r}=x\hat{x}+y\hat{y}$ the position on the focal plane and with $\overline{r}'=x'\hat{x}+y'\hat{y}+(f-p)\hat{z}$ that on the reflector aperture, the electric field on the focal plane can be expressed in terms of the scalar Green's function as follows:

$$\overline{E}_f(x,y)=\iint_{S_r}=2\left(\overline{E}^{ap}(x',y')\times\hat{\ell}_z\times\nabla_g\left(\vec{r},\vec{r}^{\,1}\right)\right)dx'dy' \tag{4A.4}$$

with $\overline{k}=\frac{\overline{r}-\overline{r}^{\,1}}{\left|\overline{r}-\overline{r}^{\,1}\right|}k$, and $g\left(\overline{r},\overline{r}^{\,1}\right)=\frac{e^{jk\left|\overline{r}-\overline{r}^{\,1}\right|}}{4\pi\left|\overline{r}-\overline{r}^{\,1}\right|}$. Because for $r >> \lambda_0$, $\nabla_y(\vec{r},\vec{r}^{\,1})\cong -j\overline{k}g(\overline{r},\overline{r}^{\,1})$ (4A.4) can then be expressed as follows:

$$\overline{E}_f(x,y)=\iint_{S_r}-j\overline{k}\times 2\left(\vec{E}^{ap}(x'y')\times\hat{i}_z\right)\frac{e^{-jk\left|\overline{r}-\overline{r}'\right|}}{4\pi\left|\overline{r}-\overline{r}'\right|}dx'dy' \tag{4A.5}$$

This expression is general for any aperture, focusing in the far or near field, and can be further simplified by considering amplitude and phase approximations in the Fraunhofer or Fresnel regions.

To calculate the radiated field in the Fresnel region, the expression in (4A.5) can be simplified by imposing the following approximations:

For the amplitude: $$\frac{1}{\left|\overline{r}-\overline{r}'\right|}\cong\frac{1}{F} \tag{4A.6}$$

For the phase: $$\left|\overline{r}-\overline{r}'\right|\cong F+\frac{(x-x')^2}{2F}+\frac{(y-y')^2}{2F} \tag{4A.7}$$

Note that the amplitude approximation implies a maximum error of 11.8% in the field amplitude for $F/D = 1$, and less for larger F/D. Usually, in antenna

problems, it is required that $F > 10D$ and the approximation given in (4A.6) is used, leading to an amplitude error of less than 5%. Thus,

$$\bar{E}_f(x,y)=\frac{-je^{-jkF}}{2\pi F}\iint_{S_r}\bar{k}\times\left(\bar{E}^{ap}(x',y')\times\hat{i}_z\right)e^{-jk\frac{(x-x')^2}{2F}}e^{-jk\frac{(y-y')^2}{2F}}dx'dy' \tag{4A.8}$$

By expanding the exponential terms, (4A.8) leads to

$$\vec{E}_f(x,y)=\frac{-je^{-jkF}e^{-jk\frac{x^2+y^2}{2F}}}{2\pi F}\iint_{S_r}\bar{k}\times\left(\vec{E}^{ap}(x',y')\times\hat{i}_z\right)e^{-jk\frac{x'^2+y'^2}{2F}}e^{jk\frac{x'x}{F}}e^{jk\frac{y'y}{F}}dx'dy' \tag{4A.9}$$

At this point, we can recall the expression derived for the aperture field in equations (4A.1) and (4A.2). We can observe that if we want to compute the field around the focal point ($z = F$), the quadratic term in (4A.9) cancels out with the quadratic phase variation introduced by the parabolic reflector (or in general by a focalizing system), leading to:

$$\begin{aligned}\bar{E}_f(x,y)&=\frac{-je^{-jkF}e^{-jk\frac{x^2+y^2}{2F}}}{2\pi F}\iint_{S_r}E_i(k_{xi},k_{yi})\,e^{-jk_{xi}x'}e^{-jk_{yi}y'}\bar{k}\\&\times\left(\hat{e}_{inc}\cdot\bar{\bar{S}}\left(k_{xi},k_{yi},x',y'\right)\times\hat{i}_z\right)e^{jk\frac{x'x}{F}}e^{jk\frac{y'y}{F}}dx'dy'\end{aligned} \tag{4A.10}$$

Let us define the equivalent magnetic currents on the reflector aperture as $\hat{e}_{inc}\cdot\bar{\bar{S}}\left(k_{xi},k_{yi},x',y'\right)\times\hat{i}_z=m_x(x',y')\hat{x}+m_y(x',y')\hat{y}$. Then it follows that, being $\bar{k}=k_x\hat{x}+k_y\hat{y}+k_z\hat{z}$, the focal plane field can be expressed in a general form for any focusing system as:

$$\begin{aligned}\bar{E}_f(x,y)=&\frac{-je^{-jkF}e^{-jk\frac{x^2+y^2}{2F}}}{2\pi F}E_i(k_{xi},k_{yi})\iint_{S_r}e^{-jk_{xi}x'}e^{-jk_{yi}y'}\\&\begin{pmatrix}-k_zm_y(x',y')\hat{x}+m_x(x',y')k_z\hat{y}+\\\left(k_xm_y(x',y')-k_ym_x(x',y')\right)\hat{z}\end{pmatrix}e^{jk\frac{x'x}{F}}e^{jk\frac{y'y}{F}}dx'dy'\end{aligned} \tag{4A.11}$$

Note that in theory $k_x\hat{x}+k_y\hat{y}+k_z\hat{z}$ is a vector that depends on the source and observation point. However, it is legitimate to assume that it is a function of the source point only when the observation point is close to the focus with respect to the focal distance F (even for small F/D). As a matter of fact $\bar{k}=\frac{\bar{r}-\bar{r}'}{|\bar{r}-\bar{r}'|}k_0\approx\frac{-\bar{r}'}{r'}k_0$ (i.e., $k_x\approx\frac{-x'}{r'}k_0$, $k_y\approx\frac{-y'}{r'}k_0$ and $k_z\approx\frac{-z'}{r'}k_0$) when $\bar{r}'\gg\bar{r}$. Therefore, the term in (4A.11) $\left(-k_zm_y(x',y')\hat{x}+m_x(x',y')k_z\hat{y}+\left(k_xm_y(x',y')-k_ym_x(x',y')\right)\hat{z}\right)$ can be assumed independent from the observation point. Moreover, in the above hypothesis,

it is possible to neglect the quadratic term $e^{-jk\frac{x^2+y^2}{2F}}$ and to express the field $\bar{E}_f(x,y)$ as a superposition of plane waves of phases $e^{jk\frac{x'x}{F}}e^{jk\frac{y'y}{F}}$ and intensity:

$$\frac{-je^{-jkF}e^{-jk\frac{x^2+y^2}{2F}}}{2\pi F}E_i(k_{xi},k_{yi})\,e^{-jk_{xi}x'}e^{-jk_{yi}y'}\begin{pmatrix}-k_z m_y(x',y')\hat{x}+m_x\\(x',y')k_z\hat{y}+\\\left(k_x m_y(x',y')-k_y m_x(x',y')\right)\hat{z}\end{pmatrix}$$

Now, if we assume that a series of plane waves, with the same polarization, is impinging on the reflector, for the linearity of the problem, the electric field on the focal plane can be calculated as a superposition of the fields generated by each of these plane waves. In the case of plane waves polarized along *y*, the expression of the field becomes:

$$\bar{E}_f(x,y)=\frac{-je^{-jkF}e^{-jk\frac{x^2+y^2}{2F}}}{2\pi F}\int\int_{-\infty}^{\infty}E_i\left(k_{xi},k_{yi}\right)\iint_{S_r}e^{-jk_{xi}x'}e^{-jk_{yi}y'}\begin{pmatrix}m_x(x',y')k_z\hat{y}+\\-k_y m_x(x',y')\hat{z}\end{pmatrix}e^{jk\frac{x'x}{F}}e^{jk\frac{y'y}{F}}dx'dy'dk_{xi}dk_{yi} \tag{4A.12}$$

Assuming that we can neglect the effect of the reflector on the polarization of the equivalent aperture field, and large *F/D* numbers and symmetry (valid for points closed to the focal plane) are present, the integrals in (4A.12) can be interchanged and the field in the reflector equivalent aperture can be expressed directly as a function of the summation of the incident plane waves, that is, as an inverse Fourier transform: $e_i(x',y')\frac{\ell}{(2\pi)^2}\int\int_{-\infty}^{\infty}E_i\left(k_{xi},k_{yi}\right)e^{-jk_{xi}x'}e^{-jk_{yi}y'}dk_{xi}dk_{yi}$
leading to:

$$\bar{E}_f(x,y)=\frac{-je^{-jkF}e^{-jk\frac{x^2+y^2}{2F}}}{2\pi F}\iint_{S_r}e_i(x',y')\begin{pmatrix}m_x(x',y')k_z\hat{y}\\-k_y m_x(x',y')\hat{z}\end{pmatrix}e^{jk\frac{x'x}{F}}e^{jk\frac{y'y}{F}}dx'dy' \tag{4A.13}$$

Appendix 4B Effective Height of the Reflector Antenna Feed

In the chapter, we make use of a simplified model of the antenna feed coupled to the reflector system, as described here. The far field of an antenna can in general be expressed as a function of the magnetic $\bar{m}_a(x',y')$ and electric $\bar{J}_a(x',y')$ currents along the surface of the antenna, S_a:

$$\bar{E}^{ant}(\theta,\phi)=\frac{jke^{-jkr}}{4\pi r}\iint_{S_a}\begin{pmatrix}\frac{\bar{r}}{r}\times\bar{\bar{I}}\cdot\bar{m}_a(x',y')-\\ \zeta\left(\bar{\bar{I}}-\frac{\bar{r}}{r}\right)\cdot\bar{J}_a(x',y')\end{pmatrix}e^{jk\sin\theta\cos\phi x}e^{jk\sin\theta\sin\phi y}dx'dy' \tag{4B.1}$$

The effective height of an antenna located in r_n when radiating in direction (r, θ, ϕ) can be calculated as:

$$\bar{h}(\theta,\phi)=\frac{\bar{E}^{ant}(r,\theta,\phi)}{I_0 jk\frac{e^{-jkr}}{4\pi r}\zeta} \tag{4B.2}$$

where I_0 is the current following on the antenna terminals when operated in transmission.

If we consider directive antennas, widely used in the terahertz regime, such as horns and lenses, we can compute the far field radiated by the antenna in terms of a radiation integral involving only magnetic equivalent currents over the aperture of the antenna (i.e., the horn aperture or an aperture defined on the top of the lens) by invoking the Schelkunoff theorem [56]. The antenna current distribution, $m_a(x, y)$ can be expressed as a function of generic function, $f_a(x, y)$ and a normalization constant v: $m_a(x, y) = f_a(x, y)$.

Then, the actual far-field pattern can be calculated directly from the Fourier transform $vF_a(k_x, k_y)$ of the equivalent current. Assuming an equivalent magnetic current along x, the far field can be expressed as [23]:

$$E_\theta^{ant}(\theta,\phi)=-j\frac{ke^{-jkr}}{2\pi r}v\sin\phi F_a(\theta,\phi) \tag{4B.3}$$

$$E_\phi^{ant}(\theta,\phi)=j\frac{ke^{-jkr}}{2\pi r}v\cos\phi\cos\theta F_a(\theta,\phi) \tag{4B.4}$$

and the effective height can be expressed as follows:

$$\bar{h}(\theta,\phi')=\frac{\bar{E}^{ant}(\theta,\phi)}{I_0 jk\frac{e^{-jk|r-r_n|=D_r}}{4\pi|r-r_n|=D_r}\zeta}=\frac{2v}{I_0\zeta}\left(-\sin\phi F_a(\theta,\phi)\hat{\theta}+\cos\phi\cos\theta F_a(\theta,\phi)\hat{\phi}\right) \tag{4B.5}$$

As an example, we can assume a feed with a circular aperture D_f (see Figure 4.13) with a uniform aperture field. In this case the Fourier transform of the equivalent current is:

$$F_a(\theta)=\pi\frac{D_f^2}{2}\frac{J_1\left(k\sin\theta D_f/2\right)}{k\sin\theta D_f/2} \tag{4B.6}$$

Let us also consider the following taper field circular distribution, which can be used to model horns and lenses, the most common antennas in the terahertz domain:

$$f_a(\rho')=J_0\left(2\frac{k_{te}\rho'}{D_f}\right)circ\left(\rho',D_f/2\right) \tag{4B.7}$$

where k_{te} = 2.11 for a –16-dB field decay at the feed aperture edges. Its Fourier transform is:

$$F_a(\theta)=\frac{2\pi D_f/2}{\left(\frac{k_{te}}{D_f/2}\right)^2-k^2\sin^2\theta}\begin{bmatrix}\frac{k_{te}}{D_f/2}J_0\left(k\sin\theta D_f/2\right)\\ J_1\left(k_{te}\right)-k\sin\theta J_0\left(k_{te}\right)\\ J_1\left(k\sin\theta D_f/2\right)\end{bmatrix} \tag{4B.8}$$

To find the normalization constant v, we assume that the power at the aperture plane, $\frac{1}{2}\iint_{S_a}\bar{E}_a(x,y)\times\bar{H}_a^*(x,y)ds$, is equal to the power radiated by the antenna; that is, $\frac{1}{2}|I_0|^2R_a$ times an efficiency factor that includes the ohmic and front-to-back ratio losses $\eta_{loss}=\eta_{ohm}\eta_{FB}$. For large apertures, typically associated with large *F/D* common in the terahertz regime, we can assume that $\frac{1}{2}\iint_{S_a}\bar{E}_a(x,y)\times\bar{H}_a^*(x,y)ds\approx\frac{1}{2}\iint_{S_a}\frac{|m_a(x,y)|^2}{4\zeta}ds$, where $m_a(x,y)=vfa(x,y)=2\bar{E}_a\times\hat{n}$. Equating both powers, one can derive the current amplitude constant to be:

$$v=2I_0\sqrt{\frac{R_a\zeta\eta_{loss}}{\iint_{S_a}|f_a(x,y)|^2ds}} \tag{4B.9}$$

Therefore, (4.20) becomes

$$\bar{h}(\theta,\phi)=\frac{4}{\zeta}\sqrt{\frac{R_a\zeta\eta_{loss}}{\iint_{S_a}|f_a(x,y)|^2ds}}\left(-\sin\phi F_a(\theta,\phi)\hat{\theta}+\cos\phi\cos\theta F_a(\theta,\phi)\hat{\phi}\right) \tag{4B.10}$$

Note that for directive antennas the power at the antenna aperture can be related to the power radiated in the far field using the following valid equivalence:

$$\iint_{S_a}|f_a(x,y)|^2ds\cong\left(\frac{k}{2\pi}\right)^2\iint_{S_a}|F_a(\theta,\phi)|^2\sin\theta d\theta\phi \tag{4B.11}$$

Appendix 4C Power Received by an Antenna in the Focal Plane of a Focusing Reflector

In this appendix we derive an expression for calculating the power received by an antenna placed in the focal plane of a general focalization system under the incidence of a plane wave coming from a direction identified by the spherical angles (α, β) with an amplitude $E_e(\alpha, \beta)$. For this purpose, we can recall the expression of the focal plane field derived in (4A.13). To calculate the power received by the focal plane array, we approximate the field in the surrounding of the nth antenna in the focal plane, which will be located in (x_n, y_n), as follows:

$$\bar{E}_f^n(x,y) \approx \frac{-je^{-jkF}e^{-jk\frac{x_n^2+y_n^2}{2F}}}{2\pi F} E_e(\alpha,\beta)\iint_{S_r} \bar{U}(x',y')e^{-jk_x x'}e^{-jk_{i}y'}e^{jk\frac{x'x}{F}}e^{jk\frac{y'y}{F}}dx'dy' \quad (4C.1)$$

where $k_x = k\sin\beta\cos\alpha$, $k_x = k\sin\beta\sin\alpha$ and $\bar{U}(x',y') = -k_z m_y(x',y')\hat{x} + m_x(x',y')k_z\hat{y} + \left(k_x m_y(x',y') - k_y m_x(x',y')\right)\hat{z}$ is the term that represents the impact of the reflector on the equivalent aperture distribution.

The integrand in equation (4C.1) is a superposition of plane waves with phase variations $e^{jk\frac{x'x}{F}}e^{jk\frac{y'y}{F}}$. The voltage induced on an antenna centered in (x_n,y_n), when excited by a plane wave coming from direction $\frac{x'}{F} = \tan\theta\cos\phi$, $\frac{y'}{F}\tan\theta\sin\phi$, can be expressed as the incoming field multiplied scalarly by the effective height of the antenna. (Note that for large *F/D* numbers, one can assume that, $\frac{x'}{F} \cong \sin\theta\cos\phi$, $\frac{y'}{F} \cong \sin\theta\sin\phi$.) Therefore, the voltage induced at the nth antenna centered in (x_n,y_n) can be expressed as the summation of the voltages induced by each of the plane waves composing the integrand of (4C.1):

$$V^n(\alpha,\beta) \approx \frac{-je^{-jkF}e^{-jk\frac{x_n^2+y_n^2}{2F}}}{2\pi F} E_e(\alpha,\beta)\iint_{S_r} \bar{U}(x',y')\cdot\bar{h}_n(x',y')e^{-jk_x x'}e^{-jk_y y'}dx'dy' \quad (4C.2)$$

where the effective height of the antenna has been expressed directly as a function of (x',y'): $\bar{h}_n(\theta,\phi) = \bar{h}_n(x',y')$. Considering that all of the antennas in the focal plane are the same, it is actually more convenient to express this effective length in a coordinate system centered at the antenna itself:

$$\bar{h}_n(x',y') = \bar{h}_0(x',y')e^{jk\frac{x'}{F}x_n}e^{jk\frac{y}{F}y_n} \quad (4C.3)$$

and, therefore,

$$V^n(\alpha,\beta) \approx \frac{-je^{-jkF}e^{-jk\frac{x_n^2+y_n^2}{2F}}}{2\pi F} E_e(\alpha,\beta)\iint_{S_r} \bar{U}(x',y')\bar{h}_0(x',y')e^{jk\frac{x'}{F}x_n}e^{jk\frac{y'}{F}y_n}e^{-jk_x x'}e^{-jk_y y'}dx'dy' \quad (4C.4)$$

Once the voltage in the equivalent circuit of the antenna in reception is known, the power received by the load can be expressed as $P_n = \frac{1}{2}|V_n|^2 \frac{R_l}{|Z_l + Z_a|^2}$, where $Z_l = R_l + jX_l$ and $Z_a = R_a + jX_a$ are the load and antenna impedances, respectively, or as a function of the impedance mismatch as $P_n = \frac{1}{8R_a}|V_n|^2 \chi_{match}$, where $\chi_{match} = \frac{4R_l R_a}{|Z_l + Z_a|^2}$.

The effective height of an antenna as given in (4B.2) can in general be expressed as a function of the magnetic $\bar{M}_s(x,y)$ and electric $\bar{J}_s(x,y)$. Substituting (4B.2) into (4C.4), after some algebraic manipulations, one arrives at the following compact expression:

$$V^n(\alpha,\beta) \approx \frac{-je^{-jkF}e^{-jk\frac{x_n^2+y_n^2}{2F}}}{2\pi F} E_e(\alpha,\beta)\left(v_m(\alpha,\beta) - v_j(\alpha,\beta)\right) \tag{4C.5}$$

where

$$\begin{aligned} v_m(\alpha,\beta) = & \iint_{S_r}\iint_{S_a} \bar{U}(x',y')\frac{\bar{r}'}{r'} \\ & \times \bar{\bar{I}} \cdot \frac{\bar{m}_a(x,y)}{\zeta I_0} e^{jk\frac{x'}{F}(x_n+x)} e^{jk\frac{y'}{F}(y_n+y)} e^{-jk_x x'} e^{-jk_y y'} dx'dy'dxdy \end{aligned} \tag{4C.6}$$

$$\begin{aligned} v_j(\alpha,\beta) = & \iint_{S_r}\iint_{S_a} \bar{U}(x',y')\left(\bar{\bar{I}} - \frac{\bar{r}'}{r'}\right) \\ & \cdot \frac{\bar{J}_a(x,y)}{I_0} e^{jk\frac{x'}{F}(x_n+x)} e^{jk\frac{y'}{F}(y_n+y)} e^{-jk_x x'} e^{-jk_y y'} dx'dy'dxdy \end{aligned} \tag{4C.7}$$

Finally, the received power can then be calculated as follows

$$P_n(\alpha,\beta) = \frac{|E_e(\alpha,\beta)|^2}{8R_a} \frac{1}{(2\pi F)^2} \left|\left(v_m(\alpha,\beta) - v_j(\alpha,\beta)\right)\right|^2 \chi_{match} \tag{4C.8}$$

Appendix 4D Integration Time in Passive Detectors

In this appendix, we provide some formulas to compute the integration time in a passive detector needed to achieve a certain signal-to-noise level. These formulas will be useful for the optimization of the FPA sampling in terms of image acquisition speed.

In a direct detection scheme, the *S/N* after detection, $(S/N)_{AD}$, can be improved with respect to the one before detection, $(S/N)_{BD}$. As a matter of fact, as described in [27]:

$$(S/N)_{AD} = (S/N)_{BD}\sqrt{\tau BW} \tag{4D.1}$$

where τ is the inverse of the postdetection bandwidth (or the integration time) and BW is the radio-frequency bandwidth. The input signal power in (4D.1) is the average power captured by each pixel of the focal plane, $< P_n^e >$. The receiver noise power before detection is characterized by the total noise equivalent power (NEP) at the input; thus, $(S/N)_{BD} = \frac{< P_n^e >}{NEP}$. By definition, the NEP is the input signal that provides, as output, a *S/N* equal to 1. A nice property of the NEP representation is that every source of noise can be treated additively. The two major contributions to the total NEP are the internal noise of the receiver (NEP_{det}), and the photon fluctuations of the signal itself (NEP_{phot}). The total NEP is then $NEP = \sqrt{NEP_{phot}^2 + NEP_{det}^2}$. It is useful to introduce a quantity, γ, that relates the photon noise to the detector noise: $NEP_{\det} = \gamma NEP_{phot}$. Hence, the total NEP can be expressed only as a function of the photon noise $NEP_{tot} = NEP_{phot}\sqrt{1+\gamma^2}$, or of the receiver noise $NEP_{tot} = NEP_{\det}\frac{\sqrt{1+\gamma^2}}{\gamma}$.

For sensitive terahertz space imaging applications, one can concentrate on an important situation: the one in which the cooled receiver does not introduce significant noise. In such a situation, the limiting noise is the photon noise only, dependent on the background. Therefore, the case where $\gamma = 0$ is commonly referred to as the background limited case.

The starting point for FPA acquisition speed optimization is (4D.1), indicating that the *S/N* improves with the integration time or the bandwidth. The integration time can be expressed as the time required to acquire an image on a specific FoV for a certain accepted signal-to-noise ratio, $(S/N)_{AD}$:

$$\tau = (S/N)_{AD}^2 \frac{NEP_{phot}^2 \left(1+\gamma^2\right)}{< P_n^e >^2} \frac{1}{BW} \tag{4D.2}$$

In a radiometric scenario, assuming a Poisson distribution for the photon noise, it is simple to demonstrate [57] that $NEP_{phot} = \sqrt{hf_0 BW < P_t >}$, where $<P_t>$ is the total power absorbed over a certain BW, h is Planck's constant ($h = 6.626068 \times 10^{-34}$ J/s) and f_0 is the central frequency. Substituting this definition for the photon noise in (4D.2), we obtain the following expression:

$$\tau = (S/N)_{AD}^2 hf_0 \frac{< P_t >}{< P_n^e >^2}\left(1+\gamma^2\right) \tag{4D.3}$$

Overall, the required integration time is inversely proportional to the useful (signal) power received and directly proportional to the total received power (since the entire power received contributes to photon noise). The useful signal is the part of the absorbed power that arrives at the receiver from the FoV through the reflector system. However, in general, the total received power differs from that desired signal: For example, a thermal contribution originating in the reflector system itself, $< P_n^i >$, which is at a certain temperature, will contribute to the total absorbed power, that is, $< P_t > = < P_n^i > + < P_n^e >$, but not to the desired signal. This signal is noise only, and typically it is referred to as the instrument background contribution. This

contribution is typically negligible in most significant cryogenically cooled reflector systems. Including these two signal contributions, (4D.3) becomes

$$\tau=(S/N)_{AD}^2\frac{hf_0}{<P_n^e>}\left(1+\frac{<P_n^i>}{<P_n^e>}\right)\left(1+\gamma^2\right) \tag{4D.4}$$

Appendix 4E Instrument Background Contribution

In passive detectors, when the reflector system is not sufficiently cold, an important noise contribution arises directly from the instrument itself. For such a contribution we can calculate the average power received by the antenna assuming that a series of plane waves arrives at the antenna from angles outside the reflector rim as:

$$<P_n^i>=\int_0^{2\pi}\int_{\theta_{sub}}^{\pi}<P_n^i(\alpha,\beta)>\sin\beta d\beta d\alpha \tag{4E.1}$$

where $P_n^i(\alpha,\beta)$ is the received power from a single plane wave. This power can be calculated from the voltage induced on the antenna, that is, $V^n(\alpha,\beta)=\bar{E}^i(\alpha,\beta)\cdot\bar{h}_0(\alpha,\beta)e^{jk_x x_n}e^{jk_y y_n}$. Therefore,

$$P_n^i(\alpha,\beta)=\frac{1}{8R_a}\left|\bar{E}^i(\beta,\alpha)\right|^2\left|\bar{h}_0(\beta,\alpha)\right|^2\chi_{match} \tag{4E.2}$$

If we include the definition of the effective height given in (4B.10), we obtain the following expression:

$$<P_n^i>=S_{ave}^i A_a\eta_{loss}\chi_{match}\int_0^{2\pi}\int_{\theta_{sub}}^{\pi}\eta_{ap}^a(\alpha,\beta)sin\beta d\beta d\alpha \tag{4E.3}$$

where S_{ave}^i is the average brightness internal to the instrument, A_a is the antenna aperture, and $\eta_{ap}^a(\beta,\alpha)$ is the antenna aperture efficiency, defined as follows:

$$\eta_{ap}^a(\alpha,\beta)=\frac{\left|\iint_{S_a}f_a(x,y)e^{jk\sin\beta\cos\alpha x}e^{jkin\beta\sin\alpha y}dxdy\right|^2}{\iint_{S_a}\left|f_a(x,y)\right|^2 dsA_a} \tag{4E.4}$$

Note that (4E.4) can be easily related to the spillover efficiency, η_s^a, as follows:

$$<P_n^i>=S_{ave}^i\eta_{loss}\chi_{match}\lambda^2\left(1-\eta_s^a\right) \tag{4E.5}$$

where $\eta_s^a = \dfrac{\int_0^{2\pi}\int_0^{\theta_{sub}} |F_a(\theta,\phi)|^2 \sin\beta d\beta d\alpha}{\int_0^{2\pi}\int_0^{\pi} |F_a(\theta,\phi)|^2 \sin\beta d\beta d\alpha}$ is the spillover efficiency, and $F_a(\theta, \phi)$ is the Fourier transform of the antenna current distribution $f_a(x, y)$.

References

[1] G. Chattopadhyay, *Submillimeter-Wave Coherent and Incoherent Sensors for Space Applications*, Smart Sensors and Sensing Technology, Publisher Springer, 2008.

[2] P. H. Siegel, "Terahertz Technology," *IEEE Trans. Microwave Theory and Tech.*, Vol. 50, No. 3, pp. 910–928, March 2002.

[3] P. H. Siegel, "Terahertz Instruments for Space," *IEEE Trans. Antennas and Propagation*, Vol. 55, pp. 2957–2965, Nov. 2007.

[4] R. R. Cladwell and M. Kamionkowski, "Echoes from the Big Bang," *Scientific American*, pp. 38–43, 2001.

[5] T. G. Phillips and J. Keene, "Submillimeter Astronomy," *Proc. IEEE*, Vol. 80, pp 1662–1678, November 1992.

[6] S. Gulkis et al., "MIRO: Microwave Instrument for Rosetta Orbiter," *Space Science Reviews*, Vol. 128, No. 1–4, pp. 561–597, Feb. 2007.

[7] L. E. Kristensen, E. F. van Dishoeck, M. Tafalla, R. Bachiller, B. Nisini, R. Liseau, and U. A. Yildiz, "Water in Low-Mass Star-Forming Regions with Herschel (WISH-LM): High-velocity H_2O Bullets in L1448-MM Observed with HIFI," *Astronomy and Astrophysics: Solar and Stellar Astrophysics*, arXiv:1105.4884 [astro-ph.SR].

[8] F. T. Barath et al., "The Upper Atmosphere Research Satellite Microwave Limb Sounder Instrument," *Journal of Geophysical Research*, Vol. 98, Issue D6, pp. 10751—10762, June 1993.

[9] J. W. Waters et al., "The Earth Observing System Microwave Limb Sounder (EOS MLS) on the Aura Satellite," *IEEE Trans. Geosciences and Remote Sensing*, Vol. 44, No. 5, pp. 1075–1092, May 2006.

[10] R. Appleby and H. B. Wallace, "Standoff Detection of Weapons and Contraband in the 100 GHz to 1 THz Region," *IEEE Trans. Antennas and Propagation,* Vol. AP-55, No. 11, pp. 2944–2956, 2007.

[11] K. B. Cooper, R. J. Dengler, N. Llombart, B. Thomas, G. Chattopadhyay, and P. H. Siegel, "THz Imaging Radar for Standoff Personnel Screening," *IEEE Trans. Terahertz Science Tech.*, Vol. 1, No. 1, pp. 169–182, Sep. 2011.

[12] H.-J. Song and T. Nagatsuma, "Present and Future of Terahertz Communications," *IEEE Trans. Terahertz Science Tech.*, Vol. 1, No. 1, pp. 256–263, Sep. 2011.

[13] D. Baumann et al., "CMBPol Mission Concept Study: Probing Inflation with CMB Polarization," *AIP Conference Proc.*, arXiv:0811.3919v2 [astro-ph], Mar. 2009.

[14] C. M. Bradford et al., "Z-Spec: A Broadband Millimeter-Wave Grating Spectrometer: Design, Construction, and First Cryogenic Measurements," *Proc. SPIE*, Vol. 5498, p. 257, 2004.

[15] E. D. Shirokoff et al., "KID Development for SuperSpec: An On-Chip, MM-Wave, Filterbank Spectrometer," *Proc. SPIE*, Vol. 8452, 2012.

[16] A. R. Gillespie and T. G. Phillips, "Array Detectors for Millimeter Line Astronomy," *Astron. Astrophys.*, Vol. 73, pp. 14–18, 1979.

[17] G. Chattopadhyay, "Heterodyne Arrays at Submillimeter Wavelengths," *Proc. XXVIIIth General Assembly of International Union of Radio Science*, New Delhi, India, Oct. 2005.

[18] C. Groppi and J. Kawamura, "Coherent Detector Arrays for Terahertz Astrophysics Applications," *IEEE Trans. Terahertz Science Tech.*, Vol. 1, No. 1, pp. 85–96, Sep. 2011.

[19] G. Chattopadhyay, N. Llombart, C. Lee, B. Thomas, C. Jung, R. Lin, A. Peralta, and I. Mehdi, "Integrated Arrays on Silicon at Terahertz Frequencies," *Proc. IEEE Intl. Symp. Ant. Prop. USNC/URSI National Radio Science Mtg.*, Spokane, WA, July 2011.

[20] D. P. Woody et al., "The CCAT 25m Diameter Submillimeter-Wave Telescope," *Proc. SPIE*, Vol. 8444, 2012.

[21] Sherman, J., III, "Properties of Focused Apertures in the Fresnel Region," *IRE Trans. on Antennas and Propagation*, Vol. 10, No. 4, pp. 399–408, July 1962.

[22] M. Born and E. Wolf, *Principles of Optics,* Pergamon, New York , 1975.

[23] C. Balanis, *Antenna Theory: Analysis and Design*, Wiley, New York, 2005.

[24] K. Iizuka, *Engineering Optics*, Third Edition, Springer, Berlin, 2008.

[25] GRASP software, TICRA.

[26] J. Johansson, *Tapered Slot Antennas and Focal Plane Imaging Systems*, Chalmers, 1988.

[27] R. C. Hansen, *Microwave Scanning Antennas,* Chapter 4, Book I, Academic Press, 1986.

[28] Y. Li and E. Wolf, "Focal Shifts in Diffracted Converging Spherical Waves," *Optics Communications*, Vol. 39, No. 4, 1993, pp. 211–215.

[29] Y. Li, E. Wolf, "Three-Dimensional Intensity Distribution Near the Focus in Systems sf Different Fresnel Numbers," *J. Opt. Soc. Am. A,* Vol. 1, No. 8, Aug. 1984, pp. 801–808.

[30] A. Garcia-Pino, N. Llombart, B. Gonzalez-Valdes, and O. Rubinos-Lopez, "A Bifocal Ellipsoidal Gregorian Reflector System for THz Imaging Applications," *IEEE Trans. Antennas and Propagation,* Vol. 60, No. 9, pp. 4119–4129, Sep. 2012.

[31] Herbert Gross, *Handbook of Optical Systems*, Wiley, New York.

[32] Nuria Llombart, Ken Cooper, Robert J. Dengler, Tomas Bryllert, and Peter H. Siegel, "Confocal Ellipsoidal Reflector System for a Mechanically Scanned Active Terahertz Imager" *IEEE Trans. Antennas and Propagation,* Vol. 58, No. 6, June 2010, pp. 1834–1841.

[33] Y. Ramat-Samii, "Reflector Antennas," in *Antenna Handbook*, Y. T. Lo and S. W. Lee, Eds., Springer, Berlin, 1983.

[34] M. J. Griffin, B. M. Swinyard, and L. G. Vigroux, "Herschel's Submillimetre Camera and Spectrometer," *Proc. SPIE*. Vol. 4850, pp. 686–697, 2003.

[35] M. Griffin, J. Bock, and W. Gear, "Relative Performance of Filled and Feedhorn-Coupled Focal-Plane Architectures," *Appl. Opt*., Vol. 41, pp. 6543–6554, 2002.

[36] P. F. Goldsmith, C.-T. Hsieh, G. R. Huguenin, J. Kapitzky, and E. L. Moore, "Focal Plane Imaging Systems for Millimeter Wavelengths," *IEEE Trans. on Microwave Theory and Tech*., Vol. 41, No. 10, pp. 1664–1675, Oct. 1993.

[37] Peter de Maagt, Daniel de Chambure, Dominic Doyle, and Gerry Crone "Planck and Herschel Instruments and Antenna Technology, " *2007 IEEE Antennas and Propagation Society International Symposium,* pp. 4361–4364, June 2007.

[38] Willard V. T. Rusch, Aluizio Prata, Jr., Yahya Rahmat-Samii, and Robert A. Shore, "Derivation and Application of the Equivalent Paraboloid for Classical Offset Cassegrain and Gregorian Antennas," *IEEE Trans. Antennas and Propagation,* Vol. 38, No. 8, Aug. 1990.

[39] S. Chang and A. Prata, Jr., "The Design of Classical Offset Dragonian Reflector Antennas with Circular Apertures," *IEEE Trans. Antennas and Propagation,* Vol. 52, No. 1, Jan. 2004.

[40] A. Monfardini, et al., *Astronomy & Astrophysics,* 521 A29, 2010; and A. Monfardini, et al., *Astrophysical Journal Supplements Series,* Vol. 194, Issue 2, June 2011.

[41] A. Luukanen, A. J. Miller, and Erich N. Grossman, "Active Millimeter-Wave Video Rate Imaging with a Staring 120-Element Microbolometer Array," *Proc. SPIE,* Vol. 5410, p. 195, 2004.

[42] I. Mehdi, B. Thomas, C. Lee, R. Lin, G. Chattopadhyay, J. Gill, N. Llombart, K. B. Cooper, and P. H. Siegel , "Radiometer-on-a-Chip: A Path Towards Super-Compact Submm Imaging Arrays," presented at *2010 SPIE Defense, Security and Sensing Conference,* Orlando, FL, April 5–9, 2010.

[43] M. C. Nuss and J. Orenstein, "Terahertz Time Domain Spectroscopy (THz-TDS)," in *Millimeter-Wave Spectroscopy of Solids*, G. Gruener, Ed. Springer, Berlin, 1997.

[44] N. Llombart, K. B. Cooper, and R. J. Dengler, "Terahertz Antenna System for a Near Video Rate Radar Imager," *IEEE Antenna Magazine*, Vol. 52, No. 5, pp. 251–259, Oct. 2010.

[45] A. Wehr and U. Lohrr, "Airborne Laser Scanning—An Introduction and Overivew," *ISPRS Journal of Photogrammetry & Remote Sensing,* Vol. 54, pp. 68–82, 1999.

[46] C. am Weg, W. von Spiegel, R. Henneberger, R. Zimmermann, T. Loeffler, and H. G. Roskos, "Fast Active THz Cameras with Ranging Capabilities," *J. Infrared Millim. Terahertz Waves*, Vol. 30, No. 12, pp. 1281–1296, 2009.

[47] R. Appleby et al., "Compact Real-Time (Video Rate) Passive Millimetre-Wave Imager," *Proc. SPIE,* Vol. 3703, pp. 13–19, 1999.

[48] A. Luukanen, P. Helisto, P. Lappalainen, M. Leivo, A. Rautiainen, H. Toivanen, H. Seppa, Z. Taylor, C. R. Dietlein, and E. N. Grossman, "Stand-Off Passive THz Imaging at 8-Meter Stand-Off Distance: Results from a 64-Channel Real-Time Imager," *Proc. SPIE*, Vol. 7309, p. 73090F, 2009.

[49] Erik Heinz et al., "Passive Submillimeter-wave Stand-off Video Camera for Security Applications," *J. Infrared Millim. Terahertz Waves,* Vol. 31, pp. 1355–1369, 2010.

[50] R. Anderton and A. Lettington, Scanning Apparatus, U.S. Patent No. 6587246.

[51] A. H. Lettington, N. E. Alexander, and D. Dunn, "A New Opto-Mechanical Scanner for Millimeter and Sub-Millimeter Wave Imaging," *Proc. SPIE*, Vol. 5789, pp. 16–23, 2005.

[52] J. A. Martinez-Lorenzo, A. Garcia-Pino, B. Gonzalez-Valdes, and C.M. Rappaport, "Zooming and Scanning Gregorian Confocal Dual Reflector Antennas," *IEEE Trans. Antennas and Propagation,* Vol. 56, No. 9, pp. 2910–2919, Sep. 2008.

[53] W. H. Steel, "The Design of Reflecting Microscope Objectives," *Australian Journal of Scientific Research, Series A: Physical Sciences*, Vol. 4, p.1, 1951.

[54] A. B. Shafer, L. R. Megill, and L. Droppleman, "Optimization of the Czerny-Turner Spectrometer," *J. Opt. Soc. Am.*, Vol. 54, pp. 879–886, 1964.

[55] C. S. Ih and K. Yen, "Imaging and Fourier Transform Properties of an All-Spherical-Mirror System," *Appl. Opt.,* Vol. 19, pp. 4196–4199, 1980.

[56] S. A. Schelkunoff, "Some Equivalence Theorems of Electromagnetics and Their Application to Radiation Problems," *Bell System Tech. J.,* Vol. 15, pp. 92–112, 1936.

[57] E. R. Brown "Fundamental of Terrestrial MM Wave and THz Remote Sensing," *THz Sensing Technology*, Vol. II, pp. 110, 2003.

CHAPTER 5

Multiband Reflector Antennas

Sudhakar Rao, Northrop Grumman Aerospace Systems

5.1 Introduction

Advanced reflector antennas supporting multiple frequency bands are required for both satellite and ground applications. These antennas have the advantages of reducing the number of reflectors, minimizing the mass, and significantly reducing the cost. The technical challenges are the reflector design, feed system supporting multiple frequency bands, and the feed assembly that separates the various frequency bands providing the desired isolation.

Conventional reflector antennas support either single or two frequency bands. Although parabolic reflector antennas are frequency independent, the feed systems have limited bandwidths. In addition, when the reflector shape is changed from the parabolic surface for shaped beam applications, the reflector also becomes band limited. Figure 5.1 shows two conventional methods of supporting two frequency bands from a common reflector antenna. The first method employs a subreflector that is made up of a frequency selective surface (FSS) to separate the low- and high-frequency band signals. The high band is reflective to FSS and therefore the high band uses the dual-reflector system. The low band is transmissive through the FSS subreflector, so single reflector optics are employed at the low band. The FSS in this case employs lowpass elements such as annular rings, cross-dipoles, or Jerusalem crosses etched on the subreflector. The Voyager spacecraft employed an S/X band Cassegrain antenna with FSS subreflector [1, 2]. Disadvantages of with this design include the loss associated with the FSS subreflector and the long coaxial line from the low-frequency feed to the back of the main reflector. The two bands have to be widely separated in order to minimize the losses due to FSS (typically > 2:1 bandwidth ratio). It also requires two feeds and a complicated FSS subreflector with limitations on the separation of the frequency bands.

The second method employs a dual-band feed and a single reflector. The high-frequency band uses a central waveguide, whereas the low frequencies are propagated through a coaxial structure [3]. The two conventional methods are illustrated in Figure 5.1. There are two separate feed points for the feed. This also requires

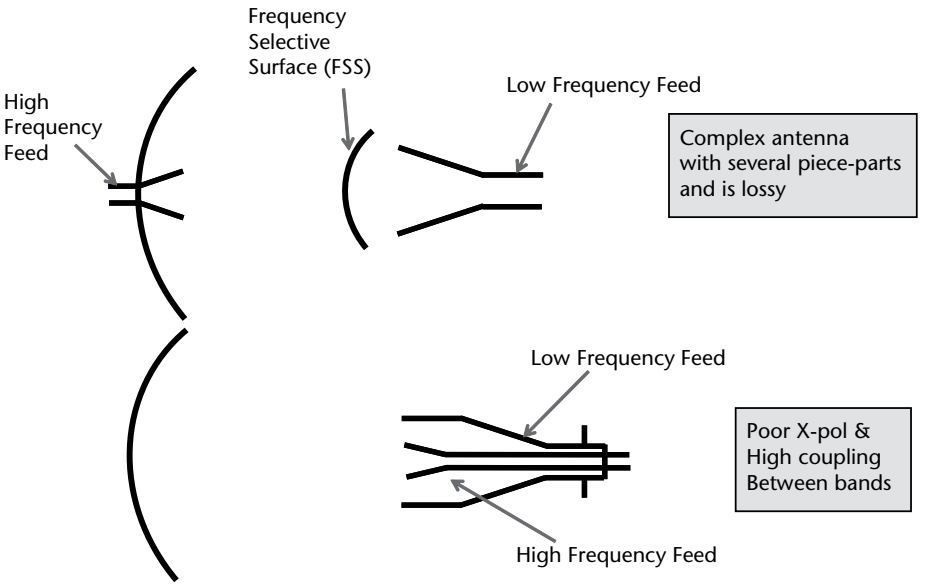

Figure 5.1 Conventional methods of generating dual-frequency bands using a common reflector antenna.

the two bands to be widely separated. The high-frequency signals leak through the outer coaxial structure, requiring either filters or absorbing material to suppress the coaxial modes at the high band. A disadvantage with this design is the poor cross-polar levels at the low-frequency band due to coaxial mode propagation that are unacceptable for space applications and most ground applications.

A number of recent developments related to advanced reflector antennas supporting multiple frequency bands are discussed in this chapter. The following developments include both reflectors and feeds:

- Dual-band antennas with a single-waveguide-type feed;
- Dual-band antennas with multiple feeds;
- Multiband antennas supporting several frequency bands;
- Stepped-reflector antennas;
- Antennas with reflective and partially reflective surfaces.

5.2 Dual-Band Reflector Antennas with Single Feeds

An advanced dual-band feed using a Cassegrain reflector is illustrated in Figure 5.2. This antenna has the advantage of covering two discrete bands that are separated up to the 3.5:1 bandwidth ratio and able to produce either similar beam shapes at two bands or different beam shapes at the two discrete bands. The bandwidth ratio is defined as the ratio of highest frequency of the highband to the lowest frequency of the lowband. To produce similar beam shapes at low and high bands, the feed needs to be designed with frequency-dependent radiation characteristics.

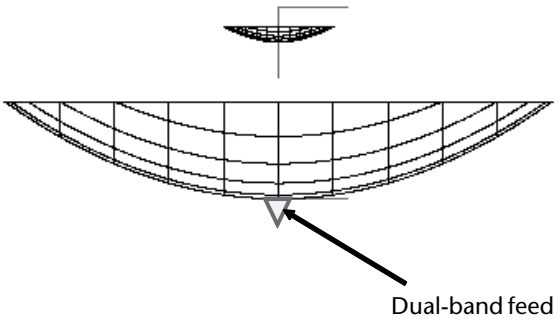

Figure 5.2 Advanced dual-band antenna with low loss. (© 2008 IEEE. From [5].)

Such a design produces a highly tapered amplitude distribution that might include sidelobes on the subreflector at the high band. In addition, the feed creates a phase distribution at the high band such that it has a 180-deg phase reversal at the outer portion of the subreflector. As a result, the secondary patterns from the antenna are significantly broadened at the high band and provide similar beam shapes at both bands that are widely separated in frequency [4].

The main challenge here is the feed system design, which is tasked with producing the desired frequency-dependent radiation characteristics. A corrugated horn can support dual bands with a limited bandwidth ratio of about 2:1, but cannot cover bands that are more widely separated than this. Also, corrugated horns have the disadvantages of increased mass due to thick corrugations. A smooth-walled multimode horn is more suited for such applications.

The reflector diameter is chosen to meet the desired gain and beamwidth requirements at the lowest frequency. The design of the horn is based on selecting the horn diameter that provides the desired illumination taper on the subreflector at the lowest frequency. An illumination taper of around 12 dB is optimum at the low band. For this application the aperture distribution is required to be more uniform at the low band and tapered at the high band. The feed horn synthesis process using mode-matching analysis was developed by Chan and Rao [5]. The required mode contents to create a tapered aperture distribution at the high band are chosen [5, 6]. Based on the mode content, the initial discontinuity points can be determined based on the mode cutoff wavelengths in a circular waveguide. Initial synthesizing of the horn geometry can be performed at the high band in order to provide the required illumination taper and gain at the high band. Final optimization of the horn's geometrical parameters can be performed by specifying the desired cost function at several frequencies, covering both the low and high bands, and synthesizing the horn using mode-matching analysis. The cost function includes desired performance parameters and can be defined as follows:

$$C_F = \sum_{i=1}^{N} \left\{ wt_r \left(\rho_i - \rho_{di}\right)^2 + wt_x \left(x_i - x_{di}\right)^2 + wt_a \left(\eta_i - \eta_{di}\right)^2 \right\} \tag{5.1}$$

where wt_r, wt_x, and wt_a are the weights of the error function for return loss, cross-polar level (relative to copolar peak), and efficiency; ρ_i and ρ_{di} are the computed and desired return loss values at a given frequency i; x_i and x_{di} are the computed and

desired cross-polar levels in the diagonal plane; and η_i and η_{di} are the computed and desired efficiency values. The parameters are expressed in decibels and an optimization routine is used to minimize the cost function by searching for the radii and slope at the break points in the horn profile.

The synthesized horn geometry is shown in Figure 5.3. It has four slope discontinuities in order to generate the desired radiation characteristic. The evaluated performance of the dual-band feed with BWR = 3.56 is shown in Table 5.1. The return loss is better than 29 dB, the axial ratio is better than 1.37 dB over the frequency band (cross-polar isolation is better than 22 dB), and the beamwidths are very close despite the wide frequency separation between the low and high bands.

The computed radiation patterns of the dual-band feed at the low and high bands are shown in Figures 5.4 and 5.5, respectively. The amplitude patterns shown in Figure 5.4 have a better than 12-dB illumination taper on the subreflector, and the phase patterns are mostly uniform with a maximum phase variation of 50 deg within the illumination angle of ±19 deg. The cross-polar levels are lower than –20 dB relative to copolar peak gain.

At the high band, the feed patterns shown in Figure 5.5 have an amplitude taper of a better than 17-dB illumination taper. The phase patterns show 180 deg phase reversal within the subreflector illumination region. This phase nonuniformity is required in order to broaden the secondary patterns.

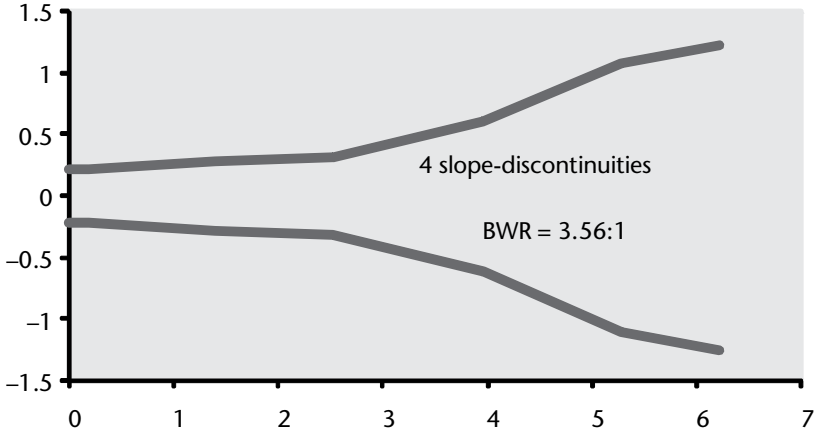

Figure 5.3 Geometry of the multimode horn covering a BWR of 3.56:1. (© 2005 IEEE. From [7].)

Table 5.1 Computed Performance of the Dual-Band Feed

Frequency	*Return Loss (dB)*	*Main Peak Gain (dBi)*	*Max AR (2 dB BW) (dB)*	*3 dB BW (deg)*
1.00	29.7	19.9	1.28	17.1
1.08	34.8	20.5	1.37	16.0
1.17	41.2	21.0	1.20	15.0
3.17	50.2	21.8	1.31	15.6
3.33	52.7	21.6	1.02	15.0
3.56	37.2	22.4	0.90	14.6

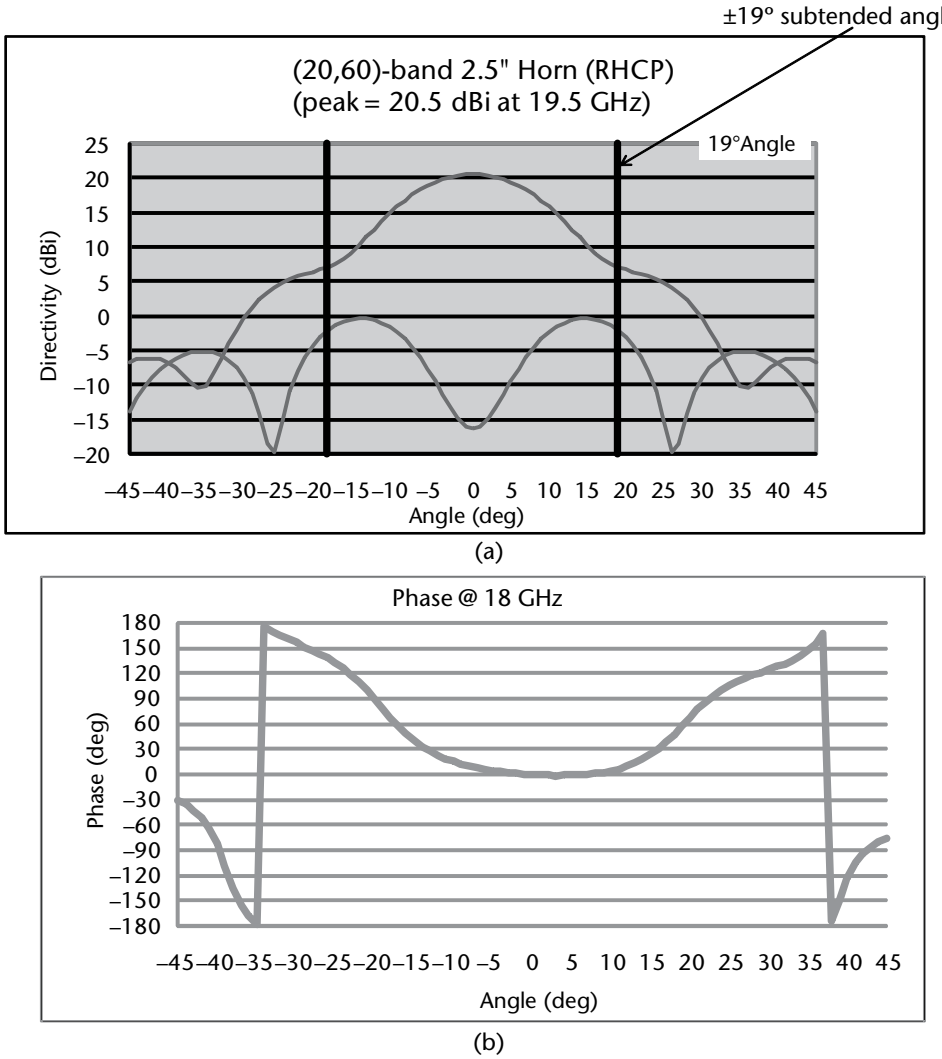

Figure 5.4 The amplitude and phase distributions of the dual-band feed on the subreflector at low band showing a >12-dB amplitude taper on the subreflector and small quadratic phase variation over the ±19-deg half subtended angle. (© 2010 IEEE. From [8].)

The computed secondary patterns at two frequencies at the low band and two frequencies at the high band are shown in Figure 5.6. The beam flattening at the high band is the result of the nonuniform phase from the feed, and it makes the antenna beamwidths at both the high and low bands similar. The peak gain values are better than 48 dBi over both bands. The cross-polar isolation is better than 26 dB over the half-power beamwidth of the antenna. This dual-band antenna has the advantages of lower cost, feed simplicity, and beam congruency over both bands.

5.3 Dual-Band Reflector Antennas with Multiple Feeds

Dual-band reflector antennas for multiple-beam applications have been extensively employed for satellites supporting personal communication services. These systems

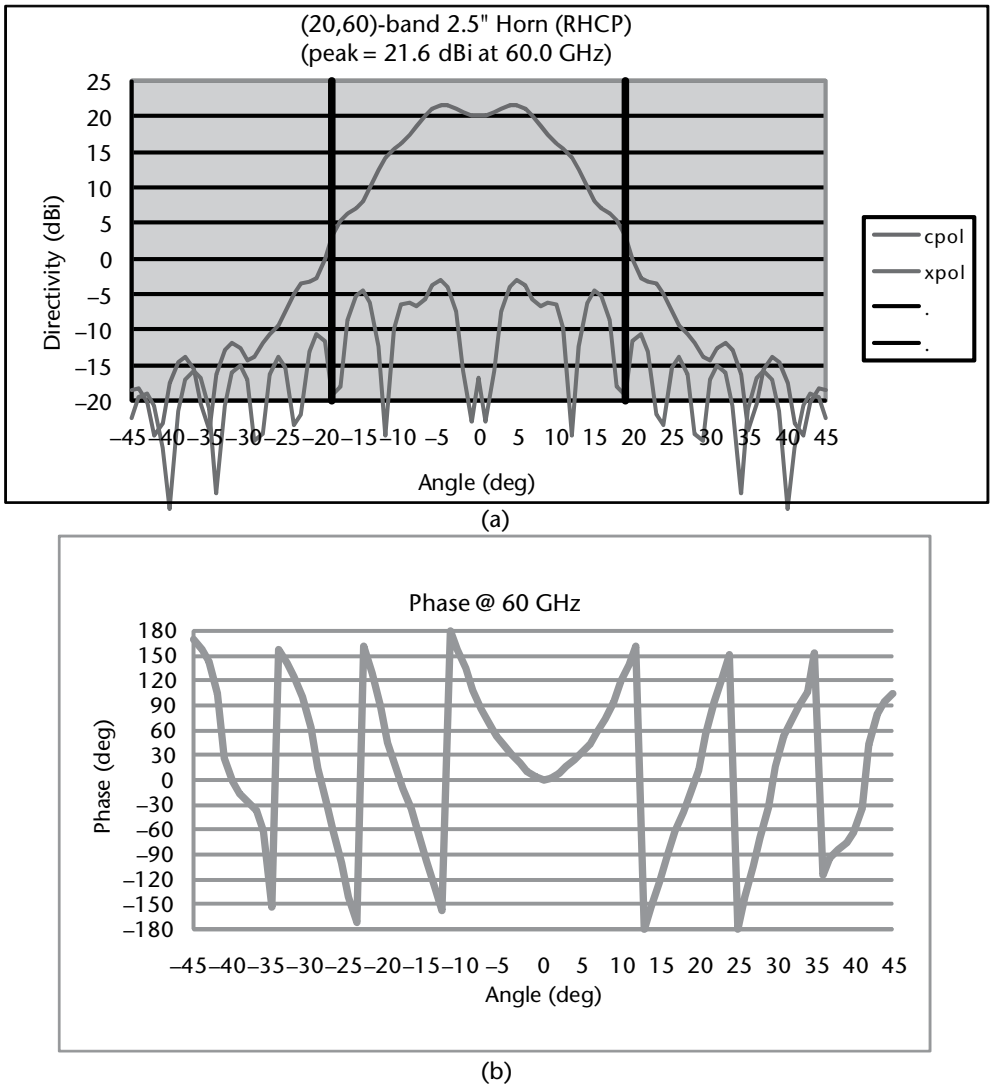

Figure 5.5 The amplitude and phase distributions of the dual-band feed on the subreflector at the high band showing 180-deg phase reversal. (© 2008 IEEE. From [9].)

are used to provide communications among several users that are spread over a given coverage region by using multiple overlapping beams [7, 8]. Communications among users is established through the ground hubs and the satellite. The users establish communication with other users using a two-way communication link via satellite and the hubs through forward (hub uplinks, satellite downconverts and downlinks to users) and return links (user uplinks to satellite, satellite downconverts and downlinks RF signals to hub). Each beam is generated using a single feed that transmits to and receives from the ground the RF signals via the reflector antenna.

A four-reflector system is typically used to generate all of the desired beams, as explained before in Section 2.3. An exemplary beam layout over the continental United States (CONUS) is shown in Figure 5.7. It employs 68 overlapping spot

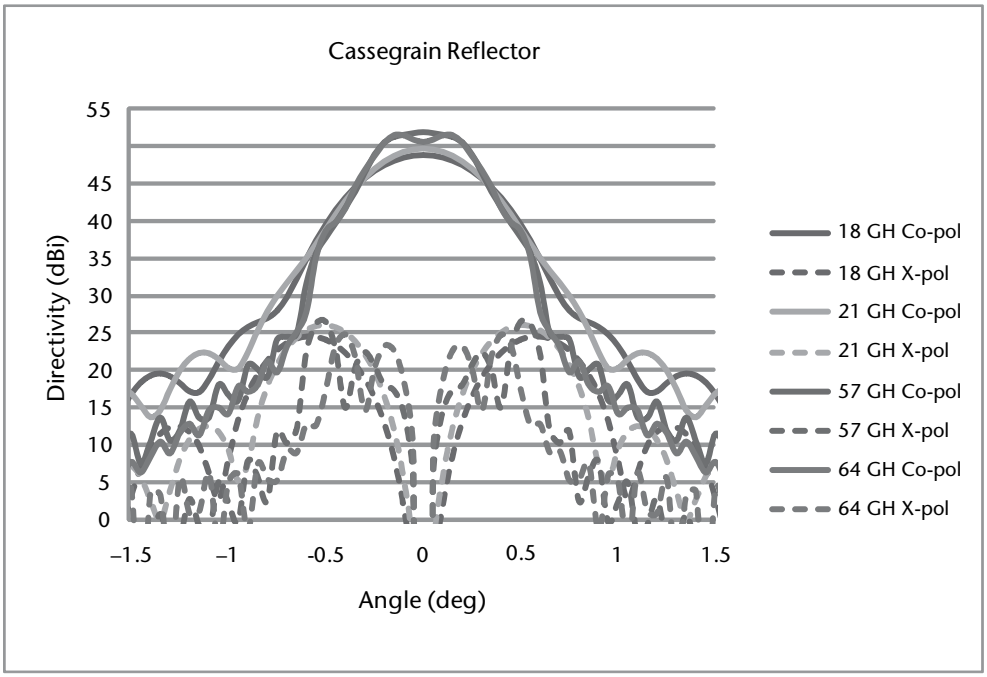

Figure 5.6 Radiation patterns of dual-band feed producing similar shapes at two widely separated bands.

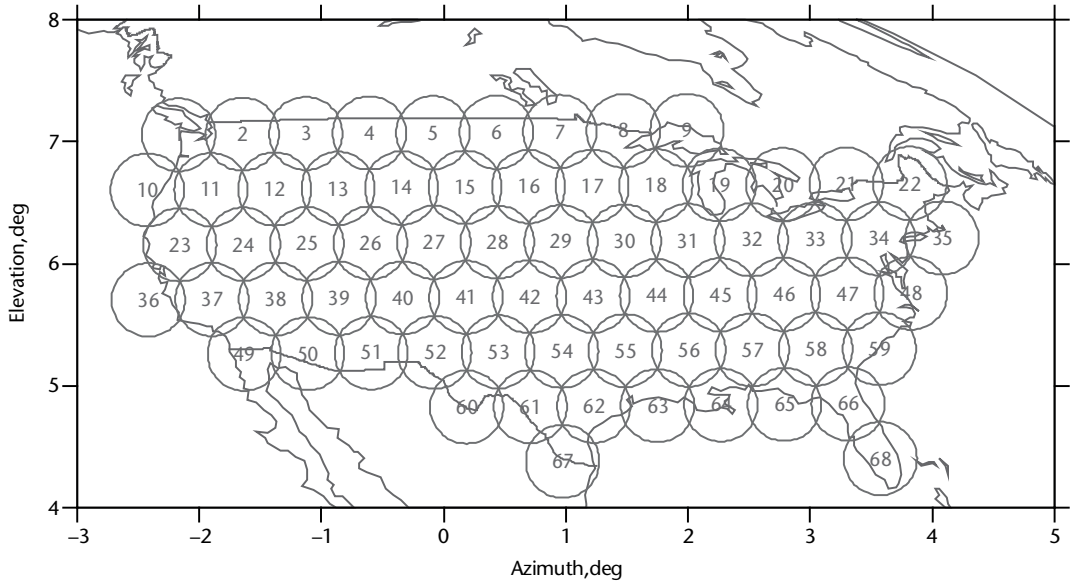

Figure 5.7 Beam layout over the CONUS for a dual-band multiple-beam antenna.

beams of 0.6 deg in diameter over the CONUS region with beam spacing of 0.52 deg. The transmitting (Tx) band is 18.3 to 20.2 GHz and the receiving (Rx) band is 28.3 to 30.0 GHz. Element diameter is dictated by the beam spacing among reuse beams (in this case it is two times the interbeam spacing) and the beam deviation

factor (sometimes referred to as scan factor) that is dictated by the offset reflector geometry (see Section 2.3.4). The feed diameter is 2.27 in. and synthesized geometry is shown in Figure 5.8.

Radiation patterns of the dual-band horn providing high efficiency values over the Rx and Tx bands are shown in Figures 5.9 and 5.10, respectively. Computed values are based on mode-matching software and agree well with the measured values. Return loss, efficiency, and cross-polar levels of the dual-band horn are summarized in Table 5.2. A number of dual-mode horns are used to illuminate each of the four reflector multiple-beam antennas (MBAs) (see Section 2.3.5) to generate the 68 overlapping spot beams on the ground, as shown in Figure 5.7. The reflector antenna geometry shown in Figure 5.11 has an 80-in. diameter, an *F/D* of 1.45, and an offset clearance height of 26 in.

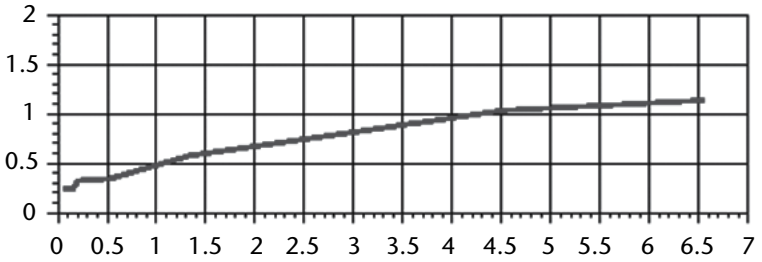

Figure 5.8 Synthesized multiflare horn geometry of dual-band feed supporting K- and Ka-band frequencies.

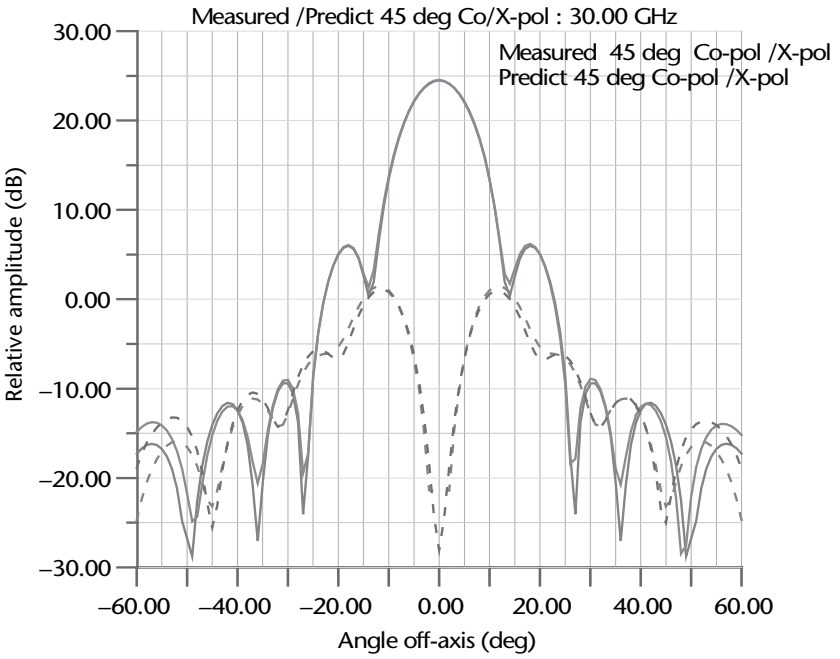

Figure 5.9 Radiation patterns of the dual-band horn at the Rx band.

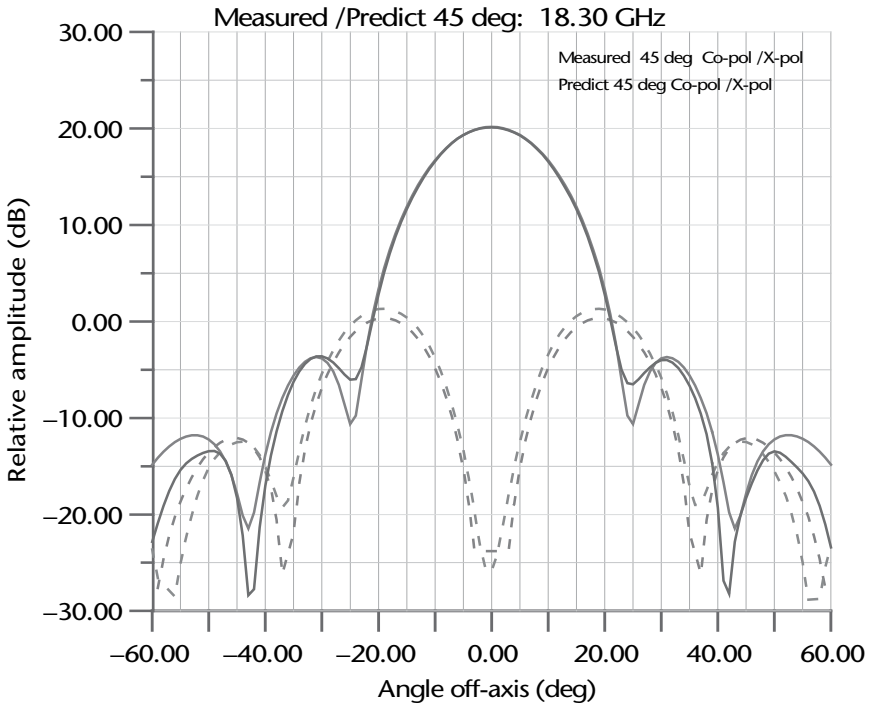

Figure 5.10 Radiation patterns of the dual-band horn at the Tx band.

Table 5.2 Performance Summary of the Dual-Band K/Ka Horn

Frequency	*Directivity (dBi)/ Efficiency*		*Cross-Polar (dB)*		*Return Loss (dB)*	
(GHz)	*Predict*	*Measured*	*Predict*	*Measured*	*Predict*	*Measured*
18.30	20.08 (83.4%)	20.10 (83.8%)	19.8	18.8	30.6	30.8
19.30	20.60 (84.5%)	20.60 (84.5%)	20.5	20.5	26.5	25.7
20.20	21.05 (85.6%)	21.1 (86.6%)	20.6	20.7	24.2	24.2
28.30	23.89 (83.9%)	23.8 (82.1%)	24.1	23.1	30.8	29.0
29.20	24.23 (85.2%)	24.2 (84.6%)	26.0	24.2	33.0	34.7
30.00	24.46 (85.1%)	24.5 (85.9%)	23.0	24.4	36.3	27.6

The antenna radiation patterns for a typical beam computed for various dual-band horn designs are shown in Figures 5.12 and 5.13. A high-efficiency horn helps to improve peak and edge-of-coverage gain (design –F) at the Tx band while reducing the peak gain and improving the edge-of-coverage gain at the Rx band; this feature is desired due to the fact that the reflector is oversized for Rx frequencies. The main beam rolloff and sidelobe patterns in Figure 5.13 indicate that the Tx sidelobe levels are lower with a high efficiency horn by about 3 dB, which helps

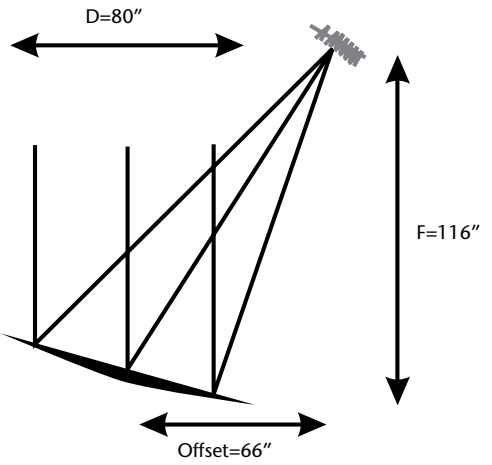

Figure 5.11 Reflector antenna geometry with multiple feeds (one of the four reflectors needed for the MBA is shown).

in copolar isolation when used with a typical four-cell frequency reuse scheme for multiple-beam antennas (see Section 2.3.5 for more details). The antenna edge-of-coverage gain for various horn designs is plotted in Figure 5.14 at the transmitting and receiving frequencies. Primary and secondary performances of dual-band MBAs are summarized in Table 5.3. Note that the high-efficiency horn improves gain over the Tx band by about 0.9 dB and improves gain by 2.0 dB over the Rx band relative to the conventional corrugated horn. More importantly, the Tx copolar isolation (C/I) is improved with the high-efficiency horn (HEH) by about 3.7 dB with a four-cell scheme with 1.2 dB of degradation in Rx C/I (it is noted that Rx C/I is less critical than Tx C/I).

5.4 Multiband Antennas Supporting Several Frequency Bands

The satellite payloads are progressively becoming more complex and support multiple services from a single satellite. This is made possible due to the advent of high-power satellites developed by several satellite manufacturers with DC power ranging from 12 to 20 kW. In addition, the recent trend toward the hosted payloads that combine the commercial payload with government payloads in a single satellite for cost reduction have created demand for the multiband antennas. A few examples of multiband antennas are described below.

5.4.1 Tri-Band Antenna

A single antenna supporting three bands covering 20, 30, and 45 GHz has been described [9, 10]. These three frequency bands potentially combine the existing Wideband Global Satellite (WGS) and Advanced EHF (AEHF) satellite into one large satellite in the future. It is designed to provide a 1.0-deg beam at 20 and 30 GHz and a 0.5-deg beam at 45 GHz. The antenna geometry is shown in Figure 5.15. It employs a 44-in. offset reflector with a focal length of 54 in. and an offset clearance of 18 in. It is fed with a tri-band multiflare horn as shown in Figure 5.16.

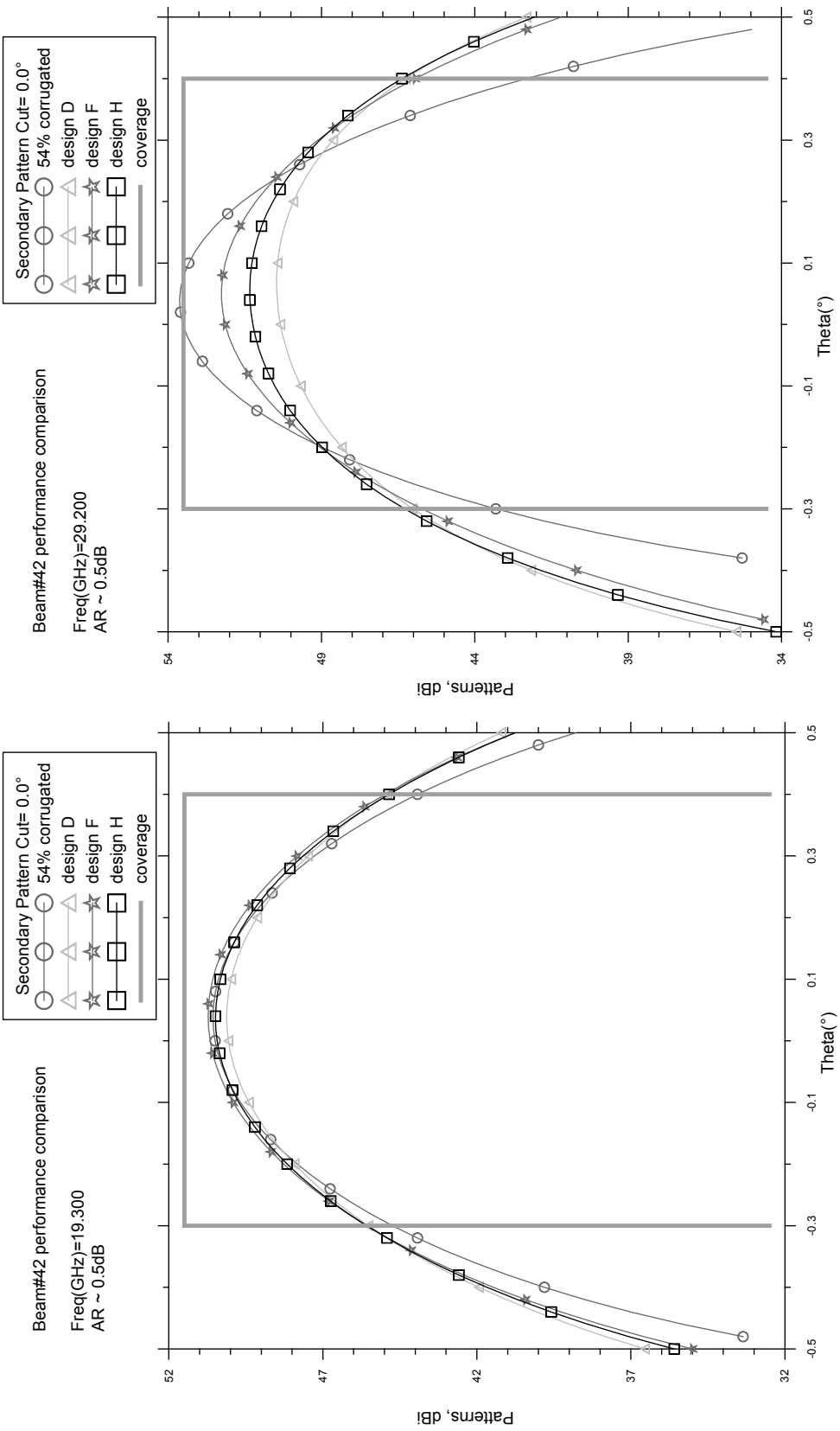

Figure 5.12 Radiation patterns of the single-offset reflector antenna with dual-band horn at the K- and Ka-bands. The various curves shown indicate different horn designs.

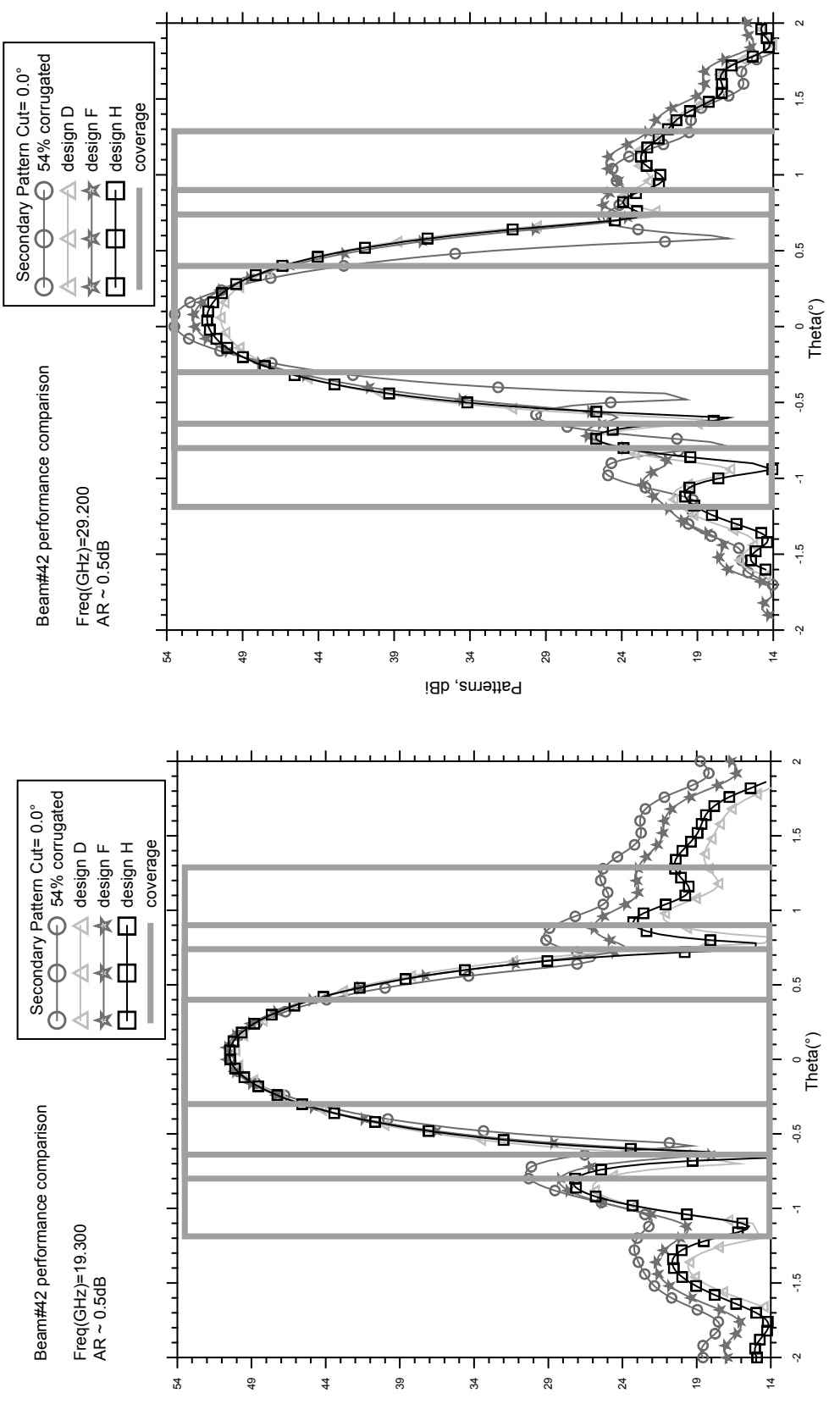

Figure 5.13 Radiation patterns of the single-offset reflector antenna showing sidelobes with a dual-band horn at the K- and Ka-bands. The various curves shown indicate different horn designs.

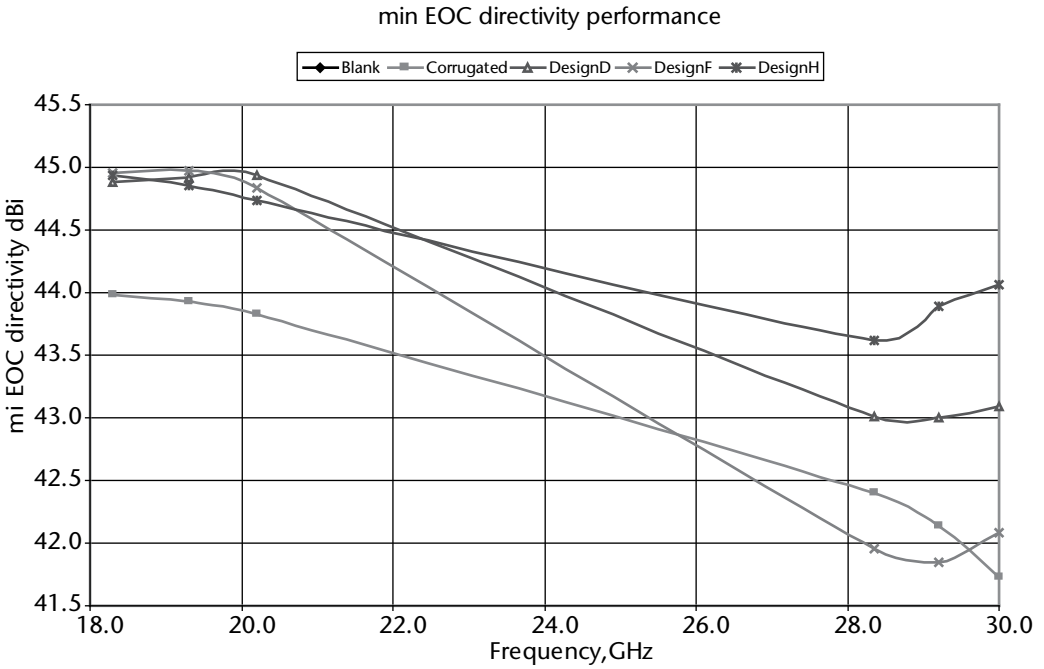

Figure 5.14 Edge-of-coverage gain performance of the multibeam reflector antenna with a dual-band horn at the K- and Ka-bands. The various curves shown indicate different horn designs.

Table 5.3 Performance Comparison of Dual-Band MBA for Two Different Horn Designs

Performance Parameter	*Conventional Horn (Corrugated)* TX/RX	*High Eff. Horn Design H* TX/RX
Efficiency %	54/52	85/85
Edge Taper, dB	7/18	13/17
Primary C/X, dB	33/33	20/23
EOC Directivity, dBi	43.8/41.7	44.7/43.7
C/I, 3-cell (dB)	11.1/13.0	14.2/11.6
C/I, 4-cell (dB)	12.0/15.8	15.7/14.5
C/I, 7-cell (dB)	18.2/19.5	22.7/21.9
C/X, dB	30.0/28.0	21.0/20.0

The feed aperture needs to be moved by about 3 in. toward the reflector in order to improve the overall performance of the tri-band antenna. This is due to the fact that the phase center of the horn at 45 GHz is inside the horn and located close to 3 in. inside the horn relative to the horn aperture. The computed performance of the tri-band antenna is summarized in Table 5.4 with no defocusing of the feed and a 3.0-in. defocusing. With the defocusing, the overall antenna gain and cross-polar levels are improved. Radiation patterns of the tri-band antenna are plotted in Figure 5.17. These patterns are computed with 3-in. defocus of the feed and provide efficient gain and cross-polar levels of lower than –20 dB. The tri-band antenna

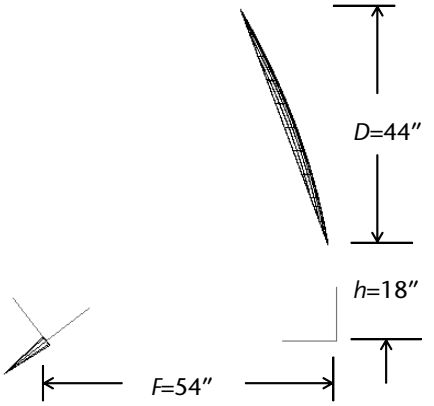

Figure 5.15 Reflector geometry for a tri-band antenna.

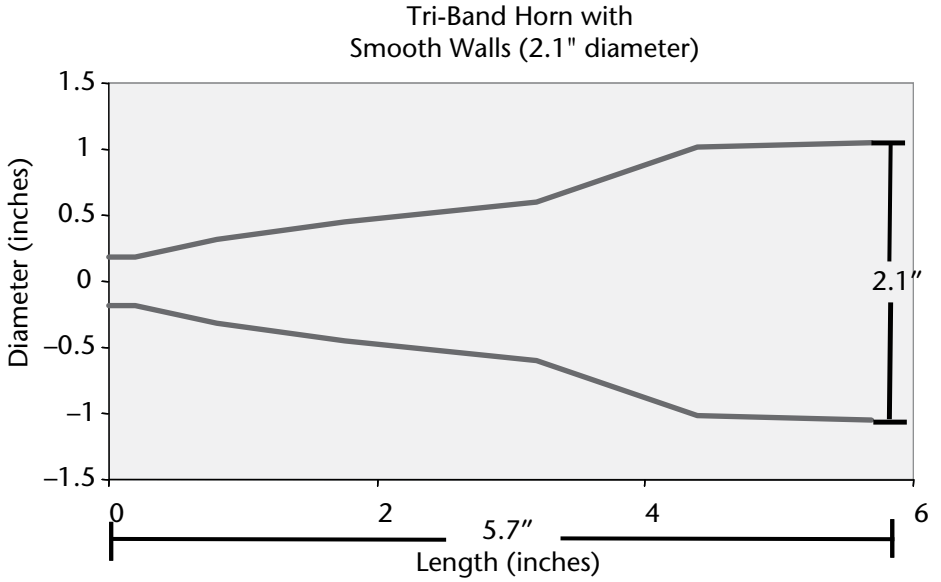

Figure 5.16 Tri-band horn geometry covering the K-, Ka-, and EHF bands.

provides congruent beams at the three bands with no differential pointing among them. This is another advantage of the tri-band antenna compared to separate antennas. The beams can be scanned over the Earth's field of view by gimbaling the main reflector by about ±5 deg and keeping the feed system stationary.

5.4.2 Multiband Antenna Supporting Five Frequency Bands

An antenna system supporting five frequency bands and three satellite services has been described recently [4, 11]. The three satellite services include direct broadcast satellite (DBS), reverse DBS (RDBS), and personal communication satellite (PCS). With the approval of RDBS bands by the Federal Communications Commission (FCC), the future satellites are expected to utilize the RDBS services in addition to DBS and PCS services. RDBS service uses the same frequency band for the Tx as

Table 5.4 Gain and Cross-Polar Summary of the Tri-Band Antenna With and Without Feed Defocus

		Defocus=0"		*Defocus=3.0"*	
Frequency (GHz)	*Coverage (degrees)*	*Cross-Polar (dB)*	*C/X (dB)*	*Cross-Polar (dB)*	*C/X (dB)*
20.7	±0.5°	41.2	19.7	41.3	21.8
30.5	±0.5°	40.8	24.7	40.1	24.2
44.5	±0.25°	45.6	16.9	46.7	20.0

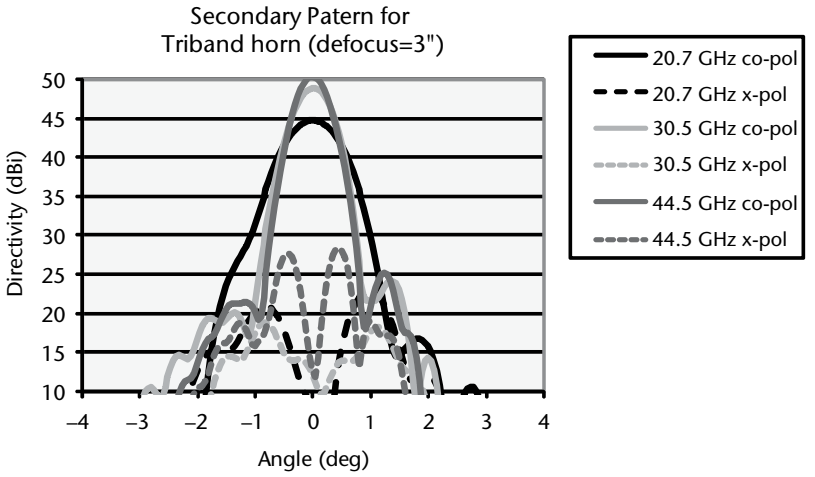

Figure 5.17 Radiation patterns (copolar and cross-polar) of the tri-band antenna at the K-, Ka-, and EHF bands.

the Rx band of the DBS. The Rx band for RDBS is the new 25 GHz that has been recently allocated by the FCC. Therefore, either DBS or RDBS service is supported at a given time along with the PCS and hence four frequency bands out of five are operational at a given time.

The synthesized multiflare horn with seven slope discontinuities is shown in Figure 5.18. The performance summary at five bands is shown in Table 5.5. Return loss is better than 26.5 dB, cross-polar levels are lower than –22 dB relative to co-polar peak gain, and efficiency values range from 74% to 82% over the five bands.

The computed radiation patterns of the multiband horn are shown in Figure 5.19. When used with the reflector, the phase patterns of the horn are important and could be used to improve the secondary patterns by changing the location of the horns relative to the focal plane for multiple beams or focal point for a single beam application. The phase patterns of the multiband horn are plotted for two positions of the horn in Figure 5.20. The first position is when the horn aperture coincides with the focal point or focal plane of the reflector (no defocus) and the second position is the optimized location when the horn is moved toward the reflector from the focal plane by 1.0 in.

The peak gain as a function of defocus distance is plotted in Figure 5.21. Larger defocus is better at high bands and no defocus is better at the lowest frequency. A 1.0 in. defocus is optimum over all five bands. Computed radiation patterns of a 100 in.-diameter offset reflector with 1.0-in. defocus are plotted in Figure 5.22.

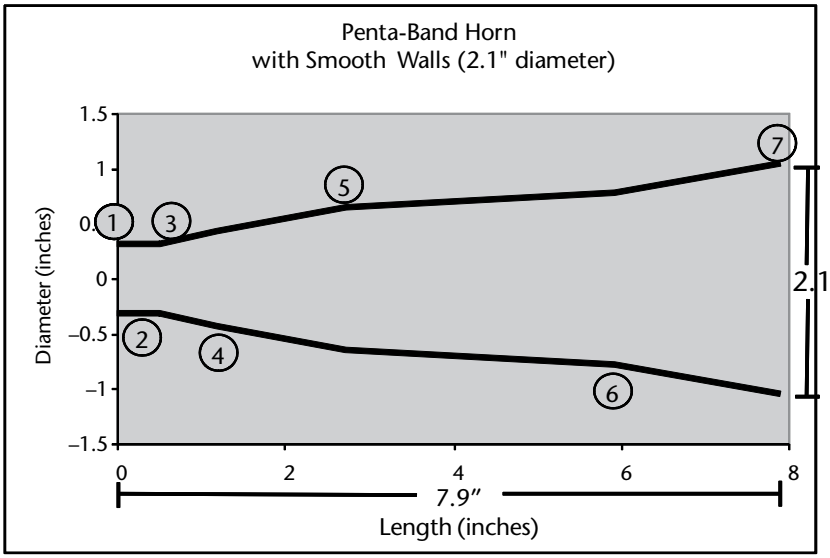

Figure 5.18 Multiflare smooth-walled horn with seven "slope-discontinuities" and the supporting five frequency bands.

Table 5.5 Performance Summary of the Multiflare Horn Supporting Five Frequency Bands.

Frequency (GHz)	*Return Loss (dB)*	*Cross-Polar (20°) (dB)*	*Efficiency (%)*
12.5	26.5	–22.3	82
17.3	48.0	–22.5	80
17.8	50.2	–23.6	80
18.4	43.6	–23.6	79
20.2	41.7	–22.1	76
24.8	50.1	–23.0	76
25.3	44.3	–23.7	76
28.5	44.0	–23.9	75
30.0	45.2	–22.1	74

The summarized performance in Figure 5.22 shows that better overall gain performance is achieved with 1.0 in. defocus. Peak gain values of 49.0 to 53.6 dBi are achieved over the five bands with edge-of-coverage gains ranging from 47.4 to 50 dBi over the bands. The cross-polar isolation (C/X) is very high at low bands and varies from 32.8 to 18.4 dB over the bands. For PCS service at 30 GHZ, a C/X of 18.4 dB is good because the interference is dominated by the copolar isolation (C/I), which is typically about 14 dB.

Figure 5.23 shows beam layout for DBS, RDBS, and PCS services over CONUS covering the top 40 designated market areas (DMAs). It requires 26 spot beams generated using four 100 in. reflectors where each reflector provides six to seven beams. The computed minimum gain contours at 12.45 GHz for all beams on one reflector are all plotted in Figure 5.24. All beams reuse the same frequency and the

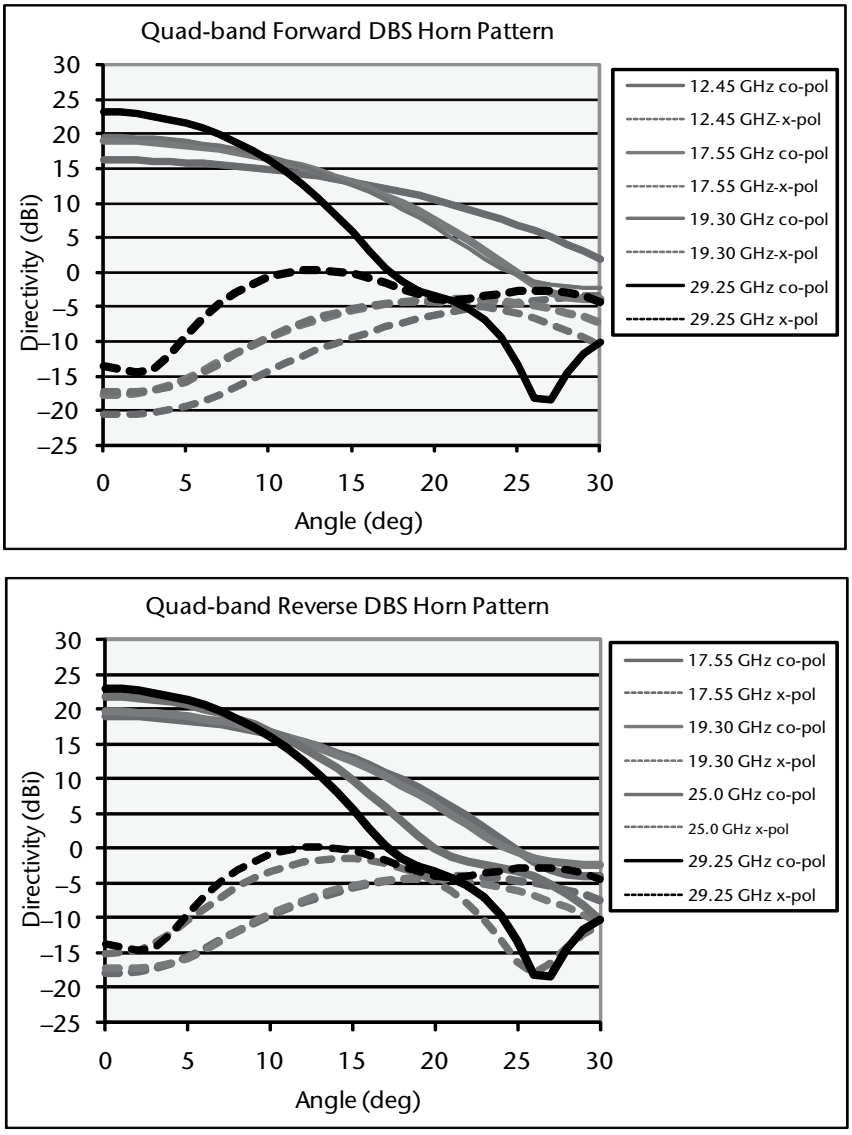

Figure 5.19 Radiation patterns of the multiflare horn at five bands. The X-axis is the polar angle θ from the antenna boresight direction.

worst-case copolar isolation (C/I) is shown as an inset in Figure 5.24. The C/I is better than 21 dB. The Tx and Rx beam plots for PCS are shown in Figures 5.25 and 5.26, respectively. The C/I values are better than 25 dB at both bands.

The overall performance of the multiband antenna over five frequency bands is summarized in Table 5.6. The feed assembly is the key hardware for these types of antennas that separate multiple frequency bands through filters and diplexers and provide dual circular polarization at each band. The feed assembly concept is illustrated in Figure 5.27. The lowest frequency band of 12 GHz is separated out through a symmetrical junction using four waveguide slots and four filters that reject all high band signals. The outputs of the four lowpass filters are combined through two H-plane junctions and a 3-dB hybrid coupler to produce dual CP

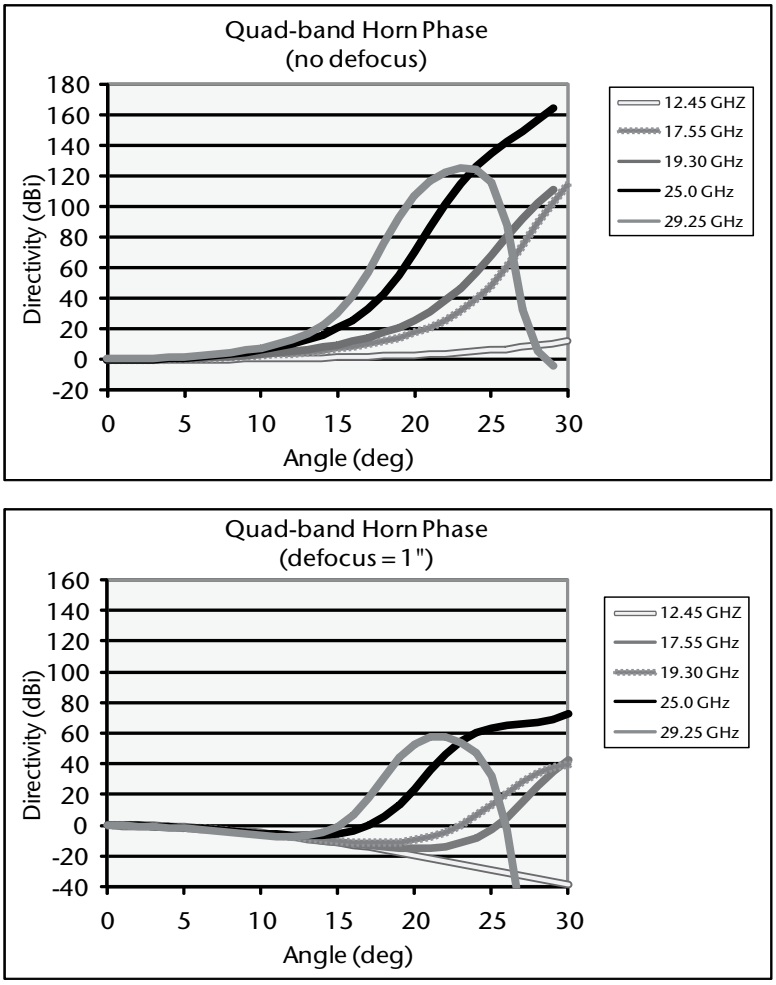

Figure 5.20 Axial defocusing effect of the horn phase patterns (1-in. defocus of feed is optimum). The X-axis is the polar angle θ from the antenna boresight direction.

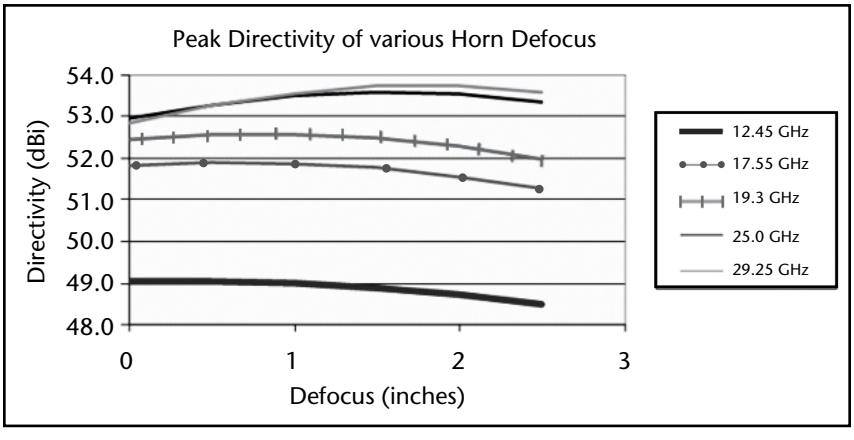

Figure 5.21 Impact of feed defocus on the antenna gain.

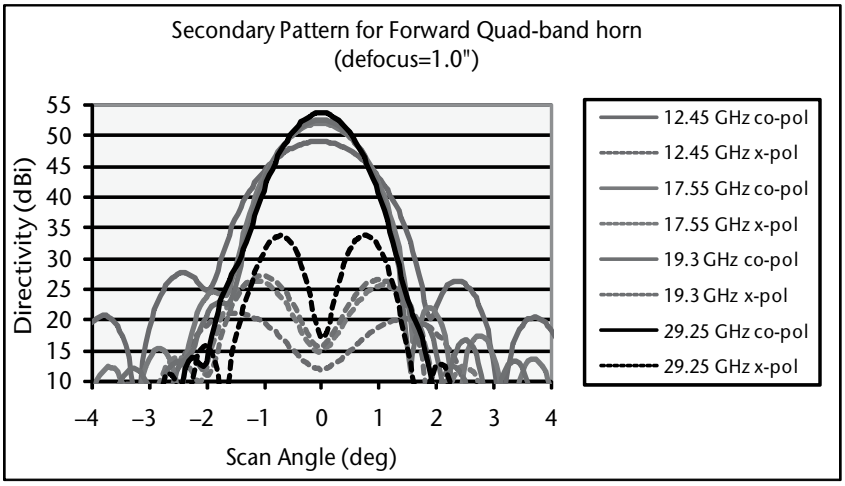

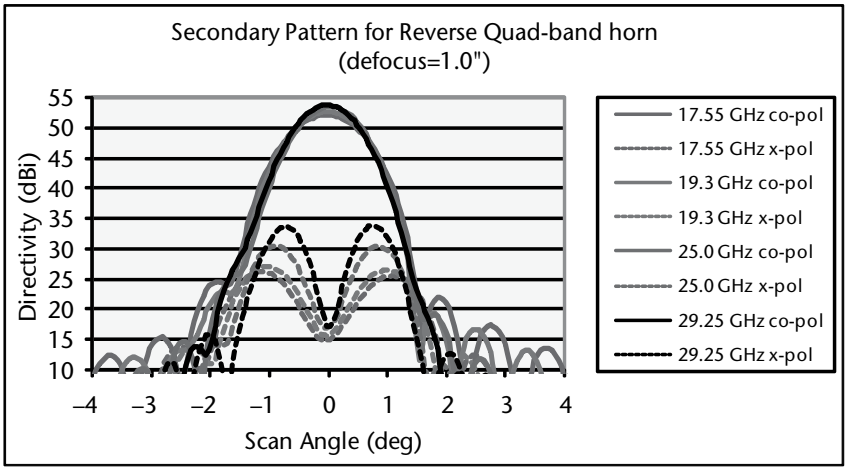

EOC Directivity

Freq	Coverage	Peak	Co-pol	C/X
12.45	±0.5°	49.0	47.4	32.8
17.55	±0.5°	51.9	49.5	28.7
19.30	±0.5°	52.6	49.8	27.4
25.00	±0.5°	53.5	50.1	23.3
29.25	±0.5°	53.6	50.0	18.4

Figure 5.22 Secondary radiation patterns of the multiband antenna with 1.0-in. defocusing of the feed (feed aperture plane is 1.0 in. toward the reflector relative to the focal plane).

ports at the Ku-band. A step in a circular waveguide after the first symmetric junction cuts off the Ku-band signals and passes the remaining four higher bands. The second symmetric junction after the step separates the 17 GHz and 20 GHz signals through four filters that act as shorts at the 25 GHz and 30 GHZ bands. The separated 17 GHz and 20 GHz signals are further isolated using two diplexers, one for each polarization. The second step in the circular waveguide acts as a short for the 17 GHz and 20 GHz signals and passes only 25 GHz and 30 GHz signals to the right of the junction. A septum polarizer is used to generate dual-CP and two diplexers are used to separate the 25 GHz and 30 GHz signals. Precise manufacturing

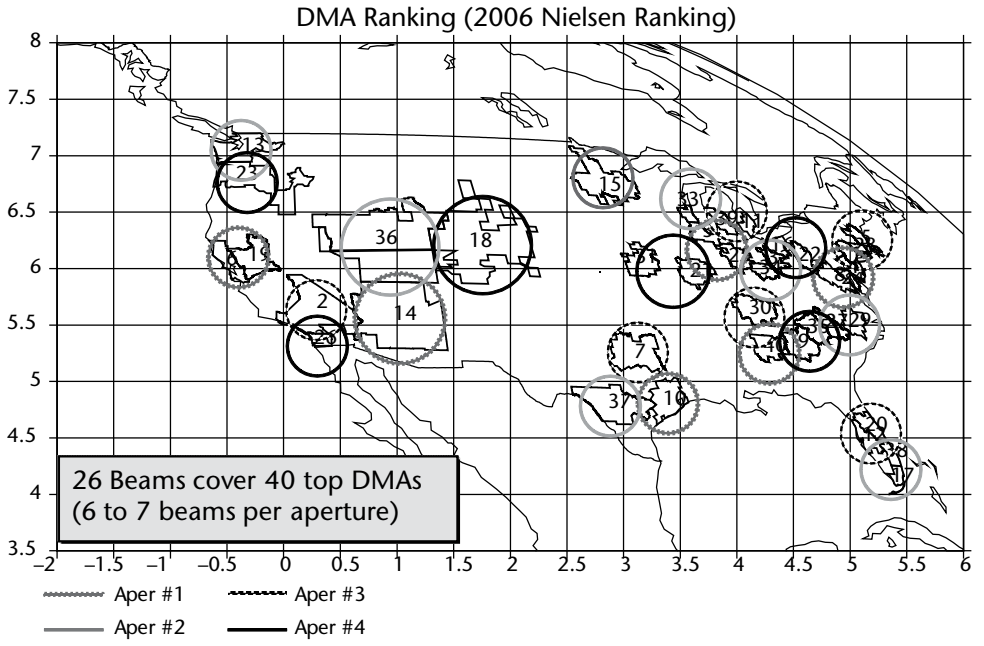

Figure 5.23 Example of multiple-beam antenna supporting DRS, RDBS, and PCS. Twenty-six beams are used to support the top 40 DMAs. The X- and Y-axes of the plot are the azimuth and elevation angles as seen from the satellite.

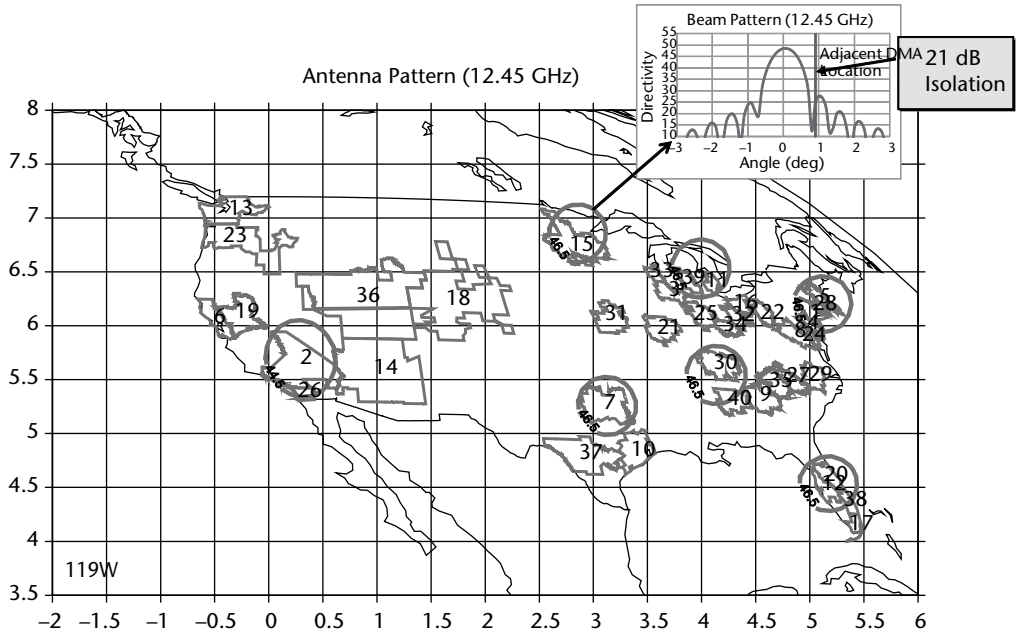

Figure 5.24 Gain contours of the multiband antenna (one of the four reflector beams shown) for DBS. The X- and Y-axes of the plot are the azimuth and elevation angles as seen from the satellite.

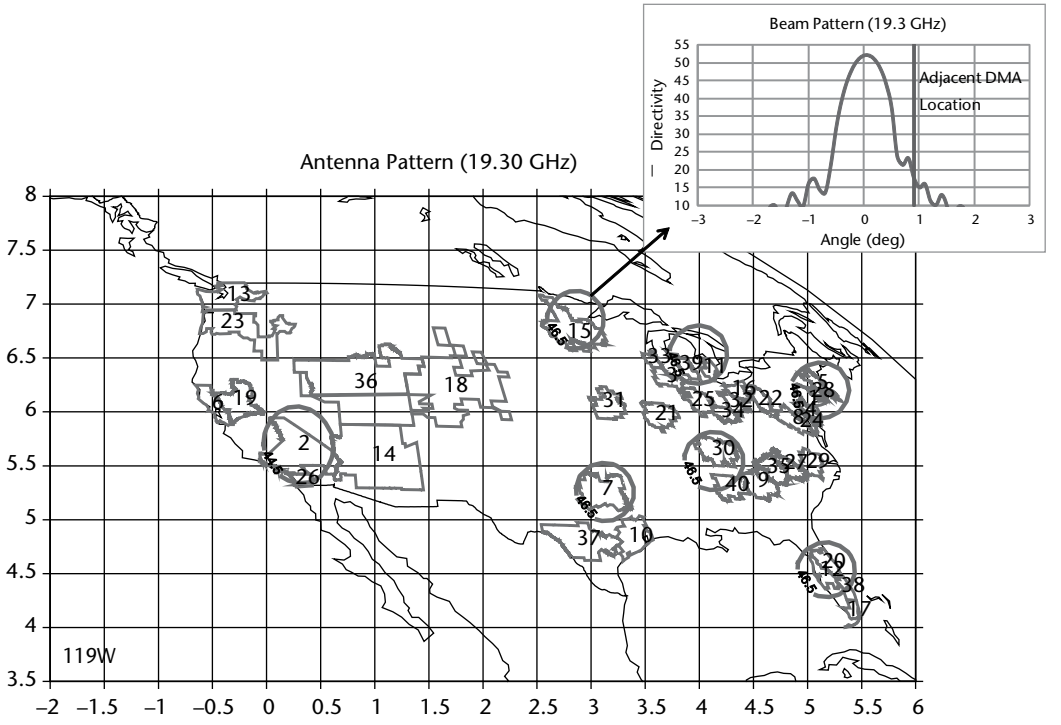

Figure 5.25 Gain contours of the multiband antenna (one of the four reflector beams shown) for the PCS Tx band. The X- and Y-axes of the plot are the azimuth and elevation angles as seen from the satellite.

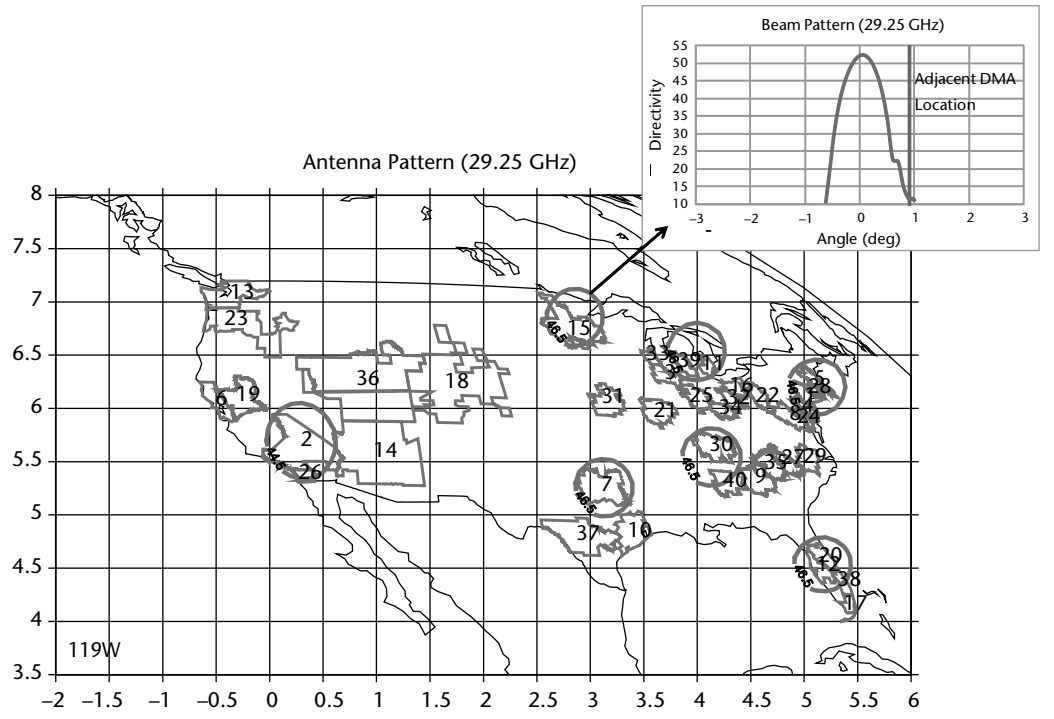

Figure 5.26 Gain contours of the multiband antenna (one of the four reflector beams shown) at the PCS Rx band (29.25 GHz). The X- and Y-axes of the plot are the azimuth and elevation angles as seen from the satellite.

Table 5.6 Performance Summary of the Multiband Antenna with Forward DBS and Reverse DBS Bands (Four Bands at a Given Time)

Forward DBS			*Reverse DBS*		
Frequency (GHz)	*EOC (dBi)*	*C/X (dB)*	*Frequency (GHz)*	*EOC (dBi)*	*C/X (dB)*
12.45	46.0	29.9	17.55	47.0	24.3
17.55	47.0	24.3	25.00	46.6	18.9
19.30	47.0	23.3	19.30	47.0	23.3
29.25	46.2	15.2	29.25	46.2	15.2

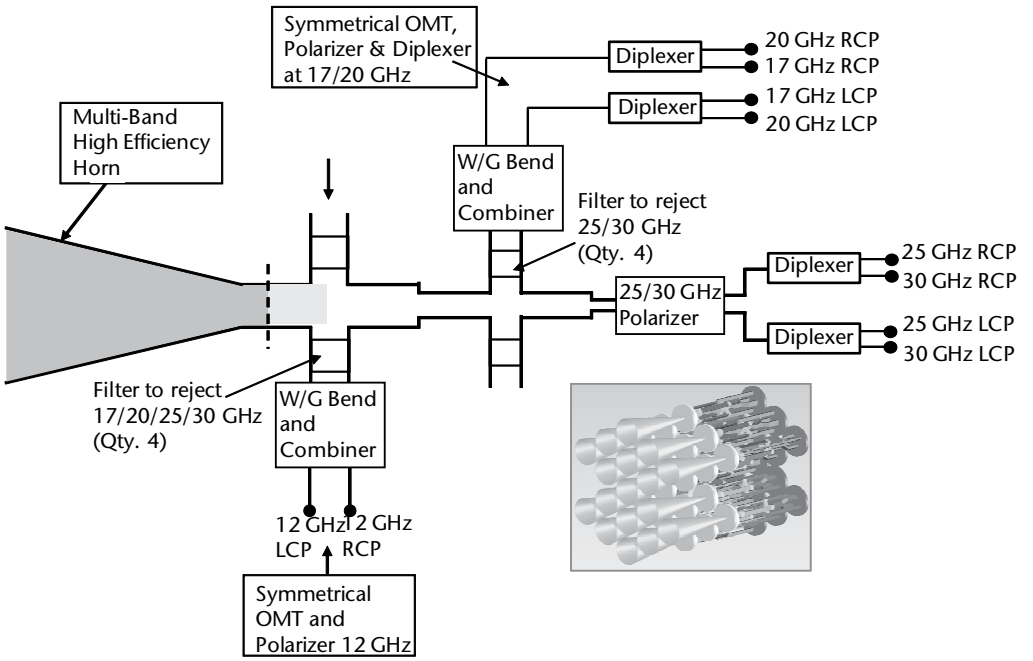

Figure 5.27 Illustration of the feed assembly block diagram separating the five bands using OMTs, filters, and diplexers with 10 beam ports and dual-CP capability at each band. (Inset: the feed array concept for MBA, courtesy of Custom Microwave Inc.)

using electroforming combined with RF analysis of the feed assembly, including the horn, enables the design and manufacture of feed assemblies that meet the stringent requirements needed for such antennas.

5.5 Stepped-Reflector Antenna

A stepped-reflector antenna (SRA) suitable for dual-band and multiple-frequency band applications has been reported recently [12–14] for multiple-beam applications. This advanced antenna utilizes reflector improvements in addition to the horn improvements that were described earlier in this chapter. A typical reflector antenna supporting 20 GHz and 30 GHz frequencies has dissimilar beamwidths at the two bands, with the high-frequency band beamwidth being smaller by about 50% compared to the low-frequency band beamwidth.

Because both bands need to cover the same area on the ground, the beamwidths have to be similar. By using a step near the outer annular region of the reflector, a 180-deg phase reversal is obtained between the inner and outer regions, thereby broadening the beam. The step height h can be designed to be a quarter wavelength at the high band, However, a quarter wave height at the high band results in about 0.17λ at the low band and impacts the low band's performance. To have a minimal impact at the low band, a frequency-dependent horn needs to be designed that produces Gaussian phase patterns at the high band while producing a near uniform phase at the low band. The combination of feed phase and reflector phase contribution can be made quarter wave at the outer annular region, which results in a smaller step size. This concept is illustrated in Figure 5.28 and has also been described in Section 2.3.5.

The SRA consists of a hybrid reflector having a central portion that is either parabolic or shaped and an outer annular ring(s) that is (are) either parabolic or shaped. The reflector size is larger than the conventional design without the step and is required to create a "flat-top" beam. Use of a slightly larger reflector is not a problem at higher frequency bands. With the combination of step height and the feed quadratic phase variations, a 180-deg phase reversal is obtained in the reflector illumination near the step region at the high band. Such a nonuniform phase distribution at the reflector aperture results in a flat-top beam shape that broadens the main beam at the high band. The flat-top beam at the high band has the advantages of higher edge-of-coverage (EOC) gain by more than 1.0 dB, improved copolar isolation (C/I) by about 3 dB, and reduced gain loss due to satellite pointing errors. The computed patterns of the SRA with and without the step ring are

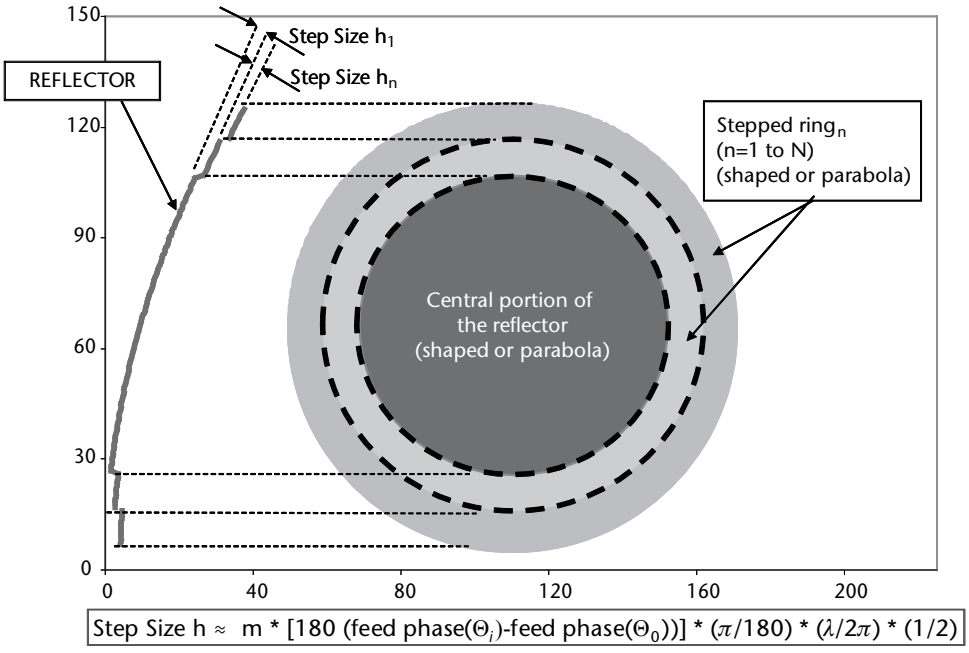

Figure 5.28 Stepped-reflector antenna concept for dual and multiple bands.

shown in Figure 5.29. The step lowers the peak gain and improves the EOC gain by about 1.0 dB at the high band without impacting the low band's performance.

The computed radiation patterns for multiple beams are shown in Figures 5.30 and 5.31 for the low and high bands, respectively. The beam is Gaussian in shape at the low band and flat-top at the high band, resulting in EOC gain improvements in both bands. The SRA can be extended to more than two bands and can be optimized with multiple steps.

5.6 Reflector Antenna with Reflective and Partially Reflective Surfaces

A hybrid antenna similar to the stepped-reflector antenna discussed in Section 5.5 has been reported in [14]. The advantage with this design is that it requires a minimum number of reflector surfaces for MBA applications, one for transmitting and another for receiving functions. This also requires no beam-forming network and uses a single horn per beam. The central portion of the reflector is fully reflective and the annular regions as shown in Figure 5.32 are partially reflective. This will create a stepped illumination on the reflector and lowers the sidelobe levels.

The reflector may include several annular regions having various reflectivity levels and thus resulting in attenuation. Since the number of reflectors required for a MBA is reduced from four to two, larger reflector sizes can be used to compensate for the attenuation caused by the annular regions. Reducing the number of apertures allows each of the reflector apertures to have an increased aperture size. The concept is illustrated in Figure 5.32, where the annular regions are made up of sparse graphite mesh, and a thin layer of Kapton coated with a resistive film such as Nichrome is bonded to the mesh. The mesh is supported by radial ribs that

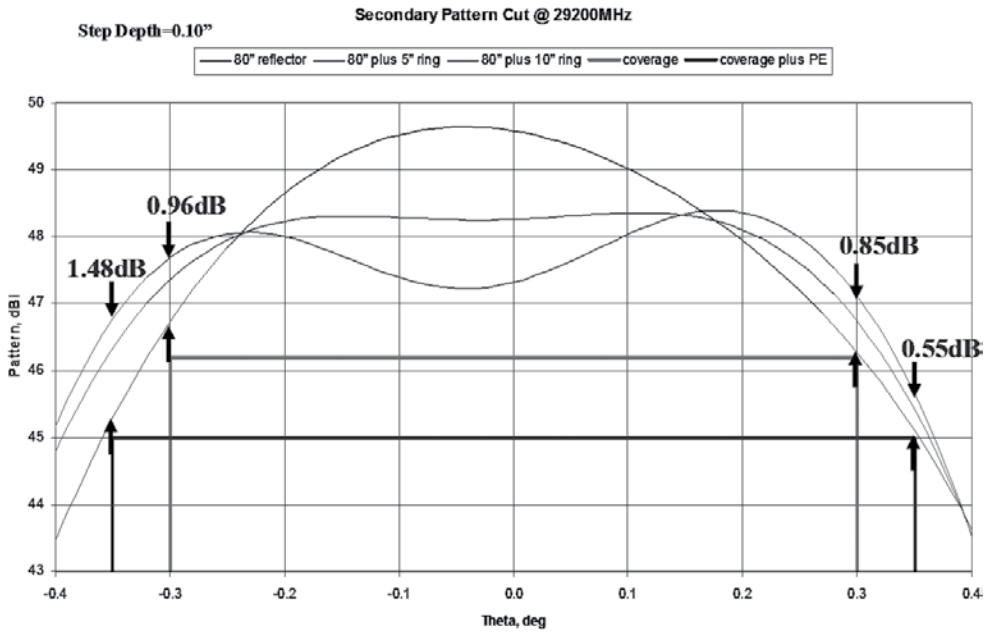

Figure 5.29 Computed patterns of the stepped-reflector antenna at the high band showing the impact of the annular step.

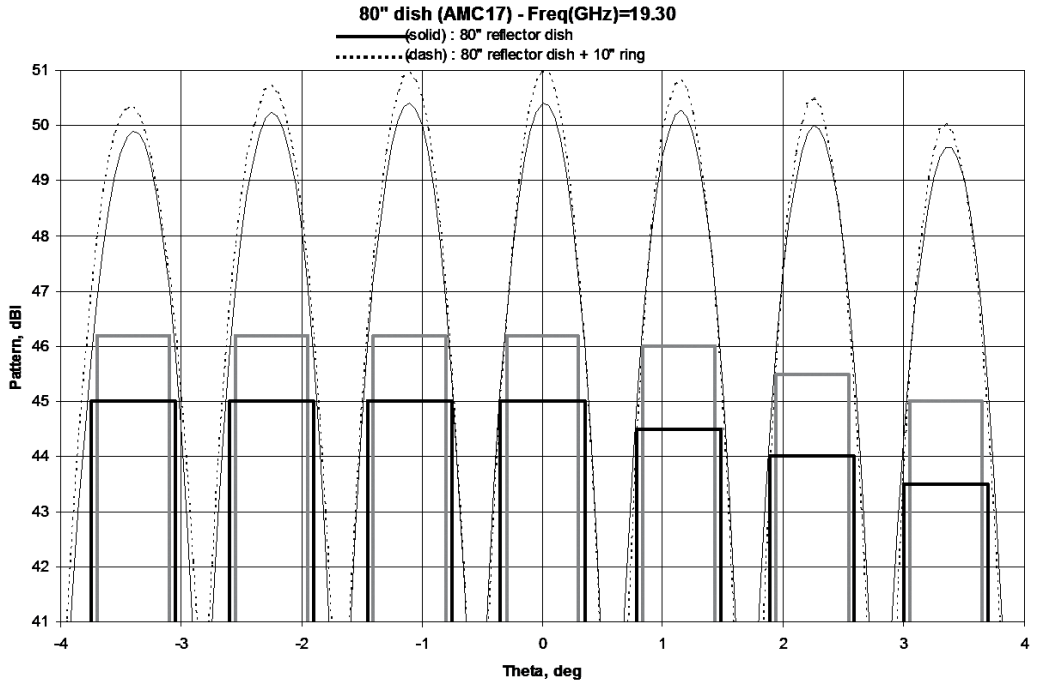

Figure 5.30 Computed radiation patterns of the stepped-reflector antenna at the low band for multiple beams. (The gain improvement at the low band is due to the use of a larger reflector with a step.)

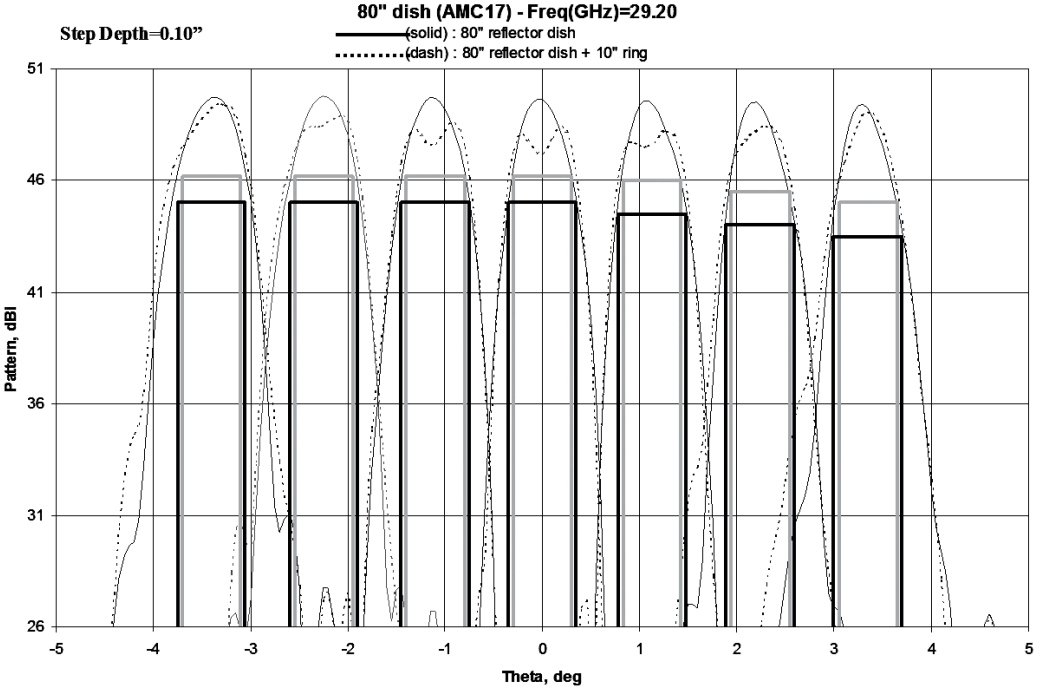

Figure 5.31 Computed radiation patterns of the stepped-reflector antenna at the high band for multiple beams. (The EOC gain improvement at the high band is due to the flat-top beam shape.)

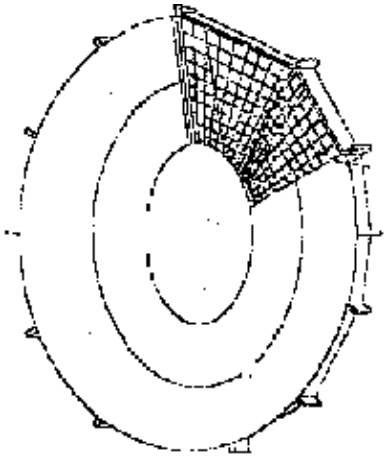

Figure 5.32 Concept of reflector with reflective and partially reflective surface.

are attached to the central section. By varying the resistivity of the film, different attenuations can be achieved over the annular regions. This method requires a larger reflector compared to conventional methods but a single reflector is needed to generate all of the beams. For example, Nichrome film of 187 Ω/square resistivity gives about a 6-dB reflective loss, whereas a 555 Ω/square film gives a 12-dB reflection loss.

Typical radiation pattern comparisons are shown in Figure 5.33 where the hybrid reflector provided about 1.5 dB more gain and about 7 dB lower sidelobe levels compared to a conventional reflector.

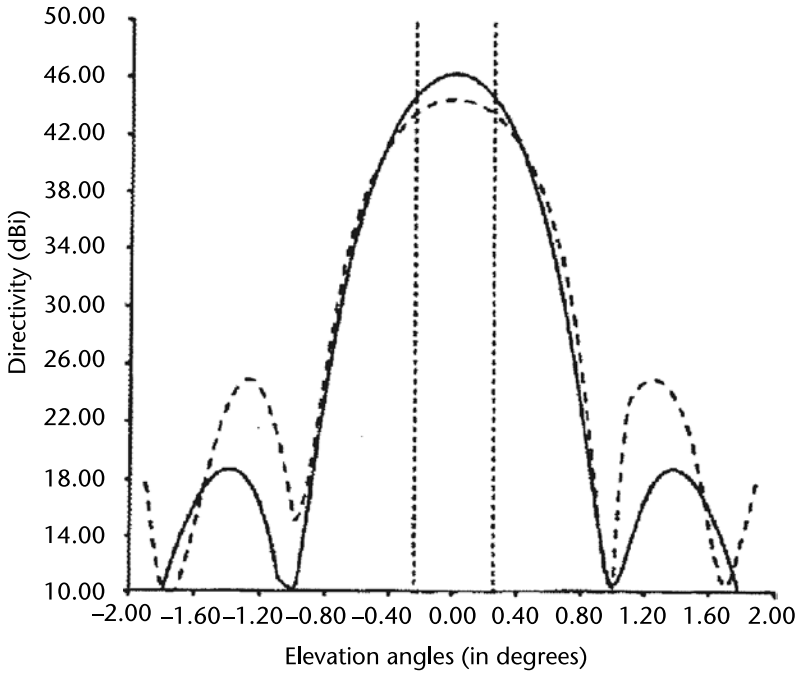

Figure 5.33 Radiation pattern comparison of conventional reflector (dotted) with reflector that has partially reflective surfaces (solid).

References

[1] R. A. Stonier, "Development of a low expansion, composite antenna subreflector with a frequency selective surface," 9th National SAMPE Technical Conference, Atlanta, GA, Vol. 9, October 1977.

[2] A. G. Brejcha and C. A. Smith, "Telemetry antenna for deep space probes," International Telemetry Conference, Los Angeles, October 1977.

[3] F. F. Dubrovka, et al., "A novel multiband coaxial feed system with low cross-polar radiation," EuCAP 2007 Conference, Edinburgh, UK, November 11–16, 2007.

[4] S. Rao, et al., "A novel antenna for wideband applications and supporting multiple bands," ISAP 2009 Conference, Bangkok, Thailand, October 20–23, 2009.

[5] K. K. Chan and S. Rao, "Design of high efficiency circular horn feeds for multibeam reflector applications," *IEEE Trans. Antennas & Propagation*, Vol. 56, pp. 253–258, January 2008.

[6] A. C. Ludwig, "Radiation pattern synthesis for circular aperture horn antennas," *IEEE Trans. Antennas & Propagation*, Vol. 14, pp. 434–440, July 1966.

[7] S. Rao et al., "Dual-band multiple beam antenna system for satellite communications," IEEE Antennas & Propagation Society Symposium, Washington, DC, July 2005.

[8] J. Wang, et al., "Dual-band multiple beam antenna system using hybrid-cell reuse scheme for non-uniform satellite communications traffic," *IEEE Trans. Antennas & Propagation*, Vol. 58, pp. 1380–1383, April 2010.

[9] S. Rao, et al., "Antenna system supporting multiple frequency bands and multiple beams," *IEEE Trans. Antennas and Propagation*, Vol. 56, pp. 3327–3329, October 2008.

[10] K. K. Chan and S. Rao, "Design of a tri-band corrugated horn," Proc. 2003 Asia Pacific Microwave Conference, Seoul, Korea, November 2003, pp. 29–32.

[11] S. Rao, et al., "Antenna system for multiple frequency bands," U.S. Patent #7737904, June 15, 2010.

[12] S. Rao and M. Tang, "Stepped-reflector antenna for dual-mode multiple beam satellite communications payloads," *IEEE Trans. Antennas & Propagation*, Vol. 54, pp. 801–811, March 2006.

[13] S. Rao and M. Tang, "Stepped-reflector antenna for satellite communication payloads," U.S. Patent #7737903, June 15, 2010.

[14] S. Rao, et al., "Multiple beam antenna using reflective and partially reflective surfaces," U.S. Patent #6759994, July 6, 2004.

CHAPTER 6

Reflector Antennas for Remote Sensing Applications

Paolo Focardi and Richard E. Hodges, Jet Propulsion Laboratory

6.1 Introduction

Remote sensing of Earth and other bodies in the solar system uses sensor technologies to detect and classify objects by means of propagated electromagnetic radiation. Sensors deployed on aircraft or satellites make it possible to collect data on a global scale that would not otherwise be practical to obtain. Remote sensing is used for a wide range of science applications ranging from global measurement of ocean topography and deforestation to the study of Jupiter's atmosphere. The military employs remote sensing techniques to collect data about opposing forces, weather conditions, and other information relevant to its mission.

Remote sensing is broadly classified as either *active* or *passive*. Active remote sensors, such as radar, transmit electromagnetic radiation toward a target and then detect the reflected or backscattered radiation. Passive remote sensors detect the radiation that is naturally emitted by an object, either due to (1) reflection of ambient electromagnetic energy incident on the object (e.g., sunlight) or (2) emission of blackbody radiation. Active sensors include many types of radars, including altimeters, which are used to accurately measure altitude; scatterometers, which measure ocean surface wind velocity; synthetic aperture radar (SAR), which is used to create high-resolution stereographic images of a planet surface; atmospheric radar, which is used to characterize properties such as precipitation and water vapor; military radars, which are used to locate, track, and identify objects such as aircraft or ground vehicles; and so forth.

Passive microwave sensors include many types of radiometers, each of which is designed for a specific purpose. Notable examples include the scanning multichannel microwave radiometer (SMMR), a five-frequency instrument primarily used to measure sea surface temperature; the TOPEX/Poseidon and Jason series radiometers, which are used to characterize tropospheric water vapor; the Microwave

Instrument for the Rosetta Orbiter (MIRO), a 190- and 564-GHz radiometer used to study comets; and the Microwave Limb Sounders (MLS), which are used to study the chemistry of ozone destruction in the Earth's stratosphere. A detailed description of these and other instruments may be found in [1].

Remote sensing system design is driven by the science requirements that define the mission. Consequently, both the system and antenna are typically custom designs that are tailored to meet the unique mission science requirements. For spaceborne remote sensing applications, reflector antennas have historically been the most widely used antenna design. Characteristics of the antenna such as beam shape and scanning capability are driven by specific system design requirements. However, some general requirements are common to most active and passive sensors. For radar, the most important requirements are gain, ability to handle high RF power, sidelobes, and cross-polarization suppression. Specific applications may also impose unique requirements that strongly influence the type of antenna used. For example, scatterometers have gain knowledge and stability requirements that preclude the use of antennas that are thermally sensitive. In contrast, radiometers require antennas with high beam efficiency, low average sidelobe level and very low internal circuit loss, whereas antenna gain is of secondary importance.

This chapter presents an overview of the various types of reflector antenna designs used for remote sensing applications. Antennas flown on historically significant missions are used to illustrate the practical implementation of each antenna type. In addition, the chapter presents notable antenna research developments that are regarded as enabling technologies for new types of sensors.

6.2 Solid Nondeployable Composite Reflectors

Reflector antennas, when feasible, have always been the preferred way of communicating with spacecraft in Earth orbit and beyond. Their simple geometry enables high gain and high data rate performance in a rugged hardware package that can support multiple frequency bands and polarization diversity. They come in forms and shapes as varied as the missions for which they were designed. The same characteristics that make them the antenna of choice for telecommunications also distinguish them as instrument antennas.

In this section we describe the most common technologies used for making solid nondeployable instrument reflector antennas and we will briefly describe the missions they were designed to support.

6.2.1 Voyager/Magellan

The high-gain antenna design used for the Voyager missions [2] was subsequently adapted for use on the Magellan spacecraft [3], and was the first of its kind to support both telecommunications and instrument systems (see Figures 6.1, 6.2, and 6.3). It was originally designed to transmit and receive in S-band and also to transmit in X-band. For Magellan, the original S- and X-band telecommunication capabilities were integrated with an S-band instrument that operated in three modes: synthetic aperture radar (SAR), altimeter, and radiometer. The Voyager reflector antenna design was attractive because minimal changes were needed to obtain the

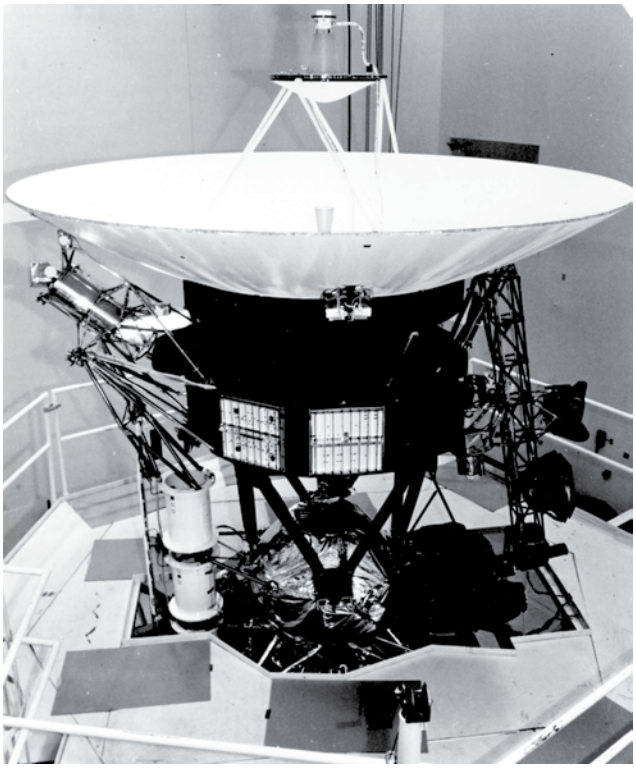

Figure 6.1 Voyager spacecraft during a vibration test. The aperture of the X-band feed horn and the shaped frequency selective surface in front of the S-band feed are clearly visible.

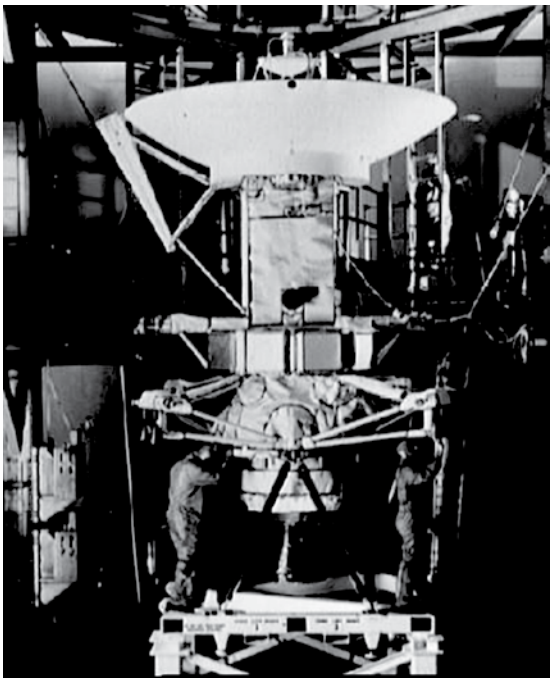

Figure 6.2 The Magellan spacecraft being prepared at Martin Marietta plant in Denver, Colorado, before being shipped to Kennedy Space Center for launch.

Figure 6.3 The Magellan spacecraft being deployed by the space shuttle Atlantis during STS-30 along with its inertial upper stage (IUS). To the left of the reflector antenna, the altimeter antenna (ALTA) instrument is also visible.

additional required functionality. The side-looking SAR provided—for the first time—a remarkably detailed map of Venus's surface, which is not visible due to the planet's dense atmosphere. The technology proven by Magellan was later used on the Shuttle Radar Topography Mission (SRTM), which provided the first global topographic maps of the Earth's surface obtained from satellite measurements.

The geometry of the antenna consists of a 3.66m paraboloidal reflector with an *F/D* of 0.338. The composite reflector is shared by both the S- and X-band feeds as shown schematically in Figure 6.4. At the higher frequency the antenna works in a Cassegrain configuration with a dual-mode circularly polarized horn feed and a shaped frequency selective surface (FSS) subreflector. At S-band, the antenna is configured as a regular prime focus reflector. The geometry of the antenna was optimized to work best in X-band. The X-band feed is designed to provide low power at the edges of the subreflector to limit the amount of spillover in the forward direction. A shaped subreflector is used in place of a classical hyperboloid to provide a uniform illumination over the main reflector as required for high aperture efficiency. The shaping algorithm creates a smaller radius of curvature near the center of the subreflector in order to direct more power toward the edges of the main reflector. To correct for the resulting phase error and achieve a constant phase aperture distribution, the main reflector is also reshaped from its nominal paraboloidal shape. However, the deviation from a paraboloid was negligible at S-band and had no significant effect on the prime focus reflector performance. A circularly polarized S-band low-gain antenna (LGA) completed the assembly and was mounted directly above, and coaligned with, the S-band feed of the high-gain antenna (HGA) as shown in Figure 6.4.

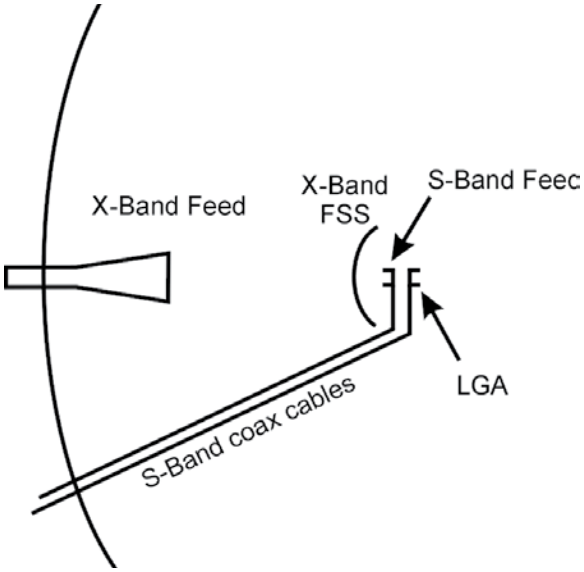

Figure 6.4 Schematic diagram of the Voyager/Magellan antenna with the subreflector made of a frequency selective surface (FSS). Also shown is the position of the low-gain antenna (LGA) in S-band.

The S-band feed is an open-ended circular waveguide with a choke to limit the spillover. Several modifications were made to support the addition of the 2385-MHz radar frequency to the telecom frequencies (2298 MHz for transmitting, 2115 MHz for receiving). The horn inherently supports both dual linear and circular polarizations, but the RF components were modified to add linear polarization input ports for the radar in addition to the existing right-hand circular polarization (RHCP) and left-hand circular polarization (LHCP) telecom ports. The feed cables were also modified to support the higher power requirements for the radar.

6.2.2 Cassini

The high-gain antenna on Cassini [4] is also a multifrequency reflector, conceptually similar to Voyager/Magellan except that it is larger and more complicated. This antenna accommodated a wide range of experimental modes, and integrating all of them on the same reflector was challenging [5]. It uses S-band for radio science experiments and to keep a radio relay link with the Huygens probe during its mission. X-band is used for telecom and Ku-band for radar imaging and altimetry of Titan. Finally, Ka-band is used for Doppler experiments, for searching for gravitational waves, and for measuring relativistic bending of solar rays. All frequency bands were designed for circular polarization (single or dual) except for Ku-band, which was linear. Apart from the reflector, all major components of Cassini's antenna are visible in Figure 6.5.

The basic design was heavily constrained by environmental requirements and by launch vehicle loads. The antenna needed to survive temperatures as high as 160°C at the Venus flyby and as low as –210°C close to Saturn. Six thick struts, well inside the aperture, were needed for the secondary reflector to survive the launch loads (Figure 6.6). The basic design was based on a typical Cassegrain configuration with a maximum aperture of 4m in diameter and an F/D of <0.33. All

Figure 6.5 Family portrait of all major components (except for the reflector) of Cassini's antenna. From top to bottom: all of the different FSSs of the subreflector, the S-band feed (left), the X-Ku-Ka-band feed (right), and the Ku-band waveguide slot arrays (center).

frequencies required on-axis pencil beams. At Ku-band, four additional fan beams were also required for radar imaging. Maximum gain was required at S- and X-band, whereas at Ku-band other critical requirements for radar imaging included minimizing the sidelobe level and integrated sidelobe ratio and maximizing the minimum gain along the range plane line. At Ka-band, a beamwidth 1.6 times larger than that achievable by the physical aperture was required as a compromise between peak gain and spacecraft attitude control capabilities at the time. The S-band subsystem is located at the prime focus of the paraboloid, while the X-, Ku-, and Ka-band subsystems are located at the Cassegrain focal plane.

The subreflector consists of a cascade of three FSSs separated by vacuum as illustrated schematically in Figure 6.7. The first one, a regular hyperboloid, reflects Ku- and Ka-band and is transparent for X-band. The second one, a shaped reflector similar to the one used by Magellan, reflects X-band. A third one is used as a matching layer for the S-band feed located at the prime focus. A triple-band feed horn and four sets of array feeds, each comprised of five 5×2 element waveguide slot arrays, are then placed in the Cassegrain focal plane. An X-band LGA atop the S-band feed completes the assembly. Figures 6.6 and 6.8 show details of the subreflector, the feed horn, the waveguide slot arrays, and the LGA.

The S-band subsystem was located at the prime focus because the feed would have been too large compared to the other bands and it would have been in conflict with the other subsystems.

Feeds for the other higher bands are located in the Cassegrain focal plane primarily to minimize transmission line losses and optimize overall efficiency. For Ku-band this location also meets the sidelobe levels required for radar imaging. A tremendous amount of work was performed by many international institutions and universities in order to predict and optimize the performance of this complex

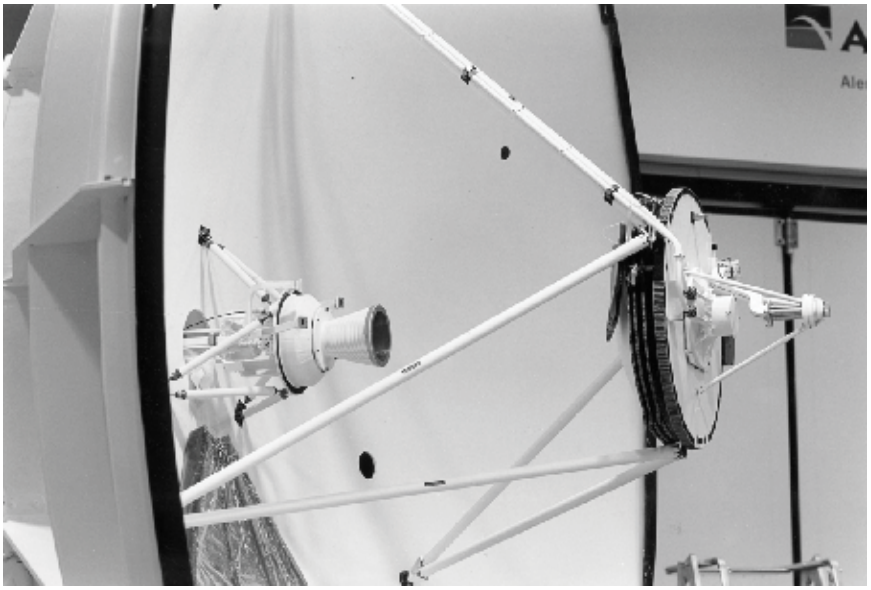

Figure 6.6 Detail of Cassini's subreflector. The different layers of the FSSs operating at X-, Ku-, and Ka-band are clearly visible. Note the X-band LGA on the back of the subreflector.

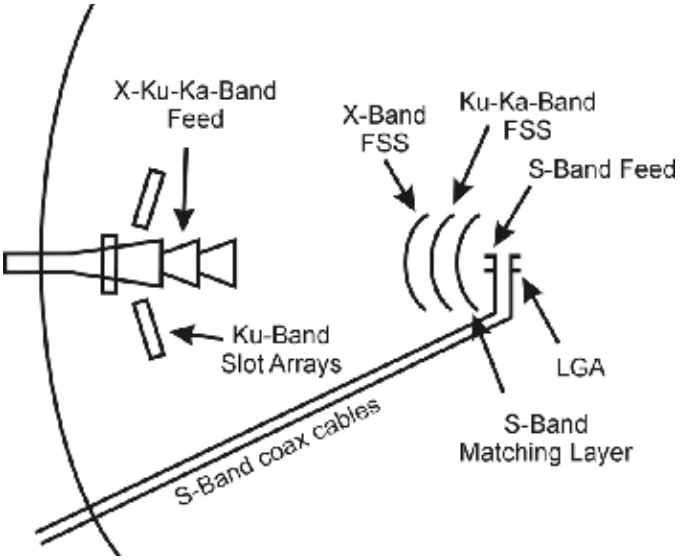

Figure 6.7 Schematic diagram of Cassini's complete antenna system.

multifrequency instrument (e.g., see [6]). Figure 6.9 shows the completed Cassini antenna.

6.2.3 CloudSat

The CloudSat mission was developed to acquire a global data set of vertical cloud structure and its variability. The primary science instrument is the Cloud Profiling Radar (CPR), a 94-GHz nadir-looking radar that measures the power backscattered

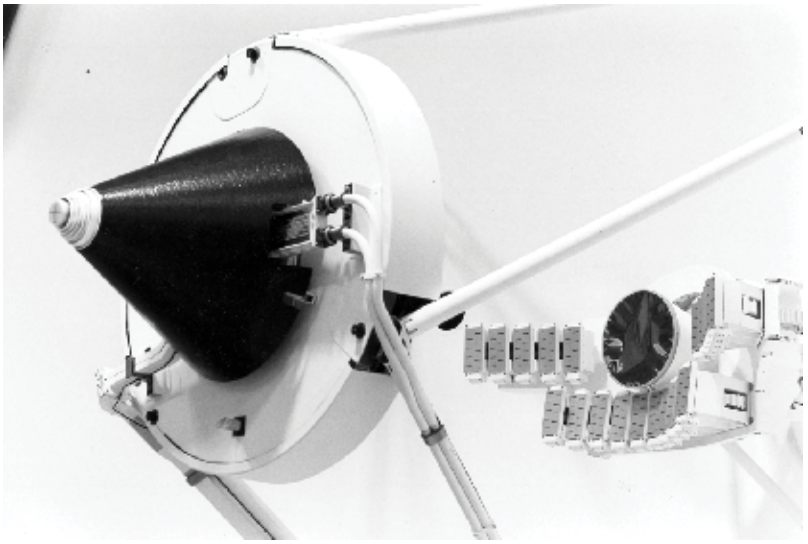

Figure 6.8 Another view of Cassini's complete feed system with the Ku-band slot arrays mounted around the feed horn.

Figure 6.9 The complete Cassini antenna before being integrated with the spacecraft.

by clouds as a function of distance from the satellite [7]. The 94-GHz operating frequency was chosen as a compromise between instrument sensitivity, antenna size, atmospheric transmission, and transmitter power. CloudSat's CPR antenna system includes a very compact 1.85m-diameter offset Cassegrain reflector (see Figure 6.10) combined with a quasi-optical transmission line (QOTL), which is used to minimize transmission line loss to the transmitter and receiver [8]. Very tight mission requirements on beamwidth (<2 km on Earth footprint), on absolute reflectivity measurement accuracy (1.5 dB), on the sidelobe level envelope (<50 dB below peak gain for angles larger than 7 deg from boresight), and on detectable

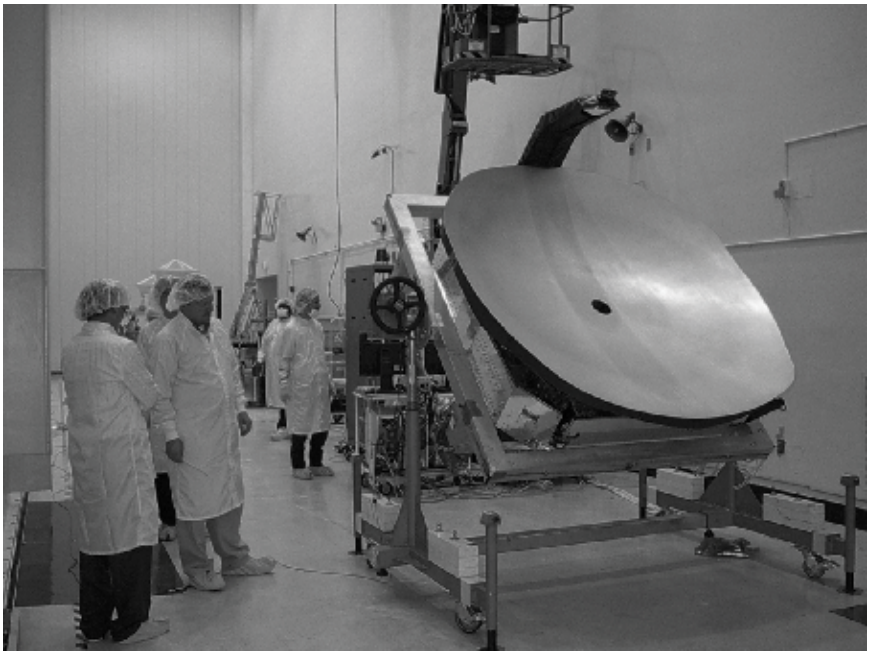

Figure 6.10 The Cloud Penetrating Radar (CPR) antenna.

cloud reflectivity (minimum detectable cloud reflectivity (Z) of –28 dBZ at the end of the two-year mission) determined the shape and size of the antenna.

The overall antenna system, illustrated schematically in Figure 6.11, includes a collimating antenna (mirrors M1, M2, and M3) and the QOTL, which consists of three more mirrors (M4, M5, and M6), a Faraday rotator, and a polarizer. The QOTL delivers the signal from the transmitter to the collimating antenna, and from the collimating antenna to the receiver on partially different paths. A signal emitted by a klystron is reflected by M6 and then goes through a polarizer and a Faraday rotator. It is then reflected by M4, which feeds the collimating antenna. Mirror M6 can also rotate on its axis and face a backup power source in case of a klystron failure. The entire QOTL is assembled just behind M1, making the entire instrument very compact. The collimating antenna and the QOTL were developed separately. To facilitate this, a corrugated circular test horn was used to provide the excitation to M3 on the collimating antenna side and to M4 on the QOTL side.

Given the high frequency at which the instrument operates, the offset Cassegrain reflector design procedure was approached from a quasi-optical point of view. The pattern of the test horn mentioned above illuminates an elliptical mirror M3, which then feeds a shaped mirror M2 through a hole in the primary mirror M1. The shapes of M2 and M1 were optimized to achieve maximum efficiency using the following procedure. The pattern of M3, fed by the test horn, is used as a source for M2. The shape of M2 is then determined by 20 points, which are used as optimization variables based on thin-plate deformation theory. Symmetry was used to limit the number of unknowns, while one point on M2 was fixed in order to fix the mirror position. A constant path length in geometrical optics (GO) then defined the shape of M1. Physical optics (PO) was used to determine the directivity of M1, the parameter to optimize in the process. The edge tapers on the hole in M1

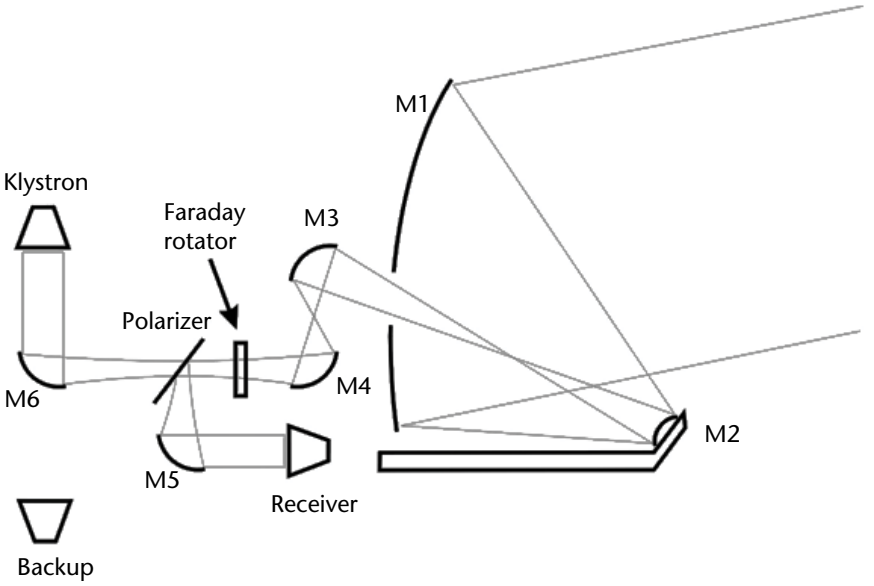

Figure 6.11 Schematic diagram of CloudSat antenna system.

and at the perimeter of M2 and M3 are 30, 23, and 25 dB, respectively, and they allowed the antenna to have very little spillover, resulting in only a 0.16-dB loss for the entire collimating antenna.

6.2.4 Aquarius

The instrument antenna for Aquarius [9] was designed to operate both as a scatterometer and a radiometer in L-band to accurately measure sea surface salinity from space on a global scale. The antenna design is a compromise between resolution on the ground and coverage. The reflector dimension was chosen as the largest that would fit in the launch vehicle in order to maximize resolution. Since the single-feed beam was too narrow to achieve the required ground coverage, three separate feeds were used to create three adjacent beams that together meet the coverage requirement.

The antenna is a 2.5m graphite composite offset reflector with an *F/D* of 0.633 and pointed 33 deg from nadir. Figure 6.12 shows the reflector and the feed subsystem. The reflector boom assembly is hinged so that it can pivot towards the feed horns for launch and then deployed once in space. The three identical L-band feed horns are located in the focal plane and are offset from the focal point and tilted to produce the required beams. These beams combine to create a total ground swath width of more than 300 km with gaps between the individual beam footprints that are smaller than 50 km. In addition, the polarization of the three horns is also clocked to obtain a properly aligned vertical polarization at the sea surface. The radiometer measures the brightness temperature of the sea surface, which is then calibrated based on the roughness information calculated by the coaligned scatterometer. The total temperature error allocation is 0.15K for the radiometer, whereas the scatterometer has an error allocation of about 0.12K. The pointing stability due to thermal and mechanical variations is required to be within 0.05 deg.

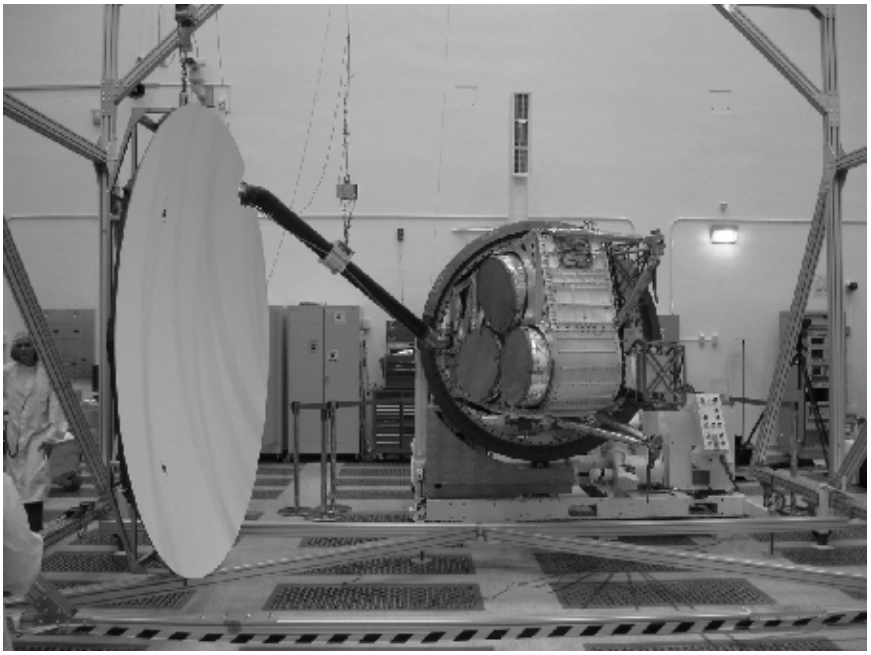

Figure 6.12 Aquarius reflector and feed subsystem.

The basic design of the reflector and feeds was originally done using a simple physical optics approach. A scale model of the entire spacecraft (roughly 1/10 scale) was fabricated and measured in order to validate the simple PO calculations (Figure 6.13). Very accurate predictions of the antenna pattern are indeed

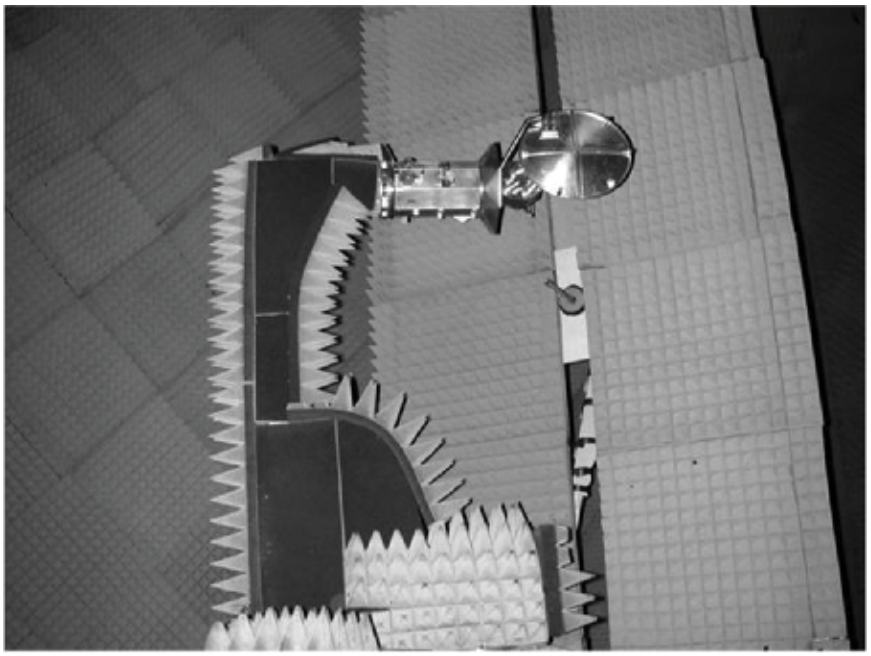

Figure 6.13 Aquarius scale model being measured on the cylindrical near-field antenna range at the Jet Propulsion Laboratory's MESA Antenna Test Facility. Note the absence of the solar panels.

necessary in order to properly calibrate a radiometric measurement. Typically the power radiated by the antenna is integrated in three major regions of space: the main beam of the antenna, the sidelobes facing Earth, and those looking at cold space. A very complex RF model of the entire spacecraft (Figure 6.14) was later developed in order to obtain more accurate predictions of the patterns produced by the three feeds in the presence of the entire spacecraft. As can be seen in Figure 6.14, this RF model is very accurate and is aimed at reproducing all of the details of the antenna performance.

6.2.5 Mars Reconnaissance Orbiter (MRO)

The Mars Reconnaissance Orbiter reflector antenna system [10] was not designed to accomplish remote sensing; instead it only supports telecommunications. However, the design is noteworthy because it has unique features that may be applicable to an instrument package such as a radar. MRO was designed with a large 3m reflector and used what is called "displaced axis" optics to minimize the blockage of the subreflector. The subreflector is shaped such that it diverts the signal coming from the feed toward the sides of the reflector without sending excessive power back into the feed. The compact nature of the subreflector minimizes blockage. Figure 6.15 shows a schematic diagram of the MRO antenna. Photos of the flight antenna are shown in Figures 6.16 and 6.17. The feed is an X-band corrugated horn in circular polarization integrated with a Ka-band disk-on-rod antenna. While the X-band link has become standard for recent space missions, the Ka-band link is also being developed in order to achieve higher data rates and support radio science. Modern instruments are capable of producing an enormous amount of data and higher rates are needed in order to limit the download time. Data rates of the order of 6 Mbps can be achieved by this antenna system.

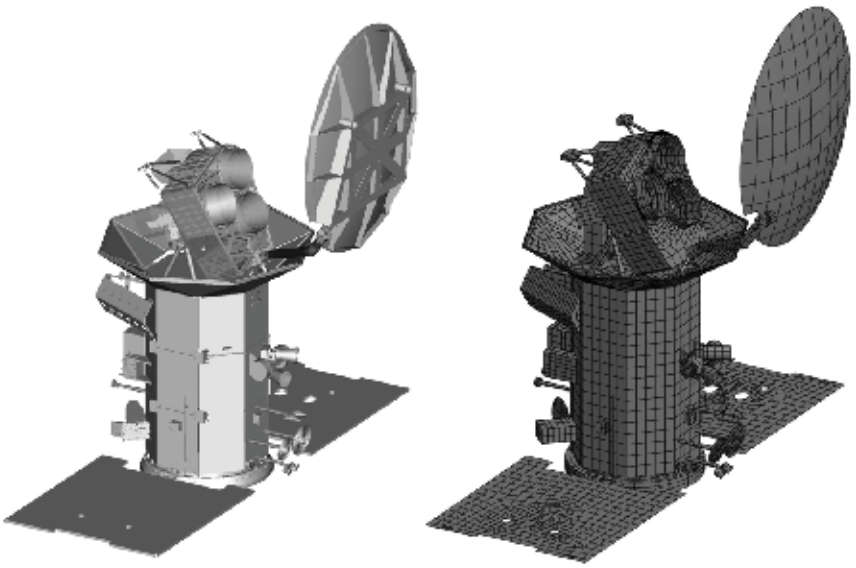

Figure 6.14 (Left) CAD model and (right) RF model of the Aquarius spacecraft.

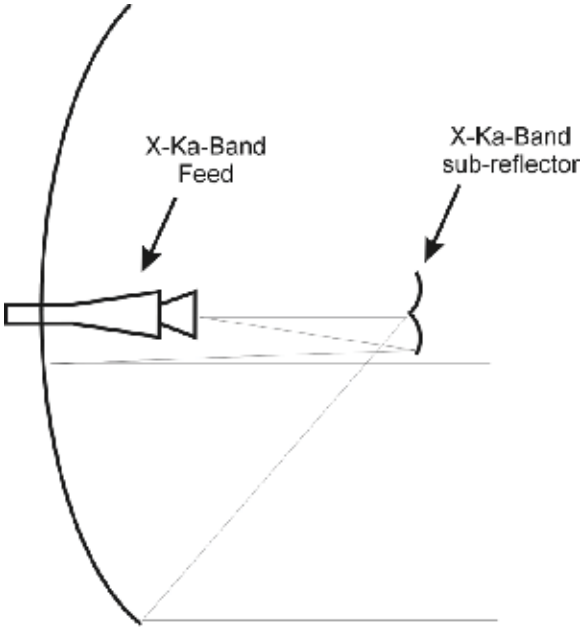

Figure 6.15 MRO antenna schematic diagram.

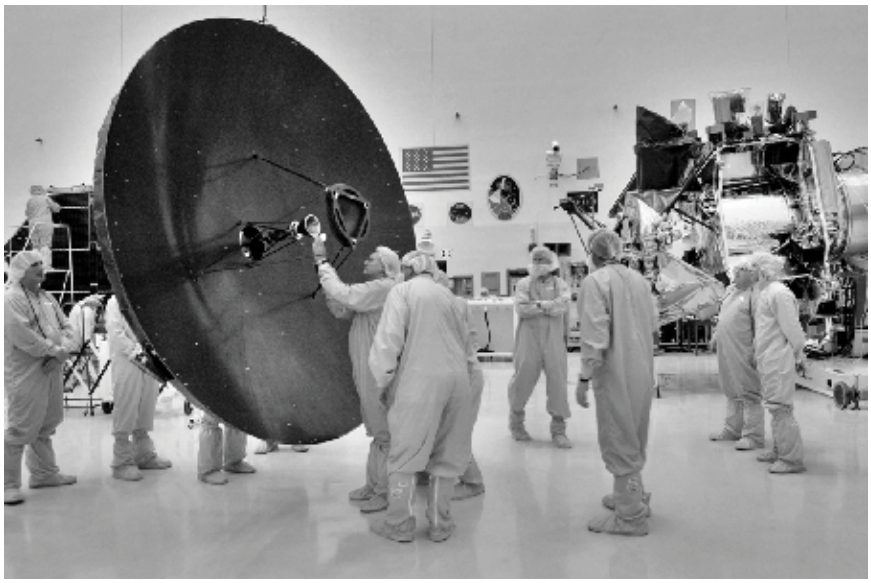

Figure 6.16 The MRO antenna is being checked before integration with the spacecraft.

6.2.6 JASON Advanced Microwave Radiometer Antenna

Since 1992, The National Aeronautics and Space Administration (NASA) and National Oceanic and Atmospheric Administration (NOAA) in the United States have partnered with CNES in France to measure the global ocean surface topography through a series of highly successful missions including TOPEX/Poseidon (1992–2006), Jason 1 (2001–present), OSTM/Jason 2 (2008–present), and Jason 3 (2014 scheduled launch). The distance between the satellite and sea surface ocean height

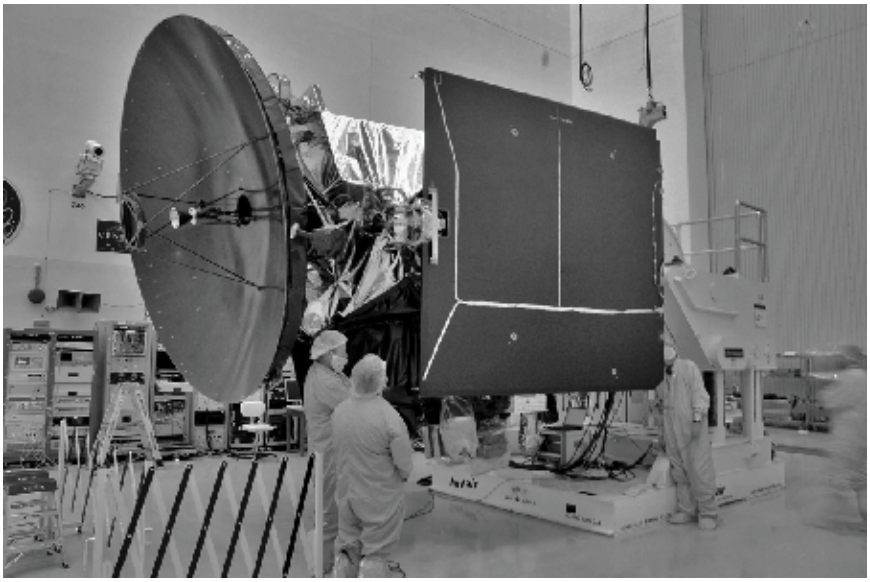

Figure 6.17 MRO's antenna after integration.

is measured using a 13.6-GHz and a 5.3-GHz radar altimeter that employs a 1.2m reflector antenna (Figure .6.18). The altimeter measures the round-trip travel time of microwave pulses transmitted by the spaceborne altimeter and reflected from the sea surface. In addition, the Advanced Microwave Radiometer (AMR) measures radiation from the Earth's surface at three frequencies (18.7, 23.8, and 34 GHz). It measures atmospheric water vapor and liquid water content in order to determine the radar signal path delays. Although the Jason 1 radiometer antenna is offset fed, four struts were added to meet launch vibration requirements (right photo in Figure 6.18). These struts cause sidelobe levels to increase, which degrades the radiometer instrument performance. For this reason, a new radiometer antenna that has no struts was designed for use on Jason 2 and 3 (see Figure 6.19). This antenna

Figure 6.18 Jason 1 spacecraft is shown at left. The larger symmetric fed reflector is the altimeter antenna. The upper reflector is the radiometer, which is also shown in the photo at right.

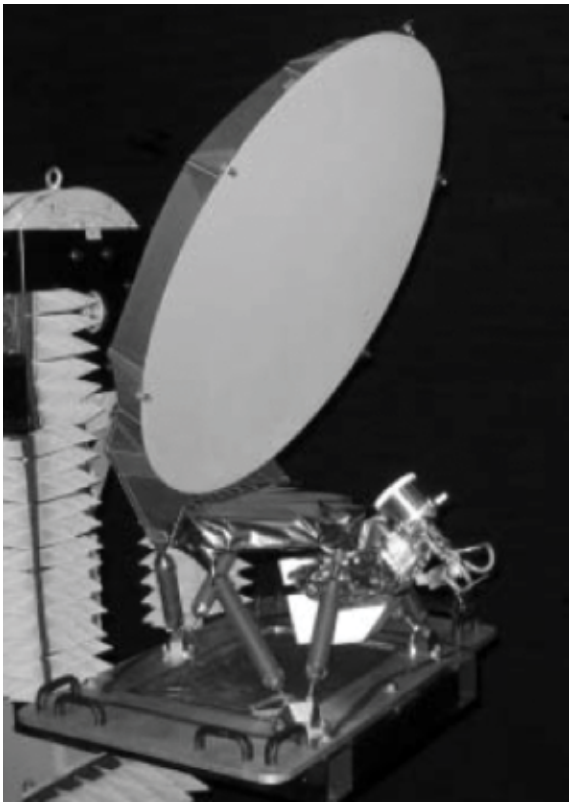

Figure 6.19 True offset-fed reflector used for the Jason 2 and 3 radiometers.

provides very low sidelobes and high beam efficiency, which results in significantly improved radiometer performance. Note that these composite reflectors are coated with a thin layer of aluminum in order to minimize conduction current losses on the reflector surface.

6.3 Deployable Reflector Antennas

6.3.1 Deployable Composite Reflectors

6.3.1.1 Segmented Folding Composite Reflectors

Deployable composite reflectors developed by Composite Technology Development (CTD) use thin graphite composite reflective surfaces that are pleated to reduce their size for stowage. CTD has developed and demonstrated this technology for both center-fed and offset-fed configurations. The center-fed reflector configuration resembles a coffee filter in the packaged state, whereas the offset-fed reflector is formed into a few large, parallel pleats. Both configurations reduce the width of the stowed reflector to about one-third of the aperture diameter. Shape memory polymer components are used within the system to constrain the reflector in the stowed shape, to control and damp deployment, and to stiffen the thin reflective surface after deployment. Both the center-fed and the offset-fed reflectors are also stiffened by a deep, thermally stable backing structure actuated with shape memory

polymer deployable beams. The packaging and deployment cycle is shown in Figure 6.20 for the center-fed reflector. Only the small portions of the reflector that consist of shape memory polymer must be heated for packaging and deployment. The on-orbit power requirement to achieve full deployment is less than 200W over a 30-min period. Full-scale engineering models of both the center-fed and offset-fed reflectors have been fabricated, cycled through multiple deployments, range tested, and thermal distortion tested. The total surface accuracy budget of these demonstration units was sufficient for Ku-band operation. Flight reflectors are expected to be capable of Ka-band and above.

6.3.1.2 Spring-Back Composite Reflectors

The spring-back reflector consists of a thin graphite mesh dish with an integrated lattice of ribs and a stiffening hoop along the rim. The reflector stows by folding, and cables along the rim hold the reflector in the stowed position (see Figure 6.21). The reflector deploys by releasing the cables so that it "springs back" to the original shape. Boeing Satellite Systems (formerly Hughes Space and Communication Company) developed this concept, which was first used on MSAT-1 in 1996 for two reflectors of 6.8m × 5.25m. Most recently it was used for NASA's next-generation Tracking and Data Relay Satellite System (TDRSS; H through J) for a reflector size of 5m. The operating frequency is up to Ka-band (27 GHz), and its mass is 20 kg with a resultant density of 0.71 kg/m^2 (without deployment structure).

The stowed volume of the spring-back reflector is quite large compared to the other deployable reflectors, and the stowed length in one direction equals the reflector diameter. For this reason, the antenna's diameter is restricted to approximately the height of the launch shroud. Although this reflector was designed for a telecom application, the concept has obvious application for instruments such as radar.

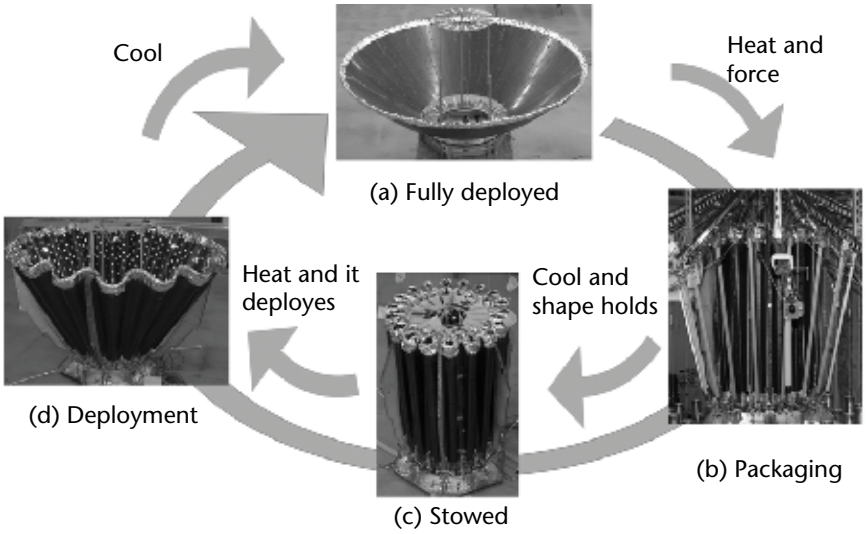

Figure 6.20 CTD shaped memory composite reflector deployment sequence. (Courtesy of Composite Technology Developments.)

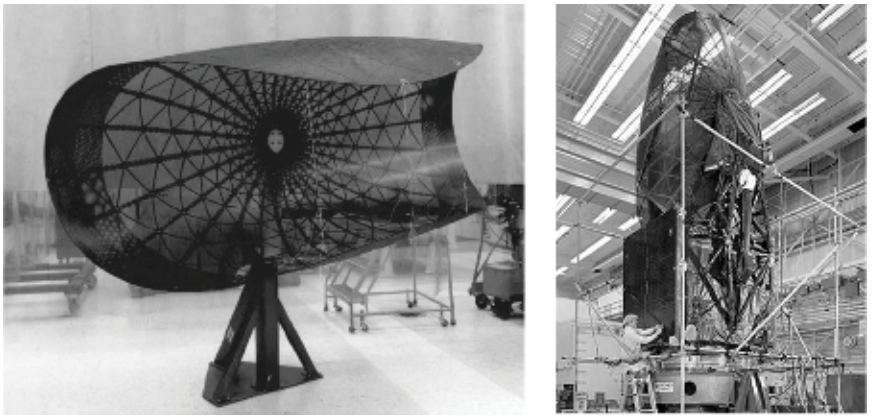

Figure 6.21 TDRSS spring-back reflector: (left) stowed configuration on a stand and (right) stowed reflector being prepared for integration with the launch vehicle. (Courtesy of Boeing Satellite Systems.)

6.3.2 Deployable Mesh Reflectors

6.3.2.1 Galileo

Although the dual S-band and X-band mesh reflector antenna system developed for Galileo [11] was designed to meet telecommunications requirements, the technology is directly relevant for current remote sensing applications such as SMAP. Galileo remains the largest and most complex antenna system flown on an interplanetary mission. Because Galileo was the first spacecraft to orbit Jupiter and endured its uniquely harsh radiation environment for 14 years, this antenna warrants careful study by present-day instrument designers.

To understand the Galileo design, it is useful to put it in the context of the time it was conceived and developed. The spacecraft was originally designed to be carried into Earth orbit on board a space shuttle and to subsequently start its journey directly toward Jupiter using a Centaur upper stage. Voyager size solid reflectors (3.66 mm) were the largest that would fit in the shuttle's bay, but the need for higher gain and data rate forced the team to select a larger deployable reflector. A 4.755m radial rib mesh reflector design that Harris Corporation had successfully used for the TDRSS was chosen for Galileo. This design included both S- and X-band capability similar to that of Voyager; but for Galileo the X-band link was intended to be the primary link because it allowed for a data rate of 134.4 kbps, the fastest data link flown on a deep space mission at that time. The dual polarization, circularly polarized, X-band horn was Cassegrain located and used an FSS subreflector similar to the Voyager/Magellan design. A linearly polarized S-band feed was located at the prime focus of the paraboloid. A low-gain antenna (LGA) in S-band originally completed the telecom system, which was mounted on top of the reflector's S-band feed and therefore coaligned with the high-gain antenna (HGA). Figure 6.22 shows a schematic diagram of the Galileo antenna.

The Galileo antenna fabrication and test was already completed when, on January 28, 1986, the space shuttle *Challenger* disaster occurred. This incident changed the Galileo deployment plan because the Centaur upper stage was deemed

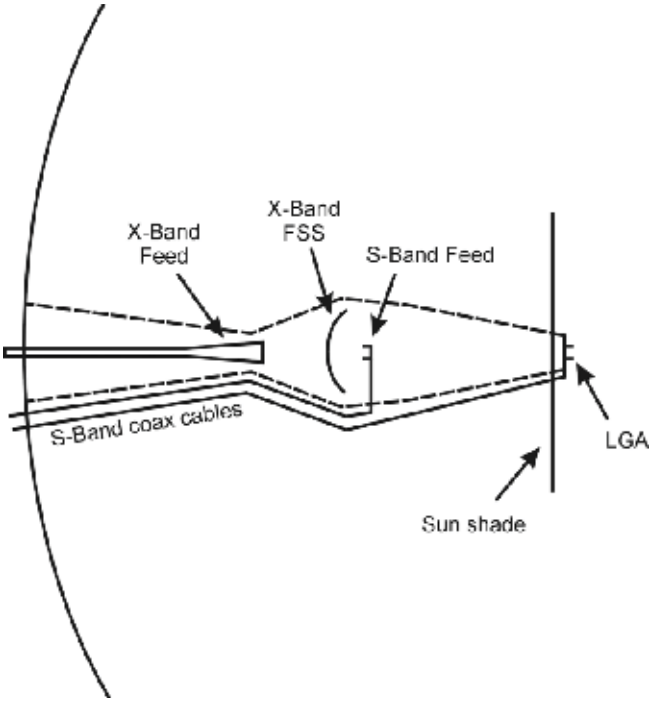

Figure 6.22 Schematic diagram of the Galileo antenna system.

unsafe to fly on a space shuttle and the U.S. Air Force's inertial upper stage (IUS) was instead chosen to boost Galileo out of Earth's gravity. A new trajectory for Galileo was designed that included one Venus and two Earth fly-bys, thus requiring 6 years to reach Jupiter. These changes in the mission plan meant Galileo would fly much closer to the sun than originally expected and therefore many parts of the spacecraft needed to be retrofitted to survive the new environment. Accordingly, two sun shades were installed: one at the top of the Cassegrain tower just below the LGA and one behind the reflector. The HGA was not opened for almost two years after launch and remained hidden behind the sun shade until the spacecraft was far enough from the sun for the mesh reflector to be opened safely. Moreover, the launch delay also resulted in the antenna being held in storage for three years and the stowed HGA was constantly sun-pointed during the early stages of the mission, conditions that the antenna was not originally designed for.

Images of both the partially and fully deployed Galileo antenna are shown in Figures 6.23 and 6.24 (the sun shades are not present in these photos). The reflector, made of a 10-openings-per-inch tricot mesh of molybdenum wires, opens as an umbrella. Unfortunately, the reflector failed to fully deploy on April 11, 1991. Although the root cause of the failure will probably never be known with certainty, the speculation is that the failure was a consequence of the launch delay associated with the *Challenger* accident. As a result, only the two LGAs were available to communicate with Earth. Despite this situation, improvements in the Deep Space Network and other measures taken to increase the data rate enabled Galileo to meet mission requirements.

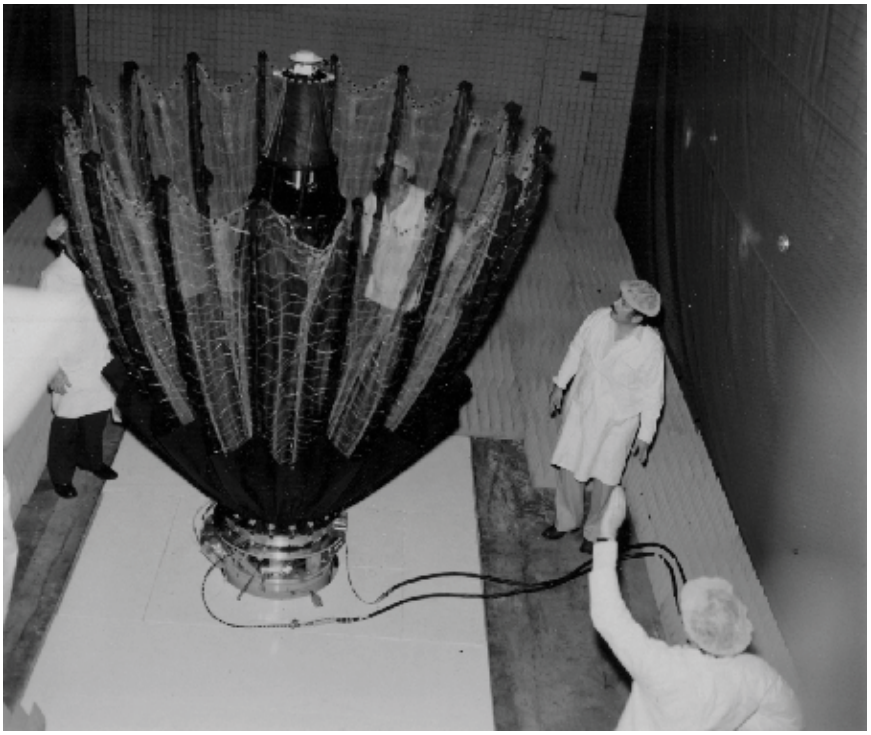

Figure 6.23 Galileo's reflector partially deployed during testing on the plane polar near-field antenna range at the Jet Propulsion Laboratory's MESA Antenna Test Facility.

6.3.2.2 SMAP

The Soil Moisture Active and Passive (SMAP) mission [12] will use an L-band radar and radiometer to measure Earth soil moisture and its freeze/thaw state. A 6m AstroMesh™ offset reflector and a dual-band, dual-polarized, L-band corrugated horn are shared by the radar and radiometer instruments. The deployable reflector, similar to the one shown in Figure 6.25, uses a 20-openings-per-inch mesh shaped by a web of Kevlar strips running across the reflector in three different directions, thereby forming a reflector of relatively flat triangular facets. The spacecraft will fly on a near-polar, sun-synchronous orbit of 680 km and is scheduled to be launched in November 2014.

The reflector has a focal length of 4.2m and an *F/D* of 0.7. It is folded into a tight bundle for launch and will deploy once in space, along with its supporting boom, to be pointed 35.5° from nadir. Once deployed, the entire instrument will spin at 14.7 rpm on top of the bus and solar panels to cover a large 1,000-km swath. It will have a spatial resolution of 40 km for the radiometer and 1 to 3 km for the radar. It will also be the first spinning mesh reflector and the first radiometer instrument based on a mesh reflector to be employed in space.

Achieving the mechanical, thermal, dynamic, and electrical stability required to use a mesh reflector proved to be significantly more challenging for the radiometric instrument than for the radar. The stability during operation of the electrical to mechanical pointing bias and the stability of the integrated power radiated in the different regions of space were also critical aspects of the design.

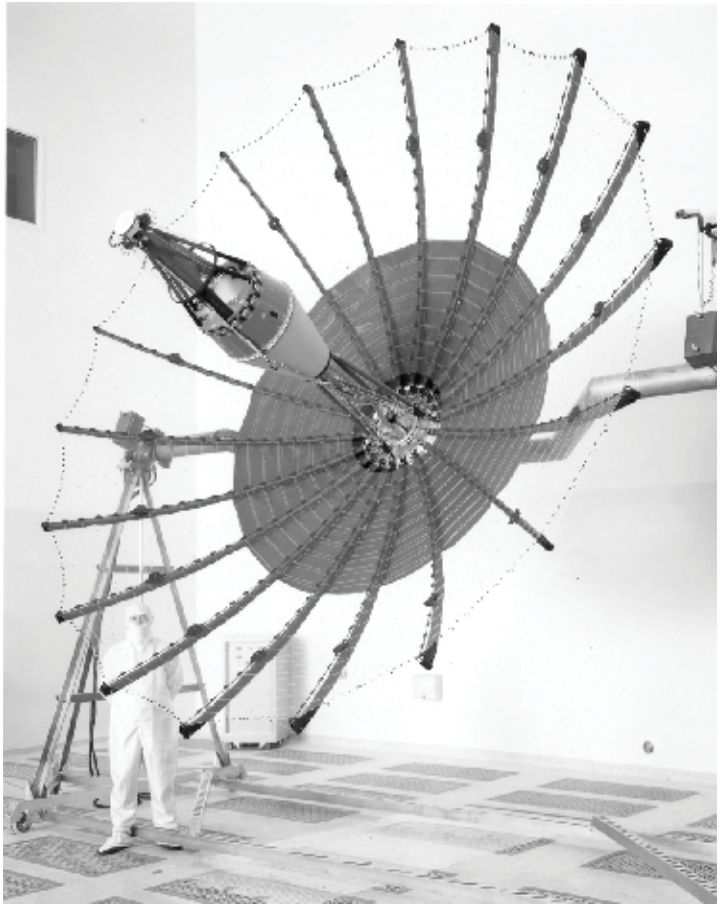

Figure 6.24 Galileo's reflector completely deployed on its ground support fixture.

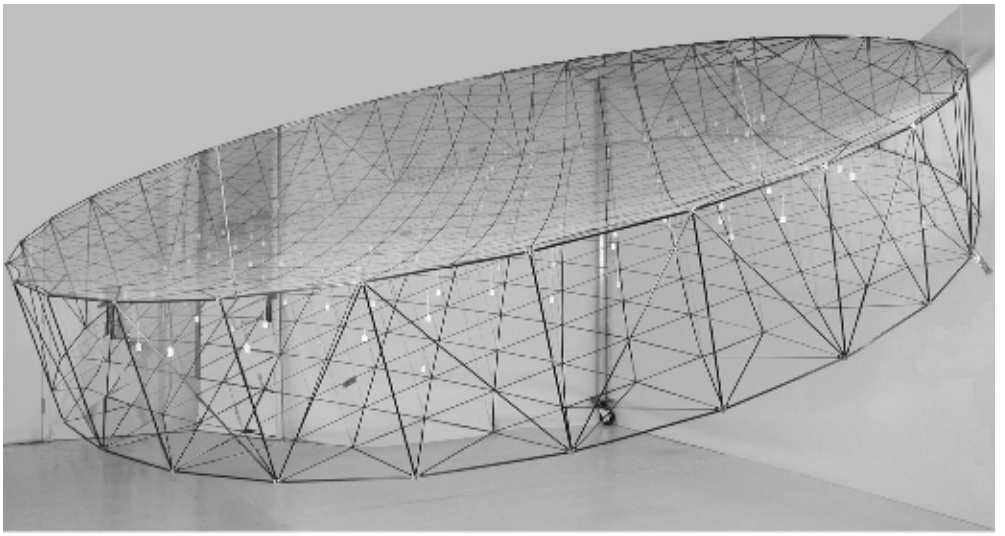

Figure 6.25 AstroMesh reflector. (Courtesy of Northrop Grumman.)

The SMAP development plan does not include measuring the flight antenna radiation pattern, and instead relies on the very accurate RF model shown in Figure 6.26 to predict the instrument performance. For more details about the SMAP RF model, see [13]. In the final layout of the spacecraft, the top corner of the solar panels intersects the 6m projected aperture of the reflector twice per revolution of the instrument. Among the many simulations, the RF model was also used to verify that this intrusion was indeed negligible from a performance standpoint. Small variations of the various parameters were observed but remained within tolerance for the instrument. For instance, the electrical pointing of the antenna is the parameter that is affected the most by the spinning, but only variations of the order of ±0.004 deg in elevation are predicted.

The radiometer electronics is located next to the feed horn in order to minimize electrical noise. The positions of these boxes and that of other instrument boxes were also used to counterbalance the spun mass of the reflector and boom. The radar electronics is located inside the bus and the signal is fed through a rotary joint at the center of the spacecraft.

As noted earlier, RF performance predictions for the antenna assembly are based on the RF model because pattern measurements of the actual reflector in a 1G environment are too costly. Instead, a 1/10 scale model of the entire spacecraft, shown in Figure 6.27, was fabricated and tested in order to verify the performance and to validate the results of the RF model. Although the scale model reflector is solid machined aluminum instead of mesh, the reflector surface is faceted to simulate the AstroMesh surface. This scale model also includes the ability to clock the spacecraft bus, solar panels, and other components on the non-spun side in order to validate the perturbations of instrument performance resulting from the antenna rotation. Test results demonstrated excellent overall agreement between the scale model measurements and the RF model.

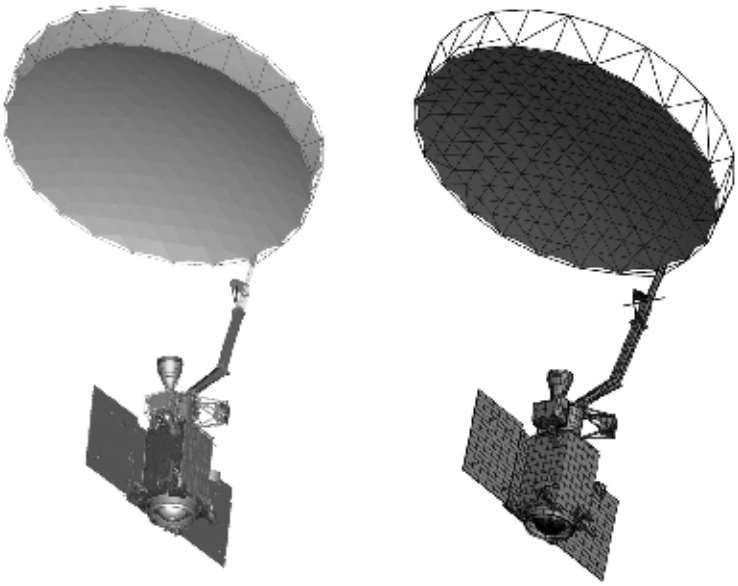

Figure 6.26 (Left) CAD model and (right) RF model of the entire SMAP spacecraft.

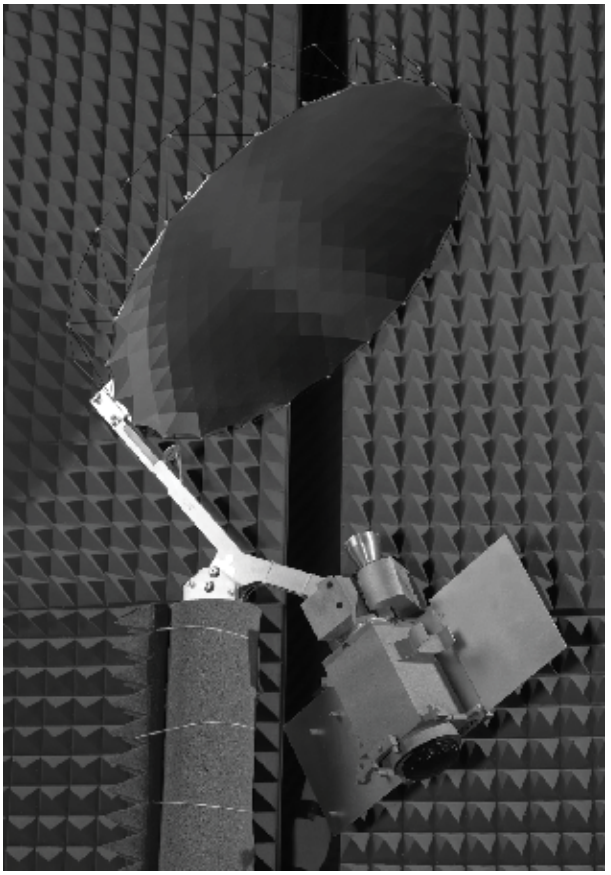

Figure 6.27 SMAP 1/10 scale model in the MESA Test Facility cylindrical near-field antenna range at NASA's Jet Propulsion Laboratory.

6.3.2.3 ISAT

In 2001, the Defense Advanced Research Projects Agency (DARPA) initiated the Innovative Space-Based Radar Antenna Technology (ISAT) program. Its focus was the development of a 300m × 3m electronic scanning radar antenna that is compatible with the stowage requirements of a conventional launch vehicle [14, 15]. One of the two ISAT concepts was a phased-array-fed reflector (PAFR). Figure 6.28 illustrates a planned 108m low-Earth-orbit (LEO) flight demonstration system. This design used a linear phased array as the feed for a deployable parabolic-cylinder mesh reflector that was developed through the critical design review (CDR) process.

On-orbit antenna deployment is performed with the antenna oriented along the gravity gradient. The antenna bays are deployed sequentially in pairs, one in each direction beginning with the outermost bays. The mesh reflector assembly is synchronously deployed with the truss structure, which supports the phased-array feed panels.

A 12m engineering unit, shown in Figure 6.29, was tested in a laboratory environment and demonstrated an rms surface error of 1 mm. Three complete axial stows and deployments were successfully completed. Thermal vacuum environmental testing to characterize surface deformation was not performed due to the associated costs and complexity.

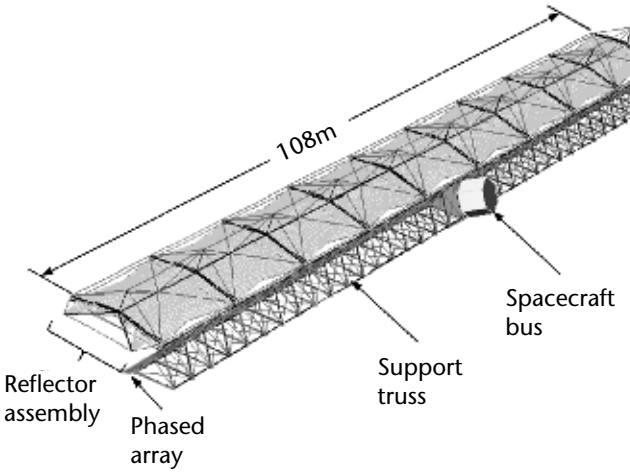

Figure 6.28 Illustration of the ISAT phased-array-fed reflector (PAFR) concept.

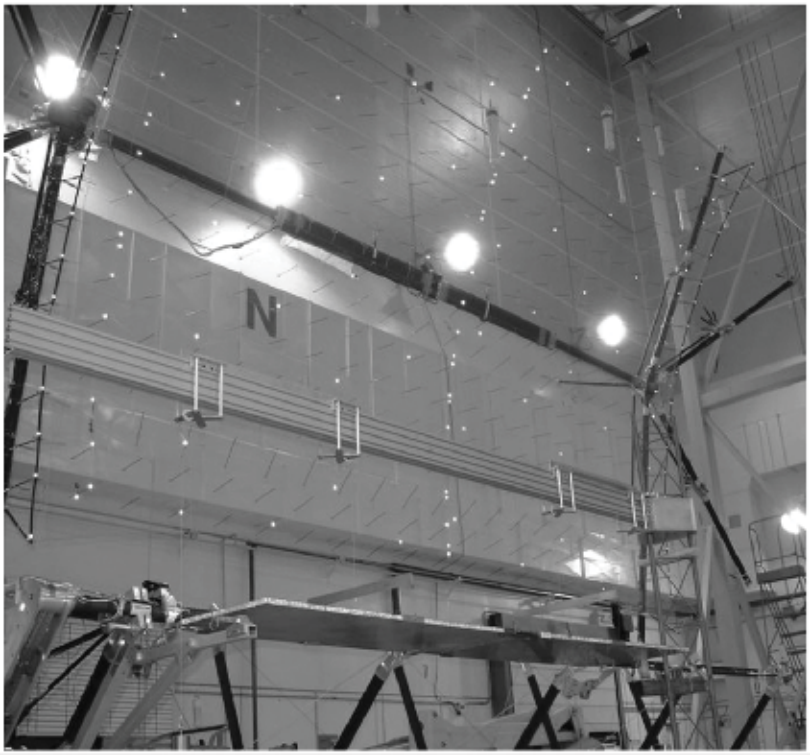

Figure 6.29 Twelve-meter engineering model of the PAFR antenna.

6.3.3 Reflectarrays

6.3.3.1 Reflectarray Technology Overview

The printed circuit reflectarray is a low-profile antenna type that evolved in the late 1980s. Reflectarrays use an array of printed circuit elements that is designed to control the phase of a reflected signal in order to create a non-Snell's law reflection

optics that enables a flat surface to function as a focused reflector comparable to a traditional parabolic reflector (Figure 6.30). The reflectarray elements control the phase of the reflected signal by adjusting some geometrical parameter, such as patch size, orientation, or the length of the transmission line. These elements are created using standard printed circuit board (PCB) fabrication methods, resulting in a low-cost reflector antenna that is readily mass produced. Reflectarrays offer the advantages of a traditional reflector, such as the simple feeding arrangement, but add many of the advantages of a phased array such as the ability to scan the beam and tailor the shape of the radiation pattern. Although reflectarrays are relatively narrowband and typically have lower overall efficiency than one can achieve with either a reflector or phased-array antenna, they are attractive for many instrument applications. Huang and Encinar provide an excellent overview of reflectarray technology including a comprehensive overview of the wide variety of design concepts that have been developed [16].

6.3.3.2 Folded Panel Deployable Reflectarrays

Reflectarrays are frequently built with the PCB material serving as the face sheet in a honeycomb sandwich configuration, resulting in a very strong and lightweight structural panel. These panels are inexpensive to build and the flat form factor is attractive for spacecraft applications because it enables the reflector to be folded, which simplifies stowage. This technical approach is well suited to instruments such as side-looking radars that require a low-cost, dual-polarization, scanned beam antenna.

Wide Swath Ocean Altimeter (WSOA)

Satellite missions began to use nadir pulsed radar altimeters to measure ocean height in 1992 with Topex/Poseidon, followed by Jason 1 in 2001 and Jason 2 in 2008. In the late 1990s, a unique experimental mission known as the Wide Swath Ocean

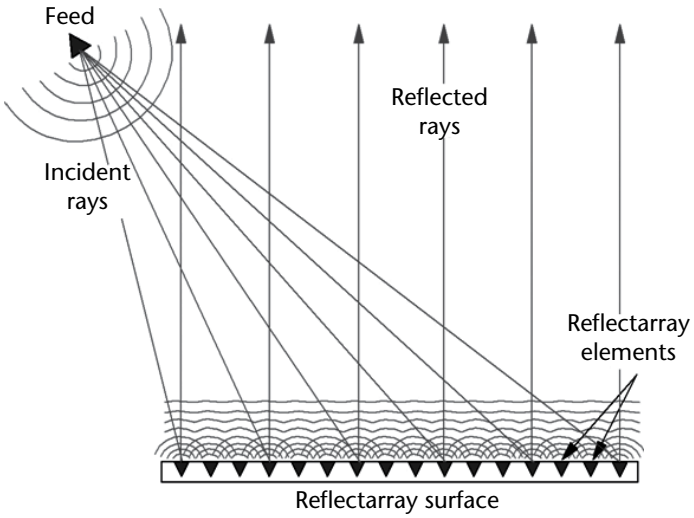

Figure 6.30 Illustration of reflectarray concept illustrating non-Snell's law optics.

Altimeter (WSOA) was proposed to produce a full three-dimensional map of ocean height. WSOA is a cross-track interferometer with a 6.4m baseline. An enabling technology for this instrument is a pair of 2.2m × 0.35m Ku-band antennas that are stowed by folding. They provide dual-beam, dual-polarization, ~20-dB sidelobes and 50% aperture efficiency in a low-mass package. Each antenna is comprised of a reflectarray and two feeds located off the focal point to produce two beams scanned ±3.3 deg from nadir.

Two Ku-band reflectarray antennas were developed for WSOA (Figure 6.31). The initial interferometer concept used a symmetric-fed piecewise parabolic (PWP) reflectarray with a 1.125m focal length in which each panel is tangent to a parabola [17]. However, due to consideration of mass, moment of inertia, and interferometric phase stability, the symmetric-fed reflectarray was abandoned in favor of an offset configuration with a 2.8m focal length [18]. Both configurations are comprised of five panels and two feeds, one for vertical polarization and one for horizontal polarization. A mechanical deployment mechanism is used to fold the flat panels into a stowage configuration for launch. The panels use variable-sized square patch reflectarray elements printed on Rogers RO4003 substrate material.

The piecewise parabolic design is used to minimize the total phase shift that must be supplied by the reflectarray elements in order to collimate the beam. This yields a more robust electrical design due to the reduced aperture phase gradient and minimization of phase wraps. A flat reflectarray was chosen for the offset-fed design in order to minimize scan loss for the two beams [19]. Breadboard tests were performed for both configurations. Performance of the two antenna designs was found to be comparable and confirmed that the analysis model accurately predicts the key antenna parameters.

Surface Water Ocean Topography (SWOT)

The proposed Surface Water Ocean Topography (SWOT) mission, currently in formulation by NASA and CNES, would employ a Ka-band radar interferometer (KaRIn) system to characterize ocean circulation at spatial resolutions of 10 km and provide a global inventory of all terrestrial water bodies whose width exceeds 50 to 100m [20].

The interferometer is formed by a pair of 5m × 0.26m reflectarray antennas separated by a 10m baseline as illustrated in Figure 6.32. The focal length is 4.37m,

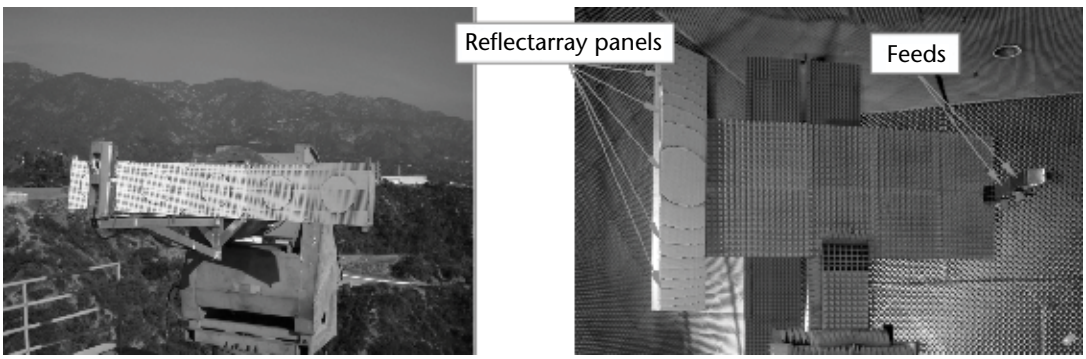

Figure 6.31 WSOA reflectarray antennas: (left) symmetric-fed PWP configuration and (right) offset-fed design.

with the focal point located near the spacecraft bus to minimize transmission losses to the transmitter/receiver. Each antenna creates two beams, one V-pol and one H-pol, which illuminate the two 10- to 70-km swaths. These antennas are a key enabler for the KaRIn instrument. Breadboard antenna test results demonstrate that the antenna will meet performance requirements [21].

6.3.3.3 Flat Membrane Reflectarrays

The flat membrane reflectarray is a relatively new antenna concept in which a reflectarray is pulled taut over a planar frame (usually circular or rectangular). This design concept offers the potential for large, ultra-lightweight instrument antennas that stow compactly. This technology is inherently less expensive than that of a traditional parabolic reflector because flat, flexible printed material is easier to fabricate, package, stow, and deploy in space. The flat membrane reflectarray antenna can employ inflatable/self-rigidizable technology in its primary structural members, thus allowing the reflectarray antenna to be collapsed and packaged into a small launch volume. However, reflectarrays are typically narrowband devices, so it is difficult to cover multiple frequency bands that are not harmonically related. In addition, the flat surface optics imposes limitations on instantaneous bandwidth due to path length differences between the source horn and various regions of the reflectarray surface.

Several experimental reflectarray antennas with different sizes and RF frequencies have been developed to demonstrate the technology. The first reflectarray antenna technology demonstration model that used inflatable structure technology was a 1m X-band reflectarray antenna [22] (Figure 6.33). The RF component consists of two layers of 1m-diameter circular Kapton membranes that are separated by a large number of small foam inserts. A urethane-coated Kevlar inflatable torus holds the RF membranes, and a hexagonal ring holds the feed, while three inflatable struts connect the torus and the hexagonal ring.

A 3m technology demonstration model of the inflatable reflectarray at Ka-band was also developed [23, 24] (Figure 6.34). This antenna is shaped like a horseshoe with a hexagonal ring to support its feed. Three asymmetrically located urethane-coated Kevlar inflatable struts connect the ring. The horseshoe-shaped

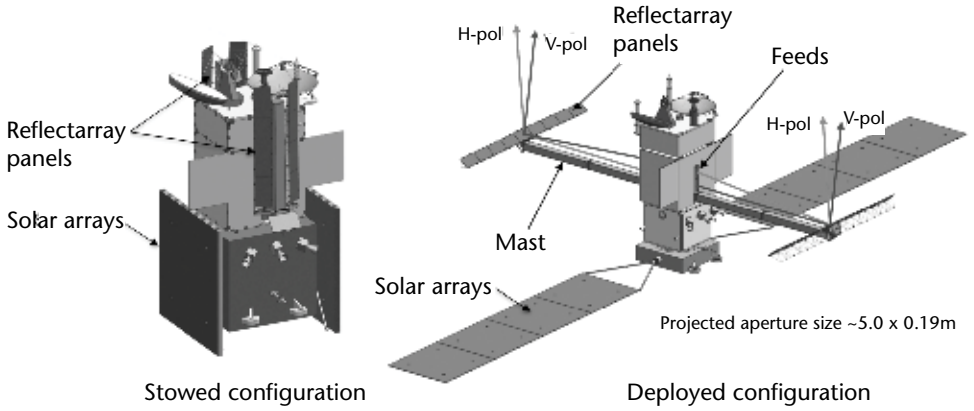

Figure 6.32 Proposed SWOT antenna configuration.

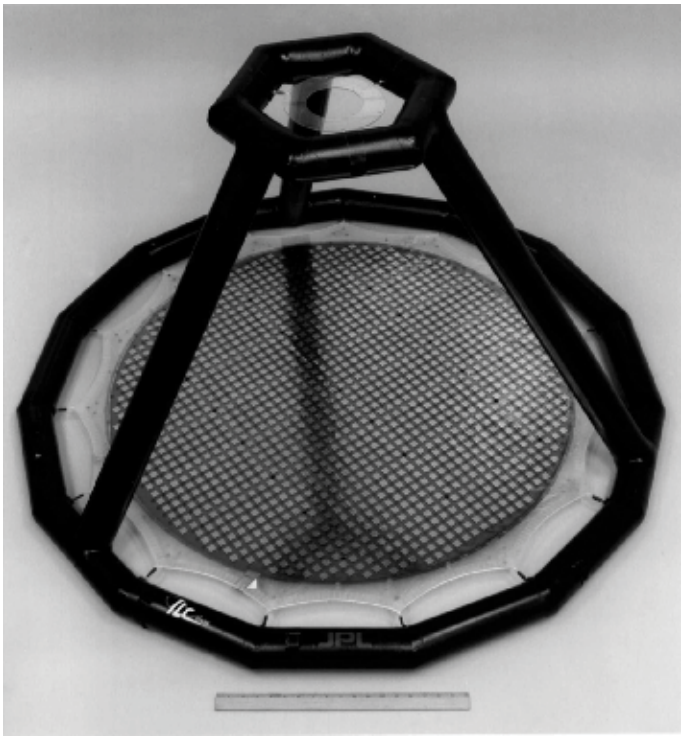

Figure 6.33 One-meter X-band flat membrane reflectarray antenna with inflatable deployment mechanism.

configuration facilitates compact stowage because the deflated support structure and membrane can be rolled up onto a rigid tube assembly without causing significant wrinkling to the membrane. The inflatable components must remain pressurized throughout the entire mission. The 3m reflectarray achieved an rms surface error of 0.16 mm (1/55 wavelength at the 32-GHz design frequency). RF tests demonstrated excellent radiation pattern characteristics, although the aperture efficiency of this demonstration unit was very low due to a design flaw in the reflectarray element design. The boom concept has been tested in the thermal/vacuum chamber and is rated at a technology readiness level of 4 to 5.

A dual X- and Ka-band, circularly polarized flat membrane reflectarray unit demonstrated that two widely spaced frequency bands can share the same aperture without introducing significant performance penalty [25]. This demonstration array employs stacked split-ring reflectarray elements that are consistent with the flat membrane reflectarray design, and it achieved approximately 50% efficiency at both bands.

6.3.4 Inflatable Reflectors and Structures

Inflatable antenna technology has been the subject of many years of research as a large deployable reflector technology that offers several potential advantages, including stowage volume and aerial density. An inflatable antenna includes four subsystems: reflector, inflation system, controlled deployment system, and structural support elements. Inflatable membrane structures ideally form a true metal

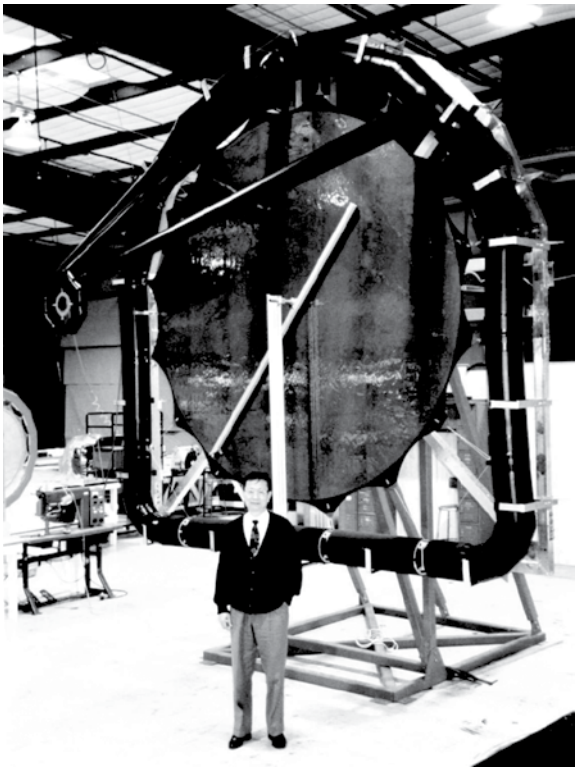

Figure 6.34 Three-meter Ka-band flat membrane inflatable reflectarray antenna.

paraboloid, compared with mesh reflectors, which provide a faceted approximation to a parabolic surface. In contrast to a flat membrane reflector, an inflatable paraboloid has a much wider bandwidth and higher efficiency, but it is more difficult to accurately create a doubly curved surface.

Although inflation methods have been successfully demonstrated in the laboratory, flexible materials will inevitably leak over an extended period of time in space as a result of micrometeoroids, radiation damage, and other factors. A variety of rigidization methods have been developed to address this issue, as discussed next.

6.3.4.1 NASA Inflatable Reflectors

The NASA-funded development of a variety of inflatable antenna projects began in the late 1950s with the Echo balloons. Echo 1 was a 31m-diameter inflated sphere made from 0.5-mil Mylar and coated with a layer of vapor-deposited aluminum. The 62-kg reflector successfully reflected radio transmissions between various locations on Earth, but failed to retain its spherical shape on orbit. Echo 2, a 41m-diameter sphere launched in 1964, served as a Comsat communications satellite for 1 year.

The Inflatable Antenna Experiment (IAE) was flown in 1996 to validate the deployment of a 14m inflatable parabolic reflector structure. Photos of the antenna experiment on orbit are shown in Figure 6.35. The basic elements of the antenna system include the (1) inflatable parabolic membrane reflector, (2) inflatable torus, which is the support structure for the reflector, and (3) 33m-long inflatable

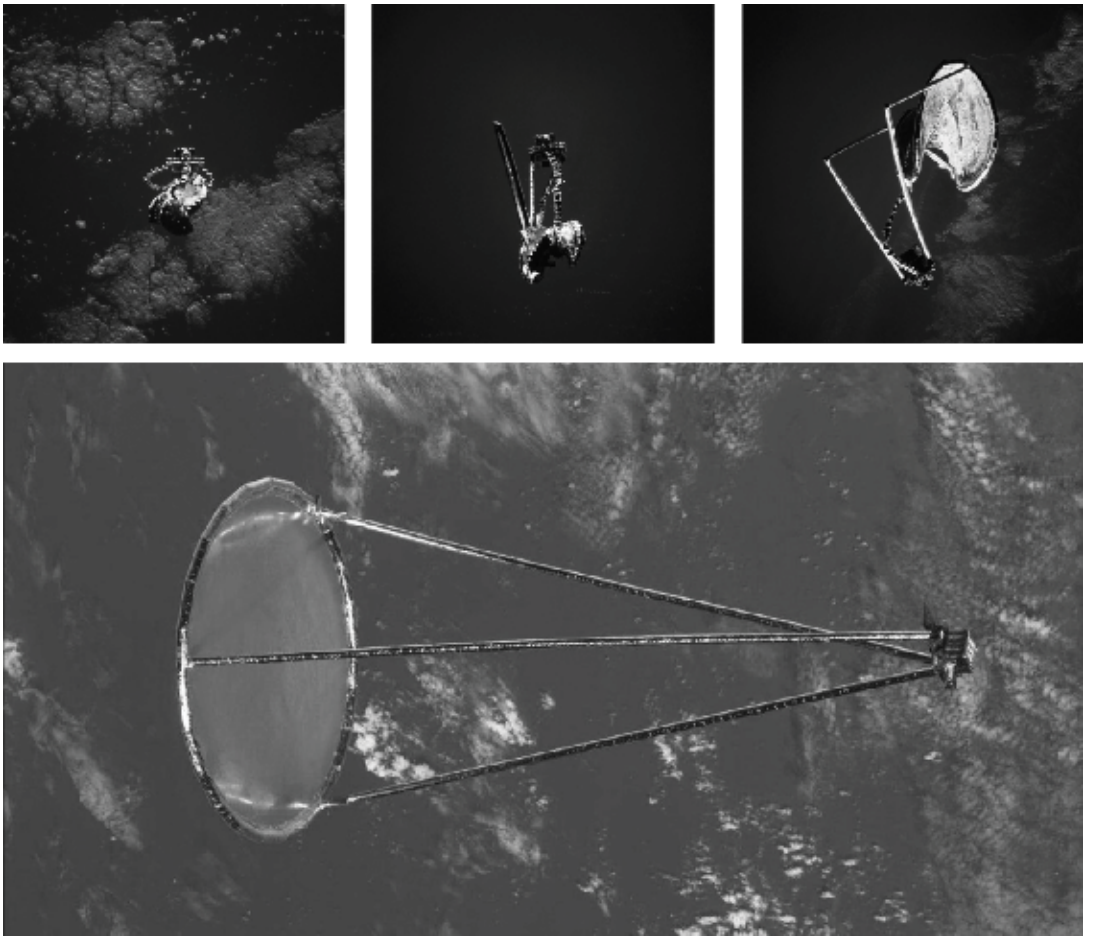

Figure 6.35 On-orbit photos of the Inflatable Antenna Experiment (IAE).

struts to support the feed structure. A canister assembly provided support for the stowed antenna and other experiment equipment. During the 90-min experiment, the L'Garde-built antenna structure deployed to the proper shape, but the reflector failed to completely inflate, precluding any in-flight measurements of surface accuracy. Nevertheless, it demonstrated that a low-cost (~$1M) reflector antenna of this size can be stowed in a small volume, survive launch loads, and inflate to a specified configuration in space. It remains the only significant inflatable reflector antenna deployed in space [26].

During the past decade, NASA funded a variety of inflatable reflector research efforts [27]. Glenn Research Center (GRC) and SRS Technologies developed a 0.3m offset inflatable thin-film polymer (CP-1) antenna, which was successfully tested at 8.4 GHz in 2004. In 2004–2005, a 4m × 6m offset thin-film inflatable antenna was fabricated and tested (Figure 6.36). The measured 3.5-mm rms surface accuracy of this antenna was concentrated in the flattened edge region, so the reflector performed better than rms surface error would suggest. The antenna achieved a directivity of 49.4 dBi (71% efficiency) at 8.4 GHz and 51.6 dBi (8% efficiency) at 32 GHz.

Figure 6.36 A 4m × 6m inflatable membrane reflector antenna in the NASA GRC near-field range.

In 2001, Johns Hopkins Applied Physics Laboratory (APL) and ILC Dover developed the Hybrid Inflatable Antenna (HIA) concept to address the perceived risk of inflatable antenna technology [28]. The HIA combines a traditional rigid parabolic antenna with an "inflation-deployed" rigidized reflector and support structures. A solid-body high-gain antenna is surrounded by a large inflated aperture in order to ensure a minimum level of performance for mission success in the event of a deployment anomaly (Figure 6.37). The HIA inflatable system stows very compactly under the rim of the fixed reflector so there is a relatively small increase in the stowed volume. A 2m, one-third scale model, prototype HIA built by ILC Dover achieved an rms surface error of approximately 1.1 mm.

6.3.4.2 Rigidizable-Deployable Structures with Inflatable Deployment Mechanism

Inflatable structures employ a radically different paradigm from conventional mechanical support structures in that gas-pressure inflation of a flexible structure replaces motor and cable actuation of solid elements. This concept has the important advantage that the stowed material can be densely packed for maximum stowage efficiency. For example, the inflatable structure designed to support a thin membrane reflectarray shown earlier in Figure 6.34 collapses into a small roll, as seen in the deployment sequence of Figure 6.38 [23]. Despite the conceptual simplicity of the inflation mechanism, the design employs a sophisticated sequence of internal baffles to control the deployment rate and provide stiffness to the deployed

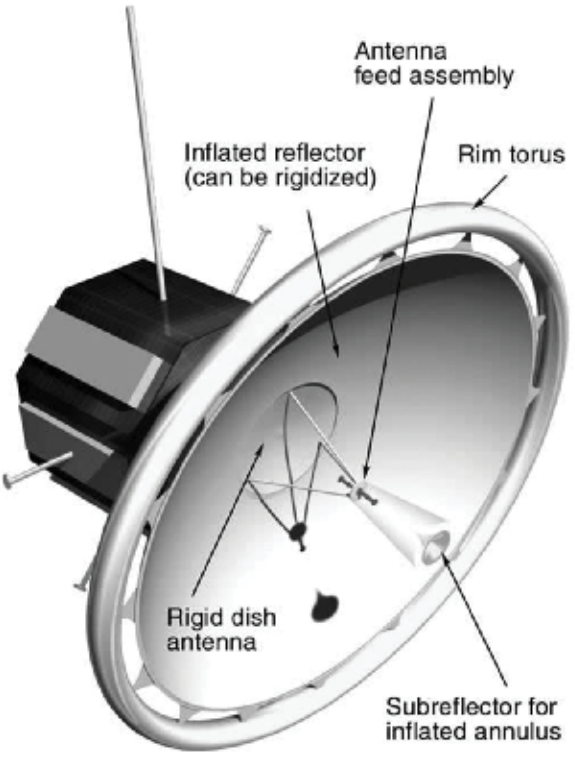

Figure 6.37 Illustration of the Hybrid Inflatable Antenna (HIA) concept in a deployed configuration.

structure. Velcro strips and constant force springs are also used to stage the deployment and increase the stiffness of the final deployed structure.

To eliminate the need to maintain constant inflation gas pressure, a variety of rigidization methods have been developed. These include passive cooling, UV exposure, inflation gas reaction, thin wall aluminum, and foam inflation. A useful description of these methods can be found in [29]. Several are currently being investigated for antenna applications. Methods referred to as inflatable-rigidizable employ a chemical or photonic mechanism to harden the antenna after deployment. Thermosetting inflatable rigidization relies on heating the material above its glass transition temperature during deployment. Currently, the most promising materials are two classes of composites: sub-Tg rigidizable thermoplastics and elastomerics, and UV and heat-cured thermoset plastics. Recent materials technology work has validated their use as high-modulus truss elements suitable for the space environment.

It was recognized during the development of the flat membrane Ka-band inflatable reflectarray (see Figure 6.38) that rigidization is essential for space missions. Consequently, ILC-Dover developed the "movie screen" deployment scheme under a Jet Propulsion Laboratory study contract for a space-applicable version of the 3m Ka-band inflatable reflectarray antenna [30–32] (see Figure 6.39). The reflectarray surface of this design is deployed by two inflatable booms in a manner similar to the unrolling of a movie screen. The inflation deployment process of the antenna only involves the unrolling and pressurization of two inflatable booms, making it possible to employ the "spring tape reinforced aluminum laminate boom" inflatable/

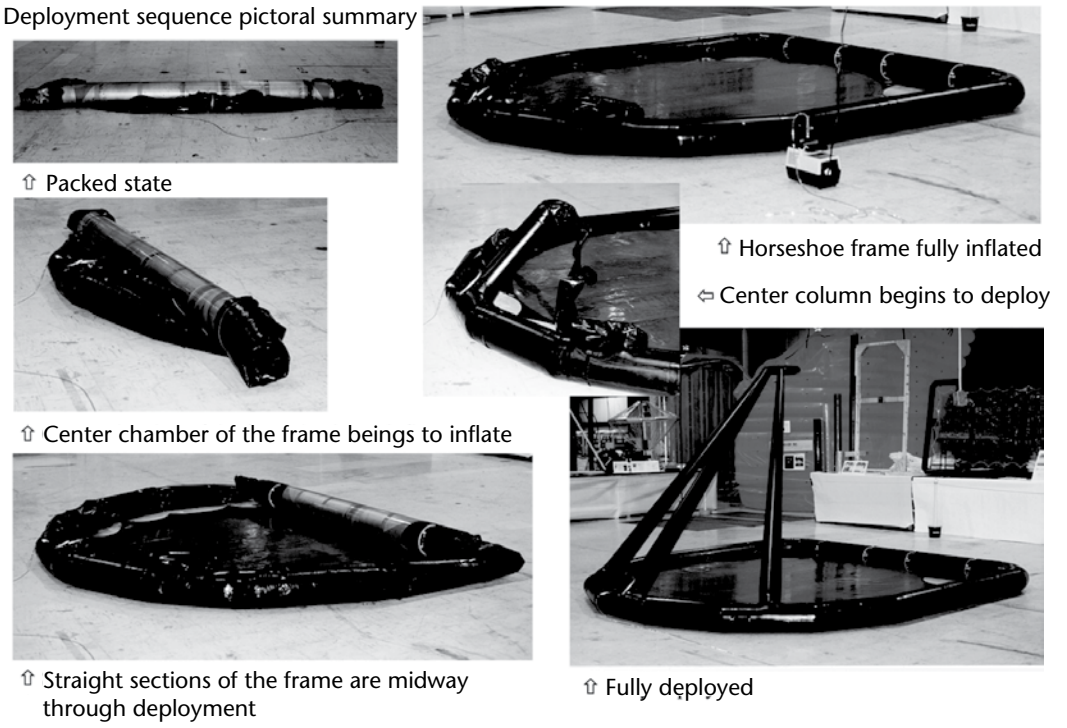

Figure 6.38 Deployment sequence of a 3m flat membrane Ka-band inflatable reflectarray.

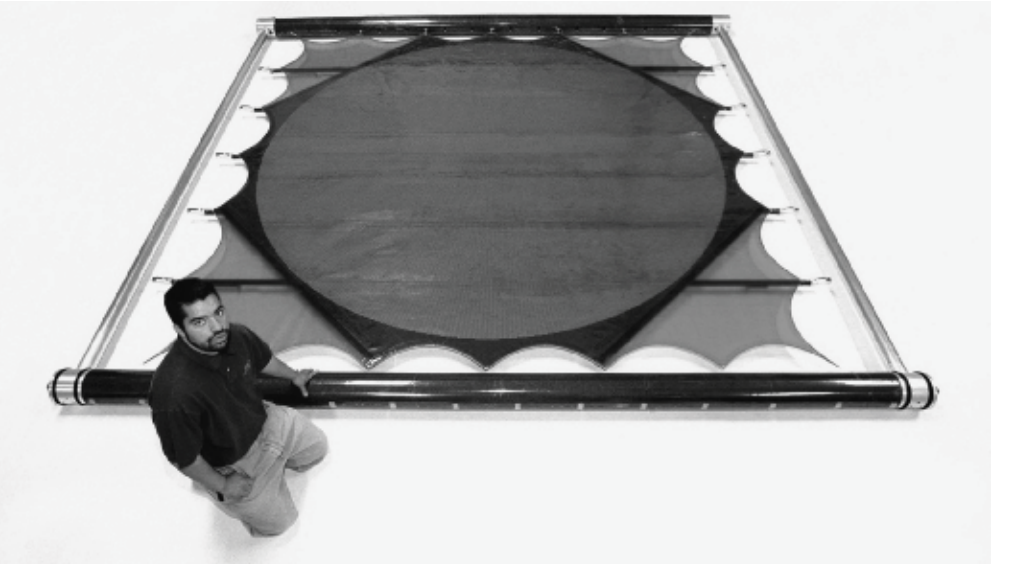

Figure 6.39 Three-meter Ka-band inflatable reflectarray antenna with "movie screen" deployment frame.

self-rigidizable boom technology [33]. A spring tape reinforced aluminum laminate boom automatically rigidizes after it is deployed by inflation pressure and needs no

internal pressure to maintain rigidity. Unlike other space rigidization approaches, this one requires no space power, curing agent, or other added-on mechanisms or devices.

6.4 Summary

This chapter provided an overview of the major types of reflector antenna designs. The majority of the historically significant antennas that have been flown are solid nondeployable composite reflectors. The Voyager/Magellan mission illustrates a symmetric shaped reflector that provides dual frequency band capability to support both telecommunications and radar instruments. The Cassini antenna demonstrates the remarkably wide range of capability that a solid reflector system can provide. It delivers channels that cover S-band (radio science), X-band (telecom), Ku-band (radar imaging and altimetry), and Ka-band (Doppler).

CloudSat illustrates the level of performance that can be achieved with a reflector optimized for a single frequency band radar antenna. The antenna is an electrically large (580 wavelength diameter) offset-fed reflector with exceptionally high efficiency (59%) and ultra-low sidelobe performance (50 dB). An important feature of this antenna is the use of a quasi-optical transmission line to achieve extremely low transmitter-to-antenna transmission line loss. At another extreme, the Aquarius mission uses an electrically small (12 wavelength diameter) multibeam antenna that supports both radar and radiometer bands.

All of the aforementioned examples are fundamentally derived from classical parabola-hyperbola optics. In contrast, the Mars Reconnaissance Orbiter reflector antenna illustrates a new "displaced axis" optics design that provides very low blockage in compact antenna design. Finally, the Jason 3 antenna illustrates the use of offset-fed reflectors for a dedicated radiometer instrument.

Although future missions will undoubtedly continue to utilize solid composite reflectors, new antenna technologies have emerged that represent enabling technologies for next-generation sensors. Novel materials have enabled development of new deployment concepts such as the CTD shaped memory composite reflector and the TDRSS spring-back reflector, which take the form of a solid composite reflector following deployment.

New mesh reflector designs have demonstrated high surface accuracy and extremely large aperture sizes, which has enabled the development of missions such as Galileo and SMAP.

Reflectarray antenna technology is of special importance for instruments because it is inexpensive and amenable to compact stowage through folding and inflation mechanisms. Moreover, reflectarrays offer unique capabilities, such as the ability to select a different focal point for each polarization, which may not be possible with a standard reflector. The NASA-proposed SWOT mission illustrates how reflectarray technology can be mission enabling. Finally, it should be noted that inflatable antennas, although not yet technically mature, have tremendous potential to produce a highly diverse set of antenna shapes that stow very compactly.

Acknowledgments

This research was carried out in part at the Jet Propulsion Laboratory, California Institute of Technology, under a contract with the National Aeronautics and Space Administration. Special thanks to Dana Turse and Robert Taylor of Composite Technology Development, Inc. for contributing material on segmented folding composite reflectors, and to Dana in particular for helping with the final review of this chapter.

References

[1] R. E. Cofield, W. A. Imbriale, and R. E. Hodges, "Instrument Packages," in *Spaceborne Antennas for Planetary Exploration*, W. A. Imbriale, Ed., Pasadena, CA: Jet Propulsion Laboratory, California Institute of Technology, pp. 341–424, 2006.

[2] Jet Propulsion Laboratory, Voyager Mission website [online]. Available: http://voyager.jpl.nasa.gov/index.html [accessed 2012].

[3] W. Johnson, "Magellan Imaging Radar Mission to Venus," *Proceedings of the IEEE,* Vol. 79, No. 6, pp. 777–790, 1991.

[4] E. H. Maize, "The Cassini-Huygens Mission to Saturn and Titan," in *Space Technology and Application International Forum—STAIF 2005*, Melville, NY, 2005.

[5] R. Mizzoni, "The Cassini High Gain Antenna (HGA): A Survey on Electrical Requirements, Design and Performance," in *IEE Seminar on Spacecraft Antennas*, London, 1994.

[6] A. Toccafondi, B. Romani, R. Mizzoni, S. Maci, and R. Tiberio, "Spherical Wave Blockage in Reflector Antennas," *IEEE Transactions on Antennas and Propagation,* Vol. 45, No. 5, pp. 851–857, 1997.

[7] E. Im, S. L. Durden, C. Wu, and T. R. Livermore, "The 94GHz Cloud Profiling Radar for the CloudSat Mission," in *IEEE Aerospace Conference Proceedings*, Big Sky, MT, 2001.

[8] S. Spitz, A. Prata, J. Harrell, R. Perez, and W. Veruttipong, "A 94 GHz Profiling Radar Antenna System," in *IEEE Aerospace Conference Proceedings*, Big Sky, MT, 2001.

[9] Aquarius Mission Website, [online]. Available: http://aquarius.nasa.gov/documents.html [accessed 2012].

[10] MRO Mission website [online]. Available: http://marsprogram.jpl.nasa.gov/mro [accessed 2012].

[11] Galileo Mission website [online]. Available: http://solarsystem.nasa.gov/galileo [accessed 2012].

[12] SMAP Mission website [online]. Available: http://smap.jpl.nasa.gov [accessed 2012].

[13] P. Focardi, P. Brown, and Y. Rahmat-Samii, "Deployable Mesh Reflector Antennas for Space Applications: RF Characterizations," Chap. 8 in *Space Antenna Handbook*, New York: Wiley, pp. 314–343, 2012.

[14] J. Guerci and E. Jaska, "ISAT—Innovative space-based-radar antenna technology," in *IEEE Int. Symp. on Phased Array Systems and Technology*, Boston, MA, 2003.

[15] S. A. Lane and T. W. Murphey, "Overview of the Innovative Space-Based Radar Antenna," *Journal of Spacecraft and Rockets,* Vol. 48, No. 1, pp. 135–145, 2011.

[16] J. Huang and J. A. Encinar, *Reflectarray Antennas*, New York: John Wiley & Sons, 2008.

[17] R. E. Hodges and M. S. Zawadzki, "Design of a Large Dual Polarized Ku Band Reflectarray for Space Borne Radar Altimeter," in *Joint IEEE Antennas and Propagat. Soc. and URSI Radio Sci. Meeting*, Monterey, CA, 2004.

[18] R. E. Hodges and M. S. Zawadzki, "A Reflectarray Antenna for Use in Interferometric Measurement of Ocean Height," in *IEEE Aerospace Conf*, Big Sky, MT, 2005.

[19] R. E. Hodges and M. S. Zawadzki, "Scanning Properties of Large Reflectarray Antennas," in *Joint IEEE Antennas and Propagat. Soc. and URSI Radio Sci. Meeting*, Monterey, CA, 2004.

[20] D. Esteban-Fernandez, L.-L. Fu, E. Rodriguez, S. Brown, and R. Hodges, "Ka-Band SAR Interferometry Studies for the SWOT Mission," in *IEEE International Geoscience and Remote Sensing Symposium (IGARSS)*, Honolulu, HI, 2011.

[21] R. E. Hodges and M. S. Zawadzki, "Ka-Band Reflectarray for Interferometric SAR Altimeter," in *Joint IEEE/URSI Int. Symp. on Antennas and Propagat*, Chicago, IL, 2012.

[22] H. Fang, M. Lou, J. Huang, and L. Hsia, "An Inflatable/Self-Rigidizable Structure for the Reflectarray Antenna," in *10th European Electromagnetic Structures Conference*, Munich, Germany, 2001.

[23] V. A. Feria, J. Huang, and D. Cadogan, "3-Meter Ka-Band Inflatable Microstrip Reflectarray," in *ESA AP 2000 Conference*, Davos, Switzerland, 2000.

[24] J. Lin, D. Cadogan, J. Huang, and V. A. Feria, "An Inflatable Microstrip Reflectarray Concept for Ka-Band Applications," in *41st AIAA/ASME/ASCE/AHS/ASC Structures, Structural Dynamics, and Material Conference*, Atlanta, GA, 2000.

[25] C. Han, J. Huang and K. Chang, "A High Efficiency Offset-Fed X/Ka Dual-Band Reflectarray Using Thin Membranes," *IEEE AP-S Transactions,* Vol. 53, pp. 2792–2798, 2005.

[26] R. E. Freeland, G. D. Bilyeu, G. R. Veal, M. D. Steiner, and D. E. Carson, "Large Inflatable Deployable Antenna Flight Experiment Results," in *Proceedings of the 48th International Astronautical Congress*, Turin, Italy, 1997.

[27] D. W. Williams, M. Collins, R. E. Hodges, R. S. Orr, O. S. Sands, L. Schuchman, and H. Vyas, "High-Capacity Communications from Martian Distances," NASA/TM-2007-214415, Cleveland, OH, 2007.

[28] C. E. Wiley, R. C. Schulze, R. S. Bokulic, W. E. Skullney, J. K. Lin, D. P. Cadogan, and C. F. Knoll, "A Hybrid Inflatable Dish Antenna System for Spacecraft," in *42nd AIAA/ASME/ASCE/AHS/ASC Structures, Structural Dynamics, and Materials Conference & Exhibit AIAA—Gossamer Spacecraft Forum*, Seattle, WA, 2001.

[29] D. Cadogan, M. Grahne, and M. Mikulas, "Inflatable Space Structures: A New Paradigm for Space Structure Design," in *49th International Astronautical Congress*, Melbourne, Australia, 1998.

[30] M. Lou and H. Fan, "Development of Inflatable Antenna Structures," in *Proceedings of the European Conference on Spacecraft Structures, Materials & Mechanical Testing*, Toulouse, France, 2002.

[31] H. Fang, M. Lou, J. Huang, U. Quijano, and L. Hsia, "Thermal Distortion Analyses of a Three-Meter Inflatable Reflectarray Antenna," in *44th AIAA/ASME/ASCE/ AHS/ASC Structures, Structural Dynamics, and Materials Conference and Exhibit*, Norfolk, VA, 2003.

[32] H. Fang, M. Lou, J. Huang, G. Kerdanyan, and L. Hsia, "An Inflatable/Rigidizable Ka-Band Reflectarray Antenna," in *43rd AIAA/ASME/ASCE/AHS/ASC Structures, Structural Dynamics, and Materials Conference and Exhibit*, Denver, CO, 2002.

[33] M. Lou, H. Fang, and L. Hsia, "Development of Space Inflatable/Rigidizable STR Aluminum Laminate Booms," in *Space 2000 Conference & Exposition*, Long Beach, CA, 2000.

CHAPTER 7

Feed Assemblies, Passive Intermodulation, Multipaction, and Corona

Clency Lee-Yow and Jonathan Scupin, Custom Microwave Inc.
Robert Reynolds and James Farrell, Boeing Satellite Development Center
Sudhakar Rao, Northrop Grumman Aerospace Systems

7.1 Introduction

Communication satellites and associated ground antennas are used for a wide variety of commercial applications including TV, telephone, data, radio, and Internet. They are also widely used by the military for the flexible exchange of information between different units of the armed forces. Most communication satellites are located in a geostationary orbit (GEO) and generally use reflector antennas to simultaneously transmit and receive RF signals using separate downlink and uplink frequency bands for communicating with antennas on Earth. The reflector antennas are illuminated directly or indirectly via a subreflector by a feed to provide high-gain coverage at specific locations on Earth. The feed assembly is key hardware in a satellite antenna. It defines the bandwidth, polarization, power handling, passive intermodulation (PIM) levels, and illumination on the reflector. It also separates various frequency bands, thus providing required isolation among the frequency bands and provides a good match with free space.

The feed assembly typically comprises a horn, orthomode transducers (OMTs), fillers or diplexers, polarizers, transitions, combining/dividing networks, and an antenna interface to the payload. It separates frequency bands, converts circular polarization (CP) to and from a linear signal, and isolates orthogonal polarizations for frequency reuse while providing a good match with free space. Reflector antennas can use a single or multiple feeds to provide the desired beam coverage. While the reflector provides desired gain and beam shape on the ground, the feed assembly dictates most of the RF performance in terms of insertion loss, return loss, axial ratio or cross-polar isolation, bandwidth, isolation among the bands for multiband payloads, high power handling, and PIM levels.

The most common frequencies used for current communication satellites are at C-, Ku-, and Ka-bands. At these frequencies the feeds can be realized in waveguide structures without being too bulky. In addition to their practical size, waveguide structures also have low loss, can handle high power, and are very reliable, all of which are very desirable features for communication satellites.

In this chapter, some insight is given into the design of commonly used feeds. The feed requirements are driven by the overall antenna requirements for beam coverage. From the feed requirements, the designers have to arrive at a concept that not only meets RF requirements but also fits in a small envelope, has low mass, is manufacturable, and can operate in the harsh space environment. The design has to be completed in a relatively short time to fit within the schedule allocated for design, fabrication, and testing of the feed.

The antenna or payload requirements drive the feed assembly design. The payload types include FSS, DBS, PCS, MSS, and so forth. Fixed satellite payloads require the feed assemblies to be dual-band supporting both uplink and downlink frequency bands. Because they employ a common feed assembly, larger bandwidth, high power handling, and PIM are the key requirements that need to be met in a multicarrier payload. On the other hand, DBS payloads use a transmit-only function from the antennas and the key requirements are power handling, thermal design, lower losses, and axial ratio. The PCS multiple beam satellites employ multiple feed assemblies for each reflector antenna. Key feed requirements are the dual-band capability, a compact assembly that can fit all hardware within the aperture diameter of the feed horn, low losses, low axial ratio, and low mass. The mobile (MSS) payloads require a feed array comprising a large number of elements and the key requirements are element efficiency and PIM. The types of beam shapes on these types of payloads that the feed assemblies and the antenna support include shaped or contoured beams, high-gain pencil beams, multiple spot beams, multiple contoured beams, and reconfigurable beams.

7.2 Feed Components

The first step in the design process is to decide on a topology that can meet both RF and mechanical requirements. A good understanding of waveguide theory, filter design, waveguide component design, performance capability, integration, and manufacturability of each type of component is necessary in order to lay out a concept that can be realized successfully without iterations. Waveguide theory [1–3], horn design [4, 5], and filter design [6, 7] are discussed in details in a number of books and will not be covered here. Instead key components will be discussed to provide some insight into how they can be integrated to realize reflector antenna feeds.

7.2.1 Bends

Bends are required to change the direction of the wave propogation in the waveguide. Bends can be in the E- or H-plane as shown in Figure 7.1. In a feed network, there are usually several of these components in series, making it critical to achieve optimal return loss for each bend in order to minimize its impact on the overall feed performance. For space applications, where small size is very desirable, mitre bends

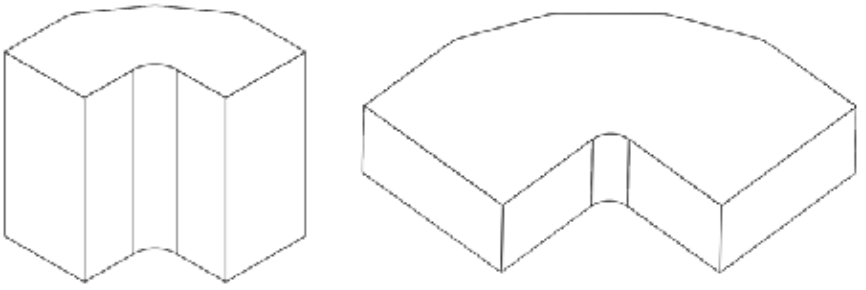

Figure 7.1 Examples of E- and H-plane bends.

offer high performance in a small space. E-plane and H-plane mitre bends can achieve better than a 50-dB return loss over more than 40% bandwidth. Depending on the fabrication method, mitre bends may have internal radii that should be included in the design and analysis.

7.2.2 Transitions

For optimal performance, waveguide feed components are usually designed in nonstandard sizes. The waveguide cross section can also be rectangular, square, circular, ridged, or coaxial depending on functionality. To minimize reflections between different sizes and cross sections, transitions or impedance transformers are used between the different waveguide sections. A number of different transitions are shown in Figure 7.2.

A transition typically consists of steps that gradually change the cross section between the two waveguide sections to be mated. The lengths and dimensions of each section can be optimized together using commercial software to minimize reflections and provide maximum power transfer. In general, a single intermediate step provides reasonable performance over a narrow band, typically a 30-dB return

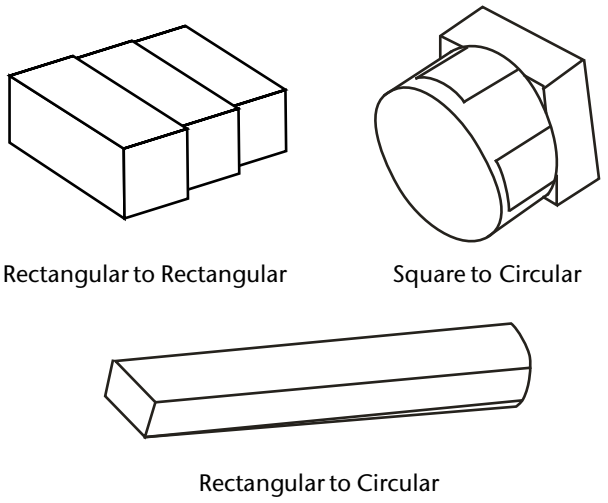

Figure 7.2 Examples of transitions.

loss over about 5% bandwidth. Three to four steps have been found to provide good performance over a wide bandwidth for most practical cases at the expense of length.

A very compact and commonly used transition between a circular and square cross section is an octagonal transition. This transition can be used to provide better than a 30-dB return loss over more than 70% bandwidth and can be very effective for matching a horn to the rest of the feed network. However the designer has to verify that the level of the TM01 mode excited with this transition is within acceptable limits so as not to have significant impact on the feed radiation patterns.

Transitions may be fabricated in a single piece by direct machining. When features are not accessible by direct machining in a single piece, split block machined pieces can be bolted or brazed together. In high-volume production, casting is a useful technique to lower costs. For closer integration with other components in a more complex assembly, electroforming can be used instead to realize a one-piece part. Machining radii if present must be accounted for during the design and analysis.

7.2.3 Filters

The design of microwave filters has been covered extensively in several well-known books [6, 7]. It is notable that the filters and diplexers required in antenna feeds are of relatively broadband performance, not the channelized filters present in multiplexers. Although the near-band rejection and group delay characteristics of these front-end filters and diplexers are not as stringent, they must have very low insertion loss, handle the full power level of all channels simultaneously without multipaction, and not contribute to the passive intermodulation of the feed. Front-end filters may be lowpass, bandpass, or highpass. Lowpass filters are typically comprised of corrugated sections, whereas bandpass filters are often of the inductive iris type. These topologies may also be designed together with a common waveguide junction to form a diplexer or a triplexer, thereby allowing transmit (Tx) and receive (Rx) signals to be combined into the same waveguide path. Figure 7.3 shows different types of filters commonly used in feed networks.

Filters may be designed to be manufactured by direct machining in pieces, which are then bolted or brazed. Machining radii if significant must be included in the RF design. This can add more time to the design process because an element with radii is not as computationally efficient as one with sharp corners.

Electroforming can be used to construct a seamless single-piece filter or diplexer with sharp corners as shown in Figures 7.3 and 7.4. Manufacturing tolerances

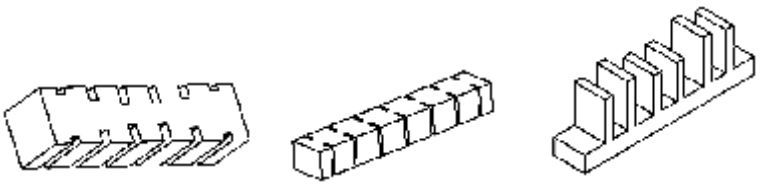

Figure 7.3 Examples of filters typically used in feed networks.

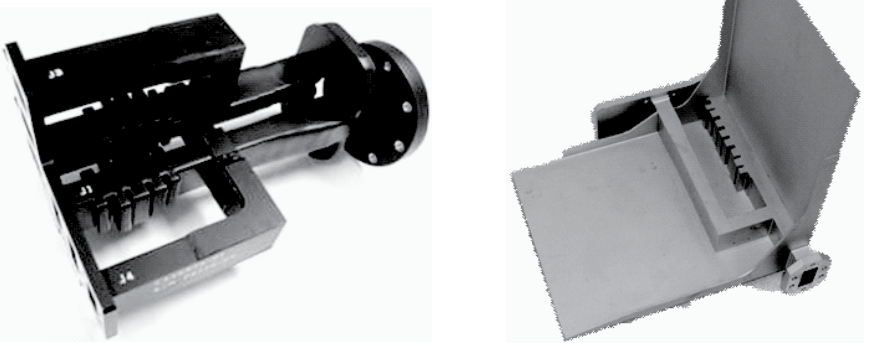

Figure 7.4 Examples of electroformed diplexers.

must be analyzed to prevent deterioration of key parameters (typically return loss is the most sensitive parameter). In some cases, tuning elements are used to compensate for manufacturing tolerances or design uncertainties. However, tuning elements are not typically amenable to high-power or low-PIM applications and therefore must be avoided for space hardware.

7.2.4 E-Plane, H-Plane, and Magic Tees

Another basic component found on many antenna feeds is a power divider/combiner. In its simplest form it is a three-port device that divides a signal equally into two paths or combines two signals into one path and is often referred to as a *tee*. An E-plane tee results in a phase shift of 180 deg between the two outputs. An H-plane tee results in a phase shift of 0 deg between the two outputs. A magic tee is a four-port combination of the two types of tees, and can perform both types of phasing operations. Examples of tees are shown in Figure 7.5.

E-plane or H-plane tees are very compact and ideally suited where tight packaging of the components is required. They can be designed to operate over more than 50% bandwidth with return losses of better than 30 dB. However special attention must be paid to the design and fabrication of the tee to ensure it is connected to a well-matched and symmetrically balanced structure. Asymmetries from design or fabrication tolerances can result in excitation of undesirable modes. Where asymmetries cannot be avoided, magic tees can be used instead with either the E- or H-port of the magic tee loaded. The magic tee is not as broadband as the simple tee, and more space is required to accommodate the extra port and the load.

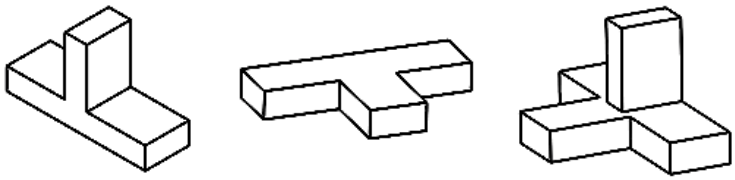

Figure 7.5 Examples of tees in feed networks.

Tees are often used when splitting power to a symmetric OMT as shown in Figure 7.6, or as components in a comparator network to perform tracking functions as shown in Figure 7.7.

7.2.5 Orthomode Transducers

An OMT is commonly used to provide dual-polarization capability for a feed. The OMT separates or combines two orthogonal linearly polarized (LP) dominant mode signals while maintaining good return loss at all ports and providing good isolation between the two orthogonal signals. Many structures have been used to realize an OMT. The particular choice depends on operational bandwidth, return loss required, feed layout, power handling capability, and manufacturing technique.

7.2.5.1 Asymmetric OMTs

When the operating bandwidth is less than about 20%, an asymmetric OMT can be used with reasonable return loss performance. This type of OMT is relatively easy to realize. Figure 7.8 shows such an OMT machined in two halves, and Figure 7.9 shows another OMT fabricated in one piece by electroforming. Isolation between the two polarizations can be greater than 60 dB at C-band when properly manufactured as shown in Figure 7.10.

7.2.5.2 Symmetric OMTs

When bandwidth greater than around 20% is required, a symmetric OMT design can extend the performance without exciting undesired modes at the higher frequencies. The trade-off is increased fabrication complexity. Symmetric OMTs may be manufactured by direct machining in pieces that are then bolted or brazed. Electroforming can be used to construct a seamless single-piece OMT, as shown in Figure 7.11, which helps reduce the risks of generating PIM in the presence of high carrier power.

Symmetric OMTs typically contain some type of matching structure in the common junction, such as posts and a vane [8] or steps. Isolation between the two

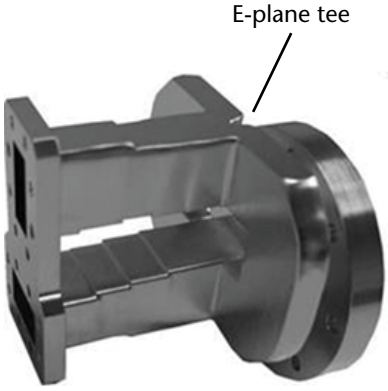

Figure 7.6 Examples of electroformed OMT with tee.

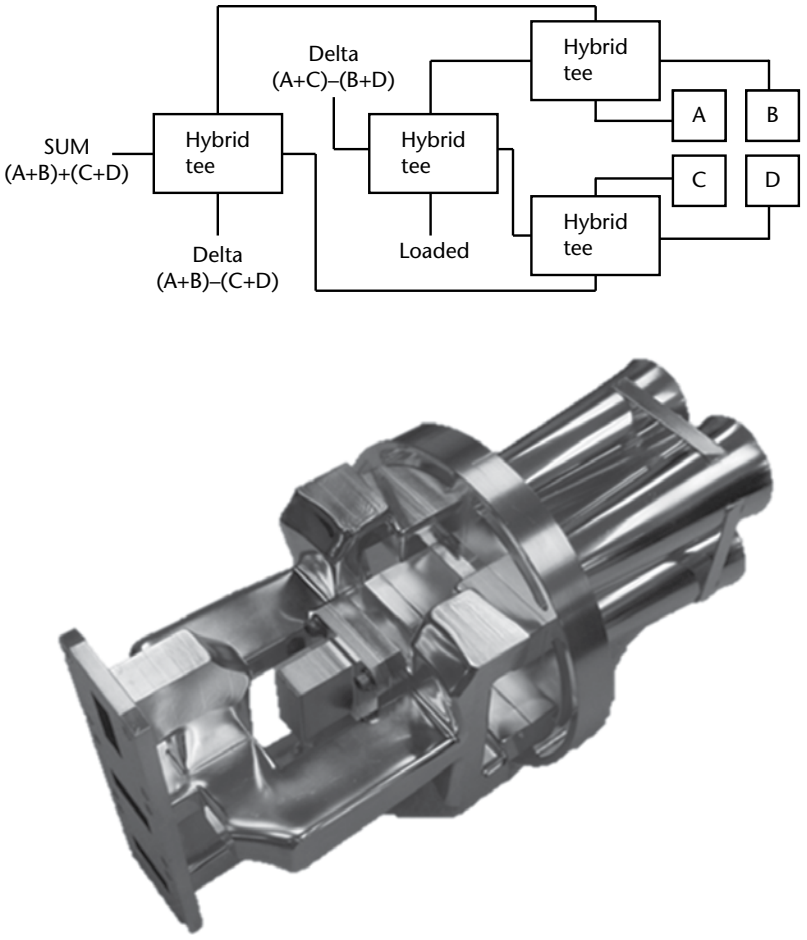

Figure 7.7 Block diagram of monopulse comparator using hybrid tees and the part realized in one piece by electroforming .

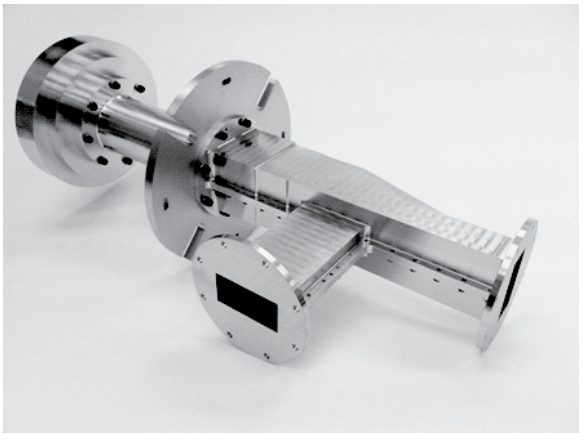

Figure 7.8 Machined asymmetric OMT.

polarizations can be greater than 55 dB at Ku-band when properly manufactured as shown in Figure 7.12.

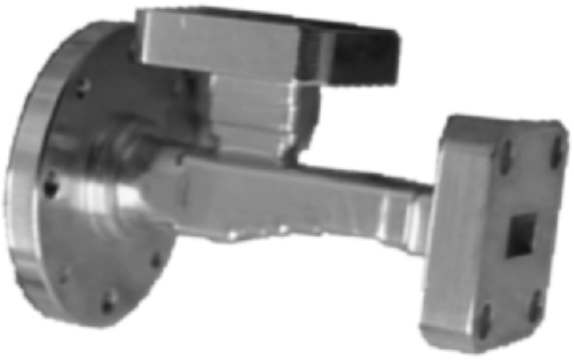

Figure 7.9 Electroformed asymmetric OMT.

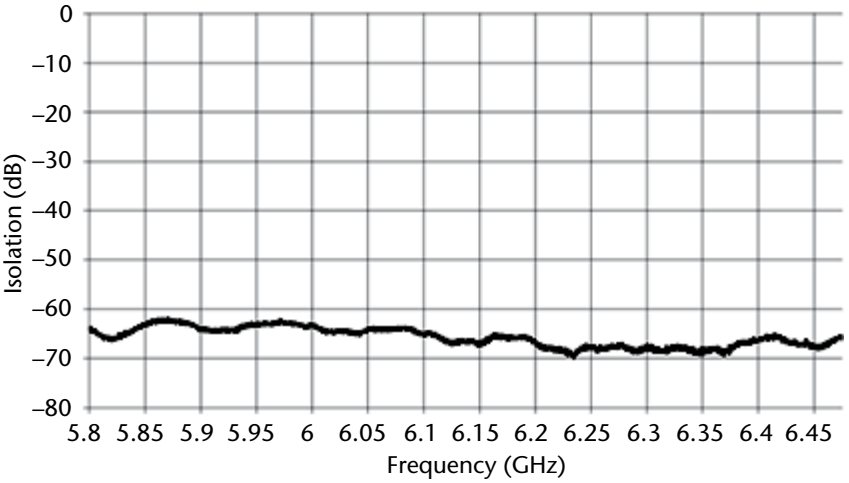

Figure 7.10 Measured polarization isolation for electroformed asymmetric OMT.

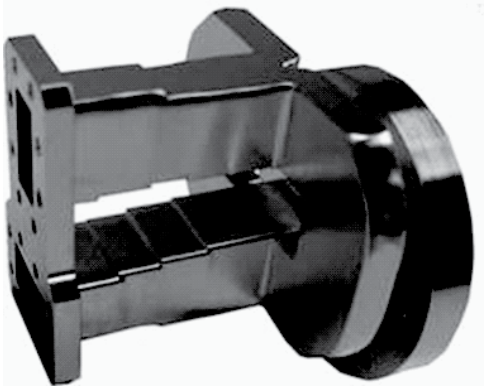

Figure 7.11 Electroformed symmetric OMT.

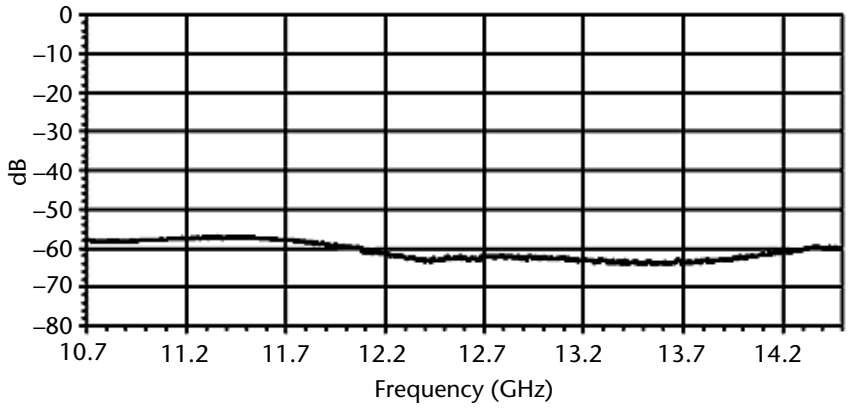

Figure 7.12 Measured polarization isolation for electroformed symmetric OMT.

7.2.5.3 Multiband Symmetric OMTs

Another symmetric OMT is the turnstile junction, which is useful when operating over multiple frequency bands. Turnstile junction OMTs can operate as diplexers, allowing both orthogonal modes at a specific frequency band to pass through the side ports, while simultaneously allowing both orthogonal modes at a second passband to pass through a rear port as shown in Figure 7.13.

Turnstile junctions may also be constructed by machining and bolting or brazing, or by electroforming. They have been used to construct feed networks operating at one, two, three, or more widely separated frequency bands. Figure 7.14 shows a feed employing two turnstile junctions in tandem to allow operation at K-, Ka-and Q-bands. With any symmetric OMT, manufacturing tolerances must be precisely controlled with respect to symmetry, or unwanted modes will be generated at the common port. These unwanted modes can manifest as large sudden changes in group delay, insertion loss drops (suck-outs or spikes), or as additional radiated cross-polarization.

7.2.6 Polarizers

Polarizers are used in CP communication systems to convert linearly polarized (LP) signals into circularly polarized (CP) signals or vice versa. A few examples are shown in Figure 7.15.

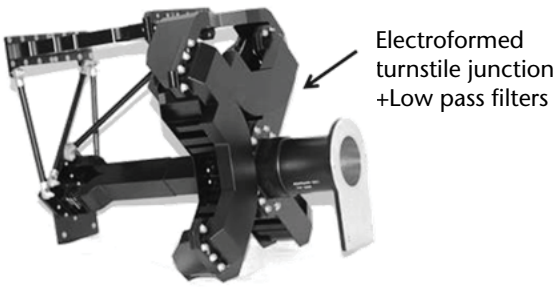

Figure 7.13 Electroformed turnstile junction as part of a 4/6-GHz circular polarized feed network.

Figure 7.14 Electroformed turnstile junction in a feed operating at K-, Ka-, and Q-bands.

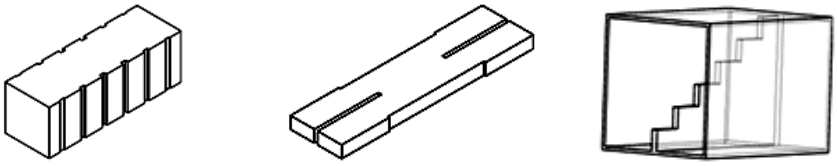

Corrugated polarizer Short-slot coupler Septum polarizer

Figure 7.15 Examples of 90-deg polarizers.

7.2.6.1 Corrugated Polarizers

Corrugated polarizers are capable of producing a very pure CP signal (0.2-dB axial ratio) over about 25% bandwidth. They can be realized in circular or square waveguide cross sections. In a square cross section, corrugations can be on two or four sides of the waveguide. They may be fabricated as machined and bolted/brazed pieces or as a single piece by electroforming. They are commonly used along with OMTs to allow for simultaneous transmission and/or reception of orthogonal CP signals (RHCP and LHCP).

7.2.6.2 Septum Polarizers

Septum polarizers are the most common type of single-band polarizers for the simple reason that they operate with dual polarizations simultaneously from a single device. They typically offer excellent performance over a narrow band (0.1 dB axial ratio, over 10% bandwidth) and can support wider bandwidths with reduced performance (0.3 dB axial ratio, over 20% bandwidth). Like other components, septum polarizers can be fabricated as machined and bolted/brazed pieces or as a single piece by electroforming.

7.2.6.3 Hybrid-Based Polarizers

Quadrature hybrids (typically short-slot couplers) can be used to generate a CP signal when used in conjunction with a turnstile OMT and a pair of tee junctions. The hybrid coupler divides a signal evenly in amplitude, with a 90-deg phase shift

between the two outputs. The two outputs can then be divided again, this time without a phase shift between the outputs, and fed into the four side ports of a turnstile junction OMT. When manufactured with high precision, a very pure CP signal can be generated at the common port of the junction over >15% bandwidth as shown in Figure 7.16.

7.2.7 Horns

Horns are the most prominent component of the feed. Most modern communication satellites use hybrid or multimode horns, consisting of corrugated or smooth-wall (profiled) designs [9–11]. Corrugated feed horns typically offer the best cross-polarization, return loss, and broadband performance at the expense of aperture efficiency, manufacturing complexity, and mass. Smooth-walled designs can offer very high efficiency at the expense of cross-polarization, but they are more easily manufactured, have lower mass, and can achieve very high performance when packaged in an array configuration for multiple spot beam antennas.

Both corrugated and smooth-wall horns are typically fabricated by direct lathe machining of aluminium billets. Both types may also be produced by electroforming, especially when very fine features are present as in submillimeter wavelengths (>60 GHz). Manufacturing tolerances must be considered in the design and analysis, particularly regarding the cross-polarization and return loss performance of these types of horns.

7.3 Feed Design

Given the typical short schedule for design, fabrication, and testing of an antenna feed for space applications, there is usually no time for prototyping or bench tuning. Design tools must be very accurate and fabrication methods precise enough to realize a feed that meets requirements that are increasingly becoming more and more demanding. It is worth mentioning that a good process has to be in place for project

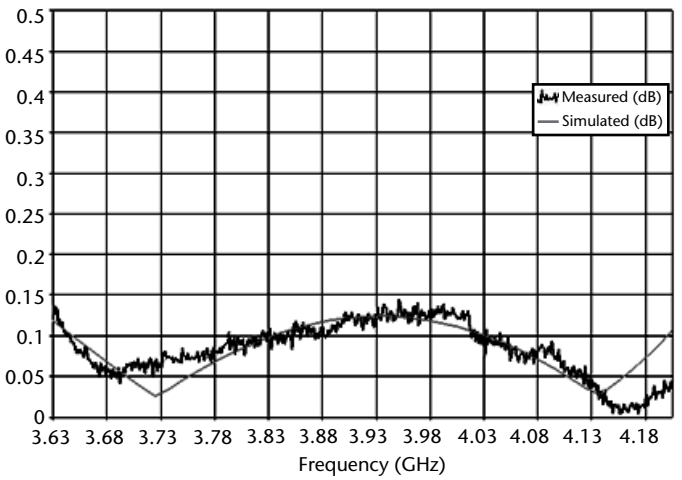

Figure 7.16 Measured vs. simulated axial ratio (<0.15 dB) from 3.625 to 4.2 GHz.

monitoring, design reviews, hardware inspection points, and testing to ensure successful and timely delivery of the feed.

7.3.1 Integrated Design Approach

Even with widely available sophisticated RF CAD tools, some designers still choose to design feed components separately. Prototypes are often produced to either prove or refine the design. The feed is then built up using an assembly of these separate components. Unfortunately deficiencies in the overall feed performance sometimes arise even if individual components exhibit good performance. This is due to the fact that interactions among the various components have not been accounted for in the design.

With the RF CAD tools and computing power available today, there is little reason why all the components of the entire feed cannot be analyzed together. If properly performed, all pertinent RF performances of the entire feed can be characterized, taking into account interactions among the various components. In addition, manufacturing tolerances can be included by performing sensitivity analysis to provide expected performance degradation after fabrication.

Taking the integrated approach one step further, the designer can consider optimizing several components together and having shared features. This approach often provides better performance over a wider bandwidth than would be possible if each component were designed separately. In addition the design is often a lot more compact. An example was shown earlier in Figure 7.13 for a diplexing junction that is comprised of a turnstile junction, lowpass filters, and harmonic reject filters.

Manufacturing by electroforming is ideally suited for this approach since it easily allows for precision fabrication of complex shapes in one piece and in a very compact layout.

7.3.2 Other Key RF Design Considerations

During the design process the designer must also keep on mind other requirements such as insertion loss, high power, multipaction [12], PIM [13], operating temperature range, size and mass constraints, port locations, achievable manufacturing tolerances, and variation over temperature. Too often some of these requirements are overlooked at the start of the design process, resulting in a waste of precious time, compromised feed performance, or worse still an unusable feed.

The PIM order and power level will often drive the manufacturing method. In general 19th-order PIM or higher is not as critical. Lower order PIM may necessitate reduction in flange joints or the use of special high-pressure or choke flanges to minimize the risk of generating PIM. The use of electroforming can eliminate seams and greatly minimize the number of flange joints and is in fact a common fabrication method used when 3rd-order PIM can be generated in the Rx band due to the harmonies of the Tx channels.

Performance variation over temperature can usually be accounted for in the design by including thermal guard bands on either side of the operating frequency band. This accounts for the expansion and contraction of the feed at the hot and

cold temperature extremes. Frequency responses, other than insertion loss, should only shift side to side as opposed to up and down for a properly fabricated feed.

7.3.3 Precision RF CAD Tools

Before the advent of sophisticated precision CAD tools and powerful computers, the feed design process could be very tedious and lengthy. Each waveguide component was designed separately using a number of different techniques, which included an empirical approach, prototyping and bench tuning, equivalent circuit models, and closed-form expressions. These methods were either limited in accuracy or can only be applied to certain specific geometries. Once each component had been realized, additional prototyping or bench tuning may have been required at the feed assembly level.

As feed requirements became more demanding and delivery schedules got shorter, these techniques were no longer adequate. With today's sophisticated CAD tools and computing power, most of the waveguide components can be designed with very high accuracy in a relatively short time. It is worth noting again that analysis of the entire feed assembly is possible with these CAD tools and is highly recommended to avoid surprises caused by interaction between the various components.

Some commonly used RF design CAD tools include CHAMP, μWave Wizard, CST Microwave Studio, FEKO, WASPNET, and ANSYS HFSS. CHAMP is used for design and analysis of rotationally symmetric horns. The fields inside each circular section of the horn can be solved and expressed as analytic solutions of Maxwell's equations. Mode matching (MM) is then used to derive the scattering matrix at the discontinuity between adjacent sections. The response of the entire structure is then obtained by cascading the matrices from each discontinuity. This method is very accurate since higher order modes between each discontinuity can be accounted for and it is very fast because of the use of analytical field solutions. However, it is limited to cross sections that can be solved analytically such as rectangular and circular.

For more arbitrary cross sections and structures, the fields for the entire component or feed can be solved using CAD tools based on the finite element method (FEM). CST Microwave Studio and ANSYS HFSS are two of the most popular FEM-based design software programs. Although these tools are very versatile, they are much slower than CAD tools based on MM due to the computation demands of FEM.

Waveguide components and antenna feeds can generally be realized using rectangular or circular cavities and waveguides. In some cases irregular shapes are needed such as for rounded corners. CAD tools such as μWave Wizard focus on using MM and their derivatives (hybrid MM/boundary contour and MM/2D finite element) wherever possible and only applying 3D FEM for the irregularly shaped portion of the structure. The fields in the irregularly shaped portion are solved using techniques based on FEM and scattering parameters computed before cascading with S-parameter matrices from the rest of the structure. The result is a CAD tool that is not only accurate but also faster for simulation and optimization of waveguide components and antenna feeds. In addition copolar and cross-polar patterns can also be part of the optimization process [14], making this type of CAD tool even more effective for feed designs.

7.3.4 Mechanical and Thermal Design

While the RF requirements drive the purpose and general design of the feed, that purpose and design has to work mechanically in the extreme environments of launch and space. The mechanical designer usually has the challenging task of optimizing size, weight, thermal, and structural integrity.

The launch environment will be the most extreme mechanical environment for any space hardware. A feed may see loads between 10 and 100g's depending on their location in the spacecraft. Some locations enjoy damping and attenuation while others could see amplification. Spacecraft subsystems typically define the vibration levels that a feed needs to meet. Shock testing is usually not performed on an antenna feeds, because all components are mechanical and metallic in nature and therefore not sensitive to shock.

As mentioned previously, the short schedule to produce feeds makes prototyping impractical. For that reason 3D modeling and finite element software is used to accurately model and analyze each unit to qualification levels. The parts, however, are tested to protoqualification or acceptance levels so they can all be used as flight hardware. Positive margins must be shown for structural analyses with factors of safety ranging between 1.25 and 3.0. The lower factors would be used with hardware that has a proven flight heritage or has accurate analysis to test correlation data. Higher factors would be used with hardware that has no proven heritage or accurate correlation. When working with electroform, factors such as material thickness variation, material property variation, and manufacturing process must be considered, because they can impact stress results. Additionally, depending on the requirements, random vibration fatigue can drive a design more strictly than overall 3σ rms stresses.

Space is the most extreme thermal environment for antenna feeds and other hardware. Spacecraft panels are temperature controlled, and even hardware that directly faces space and/or the sun may have active or passive thermal controls that keep their temperatures within appropriate operating ranges. Depending on their location on the spacecraft and the thermal controls available, a feed may see large or small temperature variations. These variations occur as cycles over the lifetime of the satellite, driven by the type of orbit. The variations are most often determined either by spacecraft subsystems or by the feed designer (with input from the spacecraft designer) using nodal-based thermal software designed specifically for analyzing spacecraft and spacecraft components. These conservatively analyzed temperatures then have 20° to 30° added onto the extremes as design and test margins of safety. The final worst-case temperatures are called the survival or nonoperating temperatures. Feeds tend to have survival temperatures between –200 and +200°C. Many boom-supported antennas and feeds are exposed to those extremes, but some locations on the spacecraft body are only subjected to –50° to +100°C.

Keep in mind that some nonmetallic materials may have strength or adhesion issues at the temperature extremes. Feeds should be analyzed for stresses induced by thermal expansion of mismatched materials and bolted joints. This causes several problems. Feeds will very often have aluminium and copper components together. These interfaces will produce higher bolt stresses, especially in shear. Because feeds are significantly alignment critical, bolt slip can be detrimental and these interfaces should be designed to prevent slip or force uniform slip. Feeds should also be

designed with interfaces to the spacecraft panel that allow for expansion without causing extreme deformation and stress. Spacecraft panels tend to be made of composite materials having expansion rates near zero, which can put high stresses on parts that are rigidly attached. Finally, thermal fatigue, although not as damaging as random vibration, can contribute to the cumulative damage index.

7.3.5 Manufacturing Methods

With precision manufacturing the waveguide components can be realized without the need for bench tuning, which not only saves time, but reduces overall program risk. Some commonly used manufacturing methods for waveguide components include direct machining using computer numerical control (CNC) mills, CNC lathes, and CNC EDM; joining two or more pieces of metal using dip brazing; and creating complex high-precision metallic parts using electroforming.

7.3.5.1 Direct Machining

Direct machining using mills and lathes is probably the most widely used method to fabricate components for antenna feeds. Aluminum 6061T6 or 7075 T7351 are the most common materials used due to their relatively low cost, low density, strength, and ease of machining. With direct machining, the parts are usually made in several pieces and/or split in halves to provide access for the cutting tool. Bolted joints are required for assembly. Wherever possible, joints are along lines of zero current to minimize impact on RF performance.

7.3.5.2 CNC EDM

To minimize bolted joints, create sharp internal corners, and machine hard-to-reach features with precision, CNC EDM is often used. In this process the desired shape is obtained by using rapidly recurring current discharges to erode away material between an electrode and the workpiece. A number of different materials can be machined using EDM including aluminum. Although this process provides better access for machining hard-to-reach internal features, it can be slow and is limited by the reach of the electrode. Multiple electrodes are required depending on the surface finish and accuracy requirements, adding to the cost and fabrication time of the part.

7.3.5.3 Dip Brazing

When tight tolerances are not required, dip brazing can be used to create thin-wall aluminum parts without bolted joints. The parts are machined, fixtured, and a brazing compound applied to the mating surfaces. The assembly is preheated and then immersed into a bath of molten salt, which melts the brazing compound to create a bond at all the joints to form the part. Variation in fillet size at the joints from the brazing compound, voids in the joints, and variations in feature sizes can affect the electrical performance of the part.

7.3.5.4 Electroforming

When direct machining, CNC EDM, or brazing is no longer practical, electroforming [15] can be used to create some of the most complex geometries with high precision. Electroforming eliminates most of the constraints associated with these other techniques and has been used for more than 30 years to produce hardware for space applications.

Electroforming is a process in which a metal component is fabricated by electrodeposition on a mandrel in a plating bath as shown in Figure 7.17. Subsequent removal of the mandrel results in a shell with the desired internal features. Examples of parts that can be created using electroforming are shown in Figure 7.18. The most common material used is copper since the plating solution can be formulated to provide very good leveling capability to allow plating in deep recesses with sharp corners. Copper also has very good electrical conductivity for low loss and good thermal conductivity to transfer heat in high-power applications.

The internal surfaces are usually left as electroformed since electroformed copper at C-, Ku-, and even Ka-band frequencies do not have significantly higher loss than silver. There is also no need to treat the copper surface for corrosion protection since the parts are normally stored in typical laboratory environments. Electroformed copper can maintain its original shine under standard laboratory environments. Electroforming provides benefits such as high precision, inspection of internal features, uniform internal plating, and fabrication of complex shapes and is ideally suited where low PIM is critical.

The high mechanical precision permitted by electroforming allows high-performance antenna feeds to be produced without the need for tuning screws. This in turn improves power handling and further reduces PIM risks. Tolerances are limited by the accuracy of the machined mandrel, which can be as tight as ±0.0002 in. Waveguide components up to 1.2 THz have been realized using electroforming.

The internal features of the final electroformed part can easily be inspected on the mandrel because the electroformed shell's internal features exactly replicate the external features of the mandrel.

If internal plating is required, it is applied on the mandrel first before electroforming. This results in a more uniform plating than can be achieved by plating in-

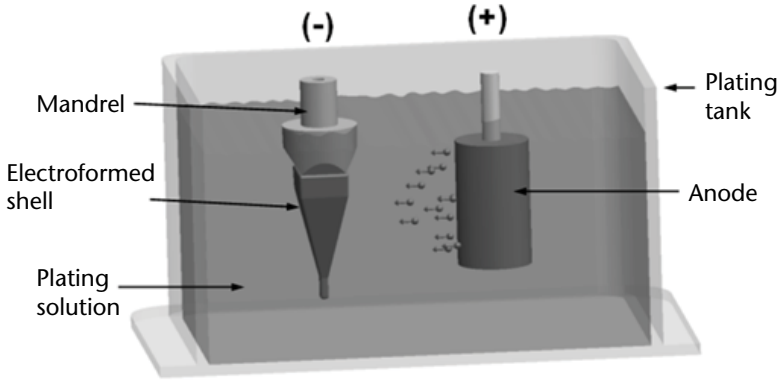

Figure 7.17 Electroforming process.

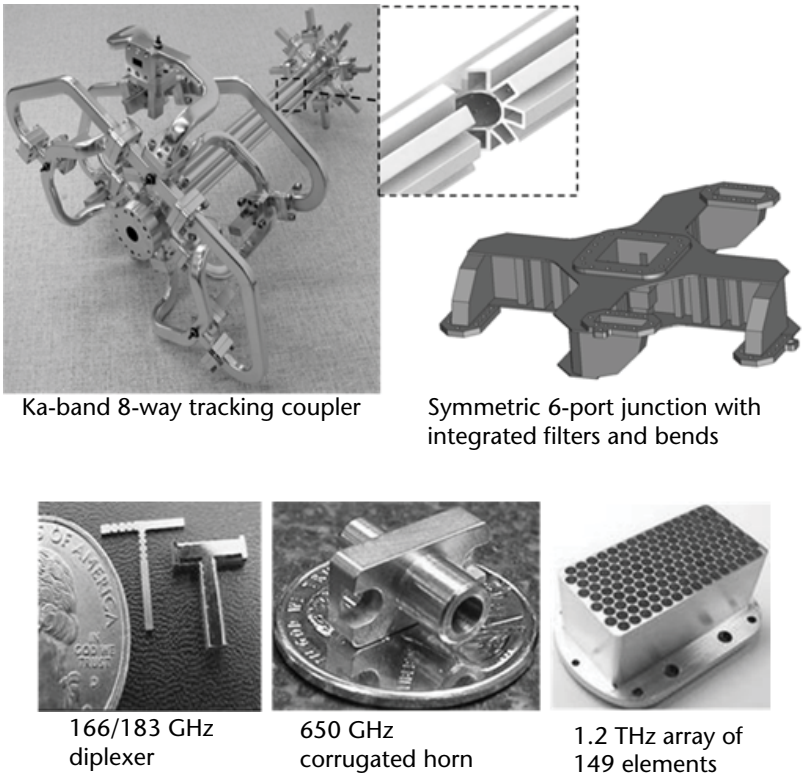

Figure 7.18 Examples of parts created by electroforming.

side a component after fabrication as would be the case with other manufacturing methods.

Electroforming is ideally suited for manufacturing high-precision parts with very complex internal geometries in a single piece without joints. This provides the designer with greater freedom to choose and locate internal features, allowing the potential for higher RF performance while maintaining a compact envelope.

The absence of tuning screws and split joints and a significant reduction in flange connections make this process ideally suited for PIM critical hardware.

7.4 Feed Examples

Using the components described earlier, a wide variety of feeds can be realized for specific applications. In some applications the feed can be very simple, whereas in others the requirements are such that the feed has to include many waveguide components. A number of feed examples are presented in this section to illustrate what can be created using the various components described earlier.

7.4.1 Standard C-Band Feed

An ultracompact C-band assembly feed with dual band (Tx and Rx) and dual CP (LHCP and RHCP) that meets stringent RF requirements, including high power

and low PIM over the standard frequency band, is shown in Figure 7.19. This configuration is based on using a turnstile junction to separate Tx from Rx signals because of the wide operating bandwidth of 56%. The common port of the junction is in a square or circular waveguide to support two orthogonal signals and is large enough to allow both Tx and Rx signals to propagate. The Rx port of the junction is reduced in size to allow only orthogonal signals at Rx frequencies to propagate.

The junction has four coupling waveguides with lowpass filters to reject the Rx signal and allow only the Tx signal to pass through. A short-slot coupler is used in the Tx path to separate the input signal into two components with equal amplitude and in-phase quadrature. The two components then excite orthogonal components in phase quadrature in the junction via H-plane tees to generate a CP signal. Exciting the other port of the short-slot coupler provides the orthogonal CP signal. A septum polarizer is connected to the Rx port of the junction to generate CP signals at Rx frequencies.

A transition is used to connect the junction and the horn with minimum impact on return loss and higher order mode excitation. All components of the feed including the horn are included in the design to ensure that overall performances at assembly level were met. The tuning-less high-performance network was realized by electroforming without any hardware iterations. The use of electroforming allowed this complex network to be built with a minimum number of flanged connections. This reduces PIM risks and allows the unit to fit within about a cubic foot, which is very compact at C-band.

A summary of measured performance is listed in Table 7.1. Excellent agreement was achieved between measurements and simulations for all electrical parameters. Typical measured copolar and cross-polar patterns are shown in Figure 7.20 along with simulated patterns.

This network can easily be reconfigured as a dual-band, dual-LP standard C-band feed by removing the Tx short-slot coupler and replacing the Rx septum polarizer with an asymmetric OMT as shown in Figure 7.21. All other components would remain unchanged.

7.4.2 Standard Ku-Band Feeds

The standard Ku-band can be realized in a layout that is simpler than for the standard C-band feed since it only has to operate over 28% bandwidth. An example

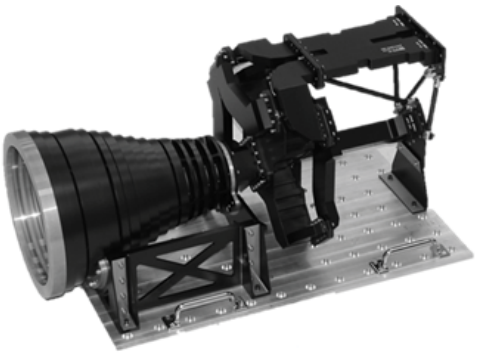

Figure 7.19 Space-qualified four-port standard C-band CP feed.

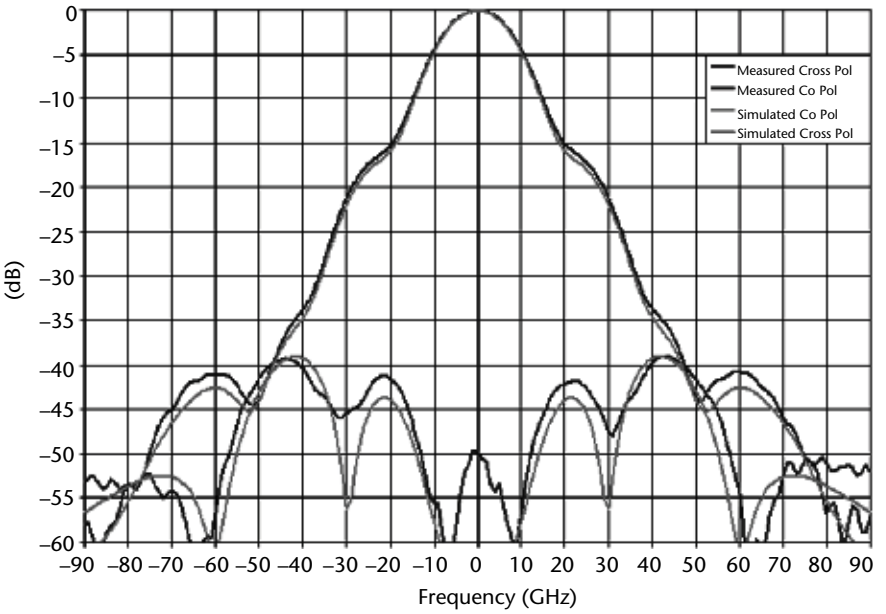

Figure 7.20 Measured vs. simulated copolar and cross-polar patterns in the 45-deg plane.

Table 7.1 Measured Performance Summary of a Four-Port CP C-Band Feed

Parameters	*Measured Performance*
Frequency	Tx: 3.625–4.2 GHz Rx: 5.85–6.425 (GHz)
Axial ratio	<0.2 dB on axis
Insertion loss	Tx: <0.15 dB Rx: <0.05 dB
Return loss	Tx: >28 dB Rx: >32 dB
Isolation	RHCP ↔ LHCP >25 dB Rx ↔ Tx >60 dB
Peak power	10 kW multipaction
PIM	<–140 dBm, 7th order
Edge taper	20 dB (±30°) typical
Cross-polar levels	<–38 dB (±30°) relative to copol peak
Size, feed	28.5 in. (L) × 12 in. (W) × 12.7 in. (H)
Mass, feed	<12 kg (with brackets)

of a dual-band, dual-LP feed is shown in Figure 7.22. A symmetric OMT is used to separate the dual-LP signals over both the Tx and Rx bands. A pair of diplexers is then used to separate the Tx and Rx bands with sufficient isolation between the bands.

This feed provides very high RF performance in a compact layout. The absence of tuning screws provides high-power handling and very low PIM at extremely low

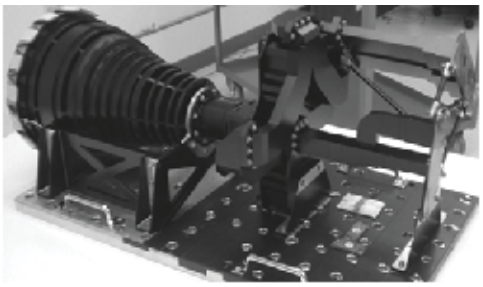

Figure 7.21 Space-qualified four-port standard C-band LP feed.

Figure 7.22 Dual-band, dual-LP standard Ku-band feeds.

temperatures. This feed has been tested and showed no evidence of third-order PIM with up to 150W carriers at –120C with a noise floor below –145 dBm.

This symmetric OMT-based layout can easily be configured for different applications. For example, adding a corrugated polarizer between the horn and the OMT provides dual CP as shown in Figure 7.23. The diplexers can also be removed or replaced with filters if fewer ports are required. Table 7.2 provides a summary of measured performance for a four-port LP feed.

In cases where both CP and LP functionality are required from the same feed, a turnstile junction can be used. Such an example is shown in Figure 7.24. Here the Tx signal is CP and the Rx signal is LP. The Tx signal could be LP by removing the short-slot coupler, and the Rx signal could be CP by using a septum polarizer.

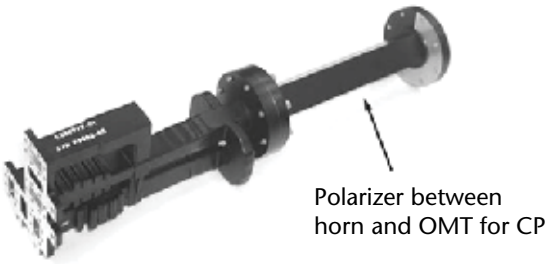

Figure 7.23 Dual-band, dual-CP standard Ku-band feed network.

Table 7.2 Measured Performance Summary of a Four-Port LP Ku-Band Feed

Parameters	*Measured Performance*
Frequency	Tx: 10.95–12.75 GHz Rx: 13.75–14.50 GHz
Insertion loss	Tx: <0.20 dB Rx: <0.25 dB
Return loss	Tx: >22 dB Rx: >21 dB
Isolation	VP ↔ HP >60 dB Tx ↔ Rx: >70 dB at Tx; >50 dB at Rx
Peak power	>9.6 kW multipaction
PIM, third order	< –140 dBm
Edge taper	20 dB (±30°) typical
Cross-polar	< –40 dB (±30°) relative to copol
Size	<15 in. long
Mass	<2.25 kg

Figure 7.24 Dual-band, CP/LP Ku-band feed.

7.4.3 K-Ka-Band Feed

The same approach and methodology used to design and build the standard C-band feed can be adapted for a compact dual-CP feed operating at K- and Ka-band frequencies. This feed is shown in Figure 7.25 and a summary of measured performances is given in Table 7.3.

7.4.4 Low Profile K-Ka-Band Network for Feed Array

The K-Ka-band feed shown earlier is based on a single turnstile junction. Although it is very compact, it is still not ideal where tight packaging is required as in an array configuration. By using a second junction, a more streamlined network can be realized as shown in Figure 7.26. In this approach, a septum polarizer is used to generate CP and the second junction is used to separate the CP signal into its linear components before recombining into the first junction. The first junction with appropriate filters is again used to separate Tx from Rx signals. Electroforming is used to fabricate this part with a minimum number of flange joints and no tuning screws. A summary of measured performance is listed in Table 7.4.

Figure 7.25 Dual-band, dual-CP K-Ka-band feed.

Table 7.3 Compact Four-Port CP K-Ka-Band Feed Measured Performance Summary

Parameters	*Measured Performance*
Bandwidth	K-band: 18% Ka-band: 12%
Axial ratio	K-band: <0.2 dB Ka-band: <0.1 dB
Insertion loss	<0.1 dB
Return loss	>30 dB
Isolation	RHCP ↔ LHCP >30 dB Ka ↔ K >60 dB
Peak power	>3.8 kW multipaction
PIM	< −140 dBm
Size, network	4 in. (L) × 3 in. (W) × 4 in. (H)
Mass, network	<350 g

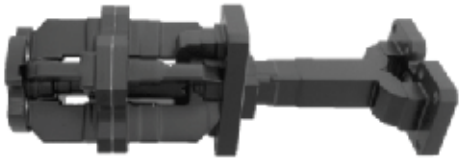

Figure 7.26 Low-profile dual-band, dual-CP K-Ka-band feed network.

7.4.5 K-Ka-Q-Band Network

An example of a tri-band dual-CP feed operating at K-, Ka-, and Q-bands was shown earlier in Figure 7.14. The design uses the turnstile junction to extract each of the frequency bands at specific locations along the feed. The challenge here is to design the junction used to extract the lowest frequency band such that excitation of higher modes is kept to acceptable levels at the higher frequencies. Precision RF CAD is used extensively to minimize higher order mode excitation while achieving acceptable RF performance in terms of band isolation, return loss, insertion loss, power handling, and axial ratio. Electroforming is again used to realize this feed network with high precision. A summary of measured performance is shown in Table 7.5.

Table 7.4 Low Profile Four-Port CP K-Ka-Band Feed Measured Performance Summary

Parameters	*Measured Performance*
Bandwidth	K-band: 10% Ka-band: 6%
Axial ratio	K-band: <0.34 dB Ka-band: <0.13 dB
Insertion loss	K-band: <0.4 dB Ka-band: <0.2 dB
Return loss	>28 dB
Isolation	RHCP ↔ LHCP >30 dB Ka ↔ K >70 dB
Peak power	>3.8 kW multipaction
Size	<2.1 in. diameter × 4.7 in. long
Mass	<300 g (flight)

Table 7.5 Measured Performance Summary for Six-Port K-Ka-Q-Band Feed

Parameters	*Measured Performance*
Bandwidth	K-band: 5% Ka-band: 3% Q-band: 5%
Axial ratio	K-band: <0.20 dB Ka-band: <0.50 dB Q-band: <0.60 dB
Insertion loss	K-band: <0.5 dB Ka-band: <0.4 dB Q-band: <0.3 dB
Return loss	>26 dB
Isolation	RHCP ↔ LHCP >20 dB K ↔ Ka >80 dB at K; >70 dB at Ka; >70 at Q K ↔ Q >80 dB at K; >70 dB at Ka; >70 at Q Ka Q >70 dB at Ka; >55 dB at Q
Peak power	>5.0 kW multipaction
Size	6 in. (L) × 4 in. (W) × 4 in. (H)
Mass	<500 g (flight network only)

7.4.6 Ku-Band Tracking Feed

Another example of a feed with a number of components packaged in a small space is shown in Figure 7.27. This is a four-horn monopulse feed used for tracking. It includes polarizers for generating CP signals and hybrids for the monopulse comparator network. A number of components are packaged in a cross section that is less than 3.1 in. × 3.5 in. Four WR62 waveguides ports provide the desired CP sum and difference signals. As with all almost all feeds produced by electroforming, no tuning is required. A summary of measured performance is listed in Table 7.6.

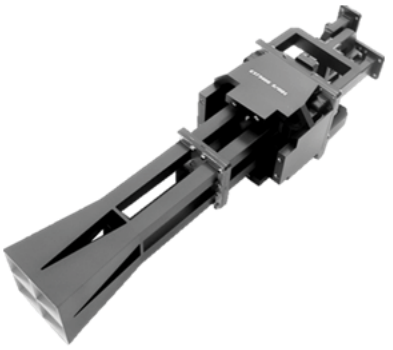

Figure 7.27 Low-profile Ku-band monopulse tracking feed.

Table 7.6 Ultracompact Ku-Band Tracking Feed Performance Summary

Parameters	*Measured Performance*
Frequency	Ku-band
Axial ratio, on axis	<0.25 dB
Return loss	>24 dB
Isolation, port to port	>30 dB
Null depth	>35 dB
Size	<3.1" × 3.5" × 11.2"
Mass	<3 lb

7.5 Qualification and Protoflight Testing

Unlike ground-based antenna systems, spaceborne antennas are not serviceable. To reduce the risk of in-orbit failure or performance degradation, the feeds are subjected to extensive testing to validate workmanship and performance. New designs typically require rigorous testing on a qualification unit to prove out the design and fabrication. Once that is done, subsequent units usually only require protoflight (PF) or acceptance testing. Qualification testing differs from PF and acceptance testing in that the hardware is exposed to more extreme levels of temperature and vibration. In addition, high-power and multipaction tests may be required depending on operating power levels. Qualification-tested hardware is not used on the satellite, because the environmental testing consumes a significant portion of its usable fatigue life.

After the feed is fabricated, preliminary tests are performed to verify RF performances. In some cases the feed is subjected to thermal conditioning at this stage to remove stresses that may have been induced during manufacturing. Once preliminary testing has confirmed that the feed is performing as expected under ambient condition, it is subjected to a formal performance validation test, which can follow the sequence as shown in Figure 7.28. The general idea for the flow is to perform a sequence of tests similar to what the feed will be subjected to during launch and subsequent operation. Some tests however are more practical when performed on

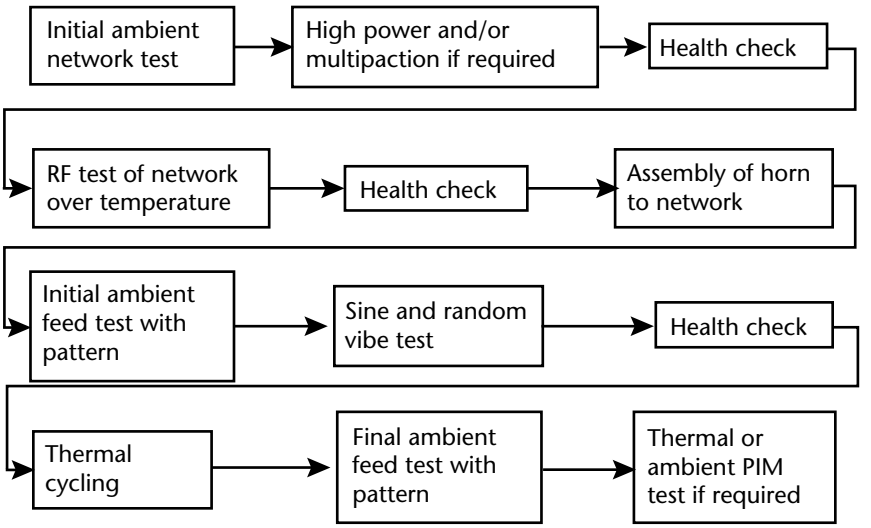

Figure 7.28 Test sequence for feed validation.

the network only, without the horn. These tests are performed at the beginning before integration with the horn.

RF tests are usually done before and after each environmental test (high power, multipaction, vibration, thermal cycling) to verify that the feed performance has not changed. Post-environmental RF tests are sometimes known as health checks and can be a subset of the tests performed before environmental tests. Changes may indicate degradation that could negatively impact the integrity of the feed. Any discrepancy detected during the formal test sequence undergoes detailed investigation with strict rules and procedures.

Ambient testing at the network level is generally performed to evaluate return loss, insertion loss, rejection between bands, group delay, axial ratio if feed is CP, and isolation between polarizations under standard room temperature, pressure, and humidity. These are usually performed using a vector network analyzer (VNA). The same parameters may need to be evaluated over temperature to ensure that performances do not degrade beyond expected levels when operating at the extreme hot and cold temperatures in space.

Ambient testing at the feed level may include return loss, rejection between bands, axial ratio if feed is CP, and isolation between polarizations under standard room temperature, pressure, and humidity. Radiation patterns may also be required to characterize gain, copolarized patterns, cross-polarized patterns, and axial ratio if the feed is CP. In general, the horn performance is not tested over temperature since it is not very practical to do so and its construction and design are such that performances are not likely to change significantly at temperature extremes. This assumption of course must be evaluated on a case-by-case basis since some horn designs and construction may be more sensitive to temperature extremes.

Thermal cycling testing is performed to ensure that the feed design, materials, and workmanship can survive the multitude of thermal cycles to which it will be subjected during operation in space. Thermal cycling can be performed in a convection heated and cooled chamber, or in a thermal vacuum chamber. If a convection

chamber is used, an inert gas is typically used to purge the chamber during testing to prevent moisture from accumulating during the cold cycles and oxidation during the hot cycles. Thermocouples are placed at specific locations along the feed to monitor its temperature during the cycles.

Sine and random vibration tests are performed to verify that the hardware will perform properly through the launch environment. The levels are flowed down by the spacecraft team and depend on where the unit will be located on the spacecraft and what type of launch vehicle will be used. Random levels are typically anywhere from 10 to 30 g over 20 to 2000 Hz. Sine levels are typically between 8 and 20 g max over 10 to 100 Hz.

Random vibration tests are the more extreme environment for feeds with higher natural frequencies. For lower frequencies, however, a sine test will produce greater displacement and can be the worst-case environment for large feeds with a first natural frequency (FNF) in that range. Both tests are usually required for a feed regardless of FNF, so for feeds with higher natural frequencies, the sine test is simply a way to verify that the first mode is not in the 10- to 100-Hz range and to make sure there are no hidden workmanship defects.

The random run times and sine sweep rates are both set to ensure that test cycles are well under the fatigue limits. In both cases accelerations are monitored at the input and at various locations on the unit. Limiting or notching may be used to keep the unit responses from going too high at resonances but must always be approved by the spacecraft team, as it changes the input levels.

PIM tests at ambient or over temperature may be required for feeds that support both uplink and downlink frequencies. When frequencies in the downlink band can mix to produce low-order PIM products that fall within the uplink band, there is a risk that these products will be produced at levels that can adversely impact the uplink signals. PIM is a serious concern that is hardly discussed in most textbooks. It is, however, very important for designers to have a good understanding of its causes and how to minimize the risk of generating PIM. This subject is discussed in more details in Section 7.7, which provides the designer some insight into PIM as it applies to antennas for communication satellites.

Multipaction testing is usually required to validate a feed design for high-power handling. If sufficient margin exists before multipactor breakdown, testing on subsequent units is usually not required. The onset of multipaction can be predicted and is well documented. Section 7.8 provides more details on this phenomenon and how to set up and perform multipaction testing.

7.6 Feed Assembly Deleterious High-Power RF Effects: Passive Intermodulation, Gas Ionization/Corona, and Multipactor[1]

Deleterious, or *harmful in an unexpected manner*, applies appropriately to high-power, high dynamic range, partial-pressure, or vacuum-based RF systems, designed without specialized attention to these effects. A perfectly good *textbook* antenna system can be designed and constructed only to discover anomalies late in the developmental or, worse yet, the application phase. However, in the space

1.

industry, experience has taught that these phenomena are anything but subtle or unexpected due to the harsh environmental conditions and limited available real estate. The space industry has dealt with these effects for many years, and they have caused substantial delays, cost, and system degradation despite detailed requirements, analysis, design, and extensive testing and qualification programs.

This section is intended as a high-power effects primer such that the antenna systems designer gains a basic understanding of the most serious *known* pitfalls that could render a perfectly good textbook design useless or cause major redesign. Special emphasis is placed on requirements, testing, qualification programs, and final verification. These are the most critical mitigation efforts and are the most likely to be underestimated because there are no formal industry standards and virtually no regularly scheduled training programs within the educational system to cover such critical issues.

7.7 Passive Intermodulation

Passive intermodulation distortion (PIM) is a phenomenon by which *passive components* and/or ordinary "metal-to-metal" contacts, found in and around medium and high-power RF transmitters, act like mixers that cause the Tx carrier energy to spread in frequency and interfere with neighboring receivers. PIM is a *parasitic* nonlinearity that is distinguished from active intermodulation (AIM), which is the result of a nonlinear transfer function commonly known to result from devices that exhibit voltage, current, or power gain such as vacuum tubes and transistors.

PIM was first observed on ships as the "rusty-bolt" phenomenon in the 1960s. It was later observed on S-band deep space systems and communication satellites in UHF and L-band systems [16]. PIM has also been observed as harmonic distortion in RF filters. It is possible on any high dynamic range system where transmitters and receivers are colocated. PIM is a routine design criterion for all communication satellites and requires special designs, materials, and extensive test programs to circumvent its occurrence on the most PIM-sensitive satellites.

7.7.1 The PIM Problem

Common items such as standard connectors, cables, filters, antenna components, thermal blankets, and supporting structures become inadvertent circuit components capable of generating substantial interference to nearby receivers. PIM interference is not stable, may exist only under a very narrow set of conditions (a single temperature, for example), and can have amplitude variations of more than 100 dB. PIM is prevalent in satellite communication systems, avionics, ships, deep space probes, cellular telephone repeaters, and any application where high-power transmitters are used in proximity to sensitive receivers. In the case of a satellite repeater, PIM will generate ring-around, self-interference.

Communication satellite PIM is an interference signal that is generated when a transmission line or radiated metal-to-metal interfaces or other nonlinear passive components are exposed to the high-power RF energy of the satellite transmitters. The interfering signal is collected by the sensitive satellite receiver and "retransmitted" as increased noise or discrete interference to the desired transmitted signal.

Sources of PIM can be located within the Tx chain of the satellite or exist externally on the spacecraft body.

Figure 7.29 shows satellite repeater PIM with separate transmitting and receiving antennas that have substantial *RF isolation* between them. The transmission paths of payload systems that have diplexed Tx–Rx antennas are far more susceptible to PIM since there is no inherent isolation between the high-power transmitter and the receiver.

7.7.2 PIM Defined

Passive intermodulation can be *functionally defined* as a conducting or transmissive medium that, above a specific power threshold, exhibits a nonlinear voltage-to-current transfer that results in the production of harmonics and or spectral spreading for a single RF Tx carrier and produces sums and differences of multiple RF Tx carriers and their harmonics.

PIM can be *physically defined* as passive transmission components, associated hardware, materials, radiated components and hardware in the environment that couples some degree of RF transmitted energy, contains a nonlinear property, and results in undesired frequency spreading of the Tx energy into Rx bands.

The effects of PIM can be subtle to the point where they are hardly noticed or will not be prevalent until multicarriers or modulation are present and then possibly only under certain environmental conditions. Even when PIM is precluded by intensive analysis and design, a testing program is typically necessary to verify workmanship or that the design was implemented properly.

The worst-case source of PIM is a form of low-pressure or loose metal-to-metal contact. Any metal-to-metal interface can produce spurious currents in the presences of RF energy, especially if it is loose [17]. However, worst-case PIM is caused by electron tunneling through angstroms-thick, insulating metal oxide layers that

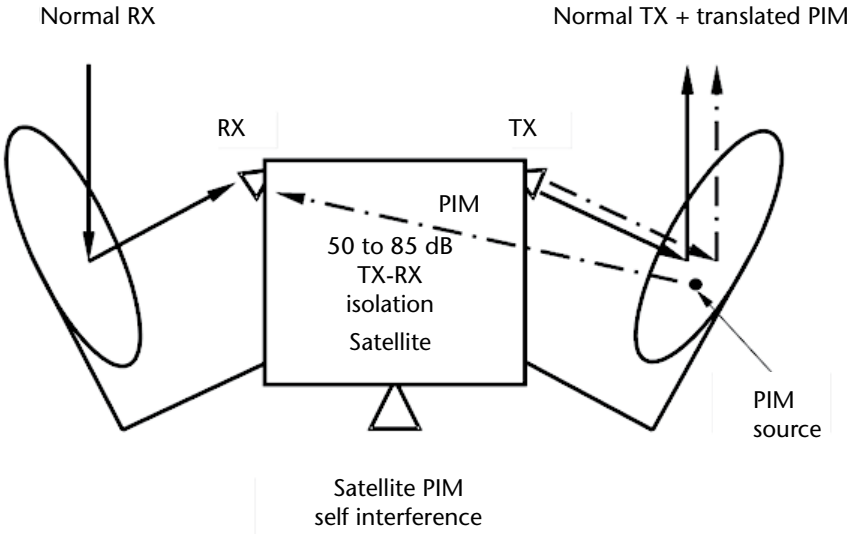

Figure 7.29 Satellite repeater PIM.

form on the surface of most metals [16]. So when two metal components are connected, there is some portion of a *metal-insulator-metal* (MIM) interface instead of a good electrical metal-to-metal contact everywhere. The presence of RF energy can cause a voltage difference between the MIM interfaces, and when the voltage potential becomes great enough, electrons tunnel across the insulating interface, resulting in a nonlinear voltage-to-current progression. This causes harmonics of a single incident radio frequency to be generated and causes harmonics of multiple incident frequencies to add and subtract with each other. The harmonics and/or the sum and difference of some harmonics can land in a payload Rx band and thus cause unwanted interference.

Therefore, sources of PIM produce *harmonic distortion* in single-carrier systems and *intermodulation distortion* in multiple-carrier systems [16] as described here:

Harmonic distortion: the appearance of integer multiple frequencies at the output of the transmitter.

Intermodulation distortion: the appearance of frequencies at the output of the transmitter equal to the *sums* and *differences* of integer multiples (harmonics) of the input frequencies.

The frequency of intermodulation products can be found by the expression in Figure 7.30.

Discrete PIM frequencies are located at the sums of integer multiples (m and n) of the carrier frequencies, which also determine PIM *order*. The multiples (m and n) can be any integer positive, negative, or zero. The example illustration in Figure 7.31 gives a partial distribution of PIM products [18, 19]. As the PIM *order* increases, the "amplitude" of the PIM generally decreases. Thus, the lower the order, the more sensitive the system is to PIM.

When Tx carriers are spaced close together, all of the intermodulation products near Tx carriers are "odd-order" products and these are the PIM products that are typically addressed on *communications systems* because Tx and Rx frequencies normally exist within the same frequency band (L-band, C-band, etc.). "Even-order" products typically have less energy than odd-order ones, but still must be considered if they dominate in the payload Rx band.

7.7.3 Causes of PIM

There are a variety of voltage, current, or thermally induced sources of PIM: MIM junctions, magnetic hysteresis, micro-arcing, and inherent material nonlinearity (molecular) as follows:

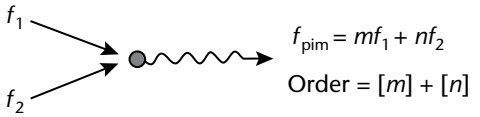

Figure 7.30 Illustration of frequency of intermodulation products and PIM order.

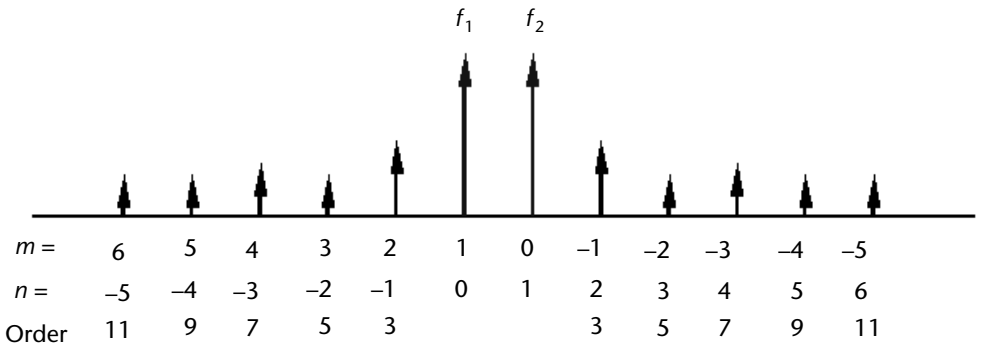

Figure 7.31 Partial distribution of PIM products.

Common Sources of Voltage-to-Current Nonlinearities [16]

- *Electron tunneling:* This penetration of a barrier of higher potential occurs as a result of MIM junctions. MIM junctions result when metals such as aluminum or stainless steel come into contact with that form surface oxides layers. Oxide layers are typically 20 to 40 Å thick.
- *Electron discharges:* Electrons bridge a gap between conductive structures (i.e., gas ionization, micro-arcing, field emission).
- *Magnetic hysteresis:* Nonlinearities are caused by the use of ferromagnetic materials, magnetic nickel, stainless steel, and so forth.
- *Carbon fiber composites and graphite materials:* PIM is probably due to low-pressure contacts between fibers providing voltage-dependent current paths.
- Certain known nonlinear materials and metals such as loaded circuit board dielectrics, conductive thin films, and so forth.
- Semiconductor (diode) junctions, dissimilar metal-to-metal contacts.
- RF switches (during transition).
- Transmission line surface finish irregularities.
- Electrothermal nonlinear effects [20] of low thermal mass transmission line components resulting in current-dependent resistance, and so forth.

Although many of the published articles discourage the use of graphite and ferromagnetic materials and the other nonlinear materials listed above, loose metallic connections or MIM junctions (Figure 7.32) are by far the most common and worst generators of PIM. They are caused by voltage-induced electron tunneling

Figure 7.32 MIM junctions.

and some are possibly combined with microdischarging. Also, since the above listed nonlinear materials and others found in the public domain can be eliminated during the design phase, the MIM interface remains the most troublesome and unpredictable source of PIM.

7.7.4 Mathematical Definition [18, 19]

Linear System

Consider a "source of PIM" to be excited by two carrier signals of frequency f_1 and f_2. The term V_i is the voltage sum of the combined signals and V_1 and V_2 are voltage amplitudes of the two carriers and t = time.

$$V_i = V_1 \cos(2\pi f_1 t) + V_2 \cos(2\pi f_2 t) \tag{7.2}$$

For a linear system the current can be expressed as:

$$I_{\text{linear}} = A_0 V_i$$

where A_0 is the amplitude coefficient of the system (gain or loss) and I_{linear} is the linear output of the current. Figure 7.33 shows the linear system response.

Nonlinear System

A nonlinear device does not obey Ohm's law, and the relation of current and voltage is a curve that is commonly represented by an *n*th-order power series:

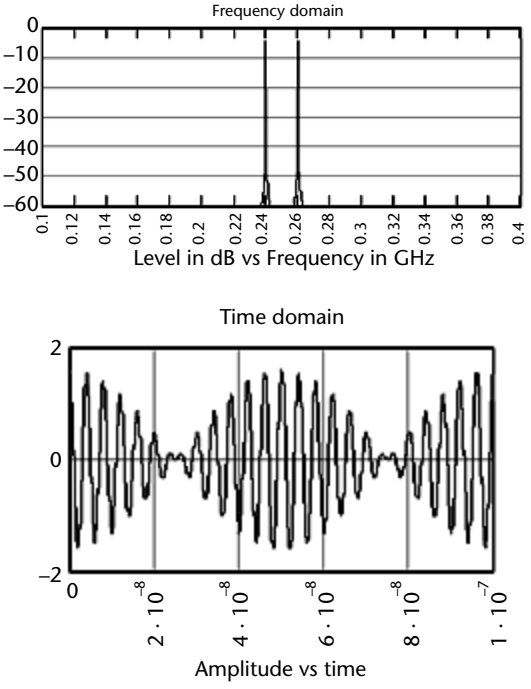

Figure 7.33 Linear system response.

$$I_{\text{nonlinear}} = A_0 V_i + A_1 V_i^2 + A_2 V_i^3 + A_3 V_i^4 + \ldots \tag{7.3}$$

The current $I_{nonlinear}$ is the sum of the linear output term $(A_0 V_i)$ plus the sum of the nonlinear terms. The amplitude coefficients $A_0 \ldots A_n$ depend on the voltage-to-current properties of the nonlinear PIM junction.

Substituting the expression for V_i from (7.2) into (7.3) gives the nonlinear spectrum of $I_{nonlinear}$ for a single condition of PIM. Figure 7.34 shows the nonlinear system response. The linear amplitude coefficient A_0 in the previous plot has been eliminated to emphasize the intermodulation energy that is present.

The curve in Figure 7.35 represents the accompanying DC to millimeter-wave nonlinear voltage-to-current characteristic (that can be measured on a PIM junction with a low-frequency curve tracer), which is dependent on the instantaneous magnitude of the transmitted signal. This curve [21] is defined by the amplitude terms: A_0, A_1, A_2, A_3,.... The previous chart in Figure 7.34 shows intermodulation products that exist close to the Tx carrier frequencies. Sources of PIM produce both *harmonic distortion* and *intermodulation distortion* over a much broader range of frequency.

The chart in Figure 7.36(a) shows a single 0.26-GHz carrier gradual taper of even- and odd-order harmonic distortion responses. The chart in Figure 7.36(b) shows the combined harmonic distortion and intermodulation distortion of a two-carrier response.

The chart in Figure 7.37 gives the specific PIM order versus frequency distribution over a broad band of frequencies for a two-carrier response.

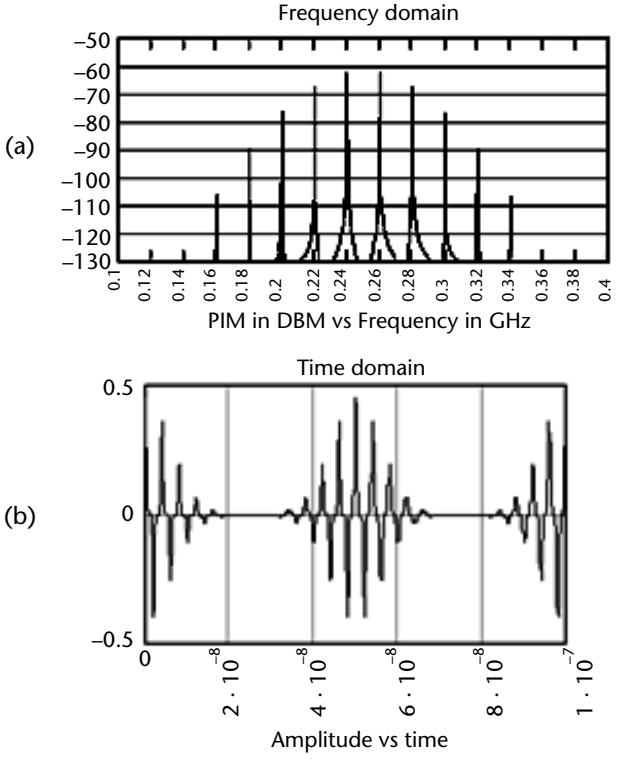

Figure 7.34 Nonlinear system response.

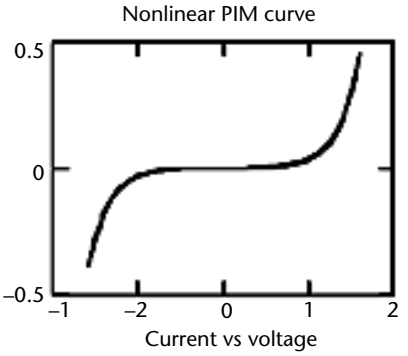

Figure 7.35 Voltage-to-current curve.

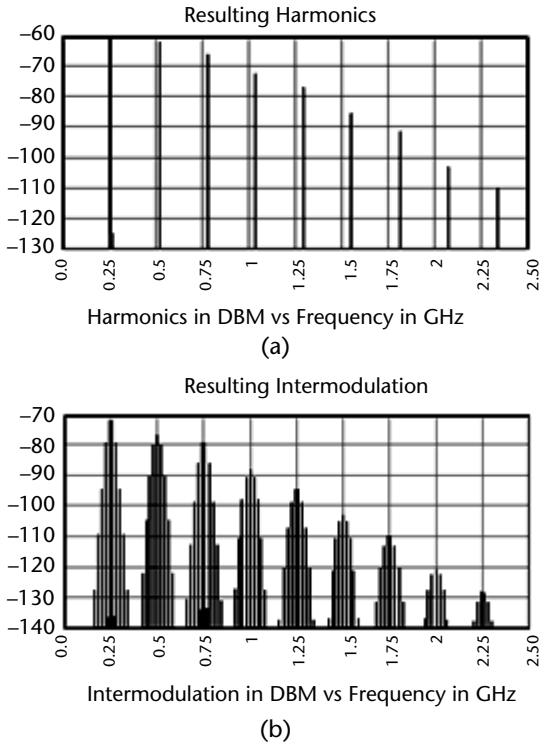

Figure 7.36 Broadband response of harmonic and intermodulation distortion.

7.7.5 PIM as a Function of Incident Power

The chart in Figure 7.38 shows a typical power transfer curve for a single third-order intermodulation product resulting from the passive nonlinearity of a standard SMA connector. In this case, the PIM appears well ordered and predictable. However, MIM junctions are routinely unstable and exhibit both nonlinearity, as shown, plus attributes of an extremely intermittent connection. This makes them both difficult to predict and difficult to measure. Therefore, the safest route is to avoid them through good design and PIM mitigation techniques.

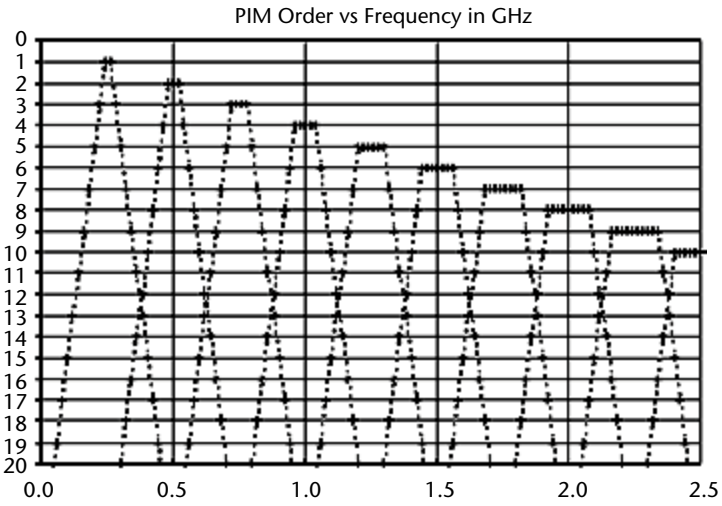

Figure 7.37 Broadband view of two-carrier PIM product distribution + PIM product of f1 = 0.24 GHz and f2 = 0.26 GHz.

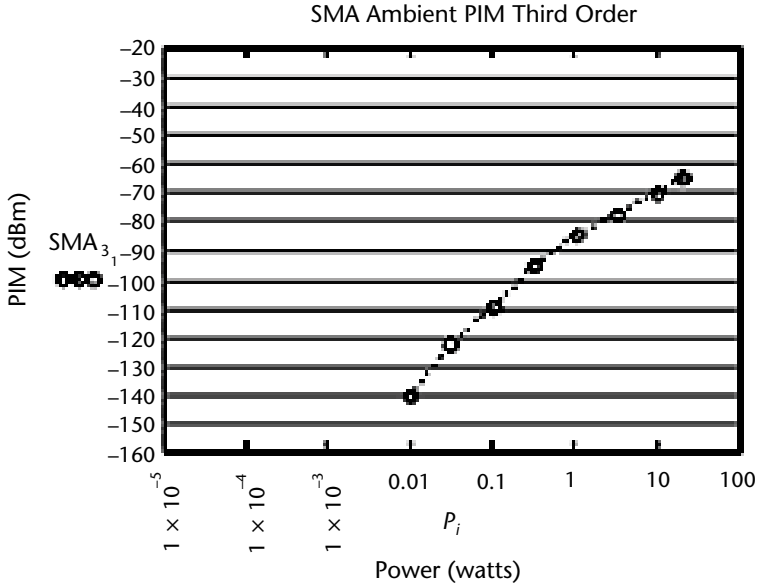

Figure 7.38 PIM as a function of incident power.

7.7.6 PIM Mitigation

PIM mitigation is an activity that is becoming increasingly prevalent due to the increased dynamic range of communication systems and an increase in the sheer number of new communication systems. PIM mitigation techniques vary widely depending on hardware, requirements, design philosophy, and local culture.

It is not the intention here to provide detailed design criterion but to raise awareness of the issue and emphasize requirements definitions and testing and

verification methods. Suffice it to say that in the presence of high-power RF, PIM can be avoided in most cases by providing an excellent oxide-free RF electrical connection or decoupling direct metal-to-metal RF paths (electrical isolation) and by avoiding known nonlinear material. Substantial design information regarding materials and hardware configuration is available within the public domain (see the list of references at the end of this chapter) and review the list in Section 7.7.3 for causes of PIM.

7.7.7 Susceptible Systems

System susceptibility begins with calculating the lowest PIM order as given above using two carriers within the Tx band of a multicarrier system or the lowest harmonic that lands within a susceptible Rx band.

A PIM order greater than 19th may not require more than good workmanship using standard RF components, construction techniques, and connectors to avoid PIM interference in many systems. However, the lowest orders will require substantial PIM mitigation especially within high-power Tx–Rx diplexed antenna systems. Separating the Tx and Rx antennas will effectively relieve excessive susceptibility within the high-power transmission line but exterior radiated hardware in proximity to the antennas may yet have extreme sensitivity even at low power especially with longer wavelengths (≥6 in.). Radiated Tx flux and Rx coupling analysis coupled with a component test program will further define PIM susceptibility.

7.7.8 Hardware PIM Requirements

Once PIM susceptibility has been established, hardware requirement compliance must be defined to ensure that system operational conditions are satisfied. This is typically done by specifying two-carrier PIM test parameters as follows:

- Transmit band, f_{low} to f_{high} – PIM energy source.
- Transmitter single-carrier power × two carriers.
- Receive bands, f_{low} to f_{high} – PIM target payload.
- Maximum allowable PIM power at the Rx antenna port (dBm) with little or no degradation to receiver noise floor considering the lowest or lowest predominant PIM order power density over the Rx channel bandwidth.
- Environmental operating conditions, specifically the thermal range of operation.
- Direction of propagation (reflected or through or radiated).

The PIM requirements for hardware in a radiated environment are the same as the above except Tx power is defined in terms of two-channel flux density at the radiated hardware location, and allowable PIM is defined as maximum PIM flux density at the Rx antenna aperture at a specified distance and angle of illumination from the radiated hardware (see Appendixes 7A and 7B).

7.7.9 PIM Test and Verification Methods

Some level of PIM testing is required to verify design and workmanship during hardware development depending on the level of risk. Tests are normally conducted at ambient temperatures for lower risk hardware or over some degree of thermal range for higher risk devices. Usually PIM is more active at lower temperatures or especially during temperature transitions.

PIM testing is normally done with two carriers set near the band edges of the Tx band. This produces the lowest order, discrete intermodulation products that fall in the receiver bandpass. The use of two carriers will force all of the energy of the PIM source to fall into a few discrete frequencies that can be predetermined by (7.1), to be more readily located during testing.

Test-Related Terms

- *Reflected PIM:* PIM energy that is excited by and is traveling back toward the source of the incident energy, usually in reference to Tx–Rx diplexed systems.
- *Transmitted PIM or through PIM:* PIM energy that is excited by and is traveling in the same direction of the incident energy.
- *Radiated PIM:* usually refers to reflected or through PIM in free space.
- *Contact PIM:* PIM generated by the contact of *any material* with another "highly" conductive material, such as a metal, while being exposed to RF fields.
- *Inherent PIM:* a form of contact PIM in which the PIM is generated by contact of the material with itself and/or inherent contacts within the material such as a conductive loading.
- *Intrinsic PIM:* a form of PIM that results from a noncontacting intrinsic molecular nonlinear feature of the material such as magnetic hysteresis or semiconductor action.
- *Thermal PIM:* A PIM test conducted while thermal cycling a device. This is a method of stimulating dormant "contact" PIMs or gap-sensitive PIMs. Some contact- or gap-related PIMs are vibration sensitive and some are not, but nearly all are thermally sensitive.
- *Ambient PIM:* A PIM test conducted at ambient temperature. This test normally accompanies some light physical manipulation, or tapping, of the device under test to stimulate contact PIMs. Some contact- or gap-related PIMs can be missed with "ambient-only" tests.

The PIM test procedure example, listed in Appendix 7C, is a generic procedure that can be used for the test configurations discussed next to verify that PIM sensitivity requirements have been met and maintained over the duration of the device under test (DUT) PIM testing.

7.7.9.1 Hardline Closed-Loop PIM Test Setups

A closed loop transmission line PIM test configuration can be set up for the transmissive or through PIM by directly connecting the Tx reject filter to the DUT output Tx–Rx diplexer or set up for reflective PIM by directly connecting the Tx reject filter to the Tx–Rx diplexer at the DUT input. This is the most versatile PIM test setup, which can also be used for antenna and/or materials radiative tests. But it is the most expensive and difficult PIM test setup to construct.

Figure 7.39 shows a Tx multiplexed, Tx–Rx diplexed transmission line setup. Other carrier power-combining methods are shown in Figures 7.40 and 7.41. The passively combined method of Figure 7.40 causes half of the transmitted power to be dissipated in the hybrid load. The actively combined method of Figure 7.41 generates high-level active intermodulation (AIM) that requires low connector leakage and/or shielding for radiated tests and a high degree of receive reject filtering up to 180 dB.

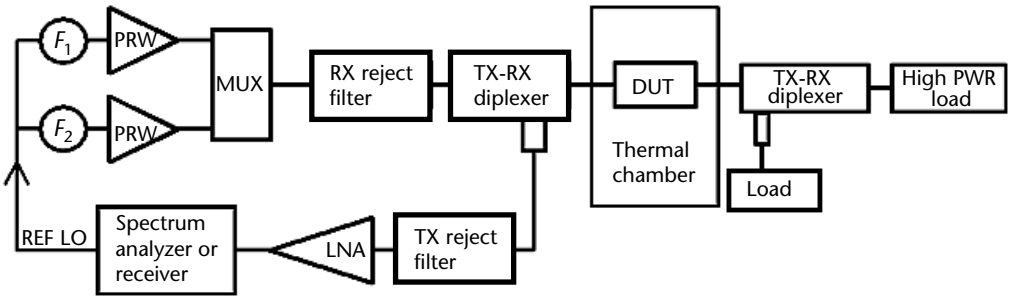

Figure 7.39 Tx multiplexed, Tx–Rx diplexed transmission line setup.

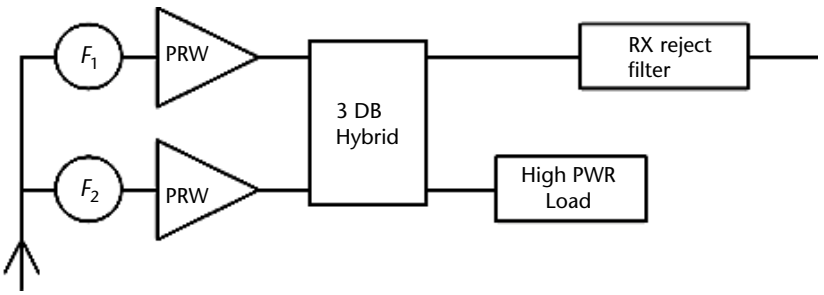

Figure 7.40 Passively combined setup.

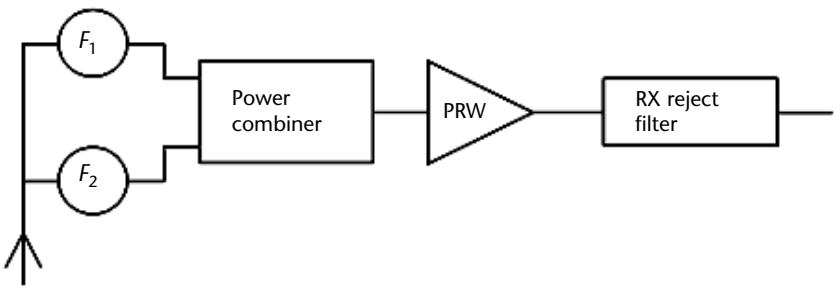

Figure 7.41 Actively combined setup.

7.7.9.2 Radiated PIM Test Setups

The space combined reflected free-space PIM test, shown in Figure 7.42, consists of a PIM test setup that transmits radiated energy to the DUT. The resulting DUT PIM energy travels back to a test setup receiver. This configuration requires minimal filtering mainly to reduce power amplifier noise that is generated in the Rx band. In most cases, standard (non-PIM design) filters can be used since the carriers are space combined. This is useful for testing reflectors, hardware samples, materials, and so forth, only in a radiative, reflective measurement configuration.

The radiated PIM test configuration of Figure 7.43 is useful for reflective/transmissive antenna or reflective free-space device/material radiated PIM testing. Shown in the reflected or Tx–Rx diplexed configuration, a separate Rx antenna or a probe used for troubleshooting may also be connected to the receiver for PIM transmissive tests.

7.7.9.3 PIM Measurement Considerations

It is preferable to use circularly polarized test antennas during radiative tests of materials and devices to overcome polarization sensitivities within the DUT. In test setups having a DUT Rx band matched source and load as in Figure 7.39:

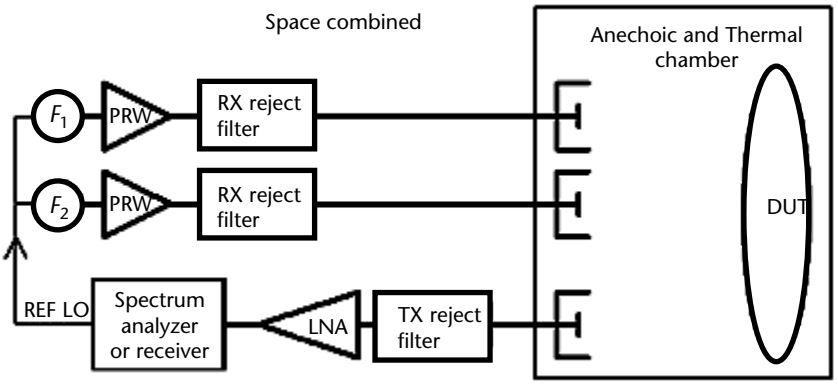

Figure 7.42 Reflected PIM test example.

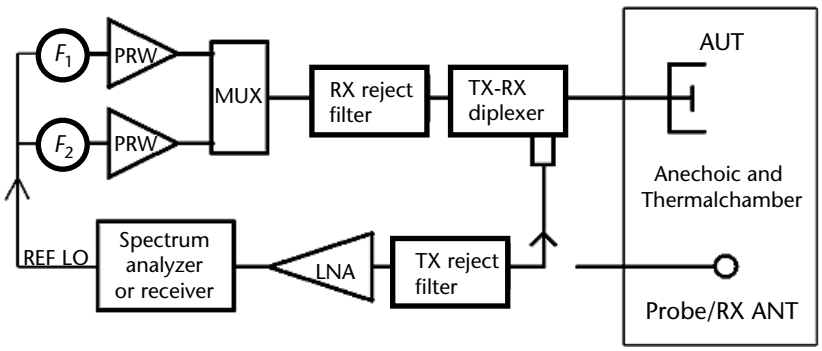

Figure 7.43 Tx multiplexed, Tx–Rx diplexed.

- Measurements in the through or transmissive configuration will contain an in-phase summation of all PIMs within the DUT.
- Measurements in the reflected configuration will result in a vector summation of distance related or distributed phase of all sources of PIM for electrically large devices with multiple sources of PIM.
- Reflected and through PIM will measure approximately the same for electrically small devices that contain multiple sources of PIM.

7.7.9.4 General Filter Requirements

The filtering pass band of the PIM test setup can be designed to cover several PIM orders so they may be selected for current and future use. For example, if the system test requirement is for a fifth- or seventh-order PIM, design the PIM test setup to enable a third-order test in which the fifth- and seventh-order PIM products can be made to land at the same Rx frequency as the third simply by setting the Tx carrier closer together within the Tx band.

- The *transmit multiplexer* must be designed to handle the full rated power of the amplifiers and provide enough channel-to-channel rejection (about –30 dB at the band edges) for the amplifiers to safely operate.
- The *receive reject filters* must be designed for low PIM operation and provide enough rejection to eliminate the passives generated by the multiplexer or combiner. Elimination of the AIM, generated by the amplifier in a single-amplifier system, can require filter rejection to a level of less than –160 dBm. Typically the rejection for passives should be –80 to –100 dB and rejection for actives should be rated according to the "third-order intercept point" of the amplifier. Low PIM connectors must be used at the DUT ports.
- The *Tx–Rx diplexer* must also be designed for low PIM operation and should have a minimum rejection of –35 dB to avoid PIM from the connector interfaces. Standard connections can be made at the Rx port, but low PIM connectors must be used at the common port and Tx port.
- The *transmit reject filter* prevents low-noise amplifier (LNA) saturation by the Tx carriers. The minimum rejection required is established by the range in decibels from the saturation input level of the LNA (its maximum output minus the gain) to the maximum output level of the transmitter. The diplexer rejection can be added to the rejection of the Tx reject filter to achieve the minimum required rejection. Typical values are –80 to –110 dB.

7.7.9.5 PIM Receive/Spectrum Analyzer

Because PIM-sensitive hardware by definition would incorporate a high dynamic range and, therefore, a very sensitive receiving system, the PIM setup receiver would also require high sensitivity. This is achieved by the use of a low-noise preamplifier and the use of narrow intermediate frequency (IF) bandwidths.

Typically PIM measurements are done at IF bandwidths between 10 and 100 Hz. This requires the receiver to have a high-stability frequency standard (reference

oscillator) and a frequency locking capability. The dynamic range of the receiver should be at least 50 dB and is normally closer to 100 dB to capture the wild variations due to PIM.

Normally, a spectrum analyzer set for 10 Hz IF resolution bandwidth is used with a 30- to 50-dB gain LNA to obtain an average noise floor of approximately –155 to –160 dBm depending on system losses.

7.7.9.6 Frequency Source

Because the ultimate sensitivity of the PIM test setup receiver is directly related to the frequency stability of the system, frequency locking capability is required. The PIM receiver and both frequency sources must be locked to the same high-stability reference oscillator.

7.7.9.7 PIM Test Setup Sensitivity and System Noise [22]

The required sensitivity of the PIM test setup receiver will be driven by the ultimate PIM sensitivity of the DUT and should be one to two orders of magnitude better that the DUT to ensure measurement margin.

The test system sensitivity can be determined by finding the kT_SB noise floor.

This is defined as follows:

$$N_{\text{floor}} = kT_SB$$

where:

B = receiver bandwidth (Hz).

T_S = system noise temperature (deg).

$k = 1.38 \times 10^{-23}$ J/K, which is Boltzmann's constant (heat capacity).

7.7.9.9 PIM Test System Noise Temperature

The system noise temperature, T_S, contains contributions from the antenna, the antenna feed, the LNA, and the PIM test setup receiver or spectrum analyzer. This consists of the following:

$$T_S = T_{ant} + T_0(L - 1) + LT_0(F_{LNA} - 1) + LT_0(F_{Rx} - 1)/G_{LNA}$$

where:

T_{ant} = antenna or load noise temperature (290 K).

L = losses between antenna and LNA (a power ratio).

F_{LNA} = LNA noise factor (a power ratio).

F_{Rx} = receiver or spectrum analyzer noise factor (a power ratio).

G_{LNA} = LNA gain (a power ratio).

T_0 = ambient temperature (290 K).

7.7.9.9 PIM Verification

It should be noted that PIM test setup verification is the most important aspect in the PIM measurement.

Because test data is relied on to qualify critical hardware, system failure can result if PIM testing does not properly detect sources of PIM. Therefore, it is crucial to have correct initial calibration and a procedure in place that will guarantee continuous PIM test setup sensitivity throughout the duration of the test.

The key items that will ensure PIM test setup verification are listed as follows:

- *Ensuring accurate initial calibration:* Includes accurate Tx power levels, absolute Rx levels, and PIM source (initiator) verification
- *Ensuring the correct intermodulation product is located:* Most of the time the correct product is easy to find and this is not an issue. However, in some cases this gets missed and a spur, electromagnetic interference (EMI), or other PIM product is inadvertently monitored in lieu of the specified product and the test is therefore invalid.
- *Ensuring calibrated setup conditions do not change midtest:* Continuously monitor Tx power and periodically recheck the PIM source.
- *Ensuring accurate final calibration:* Repeat initial calibration routine and PIM source verification.

The key elements to PIM verification can be implemented as discussed next.

Pretest Calibration

This consists of precise calibration of Tx power and Rx channel and then verification by measuring with an external calibrated standard. On hard-line tests a power meter with a high-power sensor can be used to verify Tx power at the DUT. A calibrated RF radiation meter can be used to verify Tx flux for radiated tests. The receiving channel amplitude is verified by connecting directly to a calibrated frequency source while incrementing amplitude to ensure that the receiver and data collection system track amplitude changes and absolute level.

Pretest PIM Source Initiator

Once calibration has been established, a known source of PIM such as a medium-gain antenna attached to a mixer can be used to verify radiated PIM tests or a mixer attached to a Tx coupled port can be used to monitor hard-line tests. In the radiated tests, the PIM source should be placed in a fixed position where changes in Tx power up and down are recognizable and where a significant and stable PIM level can be monitored. Placing the PIM source in this position should produce repeatable results if nothing has changed in the setup.

PIM Frequency Verification

The receiver center frequency of the PIM is verified by measuring the frequency of each Tx carrier using the Rx channel analyzer and calculating the exact PIM frequency per (7.1) of Figure 7.30 (see Section 7.7.2), then setting the Rx spectrum analyzer to that exact frequency. Install a PIM source and find the generated PIM at

or very near the calculated frequency. If measuring a repeater link or intermediate frequency, measure the carrier frequency, obtain the translation frequency from the system engineers, and again calculate as in (7.1) of Figure 7.30 (see Section 7.7.2) considering the translation frequency.

Once the exact PIM frequency has been centered, the spectrum analyzer frequency span is set to 0 Hz such that continuous monitoring for PIM over time is enabled. The spectrum analyzer and the Tx frequency source must be locked to the same local oscillator (LO) for stable frequency readings within a 10-Hz bandwidth.

PIM Test Setup Residual PIM Verification

Once the Rx channel PIM frequency has been verified, the PIM source is removed and the test setup residual PIM floor (Rx channel noise floor plus setup PIM) is verified either with a surrogate DUT or through connection (no DUT). An acceptable residual or setup PIM floor is a least 10 dB below the DUT PIM requirement at full Tx power. If the measured level is not low enough, the setup or chamber needs to be diagnosed and repaired for arbitrary sources of PIM or potential EMI ingress from external sources.

Periodic PIM Source Calibration Checks

Verification of frequency, PIM sensitivity, and Tx power needs to be taken at various points for a test that lasts longer than an hour. Because narrow IF bandwidths are used for PIM testing, frequency drift of only a few hertz can cause amplitude errors of the Rx channel. Therefore, replacing the PIM source in the known fixed position as described earlier and verifying that the PIM level is repeatable serve as verification that nothing has changed in the setup since the initial calibration. If the level has changed, set the analyzer's frequency span to 100 or 300 Hz and record the difference in level between the center frequency reading and the peak reading, then recenter the frequency and reset for 0 Hz.

Post-Test Calibration

The first step here is an end-of-test PIM source check. Next, perform the same steps as done for the pretest calibration. Record any differences.

See Appendix 7C for an example test procedure that can be used to ensure the items above are implemented during testing. This can be used as part of a boilerplate test procedure.

7.8 Multipactor, Corona, and Ionization Breakdown

This section presents an overview of known and predictable high-power RF voltage breakdown effects that are capable of causing system degradation ranging from interfering intermodulation and/or noise, to gradual hardware deterioration, to instantaneous and catastrophic hardware failure. The intention of this section is to raise awareness and give a basic understanding of the phenomena with a focus on requirements, test, and verification.

7.8.1 Multipactor

Multipactor is well known and well-documented electron discharge phenomena dating back to Philo T. Farnsworth's early 20th-century invention of the cold cathode *multipactor* vacuum tube. Farnsworth used this device as an RF oscillator for radio transmissions and also as a current amplifier for his cathode-ray tube invention.

The action of a multipactor is relatively simple and predictable. If a sufficiently high-voltage RF field is applied in a vacuum between two parallel surfaces and the electron transit time between the plates is an odd multiple of one-half cycle of the RF, multipactor is likely to initiate.

Although conditions might be right for multipactor to occur, RF voltages in microwave transmission lines typically do not have the field intensity to cause electrons to directly emit from transmission line surfaces (field emission). Therefore, some other mechanism needs to be present to generate free electrons. The free electrons will then accelerate within the RF field with sufficient momentum to initiate secondary electrons on collision with the transmission line surfaces.

Multipactor is often initiated by random energetic electrons present in the environment or by other mechanisms such as released electrons through exposure to ultraviolet (UV) light or other forms of radiation. Once initiated, gasses trapped in the surface materials may also release and ionize due to collisions with accelerated secondary electrons, obscuring pure multipactor until adequate venting evacuates the gas. This is followed by the multipactor potential to create an electron avalanche forming a sheet-like cloud of secondary electrons if the secondary electron emission (sometimes called SEE) coefficient of the surface is greater than one ($\delta > 1$) as shown in Figure 7.44.

In Farnsworth's case, a coating was applied to the surfaces to increase the secondary emission coefficient in order to actively initiate continuous multipactor discharge. In designing high-power RF or microwave transmission hardware, the effort is to have the lowest possible secondary electron emission to minimize damaging multipactor effects. However, most materials compatible with high-power microwave transmission, such as aluminum, silver, and gold, have a secondary emission coefficient that is low but still greater than one. Therefore, it is necessary to deliberately design multipactor potential out of a transmission system [23] in case the electron transit time happens to exist within the operating parameters of

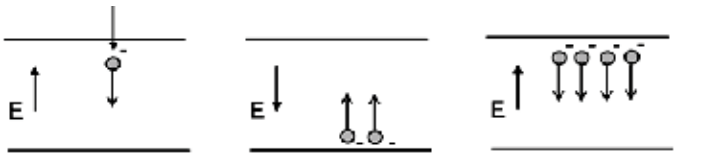

A stray electron from the environment enters and is accelerated by the RF electric field.

Striking the opposite δ=2 surface at high velocity produces 2 secondary electrons accelerating in the opposite direction.

Electrons striking the opposite surface at high velocity from a *sheet* of secondary electrons.

Figure 7.44 Illustration of electron avalanche causing multipaction.

the system. Although coatings $\delta < 1$ are available, mitigation is more reliably done by increasing the gap dimensions between the transmission path surfaces such that the electron transit time does not now match the RF operational parameters.

If multipactor is not considered in the design and multipactor discharge occurs, the system is likely to fail. The avalanche of electrons traveling back and forth perpendicular to the propagation of the RF effectively causes a low-impedance conduction path aligned with the electric field that both reflects and absorbs a substantial portion of the high-power transmitted energy. While reflected RF may be damaging to the system, the usual cause of failure is excessive RF absorption in locations along the transmission path that were not designed to dissipate the additionally generated heat. This sometimes results in a severely conductive discharge event caused by ionization breakdown from local, overheated organic materials initiating gas discharge. The resulting intense heat of an ionization breakdown is capable of vaporizing metallic components in the area that are not rated for excessive heat dissipation. In this manner, the transmission line may be destroyed.

7.8.1.1 Multipactor Susceptibility

Multipactor susceptibility is defined by frequency, gap distance, RF voltage, and surface material secondary emission coefficient [24–26]. Additionally, a high vacuum (typically $<10^{-4}$ Torr) is required along with a random energetic electron or other type of initiator. The example chart in Figure 7.45 shows predicted multipactor breakdown for a silver surface $\delta \approx 1.6$. The *X*-axis marks the frequency-gap related variable (typically referred to as the *fd* product) and the *Y*-axis defines the

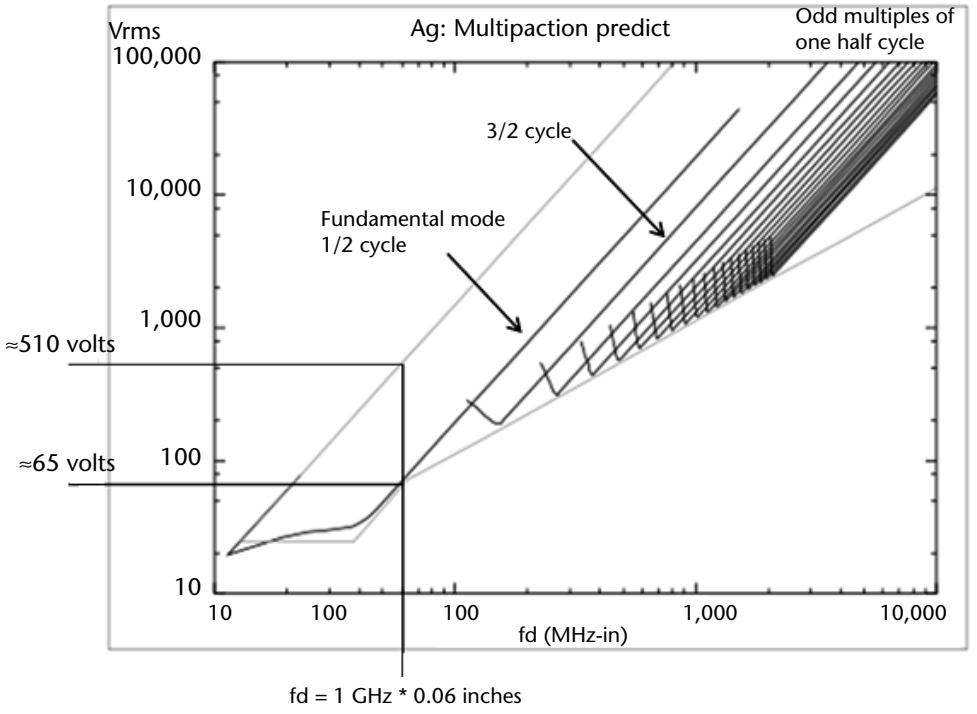

Figure 7.45 Silver multipactor curves.

operational RF voltage determined by total operational power, impedance effects, VSWR effects, and multicarrier/frequency spreading effects. The outer envelope of the chart gives the multipactor breakdown threshold for uniform fields as found between parallel plates. For example, if a frequency of 1 GHz were used in a 50-Ω transmission line that had a 0.06-in. gap between the inner conductor and outer conductor, the initial breakdown threshold would exist at approximately 65 volts rms as indicated.

Breakdown continues to occur until approximately 510V rms. As the voltage is increased beyond the upper threshold at 510V, the multipactor will terminate since the increased voltage will further accelerate the electron such that the transit time is now too rapid to synchronize with the RF half cycle. In practice, devices should be designed such that there is sufficient margin to the minimum breakdown voltage; in other words, the design should be made such that there is some amount less than 65V in this particular gap.

One variable that is not included in the chart is the time required to produce enough secondary electrons to have a noticeable effect on performance. This has been estimated to be something between 20 and 40 electron crossings to accumulate a large enough electron cloud. Although evidence exists and it is generally agreed upon, this is most likely a conservative estimate. The system multipactor susceptibility time frame is determined by the expected time-domain RF operational waveform wherein the peak power envelope exceeds the multipactor threshold in Figure 7.46 for a period lasting longer than 20 to 40 crossings. This pertains mainly to multicarrier systems where the carriers tend to sum over a very short period of time.

Figure 7.46 gives an example of five equally spaced, equal amplitude 5W carrier waves all in phase at $t = 0$ sec. Obviously, the peak power envelope far exceeds the given multipactor threshold as shown; however, the peak envelope time period falls considerably short of the 20-crossing estimate. The waveform shown is the worst case for peak power production but is not typically an operational condition. Normally, the operational condition will cause a 20-crossing time period somewhere between total average power and the worst-case peak power. Establishing the 20-crossing time base requires an operational waveform analysis and/or multipactor test to determine the multicarrier susceptibility threshold.

The power instantaneous rms voltage waveform can be calculated by the expression in Figure 7.47.

Although the multipactor peak power summation may potentially initiate multipactor, the effect to the system may not even be noticeable. This is one of the areas that requires an in-depth signal/waveform analysis or multipactor test to determine ultimate susceptibility. The other area that potentially requires significant analysis is determining the maximum operating voltage within complex hardware such as high-power filters and antenna components. Electromagnetic solvers require significant knowledge and skill to accurately predict operating voltages. Even then, modeling uncertainty, workmanship, contamination, and so forth, may require a threshold test of hardware even though a significant margin is predicted. Detailed design and analysis information, particularly EM and multicarrier, is not the purpose of this section. However, is it available and covered rather extensively in the public domain (see the references at the end of the chapter).

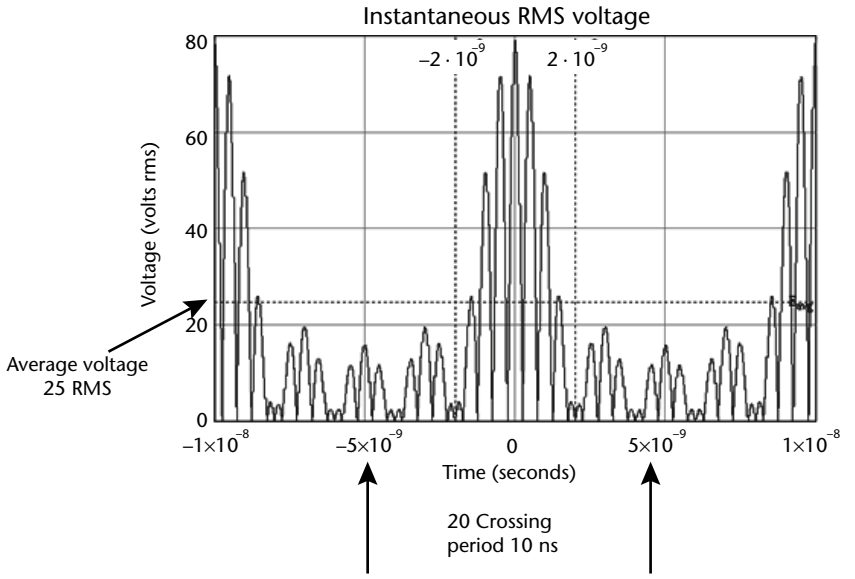

Figure 7.46 Example of an instantaneous rms voltage waveform.

Determine RMS Instantaneous Voltage:

$$e(t) = \left| \sum_{i=1}^{n} \left[\left(p_i \cdot Z_0 \right)^{\frac{1}{2}} \cos\left[\left(F_i \cdot \omega \cdot t \right) + \frac{\theta \cdot \pi}{180} \right] \right] \right|$$

Where: $\omega = 2 \cdot \pi \cdot f_o \quad f_o = 10^9$

F = carrier frequency (GHz)
p = carrier power (RMS watts)
Z_0 = line impedance (ohms)
n = number of carriers
θ = carrier phase (degrees)

Figure 7.47 Instantaneous voltage.

7.8.2 Corona and Ionization Breakdown

Other related but entirely different phenomena are corona and gas ionization breakdown [26]. Both multipactor and ionization breakdown are initiated by electron collisions. However, the major difference from multipactor is pressure. Whereas multipactor requires a vacuum of at least 10^{-2} Torr for unobstructed electron flow between the surfaces, corona and ionization exist only within a pressurized gas or partial pressure environment. When this exists, the path between the surfaces is obstructed by the gas where the mean free electron path is shorter than the electrode or surface separation such that secondary electron emission now results in collision with the gas. This results in an ionized gas rather than a pure electron cloud. Gas ionization also can exist within direct current (DC) fields, whereas multipactor is a resonant, synchronous time-based electron avalanche resulting only from AC fields.

The power density of the discharge is also pressure dependent. At pressures $<10^{-2}$ Torr, power density can range from very low at the multipactor threshold to intermittent and can have an erratically high density during high current multipactor where the electron current becomes large enough to partially short the incident energy. When this takes place, the incident RF voltage may drop below

the multipactor threshold and multipactor momentarily ceases to exist. As the RF voltage then recovers, the multipactor cycle repeats.

On the other hand, gas ionization may run the gamut from a very weak power density at low pressure (plasma globe) to an extremely intense high-current localized plasma arc at higher pressures (plasma arc welding). As such, *corona* generally refers to a nonthermal discharge, whereas arc discharge refers to high temperature or thermal discharge. Obviously, the high-pressure plasma arc is the most destructive, potentially reaching temperatures in excess of 10,000°C near atmospheric pressure. This is a major concern for satellite waveguides operating at high power densities such as WR75 and WR51 in ambient pressure [27].

If an arc is initiated by any form of vaporizing debris, the ambient gas will sustain the arc and it will travel back to the RF power source at a relatively slow speed (a few meters/second or less) until it encounters an obstacle such as a waveguide window. If temperatures are sufficient, it will crack the window and destroy the hardware. Extreme care must therefore be taken to circumvent any form of metallic debris or organic debris within the waveguide that might overheat and vaporize. This would include bonding agents commonly used in waveguide load manufacturing.

Because gas ionization breakdown involves electrically charged particles creating an electrically conductive discharge within the high-power transmission path, it appears with similar attributes as multipactor discharge. Therefore, the same screening test can be used to detect both phenomena with the only difference being the test pressure. Multipactor is always tested in high vacuum ($<10^{-4}$ Torr), whereas corona is tested from ambient pressure through partial pressure to high vacuum. Of course, inadvertent gas discharge (heat releasing trapped gases from surfaces) during corona testing can give a similar test response as multipactor depending on the monitoring scheme.

7.8.3 Hardware Test Requirements

Hardware requirements are typically given in terms of margin to analysis and/or margin to test. In simple types of hardware, where multipactor margin can be accurately predicted, analysis with significant margin may be sufficient in lieu of a test requirement. In other cases and with certain philosophies, unit tests may be required of all hardware. At a minimum in all cases, a system-level operational test in vacuum is required to discover unpredictable items such as contamination and workmanship. Requirements for multipactor tests are usually defined as follows:

- *Test average power:* The actual operational rms power considering potential limiter faults (amplifier saturation), VSWR effects, optimistic RF insertion losses, plus some small degree of margin that does not overstress the hardware but creates the operational heating effects.
- *Peak power:* This is determined from the momentary summation of rms power of each amplifier (considering all the carriers), the minimum number of electron crossings at the multipactor threshold, plus those listed in the preceding entry (test average power). It is the anticipated peak test power with some practical degree of margin to multipactor depending on the system.

During a multipactor or corona test, average and peak power are run concurrently by running a *peak power pulse* with an *average power duty cycle*. The peak power is to deliver the correct voltage to the device, while the average power is to apply the correct thermal load.

- *Operational frequency band:* This can include frequency and power of the system carriers with a requirement to test at a specific *power-weighted average frequency* (see the expression in Figure 7.48). In single-carrier devices that have a large operational band, it is sufficient to test at the worst-case frequency based on the susceptibility curves.
- *Pretest high-vacuum soak:* This is typically done at ambient temperature in high vacuum for a minimum of 12 hours for multipactor tests. In the case where the unit under test has poor venting or volatile materials, a soak of 24 hours or more may be needed to ensure the entire unit is at a vacuum pressure and not in the critical pressure region where corona may occur. For a corona test, a unit should soak in ambient air for at least an hour before beginning testing if it has recently been in a vacuum environment.
- *Operational temperature limits:* All metal devices are usually tested at the maximum operational temperature. Devices that contain dielectrics, with thermally sensitive gaps, are tested over a minimum and maximum thermal cycle. Corona tests are typically done at ambient temperature to simulate the operational environment of launch.
- *Free-electron source:* This is normally a radioactive cesium source (Cs-137) on or slightly upstream of the predicted most likely location on the hardware to break down (small gap with high voltage). Other possible free-electron sources include strontium (Sr-90) or an electron gun.
- *Multipactor initiator:* An initiator is required to prove the multipactor test setup is capable of detecting multipactor independent of the device under test. This is a device that is designed and built to break down at a known threshold near the test article's maximum input power level. Power is applied to this device prior to the actual unit under test to prove that the test equipment is sensitive enough to detect breakdown. This is ideally done both before and after the actual unit test. This is done for corona tests as well.
- *Surrogate device:* In cases where a DUT fails a high-power test, it may be necessary to have a replacement device to demonstrate that the test setup is not causing the DUT to fail. In coaxial devices, this may be a barrel; in waveguide devices, it may be a piece of regular waveguide.
- *Test pressure requirements:* Multipactor testing can occur only when pressures in the chamber are below 10^{-4} Torr (and after the soak times described earlier for the pretest high-vacuum soak). Units undergoing multipactor

Determine Power Weighted Average Frequency

Where: P = carrier power
F = frequency
n = number of carriers

$$\text{Frequency} = \frac{\sum_{i=1}^{n} (P_i \cdot F_i)}{\sum_{i=1}^{n} P_i}$$

Figure 7.48 Power-weighted average frequency.

testing should have a dry run at ambient pressure before being tested for multipactor in high vacuum. Corona is tested from ambient pressure through partial pressure to high vacuum at a controlled rate slower than the operational profile.

- *Venting requirements:* High-power vacuum tests require adequate venting such that vaporizing trapped gas will rapidly escape the high-power RF field areas and the unit internal pressure will reach high vacuum in a reasonable amount of time to test.

7.8.3.1 Multipactor Testing

There are many ways to meet the hardware test requirements outlined in the last section, but several best practices have been developed in the industry that allow for reliable results.

The most important part of a multipactor test is determining the detection methods. There are many ways to detect multipactor, and it is beyond the scope of this text to provide details, but some of the most common detection methods are listed here. It is required in any test to have at least two detection methods and it is always better to have more. A test failure is defined as simultaneous multipactor detection on two or more unrelated detection methods.

- *Nulling of forward/reverse power:* Consists of a continuously variable attenuator and phase shifter that are used to null the forward and reverse power to a level close to the noise floor of a spectrum analyzer. Any sudden increases in the null indicate an event has occurred. The null must be continuously adjusted during the test to remain useful.
- *Third harmonic noise:* A highpass filter is coupled at the output of the transmission that rejects lower harmonics. Multipactor is seen as a sudden perturbation in the third harmonic signal on a spectrum analyzer.
- *Monitoring bias current:* Current from an event is detected on a picoammeter through a bias-T and a services battery box. The RF path of the device must not have a path to ground.
- *Electron probes:* Current from an event is detected on a picoammeter through a services battery box. An electron probe is placed near a vent hole to detect the electrons.
- *Forward/reverse/output power detection:* In any test, the power levels are monitored. During an event, the input power can be substantially reflected (and the output power attenuated). This is a much slower detection methods, but an indicator nonetheless.

The test equipment used for a multipactor test can vary widely depending on the detection methods, power level required, and the test frequency. However, a typical test consists of a block diagram very similar to that shown in Figure 7.49. This test setup uses two of the most common detection methods, a forward/reflected null and third harmonic detection. The detection methods for corona are typically the same.

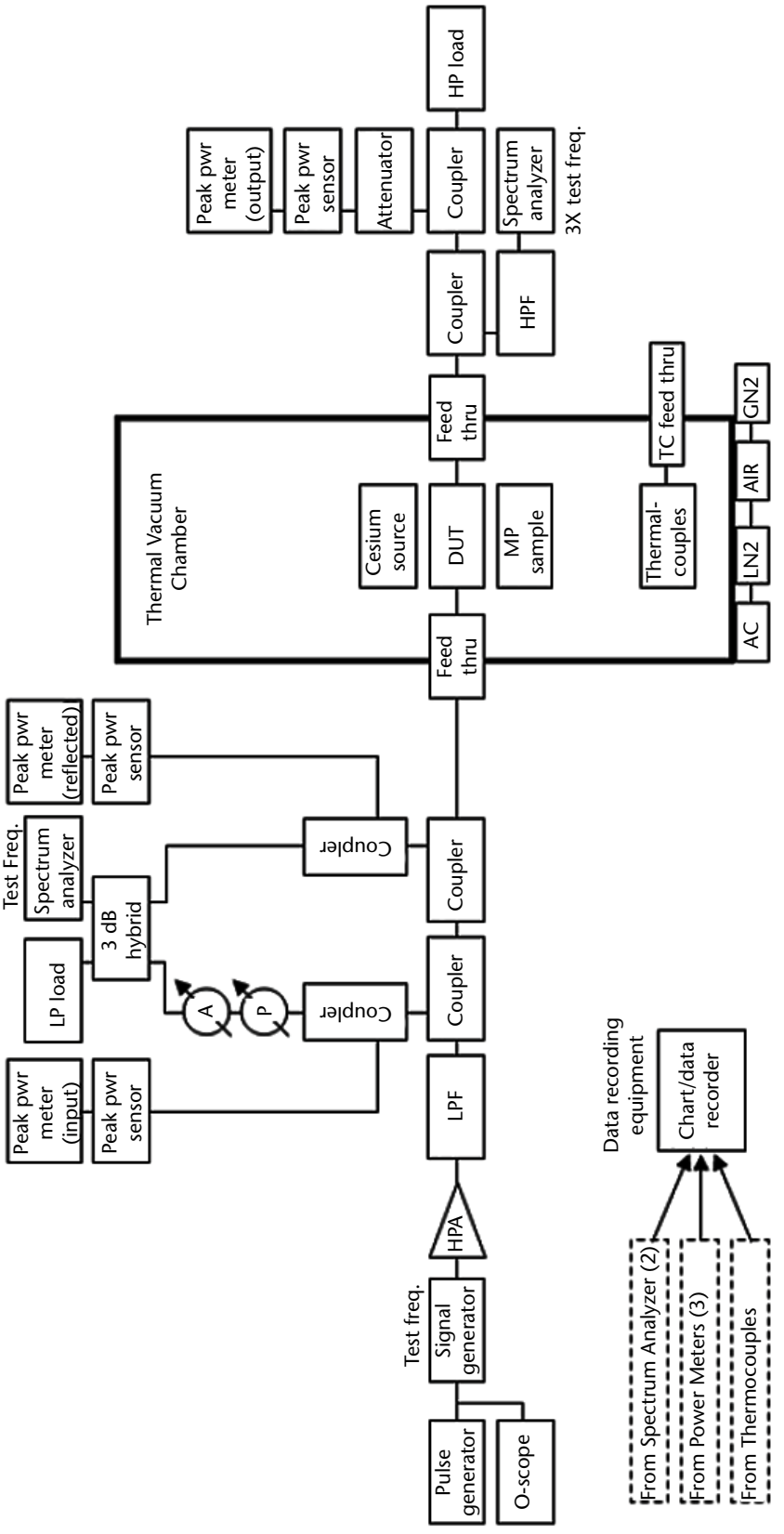

Figure 7.49 Multipactor test block diagram example.

There are a few important notes about the test equipment. First, the spectrum analyzers used must be set to a 0-Hz span (to view the data in the time domain) and have a video-out port connected to a data collection system or strip chart (to overcome the screen refresh rate) to ensure all events are detected. Simply using the maximum hold feature on the screen is not sufficient to declare success in a test because potential events could be missed. However, these events may be visible on the strip chart due to the video-out feature if the sampling rate is fast enough.

Next, the high-power amplifier (HPA) selection is very important; there are several options to meet requirements. Continuous-wave (CW) amplifiers are common and can be used if one can be located that provides a high enough power level for the test. Unfortunately, with some tests, the power level needed after adding margins is too high for a CW amplifier. Because the peak power is what matters for inducing multipactor, a very low duty cycle pulsed amplifier can be used. A CW amplifier can also be applied to obtain the required average power for heating, if needed. If a pulsed high-power amplifier is not available, a ring resonator can be used for closed loop tests. A resonant ring can passively amplify an input signal from a lower power amplifier by a factor of 10 or more. The lower the loss in the ring, the higher the amplification it provides.

To ensure that a high-power test is yielding meaningful results, several sequential steps should be followed:

1. The test equipment must be set up properly according to the block diagram and all measurement devices must be calibrated.
2. A surrogate device should be installed in place of the DUT and the power increased to full level at ambient pressure to ensure that the setup can handle the power.
3. Repeat step 2 with the DUT.
4. To demonstrate that the test setup itself is multipactor free, the surrogate device should be installed once again, but this time pumped down to vacuum and soaked. Power should be applied and all detection methods monitored for any signs of breakdown. This proves that any events seen during the test are from the DUT and not the setup. If a corona test is being performed, this step should include power on from ambient through vacuum to demonstrate the setup will not have corona effects.
5. The known multipactor device (multipactor initiator) should be installed in the chamber. (Ideally, the penetration plate will have enough ports to have the DUT and initiator devices in the chamber at once so pumpdown does not need to be repeated.) After a soak at vacuum, the power should be applied in approximately 10 incremental steps of at least 5 min each until breakdown is observed on all detection methods.
6. This step varies depending on test type. For a multipactor test, after the required vacuum soak, power may be applied to the DUT in incremental steps until full power is reached. For a corona test, power should be applied at ambient pressure and remain on through pumpdown.
7. After the required dwells and thermal cycling (if applicable), power should be applied to the initiator device again until breakdown is observed to prove that nothing changed in the test setup.

8. The final step in any test is to collect data items that are sufficient to prove to a third party that a device has successfully passed.

For either type of high-power test, several data items are required:

- First, there should be a continuous strip chart of all detection methods, power meters, and thermocouples with high enough sampling rates to ensure that all possible events were captured.
- Next, there should be evidence from the detection methods showing the breakdown of the multipactor initiator device. On a forward/reflected null, for example, there would be an image from the spectrum analyzer screen depicting the event.
- There should also be evidence that temperatures and pressures were within specification limits during the test and that all dwell times were met.
- If any events were recorded on the DUT, there should be images of the events on the detection methods and detailed descriptions of the test conditions during the event(s).

This is the general outline of the steps required for high-power testing. Required data collection is discussed next.

7.8.3.2 Strip Chart or Data Acquisition Annotation

The following items must be continuously recorded on the strip chart or within the data acquisition software. The channels with low data rate must update by at least one sample per second and detection method channels typically require a 1-kHz sampling rate or faster. It is usually difficult for an outsider to review test data from a high-power test, especially when a phase bridge is used, so data should be as well annotated as possible.

- Date and time;
- Test description (ambient, developmental, proto-qual, acceptance, etc.);
- DUT, description, model, and serial number;
- High-power test frequencies and monitoring frequencies;
- Chart *X* and *Y* parameters (what is being measured)—absolute levels and steps;
- Strip chart speed;
- Level of each monitor channel—frequency, absolute power levels and steps;
- Tx power—absolute levels and steps;
- Temperature of DUT—absolute levels and steps;
- Test setup noise floor;
- Initiator source checks;
- Tx power checks;
- Calibration pre- and post-test including absolute levels and steps;

- Any changes in spectrum analyzer or other instrument settings that deviate from the test plan;
- Any other or unexpected events that take place during the test.

Appendix 7A

7A.1 Generic PIM Test Setup Equations Related to Far-Field Tx Flux Density

Equation to solve for flux density (watts/cm^2):

$$S_{tx} = \frac{P_{tx} \cdot G_{tx}}{4 \cdot \pi \cdot R^2}$$

Equation to solve for distance(cm):

$$R = \sqrt{\frac{P_{tx} \cdot G_{tx}}{4 \cdot \pi \cdot S_{tx}}}$$

Equation to solve for transmit input power (watts):

$$P_{tx} = \frac{S_{tx} \cdot 4 \cdot \pi \cdot R^2}{G_{tx}}$$

Where:

R = distance in cm (to compare directly with a flux density probe which reads in watts/cm^2)

P_{tx} = transmit input power in watts (rms)

S = transmit flux density in watts/cm^2

G_{tx} = a power ratio derived from gain in dBi as follows:

$$G_{tx} = 10^{\frac{G_{\text{dBi}}}{10}}$$

R distance must be substantially greater than the Transitional Farfield:

$$R_{\text{TransitionalFF}} = 0.16\left(\frac{2 \cdot d^2}{\lambda}\right)$$

R need not be a greater distance than:

$$R_{\text{Farfield}} = \left(\frac{2 \cdot d^2}{\lambda}\right)$$

d = transmit antenna physical aperture (cm)
λ = wavelength (cm):

$$\lambda = \frac{30}{f_{\text{GHz}}}$$

Appendix 7B

7B.1 Generic PIM Test Setup Equations Related to Far-Field Rx Coupling

Equation to solve PIM power at source of PIM (dBm):

$$P_{pim} = P_{tx} - G_{rx} - G_{pim} - 20\log\left(\frac{\lambda}{4 \cdot \pi \cdot R}\right)$$

Equation to solve coupling from source of PIM (dB):

$$PIM_{coupling} = P_{rx} - P_{pim}$$

Or:

$$PIM_{coupling} = G_{rx} + G_{pim} + 20\log\left(\frac{\lambda}{4 \cdot \pi \cdot R}\right)$$

Where:

R distance in cm

P_{tx} = PIM test setup received PIM at spectrum analyzer in dBm

P_{pim} = PIM power at the source of PIM

G_{rx} = gain of PIM test setup receive antenna (dBi)

G_{pim} = gain of the source of PIM (0 dBi for omni radiator or +3 dBi for hemispherical)

$\text{PIM}_{\text{coupling}}$ = total loss and gain from the soruce of PIM to the setup receive antenna port in dB

Distance R must be substantially greater than the Transitional Farfield:

$$R_{\text{TransitionalFF}} = 0.16\left(\frac{2 \cdot d^2}{\lambda}\right)$$

R need not be a greater distance than:

$$R_{\text{Farfield}} = \left(\frac{2 \cdot d^2}{\lambda}\right)$$

d = transmit antenna physical aperture (cm)
λ = wavelength (cm):

$$\lambda = \frac{30}{f_{\text{GHz}}}$$

Appendix 7C

7C.1 Example Test Procedure

PIM Test Setup and Calibration Procedure:

1. Set up equipment as shown in Figure 7C.1 and photograph the installed DUT.
2. Plug in and warm up spectrum analyzers and signal generators for a minimum of 1 h before starting test.
3. Set signal generators to Tx f_1 = 3.7 GHz, Tx f_2 = 4.2 GHz (or other frequencies in between to produce a ninth-order Rx-band PIM).
4. Set power meter offset equal to measured coupling value of coupler plus WR229 waveguide loss from coupler to DUT to be able to read the absolute power level at DUT.
5. Set spectrum analyzer 1 to Rx = f_3 to 6.2 GHz (or equivalent ninth-order PIM).

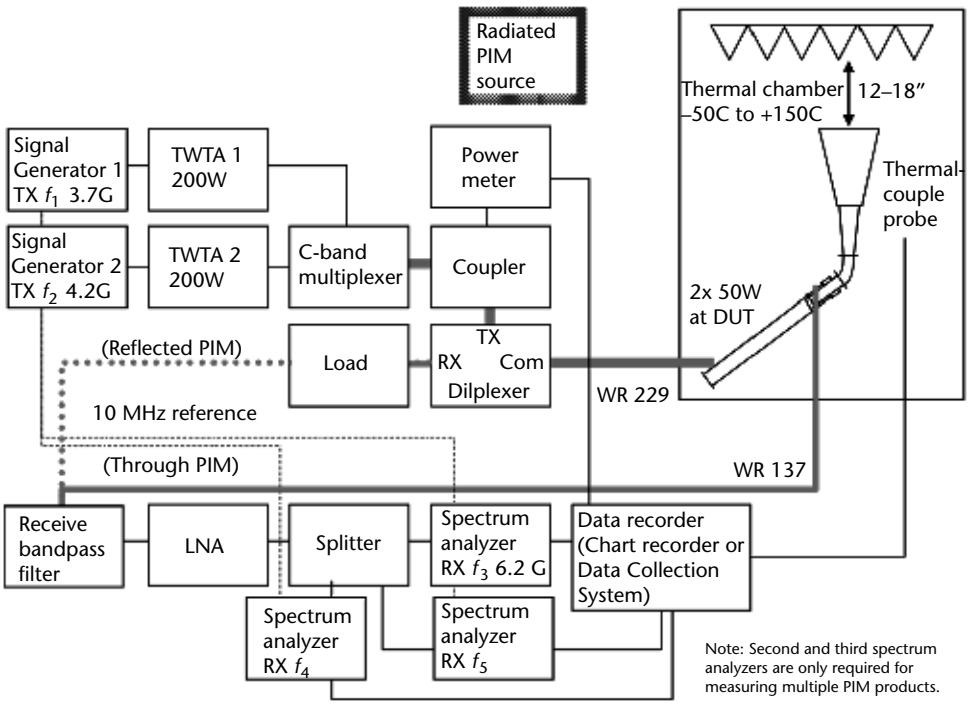

Figure 7C.1 Carrier frequencies may be adjusted between 3.7 and 4.2 GHz provided the ninth-order PIM product falls within 5.925 to 6.425 MHz.

6. Set spectrum analyzer scale to 10 dB/division, reference level to –70 dBm, and attenuation to 0 dB.
7. Inject –70-dBm signal at Rx f_3 PIM frequency into WR137 interface at DUT and set spectrum analyzer reference offset such that spectrum analyzer reads –70 dBm.
8. Center the frequency at 10-Hz IF resolution bandwidth, set frequency span to 0 Hz, then step the injected Rx signal (of step 7) down in 10-dB increments and record the resulting stair-step on the strip chart or data collection system (data recorder).
9. Set data recorder "amplitude and position offset" to read the same scale as the recorded instrument displays and to continuously monitor (or sample a minimum of 1 point/second) the spectrum analyzer output, system power, and the chamber temperature. Set chart speed to 1 mm/min for the test and 10 mm/min when performing PIM source check and frequency centering.
10. Ensure a system receiver noise floor of –150 dBm or lower (average reading).
11. Support the first DUT in the thermal chamber with Kapton-covered foam blocks and place approximately 12 to 18 in. from the absorber panel, verify absorber power handling (expect 2 W/in.^{2}; absorber power handling is 5 W/in.^{2}), and connect as shown.
12. Attach thermal couples to DUT at points 1–2 in Figure 7C.2.
13. Install radiated PIM source in an established repeatable location (ambient only).
14. Power up DUT with 2 × 50W and turn on the data recorder.
15. Set the frequency span to 100 Hz (or wider if necessary) and find the fourth-order PIM with spectrum analyzer.
16. Center the PIM on the spectrum analyzer using an IF bandwidth of 10 Hz and set frequency span to 0 Hz as in Figure 7C.3 then momentarily vary Tx power by 3 dB to ensure that the PIM source is not saturated (for power-sensitive hardware, reduce power by –3 dB). Relocate source if necessary.
17. Remove the PIM source and verify that the residual PIM level is below the "PIM product detection level" of <–145 dBm.
18. If necessary, remove or correct any sources of PIM found in the chamber or test equipment.
19. Conduct a single thermal cycle PIM test with the profile indicated in Table 7C.1 and record the results in Table 7C.2. Do not exceed 9°C/min ramp rate and dwell for 1 h at hot and cold each. Notice the indicated tolerance

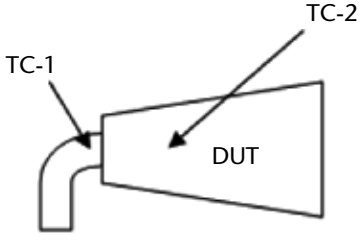

Figure 7C.2 TC location.

on hot and cold dwells in Table 7C.1. Ensure that primary thermocouple 1 (TC-1) remains within the indicated tolerance level and that the remaining TCs do not exceed the allowable extremes +150°C or –50°C. Perform a frequency check of the spectrum analyzer at both dwell points. (Can be done using an external mixer as a PIM source at power monitoring coupler.) Record all of the data on the data recorder as shown in Figure 7C.3.

20. Reinstall the radiated PIM source and record the ninth-order PIM levels at the end of the thermal PIM test and repeat calibration step 8.
21. Repeat steps 11 through 21 with second DUT.

Table 7C.1 Thermal PIM Test Procedure

Test Data							
			Thermal Cycle				
Assembly No.	*PIM Order*	*Initial Ambient*	*21°C*	*+140°C +5/–0*	*–40°C –5/+0*	*21°C*	*Final Ambient*
1	9th						
	9th						
2	9th						
	9th						

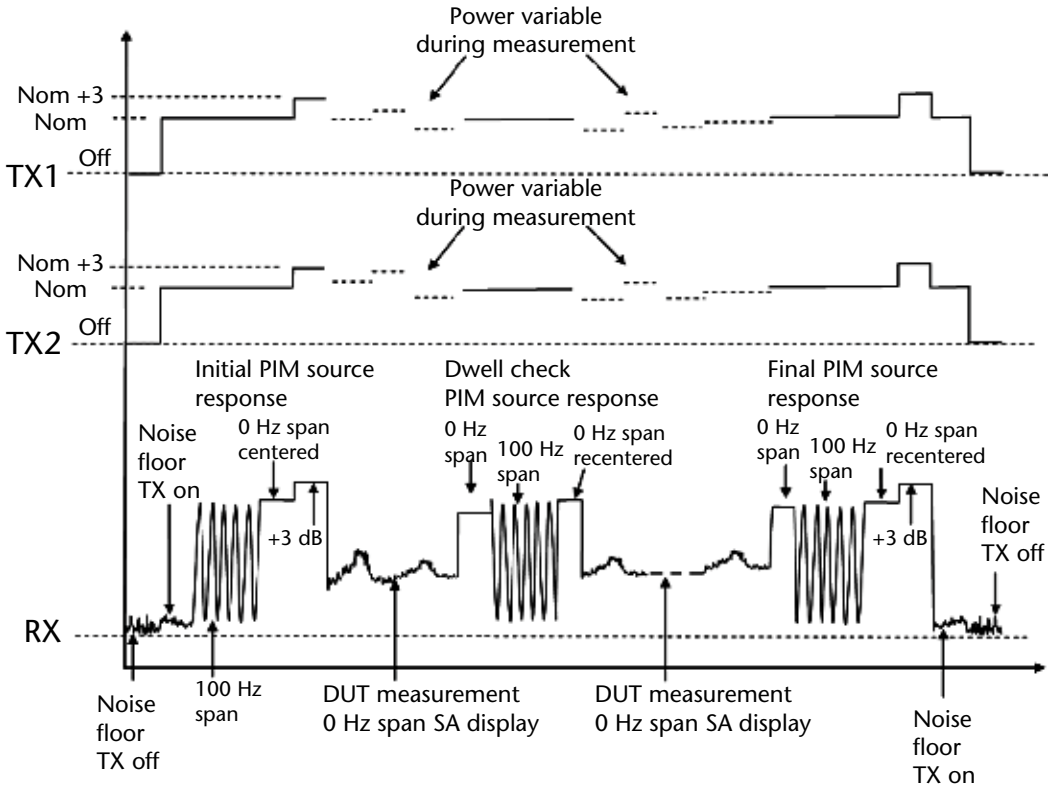

Figure 7C.3 Data recorder example of PIM source frequency centering.

22. Perform the post-thermal PIM functional test and ensure that all data have been taken and are complete.
23. Generate test report.

Equipment List: List Model, Calibration, and ID Number:

Signal generator 1 –
Signal generator 2 –
TWTA –
TWTA –
C-band multiplexer –
Coupler –
Power meter –
Diplexer –
Receive reject filter –
LNA –
Splitter –
Spectrum analyzers –
Chart recorder –

Table 7C.2 is primary maintained at 140 +5/–0 and –40 +0/–5°C.
Do not allow TC-1 through –3 to exceed +150°C or –50°C.
Maintain dew point 10°C below chamber temperature.
The following items must be continuously recorded on the strip chart or within the data acquisition software. The active channel data must update by at least one sample per second.

Strip Chart or Data Acquisition Annotation:

Date and time
Test description (ambient, pre-environmental, thermal post-environmental, spacecraft, etc.)
DUT, description, model, and serial number
PIM test Tx and Rx frequencies
Chart *X* and *Y* parameters (what is being measured)—absolute levels and steps)
Strip chart speed
PIM level of each Rx channel—frequency, absolute levels and steps
Tx power per channel—absolute levels and steps
Temperature of DUT for thermal PIM—absolute levels and steps
Test setup noise floor
Test setup residual PIM floor
PIM source checks

Table 7C.2 Thermal Cycle PIM Test Results

Time	*TC-1 (°C) (Primary)*	*TC-2 (°C)*	*TC-3 (°C)*	*TC-4 (°C) Air*	*PIM (dBm)*

PIM frequency centering

Tx power checks

Calibration pre- and post-test—absolute levels and steps

Any changes in spectrum analyzer or other instrument settings that deviate from the test plan

Any other or unexpected events that take place during the test.

References

[1] S. Silver, *Microwave Antenna Theory and Design*, New York: McGraw-Hill, 1949.

[2] C. A. Balanis, *Antenna Theory: Analysis and Design*," New York: Wiley, 1982.

[3] N. Marcuvitz, *Waveguide Handbook*, IET, 1951.

[4] P. J. B. Clarricoats and A. D. Olver, *Corrugated Horns for Microwave Antennas*," IET, 1984.

[5] R. C. Johnson, *Antenna Engineering Handbook*, 3rd ed., New York: McGraw-Hill , 1992.

[6] Matthaei, E. M. T. Jones, and L. Young, *Microwave Filters, Impedance-Matching Networks, and Coupling Structures*, Dedham, MA: Artech House, 1980.

[7] R. J. Cameron, R. Mansour, and C. M. Kudsia, *Microwave Filters for Communication Systems: Fundamentals, Design and Applications,* New York: Wiley-Interscience, 2007.

[8] A. M. Bøifot, E. Lier, and T. Schaug-Pettersen, "Simple and Broadband Orthomode Transducer," *Proc. IEE*, Vol. 137, No. 6, pp. 396–400, 1990; A. M. Bøifot, "Classification of Ortho-Mode Transducers," *European Trans. on Telecommunications and Related Technologies*, Vol. 2, No. 5, pp. 503–510, 1991.

[9] C. Dragone, "Reflection, Transmission and Mode Conversion in a Corrugated Feed," *Bell Systems Technical Journal*, Vol. 56, pp. 835–867, July 1977.

[10] K. K. Chan and S. K. Rao, "Design of High Efficiency Circular Horn Feeds for Multibeam Reflector Applications," *IEEE AP*, Vol. 56, No. 1, pp. 253–258, 2008.

[11] C. Granet, G. L. James, R. Bolton, and G. Moorey, "A Smooth-Walled Spline-Profile Horn as an Alternative to the Corrugated Horn for Wide Band Millimeter-Wave Applications," *IEEE AP*, Vol. 52, No. 3, pp. 848–854, 2004.

[12] A. D. Woode and J. Petit, "Investigations into Multipactor Breakdown in Satellite Microwave Payloads," *ESA Journal*, Vol. 14, 1990.

[13] P. Ford and A. D. Rawlings, "A Study of Passive Inter-Modulation Interference in Space RF Hardware," ESTEC Contract 111036, Final Report, May 1992.

[14] "Horn Antenna Synthesis CAD Tool," product feature, *MW Journal*, Vol. 52, No. 3, March 2008.

[15] L. J. Durney, *Electroplating Engineering Handbook*, London: Chapman & Hall, 1996.

[16] C. F. Hoeber, D. L. Pollard, and R. R. Nicholas, *Passive Intermodulation Product Generation in High Power Communications Satellites*, American Institute of Aeronautics and Astronautics,1985, pp. 2, 7, 11, 13.

[17] C. Vicente et al., "Experimental Analysis of Passive Intermodulation at Waveguide Flange Bolted Connections," *IEEE Transactions on Microwave Theory and Techniques*, 0018-9480, 2007.

[18] Lui, "Passive Intermodulation Interference in Communication Systems," *Electronics & Communication Engineering Journal,* pp. 109–112, June 1990.

[19] C. D. Bond, C. S. Guenzer, and C. A. Carosella, "Intermodulation Generation by Electron Tunneling Through Aluminum-Oxide Films," *Proceedings of the IEEE*, Vol. 67, No. 12, pp. 1647, December 1979.

[20] J. R. Wilkerson, "Passive Intermodulation Distortion in Radio Frequency Communication Systems," Doctoral dissertation, North Carolina State University, 2010.

[21] W. H. Higa, "Spurious Signals Generated by Electron Tunneling on Large Reflector Antennas," *Proc. IEEE*, Vol. 63, No. 2, p. 311, February 1975.

[22] M. E. Van Valkenburg, *Reference Data for Engineers: Radio, Electronics, Computer, and Communications*, New York: Prentice Hall, 1993, Sections 3-3, 27-15, and 34-2.

[23] A. D. Woode and J. Petit, "Design Data for the Control of Multipactor Discharge in Spacecraft Microwave and RF Systems," *Microwave Journal,* January 1992.

[24] A. J. Hatch and H. B. Williams, "Multipactor Modes of High Frequency Gaseous Breakdown," *Journal of Applied Physics*, 1954.

[25] Hughes Aircraft Co., "The Study of Multipactor Breakdown in Space Electronic Systems," NASA Contract NAS 5-3916, Report P65-49, April 1965.

[26] R. Woo, "Final Report on RF Breakdown in Coax Transmission Lines," NASA Report 32-1500, October 1970.

[27] M. Nakamura, S. Takaya, and K. Minoru, "Characteristics of High-Power Breakdown at 28 GHz," *IEEE Trans. on Microwave and Techniques,* Vol. MTT-26, No. 5, May 1978.

CHAPTER 8

Deployable Reflectors

Samir F. Bassily, Consultant (formerly with Northrop Grumman Aerospace Systems)
Mark W. Thomson, Jet Propulsion Laboratory, California Institute of Technology

8.1 Introduction

All but the smallest reflectors used on today's spacecraft are deployable in some sense. The great majority of those are substantially rigid structures that deploy by hinging about an axis using a motorized or spring-activated mechanism. The size of those reflectors is limited by the size of the booster fairings on which they are carried into space. Larger reflectors that exceed the size of the fairings need to be "folded up" for launch in some way, and "unfurled" to their full size on orbit. It is those foldable and unfurlable reflectors, simply referred to as "deployable" reflectors, which are the subject of this chapter.

After this introduction, the remainder of the chapter deals with three main subjects. Section 8.2 deals with reflector classifications. Sections 8.3 through 8.7 describe the various reflector types and styles, and Section 8.8 covers the most important subsystem design considerations/requirements for deployable reflectors.

Reflector classifications are done from two points of view. The first classification is according to the surface geometry such as parabolic vs. shaped, circular vs. elliptical, and center-fed vs. offset-fed reflectors. The second classification is according to the reflector surface type and includes rigid/segmented, semirigid, inflatable/rigidizable, woven-mesh, and knitted-mesh types. Because the knitted-mesh type reflector is the most common and most flown of all deployable reflectors, its major constituents are further discussed in Sections 8.7.1 through 8.7.4, which cover the mesh itself, the net/soft structure, the deploying structure, and the mesh/soft structure management provisions. Seven different styles of deploying structures used with knitted-mesh reflectors are discussed in Sections 8.7.3.1 through 8.7.3.7.

The subject of subsystem design considerations/requirements for deployable reflectors is discussed in Section 8.8. It includes discussions of electrical, mechanical, thermal, and environmental design drivers. The electrical requirements discussion

covers the various factors that contribute to gain-loss, as well as a brief discussion of other common requirements including side/grating lobe limits, passive intermodulations, and electrostatic discharge. The mechanical requirements discussion covers mass, frequency, and pointing requirements. Finally, a brief discussion of the thermal analysis and design aspects, as well as environmental design drivers such as radiation and solar transparency, is presented.

Reflector categories that, for various reasons, are *not* covered in this chapter are as follows:

1. *Space assembled/erected reflectors:* These were studied extensively in the early shuttle era. They are assembled/erected in low Earth orbit by astronauts from numerous subassemblies carried to orbit aboard one or more shuttle missions to form extremely large reflectors. They were believed to have the potential for producing extremely high surface accuracy for their size. To the author's knowledge, this style of reflector is no longer being pursued.
2. *One-dimensional deployable reflectors:* The ISAT radar reflectarray is one example. It utilizes a parabolic cylinder shaped reflector 300m in length and only a few meters wide; therefore, it only needs to deploy in one dimension. Several designs were being pursued by competing government contractors when the effort was terminated in the mid-2000s.
3. *Shape-memory reflectors:* These utilize phase-change materials that assume different shapes when heated (or cooled) beyond a certain phase-change temperature. Two different categories of these reflectors have been considered. In the first category, those materials are used in conjunction with inflatable reflector technology, which is further discussed in Section 8.5. In the second category, those materials are used to form the reflector surface itself in a manner analogous to the segmented and semirigid surface reflectors discussed in Sections 8.3 and 8.4, respectively, but will not be discussed here any further, since that technology is considered to be still in its early stages of development.

8.2 Reflector Classifications

To keep track of the large variety of reflectors that have been conceived, they may be classified in accordance with two main aspects. Specifically, they may be classified according to their surface geometry or according to their surface type.

8.2.1 Classifications According to Reflector Surface Geometry

Regardless of whether a reflector is fixed or deployable, its ideal surface geometry in its simplest shape is formed by intersecting a parent surface of revolution, usually paraboloidal, with a cylindrical "cookie cutter," the axis of which is parallel to the axis of the surface of revolution. In this classification, the type of the reflector depends on three aspects: the shape of the parent surface, the shape of the "cookie cutter," and the location of the surface axis versus the "cookie cutter" axis, as discussed next.

Shape of the Parent Surface

Parabolic: This type uses a paraboloidal surface of revolution. This shape comprises the vast majority of deployable reflectors (as defined herein) that have been flown.

Mildly shaped: This type may utilize a nonparabolic surface of revolution, or a paraboloidal surface wherein the focal length of the constituting parabola varies gradually as it rotates about its axis of revolution. In all cases, the mildly shaped surface always curves in the same direction: toward the reflector focus.

Arbitrarily shaped: In this type of reflector, the surface, which typically starts with a mildly shaped surface, is further perturbed by the addition of a series of higher order surface functions. The magnitudes of these surface functions are typically optimized through the use of sophisticated numerical techniques aimed at optimizing certain antenna performance parameters via reflector surface shaping. Usually, this results in forming certain "bumps" over the surface of the reflector, which may cause the surface to locally curve in a direction opposite to the general direction of the reflector surface curvature (i.e., have regions of negative curvature).

Shape of the Cylindrical "Cookie Cutter"

Circular: This shape is the most common, and obviously produces a circular reflector (when viewed along the reflector boresight). It typically produces a "pencil beam" with a circular main lobe in the far field when illuminated with a single feed located at or near the focal point. The size of that pencil beam, in degrees, is inversely proportional to the reflector diameter for a given RF wavelength. Alternatively, when illuminated with a number of independent feeds located near the focal point, it can produce what is known as a multibeam antenna.

Elliptical: As expected, using an elliptical cylinder for the "cookie cutter" produces an elliptical reflector. Also as expected, an elliptical reflector produces an elliptical or "fan" beam in its far field. The orientation of the major diameter of that beam, however, corresponds to the direction of the minor diameter of the reflector surface. This becomes obvious when you consider the inverse proportionality relationship between the beam size and the reflector diameter stated above.

Arbitrarily shaped perimeter: While not ideal, the desire to maximize the area of a reflector that can fit within the available booster fairing occasionally leads to the design of somewhat oddly-shaped reflectors. This is more common with fixed (i.e., nondeployable) reflectors. Also, with deployable mesh reflectors, the outer perimeter of the reflector often "recedes" inward between the mesh attachment points along the perimeter, resulting in a shape that more closely approximates a multifaceted polygon.

The use of noncircular and nonelliptical shaped reflectors has two drawbacks. First, since it is difficult to design a simple feed that can efficiently "illuminate" an arbitrarily shaped perimeter reflector, such a reflector will typically suffer from increased spillover losses or a high cost. Second, the corresponding nonuniform illumination of the reflector edges and the increased spillover energy manifest themselves in the form of higher level sidelobes, which are oftentimes detrimental to the system-level performance.

Location of the Surface Axis vs. the "Cookie Cutter" Axis

Center-fed reflector: This type of reflector corresponds to a reflector in which the two axes coincide. As a result, the feed (which must be located on, or near, the axis of the reflector surface) is also located near the center of the "cookie cutter," which defines the outer perimeter of the reflector. Hence, the reflector is "center fed."

Offset-fed reflector: Here, the two axes are parallel but offset relative to each other. In most practical applications, the axis of the reflector surface is located entirely outside of the "cookie cutter."

The obvious advantage of the offset-fed design is that the feed (which is located on, or near, the axis of the reflector surface) does not substantially block the path of the energy reflected off of the surface of the reflector, if at all. For this reason and because offset-fed reflector designs enhance the architectures of the spacecraft, they are prevalent. On the other hand, with a center-fed reflector, the feed—and often its support structure and feed waveguide—blocks and scatters some of the reflected energy, resulting in a loss of efficiency and the generation of sidelobes. Since the center of the reflector is where the energy density is highest, the effect of the center feed blockage and scattering on the reflector efficiency is amplified. Additionally, the energy blocked by the feed (and its support) is scattered away from the main antenna lobe and ends up adding to the energy in some of the sidelobes, which can be detrimental to system performance in certain applications. Nonetheless, there are important reasons for implementing large center-fed apertures for some applications.

8.2.2 Classification According to Reflector Surface Type

From the point of view of the type of surface used to construct a reflector, the various reflectors known to the authors may be classified into the following types:

1. *Rigid surface—one piece:* This is the basic type of surface used on fixed (nondeployable) reflectors. Because this chapter is concerned only with the deployable reflectors, this type is not discussed further.
2 *Rigid surface—segmented:* In this reflector type, the surface is divided into a collection of rigid segments connected with hinges and/or linkages. Pairs of three-segment 5m reflectors of this type were flown on several XM-Radio satellites, and at least one two-segment folding aperture was flown on a European satellite. This type is further discussed in Section 8.3.

3. *Semirigid surface:* This type is also known as the *spring-back antenna*. Two pairs of this type were flown on the Mobilesat spacecrafts, and several sets of three reflectors were flown on the TDRS-II satellites. Spring-back reflectors are further discussed in Section 8.4.
4. *Inflatable/rigidizable surface:* This type comprises a lenticular structure with an RF transparent front surface and a metalized back/reflecting surface. The surfaces may be rigidized in space using various technologies, or kept under constant, but very low, pressure for the life of the reflector mission. An Inflatable Antenna Experiment (IAE) was flown on the space shuttle, which provided a significant learning experience. This technology is further discussed in Section 8.5.
5. *Woven-mesh surface—wrap-rib reflector:* A woven-mesh surface has near-zero shear stiffness and is therefore suitable for use on the wrap-rib reflector built by Lockheed Martin. A 9.5m version was flown on the ATS-6 satellite in 1974. More discussion is given in Section 8.6.
6. *Knitted-mesh surface:* A knitted mesh has the advantage of providing extremely low extensional stiffness, excellent RF properties, and very low weight. It is suitable for use at frequencies no higher than about 50 GHz to avoid substantial reflection losses. Over half a dozen different styles of deployable reflectors utilizing this type of reflecting surface have been built and most of them successfully flown. They total well over 40 units on-orbit at the time of writing this chapter and thus represent the majority of the deployable reflectors that have been placed on orbit. Therefore, much of the discussion in the remainder of this chapter pertains to this type of reflector and its various styles.

8.3 Segmented Reflectors

As the name implies, in this type of reflector, the surface is divided into a number of substantially rigid segments. These segments are interconnected with hinges and/or linkages of various designs. The objective is to permit the stowage of one or more reflectors, each having a diameter larger than that of the launch vehicle fairing, to be carried to orbit within the available volume inside that fairing. Typically, the larger the number of segments into which a reflector is divided, the smaller the volume in which it can be stowed; or conversely, the larger the diameter of the reflector that can be stowed within a given volume. This can be described as having higher stowage efficiency. On the other hand, the larger the number of segments utilized, the larger the number of interconnecting hinges/linkages needed, which results in increased complexity, cost, mass, and RF loss. The increased RF loss is due to the increased length of the intersegment boundary seams and the increased cumulative misalignment error through the increased number of interconnecting features. It is because of this increase in complexity and RF loss that some authors estimated that this type of reflector is practically limited to 10m in diameter [1].

The use of this type of reflector is motivated by two main advantages:

1. The increased surface accuracy (at least within each individual segment) makes it suitable for use at higher frequencies (such as 40 GHz or higher).

2. It is suitable for producing arbitrarily shaped surface reflectors, wherein regions of reversed curvature may exist.

The oldest of these reflectors is the Sunflower, which was developed by TRW in the early 1980s, when they built a 4.9m engineering model [2, 3]. The reflector may employ one or two rings of segments as shown in Figures 8.1 and 8.2 [3]. Two other designs, known as DAISY and MEA, were developed by the European Space Agency (ESA) and Dornier, for which they built engineering models.

A fourth model named the Solid Surface Deployable Antenna (SSDA) was developed by DSL, of which they built a 1.5m demonstration model (Figure 8.3) [3]. Unfortunately, all of these models provide relatively poor stowage efficiency and use large numbers of segments (approximately 20 to 50 segments).

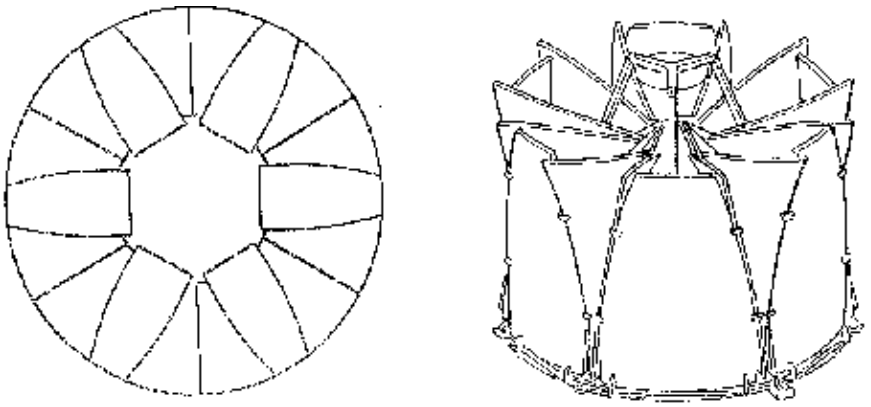

Figure 8.1 The Sunflower reflector: (a) deployed and (b) stowed. (© 1996 IEEE. From [3].)

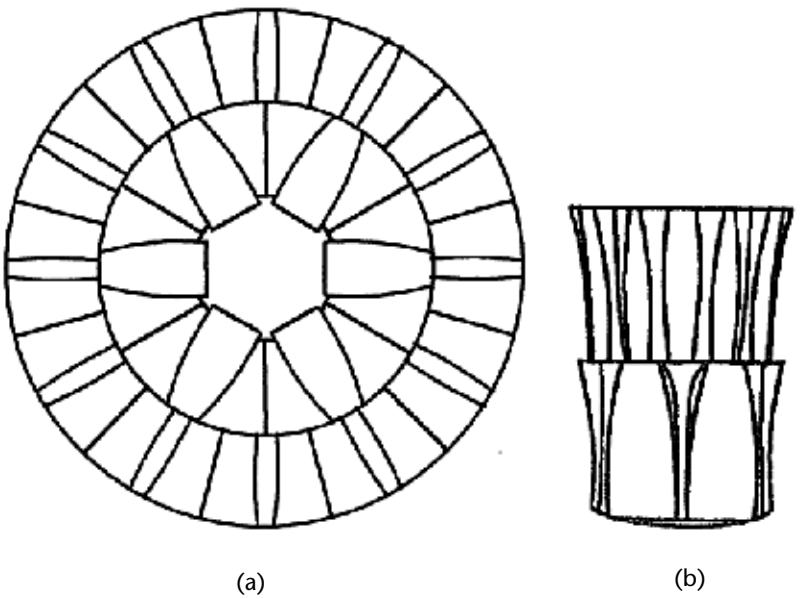

Figure 8.2 Two-tier Sunflower reflector: (a) deployed and (b) stowed. (© 1996 IEEE. From [3].)

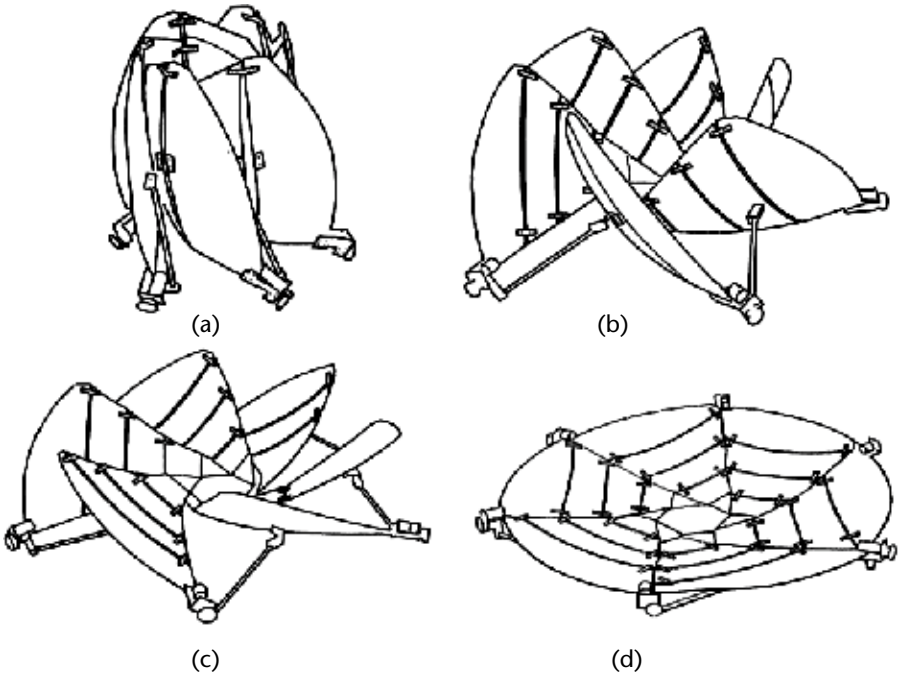

Figure 8.3 Solid Surface Deployable Antenna (SSDA) deployment sequence. (© 1996 IEEE. From [3].)

In the late 1990s, a new concept was patented by Hughes (now Boeing), in which linkages, rather than simple hinges, were used to connect adjacent segments, allowing them to stow back-to-front, instead of front-to-front, thus substantially matching each other's curvature and stow more compactly (Figure 8.4) [4]. Several concepts having from 2 to 10 segments were presented and shown to stow compactly. The company produced a number of 3-segment 5m reflectors.

A pair of those reflectors were stowed on the sides of their standard HS702 spacecraft and flown in the early 2000s in a standard 3.7m-diameter booster fairing. Those reflectors were used on the XM-Radio satellites, and are arbitrarily shaped, which made them more difficult to nest together than their paraboloidal counterparts. The fact that those reflectors were arbitrarily shaped was the reason why segmented, rather than the more common mesh, reflectors were used, since at that time, arbitrarily shaped mesh reflectors had not yet been developed. To date, those XM-Radio reflectors remain the only shaped segmented reflectors that have ever been flown.

8.4 Semirigid Surface Reflectors: Spring-Back Antennas

The spring-back antenna (SBA) concept was developed by Hughes (now Boeing) in the mid-1990s, and flown for the first time on Mobilesat-1 in 1996. Figure 8.5 [5] shows that spacecraft with two SBAs on it, one stowed and the other deployed. This novel reflector design is made of a thin graphite shell reinforced with flat strips and an outer hoop integrated into a single bonded, semiflexible assembly. That shell is elastically folded (like a taco) to form about a 300-deg arc. It is kept in this gently

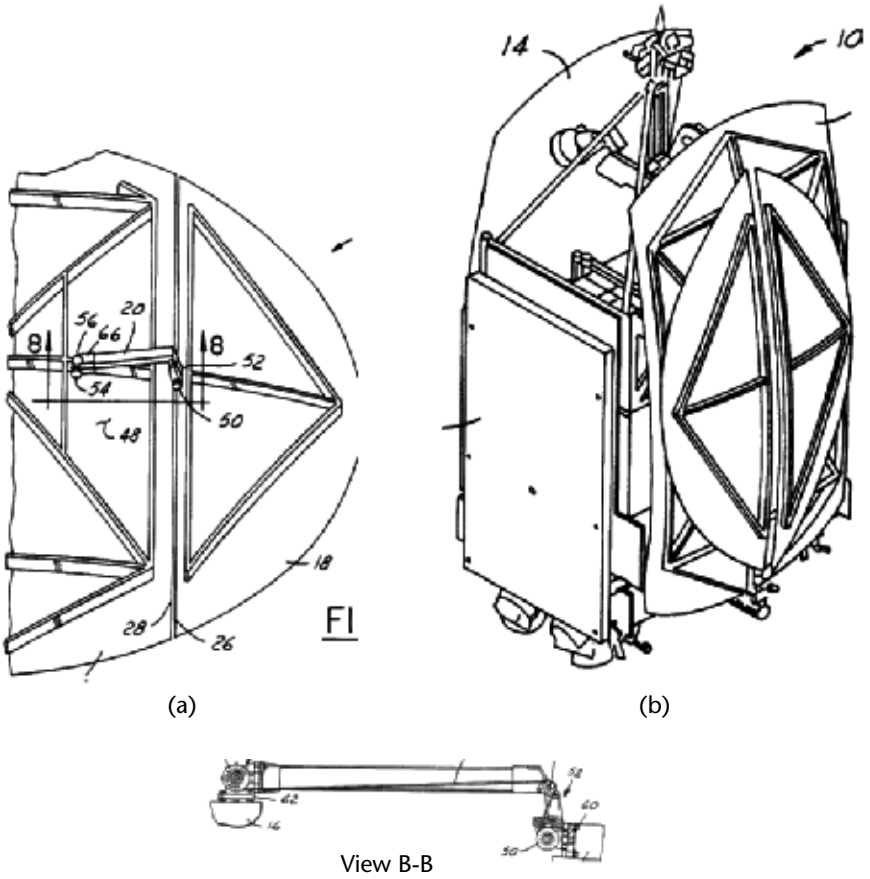

Figure 8.4 Hughes segmented reflector: (a) deployed and (b) stowed.

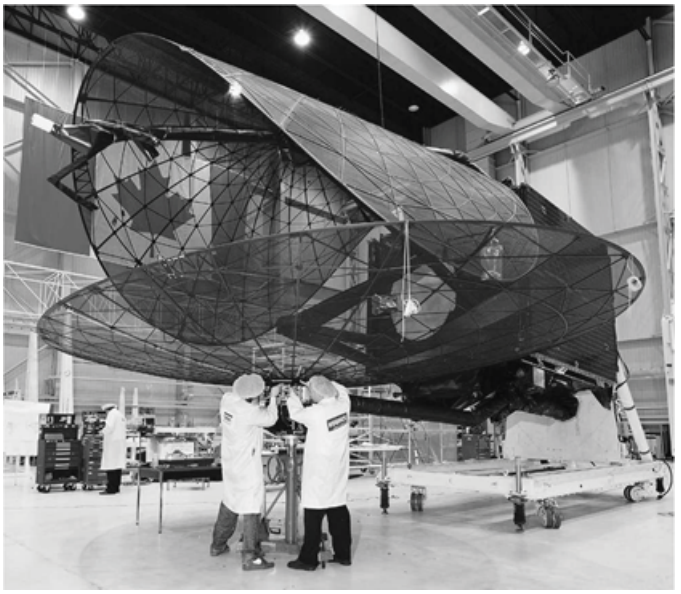

Figure 8.5 Hughes spring-back antenna: spacecraft with one reflector deployed and one partially stowed. (© 2002 IEEE. From [5].)

stowed configuration by tie cables connected to the outer hoop and to a damped release mechanism designed to absorb some of the deployment energy. A pair of such reflectors, each 5.25m × 6.8m in diameter, is nested together in their stowed configuration to form a nearly 5.3m-high, truncated cone. The reflectors are tied to each other and to external supports at several locations using launch locks in order to provide adequate strength and stiffness during launch.

Although the stowage efficiency for SBAs is low, the fact that the stowed reflector is substantially hollow, makes it possible, and even advantageous, to stow two (or three) reflectors nested together in the same space—significantly increasing that efficiency. Additionally, the fact that the SBA design is extremely simple drastically cuts down its development cycle in comparison with any other deployable reflector. In fact, this enabled the incorporation of the SBAs on the Mobilesat spacecraft in an extremely short 9-month period from conception to launch.

A more recent application for SBAs has been on the NASA TDRS second- and third-generation spacecraft, where 4.6m-diameter SBAs are used in frequencies as high as the Ku-band.

8.5 Inflatable/Rigidizable Reflectors

Much like a Mylar birthday balloon, an inflatable reflector is constructed out of two plastic membranes circumferentially seamed together to form a lenticular structure. The front membrane is kept as an RF transparent sheet, while the back one is metalized to form an RF reflective surface. In addition to completing the balloon, the front surface serves as a canopy, which helps athermalize the reflecting surface.

The reflector takes its shape on orbit by being inflated by a very low-pressure inert gas (on the order of 2 to 3 Pa). The pressure is kept particularly low for two reasons: first, to minimize the membrane stress (which is proportional to the pressure times the reflector radius, divided by the membrane thickness), and second, to minimize the mass of the gas needed to inflate the reflector and to maintain the pressure for the duration of the mission. The problem of determining the mass of the maintenance gas needed is nontrivial. At the beginning of life, the leakage rate depends primarily on the permeability of the membrane material (including any material defects). As time goes on, however, one has to account for the probability that some holes/tears may develop due to micrometeoroids or space debris. The size and number of such holes can only be determined statistically, and will obviously increase with the length of the mission life.

The first inflatable reflectors were developed in the United States by L'Garde, under Jet Propulsion Laboratory (JPL) leadership and funding. With the very low stiffness and pressures involved, ground testing had limitations and did not sufficiently reduce the development risk for the technology. JPL/NASA therefore initiated the Inflatable Antenna Experiment (IAE), together with L'Garde. The experiment involved a 14m reflector made out of 0.25-mil-thick Mylar membranes (Figure 8.6) [6]. The reflector was reinforced with an outer toroidal ring and supported by three long struts, all of which were made of 12-mil-thick Kevlar composite and pressurized to much higher pressures. The entire structure, together with the inflating equipment and pressurant, was packaged in a rectangular box about 1 m^3 in volume. The experiment was flown on the space shuttle and deployed in orbit,

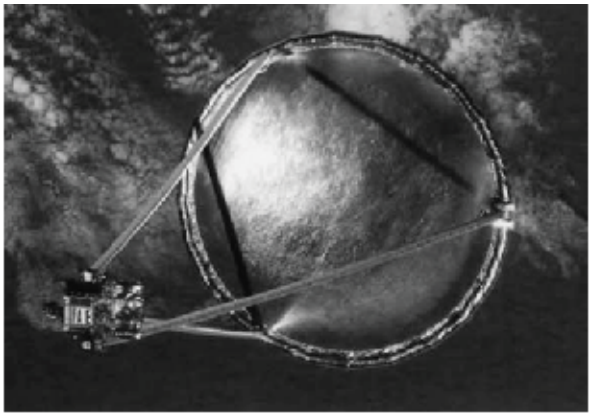

(a)

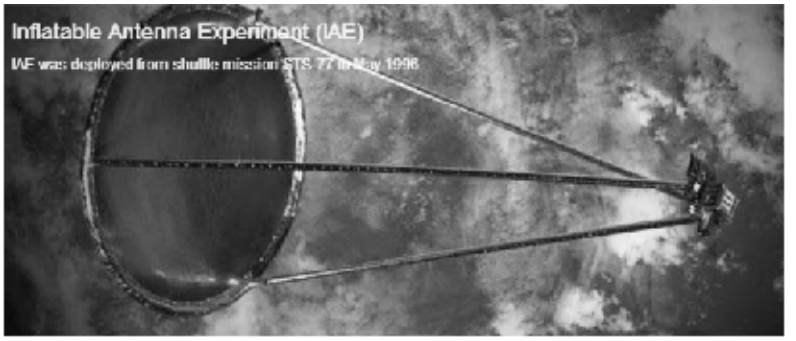

(b)

Figure 8.6 Inflatable Antenna Experiment (L'Garde) (courtesy of NASA/JPL-Caltech). (© 2008 IEEE. From [6].)

in 1996. Although the results of the experiment may not have been flawless, the experiment provided invaluable lessons learned, and remains the first and only on-orbit demonstration of the potential capabilities of inflatable precision structures.

Near the turn of the century, JPL was developing the Advanced Radio Interferometry between Space and Earth (ARISE) mission, which involved a 25m precision deployable reflector. An inflatable reflector, as one of the two options funded by JPL, was being developed by L'Garde. Although significant progress was made by both organizations, the ARISE mission is, unfortunately, no longer being pursued (most likely due to NASA funding cuts).

A rigidizable reflector structure is a subclass of the inflatable technology. It overcomes the issue of replenishing the pressurant, especially for longer missions, by using a material that turns rigid after being inflated on orbit. This is particularly advantageous for the secondary reflector structures, such as the support struts and the toroidal reinforcing ring, which require higher pressures to maintain their rigidity. Several technologies have been considered/pursued for achieving on-orbit rigidization [7] including the following:

- *Fiber-reinforced space-curable epoxy composite materials:* These materials cure in about 6 h at 110°C, which is easily achievable in direct sunlight on orbit.

- *Fiber-reinforced subglass transition temperature (sub-Tg) elastomeric materials:* Some of these are also known as "shape memory" composites. These materials become rigid at very low (sub-Tg) on-orbit temperatures, but are soft at warmer temperatures above their Tg.
- *Fiber-reinforced ultraviolet (UV) curable resins:* These materials slowly cure on orbit as they are exposed to the sun's UV rays.
- *Polymers laminated with annealed aluminum foil:* These materials can be folded during stowage/launch, and then inflated on orbit to stresses beyond the yield stress of the aluminum foil. When the pressure is removed, the prestretched foil retains much of the laminated material's shape and rigidity.

In addition to the JPL/L'Garde work on the IAE and ARISE inflatable reflectors, ESA and Contraves (a European company) have developed the Inflatable Space Rigidizable Structure (ISRS) reflector for a joint ESA/NASA program (Figure 8.7) [6]. The reflector membranes were made of Kevlar impregnated with space-curable epoxy of the type described earlier. Although the Mylar membranes used in the L'Garde reflectors are much lighter and thinner than those used on ISRS, the effect on the overall mass of the reflectors is small since the mass of the Mylar membranes represents only about 10% of the overall system mass. In return, the thicker Kevlar membranes provide much higher structural stiffness and strength, and free the reflector from the limited life constraint/risk due to the limited amount of make-up pressurant available, providing instead a nearly infinite reflector life. Kevlar also has a lower coefficient of thermal expansion (CTE) than Mylar, thus resulting in potentially lower on-orbit thermal distortion errors.

In summary, the main potential advantages of the inflatable/rigidizable technology are simplicity, high deployment reliability, high stowage efficiency, low areal mass, and low reflection loss at high frequencies. The disadvantages are the difficulty of deployment testing and obtaining high shape accuracy on the ground due to limited adjustability and limitations on accurate 1G simulation.

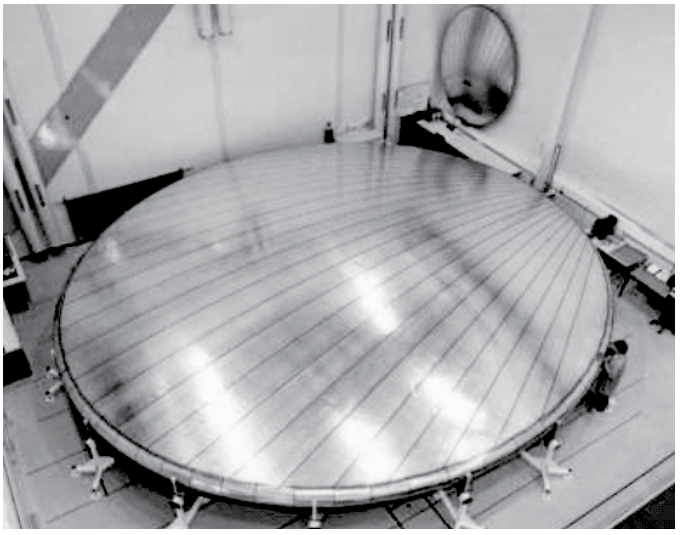

Figure 8.7 Inflatable Space Rigidizable Structure (ISRS) reflector (Contraves) (courtesy of NASA/JPL-Caltech). (© 2006 IEEE. From [6].)

8.6 Woven-Mesh Surface: The Wrap-Rib Reflector

The wrap-rib reflector was developed by Lockheed in the 1970s under a JPL contract. It consists of a central hub to which a number of radial ribs (typically one to four dozen) are attached via nearly vertical hinges. The ribs, which are shaped along the parabolic reflector surface, have either a slightly curved cross section (similar to a large carpenter tape) or a lenticular cross section (representing two face-to-face carpenter tapes). They are fabricated out of either metallic (aluminum or titanium) or composite GFRP materials. In addition to providing a place for supporting the reflector rib attachment hinge, the hub's upper and lower surfaces are extended radially outward in order to provide a toroidal-shaped compartment, which starts slightly inboard of the rib hinge locations and extends a sufficient distance outboard of those hinges to provide enough room to stow the ribs (and the mesh) as they are "wrapped" around the hub (hence the name "wrap-rib"). Figure 8.8 is a sketch of the hub design (after [8]).

To wrap the ribs, they are first rotated approximately 90 deg about their hinges until they become substantially tangential to the hub. The cross section of each rib is then flattened periodically along its length in order to permit it to wrap around the hub in a spiral fashion (like a clock spring). The reflective mesh attaches to the top edges of the ribs, and is fanfolded between the ribs and stowed with them as they are wrapped around the hub. To retain the stowed ribs and mesh in place, the outer edge of the extended lower surface of the hub is fitted with a set of spring-loaded doors, which run circumferentially around the hub. These doors are closed upward to a vertical position, and kept in place with a cable, which wraps around the hub like a bellyband. The cable is then pyrotechnically released to effect

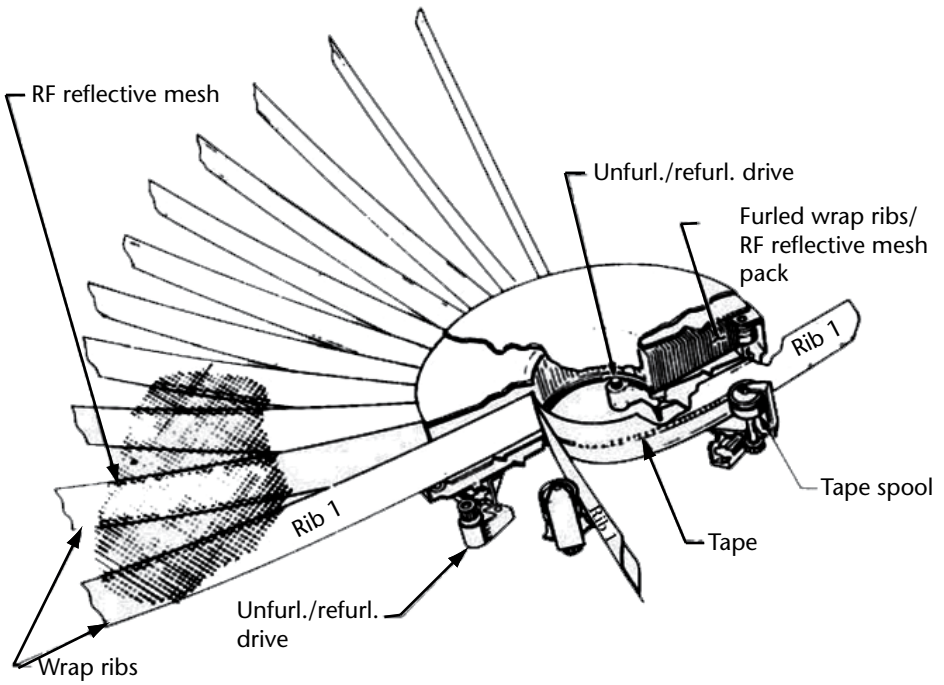

Figure 8.8 Wrap-rib reflector hub (Lockheed Martin). (© 2008 IEEE. From [9].)

deployment. The rotation of the hub during deployment may or may not be mechanically damped; if not, the deployment may be quite energetic due to the release of stored energy.

The reflective mesh of the wrap-rib reflector is usually made out of trapezoidal-shaped gores, which are seamed together proximate the ribs. Each gore forms a facet, whose shape approximates a parabola of revolution but is in fact closer to a segment of a parabolic cylinder. The curved facets are bounded by two parabolic ribs, an outer catenary member, and a part of the circumference of the central hub. Since the ribs rotate about 90 deg as they are stowed, the inner edges of the mesh gores have to undergo extremely high shear strains in the process. A mesh made of an open plain weave is therefore necessary in order to be able to withstand such large strains without excessive shear stresses. Such a woven mesh also possesses a very low Poisson's ratio, which is important to minimize "pillowing" distortion. Pillowing is a type of distortion in which the surface moves toward the center-of-curvature as it is tensioned in the radial direction.

A 9.5m wrap-rib reflector was built by Lockheed for the Application Technology Satellite in the 1960s (Figure 8.9) [6, 9]. The reflector had 48 aluminum ribs. Lockheed also built a sector of a 55m-diameter reflector having GFRP ribs with lenticular cross sections [6]. This type of closed cross section provides for a significant increase in both the torsional and lateral weak-plane stiffness of the ribs, and thus greatly improves their torsional-buckling capability.

The wrap-rib reflector is particularly suited for a center-fed antenna. In such a case, the large number of contoured ribs typically needed become identical in shape. Also, the on-orbit mechanical and thermal loads become primarily axial and radial (due to symmetry), which the ribs are best suited to handle. Finally, this symmetry permits the reflector to be designed with a free-wheeling hub, which

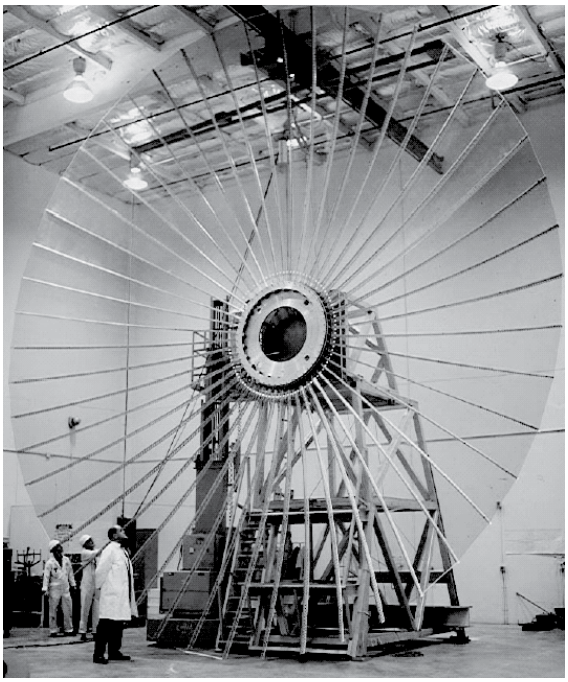

Figure 8.9 9.5m wrap-rib reflector (Courtesy of NASA/JPL-Caltech). (© 2008 IEEE. From [6].)

greatly reduces the loads at the end of deployment. On the other hand, an offset-fed antenna reflector loses all of the above advantages, becoming difficult and costly to successfully design and build.

8.7 Knitted-Mesh Surface Reflectors

Knitted-mesh surface reflectors are the most popular and prevalent among deployable reflectors that have flown in space. There are at least half a dozen different styles of reflectors, some with different substyles, that fall in this category. Most of them have been successfully used on orbit. The mesh itself is particularly suited for large deployable reflectors due to its extremely high flexibility, low mass, and excellent RF performance.

Certain basic components/systems make up a reflector of this type: the mesh, the shaping net/soft structure, the deploying structure, and the mesh/net management system. In the following subsections, each of these components/systems is discussed, as well as some of their variations as they pertain to the most common styles that have been developed.

8.7.1 The Knitted Mesh

This mesh is typically produced using a two-bar tricot machine, which was perfected for textile manufacture during the 19th century. Its density is measured by the number of openings per inch (OPI), with the typical range being 5 to 30 OPI, and the most common being 10 OPI (Figure 8.10). Practically all of the knitted reflector meshes that have been flown use gold-plated molybdenum wires with a diameter of about 1 mil. Molybdenum has an extremely high modulus of elasticity and strength that, with the resulting bending stiffness of the wire loops, provides the knitted structure with a high strain capability and relatively stable orbital tension levels. The importance of this fact to the success of these reflectors cannot be overstated. The CTE of molybdenum is fairly low, but there is a common misconception that an even lower CTE is important to control deformations and/or loads in view of the extreme on-orbit thermal behavior of the mesh, where the gold may cause temperatures to range from –180° to 300°C. However, because the mesh is a soft spring that is strained possibly up to 10% in its deployed configuration, the addition of another 0.25% of strain at the temperature extremes does little to affect the mesh tension—it simply sits there. Also, its thermal mass is too low for the mesh temperature extremes to adversely affect any adjacent structure.

The gold plating provides the benefits of excellent corrosion resistance, low contact resistance, and high electrical conductivity. Gold also facilitates the knitting process. Without gold plating, the lubricity of the wire would be too low to knit because the molybdenum base metal is highly abrasive. This mesh has several characteristics that make it particularly suited for use on deployable reflectors:

1. It has extremely low extensional stiffness as knitted and a high strain capability. As a result, it can be sufficiently prestretched so that it does not go slack on orbit without overtaxing the deployment structure that has to

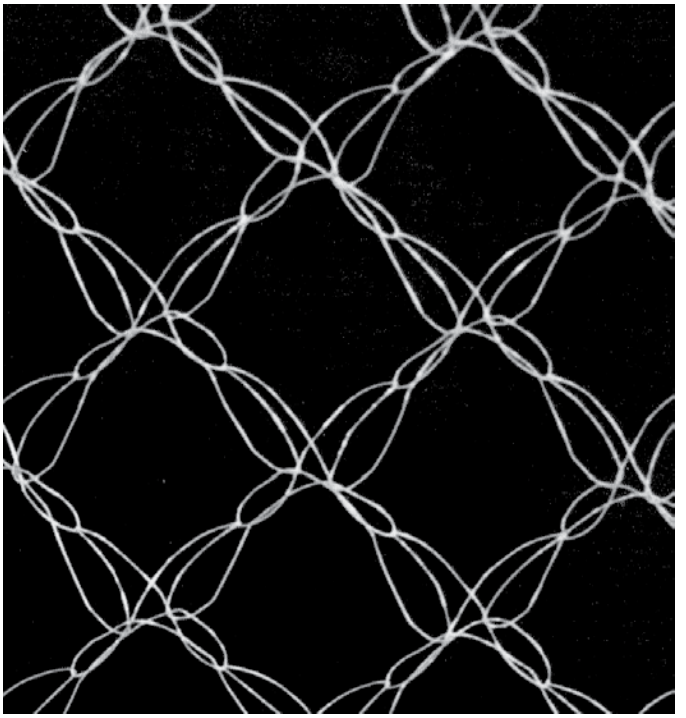

Figure 8.10 Knitted gold-molybdenum mesh close-up [9].

react to those preloads. Also, it does not kink or permanently wrinkle after being stowed for a long period of time.

2. It has excellent RF properties. Specifically, it has low reflectivity loss (up to 50 GHz, provided a sufficiently dense knit pattern is used) [10] and a high passive intermodulation (PIM) threshold (provided it is kept clean of conductive debris).
3. It has very low areal mass, 0.025 kg/m^2 is typical, which makes it suitable for large reflectors.

Because of the small diameter of the wire, as well as the excellent electrical conductivity and softness of the gold plating, the mesh exhibits very low wire-to-wire contact resistance, even after losing much of its preload at the high on-orbit temperature environment. This is essential for maintaining good RF performance.

Another knitted mesh was developed by Hughes in the mid-1990s, and was knitted out of a specially formulated "Aracon" thread, which is a DuPont material made up of nickel-plated Kevlar yarn. This net has excellent PIM characteristics and a low CTE, at the expense of somewhat higher mass and reflectivity loss. This makes it particularly suited for severe PIM environments, especially if excellent cleanliness cannot be guaranteed. Unfortunately the low bending stiffness of the Aracon fibers resulted in a mesh with nonlinear stiffness characteristics and a narrow band of deflection between the slack and fully taut states. This makes it more difficult to produce a consistently tensioned mesh in the deployed reflector.

One of the characteristics of the knitted mesh is that it has extremely low uniaxial stiffness, but a high Poisson's ratio (ν), which has a geometric average in the x

and y directions of near unity. As a result, the mesh biaxial stiffness, which has the quantity $(1 - \nu_x \cdot \nu_y)$ in its denominator, is more than an order of magnitude higher than its uniaxial stiffness. This is important for the tensioning process during reflector fabrication since it becomes very easy to biaxially overtension the mesh, and because the thermal expansion of the mesh typically results in biaxial loading.

8.7.2 The Shaping Net/Soft Structure

Because of the very low stiffness and high Poisson's ratio of the mesh, attempting to force it into a paraboloidal shape by controlling it only at a reasonably small number of points, say a few hundred, will result in a high pillowing error. *Pillowing* refers to the tendency of the mesh surface to move toward the reflector focus (or more precisely its center of curvature) in an attempt to relieve its pre-strain. An effective way to minimize mesh pillowing is to subdivide it into a collection of nearly flat "facets" that approximate the reflector's paraboloidal surface shape. The surface of the mesh within a facet stays flat if its edges are kept substantially flat and coplanar.

The above can be achieved by introducing a "net" made of cords (or straps), the openings of which will define the edges of the facet, and its vertices will be controlled to fall on the theoretical paraboloidal surface. This can be accomplished by tying those vertices directly to a hard structure, by pulling them toward that hard structure, or by pulling them toward another "net" or a set of cords located behind the net controlling the mesh. This "pulling" is achieved by a set of cords usually running substantially perpendicular to the reflector surface, which are often referred to as "drop ties" and may be adjustable and/or spring loaded. In some reflector styles, especially the older ones, additional drop ties are incorporated between the net vertices. Doing so, however, results in nonflat facets and may be less effective in controlling the mesh pillowing. In order for the mesh surface to be controlled by the net, it is either placed behind it (i.e., on its anti-focus side), where its pillowing tendency makes it naturally push against the net, or it is sewn to the net continuously or at very close intervals.

Typically, the front net divides the reflector surface into either triangular or quadrilateral facets depending on the style of the reflector. The quadrilateral facets are typically trapezoidal, or square/rectangular in shape [Figures 8.11(a) and (b)] [6, 11]. Triangular nets provide the reflector with in-plane shear stiffness, which is something that the AstroMesh Perimeter Truss reflectors greatly benefit from [Figure 8.11(c)] [12]. Actually, the AstroMesh reflector uses fairly stiff Kevlar or GFRP straps to form a net that operates on an "inextensible tensioned membrane" theory where soft tension ties preload the pseudo-geodesic net structure in the normal direction.

Quadrilateral nets, on the other hand, are used for the great majority of reflectors. Umbrella-style reflectors, which are the oldest and most manufactured/flown style, typically use trapezoidal nets, which are particularly compatible with the use of "gored" meshes. They are made up of elongated nearly triangular (or trapezoidal) segments referred to as gores, which correspond to the space between two contiguous reflector ribs. The net divides each gore into trapezoidal facets that increase in width as they get further away from the center. In the TRW and Harris umbrella-style reflectors, the facets incorporate additional intermediate drop ties in between the vertices on the wider sides, which extend in the circumferential

directions [review Figure 8.11(b)]. Because the facet vertices are located directly above the ribs, they may, in many situations, tie directly to the ribs through short, adjustable links. The intermediate drop ties, however, often need to react their loads against another set of cords located behind the main net, forming what may be either an "aft" net or a set of circumferential polygons configured much like spider webs. The collection of cords forming the main net, the drop ties, and the aft nets or circumferential cords, are often referred to as the "soft structure."

Some of the more recently developed reflectors, however, use square (or rectangular) net arrangements. These provide more uniform distribution of vertices over the surface of the reflector and are easier to fabricate and pretension. This is because they can be fabricated out of fewer, long pieces of cord, which extend from one edge of the reflector to its opposite edge, each of which can be preconditioned and pretensioned as a whole. On the other hand, the trapezoidal, spider web–type

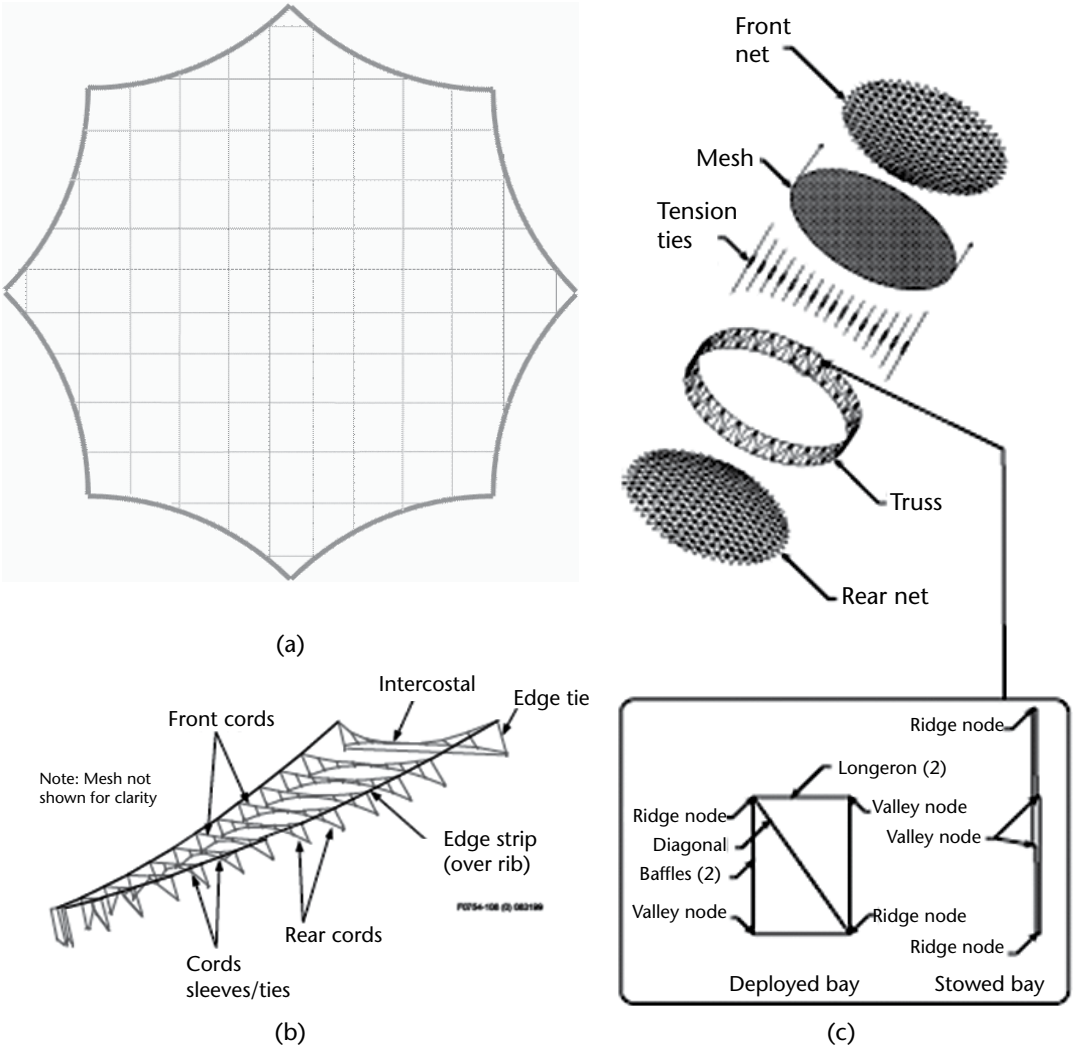

Figure 8.11 (a) Square net, (b) trapezoidal net with intermediate control points (Harris Corporation) (courtesy of NASA/JPL-Caltech) (© 2008 IEEE. From [6]), and (c) AstroMesh concept with triangular nets [12].

nets require many more cord segments, especially in the circumferential direction, which need to be fabricated, preconditioned, and pretensioned independently.

A phenomenon associated with the uniform square reflector facets, as well as the triangular facets (such as those used on the AstroMesh reflector), is that they produce significant "grating lobes." These are large, pencil-shaped, sidelobes that form at certain locations surrounding the main reflector's RF lobe, and have long been recognized for phased arrays with uniformly spaced radiating elements. The phenomenon has been described by Thomson [13] for the AstroMesh triangular net, and in the specifications of a Boeing patent [14] for the square net. Because this can be detrimental to some system designs, that same patent describes solutions that can easily be implemented in the net design. For example, Figure 8.12 shows that using nonuniform rectangular net openings can significantly reduce the levels of the grating lobes. Those net openings would be made smaller near the reflector center, and grow gradually toward the edges. This also provides additional performance advantages for two reasons:

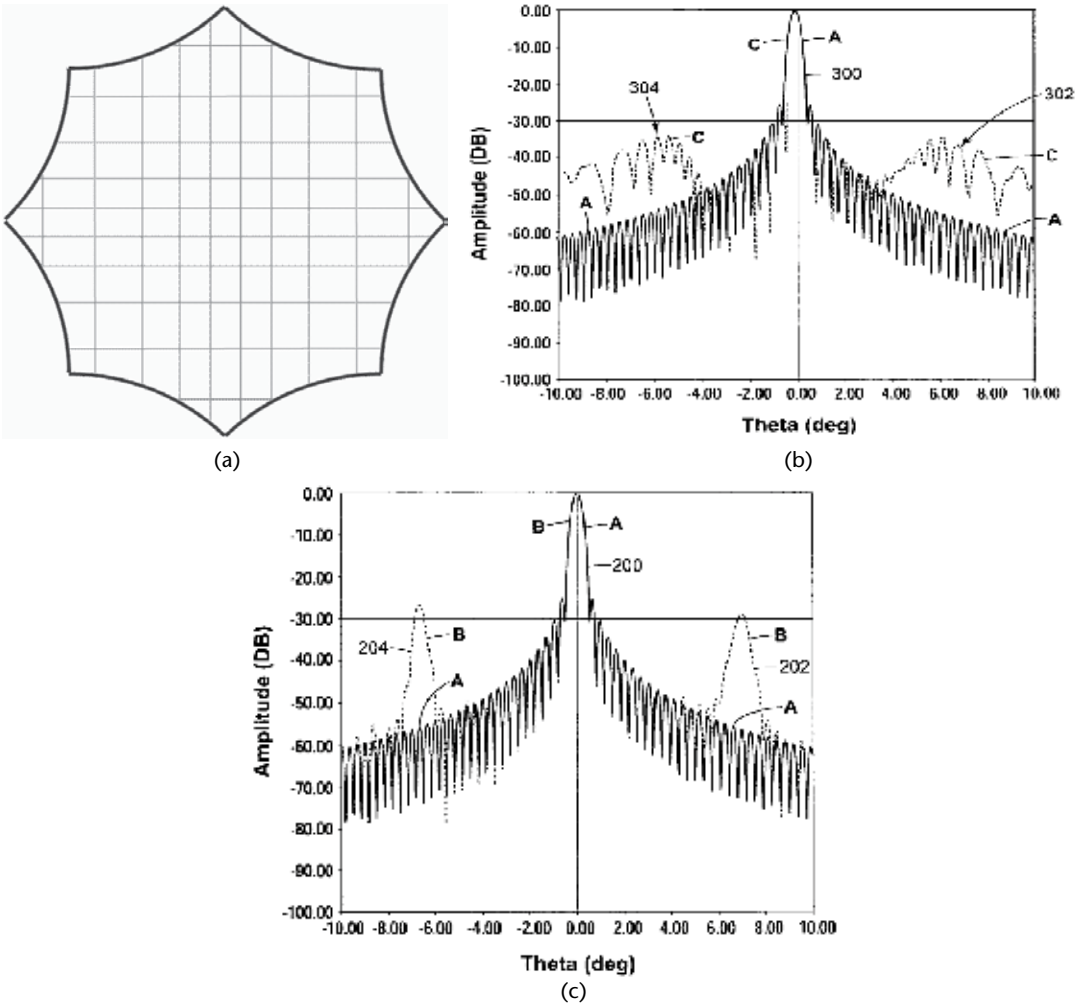

Figure 8.12 Variable-sized net openings reduce grating lobe levels [14]: (a) ideal surface, (b) uniform facets, and (c) variable facets.

1. The feed illumination is highest at the center of the reflector; therefore, smaller facets, with associated smaller deviations from the theoretical surface, are more important near the reflector center.
2. The curvature of a paraboloidal reflector surface is highest at its center; thus, smaller facets are needed to reduce surface deviations near the center than those needed near the outer edges of the reflector.

Due to the curvature of the reflector surface, there are finite angles between the adjacent mesh facets. As a result, the preload in the mesh translates into loading along the net cords in a direction normal to the surface, causing them to tend to pillow. To minimize the "net" pillowing (which translates into corresponding mesh pillowing), the net cords are usually preloaded to significantly higher loads than the mesh itself. Because the stiffness of the net cords is often in the same order as (or even higher in certain directions than) that of the deploying structure itself, a significant reduction in the net load can affect the accuracy of the final reflector surface shape. This can occur due to repeated deployments on the ground, or to thermal cycling and long-term creep on orbit. Therefore, some deployable reflector designs introduce sources of flexibility, often in the form of nonmetallic spring elements, at some interfaces between the front/back nets or cords and the deploying structure.

Because the shape of the net has a direct impact on the accuracy of the reflector surface, careful consideration must be given to its configuration and the materials used in making it. As will be discussed in more detail in Section 8.8, the size of the net openings controls the "faceting loss," whereas the accuracy by which the net vertices is located controls the "random surface loss." Therefore, while increasing the number of facets can reduce the faceting loss, because the mesh can be made to more closely "hug" the theoretical surface, it unfortunately increases the random surface loss. This is due to the corresponding significant increase in the number of vertices, which makes it harder to place all of them at their precise theoretical locations within a reasonable number of surface adjustment iteration cycles and within a reasonable time span (not to mention the increased time and cost to fabricate and assemble the components of the soft structure as a whole).

For on-orbit thermal, moisture and creep stability, graphite and quartz cords are the materials of choice for fabricating the soft structure. Although graphite is often preferred due to its higher stiffness, it poses significant risk for PIM-critical applications since the main (forward) net makes casual (i.e., low-pressure) contact with the mesh, thus promoting PIM. For those applications, quartz must be used. Additionally, because quartz fibers are much finer than graphite, braided quartz cords are very durable and can be more easily terminated by the use of special knots—and hence are preferred by some reflector designers.

Positional and preload adjustments of the various components of the soft structure have traditionally been accomplished via the use of threaded hardware. However, two Boeing/Hughes patents [15, 16] describe methods for terminating and adjusting the length of cords by using a "continually adjustable non-return knot." Several examples have been described for using this special knot for tying a cord to a structure, or for tying two cords together through a small bead. Continuous and smooth adjustment of the cord's length can be achieved by pulling its loose end through the knot, while temporarily relieving its tension [Figures 8.13(a) and (b)] [15, 16]. In some applications, a release loop is added to the knot to facilitate

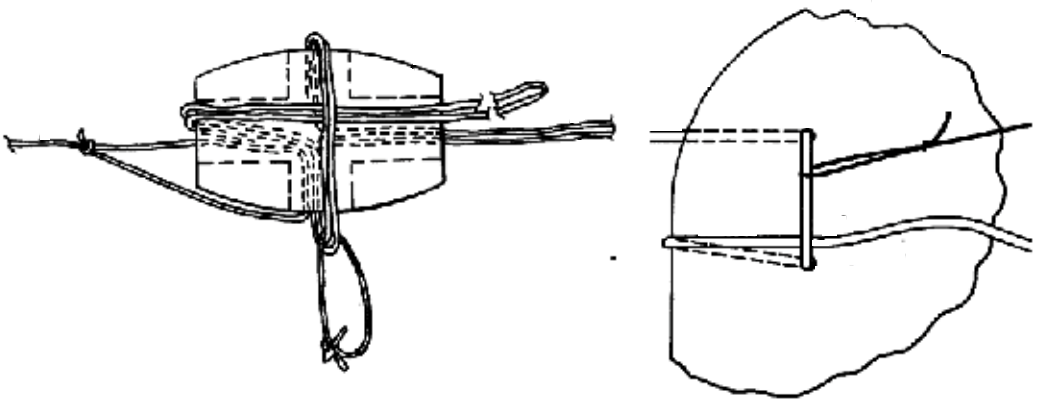

Figure 8.13 Continually adjustable non-return knot [15, 16]: (a) cord to plate and (b) cord to cord.

loosening and readjusting the cord during the surface assembly and adjustment process. The release loops are often removed after the surface adjustment is finalized and prior to the final reflector acceptance testing.

8.7.3 The Deploying Structure

As mentioned earlier, many different styles of deployable reflectors that use the knitted mesh have been developed. Those styles differ primarily in the design of the deploying structures they utilize. These reflectors have been developed in the United States, Europe, and Asia. A number of these reflector styles are discussed in this subsection. The fact that the majority of the discussion pertains to U.S.-developed reflectors is more a reflection of the authors' extent of personal familiarity with them than of their importance or efficiency. It is interesting to note that, although much of the initial development in the field of deployable reflectors has been carried out under the auspices of government entities such as JPL and other NASA centers in the United States and ESA in Europe, beginning in the mid-1990s, the torch has been transferred to the commercial arena, and much of the recent progress has been funded in support of commercial satellite programs. Progress in Asia and to a large extent in Europe, however, is still being made with the support of government funding, perhaps because it is still in the earlier stages of development.

8.7.3.1 The Radial-Rib Reflector (RRR)

The umbrella-style reflector developed by Harris Corporation for the NASA/TRW TDRS satellite was perhaps the first knitted mesh reflector developed (Figure 8.14). It is a 4.8m main reflector of a Cassegrain antenna. It comprises 18 contoured tubular graphite ribs hinged to a central hub. It uses a 10-OPI knitted mesh, except in its central region, where a denser mesh is used. It operates up to the Ku-band range. Although a dozen of these reflectors have been successfully flown, a similar one that Harris built for the NASA Galileo mission failed to deploy. Circumstantial evidence points to the failure of a launch-lock as the likely cause.

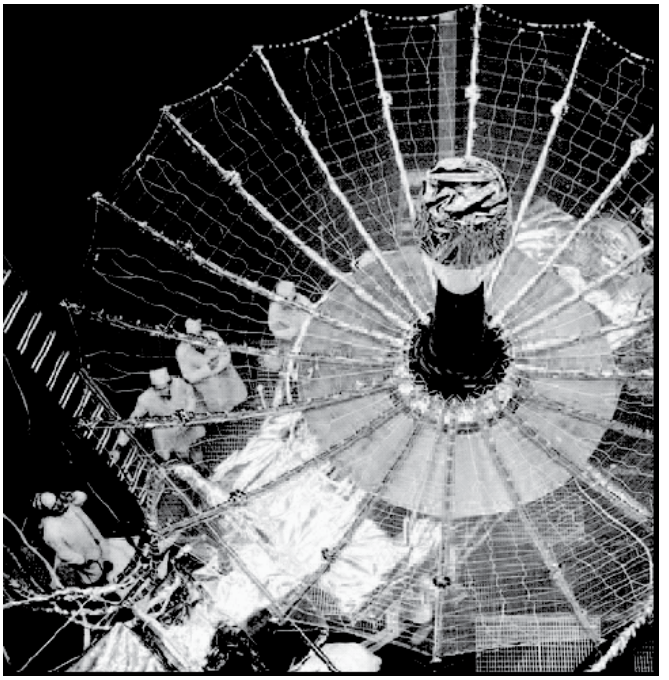

Figure 8.14 TDRS radial-rib reflector—in ground test, 12 reflectors were successfully deployed on orbit (Courtesy of Harris Corporation).

More recent RRRs built by Harris corporation use fewer straight tubular ribs (i.e., not contoured) (Figure 8.15), which are lighter and stow more compactly. Depending on spacecraft accommodations, reflectors of this style as large as 8m in diameter, may be feasible to stow in a standard 4m fairing.

A third RRR variant was developed and patented by Hughes (now Boeing) in 1997 [17]. It is designed to have a low stowage profile, such that an offset reflector with a physical size of 15m × 12.25m can be accommodated in a standard 3.7m fairing without the need to articulate the ribs. To achieve this feat, the reflector was designed with the following features:

- A very compact hub that fits near the tip of even the tightest 4m fairing nose cone.
- Efficient highly tapered contoured ribs with only 2 in. high at their tips.
- An odd number of ribs (31) that permits nesting of the long attachment rib at one reflector end between the two longest ribs from its opposite end.
- A powerful composite hub deployment apparatus [18], which comprises a composite deployment shaft that stows primarily below the hub during launch.

The contoured attachment rib was built sufficiently stiff to permit achieving a 1-Hz resonance when the entire reflector is carried from it on orbit. The remaining 30 contoured ribs were routed out of lightweight graphite honeycomb sandwich panels. They were trussed out to be so mass efficient that the longest ribs, which

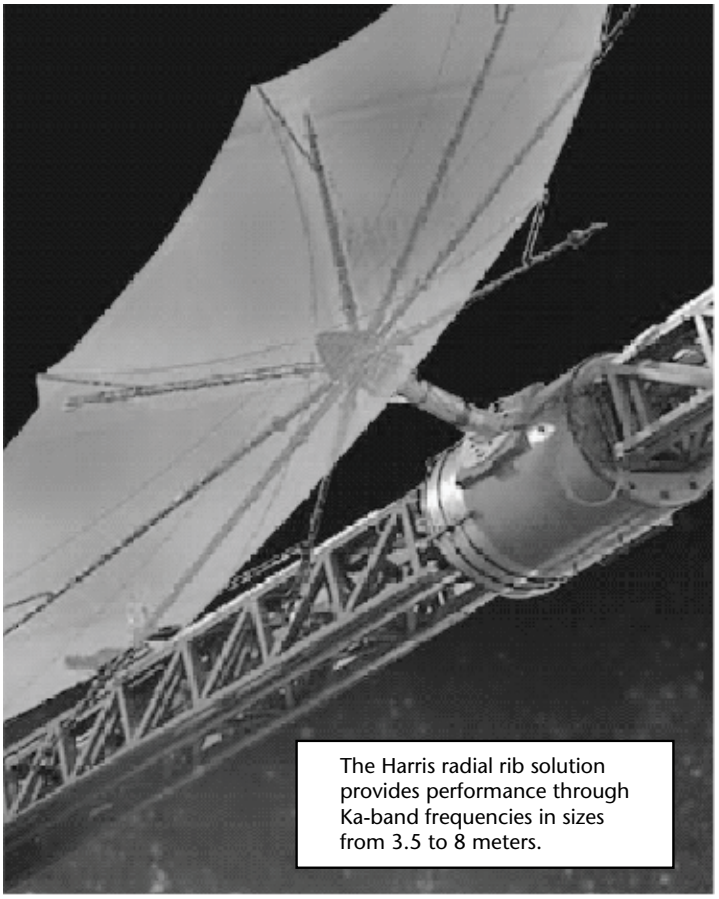

Figure 8.15 Modern radial-rib reflector (Harris Corporation).

were over 24 feet in length, weighed under 1 kg each. The entire reflector, except for the stiff attachment rib, could be deployed unassisted in a 1G field. Figure 8.16 shows deployed and stowed sketches of the antenna mounted on the Hughes Geomobile spacecraft. Figure 8.17 shows a photograph of the 15m × 12.25m engineering model reflector deployed without a 1G offloader. Figure 8.18 depicts the composite hub deployment apparatus and a typical composite honeycomb deployment rib.

8.7.3.2 The Folding-Rib Reflector (FRR)

As with a regular umbrella, folding the ribs makes for more compact stowage. Folding-rib antennas were developed by both TRW and Harris, mostly in the 1980s and 1990s. However, with TRW acquiring Astro Aerospace from SPAR around the turn of this century, including its then newly developed AstroMesh reflector technology, they limited their deployable reflector development effort to studies aimed at improving the AstroMesh reflector. Harris proceeded to develop several folding-rib umbrella designs, most of which having a single mid-rib hinge with diameters as large as 18m (an example of an FRR deployed in the test chamber is shown in Figure 8.19).

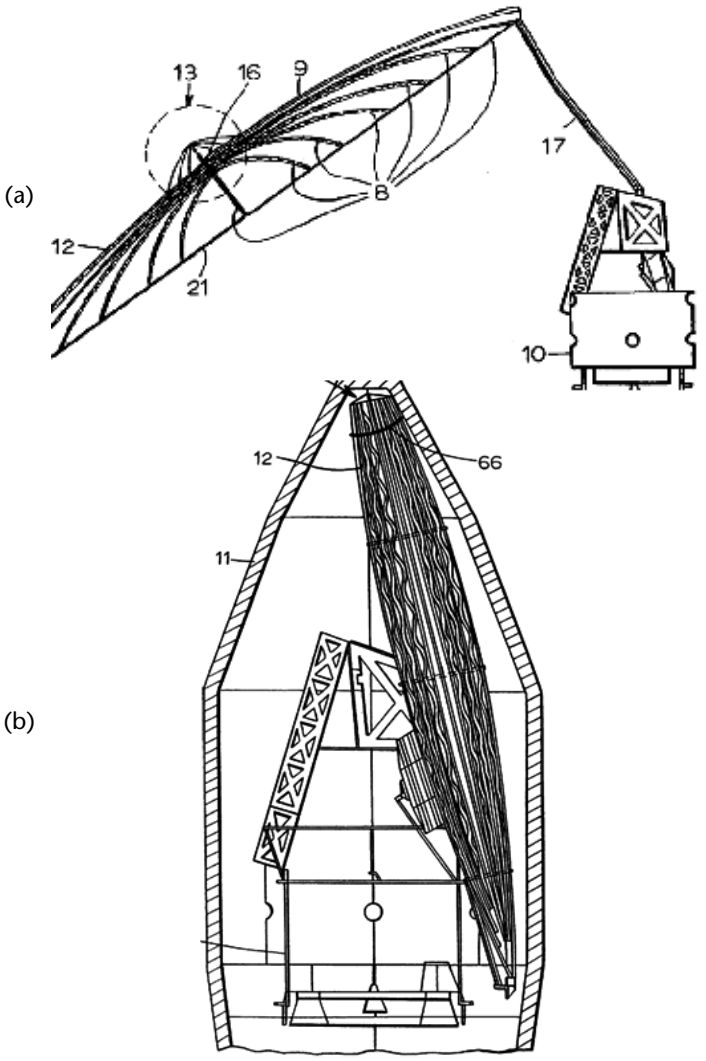

Figure 8.16 Edge-supported low-profile RRR (Hughes): (a) deployed and (b) stowed [18].

A more compact design, utilizing "bat-wing" style riblets integrated into the forward net to produce an almost fully round reflecting surface, was flown by Harris for the first time on the ICO spacecraft in 2008. This design permitted the use of even fewer and somewhat shorter ribs than their older FRR design shown in Figure 8.19, for the same required reflector diameter. Figure 8.20 is an on-orbit photograph taken from a spacecraft-mounted camera of the fully deployed ICO reflector, with the bat-wing riblets clearly visible. This design idea is applicable to all recent styles and sizes of Harris reflectors.

8.7.3.3 The Hoop-Column (Maypole) Reflector

In the 1980s, Harris developed the hoop-column (Maypole) reflector under a NASA Langley contract for the LSST program. The design was aimed at developing a large 100m-diameter parent paraboloid, of which four separate offset reflectors

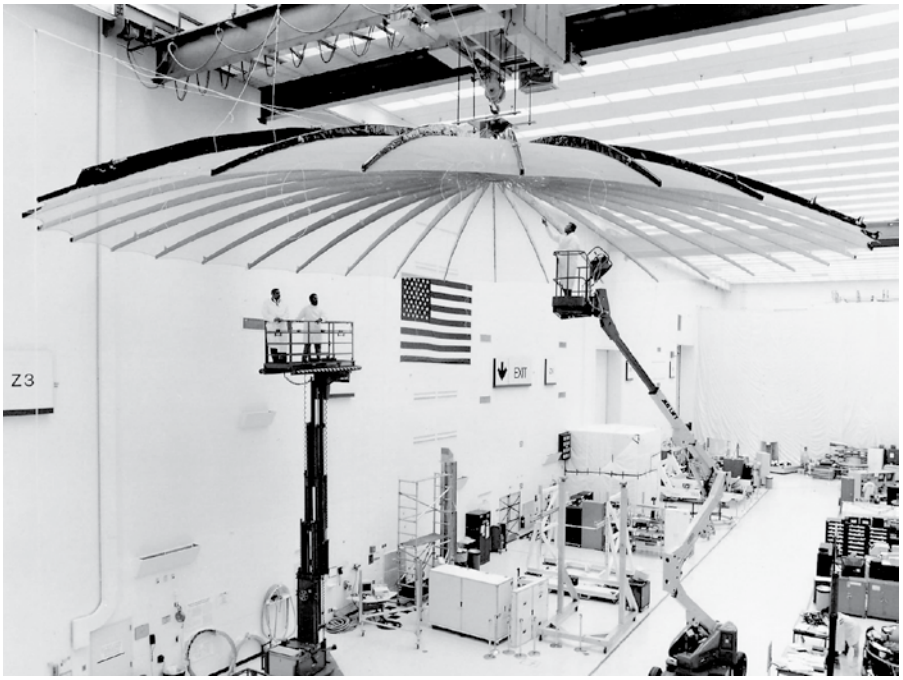

Figure 8.17 Edge-supported low-profile reflector deployed without an offloader (Hughes).

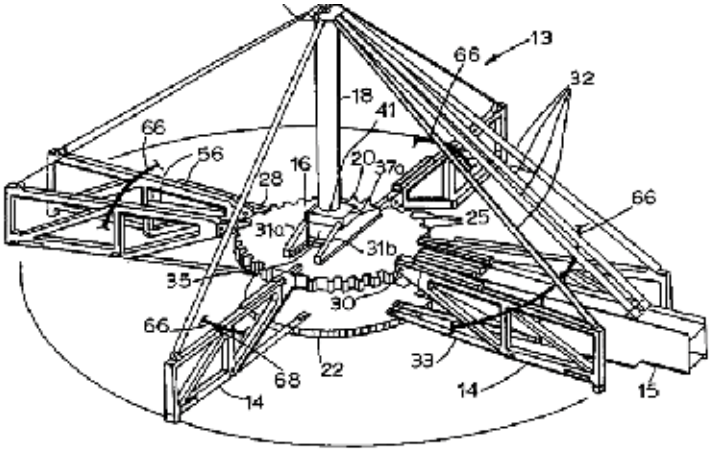

(a)

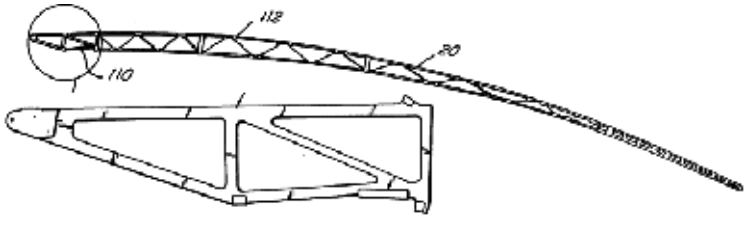

(b)

Figure 8.18 Edge-supported low-profile reflector (Hughes): (a) composite hub deployment apparatus [18] and (b) composite honeycomb profiled rib [17].

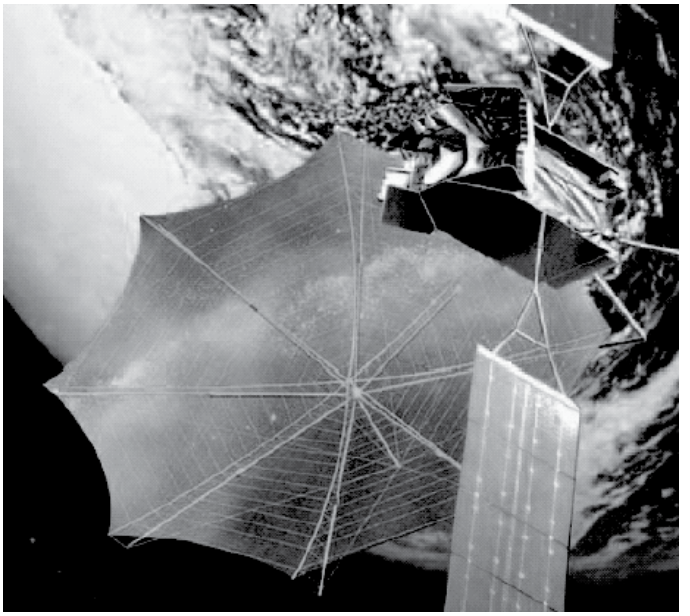

Figure 8.19 Artist's conception of folding-rib reflector deployed on orbit (Harris Corporation).

are formed. As a proof-of-concept task, Harris built and tested a 15m engineering model reflector. As the name implies, it includes a telescoping column and an articulating hoop. These are the only compression-carrying members in the system. The large mesh and net are shaped by a system of cables extending between the column and the hoop. Figures 8.21 and 8.22 show the general concept and a rough deployment sequence [19]. Because the concept is aimed at very large reflectors, it necessarily has a very high stowage efficiency. For example, this 15m model stows inside a 2.7m high by 0.9m diameter cylinder. This design was the result of the realization that as the reflector gets larger, a hoop, rather than an umbrella-type structure, is most efficient [20].

8.7.3.4 The AstroMesh Reflector

This very efficient reflector structure was developed by Astro Aerospace in the 1990s. A 12.25m version was flown on the Thuraya spacecraft in 2000 and seven other units having 9m to 12m aperture diameters have flown on various missions as of this writing. The general concept of the reflector was shown earlier in Figure 8.11(c). The deployment structure is a perimeter truss that stows by allowing the telescoping truss diagonals to expand, thus causing its bays to collapse. Deployment is effected by shortening a cable that runs continuously through the diagonals and wraps around a pair of drums located on the deployment booms at either end of the cable. This provides redundancy, since operation of either one of the drums can deploy the entire reflector.

This type of perimeter structure, which has no central structural feature, is particularly suited for use on an offset-fed reflector, where it is supported via a short boom attached to a point along the perimeter truss (Figure 8.23) [8]. As mentioned in Section 8.7.2, this reflector uses relatively stiff triangular (geodesic) front and

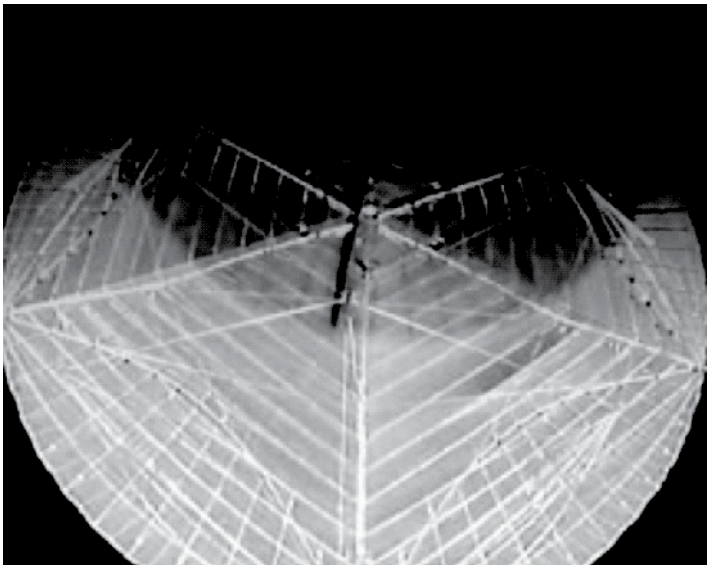

Figure 8.20 Twelve-meter ICO folding-rib reflector photographed from the spacecraft fully deployed on orbit, 2008 (Harris Corporation).

back nets fabricated out of Kevlar (or graphite) straps, which provide the reflector with much of its in-plane stiffness and thermal stability. The front and back nets are pulled toward each other by a set of spring-loaded drop ties located at each of the net vertices, which provide for a significant tension field in the nets.

Although all AstroMesh reflectors flown to date operate at the L- and S-band ranges, studies have confirmed its suitability for use at the Ku- and Ka-bands with impressive performance, for up to 12m and 6m diameters, respectively. Two other factors make this design suitable for high-frequency applications:

- Its excellent thermal distortion performance, aided by the lack of the systematic/periodic errors usually associated with the umbrella rib pattern, leaving much of the distortion as global shape changes that can be largely mitigated by active fine pointing correction [13]. Also, the inherently shorter boom makes for a lower boom thermal distortion contribution.
- Its inherently high stiffness, due to its drum-like structure, and its use of a relatively short boom with a load path that does not need to first reach the hub, as is the case with an umbrella-style reflector. The higher stiffness makes for less interaction with the spacecraft control system, resulting in better pointing stability, which is much needed for high-frequency applications, as discussed in Section 8.8.2.

As mentioned in the hoop-column reflector discussion, reflectors that are based within a circumferential ring are more suited for larger apertures than the historic umbrella type [20]. Add to this its suitability for use on offset-fed reflectors, and you have what may be considered the most efficient large reflector design available. More recent developments at Astro are aimed at further reductions in the stowed

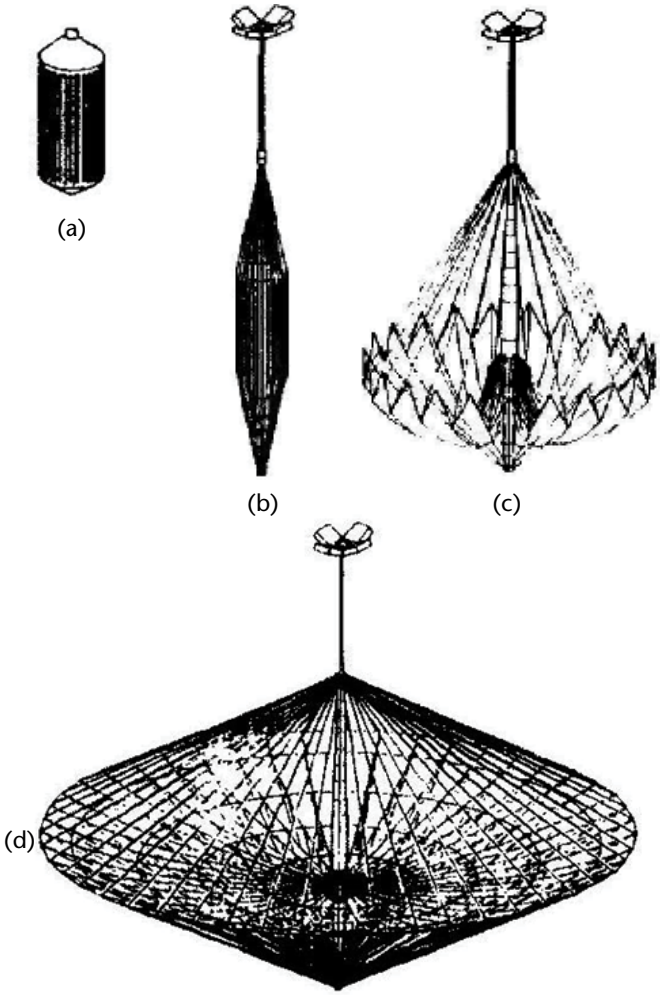

Figure 8.21 Hoop-column (Maypole) reflector deployment sequence [19]: (a) stowed, (b, c) partially deployed, and (d) deployed (courtesy of NASA/JPL-Caltech). (© 1982 IEEE. From [19].)

reflector length and diameter, in order to permit packaging reflectors as large as 100m within currently available booster fairings [9].

8.7.3.5 Other Hoop-Based Reflectors

In addition to the AstroMesh and the hoop-column, other hoop-based design reflector designs have been developed, and two of them have been flown. The largest and most recent of these is the Harris hoop-truss reflector, a 22m version of which was flown in 2010 on what became the largest commercial satellite in orbit. The deployment structure is a ring-like truss combining folding rigid tubes for its compression members with preloaded cords for its tension members. The structure shown in Figure 8.24 is an octagonal ring truss with three rigid members in each bay, plus a multitude of pretensioned cords. Additional folding mechanisms at the middle of the long sides enable compact stowage of the structure. The mesh and the forward net stretch across the top corners of the deployment structure. As with the Harris

(a)

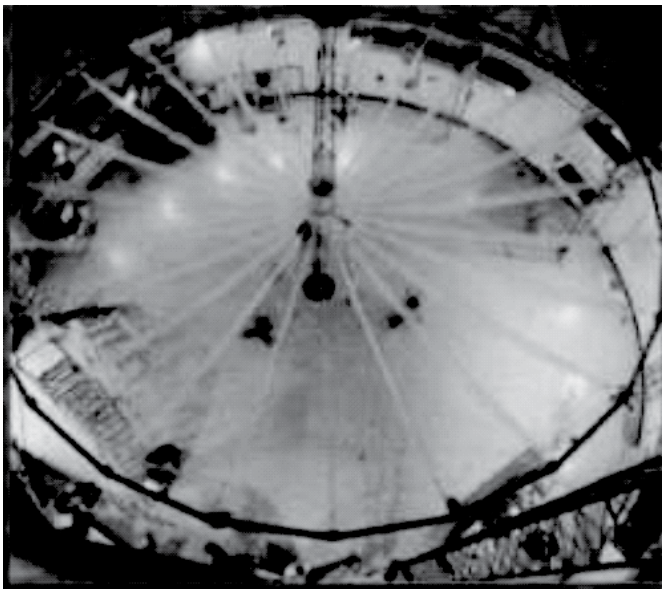

(b)

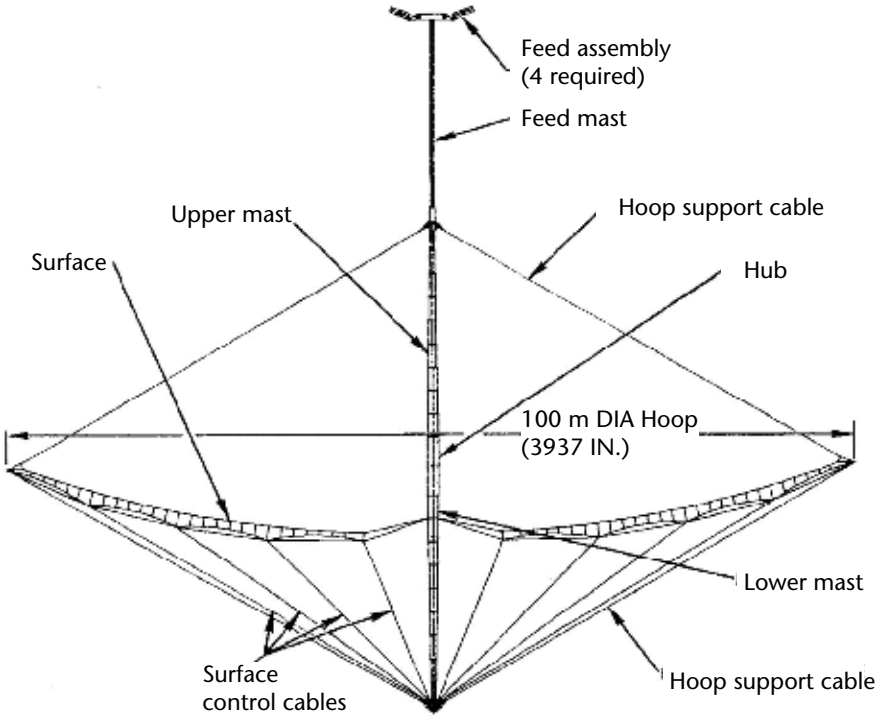

Figure 8.22 Hoop-column (Maypole) reflector [19]: (a) 15m engineering model (Harris Corporation) (© 2008 IEEE. From [6].) and (b) general concept [19].

FRR described earlier, the mesh edge is circularized using bat-wing style riblets, a few of which are visible in the photograph.

Another hoop-based reflector was developed by the Russian company Energia–GPI Space, of which a 6.4m × 5.2m version was built and deployed on the MIR

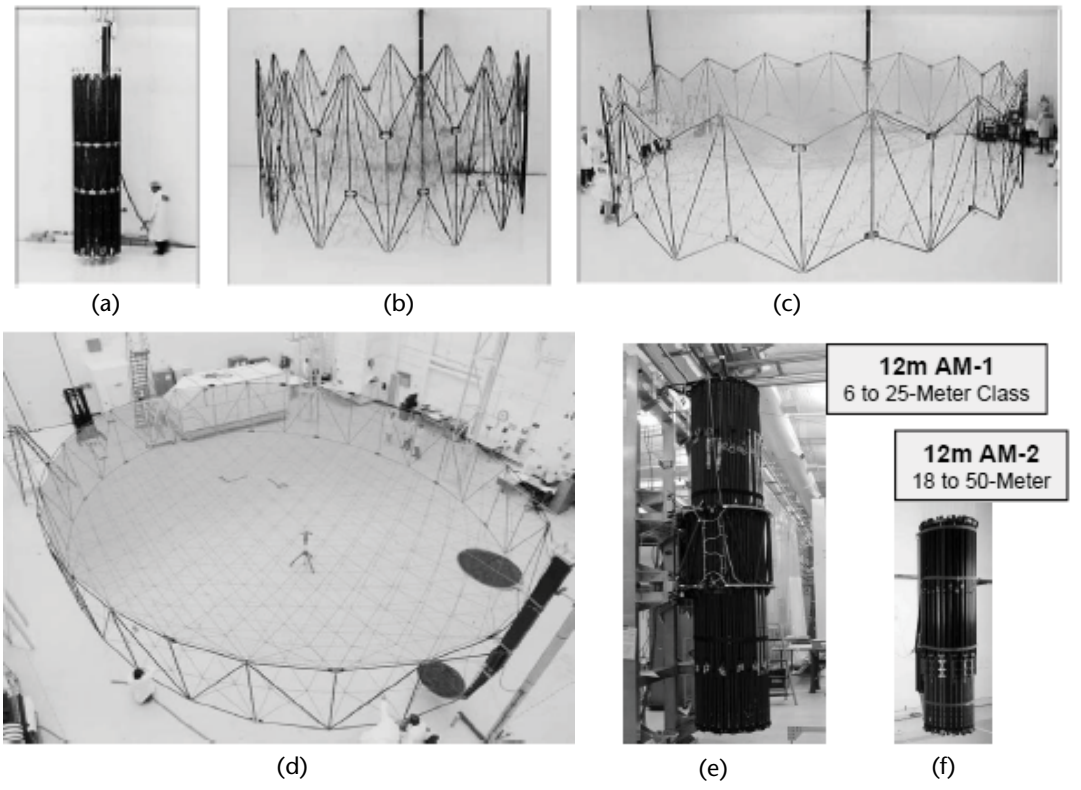

Figure 8.23 The AstroMesh reflector [9]: (a–d) deployment sequence and (e, f) AM-1 vs. AM-2 stowed models.

orbital station (Figure 8.25) [21] in July 1999. As can be seen from the photograph, the hoop structure is a cylindrical pantograph that stretches a set of radial soft ribs that connect to a central fitting (somewhat like the hoop-column reflector). The reflector stows in a compact 0.6m diameter by 1.0m high package, and weighs a total of 35 kg, including its electrical deployment system.

8.7.3.6 Modular Mesh Reflector

A new concept in deployable reflector architecture was pioneered by the National Areospace Development Agency of Japan (NASDA) on what they called the Large Deployable Reflector (LDR), of which they launched a pair on the Engineering Test Satellite VIII (ETS-VIII) in December 2006. Cameras on board the satellite photographed the reflectors as they were being deployed; the fully deployed photographs are shown in Figure 8.26 [22]. As can be seen, each reflector comprises 14 hexagonally shaped modules. The modules are 4.8m each (tip-to-tip) and the composite reflector spans 19m × 17m with a conservative inscribed projected circular aperture of 14m. Ozawa [22] describes the design of the module (Figure 8.27) as having a gold-molybdenum mesh with a triangular quartz net, quartz drop ties, and quartz spider web-shaped aft reaction cords. The deployment structure comprises six radial collapsible ribs, each looking like one of the bays of an AstroMesh reflec-

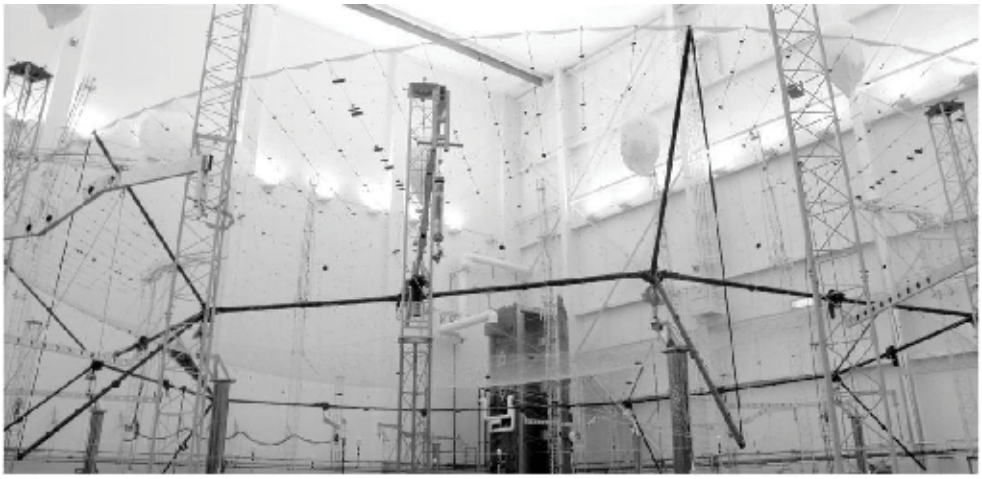

Figure 8.24 Harris hoop-truss reflector deployed (courtesy Harris Corporation).

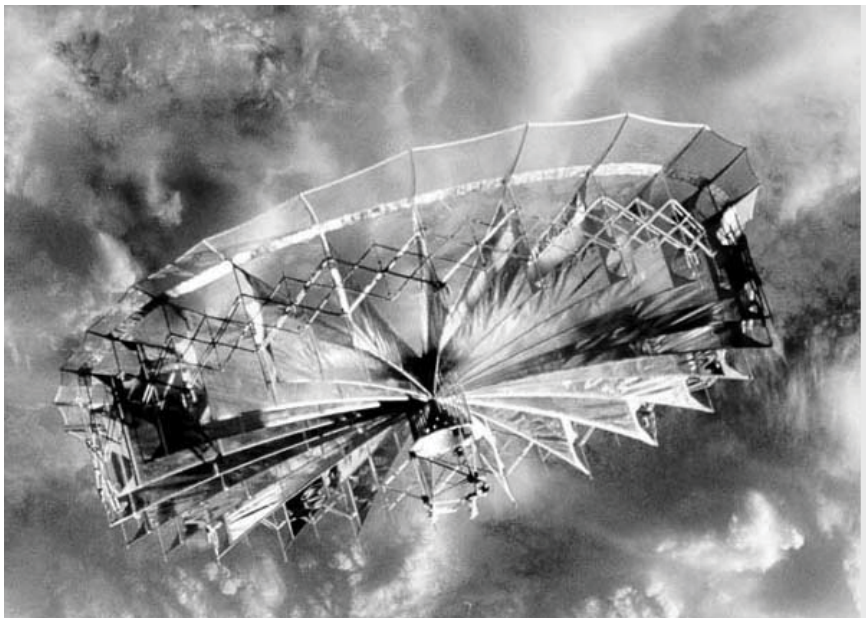

Figure 8.25 Energia-GPI Space pantograph hoop reflector experiment—deployed on MIR orbital station [21].

tor. Deployment is effected by a combination of motors for controlled reversible deployment and springs for added deployment force margins.

The advantages of a modular design are fairly obvious and significant. Of the most important are the programmatic advantages associated with the ability to build, test, and adjust the modules in parallel, in smaller/cheaper facilities. Technical advantages include more accurate surface accuracy due to better offloading accuracy, and scalability of the design to various sizes by increasing either the number or the size of the modules, or both. The design also provides for compact stowage, whereby the entire 19m × 17m reflector stows within a 1m-diameter by 4m-long package, which is more efficient than the 12 m AstroMesh reflector stowage.

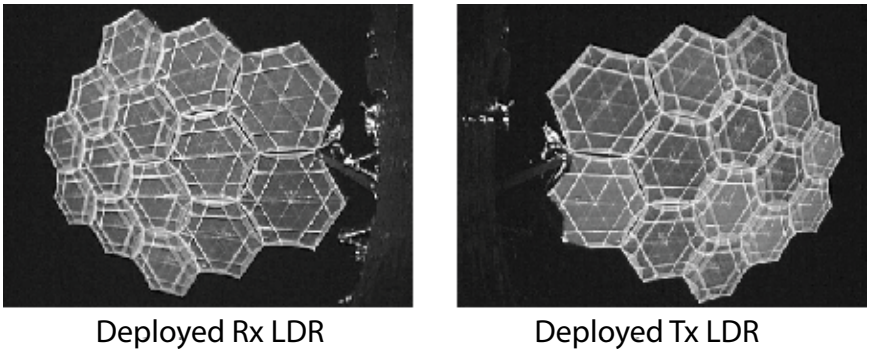

Figure 8.26 ETS-VIII large deployable reflector photograph in orbit [22] (courtesy of NASA/JPL-Caltech).

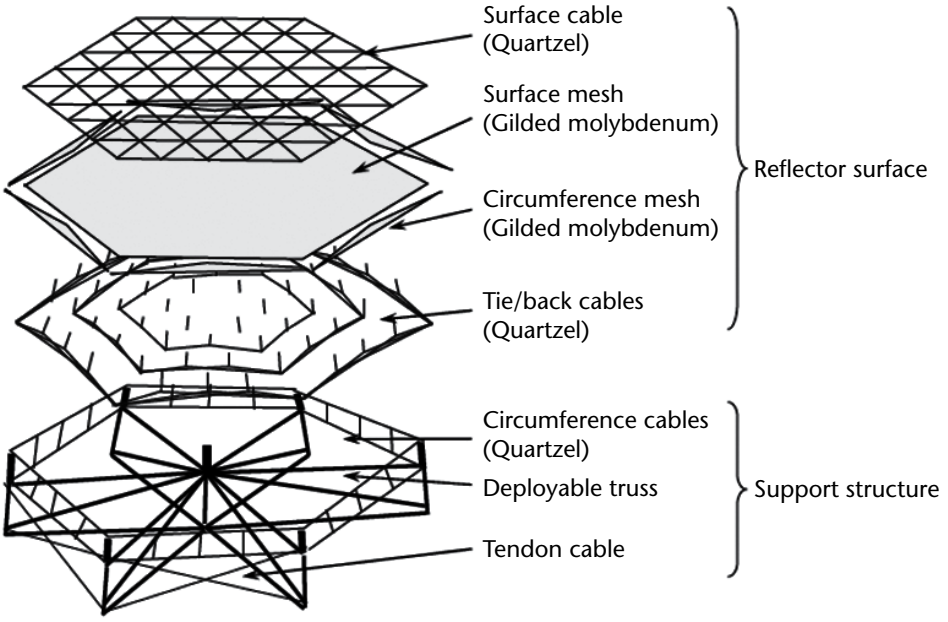

Figure 8.27 Module construction of ETS-VIII modular reflector [22] (courtesy of NASA/JPL-Caltech.).

8.7.3.7 The Arbitrarily Shaped Mesh Reflector

Although almost any mesh reflector can be used to provide a nonparaboloidal gently shaped surface, providing an arbitrarily shaped mesh surface (i.e., one that may have both positive and negative curvature regions) requires specific reflector design changes. Such a specialized reflector was developed by Boeing in 2005 with a patent filed in February 2006 (Figure 8.28) [11]. That patented reflector uses a radial-rib design as an illustration; however, other reflector styles may also be usable. Because the nature of an arbitrarily shaped surface involves higher surface curvatures (both positive and negative), and since the normal loading on the net elements is proportional to the angles between the facets surrounding them (which is proportional to the surface curvature), such a reflector requires significantly higher preloads in its net. With the higher preload comes the need for a stronger deployment mechanism

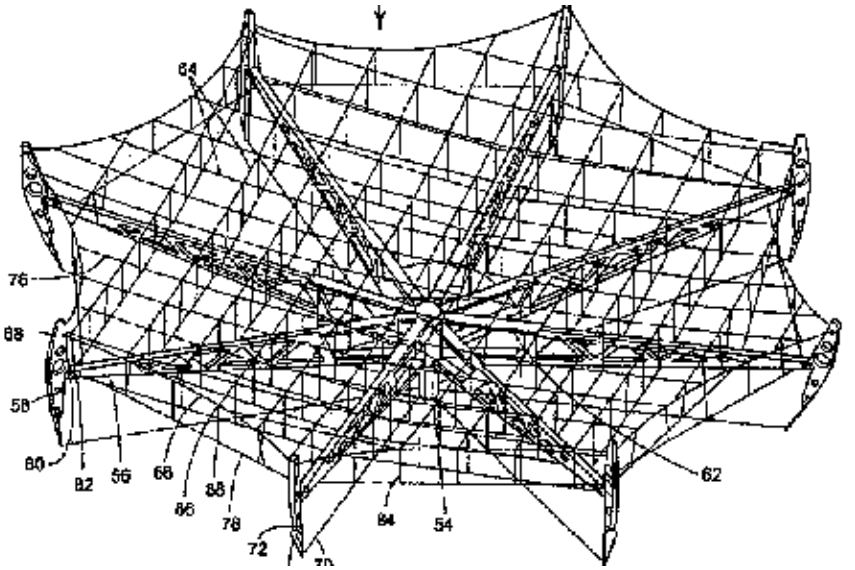

Figure 8.28 Arbitrarily shaped mesh reflector (mesh not shown) [11].

(or springs) and stronger/stiffer deployment structure (or ribs). Therefore, instead of the tubular ribs usually used on umbrella reflectors, tapered ribs routed out of composite sandwich plates are preferred. Those ribs provide the higher preloads needed. The tapered shape is consistent with the higher loads toward the roots of the ribs.

This type of reflector preferably uses a net with square (or rectangular) openings. A number of the advantages provided by rectangular nets were discussed previously in Section 8.7.2. There are two additional advantages particular to an arbitrarily shaped reflector net. First, as the net is modified during the surface adjustment process, the lengths of the web elements change slightly. With a square/rectangular net, the entire net cord, stretching from one end of the reflector to its opposite end, acts as one cord along which those changes in length can be equalized and averaged, resulting in only minimal preload changes. This effect is further aided via the use of relatively soft net cords. Second, since shaping of a surface that includes reversed curvatures requires pushing on the surface at certain locations (instead of pulling), those elements that are under compression need to be stabilized in at least two different directions. This precludes the use of intermediate edge control points for any "push" locations [as was the case with the old RRR used on TDRS and shown in Figure 8.11(b), for example].

A novel design was devised for the "push" elements used at the reversed curvature locations [Figures 8.29(a) and (b)]. That design uses a telescoping spring-loaded tube through which extends a standard, finely adjustable tension tie. The spring-loaded telescoping tube pretensions the tension tie, thus allowing it to sustain both tensile and compressive loads, as long as the compressive load does not exceed its preload. Because the tension tie itself is much stiffer than the spring-loaded telescoping tube, the stiffness and thermal expansion properties of the pair are dominated by the drop tie properties, regardless of the properties of the telescoping tube.

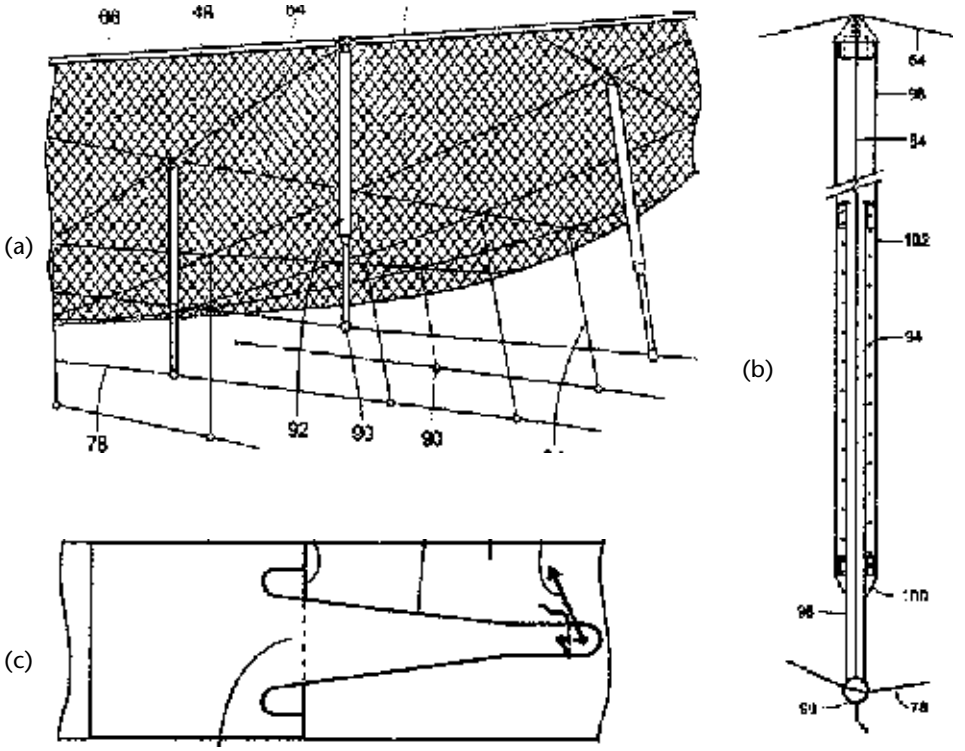

Figure 8.29 Some details for an arbitrarily shaped mesh reflector [11].

To maintain a stable high tension in the net throughout the life of the reflector and at all temperature conditions, the net cords are tensioned against eight perimeter catenary members, the ends of which are tensioned by pivot arms that terminate with composite flexures. The large flexibility of those flexures makes for a stable tension load throughout the net elements.

Similarly, stability of the tension in the aft catenary members is provided via termination of each of them at a composite flexure, which in turn attaches to one of the deployment ribs [Figure 8.29(c)]. The large flexibility of those flexures provides a high enough deflection to be an accurate indicator for the catenary initial tensions, as well as the stability of those tensions.

8.7.4 Mesh and Soft-Structure Management Provisions

The biggest risk of failure in a deployable knitted mesh reflector is that of entanglement of the mesh or the soft structure in a manner that halts the deployment or damages the reflector if deployment is "forced through." Therefore, sufficient mesh/soft structure management features are typically needed to ensure the safe and reliable deployment of the reflector. The design and placement of those features requires significant hands-on experience and is as much of an art as it is a science. Some of the principles and tools involved are:

1. The management provisions should permit only gradual release of the mesh and soft structure as deployment progresses such that the portions

released are not large or long enough to reach and entangle around other components.

2. One commonly accepted rule for assessing the adequacy of the management features at any point in the deployment process is called the "one-hand rule." It suggests that management features are inadequate if one can use a single hand to cause a portion of the mesh or soft structure to wrap around another component in such a way that the deployment tends to be halted (or damage becomes imminent). This usually indicates that additional (or different) features are needed.
3. Another important principle in designing deployment systems and mesh management devices is to design for "soft failure." This means that if a hard "snag" should develop during deployment, the deployment motor should stall (or its drive clutch capability be overcome) or at least a clear telemetry indication of off-normal behavior must be received, resulting in an automatic pause or abort command before a "hard" structural failure can occur. Breakaway features may also be provided for some of the management provisions/cords so that a snag may resolve itself with minimal or no damage. Because most deployment structures have variable mechanical advantage over a given snag at different points in deployment, and because it is not known beforehand at what point a snag will occur or what load it can develop and yet remain "safe," then using a set stall torque or clutch torque limit may compromise deployment reliability. Some system designers may thus choose to provide additional "boost" motor power, which theoretically can exceed the minimum capability of the structure, but which can only be applied through ground intervention after all other available means to resolve a deployment stall have been exhausted. Yet another useful strategy is to current-limit the motor torque in anticipation of a nominal deployment; the torque limiting value can even be varied as a function of deployment progress based on analytical results or known nominal deployment profiles. At any time during deployment, it would be possible to override the preset current limit and use a more aggressive yet "safe" limit.
4. Other safety features that are considered desirable in designing a deployable system include installation of on-orbit observation cameras, which could help and to possibly identify the cause of a hangup or a snag. Another feature that some system designers utilize is the ability to relieve built-up strain due to a snag or another anomaly by a passive backdrive capability of the actuator, or the ability to reverse the deployment motion altogether in case of a hangup. Although backing down to lower levels of strain is usually a safe strategy, full reversal of the deployment motion, however, should be considered very carefully and only be used as a last resort, especially in the absence of an adequate observation system, since backing up the deployment for any significant distance can result in large uncontrolled mesh/cord spans, which can lead to more entanglement.

A main concern in evaluating the adequacy of the management features is that the 1-G offloaders used during deployment are often inadequate, especially when

it comes to offloading the soft structure. The 1-G environment tends to cause the soft structure (and the mesh) to behave in a somewhat regular and predictable/repeatable manner. However, in zero-G any built-in or residual stresses in the soft structure (e.g., cords) cause it to move in an unpredictable manner and sometimes take bizarre shapes. This is why the one-hand rule permits manipulation of the soft structure into any shape that can be imposed on it by the use of a single hand.

Some of the features that have been successfully used for managing the mesh/soft structure include the following:

1. Attaching plastic rings or washers to the mesh/net then passing control/management elements (which may be rigid or semirigid) through them. The mesh is then draped or fanfolded between the rings for launch in a manner similar to a theatre curtain or a drape. During deployment, the control/management element is gradually withdrawn, allowing the rings to sequentially fall off and release successive portions of the mesh/net. An example of this system is described in a Boeing patent [Figures 8.30(a) and (b)] [15].
2. In another example, snaps are used to shorten certain management straps, which cause portions of the mesh/net to be "bunched up" during launch. As the deployment structure starts to deploy, it pulls on the straps, which in turn "unsnaps" the snaps in a sequential manner, permitting the mesh/net to deploy gradually. Other means, such as Velcro fasteners or looped plastic elements, may be used instead of the snaps to produce a more gradual release.
3. Other soft structures, such as cords, may be controlled by passing them through snug semiflexible "spaghetti" tubing [15] or stowing them in Ziploc bag-style pouches. The cords may also be controlled by looping them through a pair of snug-fitting holes in a fixed (or deploying) component, which keeps the cords taut during deployment by requiring them to overcome the friction force needed to pull it through those holes.
4. The patent also describes a technique in which the mesh control cords are formed into loops that are then placed around the teeth of a comb-like component. This component is kept in a locked position during launch by snubbing it against certain members of the deployment structure. As those members are deployed, the comb-like component is released and permitted to rotate to a new position, thus allowing the loops to slip off and release the cords being controlled [Figures 8.30(c) and (d)].

The possibilities are almost endless, but all control devices utilized need to be carefully characterized through multiple environmental test runs, and the adequacy of the entire management system needs to be evaluated through multiple partial and/or full cup-up and cup-down deployments.

8.8 Reflector Subsystem Design Considerations

Deployable reflector subsystem specifications typically include electrical as well as mechanical, thermal, and environmental requirements. The electrical requirements include allowable gain-loss, allowable side/grating lobe levels, passive

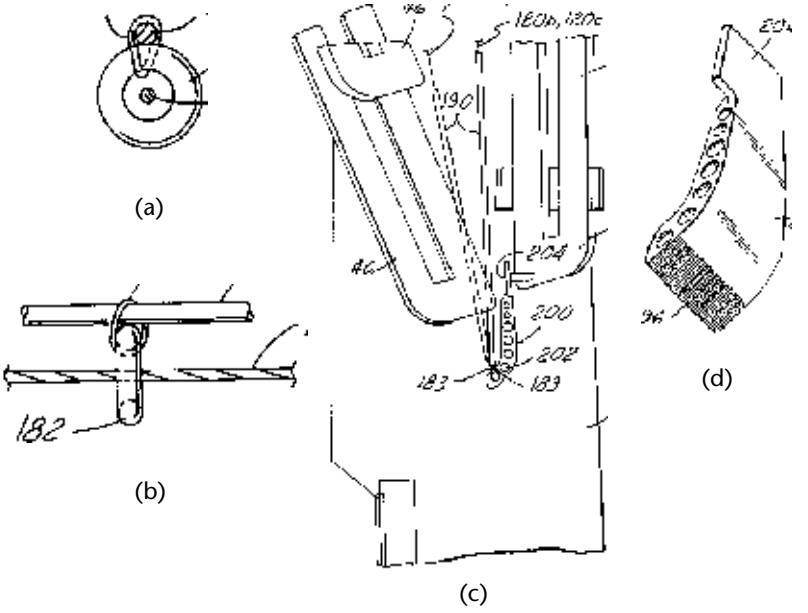

Figure 8.30 Examples of soft structure management provisions [15].

intermodulation (PIM) levels, and electrostatic discharge (ESD) requirements. The mechanical requirements include geometric requirements for both deployed and stowed configurations (e.g., aperture diameter, focal length, offset, stowed volume, shadowing, and stay-out requirements), mass properties, stowed and deployed frequencies, and pointing requirements. In this section, we discuss the electrical and critical mechanical design drivers; thermal and environmental requirements are just briefly touched on.

8.8.1 Electrical Requirements

8.8.1.1 Gain-Loss Allowance

The total allowable gain-loss from all sources for a deployable reflector subsystem is one of its most critical design drivers, and must be specified in order for the entire system to operate successfully. For commercial low- to medium-frequency reflectors (L- through Ku-band), a total loss of 0.3 dB has been shown to be achievable [13]. Using the well-known Ruze formula [23], this translates to a maximum equivalent root-mean-square (RMS) error of $\lambda/50$, where λ is the minimum operating wavelength. For a higher frequency/shorter wavelength, higher gain-loss [24] has often been permitted by the system design, especially for larger reflectors (e.g., greater than 500λ in diameter). All sources of gain-loss must be accounted for, although some of the smaller contributors are often lumped together. The following is a brief discussion of those losses:

1. *Blockage loss:* In center-fed reflectors, shadowing from the feed elements, waveguides, subreflector, and often feed supports cause effective area loss, which must be accounted for in the design. Fortunately, this type of loss is usually entirely avoidable for offset-fed reflectors. This is particularly

important for multibeam antennas (MBAs), where the size of the feed cluster can be significant. The gain-loss due to blockage is given by the following simple equation:

$$\text{Gain loss}\,(\text{dB}) = 10\,\log_{10}\left[1-\left(\frac{\text{area blocked}}{\text{total area of reflector}}\right)\right]$$

2. *Surface roughness/random loss:* This is usually due to manufacturing errors/tolerances, as well as roughness of the reflective surfaces and inaccuracies in locating/adjusting the net vertices. The RMS error of the measured reflector surface relative to the "as-designed" theoretical faceted surface can be plugged into the Ruze formula to calculate this loss contribution:

$$\text{Gain loss (dB)} = 688\,(\text{RMS error}/\lambda)^2$$

3. *Faceting loss:* The difference between the ideal surface and the faceted approximation introduced by the forward net theoretical shape is referred to as the faceting error. The faceting loss is the difference in gain performance between these two theoretical surfaces. This performance difference can be determined via RF analysis of the gains obtainable from the two surfaces. Reference [13] showed that a slightly conservative estimate for this faceting loss, at least for triangular facets, can be obtained by calculating the RMS of the differences between these two surfaces and substituting that value into the Ruze formula. This is despite the fact that the faceting error is actually a systematic error, whereas Ruze's formula was derived for random errors. This approximation is particularly convenient for preliminary designs, because it allows for easy optimization of the facet size. This optimization is important because the cost and time required to build a deployable reflector are driven, to a great extent, by the number of facets used.

   Hudgepeth [25] has derived simple relationships between the facet size (l), the focal length (F), and the faceting RMS error (W_{RMS}) for various facet shapes that can be rewritten as follows:

$$l = K(F \cdot W_{\text{RMS}})^{1/2}$$

   where $K = 7.87$ for triangular facets; 6.17 for square facets; 7.33 for rectangular facets having widths less than $0.5l$; and 6.82 for gore-shaped nets, wherein l represents the gore width at the rim.
4. *Pillowing loss:* As described in Section 8.7.2, the curvature of the reflector surface, coupled with the tension in the mesh, loads the net cords, causing them to curve slightly toward the reflector focus, which causes the mesh to curve toward the focus as well. This deviation from the theoretically flat facet surface constitutes the faceting error. It can be shown that the pillowing error is proportional to the faceting error multiplied by the ratio of the total mesh tension to the net tension. Because that tension ratio is usually

kept low (about 0.1), the pillowing error is often very small. Reference [25] provides equations for the combined pillowing and faceting errors for facets of various shapes. From those equations, one can derive the following relationship between the RMS of the pillowing error and that of the faceting error:

$$W_{\mathrm{RMS}}^{\mathrm{pillowing}} = K1 \cdot W_{\mathrm{RMS}}^{\mathrm{faceting}} \cdot (Nl/T)$$

where N is the mesh tension, l is the facet edge length, and T is the net cord tension. The constant $K1 = 0.33$ for triangular facets, and 0.2 for square facets. If Nl/T is kept below 0.1, then the pillowing RMS is only 1% to 2% of the faceting RMS. Note, however, that since the faceting and pillowing errors are directly correlated, the magnitudes of their corresponding RMSs should be added directly (and not RSSed), and the resultant RMS error can be used to calculate a combined faceting/pillowing gain-loss from the Ruze formula (for preliminary analysis).

5. *Thermal distortion and moisture desorption losses:* Due to the temperature extremes that reflectors are exposed to on orbit, thermal distortion is often a significant contributor to the reflector's gain-loss. Unfortunately, evaluating thermal distortion losses is a complex process that requires significant interdisciplinary effort involving thermal, thermomechanical, and electrical (RF) analyses interaction. It is therefore almost never performed during the preliminary design stage, but rather reserved for the final design verification stage, with an estimated "allowance" made for it in the earlier stages.

   In general, the process starts with performing transient thermal analysis for at least two orbit periods at each season (summer, winter, and equinox) using both beginning-of-life (BoL) and end-of-life (EoL) properties. Spacecraft shadowing, eclipses, and through-the-thickness gradients in the ribs/booms are important considerations for those analyses. The temperatures determined are then mapped onto a detailed thermo-structural finite element model for a large number of time steps for each season at both BoL and EoL, and the surface deflections determined. For this stage, good knowledge of the reflector's components, including soft structure stiffness and CTE properties (including rotational CTEs), as well as the uncertainty/variability of those properties, is critical. Finally, either a best-fit analysis is performed to separate elastic surface distortions from rigid body rotations/translations and defocusing, or direct RF analysis is performed to directly determine the gain-loss and beam mispointing.

   Moisture desorption effects are also evaluated in a manner analogous to thermal distortions, but by using coefficients of moisture expansion (CMEs) instead of the CTEs. The resulting distortion limits can be added as initial reflector shape distortions to all thermal distortion cases, or the resulting gain-loss evaluated and added separately (or in combination with other effects such as creep, relaxation, and radiation effects) for both BoL and EoL evaluations.

6. *Deployment repeatability, measurement uncertainty, and 1-G relief losses:* These factors represent uncertainties in the initial on-orbit shape relative

to the final measurements performed on the ground. Reasonable estimates are made for the effects of these uncertainties on the shape with the results RSSed together, and the corresponding equivalent loss added to the other gain-loss components. For example, the deployment repeatability effect is evaluated by comparing the results of successive surface measurements taken after each deployment test, excluding those separated by environmental exposures. Measurement uncertainty, on the other hand, is evaluated based on knowledge of the measurement system accuracy (typically photogrammetry), the available shooting angles, and the number of shots taken. The 1-G relief effects depend on the quality of the 1-G offloaders used, how well the soft structures are offloaded, and how large and nonlinear (cup up vs. cup down) the predicted mesh deflections are in the offloaded test environment.

7. *Mesh reflectivity loss:* Gold-molybdenum meshes are available in several densities suitable for use up to Ka-band. Reference [13] presents analytical and measured data on 10-, 20-, and 30-OPI meshes, and discusses a newer low-loss mesh for Ka-band applications (Figure 8.31) [13]. The data and discussions suggest that with the use of the appropriate mesh density, the reflectivity loss can always be kept within 0.1 dB. It also suggests that the 10-OPI mesh is suitable for use up to C-band, the 20-OPI up to Ku-band, and the 30-OPI up to Ka-band.

8.8.1.2 Other Electrical Requirements

Depending on the system design, several other electrical requirements may become important drivers for the reflector design. Low sidelobe and/or grating lobe levels may be necessary to reduce interference and improve beam-to-beam insulation, especially for MBAs. The outside perimeter shape of the deployable reflector (e.g., round vs. octagonal with perimeter catenaries as in Figure 8.12) can significantly

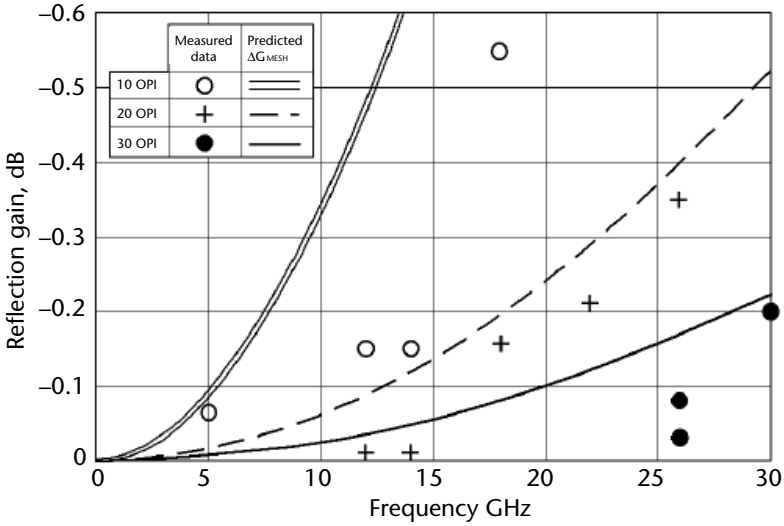

Figure 8.31 Mesh reflectivity loss [13].

affect the sidelobe levels. Additionally, as discussed in Section 8.7.2, grating lobes can develop as a result of using uniformly spaced facets, such as square or the geodesic triangular nets used on the AstroMesh reflector. Those grating lobes can be broken down to much smaller lobes by introducing variations in the net opening sizes, as described in [14] and illustrated in Figure 8.12.

For other systems, such as those using a dual-mode reflector that combines both Tx and Rx functionality, PIM avoidance can become a critical driver. For example, the FleetSatcom spacecraft built by TRW in the early 1970s was originally intended to utilize a dual-mode deployable reflector that used a woven mesh. Unacceptable PIM levels, however, forced the redesign of the system to add a separate Rx antenna in the 11th hour. Additionally, since high PIM levels are generated as a result of casual (i.e., low-pressure) metal-to-metal contacts between conductors, the wires forming the woven reflective mesh had to be welded/soldered together at each mesh wire intersection. Alternatively, woven meshes may have to use insulated wires for PIM reduction. As mentioned in Section 8.7, the gold-molybdenum knitted meshes produce acceptably low PIM levels, as long as they are kept clean from metallic debris; otherwise, a mesh woven out of Aracon threads can be used to avoid PIM under all conditions. In addition to design considerations to avoid casual metal-to-metal contact throughout the antenna system, extensive PIM testing in specially designed PIM-free facilities is also necessary for PIM-sensitive systems.

Electrostatic discharge avoidance is another design driver for many deployable reflectors. Mitigating it typically involves avoiding large nonconductive surfaces that can get charged in the space environment, and then discharged suddenly, causing either physical damage to the low-noise amplifiers (LNAs) or sufficiently frequent low-level discharges that interfere with the operation of the communications system. Although designing for ESD avoidance is typically an easy task with the use of proper ESD coatings, simultaneously avoiding both ESD and PIM is much trickier since they entail somewhat competing requirements. A number of companies, however, have developed proprietary plastics, resins, and coatings that satisfy both requirements.

8.8.2 Mechanical Requirements

Meeting the basic reflector deployed and stowed geometric requirements is the basic driver in developing the large variety of deployable reflectors discussed throughout this chapter and therefore will not be further discussed in this section.

8.8.2.1 Mass Properties

Because of the sheer size of the deployable reflectors, minimizing mass and inertia has been a major thrust in developing those reflectors. Thanks to the lightweight knitted mesh (that by itself weighs only about 0.025 kg/m^2), very lightweight mesh reflectors have been developed. An areal mass of 0.37 kg/m^2 was reported for the 12.25m AstroMesh reflector (excluding its boom and stowage cage) [12], with lower values predicted for larger reflectors [9].

8.8.2.2 Frequency Requirements

To avoid significant interaction with the attitude control system (ACS), and since deployable reflectors represent large appendages with very high inertias, a minimum deployed frequency requirement is typically specified for the reflector. For smaller reflectors and older control systems, frequencies in the range of 0.5 to 1.0 Hz were specified; however, with larger reflectors and state-of-the-art control systems, frequencies in the range of 0.1 to 0.2 Hz are tolerable with careful ACS design. Often, the deployed frequency is dominated by the boom stiffness, the stiffness of the local area of the reflector where the boom is attached, and the deployment mechanisms. Stowed frequencies, on the other hand, are specified for minimizing launch loads, just as with any other structure. It is appropriate, to a large extent, for the reflector deployment structure to be sized for deployed frequency and launch loads, but not launch frequencies. Instead, the stowage restraint subsystem, which supports the reflector in its stowed configuration, should be designed to enable the reflector system to meet the stowed frequencies.

8.8.2.3 Pointing Requirements

As deployed reflectors get larger, and higher frequencies more prevalent, the RF beams get smaller in width. For example, for communications from Martian distances at high data rates, (of the order of 1 Gbps) a joint NASA/Boeing paper [26] suggested that reflectors with diameters of the order of 1,000 wavelengths would be needed. Such a reflector would produce an RF beam of the order of 1.5 milliradians (mrad) in width. To limit the pointing loss to less than 1 dB, the pointing error from all sources needs to be less than 0.5 mrad, which represents a significant design challenge.

Pointing requirements include pointing accuracy and pointing stability. Many factors contribute to each of these, which must be carefully budgeted and verified. The deployable reflector is only one of the contributors to pointing errors. As mentioned in Section 8.8.1, under thermal distortion loss, the best-fit analysis performed on the distortion data separates the rigid body motions from the elastic distortions. Those rigid body motions represent the reflector's thermal distortion contribution to the pointing error. Similarly, the moisture distortion analysis results in a BoL contribution to pointing. In addition, to the reflector, the reflector boom, feed support, and the bus itself all contribute to the thermal and moisture distortions, and must be accounted for in the system pointing budget. Additionally, dynamic interaction between the reflector and its boom with the control system provides yet another contribution to pointing inaccuracy.

Finally, the pointing error contributors are bucketed into various groups, depending on the time domain. For example, ground alignment accuracy, launch hysteresis effects on the reflector, boom and deployment mechanisms, moisture desorption effects, and average orbital temperature distortions are all contributors to the initial "pointing accuracy," or misalignment. Often, much of the effect of this initial misalignment is mitigated by various calibrations during initial on-orbit testing. In contrast, other variable or delayed contributors are "pointing stability" contributors. Those, in turn, are usually divided into short-, medium-, and long-term stability contributors. Dynamic events due to station-keeping and momentum

dumping are typical short-term stability error contributors, while thermal distortion diurnal errors (typically occurring over one orbit period) represent medium-term contributors. Finally, long-term errors include such contributions as creep, orbital radiation effects, and the difference between the mean BoL and EoL thermal pointing contributions.

8.8.3 Thermal and Environmental Requirements

Thermal analyses and testing of deployable reflector systems are significant activities that are usually performed in the stowed, deployed, and "deploying" conditions of the reflector, with the objectives of ensuring that all materials and components remain within their safe temperature ranges and of providing data for use in the thermal distortion/pointing analyses previously discussed. In parallel with the initial analyses, thermal design and test activities take place in order to determine the appropriate thermal finishes and blankets needed, and to design and plan the appropriate testing.

Other environmental design drivers for a deployable reflector include effects of exposure to radiation and UV rays on the CTEs and dimensional stability of the materials, as well as effects of micro-meteoroids on survivability and surface integrity of the reflector (especially for an inflatable reflector). Another important requirement for all large reflectors is their optical transparency. This affects the electrical power subsystem, because the reflectors often shadow the solar panels (at least at certain times/seasons), as well as the ACS operation/fuel consumption, because solar pressures tend to push the spacecraft around. Therefore, minimum transparency requirements are often specified for deployable reflectors and could limit the acceptable mesh density; otherwise, a larger solar array (for power consideration) and/or a solar sail (for ACS considerations) may be required.

References

[1] Mikulas, M. M., and Thomson, M. "State of the art and technology needs for large space structures," Chap. 3 in *New and Projected Aeronautical and Space Systems, Design Concepts, and Loads of Flight-Vehicle Materials, Structures, and Dynamics—Assessment and Future Directions*, Vol. 1. New York: ASME, 1994, pp. 173–238.

[2] Archer, J. S., and Palmer, W. B., "Antenna technology for QUASAT application," in *Large Satellite Antennas and Space Technology*, Part 1, NASA CR-2368, 1984.

[3] Guest, S. D., and Pellegrino, S., "A new concept for solid surface deployable antennas," *Acta Astronotica,* Vol. 38, No. 2, 1996, pp. 103–113.

[4] Bassily, S. F., "System for compact stowage of segmented dish reflectors," U.S. Patent No. 6,191,757, Feb. 2001.

[5] Tan, L. T., and Pellegrino, S., "Thin-shell deployable reflectors with collapsible stiffeners: approach," *AIAA Journal*, Vol. 4-4, No. 11, Nov. 2002.

[6] Freeland, R. E., and Helms, R. G., "Deployable antenna structures technologies," Large Space Apertures Workshop, California Institute of Technology, Nov. 2008.

[7] Helms, S. K., "Development and testing of an inflatable, rigidizable space structure experiment," Thesis, Department of the Air Force, Air Force Institute of Technology, Write-Patterson Air Force Base, OH, Mar. 2006.

[8] Campbell, G. K. C., "Large Furlable Antenna Study," prepared for California Institute of Technology, JPL, Contract #945082, Lockheed Missiles and Space Company, D384797, January 20, 1975.

[9] Thomson, M. W., "Mechanical vs. inflatable deployable structures for large apertures," Large Space Aperture Workshop, Keck Institute for Space Sciences, Nov. 2008.

[10] Mobrem, M., Keay, E., Marks, G., and Slimks, E., "Development of the large aperture reflector/boom for the SMAP spacecraft," ESA/ESTEC, Noordwijk, The Nederlands, Oct. 2012.

[11] Bassily, S. F., "Arbitrarily shaped deployable mesh reflectors," U.S. Patent No. 7,595,769, Aug. 2007.

[12] Thomson, M. W., "The AstroMesh deployable reflector," Antenna Propagation Society International Symposium, IEEE, Vol. 3, 1999, pp. 1516–1519.

[13] Thomson, M. W., "AstroMesh deployable reflector for Ku- and Ka-band commercial satellites," *29th AIAA International Communications Satellite Conference and Exhibit,* May 2002, AIAA-2002-2032.

[14] Bassily, S.F., "Method and apparatus for grating lobe control in faceted mesh reflectors," U.S. Patent No. 7,570,226, Aug. 2007.

[15] Bassily, S. F., and Uribe, J., "Mesh tensioning, retention and management systems for large deployable reflectors," U.S. Patent No. 5,969,695, Oct. 1999.

[16] Bassily, S. F., and Uribe, J., "Continually adjustable non-return knot," U.S. Patent No. 5,030,037, Oct. 1999.

[17] Bassily, S. F., "Edge-supported umbrella reflector with low stowage profile," U.S. Patent No. 5,963,182, Oct. 1999.

[18] Bassily, S. F., and Rodriguez, D. J., "High-torque apparatus and method using composite materials for deployment of multi-rib umbrella-type reflector," U.S. Patent No. 6,028,569, Feb. 2000.

[19] Sullivan, M. R., "LSST (hoop/column) Maypole antenna development program, Part 1, Phase 1," NASA Contractor Report 3558, 1982.

[20] Hudgepeth, J. M., "Influence of fabrication tolerances on the surface accuracy of large antenna structures," AIAA Journal, Vol. 20, No. 5, May 1982, pp. 680–686.

[21] Energia-GPI Space website, "Space Experiment: Reflector," http://www.egs.cosmos.ru/eng/freport.htm.

[22] Ozawa, S., "Large Deployable Reflector on Engineering Test Satellite VIII," http://www.kiss.caltech.edu/workshops/apertures2008/talks/ozawa.pdf.

[23] Ruze, J., "Antenna tolerance theory—A review," *Proc. IEEE*, Vol. 54, pp. 633–640, 1966.

[24] Lowe, E., Josephs, M., and Hudgepeth, J., "Advanced deployable reflectors for communication satellites," AIAA/AHS/ASEE Aerospace Design Conference, Irvine, CA, AIAA 93-0978, Feb. 1993.

[25] Hudgepeth, J. M., "Accuracy potentials for large space antenna structures," presented at the 39th Annual Conference of the Society of Allied Weigh Engineers, SAWA Paper No. 1375, Index Category No. 18, May 1980.

[26] Hodges, R., Sands, S., Huang, J., and Bassily, S., "High capacity communications from Martian distances. Part 4: Assessment of spacecraft pointing accuracy capabilities required for Ka-Band reflector antennas," *12th Ka and Broadband Communications Conference,* Naples, Italy, Sep. 2006.

CHAPTER 9

Mechanical Aspects of Reflector Antennas for Space Applications

Michael J. Noyes and Dawn B. Valero, Applied Aerospace Structures Corporation

This chapter provides the reader with a framework and top-level understanding of the elements and requirements that must be considered in the successful design, fabrication, and testing of a spaceflight antenna reflector. It is a guide based on more than 30 years of professional and personal experience in engineering, fabricating, and testing spaceflight antenna reflectors and systems.

Because the state of the art in antenna reflector design is continually advancing, this chapter is purposely written to provide general recommendations for configuration, design approach, materials, and testing. A wealth of information is available from composite materials suppliers, technical papers, and organizations such as SAMPE, so it is left up to the reader to perform the detailed analyses, engineering, and materials research required to establish the best possible specific choices relative to the set of requirements for the particular reflector type being considered. A successful antenna reflector design is always a carefully balanced combination of many specific and interdependent choices that must all work together to achieve the best possible results.

9.1 Mechanical Considerations for Spaceflight Antenna Reflectors

The fundamental function of an antenna reflector is to collect, focus, and direct the energy radiated by an RF source, which is commonly single or multiple waveguide horns or other type of radiators. Sometimes multiple surfaces are used in the reflector antenna subsystem optics to further enhance antenna performance such as a subreflector/main reflector system. The reflector system may also contain more than one "antenna" such as a dual-shell (dual-polarized) reflector or a subreflector

that is frequency selective. In both of these cases, the antenna is effectively two antennas packaged into the same volume.

From a physical packaging perspective reflectors systems fall into three broad categories:

1. Fixed-mount reflectors that have rigid RF surface(s) and are directly mounted to the satellite structure or other fixed appendage and remain in the same relative alignment on orbit as for launch.
2. Deployable reflectors that have rigid RF surface(s) and are moved (deployed) via one or more mechanisms once on station to a different alignment or configuration from launch.
3. Furlable reflectors that have multiple-piece or deformable surfaces and are unfurled to the final desired surface shape after launch. An unfurled reflector may also be moved via one or more mechanisms once on station to a different alignment or configuration on orbit as for launch.

Note that the reflector systems of the last two entries above may also be movable or steerable on orbit to either purposefully point the antenna beam or to perform an on-orbit beam correction or fine alignment. This is quite common on satellites that have more than one antenna where the relative pointing of multiple antennas needs to be very precise.

9.2 Spaceflight Reflector Design Requirements

The exact physical requirements for a spaceflight reflector are dependent on the mission environmental and structural requirements as well as the RF performance requirements. The RF and mechanical requirements are interrelated and interdependent to varying degrees.

Antenna reflectors are primarily RF components and function as key mission-critical items in the communications payload. The primary electrical performance parameter of the reflector (gain) is directly related to its aperture size. In almost all instances for commercial communications antennas, it is desirable to have the largest aperture possible, thus increasing the gain, which reduces the amount of transmitter power required and improves the signal-to-noise ratio (SNR) of the receiving system. The optimum comsat reflector will have the largest aperture, most accurate surface figure, lowest mass, and lowest cost while satisfying all of the other mission requirements. For science missions, the reflector only needs to be large enough to take full advantage of the available bandwidth and provide an acceptable SNR.

There are many established mechanical approaches/solutions to spaceflight reflector design depending on the exact RF and mission requirements, but in the end they are all compromises to some degree made to satisfy the basic requirements discussed next. Of course, the design engineer must also comply with the two critical nontechnical program requirements of cost and schedule, which for a typical commercial program almost always significantly constrain the design space.

9.2.1 RF Requirements

9.2.1.1 Aperture Size (Gain, Beamwidth)

The ideal reflector will have an aperture size large enough to minimize the payload power requirements while still satisfying the coverage (beamwidth) requirements. For a parabolic antenna the gain increases and the 3-dB beamwidth decreases with an increase in aperture diameter.

9.2.1.2 Reflectivity of Surface

The ideal reflector will have a perfectly RF reflective (conductive) surface at the specified RF frequency resulting in no ohmic losses.

Although a homogenous, solid, and continuous surface is optimum from an RF performance perspective, nonuniform, woven, or otherwise distributed materials are often used for their acceptable electrical properties and very good mechanical, thermal, and structural properties.

In general, carbon fiber composite communications reflectors operating below 30 GHz are only occasionally metalized and reflectors operating above 60 GHz are often metalized.

9.2.1.3 Accuracy of Reflector Shape

The ideal reflector will have a perfectly accurate surface contour resulting in no losses due to scattering, diffraction, or phase-induced errors. RF performance degradation sensitivity due to surface irregularities increases as the RF frequency increases (wavelength decreases).

Reflector shape accuracy is typically measured as a rms of the deviations of measured points to their ideal locations. Extremely high frequency reflectors such as those used on radiometers often require surface contours with rms accuracies approaching the submicron level. In addition to RMS surface errors, the peak errors need to be carefully controlled for reflectors used for shaped or contoured beam applications.

9.2.2 Mechanical Requirements

9.2.2.1 Size/Volume

The reflector must fit within the available space inside of the launch vehicle fairing that is not already occupied by the satellite structure and its other appendages. This often means that the reflector must be deployed from the satellite structure or and sometimes also unfurled. As a rule, deploying and unfurling add complexity (cost), reduce the reliability of the antenna subsystem, and are employed only when definitively required by a top-level systems engineering design trade-study.

9.2.2.2 Stiffness

For launch the ideal reflector would be infinitely rigid, but in reality a reflector will be designed to have sufficiently high stiffness-to-mass ratio to prevent any dynamic

interaction or coupling between the reflector and the fundamental launch vehicle and spacecraft modes in the launch configuration.

On orbit, the reflector system needs to have a stiffness that is greater than and that does not couple unfavorably with the attitude control system frequency or other deployed appendages such as solar arrays. The on-orbit (deployed) stiffness is not very often a structural design driver for a reflector, except for large furlables, but must still be carefully considered at the system level.

Ground-handling (1G) effects must also be considered for fabrication, alignment, and RF testing. Special fixturing, tooling, and alignment procedures may be required. Great care must be exercised to ensure that the alignment achieved on the ground under 1G is replicated on orbit under 0G. For large reflectors, especially furlables, fixturing to eliminate or compensate for effects due to gravity deforming the reflector can be very challenging.

9.2.2.3 Strength

The reflector structure must be strong enough to survive launch loads (quasi-static, dynamic, acoustic, pressure, thermal), deployment loads, and on-orbit load cases (usually thermally driven). Although these are the typical minimum margin load cases, in some special instances other loads may need to be considered. For instance, it is not unusual for Mars missions to use the reflector as a part of the aero-braking surface of the spacecraft when entering orbit, and in some cases the launch vehicle fairing is jettisoned early enough during launch that free molecular heating may also be a design case.

Special consideration may also need to be made for ground handling including shipping, RF range testing, and deployment testing.

9.2.2.4 Mass

Being a spaceflight structure, the ideal reflector will have a mass that is as low as possible while meeting all of the other requirements.

The reflector may also need to carry nonstructural mass such as mechanisms, thermal control (blankets and paint) and occasionally other sensors, antennas, and balance mass.

Reducing and minimizing mass without complicating the design is often the single most effective means of also reducing fabrication costs and schedules, and because the loads are predominantly dynamically generated it also serves to reduce the interfacing loads and stresses.

9.2.2.5 Survivability (Thermal, Radiation, Atomic Oxygen, and So Forth)

The ideal materials used for reflector fabrication will not be susceptible to degradation from the on-orbit environment. The exact environments will vary depending on the mission profile, whether Earth orbit (low, medium, or geostationary) or interplanetary. For certain environments such as low Earth orbit, which still has some oxygen atom presence (atomic oxygen), additional protection will be required for a typical composite reflector structure to prevent atomic oxygen erosion.

9.2.2.6 Dimensional Stability

The ideal reflector will not deform or distort due to on-orbit effects such as temperature changes/gradients or moisture dryout. With currently known materials and manufacturing technology, it is not possible to create a perfectly stable reflector, but clever combinations of materials and design configurations can produce deformations that have very little or negligible effect on the RF performance of the reflector.

9.2.3 Reflector Geometries

9.2.3.1 Common Geometries

The most fundamental reflector shape is the parabola, which is a parabolic curve rotated about the focal axis. By means of simple ray tracing, energy originating at the focus of the parabola will be collimated and radiated parallel to the focal axis of the parabola. A center-fed system cuts the resulting surface with an aperture centered on the focal axis, and an offset system cuts the parabolic surface with an aperture parallel to the focal axis, but offset from it.

Dual-reflector systems utilizing a subreflector are also very common. The subreflector collects a larger percentage of the energy radiated by the feed and directs it more efficiently onto the main reflector, thus reducing spillover and increasing the performance (gain, efficiency) of the antenna.

Most reflectors are circular in aperture when viewed along the antenna boresight axis. An offset parabolic reflector will be elliptical when viewed in the plane of the edge of the reflector. If the reflector is of a parabolic surface contour and has a circular aperture cut in an axis parallel to the focal vector, then the rim of the reflector will also lay in a plane regardless of whether the reflector is center fed or offset. This simple geometric fact can often be used to simplify tooling, assemblies, and inspections.

Commonly used fundamental antenna reflector geometries include the following:

- Parabolic;
- Cassegrain;
- Gregorian;
- Axially displaced ellipse (ADE);
- Shaped reflectors;
- Dual-surface reflectors, either polarization selective or frequency selective.

It is interesting to note that due to commercially available antenna design software packages it is increasingly rare to see an antenna design that is a simple geometric contour and not a “shaped” modification.

9.2.3.2 Modified (Shaped) Surface Geometries

Both the reflector aperture and surface shape may be modified from the parent (simple) geometry to influence the distribution of the RF energy, thus optimizing

the antenna coverage, reducing spillover, or minimizing sidelobe levels. Modern communications antenna reflectors commonly utilize reflector surface shaping as a means to measurably improve RF performance. The antenna design starts off with simple standard parent geometry, such as a parabolic surface, and then using the RF design software, the parent surface is discretely displaced, modifying the phase front radiated from the reflector to create a far more efficient and optimized energy distribution. The magnitude of the surface deviation from the parent surface is a function of the frequency (wavelength) of the energy being radiated. Higher frequencies (shorter wavelengths) will have fundamentally less physical surface deviation than lower frequencies (longer wavelengths).

Shaped surface reflectors can present both structural and fabrication challenges, depending on the amount of physical deviation from the parent surface. At lower RF frequencies the shaping of the reflector can cause quite radical peaks and valleys that influence the geometrical structural properties and resulting stiffness of the assembly, making the reflector shell more susceptible to mechanical and thermoelastic instability. Figure 9.1 shows the manufactured surface of a somewhat typical shaped surface reflector antenna.

Fabrication of a composite reflector shell with large surface deviations also presents issues and challenges. For example, maintaining proper fiber orientations to achieve the desired mechanical properties while forming the material to the correct contour requires careful materials choices and layup designs that may include darts, patches, and ply-pattern development. Another challenge, peculiar to sandwich-style construction, is ensuring that the core conforms to and is fully bonded to both the front and rear faceskins. Obviously, if the curvature is pronounced (small radius of curvature) and assuming a constant core thickness, the front and rear faceskins will have quite different contours. When faced with this difference, a design/materials decision must be made: (i) invest in two mandrel tools, one with the front contour and one with the back, and pre-cure both skins; (ii) co-cure the rear faceskin directly against the core, supported only by the inside core and a caul-sheet on the backside; or (iii) machine or shape the core to provide the same contour to the front and rear faceskins.

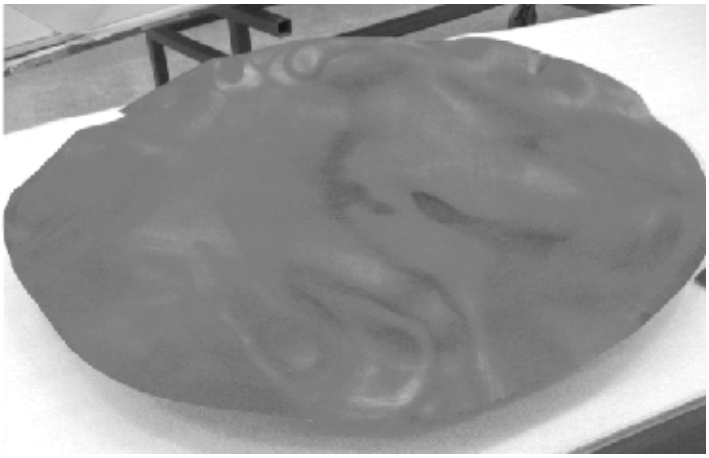

Figure 9.1 Radically shaped reflector shell. (Copyright AASC 2012.)

It is important for the mechanical design engineer to work closely with the antenna RF engineer to ensure that the fabrication techniques and implications are balanced against the theoretically optimized and idealized RF surface. It is pointless, but altogether too common, to have the RF engineer optimize the analytical RF surface to gain an additional small fraction of a decibel of performance only to discover that it is not feasible to fabricate the reflector accurately enough to realize that gain.

9.2.3.3 Modified (Noncircular) Reflector Apertures

The launch vehicle envelope available to package the reflector will almost always accommodate shapes other than the classic circular aperture. Enlarging the aperture area of the reflector can capture energy from the feed that might spill over the edge of the reflector, theoretically increasing the antenna gain. Of course, nothing is free and for a conventional reflector with a single feed a noncircular aperture will degrade some key antenna performance parameters. But with surface shaping or a multiaperture feed, it is often possible to gain an RF performance benefit from the additional area of a noncircular aperture while minimizing the resulting negative consequences. With modern RF optimization techniques, it is not uncommon to see reflector apertures that are far from circular and in some instances look square or rectangular in shape with rounded corners. These are commonly termed *super-elliptic apertures*.

9.3 Mechanical Design Considerations

Mechanical design considerations are outlined in the subsections below and possible approaches/solutions are suggested in the following construction considerations section. Although presented separately, design, analysis, test, and fabrication issues must be balanced against each other and also against the program limitations of cost and schedule.

9.3.1 Reflector Support Points and Interfaces

Probably the single most influential driver to the structural design of the reflector is the location and characterization of the support points or launch restraints. The more efficiently the reflector is supported, the less supporting structure that will be required to meet the dynamic loads and stiffness requirements. For example, a reflector that is cantilevered from one edge is going to be far more complex and challenging mechanically than one that it supported by four points equally spaced around a circular aperture. The launch configuration geometry is a key mechanical systems-level commitment, usually made very early in the program design phases. As a result the reflector design engineer often has very limited design flexibility in this regard.

The structural characteristics of the reflector launch-lock interfaces and deployment mechanisms must also be carefully considered during the reflector design and analysis activities. Although simple and idealized fixed-base assumptions for these interfaces may be convenient, the materials, stiffness, and degrees of freedom

of the restraints are often so influential that a fixed-base assumption may unrealistically drive the structural design of the reflector. Incorrect assumptions can easily lead to dramatically over- or underdesigning the reflector by either adding mass or potentially resulting in a structural failure during unit-level or subsystem testing.

The local interface mechanical properties and characteristics are just as important as the interface geometry and fixity. A carbon fiber reflector mounted to an aluminum satellite structure via titanium or other metallic interfaces/mechanisms may result in significant thermal stresses due to differences in temperature and the coefficient of thermal expansion (CTE). The reflector, satellite structure, and mechanism design teams will all need to be aware of the interface loads and the analysis assumptions used to generate them. Whether it is a restraint that needs to separate, or a hinge or gimbal that needs to deploy, static loads due to strain resulting from thermal, hygroscopic, or simple mechanical misalignment can significantly impair a mechanism's ability to function as designed.

Environmentally testing the reflector also poses similar issues with fully and correctly representing/simulating the interface characteristics. For a reflector unit-level test, it is impractical to design a vibration test fixture that accurately represents the flight structure interface; however, it should be designed such that the test considers the system-level loads, local stresses, and so forth, but not by a large margin that would overdesign the reflector and add unnecessary mass. How the reflector is going to be tested should not be overlooked and must be included or at least considered as a part of the reflector design and analysis cycle. Oftentimes the local stresses in the test configuration will not just envelop, but will be quite different from the flight stresses, and may even be a minimum margin analysis case and in some cases a design driver.

9.3.2 Mass

The mass of a reflector assembly is driven by the requirements and environments listed below but it is fundamentally dictated by the physical size (aperture), the support points (interface locations or launch locks), and the launch environment (loads). Remember that if a reflector did not have to survive the launch environment, it could be something as simple as a piece of electrically reflective foil with just enough structural stability to maintain its shape and location relative to the parent spacecraft on orbit. As with any good structural design, the design engineer logically begins with the elements that are already defined (i.e., the RF surface and interfaces) and then only adds just enough reinforcing structure to satisfy the reflector requirements. An efficient design approach with simple load paths using efficient geometry will provide the best performing, most economical solution at the lowest mass.

Reflectors are rarely a structural load path and are primarily dynamically driven; therefore, keeping the mass of the reflector low is a key contributor to keeping the launch loads low, the stiffness and stability up, and, if implemented intelligently, controlling the costs and schedule. Less material, fewer layups, less handling, less fixturing, and more robust deployment and pointing mechanisms are all beneficial natural consequences of minimizing mass. Keeping the launch-mass low is always a key goal in spaceflight design, but deliberately and carefully considering mass in every aspect of the reflector design pays off in all areas and especially

at the system level. Obviously, practical and financial limits to keeping mass to a minimum must not be disregarded. Too much emphasis on mass reduction can result in a design that is difficult and expensive to fabricate, or not structurally robust, or that employs higher cost or higher performing materials with little or no system-level benefit.

9.3.3 Stiffness

The system-level stiffness requirement for the first mode frequency of a reflector assembly in the launch configuration varies depending on the size of the reflector and the exact program requirements. For smaller assemblies (<1m) the requirement is commonly that the first mode exceed 100 Hz. If the reflector first mode frequency exceeds 100 Hz, then it will not couple with the primary modes of the spacecraft and/or launch vehicle, thus simplifying the satellite coupled loads analysis.

For certain programs, a mass versus stiffness evaluation or assessment at the systems level may be warranted. The trade-space might be to design a lighter, less complex and probably cheaper reflector that requires more analysis (inclusion in coupled loads) and possibly more testing, or to design a stiffer, more expensive, and possibly heavier reflector that is consistent with simplified and robust analysis and test assumptions.

For larger reflectors (approximately 1.5m to 2.5m) it is common to see a minimum stiffness requirement in the range of 35 to 50 Hz (or higher) depending on the critical modes of the spacecraft/launch vehicle assembly. The minimum first mode frequency is selected to ensure that the unit is safely above and does not dynamically couple with any major spacecraft or launch vehicle modes. Significant dynamic coupling can be very difficult to predict and can produce excessively high load factors. A flexible body representation of a large reflector is almost always an important part of the coupled loads cycle for the spacecraft and launch vehicle.

Very large reflectors (>2.5m) or antenna assemblies generally cannot be mounted with sufficient rigidity to the spacecraft to be safely above the spacecraft/launch vehicle modes. In such a case the reflector assembly may need to be tuned in stiffness characteristics so as to fall between and not couple significantly with any of the other major spacecraft modes. When the prediction method uncertainty is large, it is sometimes necessary to provide tuned-stiffness features in the design, allowing the modal characteristics to be measured and adjusted in the flight hardware at the subsystem- or system-level test phase. It should be obvious that this requires considerably more design and analysis effort, is particularly challenging to implement, and is not an attractive option.

9.3.4 Stability

The stability of the reflector's surface shape and its pointing orientation are the most critical elements to the on-orbit RF performance of the antenna system. Any degradation of the reflector surface figure or rigid body movement of the reflector will impact the communications payload alignment and performance and, as such, must be kept to a practical minimum.

The most obvious prime drivers for on-orbit reflector stability are the temperatures of and thermal gradients within the reflector structure. Two fundamental

design areas need to be addressed: (1) reducing the temperature extremes and thermal gradients by efficient thermal control and good thermal design, and (2) fabricating the reflector assembly from materials with a near-zero CTE and coefficient of moisture expansion (CME) so that the reflector assembly is largely unaffected by the temperature/vacuum environment.

There are limits and practical constraints to both thermal design and the ideal zero-CTE structure design and fabrication. Therefore, it is important that in addition to having a low absolute value of CTE, the reflector design configuration should have some flexibility that allows for the RF surface shape to be as insensitive as possible to temperature extremes, gradients, and magnitude/variations in CTE.

Understanding that the parameters affecting the thermal distortion of a reflector go beyond those typically incorporated into a structural finite element model (FEM) is critical. FEM techniques using 2D plate or laminate elements may be valid for dynamic and stress analysis, but discount through-thickness properties. Neglecting the mismatch between through-thickness and in-plane properties can significantly influence the accuracy of a structural model used to predict thermal distortion. Joint design is one area that tends to perform differently than what is predicted in a structural model due to highly localized characteristics that are not accounted for in a typical FEM. It is unrealistic and insufficient to purely increase the amount of elements and complexity of the structural model and expect it to account for these factors. It is very difficult to analytically account for all possible boundary condition and material property variations, and highly theoretical approaches commonly under- or overpredict thermal stresses and strains. Establishing modeling techniques that are intelligently correlated to measured thermal distortion testing of both coupons and full reflectors is a much better, accurate, and reliable process; however, it is also more time consuming and can be very expensive to execute well.

An example of how an FEM might underpredict thermal distortion is a simple multilayer composite laminate cured into a 90-deg "L" shape. The laminate will not maintain an angle of 90 deg over temperature due to the through-thickness CTE being much higher than the in-plane CTE. This effect will not be accurately predicted by a plate or laminate FEM because of the 2D simplification of that type of element. Similarly, a curved sandwich structure will behave the same way due to the high through-thickness CTE of a typical honeycomb core. Measuring through-thickness laminate CTE with any accuracy is challenging, and even if a measurement were to be successfully completed, using that value in an FEM will probably not result in an accurate distortion prediction because of the detailed micromechanical interactions of the core, film adhesive, matrix resin, and fibers. A better first-order approach is to measure distortion of a simple coupon and then tune the specific uncertain material properties in the FEM to match the measured results. There are many instances like this in the construction of a reflector that are not modeled by the typical FEM or not modeled in a way that will accurately predict the thermal distortion performance of the reflector.

9.3.5 Dynamics Considerations

The primary purpose of dynamics analysis in reflectors is to predict the mechanical accelerations, usually dimensioned relative to the acceleration of gravity on Earth

and returned to G-loading. As a starting point, systems engineers sometimes turn to the satellite/launch vehicle generic mass acceleration curve (MAC), which presents a conservative design-level G-loading as a function of the mass of the subsystem. The MAC is not usually an appropriate source for G-loading of a reflector because the reflector's distributed loading and very light mass make it an outlier from the database of all the panel-mounted components' responses that form the basis of the MAC envelope. Depending on the launch configuration, MAC-loading is sometimes way too high or way too low. A combination of design experience (heritage) and coupled loads or base-drive systems analysis is required to develop rational quasi-static design loads for antenna reflectors.

In addition to G-loading, sometimes a large stiff antenna with a significant footprint will stiffen the satellite structure to which it is mounted, which means that in addition to considering G-loading of the reflector itself, the interface and reflector structure must be able to accommodate forces and moments from satellite structure modes and transfer-orbit thermal conditions.

Because the reflector structure is very lightweight and very stiff, the design level loads are typically quite high. Nominal G-loads of 30G to 50G are common and peak local responses of as high as 100G are not unusual. High G-loading can make designing a test to envelop and verify these loads quite challenging. Because of certain basic test practical limits, it is often necessary to design the reflector structure for the test environment, which safely envelops the stresses of the flight environment, rather than designing the test to envelop flight without exceeding any structural margins.

9.3.6 Acoustics Considerations

The things that make a reflector design better from a performance standpoint—larger aperture (more surface area), higher stiffness, lower mass, and so forth—are also those things that will make it more responsive to acoustic energy. For larger aperture reflectors (>1.5m) it is common for the acoustic pressure environment to produce the highest loads (lowest structural margins) at the reflector interfaces and surrounding load-bearing areas of the structure.

The acoustic spectrum is defined by the launch vehicle/satellite top-level specification, but determining the response of the reflector structure to this dynamic pressure loading, and then backing out load factors (G's) with which to perform strength and stress analyses, can be challenging to do with any reasonable accuracy. Part of the challenge is that the reflector responses are different when mounted to the spacecraft structure than when a fixed-base or "free-free" approach is used. Two different philosophies of addressing the acoustic environment on reflectors have emerged and are discussed next. Either is valid when followed consistently.

9.3.6.1 Fixed-Base Approach

Reflectors typically exhibit higher acoustic test responses when mounted to a fixed base than when mounted to a satellite structure. Test data from multiple past program indicate that the reflector assembly's Q (dynamic response ratio) is generally and consistently higher in a fixed-base (test) configuration than on the satellite structure. In addition, a fixed-base reflector configuration will result in significant

excitation of the out-of-plane fundamental reflector modes, which will also produce significant loading and local stresses at the support interfaces. As a result, a fixed-base reflector assembly-level acoustic test almost always envelops and in some cases overtests a reflector subsystem as compared to the final assembly-level test. The loading at the support interfaces is usually enveloped by the low-frequency reactions, and the local loading of all the discrete bonded and laminated connections is commonly enveloped by the high-frequency responses. The design engineer can take advantage of this envelope if the reflector can be designed to and tested to this boundary condition without having to resort to painfully heavy or expensive structural design changes. Typically, reflector designs that are very lightweight and have well-conceived joints without significant stress-risers can be produced with this conservative approach. The significant benefit of this is that the reflector-level acoustic test becomes an excellent screen for design and workmanship of the reflector structure. Since even the in-plane interface loads are often enveloped by this fixed-base acoustic testing, sine vibration, random vibration, and static or sine-pulse testing are often not necessary.

9.3.6.2 Free-Free Approach

Acoustic testing reflectors that are supported on a highly elastic and highly damped foundation, hanging from elastic cords for example, still exhibit significant high-frequency responses, which induce representative stresses in local bond-joints and laminates. The first flexible-body (free-free) mode of a reflector is typically a twisting-style mode, which can put significant stress on the overall rib to shell joints. Responsiveness of this twisting mode and also the many high-frequency local modes of a reflector structure will make a free-free acoustic test a more than adequate screen. If a reflector design is well tested by sine, random, and/or static (proof or sine pulse) tests, then a free-free acoustic environment will avoid the likely overtest situation of a fixed-base test.

9.3.6.3 Reducing Acoustic Responses

Logically, the acoustic sound pressure environment reacts against impervious or high stiffness surfaces more than porous or compliant surfaces. It is somewhat impractical to create a highly damped reflector surface; however, it is possible to create a surface that has enough porosity that it does not respond to acoustic pressure in any significant way. The fact must not be ignored, however, that a reflector laminate with "holes" will suffer measurable degradation in RF reflective properties as the RF frequency increases, but for lower RF frequency large aperture reflectors it has proven to be a very successful solution.

One very convenient open-weave construction solution is to use a triaxial weave material. Even at 2 or 3 plies thick, it still has enough open area to significantly reduce acoustic responses while providing acceptable RF performance even above 10 GHz.

9.3.7 Thermal Considerations

Common thinking is that any materials used in a composite structure fabrication should have a glass transition temperature (Tg), the temperature when the material starts to soften, above the hot service temperature for the assembly. In reality, the published Tg does not define a phase change or change of state at an exact temperature when a polymer becomes unusable; instead, it defines the onset of softening. It is not uncommon for polymers, matrix resins, and adhesives to see use above their Tg with careful consideration of the requirements and properties at these temperatures.

Modern resin systems used for spaceflight hardware fabrication are considerably better than they were in the 1980s and early 1990s. Current modified epoxy and cyanate systems have excellent resistance to microcracking at cryogenic temperatures and have a high enough Tg that it should not pose an issue for most requirements. However, resin properties are affected by temperature, so if there is a defined structural load case at a cold or hot temperature, the analysis must account for the actual properties of the laminate at those temperatures. As a general rule, the structural properties that are most affected by temperature are going to be resin matrix driven, such as interlaminar or flatwise characteristics, and not fiber driven, such as in-plane stiffness or strength.

The design engineer must also be aware of the temperature-dependent thermal properties of composite laminates and bond joints. Thermal conductivity and especially heat capacity (sometimes referred to as thermal mass) vary considerably with temperature. For a lot of missions this can be significant when predicting temperature extremes and gradients. The heat capacity of a carbon fiber laminate will vary by more than an order of magnitude over the typical temperature ranges seen by a geostationary satellite reflector.

With careful selection, elevated-temperature curing film adhesives used for sandwich bonds should not pose an issue for most applications. However, film adhesive properties also change with temperature and in some instances this can be significant to the design. If the film adhesive is being used to bond materials with differing CTEs, such as a metallic fitting to a carbon fiber laminate, thermal strain will be induced that can cause local and sometimes global surface shape distortion. Because of the CTE mismatch between the matrix and fiber, residual strain is present in all laminates when returning to room temperature from the cure temperature, but this influence is more pronounced in sandwich construction.

For ease of fabrication, joint and fitting bonds are commonly made with room temperature curing epoxies, which can be the limiting factor to the hot service temperature extremes for the assembly. The Tg for room temperature epoxies should be carefully evaluated because many are below 100°C, which is a common design limit temperature for spaceflight reflectors. As explained above, a low Tg indicates that the temperature-dependent properties of the adhesive and the bond joint should be considered relative to the loading. A design engineer should also understand that manufacturer quoted service temperatures are not usually the Tg of the material, but the temperature when the adhesive properties drop below a certain shear strength. Once again, it should be noted that many designs are performing successfully in orbit even though they are experiencing temperature extremes beyond the Tg or recommended use temperatures of the materials used for the

construction; however, this does require careful consideration of the materials performance at those temperatures.

9.4 Construction Considerations

9.4.1 Design Configuration

The RF performance of the reflector is driven by the precision (shape, orientation, and aperture) and RF reflectivity of the reflector surface. It is the design engineer's job to maintain these RF characteristics over the on-orbit environments as best as possible while satisfying the structural, typically launch-driven, requirements for the reflector.

Any reflector design will begin with the RF surface figure provided by the antenna design engineer and the structural interfaces from the reflector to the satellite structure. For a fixed-mount reflector, the orientation (pointing) is also fixed so there is often little latitude in where the reflector aperture can be placed relative to the physical satellite structure, sensors, or other equipment that may be packaged close to the reflector and the launch vehicle fairing envelope. The interface locations from the reflector to the structure may or may not have much available real estate to attach to, and the interfacing structure may have to avoid other components such as electronics boxes mounted to the satellite underneath the reflector. The reflector thermal requirements are typically focused on the temperatures for the reflector itself. However, other requirements are occasionally imposed, such as isolating the reflector thermally from the satellite bus and payload, or perhaps using the reflector aperture as additional radiator area.

For a deployable reflector, the design team will have at least a little more latitude to package the reflector since the kinematics of deploying the reflector allow it to be stowed relative to the satellite structure with some moderate degree of flexibility. The configuration of the launch-lock and deployment mechanisms is often limited in physical location to whatever is convenient and available on the primary structure and in quantity by mass and reliability considerations.

Once the reflector surface and interfaces have been located, the goal is to provide sufficient structural support to the reflector surface at minimum mass while staying within the available envelope and maintaining the surface figure accuracy and pointing over the life of the reflector, including in the test, launch, and on-orbit environments.

9.4.1.1 Sandwich

Probably the most prevalent reflector construction medium is a thin laminate-skinned honeycomb sandwich. The front-face laminate, cured against a controlled surface mandrel (mold tool) provides the RF reflective surface. The sandwich construction, a core with a back-face laminate, provides the required structural stability and stiffness in a very mass-efficient manner. There are many viable choices for the sandwich constituents used for this type of construction. Faceskin material and form choices include uniaxial tape, woven fiber fabric, and triaxial fabric. The

honeycomb core material is often also a composite, either aramid or carbon fiber, and occasionally aluminum where the requirements allow for the higher CTE.

The reflector shell must be structurally connected to the interface locations (restraint points) to provide a load path for stowed stiffness and reacting dynamic and acoustic loads. A convenient and efficient method for doing this is to construct a reinforcing sandwich rib structure "egg crate" on the rear of the reflector shell as shown in Figure 9.2. As well as being an efficient and cost-effective method for stiffening the shell, using the same sandwich construction for the shell and the ribs also matches the CTEs, which has advantages in managing thermal distortion.

Obviously the ribs must be structurally connected to the shell, to each other at the rib nodes, and to the support interfaces. Usually this attachment is achieved via an adhesive bond fillet. In areas of higher stress, some form of carbon fiber reinforcement or angle clip will often be required to increase the load-carrying capability of the joint. These structural connections can and will drive thermal distortion to some degree due to the joint having a different stiffness and CTE than the ribs and shell. Minimizing the distortion effects should not be overlooked in the detailed design of the reflector. In addition, the strength and stiffness of these joint designs are almost always both critical and somewhat difficult to accurately predict analytically.

Once on station, the rib structure must also provide a dimensionally stable connection between the satellite body and the reflector RF surface, being the sole means of maintaining the relative pointing between the antenna system and the satellite. The link to the satellite body is usually realized via bolted joints for a fixed-mount reflector or a connection to one or more mechanisms, such as hinges or gimbals, for a deployed reflector. Because the rib structure is supporting the reflector shell, it will by default control or drive the thermal distortion of the shell contour. The challenge is to design the rib structure to provide a stable support platform to minimize thermal distortion and not drive it.

The reflector design engineer must be aware of a couple of things about predicting thermal distortion using customary analysis tools. A typical structural FEM assumes uniform and constant material properties throughout the structure

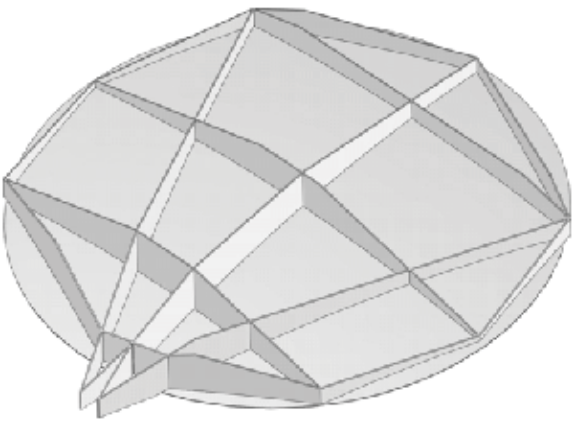

Figure 9.2 Typical egg-crate rib structure. (Copyright AASC 2012.)

as defined by the materials cards in the FEM. It also assumes a perfect geometry. The actual hardware, however, has a meaningful amount of variability in all of these values. As such, successful FEM analysis results are not necessarily sufficient to avoid resulting significant thermal instability in the reflector itself. For instance, most engineers will have been presented with the "cookie sheet in the oven" phenomenon. At an elevated temperature, a flat cookie sheet will suddenly warp into a definitively twisted alternative geometry. The facts that the cookie sheet has variability in geometry, materials properties, and thickness, is not perfectly flat to begin with, and has a low structural and geometric resistance to out-of-plane deformation mean that relatively small in-plane thermal strain differences resolve themselves as significant out-of-plane distortions. Analogous behavior can occur in a reflector assembly when the reflector rib structure consists solely of a tic-tac-toe style open-box construction. Although not necessarily shown as being required by the analysis, adding shear stability to the open boxes via triangulation or shear panel close-out is almost always a wise design choice.

9.4.1.2 Laminate/Membrane

For some reflectors it may be feasible to use a simple laminate for the reflector RF surface and not a sandwich. Laminate-style reflector construction has both potential advantages and challenges.

A laminate will more than likely be more stable thermally than a sandwich structure because it will be easier to achieve in-plane properties very close to zero CTE for a laminate than for a sandwich structure. Thermal gradients, especially through-thickness, will also be less with a laminate compared to a sandwich, potentially resulting in lower magnitudes of thermal distortion. A laminate is also potentially lower mass, takes less touch labor to fabricate, uses less material (no core, no film adhesive, etc.), and as a result is often cheaper to fabricate than a sandwich.

A laminate shell has significantly less out-of-plane stiffness, so it will not be as stable structurally as a sandwich and may be susceptible to buckling or pop-through during vibration or acoustics. Therefore, a laminate shell may require more ribs that are spaced closer together to adequately support the shell. Designing and fabricating a laminate rib structure that matches the shell properties can be quite challenging because the rib laminates are also more susceptible to buckling. If a sandwich rib structure is used to support a laminate shell, any CTE mismatch between the rib sandwich and the shell laminate will compromise the thermal distortion performance.

Many laminate shell reflectors with both sandwich and laminate rib structures have been successfully built and launched and have proven to work very well. Once again it is up to the design engineer to evaluate the design space and decide on the best approach for satisfying the requirements of each particular program.

9.4.2 Reflector Construction Materials

9.4.2.1 Carbon Fiber

Carbon fibers have electrical conductivities that can be used to produce a reflector surface with very good RF performance at frequencies of less than 30 GHz and

acceptable performance up to and in some instances beyond 60 GHz. The higher the RF operating frequency, the more critical it is to select a high-conductivity fiber and carefully consider the fiber form or weave type. As a general rule of thumb, pitch-based fibers are more conductive than polyacrylonitrile (PAN) fibers of the same modulus, and the higher the modulus (stiffness) of the fiber, the higher the electrical conductivity.

It should not be overlooked that as fiber modulus increases and the desirable electrical conductivity and RF performance also increase, that the fiber also becomes more fragile (lower strain to failure) and harder to process without causing some degree of fiber damage that weakens the laminate. Very high modulus fibers are also many times more expensive than lower modulus fibers and they tend to produce laminates with distinctly negative CTEs, which can result in thermal distortion instability, increase the overall thermal stresses, and induce increased residual strain on cooling from the cure temperature. Once again, it is the reflector design engineer who must balance RF performance against mechanical performance and fabrication/raw material costs.

Probably the most common carbon fibers found in spaceflight reflector construction are in the range of 65 to 80 msi in modulus yielding quasi-isotropic laminates in the 10- to 13-msi modulus range. A quasi-isotropic layup using 70-msi fiber with a cured fiber volume (Fv) in the range of 54% to 60% will produce a near-zero, in-plane CTE laminate. Note that weaker pitch fibers are typically preferred over PAN fibers due to their better electrical and thermal conductivity.

Fiber Orientation/Form

For a fiber-reinforced laminate reflector, the fiber is highly conductive along its length but poorly conductive between fibers or orthogonal to the fiber axis. Thus a carbon fiber laminate RF reflective surface is electrically nonisotropic. The selection and form of the carbon fiber used for the reflector surface construction must be carefully considered, because the type and orientation of the carbon fibers in the reflector surface will usually have a pronounced effect on the RF performance.

Unidirectional Material

Because the RF reflective property of a carbon fiber reflector is provided by the fiber encapsulated within the resin of the laminate, a reflector shell constructed from unidirectional material will naturally have a distinct polarizing effect on the RF energy hitting it. This is due to a combination of effects, but primarily it is a result of the conductivity of the unidirectional laminate being orders of magnitude higher in the fiber direction than in the transverse direction. The result may be an unacceptably high level of cross-polarization degradation in RF performance. Unidirectional fiber laminate reflectors have an extensive spaceflight heritage and can work very well if the RF characteristics of the laminate are understood and accounted for. Figure 9.3 shows a reflector laminate manufactured with unidirectional material.

Woven Material

Woven forms of carbon fiber (fabrics) are often used for antenna reflectors because they are easier to form to the compound curvature and shaping of the typical reflector surface than unidirectional materials. The woven form of the fiber presents a

Figure 9.3 Unidirectional laminate. (Copyright AASC 2012.)

less dramatic difference in directional conductivity to the RF energy impinging on the reflector surface. However, the fibers in a woven fabric also appear discontinuous to the RF energy so the fabric weave must be carefully selected with the RF requirements of the reflector in mind.

Fabric that is easier to form, such as a satin weave (as shown in Figure 9.4), typically has a greater effect on RF depolarization than a plain weave due to the somewhat directional properties of the surface fibers. However, a satin weave will typically have a higher RF conductivity than a similar plain weave because it appears less discontinuous to the RF field. Once again it is important to consider all aspects of the design space when selecting material fiber type and form.

Coarseness/Thickness of the Weave (Surface Roughness)

Even though a laminate reflector surface may appear to be quite smooth, the electrically conductive medium is the carbon fiber and not the resin matrix, and it is the nonconductive resin that provides the smooth surface contour. As the fiber bundles

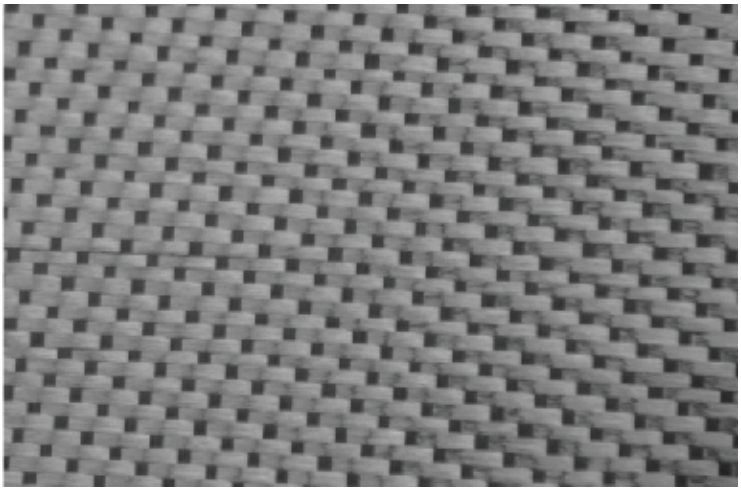

Figure 9.4 Five-harness satin weave. (Copyright AASC 2012.)

(tows) alternate over and under each other in the weave, they effectively create a rough surface than can be equated to a degradation in surface figure roughness, sometimes defined by the local surface rms (root-mean-square variation across a very fine grid of points). The roughness orthogonal to the fiber direction and the amount of tows per inch also create RF performance irregularities that can be equilibrated to surface roughness. The coarseness (weave density) and thickness of the fabric weave become more and more critical as RF frequencies increase (wavelength decreases). A thinner, finer weave will result in a smoother electrical surface and will provide measurable improvements in RF performance as frequencies increase. The design engineer must consider the exact requirements of the reflector in choosing materials since at lower frequencies a coarser and thicker material is likely to be more economical and may provide perfectly acceptable RF performance.

Because the matrix resin is a dielectric, the resin will have an effect on RF performance if the reflector surface is resin rich with the open areas of the weave being filled with resin. The dielectric constant and loss tangent of the resin system may be important for a carbon fiber reflector but will definitely be influential for a dual-surface (dielectric) reflector structure. Again, the reflector design team must account for the dielectric effect, but for most single-surface reflector applications it is not a significant driver of RF performance.

Density of the Weave (Gaps)

One way of obtaining very good mechanical properties from a woven material is to mimic unidirectional material with thin and flat tows but in a woven form. This is commonly known as a spread fabric and is so called because after weaving, the tows (fiber bundles) in the material are spread to a flat form that yields a weave with little or no open space (porosity). In addition to less porosity, the spread fabric is smoother and thinner than an unspread weave and thus provides measurably better RF surface roughness and improved RF performance at higher frequencies. Figure 9.5 shows an example of spread fabric plain weave reflector.

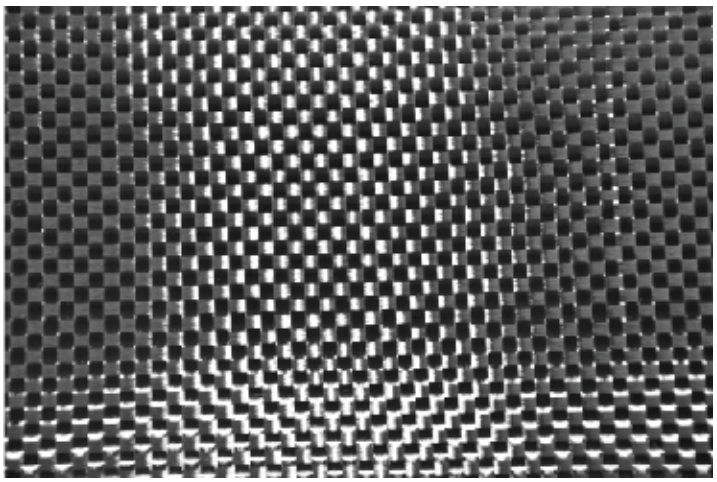

Figure 9.5 Spread fabric—plain weave. (Copyright AASC 2012.)

Triaxial Weaves

Triaxial weave material has been and is still quite commonly used for antenna reflectors. A triaxial woven material, often referred to as triax, has a three-direction (triaxial) weave rather than the common two-direction biaxial (orthogonal) woven fabrics. There are mechanical advantages to the triaxial form of the material, but there are also RF disadvantages.

A triaxial weave is typically less dense (more porous) and thicker than an equivalent areal weight biaxial weave, which can measurably degrade the electrical performance at higher RF frequencies. Triax does, however, have some desirable mechanical advantages in that a single ply is extremely close to quasi-isotropic so the number of plies can be very small; in fact, a single ply is often adequate. A laminate constructed with very few open-weave plies results in a porous laminate structure that is not responsive to acoustic energy; this can significantly reduce loads on larger aperture (surface area) reflectors. Figure 9.6 shows a reflector surface with triaxial weave construction.

Note that due to the naturally high in-plane shear stiffness of the triangular weave, triaxial materials do not form as readily to curved or shaped surfaces as do biaxial materials.

Laminate Matrix

The customary laminate matrix material is an elevated temperature cured resin polymer, usually a modified epoxy or cyanate, specifically formulated to work with the desired fiber in the thermal and deep space radiation environment. There are a relatively small number of space-qualified resin systems with heritage in spaceflight reflector construction that possess acceptable radiation resistance and exhibit very good structural integrity over the wide temperature ranges experienced. Almost all resins available today are blends or hybrids of various elements that add toughness, strength, stability, radiation resistance, and so forth.

The matrix resin has a distinct set of properties that must be considered in the design and manufacture of the reflector laminates, sandwiches, and assemblies. Most obviously, the resin is an electrically nonconductive polymer and it is also an extremely good thermal isolator. The resin has a much lower modulus than the carbon fiber, but a CTE that can be orders of magnitude higher. The resin will also

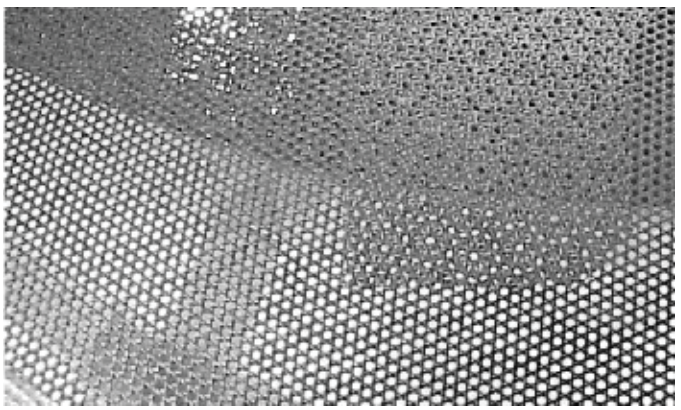

Figure 9.6 Triaxial weave material. (Copyright AASC 2012.)

exhibit a change in volume relative to ambient humidity, known as the coefficient of moisture expansion (CME).

Filled Matrix Resins

Current development activities are evaluating the addition of nanofiber and/or particle fillers to resin matrices to improve the less desirable resin properties. For example, carbon fillers can increase conductivity, lower CTE, lower CME, reduce resin shrinkage, and increase resin modulus. Of course, almost all benefits come with compromise; the fillers can have some nondesirable effects such as reducing toughness, and as a result may affect certain laminate properties. These specialized resins definitely deserve consideration and will likely become more common in the future if only for specialized applications that can take full advantage of the specific customized properties.

Low-Moisture Matrix Resins

All polymer resin matrices possess varying degrees of affinity for moisture and as such they will expand according to the increasing humidity of the surrounding environment. Of the most common resin systems, epoxies possess the highest CMEs, whereas the CMEs of cyanate esters are measurably less and the CMEs of the somewhat-specialized cyanate siloxanes are very low. These three types are broad categories of resins and within each there are specific resin formulations that have measurably lower CMEs than others.

For a conventional laminate, cured under vacuum in an oven or autoclave, the cured resin will be at its zero-stress state at the cure temperature (or thereabouts) and zero humidity. As the resin reabsorbs moisture in the ambient environment, the resin will expand and impart micromechanical stresses into the laminate. Conversely after launch, the resins will dry out and shrink. The hygroscopic effects on most reflector assemblies are measurable and may be of a magnitude that makes CME a design consideration; this is especially true with dual-surface reflectors.

9.4.2.2 Dual-Surface Reflector Materials

Certain reflector designs require one or more of the reflector shells to be RF transparent or transmissive to certain RF polarizations or frequencies and highly reflective to others. This adds additional RF requirements beyond reflectivity, and results in a new set of mechanical challenges due to the introduction of another subset of materials with their own distinct properties and characteristics.

RF Circuitry

For RF transmissive reflectors the RF conductive surface of the reflector is a discrete pattern of conductive elements that may be a linear polarization grid, or a resonant element pattern such as a ring or other types of RF features such as dipoles. These features are almost always required to be highly conductive, so the design engineer has to decide on the best materials, form, and fabrication techniques to satisfy the additional RF requirements while maintaining the typical mechanical and thermoelastic requirements. RF reflective (conductive) features on reflectors have successfully used copper, aluminum, and carbon fiber elements. There is always a size and

often a positional dimensional tolerance that is required with the RF elements that will limit the possible approaches to achieving the feature pattern accurately on the completed reflector shell. There have been a wide variety of successful construction and fabrication methods for applying the RF features that have been qualified and all have associated specific challenges or compromises. An example of an RF transmissive aramid fiber laminate subreflector constructed using frequency selective material is shown in Figure 9.7.

RF Transmissive Materials

Once the RF element design has been established, it will need a substrate (reflector shell) to accurately position the element in the antenna system. In addition to providing the required stiffness, strength, and thermoelastic stability, the substrate must incur the minimum possible impact on the RF energy passing through the reflector shell. It is easier to think of the reflector shell in this case as a radome, which is designed to have the lowest possible impact on the RF performance as possible.

As a starting point if the design engineer considers typical radome materials he or she is presented with glass fiber, quartz fiber, aramid fibers (Kevlar^{R}), and other more specialized options such as ceramics and poly-*p*-phenylenebenzobisoxazole (PBO or Zylon^{R}). Assuming that the same structural considerations are made as for a solid-surface carbon fiber shell reflector, a reasonable starting point is to directly replace the carbon fiber of the solid surface design with the dielectric fibers required for the transmissive design. This is a very good starting point but results in very distinct structural differences that must be considered:

- *Stiffness:* The typical dielectric fiber has a modulus that is less than half that of the commonly used carbon fiber, reducing the critical structural stiffness characteristics of the reflector assembly. Increasing the core thickness and

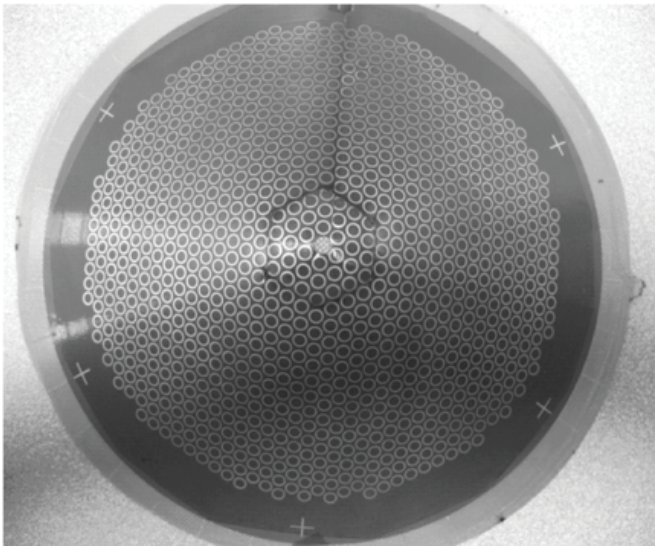

Figure 9.7 Frequency-selective subreflector surface. (Copyright AASC 2012.)

the number of supporting ribs begins to address the issue for the assembly; however, the resulting effects on RF performance must also be considered. A thicker reflector shell and more ribs, which will also need to be RF transmissive, will almost certainly result in measurable degradation to the reflector RF performance.

- *CTE:* The lower modulus of the dielectric fiber also makes designing a thermally stable structure much more challenging because the laminate is influenced to a greater degree by the high positive CTE of the resin matrix materials and adhesives used for assembly of ribs and so forth. This, combined with the fact that common fibers such as glass and quartz have distinctly positive CTEs, results in a structure with anything but a zero CTE making a design that has low thermal distortion very challenging. This does present a challenge to the design engineer, but note that some very clever proprietary solutions to minimizing the critical out-of-plane distortions while allowing significantly higher in-plane dimensional changes have been qualified and flown.
- *CME:* For reasons similar to those for the increase in CTE (lower fiber modulus), CME is also going to be higher for a dielectric fiber laminate because the fiber has less influence over the higher CME resin matrix. In the case of an aramid fiber where the fiber itself has a measurable CME, the resulting shell moisture shrinkage can be even more significant.
- *Thermal and radiation effects:* Most of these dielectric fibers also have increased susceptibility to the on-orbit radiation environment and also to large numbers of thermal cycles. These factors must be recognized and accounted for, but will be easier to manage if the reflector assembly has thermal control that covers the critical material surfaces.

9.5 Manufacturing Considerations

9.5.1 Mold Tooling

The reflector surface mold tool is logically the most critical piece of tooling in the reflector fabrication process because it ultimately governs the surface figure (RF prescription) and accuracy of the flight reflector. There are relatively few well-established tooling materials and fundamental designs used for the majority of composite reflector fabrication.

9.5.2 Mold Tool Surface Accuracy

Surface figure, the geometric fit of the as-built surface to the ideal surface, is the primary requirement for a reflector mold tool. The specified reflector accuracy ultimately dictates the mold construction, materials, and machining and finishing techniques that will be required. Tools with optical mirror-type surface accuracies can be produced but are almost always too time consuming and costly for a com-

munications antenna reflector so it is up to the design engineer to evaluate the available options and select the one that best suits the current set of requirements.

The as-delivered room temperature accuracy of the mold tool is only one aspect of realizing a successful design. Because the reflector shell laminate or sandwich shape will be formed at the laminate cure temperature, the tooling should also match the reflector laminate or sandwich CTE or may need to have the surface figure thermally compensated to the cure temperature.

9.5.2.1 Machining Accuracy

The practical machining accuracy that can be achieved is dependent on size, tool design (rigidity), and machine tool accuracy. It is quite possible to cut a tool surface to a profile accuracy of a few thousandths of an inch or less on smaller tools using a gantry milling machine yielding a surface rms of less than 1 mil on smaller tools (<30 in.) and 2 mils on tools up to around 90 in. Tools of 120 in. or more in diameter have been produced with surface accuracies of less than 0.0015 in. with additional time spent to finesse the surface by repeated measurement and handwork.

9.5.2.2 Postmachining Operations (Benching)

The most common technique used for machining contoured surface tools is to use a ball end or radiused-type milling cutter and "raster" the required surface on a five-axis CNC milling machine. This process leaves a machined surface with a washboard-type ridged surface. With the correct choice of cutter radius and path spacing, the depth of the resulting ridges can be very small, often less than 1 mil.

Once the machining of the surface has been completed, the surface must be hand finished to remove the peaks of the ridges down to the same level as the valleys. This finishing step, often called benching, levels the surface to the low spots of the troughs, which were controlled during machining to the desired surface contour. Figure 9.8 shows the photograph of a machined tool during the benching process.

The skill required to perform this task is relatively high, but by using shop aids such as machinist's blue dye and a semistiff sanding tool to bridge the ridges, an

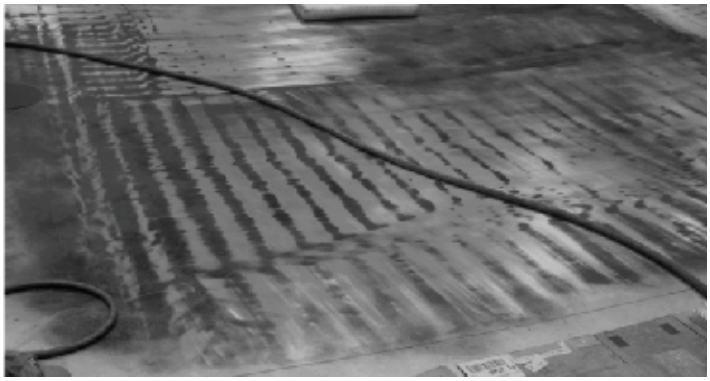

Figure 9.8 Mold tool benching. (Copyright AASC 2012.)

experienced technician can efficiently produce a very smooth and accurate finished tool surface.

9.5.2.3 Measurement Limitations

Surface contour inspection measurements of a very large and heavy mold tool can be somewhat challenging. Often it is not practical to move the tool onto a coordinate measuring machine or similar fixed inspection station, so the tool must be measured *in situ*. Inspecting the tool using the machine used for creating the tool is acceptable as a first-order inspection, but it does not isolate any errors present in the machine itself and is rarely used to accept the final tool contour. The tool is typically much better supported on the bed of the machine than it is in service, so gravity distortion (sag) effects may not be accurately assessed with a measurement on the machine. Ideally the tool should be inspected in the configuration in which it will be used, typically on an autoclave cart or perhaps a cure table for smaller tools.

Remote dimensional inspection methods for tooling are quite common such as a laser tracker, Romer™ arm, and occasionally photogrammetry. The measurement accuracy limitations of these methods must be considered and evaluated by the design engineer. The dimensional accuracy of both photogrammetry and laser tracker methods is largely driven by angular resolutions, so dimensional accuracy decreases as the measurement distance increases. As a rule of thumb, single-point measurement accuracies of better than 0.001 in. even on smaller parts should not be expected without special consideration for the setup, measurement technique, and data processing.

9.5.2.4 1G Effects

Mold tools can be very heavy. Steel, Invar, or bulk graphite tools for 2.5m reflectors can weigh 10,000 lb or more. Heavy tools maintain their surface contour during machining because they are well supported on the machine bed. However, once the tool is moved off the machine, it will distort to some degree, degrading the surface figure accuracy. To ensure that the tool maintains its accuracy during layup, curing, and assembly operations, the structural design and in-use support of the tool must be carefully engineered. If in-house experience in tool design is not available, then contracting a tool designer or manufacturer that has design and analysis capability may be the best or only option.

9.5.2.5 Stability During Curing/Assembly

As the contour of the reflector composite laminate/sandwich is established at the cure temperature of the resin system/adhesive, it is important to understand the surface figure of the mold tool at the cure temperature. The CTE of the tool material obviously has a profound effect, but the difference between the CTE of the part being cured and the tool must also be addressed. Ideally the tool and the part should have close to the same CTE. If the tool and part CTEs match and the tool has the desired contour at room temperature, so will the part, because they will both expand and contract at the same rate.

It is possible and not uncommon to design a tool out of a more economical, higher CTE material by thermally compensating the tool contour such that when the composite part cools back to room temperature it has the desired contour. This technique is very common for making composite tubes where it is desirable to have the tool shrink more than the part so that the part will slide off the tool after curing.

Depending on the final accuracy requirement for the reflector and whether the tool is to be used for multiple cures, the stability of the tool contour may also be very important. Conditioning the tool through a few temperature (cure) cycles before final machining to allow for any stress relief or relaxation to occur can be critical to the long-term stability of the tool contour.

9.5.3 Mold Tool Design Considerations

9.5.3.1 Size/Mass

As layup curing tools become larger in size, the mass of the tool and its carrier or cart becomes more and more important to consider. The greater the mass of the tool, the longer it will take to heat up and cool down during the cure cycle. Thicker sections of the tool will also tend to heat up more slowly than thinner sections, which can cause uneven curing and warping of the part. In a simplistic way this can be compared to how a potato chip cooks from the outside edge toward the center, causing it to warp. The logistics of moving the tool around the facility must also be considered. The load-bearing capacity of the flooring, ramps, or steps in the path from the layup room to the autoclave, installing the tool into the autoclave, and the capacity of the rails in the autoclave may have a distinct influence on the final tooling design and tool material choice.

9.5.3.2 Cost

The cost of the completed tool is driven by size, required accuracy, choice of raw material, and complexity of fabricating the tool. The relative price of different tooling approaches also varies as the size increases. For a very small tool, a machined Invar configuration may actually be the most economical because it can be processed from a billet of raw material with only NC programming and machining costs. However, a larger Invar tool will be on the high end of the price scale, because it requires forming of various individual pieces of Invar plate, welding, and heat treating steps before it even reaches the five-axis NC mill for contouring.

9.5.3.3 Tooling Features

Both the reflector mold tool and the reflector shell produced from the tool will require some form of physical reference to establish the base reflector coordinate system to facilitate accurate assembly and alignment. These features can be accurately located and machined as features on the tool during machining and then transferred to the composite shell during or after cure. Locating holes or pins in the tool and bosses or inserts in the reflector shell are simple and effective at establishing the nominal reflector shell coordinate system for assembly.

In some instances it is both convenient and efficient to assemble the reflector face down on the mold tool, in which case incorporating features that the locate backing structure and interfaces into the tool should be considered.

9.5.4 Mold Tool Material Options

Over the years many mold tool materials have been used including wood, plaster, and other readily machinable options that are relatively stable and will survive the required curing temperatures. However, the industry has largely evolved to the basic tool material options discussed next.

9.5.4.1 Metallic Tools

Invar 36

Invar is a high nickel content steel that is available in many different alloys, each possessing specific properties. The lowest CTE formulation of Invar commercially available is Invar 36 (36% nickel) and it is the most commonly used type for reflector mold tools. Approximately the same density as steel, large Invar tools usually have the front surface formed and welded to an open rib style backing structure, heat treated to relieve welding stresses, and then machined. Depending on the size, Invar 36 mold tools are often comparable in cost to bulk graphite, they are lighter weight, and they possess relatively good thermal conductivity and a very low CTE comparable in magnitude to bulk graphite. The lower mass and relatively uniform thickness of a fabricated Invar tool can have distinct advantages for certain high-accuracy reflector applications due to the ability to far better control tool heating during the cure cycle. An Invar reflector mold tool is shown in Figure 9.9.

Figure 9.9 Invar reflector mold tool. (Copyright AASC 2012.)

Steel

Steel tooling is quite commonly used for glass fiber or quartz fiber laminates and sandwiches that have a CTE similar to that of steel, or for assemblies that do not require a highly accurate surface contour. Steel mold tools (see Figure 9.10) are more economical than Invar due to the lower materials costs, lighter weight than bulk graphite, good thermal conductivity, and lower CTE than aluminum.

Aluminum

Aluminum is rarely used as an elevated temperature cure reflector shell mold tool due to its high CTE. However, it is commonly used for tube mold tools or assembly tooling due to its light weight and relatively economical fabrication costs.

9.5.4.2 Composite

The composite tooling description covers a wide range of tooling configurations: castings, simple laminates, supported laminates, sandwich structures, shell and core, and many more including hybrids. Simple composite tools (skin and core) are probably going to have accuracies and CTEs that are larger than those required for a precision reflector fabrication; however, they may be viable for lower accuracy requirement parts. They are also likely to have temperature limitations constraining their use to room or lower temperature cures.

Many years ago fabricated composite tooling was used for the construction of many high-accuracy reflectors (see Figure 9.11). Composite tooling was (and is) potentially the most accurate medium because the tool construction and materials can be designed to mimic the part being cured on it for a near-perfect match in CTE and thermal properties. The challenge is how to assemble the tool surface to the stiffening structure required to support it while maintaining good structural joint integrity at typical cure temperatures and pressures. Room-temperature epoxies would be a logical and convenient choice for a rib-supported structure; however, they have service temperature limitations that may preclude their use.

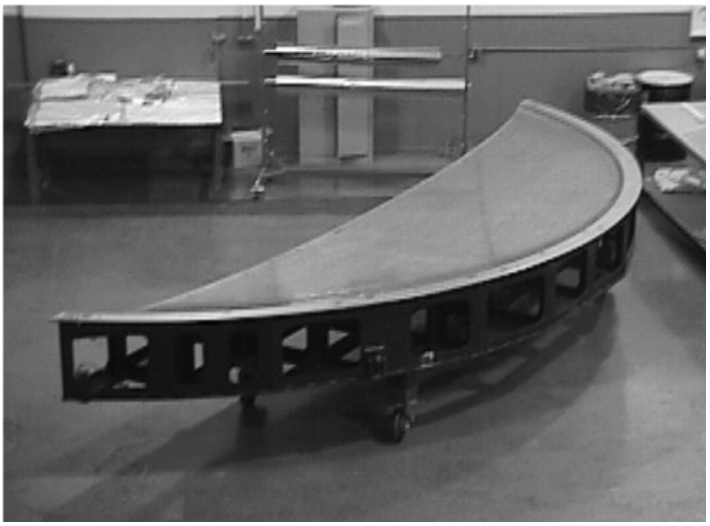

Figure 9.10 Steel mold tool. (Copyright AASC 2012.)

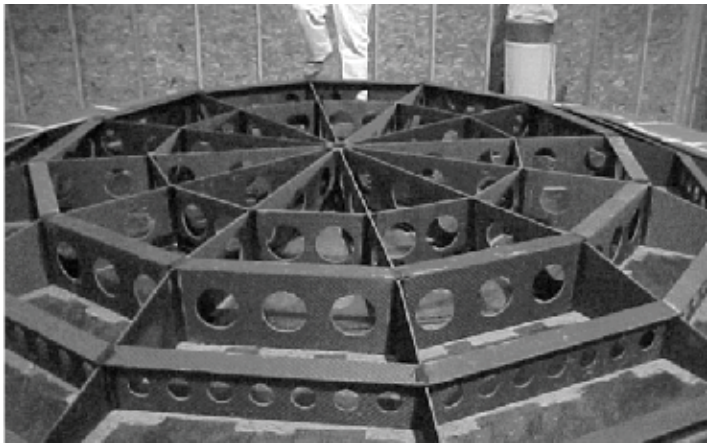

Figure 9.11 Composite mold tool, rear view. (Copyright AASC 2012.)

The unfortunate result is that fabricating high-accuracy composite tools like this becomes as challenging as the flight reflector and as a result they have lost favor to bulk graphite and Invar.

There have been recent developments in tools constructed from a carbon core with a machinable carbon molding compound skin. The core is rough machined undersize to accommodate the molding compound thickness. The compound is then applied to the core and the tool assembly cured, resulting in a blank that may be within a few tenths of an inch of the final contour. Once the tooling blank has been created, it is then machined like a typical bulk graphite tool, then benched and sealed. To this point tool to part replication accuracies have not been quite as good as equivalent bulk graphite or Invar tools; however, as the technology matures this type of tooling design may become a very attractive option, especially for large tools where weight and thermal mass become significant challenges.

9.5.4.3 Bulk Graphite

Bulk graphite tools are constructed from amorphous sintered graphite blocks machined and bonded together to form a tooling blank large enough to fit the desired shape. Once bonded together, the blocks are CNC machined, hand finished, and sealed to produce a vacuum-tight tool surface. The processes, adhesives, and sealers are very specialized and use competition-sensitive formulations. As such, there are relatively few tooling houses that can successfully produce bulk graphite tooling. Machining bulk graphite is also a very dirty and hazardous process due to the graphite dust that is created. Bulk graphite does have a very low CTE, comparable to that of Invar; however, the CTE can be slightly directional. For larger tools requiring extreme cure accuracies, the slightly positive and directional bias of the bulk graphite thermal expansion should be considered in the tool design. Figure 9.12 shows an example of a bulk graphite mold for shaped reflectors.

Bulk graphite tools are often comparable in cost to Invar depending on the size (and volume). Larger bulk graphite tools tend to be more massive than Invar due to the bulk volume of material involved compared to the thinner Invar weldment-type construction. The thermal conductivity of bulk graphite is acceptable, but the

Figure 9.12 Bulk graphite shaped reflector mold tool.

mass makes heating very large tools at a rapid enough rate somewhat challenging. Imbedding electrical heaters in the bulk graphite tool may be necessary in some instances.

9.5.5 Composite Fabrication Equipment Requirements

9.5.5.1 Processing

Composite spaceflight hardware processing requires a controlled clean area with temperature and humidity monitoring, if not controls. Environmental controls are critical for all layup activities (uncured materials) and generally important for assembly activities unless the hardware is easily and thoroughly cleaned once completed.

Contamination Control

Contamination control is critical at all times while processing composite hardware. Mold release operations must be performed in a separate room that has a completely stand-alone and separate air handling system. It is preferred that mold releases be wiped on rather than sprayed to avoid inadvertent direct or secondary contamination of flight hardware. Uncured mold release on clothing, gloves, shoes, tools, or shop aids must be very carefully controlled.

Many bond failures have been attributed to contamination of the bond surfaces with mold release, fingerprints, oils from compressed air sources, and so forth. Thorough abrading and cleaning of faying surfaces before bonding will remove most contaminates, but not silicones. As a rule, free or uncured silicones should be isolated from any composite hardware fabrication activities. Silicone-based painting, room temperature vulcanizing (RTV) bonding for optical solar reflectors (OSRs) or solar cells, or similar specialized activities must be carefully planned and separated from composite structure and bonding activities. It is common practice for a water-break test to be performed on critical bond surfaces before adhesive application to verify that there is no surface contamination that would prevent a successful structural bond.

For reflectors with dielectric shells, contamination of ribs or other RF transmissive components from conductive materials such as metal shavings and even carbon fiber or carbon dust must also be eliminated or at the least very carefully controlled. Conductive inclusions in an RF transmissive reflector shell or structure can result in devastating impacts to the RF performance especially from passive intermodulation (PIM). It most instances it is required that all layups be performed in an area that is not used for any conductive materials processing such as carbon fiber layups or processing or metal bonding and it is preferred that all assembly bonding operations be handled in an area with similar requirements. For the fabrication of some reflectors with particular sensitivity to PIM, it is not unusual to require that the machine used for running the pre-preg either be a dedicated non-carbon machine or that it be scrupulously cleaned before the dielectric pre-preg is run through it.

Laminates

Due to the harsh environment and temperatures involved, virtually all spaceflight reflector hardware uses elevated temperature curing resins systems for laminate and sandwich structures. The rigorous structural requirements of a spaceflight antenna dictate that autoclave curing is more often required than oven curing because it produces a higher quality part. Autoclave-cured laminates will have better ply consolidation, lower void content, and, as a result, more consistent and better mechanical properties than similar oven-cured laminates. Figure 9.13 shows a 16-ft × 30-ft autoclave facility at the AASC facility in Stockton, California. As noted earlier, layups will virtually always have a requirement to be performed in a controlled clean area with temperature and humidity control. The design engineer should also be aware of the susceptibility of certain materials and processes to the presence of moisture and solvents that can affect the curing chemistry and result in compromised laminates. Note that a white powdery residue or caste on the surface of a cured laminate is often a sign of a potentially serious cure issue.

Figure 9.13 A 16-ft x 30-ft autoclave. (Copyright AASC 2012.)

Sandwiches

Sandwich bonds can be satisfactorily made using an oven because the pressures involved (commonly vacuum only) are considerably less than those used for a laminate cure. Also the heat-up rate is less critical for a sandwich bond. It is customary to perform sandwich bond layups in a controlled clean area with temperature and humidity control. Also remember that sandwich structures should be vented to allow for pressure equalization during launch ascent. Aluminum cores can be purchased already perforated, but composite core materials are not usually vented and this must be accounted for in the design or addressed by adding vent paths to the core.

Assemblies

Other than the specialized equipment and facilities required for processing laminates and sandwiches and performing end item inspections and alignments, there is relatively little in the way of expensive equipment that is required for assembly of the reflector. A well-designed and manufactured set of tooling to locate critical structural elements and interfaces and common hand tools and shop aids will be adequate in almost all instances. As is always the case for spaceflight hardware, it is customary to perform assembly operations in a clean area that is monitored for temperature and humidity control.

9.5.5.2 Surface Measurement

Inspection of the reflector surface figure and alignment against the program specifications is a key requirement and a critical measurement step. The industry has largely gravitated to one of three methods: coordinate measuring machine (CMM), laser tracker, or digital photogrammetry. Other techniques, including hybrids of these methods, are constantly being developed, but as of this writing they have either not achieved the accuracy or repeatability required for most spaceflight reflector inspections or they are too expensive or not practical for the types of alignments and inspections typically needed in the fabrication and inspection of a spaceflight reflector.

Laser Tracker

A laser tracker is a very convenient portable measurement system that uses a laser beam to accurately measure a target placed on the part being inspected. The target usually used for laser tracker measurements is called an spherically mounted retroreflector (SMR) and consists of three mirrored faces representing the sides of the corner of a cube with the apex being located exactly at the center of a sphere. Any light ray that enters the reflector portion of the SMR will be reflected back to the source along a path that is equivalent to the distance from the laser tracker head to the center of the sphere and back to the laser tracker. The laser tracker calculates the location of the SMR by angular encoders in the laser tracker head and distance (flight time and phase differential) to the SMR and back. Laser tracker ranging is extremely accurate and consistent over long distances; however, the azimuth and elevation accuracy of the laser tracker does degrade with distance due to the accuracy of the digital encoders resolving the pointing angles. A good laser tracker operator

will carefully set up the inspection measurement to minimize the limitations of the angular encoder accuracy.

Laser tracker measurement (see Figure 9.14) is a contacting measurement, and data capture occurs over a period of time so this must be accounted for. If the part being measured can be measurably deflected by contact pressure of the SMR or is not rigidly mounted relative to the laser tracker head for inspection, it will be very difficult if not impossible to perform an accurate inspection.

Photogrammetry

Photogrammetry is the process of determining the positions of features from multiple photographic images. It should be immediately apparent that this method is noncontacting and instantaneous, eliminating two of the challenges of laser tracker measurement. It is critical for each image (photograph) to contain a known scale and for a series of images to be taken that provides a wide range of viewing angles of the part being inspected. The accuracy of the measurement will also increase relative to the number of images used in the measurement data set. Measurement resolutions of 0.001 in. or slightly better can be achieved at close distances with a well-thought-out measurement setup; however, as with the laser tracker measurement method, the accuracy decreases with distance in this case primarily due to the resolution of the charge-coupled device sensor and optics in the camera.

For spaceflight hardware inspection the features being "measured" in each photograph are typically retroreflective targets consisting of a small accurately cut circular piece of higher reflective material with a self-adhesive backing. "Targets" can be a variety of sizes from less than 0.1 in. in diameter to 0.25 in. in diameter or more. For a reflector inspection the surface would be populated with a distribution of targets at a spacing and density designed to provide a good characterization of the surface being inspected. In addition, retroreflective targets would be placed at the reflector interfaces and known tooling locations on the reflector shell surface to establish the nominal coordinate system.

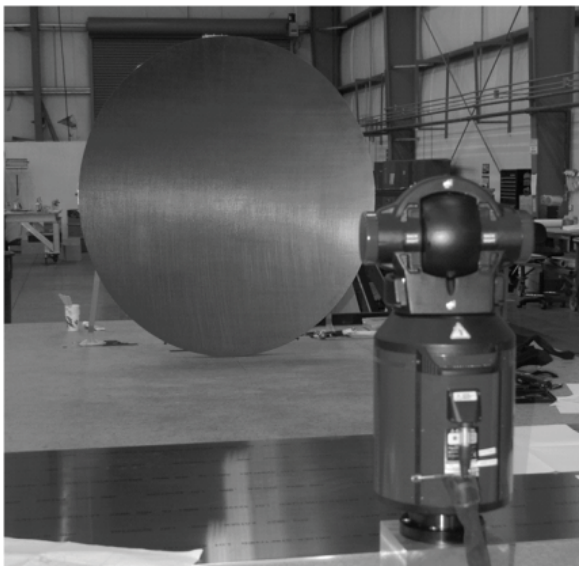

Figure 9.14 Laser tracker measurement of 1.3m reflector. (Copyright AASC 2012.)

Photogrammetry also lends itself to taking measurements in different environments such as in vacuum or at temperature to establish the thermoelastic performance of a reflector assembly. There are obviously significant challenges in performing the measurements and performing them accurately, but nonetheless there are companies (albeit limited) that have established accurate techniques for performing these measurements. A photogrammetry measurement setup is illustrated in Figure 9.15.

9.5.5.3 Alignment

Proper alignment of the reflector at the antenna subsystem level to the feed and spacecraft coordinate system requires knowledge of the reflector surface figure and its orientation and location relative to the boresight of the antenna subsystem. To establish this alignment, certain tooling references on the reflector are extremely useful to avoid having to remeasure the reflector surface for each alignment step. Tooling hole (or similar) features established from the mold tool provide easily measured locational references for the reflector alignment. Optical cube(s) may also be useful for measuring and characterizing the fixed antenna or deployed reflector angles (pointing) relative to the satellite master reference cube and also to check deployment angles and deployment repeatability.

9.6 Mechanical and Environmental Testing

Risk reduction testing occurs at all levels of the fabrication and assembly of a reflector, not just on the completed assembly. Integrating deficient material or an out-of-specification component into a reflector assembly that is not identified until the end item is tested would be devastating to the program schedule and budget.

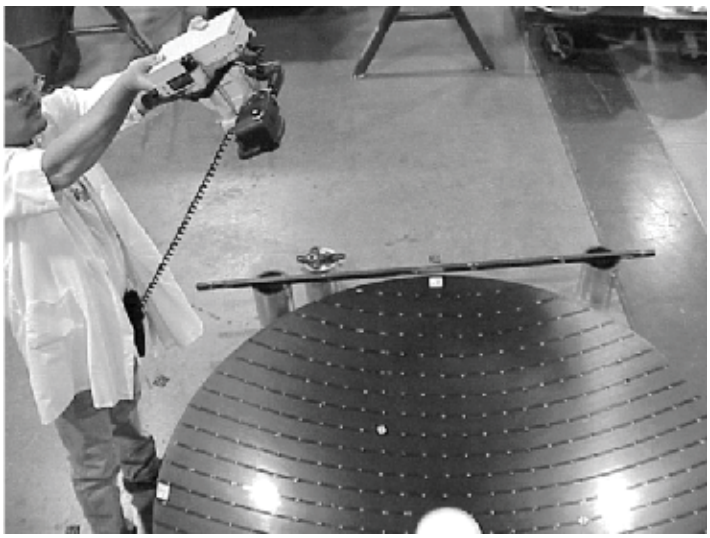

Figure 9.15 Reflector inspection using photogrammetry. (Copyright AASC 2012.)

9.6.1 Fabrication In-Process Testing

Due to the schedule, time, and material investment in a reflector assembly, it makes sense to screen the materials, processes, and subassemblies throughout the fabrication process to capture issues as early as possible.

9.6.1.1 Material Acceptance and In-Process Testing

All of the constituent materials used for a composite assembly should be screened as part of an incoming receiving test to ensure that they meet minimum requirements before being used for hardware fabrication. Material acceptance testing establishes that the purchased materials are compliant with their respective specifications.

Even though the laminate fiber and matrix properties will have been confirmed via material acceptance testing, it is still necessary to validate the production process variables. It is especially critical to perform in-process testing to confirm that the flight laminate layup matches the drawing and has been processed to the prescribed cure cycle and that the fiber volume and void content are within drawing tolerance. Sandwich bonds are customarily checked by performing in-process destructive testing by flatwise tension testing of an offcut or tag end of the sandwich. The integrity of sandwich bonds can also be checked by nondestructive evaluation, often through-transmission ultrasonic testing (see below).

Due to the specific geometry of reflectors, room-temperature bonds for fittings and ribs often cannot be reasonably proof loaded except at assembly-level environmental testing. Therefore, it is especially critical to check that the bond surfaces have been prepared correctly, often by means of the water-break test. In addition, inspectors must verify that the adhesive has been applied correctly by visual inspection and that the adhesive has been mixed and cured correctly by performing a hardness test on a sample of the adhesive, often called a "hockey puck."

9.6.1.2 Nondestructive Testing

In many instances it makes sense to perform a level of nondestructive testing (NDT) or nondestructive evaluation (NDE) during the fabrication of the assembly to identify and isolate any structural integrity issues before considerable time and effort have been invested in the hardware. Common NDE techniques in use for spaceflight hardware are coin tap and ultrasonic inspection including the use of through-transmission ultrasonic (TTU) scanning. Although it may sound crude, an experienced operator can identify extremely small flaws with a simple coin tap (nickel) test.

Most automated TTU scanners are designed for scanning flat panels and can usually only scan in the X,Y-plane (not Z). This means that a reflector shell sandwich that is not within a few inches of being flat presents a significant challenge when performing an automated TTU scan, requiring either an automated Z-axis capability or that the surface be scanned in smaller area segments that do meet the flatness deviation requirement. Figure 9.16 shows a TTU air scanner setup for a sandwich cylinder.

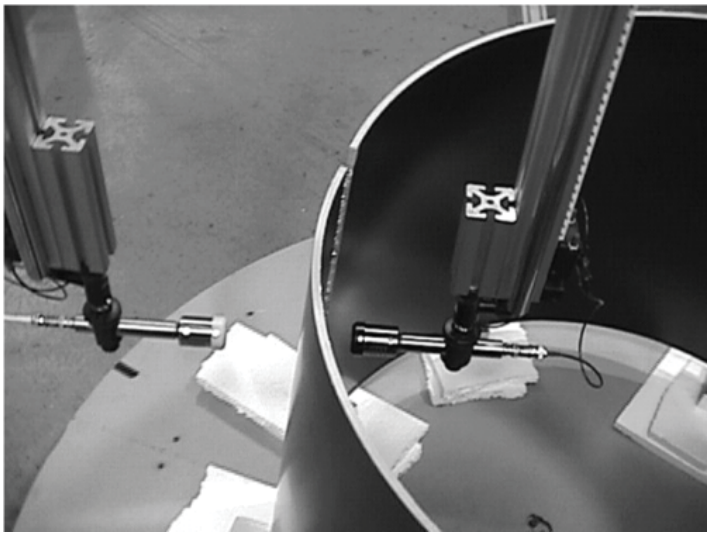

Figure 9.16 TTU air scan. (Copyright AASC 2012.)

9.6.2 Reflector Assembly Acceptance and Environmental Testing

Any spaceflight component must undergo rigorous ground testing before launch to ensure that it will survive the launch environment and satisfactorily meet all design requirements once on station. Although a satellite reflector is primarily an electrical payload component, it is a passive device and its mechanical testing is similar to that of a lightweight structural component such as a solar array substrate. Therefore, the customary testing is very different that that for an electrical component and tailored somewhat differently to a typical structural component.

The preferred and customary order of reflector-level environmental testing is as follows:

- *Dimensional inspection:* This is the baseline surface figure and interface location inspection that will used as the "before" comparison standard. This inspection is repeated as an intermediate or post-test inspection as part of the test success criteria to establish that the structural integrity of the reflector has not been compromised.
- *Low amplitude sine signature/modal:* For some larger reflectors or reflectors with specific structural requirements, it may make sense to establish a baseline for the modal signature characteristics of the reflector before any testing is performed. The signature can be repeated as an intermediate or post-test inspection as part of the test success criteria to establish that the structural integrity of the reflector has not been compromised.
- *Thermal cycle:* This test is extremely effective at screening out bad laminates, bonds, or bond prep that may not have been caught by in-process testing or NDE.
- *Thermal distortion:* The thermal distortion test is really only placed here in the flow sequence out of convenience because it can be combined with the thermal cycling test to save setup and test time. Thermal distortion testing

can be performed at any point in the test sequence and in some instances it may be warranted to measure thermal distortion at a lower level of assembly, say for a subreflector, that cannot be surveyed well at the assembly level.

- *Static proof load:* For some larger reflectors or reflectors with specific structural requirements, it may be appropriate to perform a static proof load test of certain interfaces if possible. Note, however, that reacting the applied load often makes a static load test impractical.
- *Sine vibration/sine pulse:* The intent of this test is to excite the reflector at the lower frequencies (<100 Hz) to quasi-statically load the reflector.
- *Acoustics:* The intent of this test is to acoustically excite the reflector structure in the higher frequency ranges and may also be used to load the reflector interfaces.

Between and after each of these tests there should be an inspection or verification step to ensure that no permanent damage or degradation has occurred to the reflector assembly. Depending on the exact reflector design and end item requirements, the inspections may be one or more of the following: visual inspection, dimensional inspection, nondestructive evaluation (such as TTU or coin tap), and modal signature.

9.6.2.1 Thermal Cycling

Thermal cycling is a critical test of composite and bonded structural assemblies. In any composite reflector assembly, there are many interfaces between materials with dramatically different CTEs and stiffnesses where thermal strain can create large stresses. Fiber to matrix, core to faceskin, metallic fittings to composite laminate and/or core, and adhesive-filled joints are the most obvious but there are many other areas where thermally induced strain can overstress an assembly.

Exercising the assembly by thermal cycling is a very effective way of validating that the bond joints at critical interfaces were prepared and bonded correctly before any other environmental testing is performed. Depending on the hot temperature requirement, thermal cycling may also post-cure the room-temperature curing adhesives to some extent, which in almost all cases will cause them to shrink, inducing some small level of additional strain. Thermal cycling also has the effect of relieving and balancing the strains in the assembly, which for a reflector in which surface figure is a key design parameter is a critical step in dimensionally stabilizing the assembly.

It may be wise to perform thermal conditioning at lower levels of assembly, laminates, sandwiches, and subassemblies if they contain critical structure or structural bonds in order to reduce technical risk at the top-level assembly.

Because certain construction elements of the reflector have an affinity for moisture, it is very important to conduct any cold thermal cycling in a "dry" environment to prevent icing, but more importantly to prevent the freezing of moisture present in the polymers or voids in the assembly from causing microcracking or other failures. It is common to conduct thermal cycling in a dry nitrogen environment and to bake out the moisture from the assembly for a 12- to 24-h period before commencing cold cycling.

9.6.2.2 Thermal Vacuum/Balance

Thermal cycling in an ambient pressure dry environment is usually adequate for testing an antenna reflector unless there are specific reasons to perform a vacuum test.

For certain science missions it may desirable to remove as much condensable volatile content as possible that could degrade optical instruments or other sensitive equipment on orbit. In these cases an extremely sensitive measuring device, a thermoelectric quartz crystal microbalance (TQCM) is placed in the vacuum chamber and is used to measure the rate at which the volatiles are being released from the hardware. During TQCM bake-out the hardware will remain in the vacuum chamber until the desired rate of condensable volatile emissions is achieved, which can take from a few hours to many days depending on the reflector materials, the thickness of the materials in the construction, and the bake-out temperature.

Another reason for a vacuum test could be to correlate an analytical thermal model. Most reflector designers will have a database on the key thermal properties of reflector materials (laminates/sandwiches) and construction elements such as bond joints that may have been established from simple materials or coupon tests. However, there are many possible areas for the analytical model to under- or over-predict temperatures and gradients that can significantly affect the performance of the reflector on orbit. Empirically correlating any hardware design to the thermal model at least once significantly reduces the analytical uncertainty.

9.6.2.3 Thermal Distortion

As outlined previously the surface contour and contour stability over on-orbit environments is a critical parameter for a reflector and one that should be validated for a certain design if not each unit before launch. If the reflector distorts in an undesirable or unpredicted way, the resulting distortion can have profound effects on the RF beam shape and pointing, compromising the satellite payload performance—sometimes in a catastrophic way.

The ability to perform thermal distortion measurements at temperature to the accuracies required is a challenging and specialized capability that is for the most part limited to the satellite prime contractors and only a couple of composite manufacturers. With very few exceptions the customary measurement technique is photogrammetry, which is a noncontacting technique that uses retroreflective targets placed on the reflector assembly. The camera used for the measurements is limited in the temperature range to which it can be exposed, so it must be fairly well isolated from the thermal (or thermal vacuum) chamber environment. Also photogrammetry is dependent on photographs from multiple view angles requiring that either the unit under test or the camera be repositioned multiple times during the test. A scale reference that is stable over the test temperature range is also required to be located in the chamber in a fixed location relative to the unit under test. Thermal distortion test setup for multiple reflectors is shown in Figure 9.17.

Virtually all thermal distortion tests of reflectors will be designed to establish the thermally induced deformation of the reflector relative to the satellite attachment interface, which may be a set of "feet" for a fixed-mount reflector or a single hinge or gimbal interface for a deployable or steerable reflector.

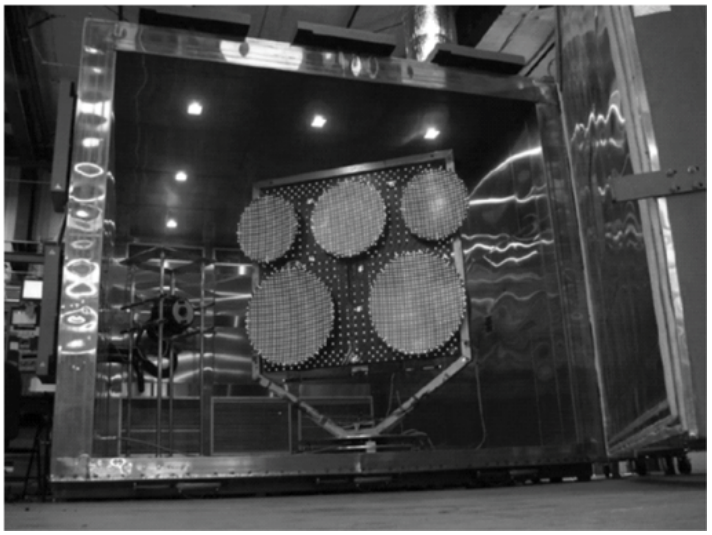

Figure 9.17 Thermal distortion testing of multiple reflectors. (Copyright AASC 2012.)

In addition, it is almost always the case that the results of a thermal distortion test will not represent any particular on-orbit environment. Bulk temperature test cases are used to correlate the structural FEM, which is then used in conjunction with thermal analysis results to predict the actual on-orbit thermal distortion. The on-orbit thermal prediction profiles are generated from the analytical thermal model, which may have also been previously correlated to the hardware in a thermal balance test.

9.6.2.4 Acoustic Vibration

For large surface area lightweight reflectors, acoustic excitation (high-frequency pressure loading) is often the structural design driver in the direction normal to the reflector surface. In-plane loads are usually driven by quasi-static conditions derived from coupled loads analysis or transfer orbit thermal loading. Medium and small reflector designs are more likely driven by random vibration inputs, both in plane and out. For all reflectors, the acoustic environment is an excellent workmanship test because its high-frequency pressure loading exercises laminates and joints globally, even those that are not in the launch configuration's primary load path.

Whether the reflector structural margins of safety are acoustically driven is somewhat dependent on the reflector mounting interface configuration and geometry, which will govern the load distribution into the structure. For smaller reflectors the bounding environment is likely to be a combination of sine (quasi-static) loads at the lower frequencies (<100 Hz) combined with random vibration loads at the higher frequencies. The breakpoint between a reflector being acoustically driven or sine/random driven is in the 1.5m aperture size range for a nonporous surface reflector. Larger surface area reflectors are usually acoustically driven by the acoustic energy exciting the reflector directly, and smaller ones are often driven by random vibration input from the panel or structure that the reflector is mounted to exciting the reflector.

It is very important to understand how the acoustic test setup correlates with the flight configuration. If the acoustic test configuration is hard mounted to the flight interfaces, then the test is usually enveloping of the flight-like configuration; however, careful analysis of the design and test configurations must be performed to ensure that a significant overtest condition is not created by the test fixture interfaces being too stiff.

If the fixturing that supports the reflector responds to the acoustic energy or is dynamically coupled to the reflector responses, a significant overtest is also likely so this must be carefully considered. Similarly, it is also possible to undertest the unit by having unrealistically flexible boundary conditions. For some reflector designs where the acoustics do not drive the interface loads, it may be valid to hang the reflector on bungee cords (free-free) for the test. The key is to understand and analyze both the flight and the test configurations and how well they correlate.

9.6.2.5 Vibration (Sine, Random, Pulse)

The purpose of vibration testing is to expose the interfaces and critical areas of the reflector assembly to flight-like structural loading and to verify the predicted fundamental frequency characteristics.

For dynamic testing it is especially important to understand how the testing relates to the launch environment. The test scheme should, as much as possible, be designed to fully and realistically test the assembly to the flight environment in the flight configuration without significant under- or overtesting. Analysis of the test configurations is critical because, as much as it is not desirable and should be avoided, it is not unusual to have the test condition become a design driver.

In reality, a reflector design is often driven by the unit-level test environment because the flight-level environment or boundary conditions are uncertain and as such the unit-level vibration requirements are specified with some if not considerable additional margin. Unless it drives a lot of cost and mass, the system design team will often assess the risk, and determine that it is easier and better to design to an enveloping simply described and implemented test condition as opposed to designing to a flight configuration with complex interface stiffness and uncertain loads. The test environment levels and boundary conditions are often more predictable and verifiable than the system-level test or flight, and the systems engineers can determine that the test condition bounds the stresses of the flight condition more readily than they can predict the exact flight condition.

Because the reflector assembly is rarely required to act as a part of the satellite structure, it is common for the loads at the interfaces to be driven purely dynamically due to the vibration environment acting on the mass of the reflector assembly. Depending on the reflector interface design details, the critical strength margins at the interfaces may be driven dynamically (quasi-static loads) or acoustically and it is important to understand this when designing the tests and test fixtures.

9.7 Concluding Remarks

A successful and efficient reflector design is a system-level balancing act between a large number of requirements, but ultimately it boils down to cost versus

performance and as with most things the cost performance benefit is not linear but exponential. Understanding the impact on system-level performance of all the specific antenna-level requirements, such as reflector surface rms, pointing, mass, stiffness, and so on, is key to trading off technical requirements while remaining within a program's cost and schedule requirements. The antenna RF design engineer should understand what is reasonable and achievable within the program cost and mass budgets for surface rms, pointing and on-orbit degradation due to thermal distortion, and so on, and allow enough margin in the RF design to accommodate these aspects. If that is not done, the reflector mechanical design engineer may be forced into a more complex and expensive design that exceeds mass, cost, and perhaps schedule requirements and still may not meet the requirements specified by the RF antenna design engineer.

Mechanically, reflector designs are a finely tuned recipe of tooling, materials, fabrication techniques, construction elements, joint designs, fittings, and so on, that all work together in a balanced way. So many variables are involved in a good design that it is critical for the whole team to be thinking about fabrication and tooling while evolving the reflector structural design. For instance, designing a reflector that incorporates "blind" bond joints will introduce fabrication challenges that could lead to extra tooling, additional labor, increased process variability, and inherent inaccuracies, resulting in degradations in joint performance. Sometimes design elements like this are inevitable or the lesser of two evils, but the earlier in the design cycle that these challenges are identified, the more likely it is that they can be incorporated into the design with minimum impact to the reflector performance.

Many of the most successful reflector designs are by far the simplest in configuration, selection of materials, complexity, and required tooling. Almost without exception this and is a result of effective communication between the RF antenna design engineer, the antenna subsystem engineer, and the satellite subsystem engineer with everyone involved being aware of what is possible within the program cost, schedule, and mass budgets.

About the Editors

Sudhakar Rao received his B.Tech from Regional Engineering College, Warangal, India, in 1974, his M.Tech from Indian Institute of Technology, Kharagpur, in 1976, and his Ph.D. from the Indian Institute of Technology, Madras, in 1980, all in electrical engineering. He was a post-doctoral fellow at the University of Trondheim, Norway, and later worked as a research associate at University of Manitoba, Canada, during 1981–1983.

Dr. Rao contributed to more than 60 satellite programs during his 38 years of professional experience that involved conceptual design, payload trades, detailed component design, and hardware test for both commercial and military satellites. Dr. Rao's original work on the development of analytical models/templates for complex radiation of satellite payloads was adopted by the CCIR/ITU as an international standard in 1992. He has published more than 150 technical papers, holds 40 U.S. patents, 2 trade secrets, and is listed in *Marquis Who's Who in the World, Who's Who in America,* and *Who's Who in Science and Engineering*. He is currently working as a technical fellow in the Electronics and Payload directorate of Northrop Grumman Aerospace Systems, Redondo Beach, CA. His previous work experience includes corporate senior fellow at Lockheed Martin (2003–2010), chief scientist & technical fellow at Boeing/Hughes (1996–2003), staff scientist at SPAR Aerospace Limited, Canada (1983–1996), senior scientist at Electronics and Radar Devl. Establishment, India (1980–1981), and technical officer at ECIL, Hyderabad, India (1976–1977)

He is an IEEE Fellow, an IETE Fellow, Chair of the IEEE APS Industry Initiatives Committee, Associate Editor for the IEEE AP-Magazine's *Antenna Applications Corner,* reviewer for IEEE APS since 1983, technical program committee member for the IEEE APS/URSI symposium since 2003, and is the member of the IEEE APS AdCom during 2010–2013. Dr. Rao received several awards during his career that include the 2008 Asian American Engineer of the Year (AAEOY) award, the 2008 IEEE Delaware Valley Engineer of the Year Award, 2006 IEEE Benjamin Franklin Key Award, the professional excellence award from Council of Indian Origin (CIO) in Greater Philadelphia in 2009, Lockheed Martin's inventor of new technology awards in 2005 and 2007, Lockheed Martin's invention and publication awards in 2005 and 2006, and Boeing's Special Invention Award in 2002. Dr. Rao received the IEEE Judith Resnik Technical Field Award in 2009 for his pioneering work in aerospace engineering.

Satish Kumar Sharma received his B. Tech. from Kamla Nehru Institute of Technology, Sultanpur, in 1991 and his Ph.D. degree from the Indian Institute of Technology (IIT), Banaras Hindu University (BHU), Varanasi, in 1997, both in electronics engineering. From March 1999 to April 2001, he was a post doctoral fellow in the Department of Electrical and Computer Engineering, University of Manitoba, Manitoba, Canada. He was a senior antenna engineer with InfoMagnetics Technologies Corporation in Winnipeg, Manitoba, Canada, from May 2001 to August 2006. Simultaneously, he was also a research associate at the University of Manitoba from June 2001 to August 2006.

In August 2006, he joined San Diego State University (SDSU), San Diego, as an assistant professor in the Department of Electrical and Computer Engineering. Since August 2010, he has been an associate professor. He is also director of the Antenna and Microwave Laboratory (AML). He teaches courses in applied electromagnetics, and advises several B.S., M.S. and Ph.D. students. He also served as visiting professor and principal electrical engineer at Space Systems Loral, Palo Alto, CA during the summer months of 2009 and 2010, respectively. He is author/coauthor of more than 125 research papers published in the refereed international journals and conference proceedings. He is co-author of the chapter "Printed Antennas for Wireless Applications," in the book *Microstrip and Printed Antennas: New Trends, Techniques and Applications,* (Wiley Inter-Science, UK). He also holds 1 U.S. patent.

Dr. Sharma received the National Science Foundation's prestigious faculty early development (CAREER) award in 2009, and the Young Scientist Award of URSI Commission B, Field and Waves, during the URSI Triennial International Symposium on Electromagnetic Theory, Pisa, Italy, in 2004. He was area editor of International Journal of Electronics and Communications (Elsevier, UK). Currently, he serves as an associate editor of *IEEE Transaction on Antennas and Propagation.* He was chair of the Student Paper Contest of the IEEE Antennas and Propagation Society Symposium 2008, co-chair of the Student Paper Contests of the International Microwave Symposium 2010 and IEEE Applied Electromagnetic Conference (AEMC) 2011, and currently serves as a Chair of the Student Paper Contest of the ACES 2013. He also served on the subcommittee of the Education Committee for the IEEE Antennas and Propagation Society for the organization of the Student Paper Contests. He is a senior member of IEEE, full member of the USNC/URSI, Commission B, fields and waves, and a member of the Applied Computational Electromagnetic Society (ACES).

Lotfollah Shafai received B.Sc. from the University of Tehran in 1963 and an M.Sc. and a Ph.D. from the Faculty of Applied Sciences and Engineering, University of Toronto, in 1966 and 1969, respectively.

In November 1969, he joined the Department of Electrical and Computer Engineering, University of Manitoba as a sessional lecturer, assistant professor (1970), associate professor (1973), and professor (1979). To enhance the University of Manitoba contact with industry, in 1985 he established the Institute for Technology Development, and was its director until 1987, when he became the head of the Electrical and Computer Engineering Department. His assistance to industry was instrumental in establishing an Industrial Research Chair in Applied Electromagnetics at the University of Manitoba in 1989, which he held until July 1994.

In 1986, he established the symposium on Antenna Technology and Applied Electromagnetics, ANTEM, at the University of Manitoba, which has grown to be the premier Canadian conference in antenna technology and related topics.

He has been the recipient of numerous awards. In 1978, his contribution to the design of a small ground station for the Hermes satellite was selected as the most Meritorious Industrial Design. In 1984, he received the Professional Engineers Merit Award, and in 1985 he received "The Thinker" Award from Canadian Patents and Development Corporation. From the University of Manitoba, he has received the "Research Awards" in 1983, 1987, 1989, 1999, and 2000; the Outreach Award in 1987 and the Sigma Xi Senior Scientist Award in 1989. In 1990 he received the Maxwell Premium Award from IEE (London), and in 1993 and 1994 he received the Distinguished Achievement Awards from Corporate Higher Education Forum. In 1998 he received the Winnipeg RH Institute Foundation Medal for Excellence in Research. In 1999, he received the Professional Engineers "Outstanding Engineering Achievement Award," and from Winnipeg Chamber of Commerce "Innovation of the year Award" for the design of dual-band satellite pico-terminal. He is a life Fellow of IEEE and a life Fellow of The Royal Society of Canada. He was a recipient of the IEEE Third Millenium Medal in 2000, and in 2002 was elected a Fellow of The Canadian Academy of Engineering and Distinguished Professor at the University of Manitoba. In 2003 he received an IEEE Canada "Reginald A. Fessenden Medal" for "Outstanding Contributions to Telecommunications and Satellite Communications," and a Natural Sciences and Engineering Research Council (NSERC) Synergy Award for "Development of Advanced Satellite and Wireless Antennas." He holds a Canada Research Chair in Applied Electromagnetics and was the International Chair of Commission B of the International Union of Radio Science (URSI) for 2005-2008. In 2009, he was elected a Fellow of the Engineering Institute of Canada, and was the recipient of IEEE Chen-To-Tai Distinguished Educator Award from IEEE antennas and Propagation society. In 2011, he received the Killam Prize in Engineering from the Canada Council, for his "outstanding Canadian career achievements in engineering, and his research on antennas."

List of Contributors

Dr. S. Bassily, Consultant
Dr. G. Chattopadhyay, Jet Propulsion Laboratory
Mr. J. Farrell, The Boeing Company
Prof. A. Ferni, University of Florence
Dr. P. Focardi, Jet Propulsion Laboratory
Dr. R. Hodges, Jet Propulsion Laboratory
Dr. Y. Inasawa, Mitsubishi Electric Corporation
Dr. Y. Konishi, Mitsubishi Electric Corporation
Dr. C. Lee-Yow, Custom Microwave Inc.
Prof. N. Llombart, Delft Univ. of Technology
Prof. A. Neto, Delft Univ. of Technology
Mr. M. Noyes, Applied Aerospace Structures Corporation
Dr. C. Ravipati, Intelsat Corp.
Mr. R. Reynolds, The Boeing Company
Mr. J. Scupin, Custom Microwave Inc.
Mr. M. Takikawa, Mitsubishi Electric Corporation
Mr. M. Thomson, Jet Propulsion Laboratory
Ms. D. Valero, Applied Aerospace Structures Corporation
Dr. S. Yamamoto, Mitsubishi Electric Corporation

Index

Q

R

S

T